# Topics beyond the Standard Cosmological Model

Matteo Puel

Department of Physics

McGill University, Montréal

July, 2023

A thesis submitted to McGill University in partial fulfillment of the requirements of the degree of

Doctor of Philosophy

*To my parents and my brother*

# Abstract

The standard cosmological model, also known as the Lambda-Cold-Dark-Matter ($\Lambda$CDM) scenario, is a rather simple but yet very predictive model describing the evolution and matter-energy content of the Universe. Despite its multiple successes, it suffers from a number of unresolved mysteries, such as the source of inflation and the mechanism of generating the observed baryon asymmetry. Perhaps more importantly, the $\Lambda$CDM model does not address the nature of its main pillars: dark energy and Dark Matter (DM).

The aim of this thesis is to advance our understanding about the major mysteries of the $\Lambda$CDM scenario, particularly focusing on the role of DM and its possible interactions with Standard Model particles, such as neutrinos.

We will start by building a "little theory of everything", where inflation, baryogenesis, neutrino masses and production of asymmetric DM can be explained in an experimentally-consistent and unified picture, using the Affleck-Dine mechanism as a key ingredient. In such a scenario, the asymmetric DM abundance observed today is achieved via the annihilation of DM particles with their antiparticles, which freezes out in the early Universe.

However, if a small DM-number violating mass term between particles and antiparticles is allowed, DM oscillations can be reactivated at late times and the resulting DM annihilation might solve one of the long-standing issues of the $\Lambda$CDM model at galactic scales, known as the core-cusp problem.

Since neutrinos and DM are fundamental ingredients in the "little theory of ev-

erything", it comes natural to question whether a potential interaction between them could be constrained using astrophysical or cosmological probes. We will show that strong bounds on the scattering cross section between neutrinos and DM can be derived by studying the flux attenuation of neutrinos emitted by active galactic nuclei, such as the blazar TXS 0506+056 and the radio galaxy NGC 1068, because they have to pass through a dense DM spike surrounding the central black hole.

# Abrégé

Le modèle cosmologique standard, ègalement connu sous le nom de scénario Lambda-Cold-Dark-Matter ($\Lambda$CDM), est un modèle plutôt simple mais très prédictif décrivant l'évolution et la composition matière-énergie de l'Univers. Malgré ses multiples succès, il souffre de plusieurs mystères non résolus, tels que l'origine de l'inflation et le mécanisme de génération de l'asymétrie baryonique observée. Peut-être plus important encore, le modèle $\Lambda$CDM ne répond pas à la nature de ses piliers principaux : l'énergie sombre et la matière noire (DM).

L'objectif de cette thèse est d'avancer dans notre comprèhension des principaux mystères du scénario $\Lambda$CDM, en mettant l'accent particulièrement sur le rôle de la matière noire et de ses interactions possibles avec les particules du Modèle Standard, telles que les neutrinos.

Nous commencerons par construire une "petite théorie de tout", où l'inflation, la baryogenèse, les masses des neutrinos et la production de matière noire asymétrique peuvent être expliquées dans un cadre cohérent avec les expériences, en utilisant le mécanisme d'Affleck-Dine comme ingrédient clé. Dans un tel scénario, l'abondance de matière noire asymétrique observée aujourd'hui est obtenue grâce à l'annihilation des particules de matière noire avec leurs antiparticules, qui s'est figée dans l'Univers primitif.

Cependant, si un petit terme de masse violant le nombre de matière noire entre particules et antiparticules est autorisé, les oscillations de matière noire peuvent être réactivées è des époques tardives et l'annihilation résultante de matière noire pourrait

résoudre l'un des problèmes de longue date du modèle $\Lambda$CDM à l'échelle galactique, connu sous le nom de problème du cœur-pointe.

Étant donné que les neutrinos et la matière noire sont des ingrédients fondamentaux dans la "petite théorie de tout", il est naturel de se demander si une interaction potentielle entre eux pourrait être contrainte en utilisant des sondes astrophysiques ou cosmologiques. Nous montrerons que des limites strictes sur la section efficace de diffusion entre neutrinos et matière noire peuvent être déduites en étudiant l'atténuation du flux de neutrinos émis par les noyaux actifs de galaxies, tels que le blazar TXS 0506+056 et la galaxie radio NGC 1068, car ils doivent traverser une région dense de matière noire entourant le trou noir central.

# Acknowledgements

My five-year journey at McGill and in Montreal would not have been possible without the invaluable support of many people.

First and foremost, I am particularly grateful to Prof. Jim Cline, whose constant support, patience, and tireless guidance have been instrumental in my growth as a scientist and as a person. His belief in me has been a constant motivation to push my boundaries and achieve more than I thought possible. From the beginning, he treated me as a colleague and made me feel like part of a family.

I would like to extend my gratitude to my Ph.D. committee members, Prof. Alex Maloney and Prof. Robert Brandenberger, for their support and guidance throughout my Ph.D. journey. Robert's teachings on approaching new ideas with a critical and open-minded mindset have been invaluable, and his kindness and patience have made a significant impact.

I am also thankful to the wonderful physicists I had the opportunity to collaborate and interact with during my time here, including Takashi Toma, Guillermo Gambini, Samuel McDermott, Gonzalo Alonso-Álvarez, Marta Reina-Campos, Jean-Saumel Roux, Benoit Laurent, Samuel Laliberte, Ziwei Wang, Heliudson Bernardo, Ken Ragan, Katelin Schutz, Andreas Warburton, Keshav Dasgupta, Simon Caron-Huot and Charles Gale. Each member of Jim's group has been a good friend, and I have learned something valuable from each of them.

I feel grateful for my wonderful officemates who have been there for me through both high and low moments, both in the office and outside of it: Shreya Saha, Trevor

Shillington, Beatrix Mühlmann, Megan Cowie, Alessandro Ambler, Bryce Cyr, Antara Paul, Christina Ann Nelson, Matthew Rigby, and Rikke Plougmann. Shreya, you have been an exceptional desk-mate and listener, and I cherish our talks and laughter. Thank you for the delicious meals, the long walks and for always being there when I needed support. Trevor, you are a true friend and always up for fun; I appreciate your companionship and positivity. Beatrix, I am thankful for the countless dinners, walks to Mount Royal, and enjoyable evenings we spent together. Megan, thank you for sharing so many moments, from the preparation of the Ph.D. preliminary exam to the fun times on the volleyball court with the physics team.

Outside the office, I am incredibly grateful to have been surrounded by an amazing group of friends, many of whom I met through the McGill men's volleyball team. To Mahdi, Emile, Han, Maël, Martin, Anne, Jannsen, Abhilash, and Brent, I want to express my heartfelt appreciation. Our time together has been filled with laughter, camaraderie, and unforgettable moments that will forever hold a special place in my heart. Thank you for being a part of my life. I love you all. Additionally, I want to thank my housemates, especially Bahaa and Antoine, for the enjoyable dinners and time spent together.

Despite being on the other side of the ocean, my long-time friends Michele P., Giacomo, Marta, Anna, Donato, Michele G., Emilio, Alessandra, Elide, Damiano, Luca, Alessio, Diego, Luana, Romina, Chiara, Ilaria and Sunny have been a constant source of support throughout my Ph.D. journey. In particular, I want to extend a heartfelt thank you to Michele P., Giacomo, and Alessandra for their true friendship, always being available for a chat, for lending a listening ear, and offering valuable advice. Your support and encouragement have meant the world to me and have kept me going during moments of doubt.

Words would truly fail to express the immense support and love I received from my family during these years. To my parents, Fiorella and Bruno, and my brother Simone, you have been my rock, a constant source of encouragement, and the reason I have been able to reach this milestone. Your unwavering belief in me and your sacrifices have been the foundation of my journey, and I am forever grateful. To my uncles, aunts, and cousins, thank you for always being there with your love and support. But most importantly, I want to express my heartfelt gratitude to my grandma Maria, who has been an extraordinary role model of strength and resilience. Your determination and spirit have inspired me to persevere through challenges and never give up. Your presence in my life has been a true blessing.

Lastly, I want to thank every person I encountered along this transformative Ph.D. journey. Each interaction, conversation, and experience has played a role in shaping the person I have become today. Your presence, whether big or small, has contributed to my growth, both personally and academically. Thank you for being a part of this incredible journey with me.

## Acknowledgements of funding

The research described in this thesis was possible thanks to the generous financial support from several sources. In no particular order, they are:

- Highly Qualified Personnel Scholarship from the Arthur B. McDonald Canadian Astroparticle Physics Institute at Queen's University, which is funded by the Canada First Research Excellence Fund (CFREF).
- SAPIN grant from the Natural Sciences and Engineering Research Council of Canada (NSERC).
- Trottier MSI Graduate Awards from the Trottier Space Institute at McGill.
- Dr. Donald G. Hurst Fellowship from the Faculty of Science at McGill University, established by the great generosity of Dorothy Reid and her family.

# Contents

# List of Tables

# List of Figures

# Preface

The present manuscript-based thesis is a collection of most of the successful projects I have worked on during my Ph.D. at McGill University. It consists of an introduction, followed by five research articles already published in peer-reviewed journals, and a conclusion.

More specifically, Chapters 1-3 provide an overview of the standard cosmological model, focusing on its main ingredients and on the limitations that have convinced the scientific community to search for extensions. Chapters 4-8 contain all the original contributions to the field made by myself and my collaborators. Chapter 9 presents the concluding remarks and future prospects.

As regards the original work, since it is common practice in theoretical high energy physics to list authors in alphabetical order, I will identify my contributions below. Following it, I will introduce the units and conventions used throughout the thesis.

## Author contributions

**Chapter 4:** J. M. Cline, M. Puel and T. Toma, *Affleck-Dine Inflation*, Phys. Rev. D 101, 043014 (2020), [arXiv:1909.12300].

The project was initiated by Jim Cline and I based on discussions we had during the course Jim gave in the fall of 2019 at McGill University on particle cosmology, whose material is covered in Ref. [1] and includes the Affleck-Dine baryogenesis scenario. All three authors contributed to the conceptualization of the problem and carried out the bulk of the analysis. In particular, I wrote an independent numerical code to solve the adiabatic and isocurvature perturbations and to scan the parameter space via a Markov Chain Monte Carlo technique, which helped to cross check each other results. The main text of the paper was written by Jim, with inputs from Takashi Toma and I.

**Chapter 5:** J. M. Cline, M. Puel and T. Toma, *A little theory of everything, with heavy neutral leptons*, J. High Energ. Phys. 2020, 39 (2020), [arXiv:2001.11505].

The project is an extension of the previous work, originated from a discussion Jim had with Joachim Kopp during his CERN visit in the fall of 2019. All three authors contributed equally to the conceptualization of the problem and everyone cross checked each other computations in an independent manner. In particular, I was in charge of deriving the electroweak precision data and laboratory constraints (section 5.4.1), computing the heavy neutral lepton weak decays (section 5.4.3, including the appendix), and taking care of the dark matter indirect detection bounds (section 5.6.2). I helped in writing the manuscript, particularly the sections I mostly worked on. I also produced all the figures except for one (Figure 5.2).

**Chapter 6:** J. M. Cline, G. Gambini, S. D. McDermott and M. Puel, *Late-Time Dark Matter Oscillations and the Core-Cusp Problem*, J. High Energ. Phys. 2021, 223 (2021), [arXiv:2010.12583].

The project was conceived by Jim and Samuel McDermott during their visit to CERN in the fall of 2020. The initial part of the work was started by Jim and Guillermo Gambini, who developed the general oscillation formalism and applied it to early-time cosmology (sections 6.2, 6.3, 6.4 and appendix 6.D). I joined the project in May 2021 and I was in charge of developing the N-body galactic simulation to test whether the model could solve the core-cusp problem. I modified the `GADGET-2` code [2] by adding dark matter scattering and annihilation, and I tested the new implementations with existing examples. Furthermore, I led the comparison between our results with observational data, in terms of the galactic rotation curve for dwarf galaxies and projected stellar velocity dispersion along the line of sight for galaxy clusters. I wrote section 6.6 and appendix 6.C, and helped writing other sections of the paper like section 6.5. I also produced all the figures of the manuscript except for two (Figures 6.4.1 and 6.5.2) and took care of most of the referees' comments.

**Chapter 7:** J. M. Cline, S. Gao, F. Guo, Z. Lin, S. Liu, M. Puel, P. Todd and T. Xiao, *Blazar constraints on neutrino-dark matter scattering*, Phys. Rev. Lett. 130 (2023) 9, 091402, [arXiv:2209.02713].

The paper was the outcome of the summer 2022 project for Shan Gao, Fangyi Guo, Zhongan Lin, Shiyan Liu, Phillip Todd and Tianzhuo Xiao, who are undergraduate physics students in the honour program at the time of writing. With Jim's help, I led the work not only in terms of the physics content and underlying analysis, but also as a mentor for the summer students. More specifically, I was responsible for: literature review, collection of input information such as the neutrino flux and IceCube data, modelling of the dark matter spike, and comparison of our results with previous limits on dark matter scattering cross section with neutrinos and electrons. The computation of the neutrino flux attenuation was independently carried out by all the authors, and the application to a realistic particle physics model was led by Jim, while I cross-checked his computation. I also produced all the plots of the paper. Most of the original manuscript was written by Jim, whereas I wrote the remaining parts (section 7.5 and parts of sections 7.2 and 7.3) and took care of all the referees' comments.

**Chapter 8:** J. M. Cline and M. Puel, *NGC 1068 constraints on neutrino-dark matter scattering*, JCAP 06 (2023) 004, [arXiv:2301.08756].

The project was conceived as a follow-up of the previous work and the idea came after a discussion with Matthew Lundy and Samantha Wong during a lunch talk I gave at the Trottier Space Institute at McGill. Both authors contributed to the conceptualization and writing stage. In particular, I carried out the analysis in sections 8.2, 8.3, 8.4, 8.5, and wrote these sections and part of the conclusions. Jim took care of the remaining sections. I cross-checked his results, produced all the plots of the manuscript and addressed the referee's comments.

# Units and Conventions

In the thesis, I decided to adopt the so-called natural or high energy physics units, if not otherwise stated, because of their wide use in particle physics, astrophysics and cosmology. In this system, the fundamental constants $\hbar = c = k_B = 1$ and there is only one important dimension, the energy (expressed generally in some power of the eV). In particular, one has

$$[\text{Energy}] = [\text{Mass}] = [\text{Temperature}] = [\text{Length}]^{-1} = [\text{Time}]^{-1}\,, \tag{1}$$

and the numerical conversion factors with the International System of units are

$$\begin{aligned}
\text{Energy:} \qquad & \text{eV} = 1.6022 \times 10^{-19}\ \text{J}\,, \\
\text{Mass:} \qquad & \text{eV} = 1.7827 \times 10^{-36}\ \text{kg}\,, \\
\text{Temperature:} \qquad & \text{eV} = 1.1605 \times 10^{4}\ \text{K}\,, \\
\text{Length:} \qquad & \text{eV} = 5.0677 \times 10^{6}\ \text{m}^{-1}\,, \\
\text{Time:} \qquad & \text{eV} = 1.5193 \times 10^{15}\ \text{s}^{-1}\,.
\end{aligned} \tag{2}$$

We also adopt the convention $M_{Pl} = G^{-1/2} = 1.22 \times 10^{19}$ GeV and $m_{Pl} = (8\pi G)^{-1/2} = 2.43 \times 10^{18}$ GeV to refer to the Planck mass and the reduced Planck mass, respectively, where $G$ is the Newton's gravitational constant.

The metric signature adopted throughout the thesis is the mostly minus convention $(+, -, -, -)$, which is commonly used in the particle physics community. Greek indices $\mu, \nu = 0, 1, 2, 3$ will be devoted to space-time vector components, whereas Latin indices $i, j = 1, 2, 3$ will be used to indicate the spatial components only.

## Bibliography

[1] J. M. Cline, "TASI Lectures on Early Universe Cosmology: Inflation, Baryogenesis and Dark Matter," *PoS* **TASI2018** (2019) 001, `arXiv:1807.08749 [hep-ph]`.

[2] V. Springel, "The Cosmological simulation code GADGET-2," *Mon. Not. Roy. Astron. Soc.* **364** (2005) 1105–1134, `arXiv:astro-ph/0505010`.

Chapter 1

# Our observable Universe

The standard model of cosmology, also known as either the Lambda-Cold-Dark-Matter ($\Lambda$CDM) model, hot Big Bang model or simply concordance cosmological model, stands as the prevailing framework for understanding the origin, evolution, and composition of our vast Universe. Developed through decades of scientific research and observations, this model provides a comprehensive explanation of the Universe's structure, dynamics, and fundamental properties. At its core, the $\Lambda$CDM model embraces the concept of an expanding, large-scale homogeneous and isotropic Universe, and incorporates the influence of dark matter, dark energy, and the remnants of a hot Big Bang. By integrating diverse fields of study, such as astrophysics, particle physics, and general relativity, this model offers a compelling narrative that unveils the intricate tapestry of our cosmic existence.

Its remarkable success rests on several key observations, including: the Hubble diagram, which displays the velocity of galaxies as a function of their distance; the light element abundances; the temperature and polarization anisotropies in the cosmic microwave background (CMB), and the large-scale structure (LSS) of the Universe. We will briefly describe these observational pillars here, in addition to present evidences of the two dominant components of the Universe, dark matter and dark energy. All these ingredients will allow us to introduce the $\Lambda$CDM model in its full glory in chapter 2 and its limitations in chapter 3. The content of this chapter, as well as the next two, is heavily based on several standard cosmology textbooks and references (*e.g.* Refs. [1–9]), with input from the more recent literature due to the fast-paced development in the field of cosmology.

## 1.1 Hubble diagram

In his seminal paper of 1929 [10], Edwin Hubble showed that galaxies are receding from us in all directions, with more distant galaxies moving away faster in proportion to their distance. His famous plot, Fig. 1.1, shows a simple linear relationship between a galaxy's radial velocity $v$ and its distance $d$ from us

$$v \approx H_0 \, d \,, \tag{1.1}$$

where the slope parameter $H_0$ is called *Hubble constant*. Such an equation, known today as the *Hubble-Lemaître law*, is the first solid evidence that the Universe is expanding.

In an expanding Universe, the distance separating galaxies from us was smaller in the past compared to its current value. To quantify this evolution, we introduce the scale factor $a(t)$ as the ratio between the distance $d(t)$ between two objects at a given time $t$ and their present-day distance $d_0$. The scale factor $a$ ranges between 0 and 1, with larger values corresponding to later cosmic times. Consequently, the distance $d(t)$, referred to as the *proper* or *physical distance*, evolves over time, whereas the *comoving distance* $d_0$ remains constant. The latter distance can be understood as the spatial separation on a cosmic grid between two coordinate points, where each point corresponds to an observer at rest. A direct consequence of this expansion is the stretching of the physical wavelength of light emitted by distant objects, proportional to the scale factor, resulting in an observed wavelength that is greater than the one at which the light was originally emitted. This stretching factor is commonly defined as the redshift $z$

$$1 + z \equiv \frac{\lambda_{\rm obs}}{\lambda_{\rm emit}} = \frac{1}{a_{\rm emit}} \,, \tag{1.2}$$

which is used as a standard measure of distances in cosmology.

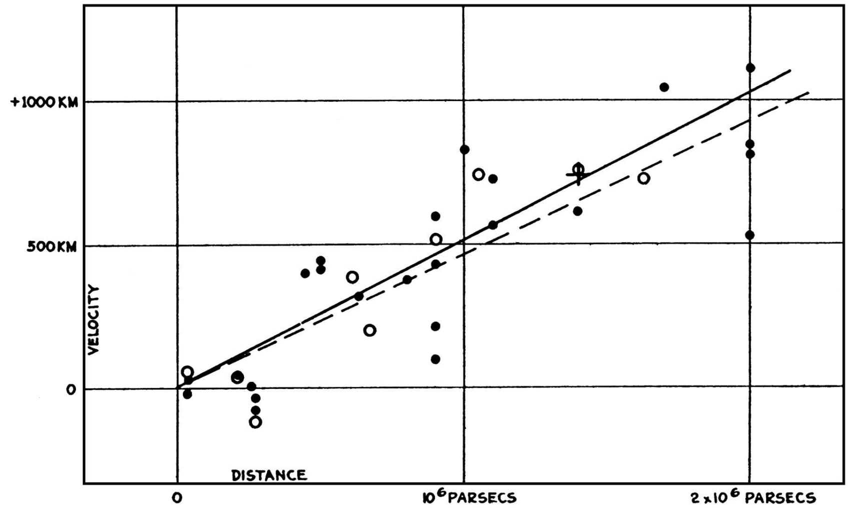

Figure 1.1: Velocity-distance relation among extra-galactic "nebulae", equivalent to today's concept of galaxies, as found by Hubble in 1929. The radial velocities, adjusted for solar motion (although labeled incorrectly), are plotted against estimated distances derived from the properties of Cepheid stars hosted in each galaxy considered in the analysis. The black discs and solid line represent the solution obtained by considering each galaxy individually in accounting for solar motion, whereas the circles and dashed line depict the solution derived from grouping the galaxies together. The cross denotes the average velocity corresponding to the mean distance of 22 galaxies for which individual distance estimations were not possible. Figure taken from Ref. [10].

The Hubble law in Eq. (1.1) is exactly what is expected in an expanding Universe. In fact, if $d(t) = a(t)\, d_0$ is the physical distance between two galaxies at time $t$, with comoving distance $d_0$, their relative velocity $v(t)$ is given by

$$v(t) = \frac{d}{dt}\Big(a(t)\, d_0\Big) = \dot{a}\, d_0 = H(t)\, d(t)\,, \qquad (v \ll c) \tag{1.3}$$

where we assumed no comoving motion between the two galaxies so that $\dot{d}_0 \equiv d(d_0)/dt = 0$ (*i.e.* no *peculiar* velocity). Here, the over-dot indicates the derivative with respect to the physical time $t$ and we introduced the *Hubble parameter*

$$H(t) \equiv \frac{\dot{a}}{a}\,, \tag{1.4}$$

which quantifies changes in the time-evolution of the scale factor and hence measures the expansion rate of the Universe. Equation (1.3) reduces to Eq. (1.1) at the present time $t_0$ if $H(t_0)$ is identified as the Hubble constant $H_0$ (recall $a(t_0) = 1$, by definition). By dimensional analysis, $H_0$ has units of velocity per distance and it is usually parameterized by a dimensionless number $h$ (not related to the reduced Planck's constant $\hbar$) via

$$
\begin{aligned}
H_0 &= 100\, h \ \mathrm{km\, s^{-1}\, Mpc^{-1}} \\
&= h/(9.8 \times 10^9 \ \mathrm{yr}) \\
&= h/(2998 \ \mathrm{Mpc}) \\
&= h\,(2.13 \times 10^{-33} \ \mathrm{eV}/\hbar)\,,
\end{aligned}
\tag{1.5}
$$

where $\mathrm{Mpc} \approx 3.086 \times 10^{22}$ m is the standard cosmological length scale.

Based on current measurements, the Hubble constant is estimated to be around $h \simeq 0.7$, although its precise value has been a subject of ongoing debate since Hubble's initial measurement of approximately $h \simeq 5.5$ in 1929. This controversy persists today, with deviations of about $\sim 10\%$ from different measurements. To mitigate the impact of this uncertainty, cosmologists commonly adopt the unit of length as $h^{-1}$ Mpc. Similarly, associated units such as $h^{-1}M_\odot$ for masses (where $M_\odot \approx 1.988 \times 10^{30}$ kg is the solar mass) are employed. This adoption allows cosmological computations to be less dependent on the specific value of the Hubble constant. Throughout this thesis, we will adhere to this convention, utilizing $h^{-1}$ Mpc and related units ensuring that our calculations remain robust regardless of the exact value of the Hubble constant.

As a final remark, the redshift $z$ in Eq. (1.2) is also used as a measure of velocities in cosmology because a star's or galaxy's velocity $v$ is linked to $z$ via the Doppler effect. In fact, the light emitted by a moving object will be observed with a shifted wavelength according to

$$
\frac{v}{c} = \frac{\lambda_{\mathrm{obs}} - \lambda_{\mathrm{emit}}}{\lambda_{\mathrm{emit}}} = z\,, \qquad (v \ll c) \tag{1.6}
$$

assuming the object's velocity is due only to the Universe expansion (*i.e.* no peculiar motion) and it is much smaller than the speed of light $c$. Therefore, measuring the redshift of known spectral lines in the spectrum of a galaxy allows one to estimate the galaxy's velocity.

## 1.2 Big Bang Nucleosynthesis

Just as a gas of particles confined in a box experiences a decrease in temperature and density over time when allowed to expand, the Universe should have followed a similar pattern if it has been expanding since its creation: it was considerably hotter and denser at early times compared to its present state, comprising (at least) all known particles.

Since the latter and their interactions are well-described within the framework of the Standard Model (SM) of particle physics, which we will briefly summarize in section 2.4.1, we can investigate phenomena that took place during early stages of the Universe. In particular, until the temperature of the Universe exceeded approximately the MeV scale, the formation of neutral atoms and bound nuclei was impeded by the abundance of high-energy photons present at that time. As the Universe gradually cooled below the typical energies required for nuclear binding, a process known as *Big Bang Nucleosynthesis* (BBN) commenced, leading to the formation of light elements such as deuterium, helium, and lithium.

The expected abundance of such elements can be precisely computed once the rates of the relevant SM nuclear reactions are known (see *e.g.* Ref. [11]) and the expansion of the Universe is properly taken into account. The results almost solely depend on the *baryon-to-photon ratio* $\eta = n_b/n_\gamma$, where $n_b$ and $n_\gamma$ are the baryon and photon number density at the time of BBN, respectively, in addition to the effective number of relativistic species $N_{\text{eff}}$, which will be defined in section 2.5.1. [1] In principle, the parameter $\eta$ could be predicted if a complete theory of baryogenesis, the process through which the asymmetry between matter and antimatter we observe

[1] The baryon density is the combination of the densities of protons and neutrons since both species have baryon number one and these were the only baryons present at that time.

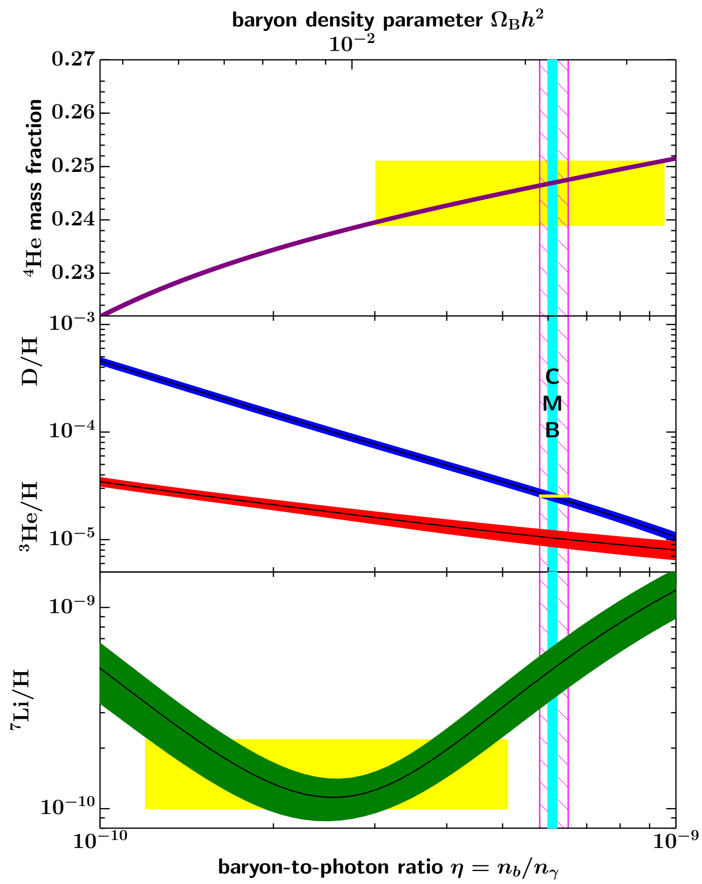


Figure 1.2: Primordial abundances (normalized by the hydrogen number density) of $^4$He, D, $^3$He and $^7$Li as a function of the baryon-to-photon ratio $\eta$ and the baryon density parameter $\Omega_b h^2$. The colored curves and associated shaded bands are the 95% C.L. predictions of the standard model of BBN [12]. The yellow boxes are the observed light element abundances. The cyan vertical band indicates the 95% C.L. inference of the baryon density from the Cosmic Microwave Background (see next section), whereas the shaded magenta band indicates the 95% C.L. BBN concordance range. Figure taken from Ref. [9].

today originated, was available. Since this is not the case, the baryon-to-photon ratio is treated as a free parameter. Fig. 1.2 shows the BBN predictions as a function of $\eta$ for the abundances of $^4$He, D, $^3$He and $^7$Li, along with their measured values.

Determining the abundances of light elements as they were shortly after the BBN era poses challenges due to subsequent changes caused by stellar nucleosynthesis. For instance, the ubiquitous production of $^4$He through hydrogen fusion in stars via the *pp*-chain makes it necessary to search for regions of hot ionized gas in "metal-poor" galaxies known as extra galactic HII regions [13]. In contrast, deuterium (D) primarily originates from BBN since, although it can also be produced in stars, it rapidly undergoes processing onto heavier nuclei [14]. The most reliable indicator of the primordial value of D is its measurement in the intergalactic medium at high redshifts, achieved by examining subtle absorption features in the spectra of distant, low-metallicity quasars. Extrapolating the primordial abundances of $^3$He and $^7$Li from observations is more challenging due to several factors. Firstly, the measurements for $^3$He rely primarily on the Solar system and solar-metallicity HII regions in our Galaxy, leading to limited data quality [15]. Secondly, estimating the abundance of $^7$Li requires studying metal-poor stars in the Galactic halo [16], which exhibit properties that are still not fully understood [17, 18].

The $\eta$ ranges in Fig. 1.2, as described by the yellow boxes, are not fully overlapping but are within a factor $\sim 2$ of each other. However, the lithium abundance disagrees with the precise deuterium abundance and the less restrictive $^4$He abundance, indicating the presence of the so-called "lithium problem", whose past solutions have invoked unknown systematics or new physics [9]. If one excludes the $^7$Li constraint, the concordant range of $\eta$ from BBN is primarily determined by the deuterium abundance, resulting in [9]

$$\eta_{\rm BBN} \approx (6.143 \pm 0.190) \times 10^{-10} \,. \tag{1.7}$$

Despite the lithium problem, it is remarkable to think we can accurately predict the primordial light element abundances, spanning over nine orders of magnitude, just using well-known microphysics. This inspires confidence in our extrapolation to understand the Universe during its earliest stages.

The value of $\eta$ in Eq. (1.7) can be translated into the baryon abundance $\Omega_b$ in the Universe, which we will define appropriately in section 2.3, via

$$\Omega_b h^2 = \frac{\eta}{2.7 \times 10^{-8}} \approx 0.02244 \pm 0.00069 \qquad ({\rm BBN})\,, \tag{1.8}$$

where $h$ is the dimensionless Hubble constant in Eq. (1.5). Taking $h \sim 0.7$, one finds that ordinary matter contributes at most 5% of the total energy budget of the

Universe today, which we will see is insufficient to explain all the structures visible in the Universe. BBN hence provides compelling evidence for the existence of a non-baryonic form of matter, dubbed as dark matter (DM), which we will present in sections 1.5 and 2.4.3 and amply study throughout the thesis.

Constraints on the value of $\Omega_b h^2$, and hence on $\eta$, come also from precision measurements of the Cosmic Microwave Background (CMB) temperature anisotropies [19], which we will introduce in the next section. Although BBN ($z_{\rm BBN} \sim 10^{10}$) and CMB ($z_{\rm CMB} \sim 10^3$) are two widely separated epochs in the history of the Universe, governed by very different physics, the value of $\eta$ found by the Planck CMB mission yields [20]

$$\Omega_b h^2 = 0.02230 \pm 0.00021 \qquad (\text{CMB})\,, \tag{1.9}$$

corresponding to

$$\eta_{\rm CMB} = (6.104 \pm 0.058) \times 10^{-10}\,, \tag{1.10}$$

in striking agreement with $\eta_{\rm BBN}$, as shown in Fig. 1.2. This is a crucial test of the standard $\Lambda$CDM model, which predicts no change in the value of $\eta$ between BBN and CMB epochs. Once the CMB and BBN values are combined, one finds $\eta = (6.129 \pm 0.039) \times 10^{-10}$ and $\Omega_b h^2 = 0.02239 \pm 0.00014$.

## 1.3 Cosmic Microwave Background

The accidental discovery of a microwave background radiation, now known as the CMB, was made by Arno Penzias and Robert Wilson in 1965 [21], who detected a constant electromagnetic "noise" emanating from all directions in the sky.

The existence of the CMB can be well explained within the framework of an expanding Universe, specifically as a result of the interaction between photons and electrons via Thomson scattering. During the epoch when the temperature of the Universe was approximately at the $\sim$ eV scale, free electrons and protons started to combine forming neutral hydrogen in a process known as *recombination*. From that moment on, the Universe became transparent to electromagnetic radiation and the photons released from this "last scattering" surface, at a redshift of around $\sim 1100$, make the CMB today.

Since the interaction between photons and electrons prior to the last scattering kept the former in thermal equilibrium, the CMB photons should exhibit a black-body spectrum given by

$$I_\nu(T) = \frac{4\pi\hbar\nu^3/c^2}{\exp\left(2\pi\hbar\nu/k_B T\right) - 1}\,, \tag{1.11}$$

where $\nu$ is the photon frequency and $k_B$ is the Boltzmann's constant. This is indeed what is shown in the left panel of Fig. 1.3, where observations by the FIRAS instrument aboard the COBE satellite are compared to the black-body spectrum, finding a perfect agreement for a mean temperature $T = 2.728$ K [22]. Even more striking is the evidence that the CMB provides the best black-body spectrum ever measured so far, telling us that the early Universe was very smooth and isotropic. [2] Anisotropies were also discovered by the same COBE satellite in 1992, showing fractional temperature fluctuations of the order of $10^{-5}$ [23]. They were later validated and mapped with remarkable precision by the WMAP mission in the early 2000s and, more recently, by the Planck satellite which has provided additional insights into the CMB, revealing subtle deviations from homogeneity also in terms of polarization and lensing effects. Today, the temperature of the CMB is known to be $T_0 = (2.72548 \pm 0.00057)$ K [24].

The standard statistical tool to study small fluctuations over a homogeneous and isotropic background is to Fourier transform the distribution describing the anisotropies, which in the case of the CMB is the space-dependent temperature field across the sky. In fact, in Fourier space, large and small scales completely decouple from each other at linear order. For the CMB and the large-scale structure, the latter of which will be presented in the next section, the most important statistic is the two-point correlation function. When measured using Fourier-space fields, it is called the *power spectrum* and its physical meaning is to describe the spread or variance of the distribution: the larger is the amplitude of the power spectrum, the

[2] Smoothness, or homogeneity, in the context of the Universe implies that it exhibits uniformity at every point, displaying translation invariance. Isotropy, on the other hand, signifies that the Universe possesses uniformity in all directions, showcasing rotation invariance.

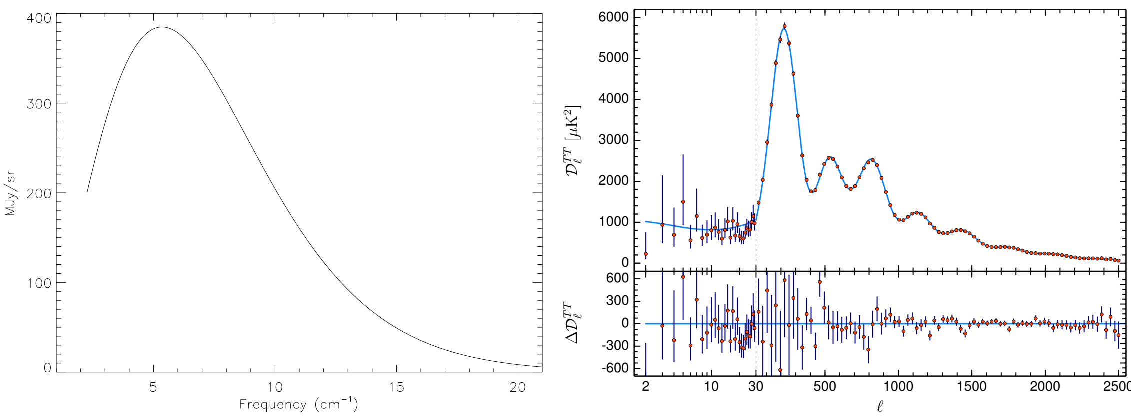


Figure 1.3: *Left*: Intensity of the CMB radiation as a function of frequency from the Far InfraRed Absolute Spectrophotometer (FIRAS), aboard the COBE satellite. The line shows a black-body spectrum with $T_0 = 2.728$ K, as given by Eq. (1.11) if converted in the appropriate units. The error-bars on the measurements are also present but are smaller than the line width. Taken from Ref. [22]. *Right:* Power spectrum of CMB temperature anisotropies. Data points as measured by the Planck satellite are shown in red along with their associated $\pm 1\sigma$ uncertainties. The blue line is the best-fit prediction of the $\Lambda$CDM model, which involves only six free parameters. Residuals between the data and the best-fit model are shown in the lower panel. Figure taken from Ref. [20].

larger are the deviations from a smooth background. Since the CMB temperature is a two-dimensional field depending only on the angular coordinates of a point in the sky, instead of taking its Fourier transform one expands it in spherical harmonics. Concretely, defining $\delta T(\hat{n})$ as the CMB temperature anisotropy in the unit direction $\hat{n}$, we can write

$$\delta T(\hat{n}) \equiv \frac{T(\hat{n}) - T_0}{T_0} = \sum_{\ell=1}^{+\infty} \sum_{m=-\ell}^{+\ell} a_{\ell m} Y_{\ell m}(\hat{n})\,, \tag{1.12}$$

where $Y_{\ell m}(\hat{n})$ are the spherical harmonics and the coefficients $a_{\ell m}$ encapsulate the temperature fluctuations. Their correlation in two different directions $\hat{n}$ and $\hat{n}'$ in the sky, averaged over the full sky, gives

$$\langle \delta T(\hat{n}) \delta T(\hat{n}') \rangle = \sum_{\ell=1}^{\infty} \frac{2\ell+1}{4\pi}\, C_\ell^{TT}\, P_\ell(\hat{n} \cdot \hat{n}')\,, \tag{1.13}$$

where $P_\ell$ are the Legendre polynomials, $\ell \sim 2\pi/\theta$ for small polar angular separations

$\theta$, and the coefficients $C_\ell^{TT}$ are the angular power spectrum

$$C_\ell^{TT} \equiv \langle\, |a_{\ell m}|^2 \,\rangle = \frac{1}{2\ell+1} \sum_{m=-\ell}^{+\ell} |a_{\ell m}|^2 \,. \tag{1.14}$$

If the temperature fluctuations $\delta T$ are Gaussian, as it appears to be the case, all the information contained in the CMB maps can be compressed into $C_\ell^{TT}$. The right panel of Figure 1.3 shows the most recent Planck data of the CMB angular power spectrum, expressed in terms of the quantity $\mathcal{D}_\ell^{TT} \equiv \ell(\ell+1)\, C_\ell^{TT}/(2\pi)$, as a function of the angular scale $\ell$, and they are superimposed by the best-fit prediction of the $\Lambda$CDM model. The agreement between the data points and the theoretical curve is remarkable, particularly when considering that it is a six-parameter fit.

The distinctive peak structure observed in the CMB power spectrum at small scales (*i.e.* large $\ell$) can be explained by the interplay between gravity and the pressure of the primordial fluid [25, 26]. Before recombination, baryons and photons formed a single fluid known as the photon-baryon fluid, which underwent compression and expansion due to gravity and pressure variations. This led to *acoustic oscillations*, similar to sound waves, and depending on the fluid's phase during photon decoupling, the emerging photons exhibited different temperatures. These fluctuations provide valuable information about the abundance of baryons during recombination.

Through the lens of the $\Lambda$CDM model, we gain insight into the Universe by examining the structure of the CMB angular power spectrum [27, 28]. The first peak reflects the abundance of baryonic matter, while the subsequent peaks carry signatures of the non-baryonic mass density. Specifically, the position of the first peak and the relative heights of the second and third acoustic peaks indicate that the Universe is flat and predominantly composed of cold dark matter (CDM), with a density ratio $\Omega_c$ about five times larger than that of ordinary baryonic matter $\Omega_b$.

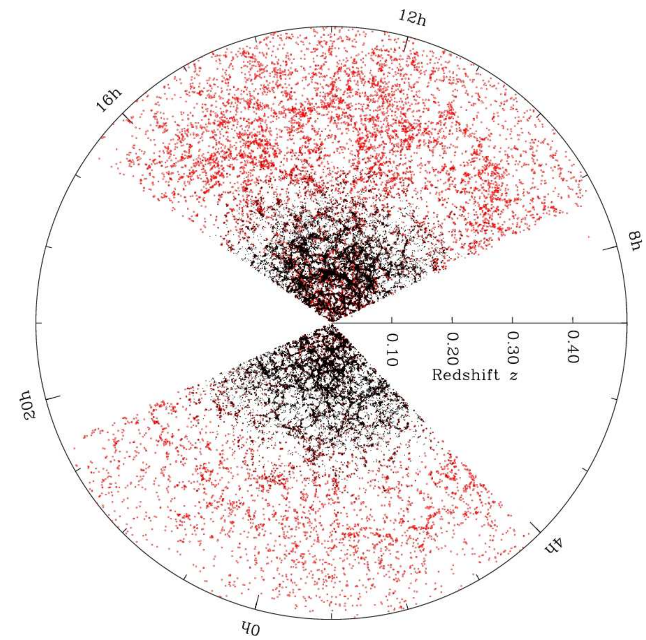


Figure 1.4: SDSS-III redshift map of the galaxy distribution. It appears clumpy on small scales, but it becomes more uniform on large scales, corresponding to early times. Figure taken from Daniel Baumann's lecture notes on Cosmology for Part III Mathematical Tripos in Cambridge (`http://www.damtp.cam.ac.uk/user/db275/cosmology.pdf`). The extended version containing SDSS-IV data can be found in Ref. [29].

## 1.4 Large-Scale Structure

The existence of inhomogeneities, often referred to as structure, within the Universe was recognized prior to the discovery of CMB anisotropies. This understanding stemmed from redshift maps depicting the distribution of luminous galaxies in the local Universe, obtained from surveys such as the Sloan Digital Sky Survey (SDSS) and the Two Degree Field Galaxy Redshift Survey (2dFGRS). These maps, an example of which is illustrated in Fig. 1.4, clearly demonstrate that galaxies are neither homogeneously nor randomly distributed. Instead, the Universe exhibits structure on large scales. The distribution of galaxies and matter on cosmological scales is commonly referred to as large-scale structure (LSS).

Similar to the analysis of the CMB, the study of matter inhomogeneities involves investigating their properties in Fourier space, which allows for a separation of large and small scales. In this context, the variable of interest is the density of galaxies as a function of their three-dimensional positions in the sky, denoted as $n_g(\vec{x})$. By defining $\bar{n}_g$ as the mean number density across the entire galaxy survey, the matter inhomogeneities can be characterized using the quantity $\delta_g(\vec{x}) = [n_g(\vec{x}) - \bar{n}_g]/\bar{n}_g$, or its Fourier transform $\tilde{\delta}_g(\vec{k})$. The galaxy power spectrum $P_g(k)$, which reveals the distribution of matter in Fourier space, can be computed by evaluating the two-point correlation function of $\tilde{\delta}_g$ [2, 3]

$$\langle \tilde{\delta}_g(\vec{k}) \tilde{\delta}_g^*(\vec{k}') \rangle = (2\pi)^3 \delta^{(3)}(\vec{k} - \vec{k}')\, P_g(k)\,, \tag{1.15}$$

where $\delta^{(3)}(\cdot)$ is the three-dimensional Dirac delta function, and the angular brackets denote an average over the whole ensemble. The left panel of Fig. 1.5 presents the galaxy power spectrum obtained from the SDSS/BOSS survey, showcasing its remarkable agreement with the predictions of the concordance $\Lambda$CDM model.

The galaxy power spectrum $P_g(k)$ exhibits intriguing oscillations around $k \simeq 0.1\, h$ Mpc$^{-1}$, known as Baryon Acoustic Oscillations (BAO), originating from the epoch of recombination. During photon decoupling, the tightly coupled photon-baryon fluid underwent acoustic oscillations in the primordial plasma before transitioning to a decoupled state. As the pressure within the fluid dissipated, it left behind fixed ripples of baryonic matter at a characteristic radius of approximately $\simeq 147$ Mpc, known as the sound horizon. The force of gravity then attracted more baryons and DM toward these initial density perturbations, eventually giving rise to the formation of galaxies and the observed LSS. This feature is imprinted in the correlation function $\xi$ of galaxy number density in position space, as illustrated in the left panel of Fig. 1.5. BAO serves as a "standard ruler" since the size of the baryonic ripples can be accurately measured without relying on any specific cosmological model.

To facilitate the comparison between theory and observations, linear perturbation theory around a smooth background is commonly employed, as shown in the left panel of Fig. 1.5. This approach provides a semi-analytical framework, eliminating the need

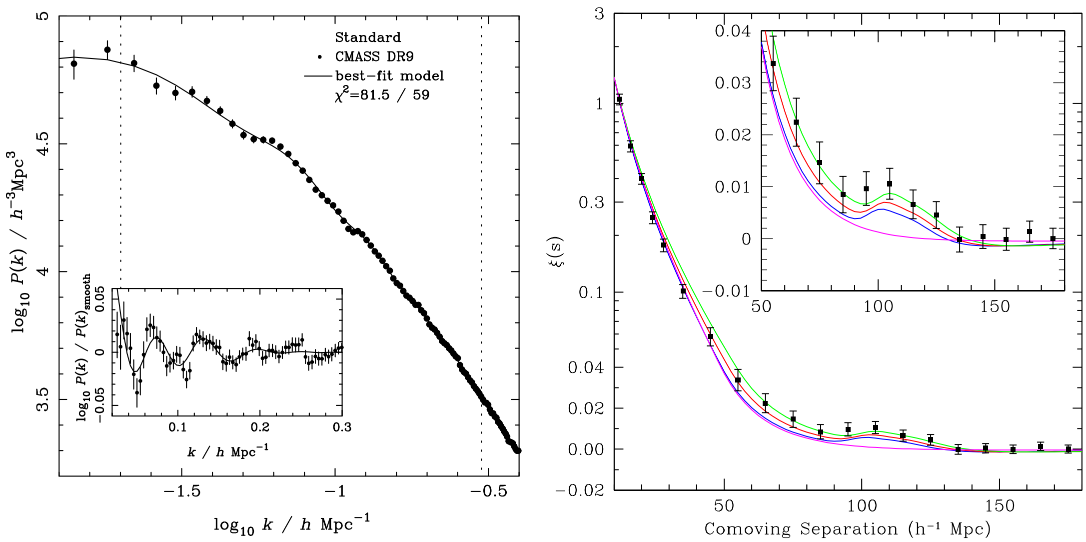


Figure 1.5: *Left*: The power spectrum $P_g(k)$, as measured from the CMASS sample of the SDSS-III BOSS catalogue (points), compared to the theoretical prediction from the best-fit ΛCDM model (solid line). The inset zooms in on the BAO feature, which is used as a standard ruler. Figure taken from Ref. [30]. *Right*: The Baryon Acoustic peak observed in the correlation function $\xi(s)$, as inferred from the SDSS galaxy sample. The peak's amplitude is sensitive to the total matter density. The models shown are with $\Omega_m h^2 = (\Omega_b + \Omega_c)h^2 = 0.12$ (green line), 0.13 (red line) and 0.14 (blue line), all with $\Omega_b h^2 = 0.024$. The purple line corresponds to the case with $\Omega_b = 0$. Taken from Ref. [31].

of computationally intensive simulations. However, linear perturbation theory is applicable only to small perturbations, imposing limitations on the size range of matter inhomogeneities that can be effectively studied using this method. Perturbations on scales smaller than approximately $\sim$ 10 Mpc have undergone significant growth in the late Universe, leading to nonlinearity with fractional density fluctuations exceeding unity. In contrast, large-scale matter perturbations remain small as they have undergone less evolution. Thus, the Universe appears homogeneous and isotropic on scales larger than about $\mathcal{O}(100\,h^{-1}$ Mpc) [32]. Similarly, the anisotropies in the CMB are small due to their origin at early times and the fact that the photons comprising the CMB did not cluster during their journey to us.

The CMB and LSS offer distinct views of the Universe, primarily due to the amplitude of perturbations. The early Universe, as observed through the CMB, appeared remarkably smooth, while the present-day Universe observed through galaxy surveys exhibits significant inhomogeneity. This transition is driven by the influence of gravity, for which small-scale perturbations undergo nonlinear growth first and then hierarchical assembly, contributing to the formation of larger structures. The growth of structure is governed by the interplay between gravitational instability, causing the collapse of overdense regions, and the outward pull from the expanding background. Therefore, LSS is intricately linked to the underlying physics of the background Universe, including its composition, evolution, and curvature.

## 1.5 Evidence of Dark Matter

Evidence for the existence of additional matter beyond what is observable, known as dark matter (DM), has been observed across various scales in the Universe, ranging from dwarf galaxies to the largest cosmological scales. While we will highlight some notable examples of this evidence, a comprehensive review and historical account of DM can be found in Refs. [33, 34].

### 1.5.1 Cluster scale

In 1933, astronomer Fritz Zwicky made a significant observation when he computed the velocity dispersion of galaxies in the Coma cluster, located $\sim$ 100 Mpc away from Earth. He found that the apparent velocities of eight galaxies exhibited a large scatter, surpassing thousands of km/s [35]. This observation was unexpected because, according to the virial theorem, one would anticipate an average galaxy's velocity $v$ in the Coma cluster with mass $M$ and mean galaxy separation $r$ [3]

$$v \simeq \sqrt{\frac{GM}{2r}} \tag{1.16}$$

[3]The virial theorem states that, for a steady, spherical and self-gravitating system of $N$ objects of average mass $m$ and average orbital velocity $v$, the total average kinetic energy $T$ is $T = -U/2$ where $U$ is the potential energy. In particular, $T = Nmv^2/2$ and $U = -N(N-1)Gm^2/(2r)$ [36]. In the limit of $N \gg 1$, one derives Eq. (1.16).

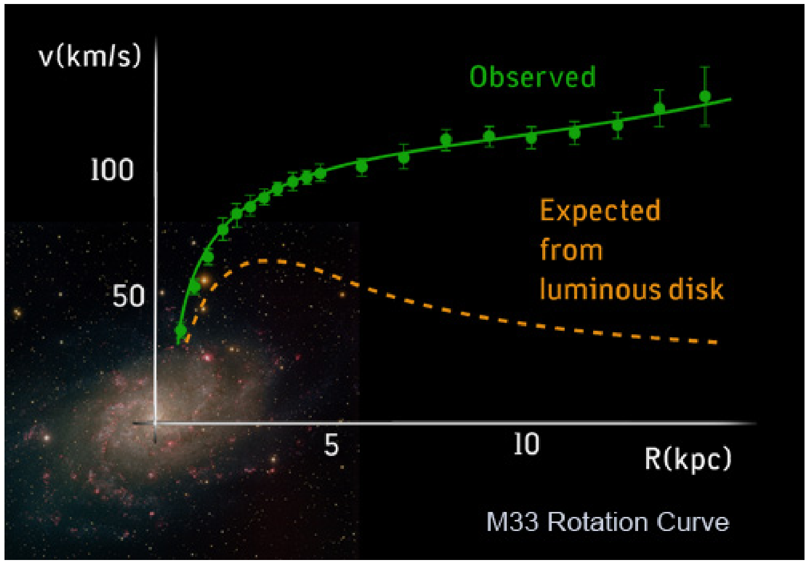

Figure 1.6: Observed and predicted rotation curves for the galaxy M33, also known as the Triangulum Galaxy. Source: © M33 Image: NOAO, AURA, NSF, T. A. Rector. `https://www.learner.org/courses/physics/unit/text.html`

to be around a few hundreds of km/s [35]. Zwicky confirmed this conclusion in a subsequent 1937 paper, where he estimated the mass-to-light ratio of the Coma cluster to be about $\sim 500$ (equivalent to $\sim 8$ with the present-day value of $H_0$ [34]), again employing the virial theorem [37]. [4] These findings led Zwicky to infer the presence of significant amounts of non-luminous matter in the cluster, necessary to hold galaxies together.

### 1.5.2 Galactic scale

The existence of DM was rediscovered in the 1970s by Vera Rubin and her collaborators, who analyzed the rotation curves of various galaxies, including the Andromeda (M31) galaxy [38, 39].

The expectation was that, similar to the planets in our Solar System, stars within a spiral galaxy should exhibit Keplerian motion. Assuming circular motion and that the mass of the galaxy is concentrated in a disk of radius $R$, where $M(r) \approx M$ for

[4] The mass-to-light ratio of an astrophysical object is the ratio between its stellar mass and its stellar luminosity. Typically, it is measured in terms of the solar mass and solar luminosity.

$r \geq R$, the velocity of the stars should follow a specific pattern. It should decrease with increasing distance from the galactic center according to

$$v(r) = \sqrt{\frac{GM(r)}{r}} \quad \xrightarrow{\text{r>R}} \quad v(r) \approx \sqrt{\frac{GM}{r}} \propto \frac{1}{\sqrt{r}}\,, \tag{1.17}$$

based on Newtonian gravity and the distribution of luminous matter.

However, Rubin's results revealed a striking deviation from these predictions. The optical data indicated that the rotation curves of stars remained nearly flat, meaning that the velocities of stars continued to increase with distance from the galactic center until reaching a limit (as depicted in Figure 1.6, for example). This constant velocity contradicted the expected decrease based on luminous matter alone. To explain this discrepancy, it is necessary to postulate the existence of an additional halo of invisible matter surrounding the galaxy, extending far beyond the observed stellar disk. This evidence strongly suggests the presence of DM in galaxies, contributing to the mass distribution at large galactic radii.

### 1.5.3 Gravitational lensing

In the 1970s, gravitational lensing emerged as another method to investigate the presence and distribution of DM. According to general relativity, mass causes the surrounding space to curve, leading to the bending of light rays passing through its vicinity. Gravitational lensing provides important information about the source, the lensing object, and the large-scale geometry of the Universe when they are at cosmological distances from each other.

One notable example is the 'Bullet cluster', shown in Figure 1.7, where a sub-cluster collided with a larger one. During this event, galaxies passed through each other without interaction, as confirmed by the gravitational lensing map (blue in the left panel or green contours in the right panel). However, the majority of a cluster's visible mass exists in the form of extremely hot gas emitting X-ray radiation (pink or red in Figure 1.7). Comparing the X-ray emission with the gravitational lensing map reveals a discrepancy: the regions of strong X-ray emission and the highest mass

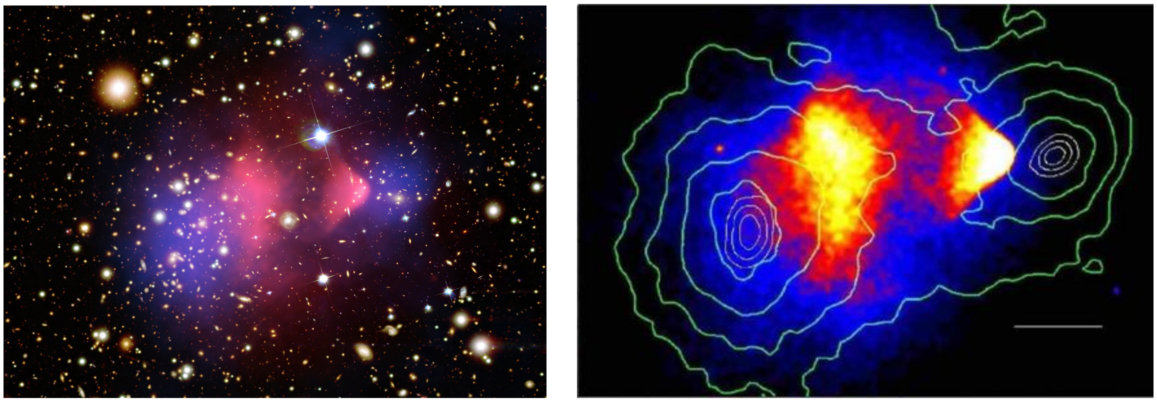

Figure 1.7: *Left:* Composite image of the colliding 'Bullet cluster', obtained with gravitational lensing. The lensing mass map is shown in blue, and the X-ray observations tracing the gas component are shown in pink. X-ray: NASA/CXC/CfA/Markevitch et al. [40]; Lensing Map: NASA/STScI; ESO WFI; Magellan/U.Arizona/Clowe et al. [41]; Optical: NASA/STScI; Magellan/U.Arizona/Clowe et al. [41]. *Right:* Lensing map, reconstructed using weak lensing data (green contours) and Chandra X-ray emissivity image of the same cluster. The white bar indicates a distance of 200 kpc. Figure taken from Ref. [41].

concentrations do not overlap, indicating that the dominant mass in the clusters is non-baryonic. This observation implies that DM interacts weakly, if at all, with gas or itself and behaves effectively as a collisionless entity. Additionally, if DM is described by a particle, it should be electrically neutral.

### 1.5.4 Cosmic web

Our current understanding of the LSS (section 1.4) is still incomplete, as its evolution from primordial density fluctuations is primarily driven by gravity, resulting in non-linear growth at small scales. Additionally, theoretical predictions must be compared with observations of the luminous Universe, where dissipative effects play a crucial role [33]. N-body cosmological simulations, particularly based on the $\Lambda$CDM model, have become a widely adopted approach to studying LSS formation.

Notably, the `Millennium-XXL` simulation [42], with its large number of DM-only particles, provides a comprehensive representation of the Universe's structure, including filaments, superclusters, walls, and voids, as seen in the left panel of Fig. 1.8. Comparisons between simulation outcomes and galaxy redshift survey data, such as

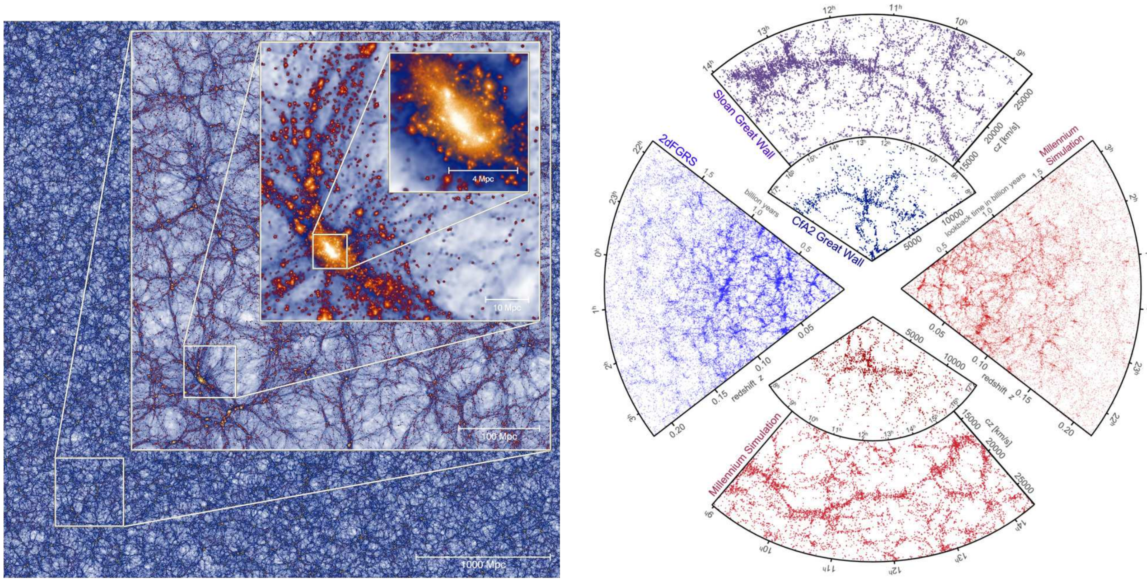


Figure 1.8: *Left:* Mass density field in the `Millennium-XXL`, in a cubical region with side $\sim$ 4.1 Gpc containing $\simeq 0.3 \times 10^{12}$ DM-only particles, focusing on the most massive halo present in the simulation at $z = 0$. Each inset zooms by a factor of eight from the previous one. The mass and length resolutions are $m_p = 8.456 \times 10^9$ $M_\odot$ and $\epsilon = 13.7$ kpc, respectively. Figure taken from Ref. [42]. *Right:* Comparison between the galaxy distributions from redshift surveys and the outcome of the `Millennium` simulation. The top and left wedges are the result from the 2dFGRS and SDSS galaxy surveys, whereas the bottom and right wedges are obtained by the N-body simulation and are matched to the structures observed by the surveys. From Ref. [43].

SDSS and 2dFGRS, reveal remarkable agreement, as shown in the right panel of Fig. 1.8.

The success of DM-only simulations in matching observational data suggests that baryonic matter's role in the overall evolution of the Universe is negligible and only becomes significant at galactic scales. DM particles used in these simulations are stable, collisionless, dissipationless, and "cold", meaning they are non-relativistic. These properties imply that DM particles should be heavy and long-lived enough to explain the structures and substructures observed today.

However, at galactic scales, numerical simulations have shown some discrepancies between predictions of the $\Lambda$CDM model and observational data, which will be discussed further in chapter 3 after a more thorough understanding of DM is presented in section 2.4.3.

In addition to the DM evidence presented in this section, CMB (section 1.3) and BBN (section 1.2) data provide strong and detailed information about the existence of DM and its cosmological properties.

## 1.6 Late-time accelerated expansion

The discovery of the Hubble law, as expressed in Eq. (1.1), was made possible through Henrietta Leavitt's study of Cepheid variable stars in the early $20^{\text{th}}$ century [44]. Cepheids are considered "standard candles" because their pulsation period is universally related to their intrinsic brightness (absolute magnitude), denoted by $M$ [45, 46].

Using the apparent magnitude $m$, which is determined by directly measuring the star's flux $F$ at Earth, $m = -(5/2)\log_{10} F + \text{constant}$, the star's luminosity distance $d_L$ can be inferred via [3]

$$\begin{aligned} \mu &\equiv m - M \\ &= 5\log_{10}(d_L/10\,\text{pc}) + K\,, \end{aligned} \tag{1.18}$$

where $K$ represents a correction factor accounting for effects such as light absorption by interstellar dust. The quantity $\mu$ is commonly referred to as the *distance modulus*. Equation (1.18) can be applied to various standard candles, including Cepheids, the tip of the Red Giant branch (TRGB), and Type Ia Supernovae (SNe Ia), where the absolute magnitude $M$ or the luminosity $L$ can be estimated based on physical properties of the system or empirical observational relations. In the case of SNe Ia, the characteristic time it takes for the luminosity to decay after the peak has been found to be universal once the luminosity-decline rate relation, known as Phillips relationship [47–49], is taken into account.

In the late $20^{\text{th}}$ century, two groups measured the apparent magnitudes of numerous SNe Ia and provided direct evidence for an accelerating Universe [51, 52]. This acceleration is best explained by the presence of dark energy. Fig. 1.9 illustrates the updated investigation of SNe Ia data using the $\Lambda$CDM model, which allows for the determination of cosmological parameters. The two free parameters in question are

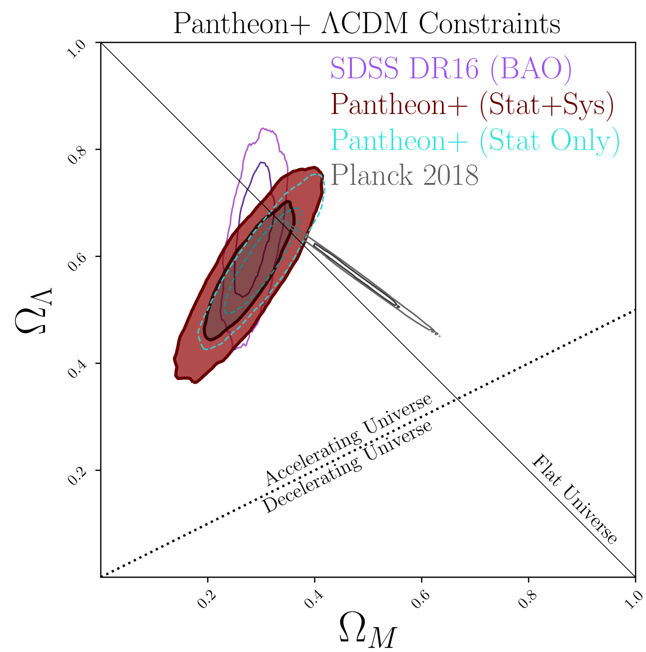


Figure 1.9: 68% and 95% Confidence Level (C.L.) contours for the abundance of non-relativistic matter $\Omega_m$ and dark energy $\Omega_\Lambda$, assuming the ΛCDM model, from the Pantheon+ dataset as well as from CMB (Planck 2018) and BAO data-sets. Two lines are included for reference: one for a flat Universe, where $\Omega_m + \Omega_\Lambda = 1$, and the other indicating an accelerating Universe. Figure taken from Ref. [50].

the normalized matter density $\Omega_m$ and the abundance of dark energy $\Omega_\Lambda$, which is assumed to be described by a cosmological constant Λ but is not limited to a flat Universe. Notably, a Universe with $\Omega_\Lambda = 0$ is inconsistent with observations and, instead, SNe data suggest a concordance value of $\Omega_\Lambda \sim 0.7$.

It is worth mentioning that another piece of evidence for dark energy arises from the BAO standard ruler, discussed in section 1.4, which provides an independent means to infer the abundance of dark energy. [3].

The abundance of DM and dark energy, as supported by multiple independent lines of evidence, strongly validates the ΛCDM model. However, the question of why the early Universe exhibited remarkable smoothness lies beyond the scope of this model. To address this question, the theory of inflation has been extensively studied because its predictions, such as the absence of spatial curvature, have been confirmed by CMB measurements. In an upcoming chapter, we will delve into this theory, but not before introducing the concordance ΛCDM model, which will be the focus of the next chapter.

# Bibliography


[1] E. W. Kolb and M. S. Turner, *The Early Universe*, vol. 69. 1990.

[2] S. Dodelson, *Modern Cosmology*. Academic Press, Amsterdam, 2003.

[3] S. Dodelson and F. Schmidt, *Modern Cosmology*. Academic Press, Amsterdam, 2020.

[4] V. Mukhanov, *Physical Foundations of Cosmology*. Cambridge University Press, Oxford, 2005.

[5] S. Weinberg, *Cosmology*. Oxford University Press, 2008.

[6] O. F. Piattella, *Lecture Notes in Cosmology*. UNITEXT for Physics. Springer, Cham, 2018. `arXiv:1803.00070 [astro-ph.CO]`.

[7] P. J. E. Peebles, *Principles of physical cosmology*. Princeton University Press, 1994.

[8] D. Baumann, *Cosmology*. Cambridge University Press, 7, 2022.

[9] **Particle Data Group** Collaboration, R. L. Workman *et al.*, "Review of Particle Physics," *PTEP* **2022** (2022) 083C01.

[10] E. Hubble, "A relation between distance and radial velocity among extra-galactic nebulae," *Proc. Nat. Acad. Sci.* **15** (1929) 168–173.

[11] C. Angulo *et al.*, "A compilation of charged-particle induced thermonuclear reaction rates," *Nucl. Phys. A* **656** (1999) 3–183.

[12] B. D. Fields, K. A. Olive, T.-H. Yeh, and C. Young, "Big-Bang Nucleosynthesis after Planck," *JCAP* **03** (2020) 010, `arXiv:1912.01132 [astro-ph.CO]`. [Erratum: JCAP 11, E02 (2020)].

[13] Y. I. Izotov, T. X. Thuan, and N. G. Guseva, "A new determination of the primordial He abundance using the He i $\lambda$10830 Å emission line: cosmological implications," *Mon. Not. Roy. Astron. Soc.* **445** no. 1, (2014) 778–793, `arXiv:1408.6953 [astro-ph.CO]`.

[14] R. I. Epstein, J. M. Lattimer, and D. N. Schramm, "The Origin of deuterium," *Nature* **263** (1976) 198–202.

[15] D. S. Balser and T. M. Bania, "Green Bank Telescope Observations of $^3$He$^+$: HII Regions," *Astrophys. J.* **156** (2018) 280, `arXiv:1810.09422 [astro-ph.GA]`.

[16] D. S. Aguado, J. I. G. Hernández, C. Allende Prieto, and R. Rebolo, "Back to the Lithium Plateau with J0023+0307 with [Fe/H]<-6," *Astrophys. J. Lett.* **874** (2019) L21, `arXiv:1904.04892 [astro-ph.SR]`.

[17] W. Aoki *et al.*, "Lithium Abundances of Extremely Metal-Poor Turn-off Stars," *Astrophys. J.* **698** (2009) 1803–1812, `arXiv:0904.1448 [astro-ph.SR]`.

[18] L. Sbordone *et al.*, "The metal-poor end of the Spite plateau. 1: Stellar parameters, metallicities and lithium abundances," *Astron. & Astrophys.* **522** (2010) A26, `arXiv:1003.4510 [astro-ph.GA]`.

[19] G. Jungman, M. Kamionkowski, A. Kosowsky, and D. N. Spergel, "Cosmological parameter determination with microwave background maps," *Phys. Rev. D* **54** (1996) 1332–1344, `arXiv:astro-ph/9512139`.

[20] **Planck** Collaboration, N. Aghanim *et al.*, "Planck 2018 results. VI. Cosmological parameters," *Astron. Astrophys.* **641** (2020) A6, `arXiv:1807.06209 [astro-ph.CO]`. [Erratum: Astron.Astrophys. 652, C4 (2021)].

[21] A. A. Penzias and R. W. Wilson, "A Measurement of excess antenna temperature at 4080-Mc/s," *Astrophys. J.* **142** (1965) 419–421.

[22] D. J. Fixsen, E. S. Cheng, J. M. Gales, J. C. Mather, R. A. Shafer, and E. L. Wright, "The Cosmic Microwave Background spectrum from the full COBE FIRAS data set," *Astrophys. J.* **473** (1996) 576, `arXiv:astro-ph/9605054`.

[23] **COBE** Collaboration, G. F. Smoot *et al.*, "Structure in the COBE differential microwave radiometer first year maps," *Astrophys. J. Lett.* **396** (1992) L1–L5.

[24] D. J. Fixsen, "The Temperature of the Cosmic Microwave Background," *Astrophys. J.* **707** (2009) 916–920, `arXiv:0911.1955 [astro-ph.CO]`.

[25] D. Baumann, "Primordial Cosmology," *PoS* **TASI2017** (2018) 009, `arXiv:1807.03098 [hep-th]`.

[26] W. Hu and S. Dodelson, "Cosmic Microwave Background Anisotropies," *Ann. Rev. Astron. Astrophys.* **40** (2002) 171–216, `arXiv:astro-ph/0110414`.

[27] V. F. Mukhanov, "CMB-slow, or how to estimate cosmological parameters by hand," *Int. J. Theor. Phys.* **43** (2004) 623–668, `arXiv:astro-ph/0303072`.

[28] W. Hu and N. Sugiyama, "Anisotropies in the cosmic microwave background: An Analytic approach," *Astrophys. J.* **444** (1995) 489–506, `arXiv:astro-ph/9407093`.

[29] **SDSS** Collaboration, M. R. Blanton *et al.*, "Sloan Digital Sky Survey IV: Mapping the Milky Way, Nearby Galaxies and the Distant Universe," *Astron. J.* **154** no. 1, (2017) 28, `arXiv:1703.00052 [astro-ph.GA]`.

[30] L. Anderson *et al.*, "The clustering of galaxies in the SDSS-III Baryon Oscillation Spectroscopic Survey: Baryon Acoustic Oscillations in the Data Release 9 Spectroscopic Galaxy Sample," *Mon. Not. Roy. Astron. Soc.* **427** no. 4, (2013) 3435–3467, `arXiv:1203.6594 [astro-ph.CO]`.

[31] **SDSS** Collaboration, D. J. Eisenstein *et al.*, "Detection of the Baryon Acoustic Peak in the Large-Scale Correlation Function of SDSS Luminous Red Galaxies," *Astrophys. J.* **633** (2005) 560–574, `arXiv:astro-ph/0501171`.

[32] K. K. S. Wu, O. Lahav, and M. J. Rees, "The large-scale smoothness of the Universe," *Nature* **397** (1999) 225–230, `arXiv:astro-ph/9804062`.

[33] J. Silk *et al.*, *Particle Dark Matter: Observations, Models and Searches*. Cambridge Univ. Press, Cambridge, 2010.

[34] G. Bertone and D. Hooper, "History of dark matter," *Rev. Mod. Phys.* **90** no. 4, (2018) 045002, `arXiv:1605.04909 [astro-ph.CO]`.

[35] F. Zwicky, "Die Rotverschiebung von extragalaktischen Nebeln," *Helv. Phys. Acta* **6** (1933) 110–127.

[36] M. Roos, "Dark Matter: The evidence from astronomy, astrophysics and cosmology," `arXiv:1001.0316 [astro-ph.CO]`.

[37] F. Zwicky, "On the Masses of Nebulae and of Clusters of Nebulae," *Astrophys. J.* **86** (1937) 217–246.

[38] V. C. Rubin and W. K. Ford, Jr., "Rotation of the Andromeda Nebula from a Spectroscopic Survey of Emission Regions," *Astrophys. J.* **159** (1970) 379–403.

[39] V. C. Rubin, W. K. Ford, Jr., and N. Thonnard, "Extended rotation curves of high-luminosity spiral galaxies. IV. Systematic dynamical properties, Sa through Sc," *Astrophys. J. Lett.* **225** (1978) L107–L111.

[40] M. Markevitch, "Chandra observation of the most interesting cluster in the universe," *ESA Spec. Publ.* **604** (2006) 723, `arXiv:astro-ph/0511345`.

[41] D. Clowe, M. Bradac, A. H. Gonzalez, M. Markevitch, S. W. Randall, C. Jones, and D. Zaritsky, "A direct empirical proof of the existence of dark matter," *Astrophys. J. Lett.* **648** (2006) L109–L113, `arXiv:astro-ph/0608407`.

[42] R. E. Angulo, V. Springel, S. D. M. White, A. Jenkins, C. M. Baugh, and C. S. Frenk, "Scaling relations for galaxy clusters in the Millennium-XXL simulation," *Mon. Not. Roy. Astron. Soc.* **426** (2012) 2046, `arXiv:1203.3216 [astro-ph.CO]`.

[43] V. Springel, C. S. Frenk, and S. D. M. White, "The large-scale structure of the Universe," *Nature* **440** (2006) 1137, `arXiv:astro-ph/0604561`.

[44] H. S. Leavitt, "1777 variables in the Magellanic Clouds," *Harvard Obs. Annals* **60** (1908) 87–108.

[45] G. F. Benedict *et al.*, "Astrometry with hubble space telescope: a parallax of the fundamental distance calibrator delta cephei," *Astron. J.* **124** (2002) 1695–1705, `arXiv:astro-ph/0206214`.

[46] G. F. Benedict, B. E. McArthur, M. W. Feast, T. G. Barnes, T. E. Harrison, R. J. Patterson, J. W. Menzies, J. L. Bean, and W. L. Freedman, "Hubble Space Telescope Fine Guidance Sensor Parallaxes of Galactic Cepheid Variable Stars: Period-Luminosity Relations," *Astron. J.* **133** (2007) 1810–1827, `arXiv:astro-ph/0612465`. [Erratum: Astron.J. 133, 2980 (2007)].

[47] M. M. Phillips, "The Absolute Magnitudes of Type IA Supernovae," *Astrophys. J. Letter* **413** (1993) L105.

[48] I. P. Pskovskii, "Light curves, color curves, and expansion velocity of type I supernovae as functions of the rate of brightness decline," *Soviet Astronomy* **21** (1977) 675.

[49] Y. P. Pskovskii, "Photometric classification and basic parameters of type I supernovae," *Soviet Astronomy* **28** (1984) 658–664.

[50] D. Brout *et al.*, "The Pantheon+ Analysis: Cosmological Constraints," *Astrophys. J.* **938** no. 2, (2022) 110, `arXiv:2202.04077 [astro-ph.CO]`.

[51] **Supernova Search Team** Collaboration, A. G. Riess *et al.*, "Observational evidence from supernovae for an accelerating universe and a cosmological constant," *Astron. J.* **116** (1998) 1009–1038, `arXiv:astro-ph/9805201`.

[52] **Supernova Cosmology Project** Collaboration, S. Perlmutter *et al.*, "Measurements of $\Omega$ and $\Lambda$ from 42 high redshift supernovae," *Astrophys. J.* **517** (1999) 565–586, `arXiv:astro-ph/9812133`.

Chapter 2

# Building the $\Lambda$CDM model

To unravel the complex evolution and history of the Universe, the theory of General Relativity (GR) stands as an essential framework. GR can be conceptually divided into two fundamental components that, when combined, provide a cohesive understanding of the cosmos. The first component is the metric, which characterizes the geometry of spacetime, governing the kinematics of particles moving in it. The second component encompasses the energy content, including matter, radiation, and other forms of energy.

The distribution and behavior of this energy content directly influence the shape of spacetime through the Einstein equations, establishing a profound interconnection between the Universe's geometry and the distribution of energy within it. In this chapter, we will initially introduce the metric for an expanding Universe and explore particle kinematics. Subsequently, we will delve into the energy content and its dynamic nature in section 2.3. The foundation of this chapter draws heavily from standard cosmology textbooks. [1–8].

## 2.1 The FLRW metric

The metric in GR describes the actual distance between infinitesimally close points in spacetime, and it depends on the chosen coordinate system. The distance, denoted as $ds^2$, is however invariant, ensuring the same measurement outcome regardless of the coordinate system used.

In GR, the metric takes on a deeper meaning by incorporating gravity, allowing us to describe particles moving freely in a curved spacetime. This concept is based on *general covariance*, where an observer in a uniform gravitational field makes identical measurements to one in an accelerated reference frame. In four-dimensional spacetime, the metric includes time intervals as its zeroth component, represented by

$$ds^2 = \sum_{\mu,\nu=0}^{3} g_{\mu\nu}\, dx^\mu dx^\nu \equiv g_{\mu\nu}\, dx^\mu dx^\nu \,. \tag{2.1}$$

The metric $g_{\mu\nu}$ is symmetric, with four diagonal and six independent off-diagonal components. The proper-time interval, described by $ds^2$, measures the time elapsed between two spacetime events when the observer is at rest with respect to them. If $ds^2 > 0$, it is called timelike, indicating a spatial separation less than the distance light can travel. For $ds^2 < 0$, it is called spacelike, and for $ds^2 = 0$, it is lightlike.

In special relativity, the metric of Minkowski spacetime is given by $g_{\mu\nu} = \eta_{\mu\nu}$, where $\eta_{\mu\nu} = \mathrm{diag}(1, -1, -1, -1)$. In an expanding Universe that is isotropic and homogeneous, the metric can be understood qualitatively by considering that points in a cosmic grid move away from each other in proportion to the scale factor $a(t)$. Thus, in an Euclidean or "flat" Universe, the metric is similar to the Minkowski metric, with spatial coordinates multiplied by the scale factor. This leads to the Friedmann-Lemaître-Robertson-Walker (FLRW) metric for an Euclidean Universe given by

$$g_{\mu\nu} = \begin{pmatrix} 1 & 0 & 0 & 0 \\ 0 & -a^2(t) & 0 & 0 \\ 0 & 0 & -a^2(t) & 0 \\ 0 & 0 & 0 & -a^2(t) \end{pmatrix} , \tag{2.2}$$

which can be generalized to include open or closed Universes, obtaining [1]

$$ds^2 = dt^2 - a^2(t)\left[\frac{dr^2}{1-kr^2} + r^2(d\theta^2 + \sin^2\theta d\varphi^2)\right] , \tag{2.3}$$

where $(t, r, \theta, \varphi)$ are comoving coordinates, and $k$ is the curvature index taking the values of $+1, -1, 0$ for spaces of constant positive (close Universe), negative (open Universe), or zero spatial curvature (flat Universe), respectively. [1]

The FLRW metric, known before the discovery of the CMB and galaxy surveys [9], was initially proposed by Friedmann in 1922 as a possible solution to the Einstein equations [10, 11]. It was further developed independently by Robertson [12, 13] and Walker [14] in the 1930s based on geometrical considerations and the assumption of a homogeneous and isotropic Universe. Lemaître's work was also influential in its development [15, 16]. This metric embodies the *cosmological principle*, which assumes no preferred direction or position in the cosmos.

## 2.2 Particle kinematics

Equipped with the FLRW metric (2.3), we can now explore particle motion within this background. Throughout this thesis, we will primarily focus on a flat Universe ($k = 0$) since precise observations of CMB temperature anisotropies (as discussed in the previous chapter) strongly indicate the spatial curvature to be nearly zero.

In Minkowski spacetime, a particle moves along a straight line in the absence of external forces. However, in curved spacetime, the concept of a straight line is generalized to a geodesic, which represents the shortest path between two points. GR states that a particle follows a geodesic when subject only to the force of gravity. To derive the geodesic equation, we generalize Newton's second law in four-dimensional spacetime without any forces, yielding [17]

$$\frac{d^2x^\mu}{d\lambda^2} + \Gamma^\mu_{\alpha\beta}\frac{dx^\alpha}{d\lambda}\frac{dx^\beta}{d\lambda} = 0\,, \tag{2.4}$$

where $\lambda$ is an auxiliary parameter that increases monotonically along the particle's path, replacing the concept of time as one of our coordinates. The quantity $\Gamma^\mu_{\alpha\beta}$

[1] In Eq. (2.3), the coordinate $r$ is dimensionless, meaning that $a(t)$ has to have dimensions of length, and $r$ ranges from 0 to 1 for $k = +1$. Alternatively, $a(t)$ can be dimensionless but the curvature index $k$ must have dimensions of an inverse length squared.

represents the Christoffel symbol and is defined in terms of the metric as

$$\Gamma^{\mu}_{\alpha\beta} = \frac{1}{2} g^{\mu\nu} \Big[ \partial_\beta g_{\alpha\nu} + \partial_\alpha g_{\beta\nu} - \partial_\nu g_{\alpha\beta} \Big] \,, \tag{2.5}$$

which is symmetric in the lower indices. Here, $g^{\mu\nu}$ represents the inverse of the metric $g_{\mu\nu}$, satisfying $g^{\mu\alpha} g_{\alpha\nu} = \eta^{\mu}_{\nu}$. In the above expression, we have used the shorthand notation $\partial_\alpha \equiv \partial/\partial x^\alpha$.

Applying the FLRW metric (2.2), Eq. (2.4) for the case of a massless particle, like a photon, with energy $E$ at time $t$ leads to [3]

$$\dot{E} + \frac{\dot{a}}{a} E = 0 \,, \tag{2.6}$$

whose solution is

$$E(a) = E_i \left( \frac{a_i}{a} \right) , \tag{2.7}$$

with $E_i$ the particle's energy at time $a_i$. Hence, we find that the energy or momentum of a massless particle decreases as the Universe expands. This implies that the wavelength of light emitted by distant objects increases linearly with the scale factor, confirming the earlier argument presented in the previous chapter when defining the concept of redshift in Eq. (1.2). For massive particles, it is possible to show that Eq. (2.7) holds true only for the magnitude of the three-momentum and not for the particle's energy [1].

In cosmology, understanding distances and horizons is a crucial aspect. By revisiting Eq. (2.3), we can express it in a simpler way using the conformal time $\tau$, defined by

$$d\tau \equiv \frac{dt}{a(t)} \,, \tag{2.8}$$

yielding

$$ds^2 = a^2(\tau) \left[ d\tau^2 - \frac{dr^2}{1 - kr^2} - r^2 (d\theta^2 + \sin^2\theta d\varphi^2) \right] . \tag{2.9}$$

The name "conformal time" becomes evident from this expression: when expressed in terms of $\tau$, the flat FLRW metric becomes conformal to the Minkowski metric $\eta_{\mu\nu}$.

In other words, the line element is equal to the Minkowski line element multiplied by the scale factor $a(\tau)$, serving as a conformal factor. The conformal time $\tau$ holds a profound physical meaning as it defines the causal structure of the Universe. Due to the isotropy of spacetime, we can choose a coordinate system where light travels only radially (*i.e.* $\theta = \varphi =$ constant). In this case, Eq. (2.9) reduces to

$$ds^2 = a^2(\tau)[d\tau^2 - dr^2]\,, \tag{2.10}$$

assuming a flat Universe for simplicity, although this assumption is not necessary [8]. Since photons travel along null geodesics, $ds^2 = 0$, their path is defined by $\Delta r = \pm\Delta\tau$, where the plus sign corresponds to outgoing photons and the minus sign to incoming photons. In other words, light rays in the $r$-$\tau$ plane correspond to straight lines at a 45° angle, defining the light cone for any observer in the spacetime. We can then define two distinct cosmological horizons based on the visual representation illustrated in Fig. 2.1. These horizons are as follows:

- The (comoving) *particle horizon* represents the maximum comoving distance $\tau$ that light could have traveled since $t = t_i$ (recall $c = 1$)

  $$\chi_{\rm ph}(\tau) = \tau - \tau_i = \int_{t_i}^{t} \frac{dt'}{a(t')}\,. \tag{2.11}$$

  If $t_i = 0$, commonly associated with the Big Bang, then $\chi_{\rm ph} = \tau$. As depicted in Fig. 2.1, the size of the particle horizon at time $\tau$ can be visualized as the intersection of the past light cone of an observer $p$ with the spacelike surface $\tau = \tau_i$. Causal influences must originate from within this region.

- The (comoving) *event horizon* gives the maximum distance from which an observer at time $t_f$ can receive a signal emitted at any time later than $t$. It is defined by

  $$\chi_{\rm eh}(\tau) = \tau_f - \tau = \int_{t}^{t_f} \frac{dt'}{a(t')}\,. \tag{2.12}$$

  In other words, the event horizon reveals the events that we will be able to see or impact in the future, assuming light can travel undisturbed and without

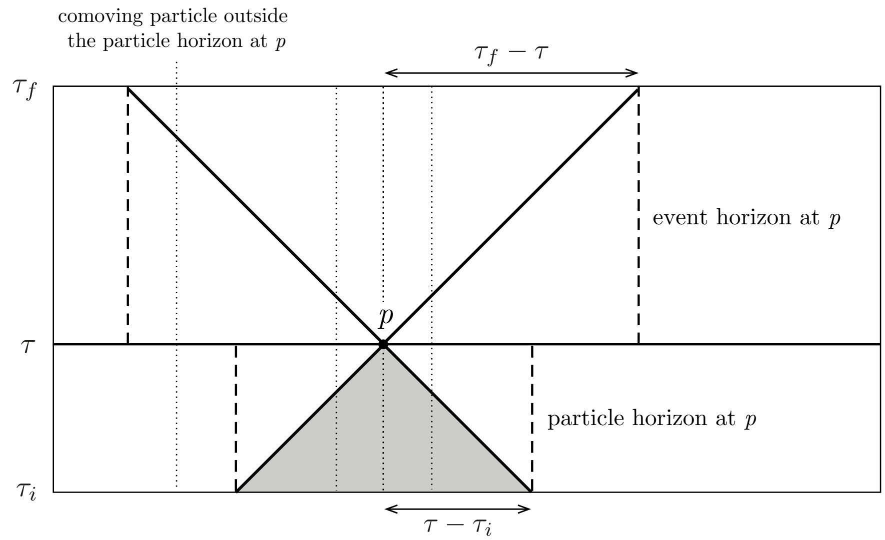


Figure 2.1: Illustration of horizons in a spacetime diagram. Dotted lines represent the worldlines of comoving objects. The event horizon corresponds to the maximum distance from which signals can be emitted by an observer located at $p$. Conversely, the particle horizon represents the farthest distance in the past from which signals can be received. Taken from Ref. [8].

interaction along its path.

The physical horizons at time $t$ can be obtained by multiplying the corresponding comoving horizons by the scale factor $a(t)$.

The introduction of the conformal time $\tau$ in Eq. (2.8) provides an easy way to define distances in a flat FLRW Universe. However, when dealing with non-zero curvature, we need to start directly from the line element in Eq. (2.3) to define distances, for which we refer interested readers to Refs. [3, 8]. Let's consider the comoving distance between us and a distant light source. In a small time interval $dt$, light travels a comoving distance $dx = dt/a$. Therefore, the total comoving distance traveled by light emitted from an object at time $t$ when the scale factor was $a$ (or redshift $z = 1/a - 1$) is given by

$$\chi(t) = \int_t^{t_0} \frac{dt}{a} = \int_{a(t)}^1 \frac{da'}{a'^2 H(a')} = \int_0^z \frac{dz'}{H(z')} \,. \qquad (2.13)$$

For small redshift $z$, the comoving distance can be approximated as $\chi \approx z/H_0$, which corresponds to the Hubble law discussed in the previous chapter (see Eqs. (1.1) and (1.6)). However, the comoving distance $\chi$ is not directly observable. Instead, we rely on two related quantities: the luminosity distance and the angular diameter distance.

One method of determining distances in astronomy involves measuring the flux from an object of known luminosity, often referred to as a "standard candle". In a static Euclidean space, the flux $F$ (energy per second per receiving area) observed at a distance $d$ from a source with luminosity $L$ (energy emitted per second) is given by

$$F = \frac{L}{4\pi d^2} \,. \tag{2.14}$$

However, in an expanding Universe described by the FLRW metric, three modifications are needed:

- The distance $d$ between the observer and the source has changed between the emission and detection times, as given by the comoving distance $\chi(a)$ in Eq. (2.13).
- The rate of photon arrival is lower than the rate of emission by a factor of $a$ due to the expansion.
- The energy of photons at detection is lower than at emission due to expansion, as described by Eq. (2.7).

Thus, the observed flux from a source with luminosity $L$ at a coordinate distance $\chi$ and redshift $z$ is given by

$$F = \frac{La^2}{4\pi\chi^2(a)} \,. \tag{2.15}$$

By comparing Eq. (2.15) with Eq. (2.14), we can define the *luminosity distance* in an expanding Euclidean Universe as

$$d_L = \frac{\chi}{a} = (1+z)\,\chi \,. \tag{2.16}$$

Another approach to determine distances in astronomy involves measuring the angle $\theta$ subtended by an object of known physical size $l$, often referred to as a "standard ruler." For cosmological objects where $\theta$ is small, the distance to the object is given simply by

$$d_A = \frac{l}{\theta}\,, \tag{2.17}$$

and it defines the *angular diameter distance*. In an expanding Universe, the comoving size of the object is $l/a$, where $a$ is the scale factor at the time of photon emission. Using Eq. (2.13), we can infer the subtended angle in a flat Universe as $\theta = (l/a)/\chi(a)$. Therefore, comparing with Eq. (2.17), we find that

$$d_A = a\,\chi = \frac{\chi}{1+z}\,. \tag{2.18}$$

It is important to note that the angular diameter distance measures the distance between us and a source at the time of photon emission. We observe that the angular diameter and luminosity distances are not independent but related by

$$d_A = a^2\, d_L = \frac{d_L}{(1+z)^2}\,, \tag{2.19}$$

which holds true even for a curved Universe [3].

## 2.3 Particle dynamics

In the previous discussion, the dynamics of a FLRW Universe were implicitly present through the time dependence of the scale factor $a(t)$. To make this time dependence explicit, one needs to solve for the evolution of the scale factor by employing the Einstein equations [2]

$$R_{\mu\nu} - \frac{1}{2}g_{\mu\nu}R \equiv G_{\mu\nu} = 8\pi G\, T_{\mu\nu}\,, \tag{2.20}$$

[2]The left-hand side of the Einstein equation (2.20) is not uniquely defined. It is possible to include a term $-\Lambda g_{\mu\nu}$, where $\Lambda$ is a constant, without affecting the conservation of the stress tensor described by Eq. (2.25). Einstein originally introduced such a term and referred to it as the *cosmological constant*. However, in modern practice, this term is moved to the right-hand side and treated as a contribution to the stress-energy tensor in the form $T^{(\Lambda)}_{\mu\nu} = \Lambda g_{\mu\nu}/(8\pi G) \equiv \rho_\Lambda\, g_{\mu\nu}$.

where $G_{\mu\nu}$ is the Einstein tensor, representing the "spacetime curvature", $R_{\mu\nu}$ is the Ricci tensor, $R = g^{\mu\nu} R_{\mu\nu}$ is the Ricci scalar (contraction of the Ricci tensor), and the energy-momentum (or stress-energy) tensor $T_{\mu\nu}$ is a symmetric tensor describing the matter and energy content of the Universe. The Ricci tensor is defined in terms of the Christoffel symbols from Eq. (2.5) as

$$R_{\mu\nu} = \partial_\alpha \Gamma^\alpha_{\mu\nu} - \partial_\nu \Gamma^\alpha_{\mu\alpha} + \Gamma^\alpha_{\beta\alpha} \Gamma^\beta_{\mu\nu} - \Gamma^\alpha_{\beta\nu} \Gamma^\beta_{\mu\alpha} \,. \tag{2.21}$$

For the stress-energy tensor $T_{\mu\nu}$, the assumptions of isotropy and homogeneity lead to the coarse-grained energy-momentum tensor taking the form of a *perfect fluid* [8]

$$T_{\mu\nu} = (\rho + P)\, u_\mu u_\nu - P\, g_{\mu\nu} \,, \tag{2.22}$$

where $\rho(t)$ and $P(t)$ represent the energy density and pressure of the fluid, and $u_\mu$ is its four-velocity. In the frame comoving with the fluid (where the fluid is at rest), we have $u_\mu = (1, 0, 0, 0)$, and thus

$$T^\mu{}_\nu = g^{\mu\alpha} T_{\alpha\nu} = \begin{pmatrix} \rho(t) & 0 & 0 & 0 \\ 0 & -P(t) & 0 & 0 \\ 0 & 0 & -P(t) & 0 \\ 0 & 0 & 0 & -P(t) \end{pmatrix} . \tag{2.23}$$

The energy density and pressure of the fluid are generally related by an equation of state, often assumed to follow that of a barotropic fluid, where the pressure depends only on the density, $P = P(\rho)$. A widely used parameterization is a linear relationship between $P$ and $\rho$, given by

$$P = w\, \rho \,, \tag{2.24}$$

where $w$ represents the equation of state parameter. This simple parameterization effectively describes various species in the known Universe.

The evolution of energy density and pressure of a perfect fluid can be derived from the conservation of the stress-energy tensor, which in GR is expressed as

$$\nabla_\mu T^\mu{}_\nu = \partial_\mu T^\mu{}_\nu + \Gamma^\mu_{\mu\alpha} T^\alpha{}_\nu - \Gamma^\alpha_{\mu\nu} T^\mu{}_\alpha = 0\,, \tag{2.25}$$

for a non-interacting fluid, where $\nabla_\mu$ denotes the covariant derivative. This equation extends the conservation of energy and momentum for a non-interacting fluid in special relativity, $\partial_\mu T^\mu{}_\nu = 0$, which gives rise to the continuity equation and the Euler equation. Using the FLRW metric of Eq. (2.2), the $\nu = 0$ component of Eq. (2.25) leads to the generalized continuity equation

$$\dot{\rho} + 3H(\rho + P) = 0\,, \tag{2.26}$$

where we recall $H = \dot{a}/a$ is the Hubble parameter. A more useful form of this expression can be derived for fluids with equation of state given by Eq. (2.24). In fact, Eq. (2.26) becomes

$$\frac{d\ln\rho}{d\ln a} = -3(1+w)\,, \tag{2.27}$$

whose solution for time-independent $w$ scales as

$$\rho(a) \propto a^{-3(1+w)}\,. \tag{2.28}$$

Examples of particular interest include:

- Non-relativistic matter, characterized by $P \ll \rho$, resulting in $\rho_m \propto a^{-3}$ that reflects the expansion of volume $V \propto a^3$. Baryons and DM (at least the majority of it) can be treated as non-relativistic matter.

- Radiation, representing relativistic particles with $P = \rho/3$, giving $\rho_r \propto a^{-4}$. The dilution now includes the redshifting of energy, with $E \propto a^{-1}$. Photons and neutrinos (for most of their cosmological history) can be treated as radiation.

- Vacuum energy or dark energy, characterized by $P = -\rho$. The energy density remains constant as $\rho_\Lambda \propto a^0$, meaning that the energy density does not dilute with the expansion of the Universe.

To determine the behavior of the scale factor over time, we have to solve the Einstein equations given in Eq. (2.20) with the FLRW metric from Eq. (2.3) and the energy-momentum tensor from Eq. (2.22). Although there are ten equations in principle, corresponding to the ten independent components of the symmetric tensor $g_{\mu\nu}$, the symmetries of the metric lead to only two non-zero independent differential equations. The latter are derived from the time-time and space-space components of $R_{\mu\nu}$, resulting in the *Friedmann equations*

$$\left(\frac{\dot{a}}{a}\right)^2 = \frac{8\pi G}{3}\rho - \frac{k}{a^2}\,, \tag{2.29}$$

and

$$\frac{\ddot{a}}{a} = -\frac{4\pi G}{3}(\rho + 3P)\,. \tag{2.30}$$

Here, $\rho$ and $P$ represent the total energy density and pressure of the Universe, respectively, including all species contributions.

The second Friedmann equation, Eq. (2.30), reveals that in an expanding Universe ($\dot{a} > 0$) filled with ordinary species that satisfy the strong energy condition, $\rho + 3P \geq 0$, we have $\ddot{a} < 0$. This implies a singularity in the finite past known as the Big Bang, where $a(t_i) = 0$. However, this conclusion relies on the assumption that GR and the Friedmann equations remain valid at arbitrarily high energies and that no exotic forms of matter become dominant in such regimes.

By combining the first Friedmann equation, Eq. (2.29), with the result from the continuity equation, Eq. (2.28), we can determine the time evolution of the scale factor during different epochs, depending on which species dominate the energy density of the Universe. Specifically, we find that

$$a(t) \propto \begin{cases} t^{2/[3(1+w)]} & w \neq -1\,, \\ e^{Ht} & w = -1\,, \end{cases} \tag{2.31}$$

where $a(t) \propto t^{2/3}$, $a(t) \propto t^{1/2}$, and $a(t) \propto \exp(Ht)$ correspond to a flat Universe dominated by non-relativistic matter ($w = 0$), radiation ($w = 1/3$), or vacuum energy

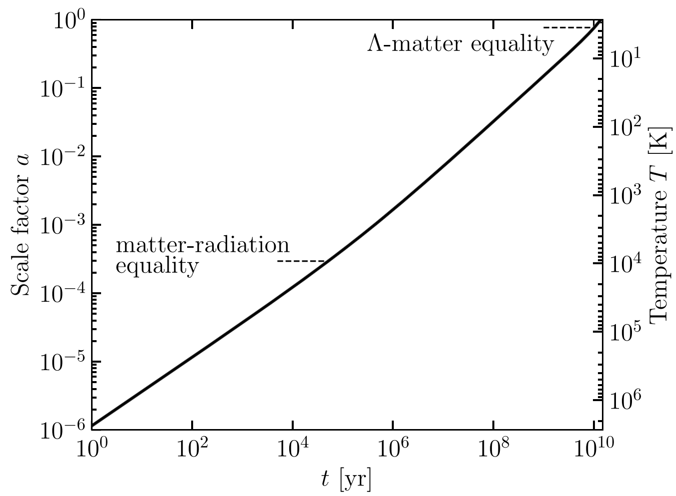


Figure 2.2: Evolution of the scale factor with cosmic time. The present-day Universe is located in the upper-right corner of the plot, where $a(t_0) = 1$ and the temperature is approximately $T = T_0 \simeq 2.73$ K. In the early Universe, radiation dominated, causing the scale factor to increase as $\propto t^{1/2}$. At the marked point, the Universe transitioned to matter domination, with $a(t) \propto t^{2/3}$. More recently, the expansion rate changed again due to the influence of dark energy, causing the scale factor to evolve exponentially. Figure taken from Ref. [3].

($w = -1$), respectively. Furthermore, if the scale factor $a(t)$ follows a power law $a \propto t^n$, the conformal time $\tau$ defined in Eq. (2.8) scales as $a(\tau) \propto \tau^{n/(1-n)}$. The different time dependencies of $a(t)$ for the different species suggest that the evolution of the Universe was initially driven by radiation, followed by a phase dominated by non-relativistic matter, and eventually, dark energy became the dominant component in driving the cosmic expansion. Fig. 2.2 illustrates the cosmic time evolution of the scale factor based on our current understanding of the Universe.

The expansion rate of the Universe is described by the Hubble parameter $H = \dot{a}/a$, where $a$ is the scale factor. As indicated by Eq. (2.31), it generally follows a $t^{-1}$ dependence. Its present value is the Hubble constant $H_0$. For a flat Universe, the current critical density is defined as [18]

$$\begin{aligned} \rho_{\text{crit}} = \frac{3H_0^2}{8\pi G} &= 1.87834 \times 10^{-29}\, h^2 \ \text{g}\,\text{cm}^{-3} \\ &= 1.053672 \times 10^{-5}\, h^2 \ (\text{GeV})\,\text{cm}^{-3}\,, \end{aligned} \tag{2.32}$$

To analyze the energy content of the Universe, we introduce dimensionless density parameters

$$\Omega_i \equiv \frac{\rho_i}{\rho_{\rm crit}}\,, \tag{2.33}$$

in terms of which Eq. (2.29) can be recast as

$$\frac{H^2}{H_0^2} = \frac{\Omega_r}{a^4} + \frac{\Omega_m}{a^3} + \frac{\Omega_k}{a^2} + \Omega_\Lambda\,, \tag{2.34}$$

where $\Omega_k \equiv -k/H_0^2$ represents the curvature density parameter. The quantities $\Omega_i$ in Eq. (2.34) should be considered as the present-day abundances of the respective species and not as $a$-dependent quantities. Here $i = r, m, \Lambda$ stands for radiation, matter and dark energy components.

Evaluating the equation above for the present time yields the golden rule of cosmology

$$\sum_i \Omega_i + \Omega_k = 1\,, \tag{2.35}$$

which reveals that in a closed Universe ($k = +1$), the sum of the density parameters exceeds one, while in an open Universe ($k = -1$), it is less than one. In a flat Universe, the sum precisely equals one.

## 2.4 Concordance model and energy content

Observations from different probes, including the CMB, BBN, LSS, and supernovae, provide strong evidence that the Universe is flat and composed of radiation ('$r$'), matter ('$m$'), and dark energy ('$\Lambda$'). Their present-day abundances, based on the $\Lambda$CDM model, are approximately [19]

$$\Omega_r \approx 9.4\times 10^{-5}\,, \qquad \Omega_m \approx 0.32\,, \qquad \Omega_\Lambda \approx 0.68\,, \qquad \Omega_k \lesssim 0.001\,. \tag{2.36}$$

The matter component is further divided into ordinary matter (baryons, '$b$') and (cold) dark matter (CDM, '$c$'), with approximate values

$$\Omega_b \approx 0.05\,, \qquad \Omega_c \approx 0.27\,. \tag{2.37}$$

However, the exact value of the Hubble constant $H_0$ is still uncertain due to a discrepancy between early and late-time probes, resulting in the *Hubble tension*, with values ranging from $\approx$ 67 km/s/Mpc to $\approx$ 73 km/s/Mpc [20–23]. Dark energy is consistent with having an equation of state similar to a cosmological constant, with $w_\Lambda \simeq -1$. The curvature, on the other hand, contributes less than 1% to the total energy budget, making its effects negligible at earlier times when matter and radiation dominate. Hence, for simplicity, we set $\Omega_k \equiv 0$ for the rest of the thesis. This model, described by Eqs. (2.36) and (2.37), is known as the ΛCDM model or the concordance cosmological model due to its excellent agreement with various cosmological datasets.

In the following sections, we will briefly explore the species that constitute the ΛCDM model, starting with the well-known visible sector that fits well within the Standard Model (SM) of particle physics.

### 2.4.1 Standard Model of particle physics

The SM of particle physics is a gauge theory that incorporates the strong, weak, and electromagnetic interactions within the framework of the $\mathrm{SU}(3)_C \otimes \mathrm{SU}(2)_L \otimes \mathrm{U}(1)_Y$ gauge group. It provides a comprehensive description of all known particles up to energies of around $\mathcal{O}(1\ \mathrm{TeV})$. Our aim here is to provide a brief introduction to the SM in order to establish the foundational understanding necessary for the subsequent chapters. For a more detailed review of the SM, we recommend referring to works such as Refs. [18, 24–28].

#### 2.4.1.1 Particle content and interactions

At the fundamental level, matter is composed of leptons and quarks. Leptons are spin-1/2 particles that interact through the electromagnetic and weak interactions, forming pairs such as the electron ($e^-$) and its neutrino ($\nu_e$), the muon ($\mu^-$) and its neutrino ($\nu_\mu$), and the tau lepton ($\tau$) and its neutrino ($\nu_\tau$). Quarks, also spin-1/2 particles, interact through the strong and electroweak interactions, and come in pairs: up ($u$) and down ($d$), charm ($c$) and strange ($s$), and top ($t$) and bottom ($b$). The electric charge of the "up" version of each quark is $+2/3$, while the "down" version has a charge of $-1/3$. Each quark type has three colors, analogous to electric charge, resulting in color singlet combinations known as hadrons: baryons (quark triplets) and mesons (quark-antiquark pairs). The absence of free colored states, a phenomenon called confinement, is a fundamental aspect of nature. Each quark or lepton pair is referred to as a generation and there is evidence for only three generations at the time of writing.

The interactions of quarks and leptons are mediated by gauge bosons, which are spin-1 particles. The photon ($\gamma$) mediates the electromagnetic interaction, the $W^\pm$ and $Z^0$ bosons mediate the weak interactions, and the eight gluons ($G$) mediate the strong interaction. All these forces operate at the level of quarks and leptons. For instance, the strong nuclear force, which binds nucleons together, is now understood as a residual force between color-neutral objects composed of quarks.

The SM is described by Yang-Mills gauge theories, which implement symmetries that organize particle states and describe the dynamics of interactions. The gauge theory for the strong, weak, and electromagnetic interactions in the SM is $\mathrm{SU}(3)_C \otimes \mathrm{SU}(2)_L \otimes \mathrm{U}(1)_Y$. The $\mathrm{SU}(3)_C$ part corresponds to quantum chromodynamics (QCD) and describes the strong (color) interaction, while the $\mathrm{SU}(2)_L \otimes \mathrm{U}(1)_Y$ part describes the electroweak interaction. Here the subscript $C$ stands for color, $L$ for left-handedness, and $Y$ for (weak) hypercharge, while $\mathrm{SU}(N)$ is the group of special unitary transformations of $N$ objects.

To illustrate gauge symmetry and gauge theory, consider the familiar $\mathrm{U}(1)_{\mathrm{EM}}$ gauge theory of electromagnetism (quantum electrodynamics, or QED). Its Lagrangian density is

$$\mathcal{L}_{\mathrm{QED}} = i\bar{\psi}\gamma_\mu D^\mu \psi - m_e \bar{\psi}\psi - \frac{1}{4} F^{\mu\nu} F_{\mu\nu}\,, \tag{2.38}$$

where $\psi$ represents the electron spinor, $m_e$ is the electron mass, $D_\mu = \partial_\mu + igA_\mu$ is the gauge-covariant derivative, $F_{\mu\nu}$ is the electromagnetic field-strength tensor, $A_\mu$ is the electromagnetic potential (gauge field), and $\gamma_\mu$ are the Dirac gamma matrices. The Lagrangian exhibits gauge symmetry, as it remains invariant under position-dependent gauge transformations of the form

$$\begin{aligned} \psi &\quad\rightarrow\quad \exp\left[iq\chi(x)\right]\psi\,, \\ A_\mu &\quad\rightarrow\quad A_\mu - \frac{1}{q}\partial_\mu\chi(x)\,, \end{aligned} \tag{2.39}$$

where $\chi(x)$ is a scalar function dependent on space-time coordinates. This local U(1) (phase rotation) symmetry arises due to the fact that $\chi(x)$ varies with space-time coordinates. In contrast, global symmetries have position-independent transformations. The introduction of the gauge field is necessary to maintain gauge invariance, a principle that requires all terms in the Lagrangian to respect the local symmetry. The presence of the gauge field gives rise to a force mediated by it.

The multiplet structure of particles reflects the underlying symmetries of nature. The gauge bosons reside in the adjoint representation of the SM gauge group: the eight gluons correspond to the adjoint representation of $\mathrm{SU}(3)_C$, the $W^\pm$ and $W^0$ bosons form a triplet under $\mathrm{SU}(2)_L$, and the $B^0$ boson is a singlet under $\mathrm{SU}(2)_L$. The photon and $Z^0$ boson are linear combinations of the $W^0$ and $B^0$ bosons, as we will see in the next subsection. Quarks, which are triplets under $\mathrm{SU}(3)_C$, and leptons, which are color singlets, follow the fundamental representation of the SM gauge group.

The electroweak part of the SM introduces an important concept known as chirality or handedness. The left- and right-handed components of quarks and leptons [3]

$$\psi_L = P_L\psi = \frac{1-\gamma_5}{2}\psi\,, \qquad \psi_R = P_R\psi = \frac{1+\gamma_5}{2}\psi\,, \qquad \psi = \psi_L + \psi_R\,, \tag{2.40}$$

participate differently in electroweak interactions. Here, $\gamma_5 = i\gamma_0\gamma_1\gamma_2\gamma_3 = \left(\begin{smallmatrix} 0 & 1 \\ 1 & 0 \end{smallmatrix}\right)$

[3] In the ultrarelativistic limit, the fields $\psi_{R,L}$ have a simple physical interpretation: a left-handed fermion is one whose spin is anti-parallel to its momentum vector (negative helicity), and a right-handed fermion is one whose spin is parallel to its momentum vector (positive helicity).

where $\gamma_i$ are the Dirac gamma matrices. In particular from Eq. (2.40), left-handed components form doublets under $SU(2)_L$, while right-handed components are singlets. This distinction violates parity symmetry, $\psi_R \leftrightarrow \psi_L$, as left- and right-handed components transform differently under the electroweak gauge group. Quarks and leptons also have different hypercharge assignments, further breaking parity symmetry.

Hypercharge ($Y$) in the context of the $SU(3)_C \otimes SU(2)_L \otimes U(1)_Y$ gauge group is related to the third component of weak isospin ($t_3$) and electric charge ($q$) by $q = t_3 + Y/2$. The upper components of lepton and quark doublets have $t_3 = 1/2$, while the lower components have $t_3 = -1/2$. On an important note, the right-handed neutrino ($\nu_R$) is a singlet under all interactions of the gauge group, characterized by $t_3 = 0$, $q = 0$, and $Y = 0$. Currently, it has not been observed in nature, although ongoing searches aim to determine its presence, as its existence would suggest a need to extend beyond the SM. The gauge bosons of $SU(2)_L$, namely $W^\pm$ and $W^0$, also possess weak isospin and transform as a triplet with $t_3(W^+) = 1$, $t_3(W^0) = 0$, and $t_3(W^-) = -1$. On the other hand, the gauge boson $B^0$ of $U(1)_Y$ does not carry hypercharge or weak isospin, which is a characteristic feature of Abelian gauge groups.

The Noether theorem reveals that every symmetry present in the Lagrangian corresponds to a conservation law. Thus, the charges associated with the generators of the $SU(3)_C \otimes SU(2)_L \otimes U(1)_Y$ gauge group, including color, weak isospin, and hypercharge, are conserved quantities. In addition to these charges arising from gauge symmetries (internal symmetries), the theory also possesses accidental global symmetries that result in additional conserved quantities. Baryon number ($B$) and the lepton flavor numbers ($L_e, L_\mu, L_\tau$) are exact conserved quantities. [4]

On a final note, the SM encompasses a range of other fascinating phenomena, including the Cabibbo-Kobayashi-Maskawa (CKM) mixing in the quark sector [29, 30], where quark flavor eigenstates and mass eigenstates differ leading to transitions among different quark generations.

[4] However, it should be noted that baryon number ($B$) conservation is violated by quantum mechanical effects related to instantons, which arise from "triangle diagrams". While $B$ is conserved classically, its conservation is anomalous at the quantum level. See section 3.3 for further details.

#### 2.4.1.2 The Higgs sector

In the SM, if we only consider the particle content described so far, all fermions and gauge bosons would be massless. However, experimental observations indicate that the weak interaction is short-range, with the gauge bosons having mass $M_W \simeq 80$ GeV and $M_Z \simeq 91$ GeV. The missing ingredient is the *spontaneous symmetry breaking* (SSB) of the $\mathrm{SU}(2)_L \otimes \mathrm{U}(1)_Y$ gauge group into the electromagnetic $\mathrm{U}(1)_{\mathrm{EM}}$ symmetry. This SSB is achieved by a scalar field known as the Higgs field, whose quanta were discovered in 2012 by both ATLAS and CMS Collaborations at CERN [31, 32]. The Higgs field, denoted as $H$, is a complex scalar $\mathrm{SU}(2)_L$ doublet with hypercharge $Y = \pm 1$. Its Lagrangian is described by

$$\mathcal{L}_{\mathrm{Higgs}} = (D^\mu H)(D_\mu H) - V(|H|)\,, \tag{2.41}$$

where $V(|H|)$ is the Higgs or scalar potential. The latter can be expressed as

$$V(|H|) = -m^2|H|^2 + \lambda |H|^4\,, \tag{2.42}$$

where

$$H = \frac{1}{\sqrt{2}} \begin{pmatrix} H^+ + iH^- \\ h + iH^0 \end{pmatrix}\,, \tag{2.43}$$

$$|H|^2 = H^\dagger H = ({H^+}^2 + {H^-}^2 + h^2 + {H^0}^2)/2\,, \tag{2.44}$$

with $H^+, H^-, H^0$ and $h$ four real scalar fields and $m$ and $\lambda$ are arbitrary parameters.

Provided that $-m^2 < 0$ in Eq. (2.42), the scalar potential $V(|H|)$ is minimized for a non-zero vacuum expectation value (VEV) of the Higgs field, $\langle |H|^2 \rangle = m^2/(2\lambda) \neq 0$, breaking the $\mathrm{SU}(2)_L \otimes \mathrm{U}(1)_Y$ symmetry down to $\mathrm{U}(1)_{\mathrm{EM}}$. As a result of this symmetry breaking, some of the gauge bosons associated with $\mathrm{SU}(2)_L \otimes \mathrm{U}(1)_Y$ acquire mass, arising from the square of the covariant derivative

$$D_\mu H = \partial_\mu H + ig\frac{\tau_a}{2} W^a_\mu H + ig'\frac{Y}{2} B_\mu H\,. \tag{2.45}$$

Here, $g, g'$ are the $\mathrm{SU}(2)_L$ and $\mathrm{U}(1)_Y$ coupling constants, respectively, $W_\mu^a$ are the three gauge fields associated with $\mathrm{SU}(2)_L$, $B_\mu$ is the gauge field associated with $\mathrm{U}(1)_Y$, and $\tau_a$ are the Pauli matrices. The $W^\pm$ bosons gain a mass given by $M_W^2 = \frac{1}{4}g^2v^2$, while the $Z^0$ boson acquires a mass $M_Z^2 = \frac{1}{4}(g^2+g'^2)v^2$, where $v = m/\sqrt{\lambda} = 246$ GeV is the VEV of the Higgs field. The photon ($A^\mu$) remains massless. In terms of the original neutral gauge fields $W_\mu^3$ and $B_\mu$, $A^\mu$ and the $Z^0$ boson are given by

$$\begin{aligned} Z^\mu &= \cos\theta_W W^{3\mu} - \sin\theta_W B^\mu \,, \\ A^\mu &= \sin\theta_W W^{3\mu} + \cos\theta_W B^\mu \,, \end{aligned} \tag{2.46}$$

where $\theta_W$ is the weak or Weinberg's angle, whose value is $\sin^2\theta_W \approx 0.23$ [18]. Through the Higgs mechanism, the four original Higgs fields have become the longitudinal components of the $W^\pm$ and $Z^0$ bosons and the neutral Higgs particle. The latter, denoted by $h$, also appears with a mass of $M_h = \sqrt{2}m$, where $m$ is the mass scale associated with the Higgs potential.

The Higgs mechanism also provides a solution to the problem of fermion masses. In the electroweak theory, a fermion mass term of the form $m\bar{\psi}\psi = m(\bar{\psi}_L\psi_R + \bar{\psi}_R\psi_L)$, called Dirac mass term, is forbidden by gauge symmetry because right- and left-handed components sit in different representations. However, the Higgs field enables the formation of $\mathrm{SU}(2)_L$ gauge singlets, and a Yukawa coupling term of the form

$$\mathcal{L}_f = -y^f\bar{\psi}_L H\psi_R \tag{2.47}$$

can arise in the Lagrangian. When the Higgs field $H$ acquires its VEV, this term leads to a fermion mass $m_f = y^f v/\sqrt{2}$. Thus, fermions acquire mass through their interaction with the Higgs field. This is not possible for neutrinos, because there is no right-handed neutrino $\nu_R$ included in the theory. We will give a closer look at neutrinos next, because they will play a vital role throughout the thesis.

### 2.4.2 Neutrinos

To introduce a mass term for neutrinos, it is necessary to go beyond the SM. In the following discussion, we will refer to the neutrinos that are part of the lepton $\mathrm{SU}(2)_L$ doublets and are singlets of the subgroup $\mathrm{SU}(3)_C \otimes \mathrm{U}(1)_{\mathrm{EM}}$ as "active" neutrinos, denoted as $\nu_L$. On the other hand, the neutrinos that do not possess any gauge interactions within the SM and are singlets of the complete SM gauge group $\mathrm{SU}(3)_C \otimes \mathrm{SU}(2)_L \otimes \mathrm{U}(1)_Y$ are referred to as "sterile" neutrinos, denoted as $\nu_R$. We will follow closely Ref. [18].

#### 2.4.2.1 Neutrino masses

Neutrino mass terms can be constructed in two ways within the framework of gauge-invariant and renormalizable operators

$$-\mathcal{L}_{M_\nu} = M_{D,ij}\bar{\nu}_{R,i}\nu_{L,j} + \frac{1}{2}M_{N,ij}\bar{\nu}_{R,i}\nu^c_{R,j} + \text{h.c.}\,, \tag{2.48}$$

where $\nu^c$ is the neutrino charge-conjugated field, $M_D$ is a complex matrix of dimension $n \times 3$ and $M_N$ is a symmetric $n \times n$ matrix. Here we have also introduced the flavour indices $i, j$, and "h.c." denotes the Hermitian conjugated terms.

The first term, arising from electroweak symmetry breaking, is generated by a Yukawa interaction

$$y_{\nu,ij}\,\bar{\nu}_{R,i}\tilde{H}^\dagger L_{L,j} \qquad \Longrightarrow \qquad M_{D,ij} = y^\nu_{ij}\frac{v}{\sqrt{2}}\,, \tag{2.49}$$

similarly to the one given in Eq. (2.47). Here we used the standard notation in which $L^T_{L,\ell} = (\nu_\ell, \ell)_L$ represents the $\mathrm{SU}(2)_L$ lepton doublet for the lepton $\ell$, $H$ is the Higgs doublet and $\tilde{H} = i\sigma_2 H^* = (h^{0\,*}, -h^-)^T$ with $\sigma_2$ is the Pauli matrix. The term in Eq. (2.49) conserves total lepton number but can break lepton flavor symmetries.

The second term in Eq. (2.48), known as the Majorana mass term, involves two sterile neutrino fields and breaks lepton number by two units. The form of $M_N$ depends on the model and we will see later one way to do it. Majorana mass terms are prohibited for charged fermions due to electric charge conservation.

The Lagrangian in Eq. (2.48) can be written more compactly as

$$-\mathcal{L}_{M_\nu} = \frac{1}{2}(\bar{\vec{\nu}}_L^c,\, \bar{\vec{\nu}}_R) \begin{pmatrix} 0 & M_D^T \\ M_D & M_N \end{pmatrix} \begin{pmatrix} \vec{\nu}_L \\ \vec{\nu}_R^c \end{pmatrix} + \text{h.c.} \equiv \bar{\vec{\nu}}^c M_\nu \vec{\nu} + \text{h.c.}\,, \tag{2.50}$$

where $\vec{\nu} = (\vec{\nu}_L, \vec{\nu}_R^c)^T$ is a $(3+n)$-dimensional vector.

The matrix $M_\nu$ is complex and symmetric and can be diagonalized by a unitary matrix $V^\nu$ of dimension $(3+n)$, such that

$$(V^\nu)^T M_\nu V^\nu = \text{diag}(m_1, m_2, \ldots, m_{3+n})\,. \tag{2.51}$$

The weak eigenstates $\nu_L$ can be expressed in terms of the resulting mass eigenstates $\nu_M$ as

$$\nu_{L,i} = P_L \sum_j^{3+n} V_{ij}^\nu \, \nu_{M,j}\,, \tag{2.52}$$

with $i = 1, 2, 3$ and $P_L$ is the left-handed projection operator in Eq. (2.40). Unlike charged fermions represented by four-component spinors, Majorana neutrinos are described by two-component spinors, as they satisfy the Majorana condition $\nu_M = \nu_M^c$.

Two notable scenarios arise from Eq. (2.48):

1. If $M_N = 0$, only the Dirac mass term is allowed, resulting in the diagonalization of $M_D$ through two $3 \times 3$ unitary matrices

$$(V_R^\nu)^\dagger M_D V^\nu = \text{diag}(m_1, m_2, \ldots, m_{3+n})\,. \tag{2.53}$$

   The weak eigenstates $\nu_L$ can be expressed in terms of the resulting mass eigenstates $\nu_D$ as

$$\nu_{L,i} = P_L \sum_j^{3+n} V_{ij}^\nu \, \nu_{D,j}\,, \tag{2.54}$$

   with $i = 1, 2, 3$. Because all leptons will acquire their mass via the same mechanism, this scenario can not explain why neutrinos are observed to be much lighter than the corresponding charged fermions.

2. If the mass eigenvalues of $M_N$ are much larger than the electroweak scale $v \simeq 246$ GeV, the diagonalization of $M_\nu$ leads to three light neutrinos $\nu_l$ and $n$ heavy neutrinos $N$

$$-\mathcal{L}_{M_\nu} = \frac{1}{2}\bar{\nu}_j M_l \nu_l + \frac{1}{2}\bar{N} M_h N \,, \tag{2.55}$$

with

$$M_l \simeq -V_l^T (M_D^T M_N^{-1} M_D) V_l \,, \qquad M_h \simeq V_h^T M_N V_h \,, \tag{2.56}$$

and $V_h$ and $V_l$ are $3 \times 3$ and $n \times n$ unitary matrices respectively. The masses of the heavy states are proportional to $M_N$, while the masses of the light states are inversely proportional to $M_N$. This scenario is known as the *see-saw mechanism* [33–37]. Both heavy and light states are Majorana particles and the former are mostly right-handed while the latter are mostly left-handed.

The Majorana mass term in Eq. (2.48) can be generated from new physics at a scale $\Lambda_{\rm NP}$ larger than the electroweak scale. The leading operator associated with this new physics is the 5-dimensional Weinberg operator [38]

$$\mathcal{O}_5 = \frac{z^\nu_{ij}}{\Lambda_{\rm NP}} (\bar{L}_{L,i} \tilde{H})(\tilde{H}^T L^c_{L,i}) + \text{h.c.} \,, \tag{2.57}$$

which violates lepton number by two units. After electroweak symmetry breaking, this operator generates a Majorana mass term for the left-handed neutrino fields

$$-\mathcal{L}_{M_\nu} = \frac{z^\nu_{ij}}{2} \frac{v^2}{\Lambda_{\rm NP}} \bar{\nu}_{L,i} \nu^c_{L,j} + \text{h.c.} \,, \tag{2.58}$$

resulting in a mass matrix $(M_\nu)_{ij} = z^\nu_{ij} \frac{v^2}{\Lambda_{\rm NP}}$. Compared to the Dirac mass matrix, this Majorana mass term is suppressed by $v/\Lambda_{\rm NP}$, providing a natural explanation for the smallness of neutrino masses compared to those of charged fermions.

Another important effect coming from Eq. (2.58) is that lepton flavour mixing and $CP$ violation are expected in the absence of additional symmetries on the Yukawa-like coefficients $z^\nu_{ij}$. We will discuss these effects next.

#### 2.4.2.2 Lepton mixing

Let us denote the neutrino weak or interaction eigenstates as $(\nu_{L,e}, \nu_{L,\mu}, \nu_{L,\tau}, \nu_{R,1}, \ldots, \nu_{R,n})$ and their mass eigenstates as $(\nu_1, \nu_2, \nu_3, \nu_4, \ldots, \nu_{n+3})$. Similarly, we label the mass and interaction eigenstates for charged leptons as $\ell = (e, \mu, \tau)$ and $\ell^I = (e^I, \mu^I, \tau^I)$, respectively.

The interactions of neutrinos with themselves (neutral current, NC) and with their corresponding charged leptons (charged current, CC) within the SM are dictated by $\mathrm{SU}(2)_L$ gauge invariance. The interaction Lagrangians are given by [5]

$$
\begin{aligned}
-\mathcal{L}_{\mathrm{CC}} &= \frac{g}{\sqrt{2}} \sum_{\ell} \bar{\nu}_{L,\ell} \gamma^{\mu} \ell_L^{I-} W_{\mu}^{+} + \text{h.c.}\,, \\
-\mathcal{L}_{\mathrm{NC}} &= \frac{g}{2\cos\theta_W} \sum_{\ell} \bar{\nu}_{L,\ell} \gamma^{\mu} \nu_{L,\ell} Z_{\mu}^{0}\,.
\end{aligned}
\tag{2.59}
$$

In the mass basis, the CC interaction takes the form

$$
-\mathcal{L}_{\mathrm{CC}} = \frac{g}{\sqrt{2}} (\bar{e}_L, \bar{\mu}_L, \bar{\tau}_L) \gamma^{\mu} U (\nu_1, \nu_2, \nu_3\ \ldots, \nu_{n+3})^T\, W_{\mu}^{+} + \text{h.c.}\,, \tag{2.60}
$$

where $U$ is a $3 \times (3+n)$ matrix with $UU^{\dagger} = I_{3\times 3}$ if $n = 3$, but in general $U^{\dagger}U \neq I_{(n+3)\times(n+3)}$ [39–41]. The structure of the mixing matrix $U$ can be obtained by comparing $-\mathcal{L}_{\mathrm{CC}}$ in the mass and interaction bases, using Eqs. (2.54) and (2.52) for neutrinos, and expressing the weak-doublet components of the charged lepton fields as

$$
\ell^I_{L,i} = P_L \sum_{j=1}^{3} V^{\ell}_{ij}\, \ell_j\,. \tag{2.61}
$$

The resulting form of $U$ is given by [18]

$$
U_{ij} = \mathcal{P}_{\ell,ii} V^{\ell\,\dagger}_{ik} V^{\nu}_{kj} (\mathcal{P}_{\nu,jj})\,, \tag{2.62}
$$

where $\mathcal{P}_{\ell,\nu}$ are diagonal $3 \times 3$ matrices absorbing unphysical phases. The matrix $U$

[5]The NC interactions determines the decay width of the $Z$ boson into light ($m_{\nu} \leq M_Z/2$) left-handed neutrino states. Thus, from the measurement of the total decay width of the $Z$ one can infer the number of such states. At the present, the measurement implies $N_{\nu} = 2.984 \pm 0.008$ [18].

contains a total of $5n+4$ (Dirac) or $6(n+1)$ (Majorana) real parameters, with $3(n+1)$ angles and $2n+1$ (Dirac) or $3(n+1)$ (Majorana) physical phases.

For the case of $n = 0$ (3 Majorana neutrinos), the mixing matrix $U$ is similar to the CKM matrix for quarks and has six independent parameters. It can be parameterized as

$$U = \begin{pmatrix} 1 & 0 & 0 \\ 0 & c_{23} & s_{23} \\ 0 & -s_{23} & c_{23} \end{pmatrix} \cdot \begin{pmatrix} c_{13} & 0 & s_{13}e^{-i\delta_{CP}} \\ 0 & 1 & 0 \\ -s_{13}e^{-i\delta_{CP}} & 0 & c_{13} \end{pmatrix} \cdot \begin{pmatrix} c_{12} & s_{12} & 0 \\ -s_{12} & c_{12} & 0 \\ 0 & -s_{23} & 1 \end{pmatrix} \cdot \begin{pmatrix} e^{i\eta_1} & 0 & 0 \\ 0 & e^{i\eta_2} & 0 \\ 0 & 0 & 1 \end{pmatrix} , \tag{2.63}$$

where $c_{ij} = \cos\theta_{ij}$, $s_{ij} = \sin\theta_{ij}$, $\theta_{ij} \in [0, \pi/2]$, and $\delta_{CP}, \eta_i \in [0, 2\pi]$. If the 3 neutrinos are Dirac, the Majorana phases $\eta_1$ and $\eta_2$ can be absorbed, resulting in a matrix similar to the CKM matrix with just one phase, often called the Pontecorvo-Maki-Nakagawa-Sakata (PMNS) mixing matrix [42, 43]. When the charged leptons have no other interactions besides the SM ones, their interaction eigenstates can be identified with the corresponding mass eigenstates up to phase redefinition.

#### 2.4.2.3 Neutrino oscillations

Neutrino masses and lepton flavor mixing lead to the non-conservation of lepton flavor during neutrino propagation. This phenomenon is known as *neutrino oscillations* and has been extensively studied [42, 44–46]. In this discussion, we focus on vacuum oscillations, which are the simplest case, although matter effects become important when neutrinos travel through dense media. For a comprehensive review, we refer the reader to Ref. [18].

The concept of neutrino oscillations is based on the idea that a weak eigenstate $\nu_\alpha$, typically produced through a CC interaction with a charged lepton $\ell_\alpha$, is actually a linear combination of mass eigenstates $\nu_i$

$$|\nu_\alpha\rangle = \sum_{i=1}^{n} U^*_{\alpha i} \, |\nu_i\rangle \ , \tag{2.64}$$

where $n$ here is the number of light neutrino species. After traveling a distance $L \simeq ct$, the state evolves as

$$|\nu_\alpha(t)\rangle = \sum_{i=1}^{n} U_{\alpha i}^* \; |\nu_i(t)\rangle \; . \tag{2.65}$$

If this neutrino undergoes a CC interaction, producing a charged lepton $\ell_\beta$ via $\nu_\alpha(t)N' \to \ell_\beta N$, the transition probability is given by

$$P_{\alpha\beta} = |\big\langle \nu_\beta | \nu_\alpha(t) \big\rangle|^2 = |\sum_{i=1}^{n}\sum_{j=1}^{n} U_{\alpha i}^* U_{\beta j} \big\langle \nu_i | \nu_j(t) \big\rangle|^2 \, . \tag{2.66}$$

Assuming that $|\nu_i\rangle$ is a plane wave, with $|\nu_i(t)\rangle = e^{-iE_i t}\,|\nu_i(0)\rangle$, where $m_i$ is the mass and $E_i = \sqrt{p_i^2 + m_i^2} \simeq p + m_i^2/(2p)$ is the energy of the relativistic neutrino mass eigenstate $\nu_i$ (using $p_i \simeq p_j \equiv p \simeq E$), we can express Eq. (2.66) as [18]

$$\begin{aligned} P_{\alpha\beta} =& \delta_{\alpha\beta} - 4\sum_{i<j}^{n} \mathrm{Re}[U_{\alpha i} U_{\beta i}^* U_{\alpha j}^* U_{\beta j}] \, \sin^2 X_{ij} \\ &+ 2\sum_{i<j}^{n} \mathrm{Im}[U_{\alpha i} U_{\beta i}^* U_{\alpha j}^* U_{\beta j}] \, \sin{(2X_{ij})} \, , \end{aligned} \tag{2.67}$$

where we used the orthogonality of the mass eigenstates, $\big\langle \nu_j | \nu_i \big\rangle$ and

$$X_{ij} = \frac{(m_i^2 - m_j^2)L}{4E} = 1.267 \, \frac{\Delta m_{ij}^2}{\mathrm{eV}^2} \, \frac{L/E}{\mathrm{m/MeV}} \tag{2.68}$$

is the oscillation phase. Notably, the first term in the right-hand-side of Eq. (2.67) is $CP$ conserving, while the last term is $CP$ violating. If we started from an antineutrino state, it is possible to show that we would have ended up with a similar expression for $P_{\alpha\beta}$ but with the exchange $U \to U^*$.

Equation (2.67) exhibits oscillatory behavior in distance, with oscillation lengths

$$L_{0,ij}^{\mathrm{osc}} = \frac{4\pi E}{|\Delta m_{ij}^2|} \, . \tag{2.69}$$

Therefore, neutrinos must have non-zero mass splittings ($\Delta m_{ij}^2 \neq 0$) and non-vanishing mixing elements ($U_{\alpha i} U_{\beta j} \neq 0$) in order to undergo flavor oscillations. Notably, the Majorana phases cancel out in the oscillation probability, as expected due to the total lepton number conservation in flavor oscillations.

Observations of neutrino oscillations across various experiments have provided compelling evidence that requires the mixing between the three flavor neutrinos in three distinct mass eigenstates [18]. There are two possible orderings for the neutrino mass spectrum:

- Normal ordering (NO), with $m_1 < m_2 < m_3$;
- Inverted ordering (IO) with $m_3 < m_1 < m_2$.

The data also indicate a hierarchy in the mass splittings, with $\Delta m_{21}^2 \ll |\Delta m_{31}^2| \simeq |\Delta m_{32}^2|$. Based on the value of the lightest neutrino mass, the neutrino mass spectrum can be classified as:

- Normal hierarchy (NH): $m_1 \ll m_2 < m_3$, with approximate values of $m_2 \simeq 8.6 \times 10^{-3}$ eV ($\sim \sqrt{\Delta m_{21}^2}$) and $m_3 \simeq 0.05$ eV ($\sim \sqrt{\Delta m_{32}^2 + \Delta m_{21}^2}$).
- Inverted hierarchy (IH): $m_3 \ll m_1 < m_2$, with approximate values of $m_1 \simeq 0.0492$ eV ($\sim \sqrt{\Delta m_{32}^2 + \Delta m_{21}^2}$) and $m_2 \simeq 0.05$ eV ($\sim \sqrt{|\Delta m_{32}^2|}$).
- Quasi-degenerate spectrum: $m_1 \simeq m_2 \simeq m_3 \gg \sqrt{|\Delta m_{32}^2|}$.

### 2.4.3 Dark matter

The multitude of evidence for DM, as discussed in section 1.5, supports the existence of a non-baryonic matter species that is electromagnetically neutral, gravitationally interacting, stable, and has negligible velocities for structure formation. This type of matter is known as cold DM (CDM). In the framework of the ΛCDM model, CDM contributes to approximately 27% of the critical density of the Universe, or about 85% of the total matter density. However, only a small fraction of DM, ranging from at least around 0.5% (based on neutrino oscillations) to at most about 1.5% (from combined cosmological constraints), is accounted by the three SM neutrinos [18], whereas the fundamental nature of the majority of DM remains unknown.

#### 2.4.3.1 Popular candidates

Numerous beyond the SM (BSM) theories have been proposed to explain DM [18]. Some of these models are considered more motivated due to their potential solutions to other particle physics problems or their ability to explain anomalous experimental or observational signals.

One extensively studied class of DM candidates is Weakly Interacting Massive Particles (WIMPs), which arise in many BSM theories addressing the hierarchy problem [6] and provide a simple mechanism to explain the observed relic abundance via thermal freeze-out, which we will describe in section 2.5.3. Perhaps the most notable example of WIMP is the neutralino, which arises in the context of the minimal supersymmetric extension of the SM (MSSM) and it is a mixture of the Higgses and electroweak gauge bosons superpartners [49]. WIMPs were and are still very popular DM candidates because their mass is predicted to lie close to the electroweak scale and hence they might be produced in particle accelerators or colliders (see next subsection).

Another well-studied DM candidates are axions. Initially introduced to solve the strong $CP$ problem in QCD [50], axions were found to be capable of accounting for all of DM [51, 52] for masses in the range $m_a \in [10^{-6}, 10^{-2}]$ eV [53]. In addition to the QCD axion, string theory predicts a range of axion-like particles (ALPs) with exponentially suppressed masses, making them lighter but still viable as DM candidates [54]. A cosmologically interesting mass scale is around $m_a \sim 10^{-22}$ eV, as it corresponds to a de-Broglie wavelength comparable to the size of the smallest observed gravitationally collapsed structures, which are on the order of a few kpc. These ultra-light bosons, often referred to as wave or *fuzzy DM* candidates, typically exhibit soliton-like cores in the density profile of galaxies. This feature offers a potential solution to the small-scale structure problems encountered in the $\Lambda$CDM model [54] (see section 3.1.5 for further explanation of these issues).

Sterile neutrinos have also been popular DM candidates [55, 56] due to their connection with neutrino mass and mixing problems. The observation of a 3.5 keV X-

[6] The hierarchy problem relies on the question of why the electroweak scale, described by the Higgs VEV $v \simeq 246$ GeV, is much smaller than the Planck scale $M_{Pl} \sim 10^{19}$ GeV [47, 48].

ray line in some galaxy clusters [57, 58] and the galactic center [59] sparked interest in sterile neutrinos as DM candidates, but the absence of the signal in other clusters [60] and dwarf galaxies [61, 62] has cast doubts on its origin.

Other extensively studied DM candidates include light vector bosons like "dark photons" [63] and models with rich dark sectors like mirror DM [64, 65].

The search for DM can be divided into three categories based on the nature and interactions of the DM candidate with SM particles: collider searches, direct detection, and indirect detection. These strategies will be briefly described next.

#### 2.4.3.2 Collider searches

Assuming that DM interacts with SM particles through additional interactions apart from gravity and has a mass around the electroweak scale, it is possible for DM to be produced in particle accelerators and colliders. Extensive searches for DM have been conducted by the CMS and ATLAS collaborations at the LHC in *pp* collisions [66, 67].

The typical signature involves missing energy and momentum at the interaction vertices, during particle reconstruction. This arises due to the feeble interaction between SM and DM particles, allowing the latter to evade detection once produced. Other signals may manifest as peaks in di-jet or di-lepton invariant mass distributions, or excesses of events in the di-jet angular distribution caused by DM mediators [66].

So far, no significant signal for DM has been observed in the LHC experiments [18]. Instead, limits have been set on DM masses, couplings, and cross-sections. The latter can be compared, usually in a model-dependent manner, with direct detection experiments [68].

#### 2.4.3.3 Direct detection

Direct detection experiments aim to observe the recoil energy resulting from elastic or inelastic scattering of galactic DM particles with atomic nuclei or electrons in the detector material [69, 70]. The predicted event rate depends on the DM mass $m_\chi$, scattering cross section $\sigma_s$, and astrophysical parameters such as the local DM density $\rho_0 \equiv \rho_\odot$, velocity distribution $f(\vec{v})$, circular speed $v_{\mathrm{circ}}$, and escape velocity $v_{\mathrm{esc}}$.

The local DM density, denoted as $\rho_0$, is an average over a volume of a few hundred parsecs in the Solar neighbourhood, distant $r_\odot \simeq 8.5$ kpc from the Galactic centre and it can be determined using two techniques [71]:

1. Local measures, which rely on the vertical motion of tracer stars near the Sun;

2. Global measures, which extrapolate $\rho_0$ from the measured rotation curve, with assumptions about the Galactic halo shape.

Recent determinations from global methods give $\rho_0 \in (0.2 - 0.6)$ GeV/cm$^3$, while local techniques yield $\rho_0 \in (0.3 - 1.5)$ GeV/cm$^3$, considering the main uncertainty due to the contribution of baryons to the local dynamical mass of our Galaxy [18].

The circular speed of the Milky Way, denoted as $v_{\rm circ}$, is inferred from the Sun's velocity relative to the Galactic center and local radial force measurements. These methods give $v_{\rm circ} \in (218 - 246)$ km/s [18]. The escape velocity has been estimated to be $v_{\rm esc} = 533^{+54}_{-41}$ km/s [72].

The local velocity distribution, denoted as $f(\vec{v})$, of DM particles cannot be directly measured. It is typically derived from simulations. In many experiments, the analysis is based on the Standard Halo Model (SHM), which assumes an isotropic, isothermal sphere of DM with a density profile of $\rho(r) \propto r^{-2}$. The velocity distribution in the SHM is Maxwellian, with a velocity dispersion $\sigma_v = v_{\rm circ}/2$, and is truncated at the escape velocity $v_{\rm esc}$ [73]. Recent measurements from the Gaia satellite support the SHM when additional anisotropies are included [74, 75].

The event rate for DM scattering off nuclei can be described by the differential scattering rate $R$ as a function of nuclear recoil energy $E_R$ [76, 77]

$$\frac{dR(E_R,t)}{dE_R} = N_T \frac{\rho_0}{m_\chi} \int_{v_{\rm min}}^{v_{\rm esc}} d^3v\, |\vec{v}| f(\vec{v} + \vec{v}_\oplus(t))\, \frac{d\sigma_s}{dE_R} \,. \qquad (2.70)$$

Here, $N_T$ is the number of target nuclei with mass $m_N$, $v$ represents the particle speed in the experiment's rest frame, and $f(\vec{v} + \vec{v}\oplus(t))$ is the velocity distribution in the Earth's frame. The quantity $v_{\rm min}$ corresponds to the minimum DM velocity required to produce a recoil energy $E_R$. For elastic scattering, it can be estimated as $v_{\rm min} =$

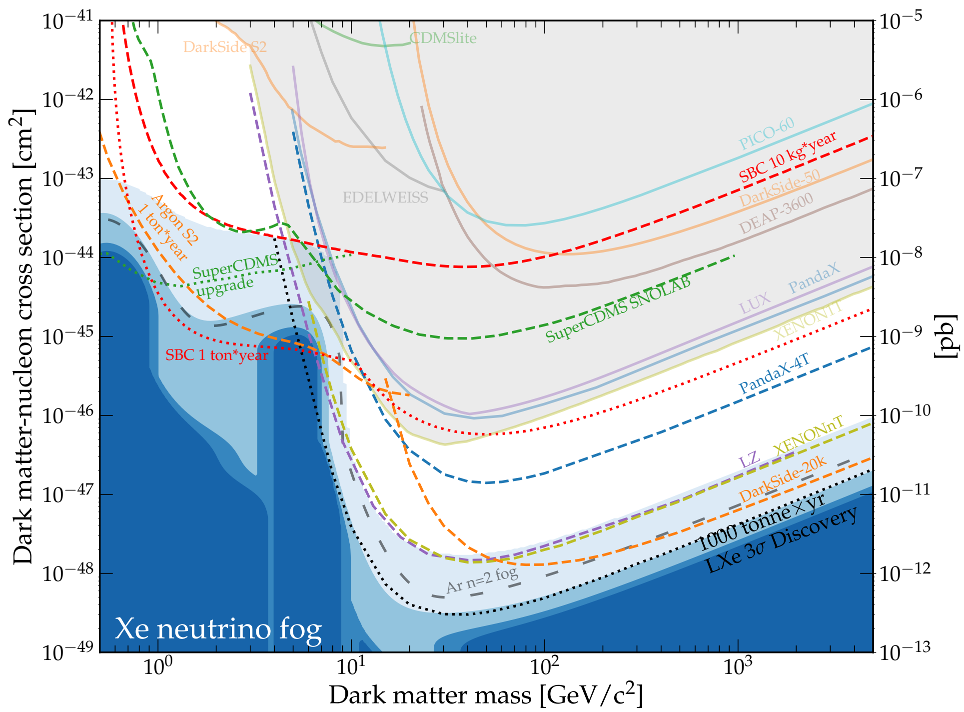


Figure 2.3: Upper limits on the SI DM-nucleon scattering cross section as a function of the DM mass. The shaded gray region represents the currently excluded parameter space, while the dashed curve represents the expected 90% C.L. exclusion sensitivity of upcoming and future experiments. Note that $1, \mathrm{b} \equiv 1, \mathrm{barn} = 10^{-24}, \mathrm{cm}^2$. Figure taken from [78].

$\sqrt{m_N E_R / 2m_r^2}$, where $m_r = (m_N\, m_\chi)/(m_N + m_\chi)$ is the reduced mass. For inelastic scattering, with nuclear excitation energy $E^*$, it becomes $v_{\min} = \sqrt{m_N E_R / 2m_r^2} + E^*/\sqrt{2 m_N E_R}$.

The differential cross section in Eq. (2.70) can be expressed as

$$\frac{d\sigma_s(E_R, v)}{dE_R} = \frac{m_N}{2m_r^2 v^2}\left[\sigma_0^{\mathrm{SI}} F_{\mathrm{SI}}^2(E_R) + \sigma_0^{\mathrm{SD}} F_{\mathrm{SD}}^2(E_R)\right], \tag{2.71}$$

where the first term represents the spin-independent (SI) contribution, associated with the charge/mass coupling of the nucleus, and the second term represents the spin-dependent (SD) contribution, related to the DM particle's coupling to the nucleus spin. The nuclear form factors $F^2(E_R)$ account for the nucleus substructure and are calculated in Refs. [79, 80], while $\sigma_0$ denotes the cross sections at zero momentum transfer, $q = \sqrt{2 m_N E_R} \sim 0$. The cross sections $\sigma_0$ are often expressed in terms of single-nucleon cross sections and effective couplings of the DM particle to protons and neutrons. Figure 2.3 illustrates recent limits on the SI DM-nucleon scattering cross section.

Searches for DM-nucleus scattering become less sensitive for DM particle masses below the GeV scale, due to energy thresholds typically in the range of a few hundred eV to a few keV. An alternative approach is to search for DM scattering off bound electrons, enabling the transfer of the entire kinetic energy to the material [81]. This allows for deriving constraints on the DM-electron scattering cross section $\sigma_{e\chi}$ by comparing observed counts to expected background ones [82].

#### 2.4.3.4 Indirect detection

Indirect detection aims to detect the products of DM annihilation or decay, such as photons, neutrinos, and antimatter particles.

The production rate of these particles depends on the annihilation cross section $\langle \sigma_a v \rangle$ or decay rate $\tau_\chi$, the density of DM particles $\rho_\chi$ in the region of interest, and the number of final-state particles $N_f$ produced. For a final-state particle $f$, the production rate per unit volume from DM annihilation $\Gamma_f^A$ or decay $\Gamma_f^D$ is given by [18]

$$\Gamma_f^A = \frac{1}{4} \frac{\rho_\chi^2}{m_\chi^2} \langle \sigma_a v \rangle N_f^A \,, \tag{2.72}$$

$$\Gamma_f^D = \frac{\rho_\chi}{m_\chi} \frac{1}{\tau_\chi} N_f^D \,, \tag{2.73}$$

where $m_\chi$ is the DM mass. The thermally-averaged cross section for DM annihilation times relative velocity is denoted by $\langle \sigma_a v \rangle$, which will be defined later in Eq. (2.97). Equation (2.72) should be multiplied by a factor of 2 if the DM particle is its own antiparticle.

The flux of photons and neutrinos from DM annihilation or decay is obtained by integrating the production rate $\Gamma_f$ over the appropriate angular region $\Delta\Omega$ along the line of sight [7]

$$\Phi_f = \frac{dN_f}{dtdA} = \int_{\Delta\Omega} \frac{d\Omega}{4\pi} \int_{\text{l.o.s.}} d\ell \, \Gamma_f \, . \tag{2.74}$$

Typically, this expression is divided into a particle physics factor, dependent on $m_\chi$ and $\langle \sigma_a v \rangle$ or $\tau_\chi$, and an astrophysical factor that only depends upon the observational target. The astrophysical factor is often referred to as the $J$-factor and denoted as $J_{\Delta\Omega}(\psi)$, where $\psi$ indicates the direction of the line of sight. It is defined as [84]

$$J_{\Delta\Omega}(\psi) = \int_{\Delta\Omega} \int_{\text{l.o.s.}\,(\psi)} d\ell \, \mathrm{d}\Omega \, \rho_\chi^2(\ell, \Omega) \, . \tag{2.75}$$

Searches for DM annihilation or decay products focus on targets with large $J$-factors, which correspond to regions expected to be DM-dominated with high $\rho_\chi$ and provide a high signal-to-noise ratio. Examples include nearby dwarf galaxies and the inner region of the Milky Way. By accurately modeling the astrophysical background, constraints on the DM mass versus annihilation cross section or decay rate can be derived if no excess observation is made.

As regards the DM density profile $\rho_\chi$, its shape can be derived from numerical simulations. N-body simulations containing only CDM particles, similar to those discussed in section 1.5.4, have found that the DM density distribution inside galaxies appears to be approximately universal and well-modeled by the Navarro-Frenk-White (NFW) profile [85]

$$\rho_{\text{NFW}}(r) = \frac{\rho_s}{\left(\dfrac{r}{r_s}\right)\left(1 + \dfrac{r}{r_s}\right)^2} \, , \tag{2.76}$$

where $r_s$ is the scale radius and $\rho_s$ is the scale density. Another frequently profile used in literature is the Einasto profile [86]

$$\rho_{\text{Ein}}(r) = \rho_s \exp\left\{ -\frac{2}{\alpha}\left[\left(\frac{r}{r_s}\right)^\alpha - 1\right]\right\} . \tag{2.77}$$

Although both the NFW ('cuspy') and Einasto ('mild') profiles are preferred by DM-

[7]The differential flux is obtained as $d\Phi_f/dE$, so the quantity $N_f$ in Eqs. (2.72) and (2.73) should be replaced by the differential flux $dN_f/dE$ at the production site, considering the appropriate redshift for cosmologically distant sources (see Ref. [83]).

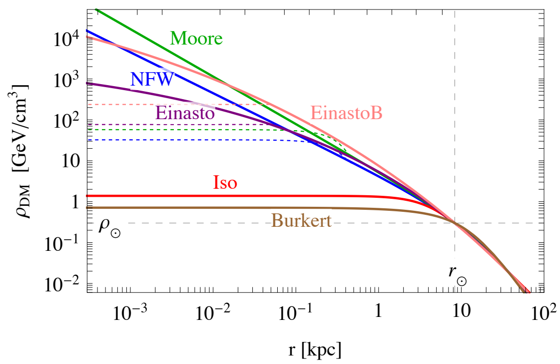


| DM halo | $\alpha$ | $r_s$ [kpc] | $\rho_s$ [GeV/cm$^3$] |
|---|---|---|---|
| NFW | – | 24.42 | 0.184 |
| Einasto | 0.17 | 28.44 | 0.033 |
| EinastoB | 0.11 | 35.24 | 0.021 |
| Isothermal | – | 4.38 | 1.387 |
| Burkert | – | 12.67 | 0.712 |
| Moore | – | 30.28 | 0.105 |

Figure 2.4: *Left:* Comparison of four DM density profiles for the Milky Way: cupsy (NFW, Moore [88]), mild (Einasto), smooth (Isothermal, Burkert), and steeper (EinastoB). *Right:* Table of scale radius $r_s$ and characteristic density $\rho_s$ values for the six profiles depicted in the figure, describing the DM density distribution of the Milky Way. Figure and values taken from Ref. [89].

only simulations, the inclusion of baryons can alter the inner slope of the profile, resulting in smoother profiles like the Burkert [87] and the modified isothermal profiles [84]

$$\rho_{\rm Burk}(r) = \frac{\rho_s}{\left(1+\dfrac{r}{r_s}\right)\left[1+\left(\dfrac{r}{r_s}\right)^2\right]}, \qquad \rho_{\rm Iso}(r) = \frac{\rho_s}{1+\left(\dfrac{r}{r_s}\right)^2}. \tag{2.78}$$

These profiles are compared for the Milky Way in Figure 2.4. Importantly, they are normalized to the same density $\rho_0$ at the location of the Sun. This means that the choice of DM halo profile does not impact constraints from direct detection experiments, but it does affect indirect detection limits.

Although the slope of the DM density profile is expected to increase from the outer regions to the center of a galaxy, the exact power-law index in the innermost regions remains uncertain. This unknown is related to the so-called core-cusp problem, which we will present in section 3.1.5.

### 2.4.4 Dark energy

As found in sections 1.6 and 2.4, current measurements support the idea that dark energy can be described by a cosmological constant $\Lambda$. However, this is the simplest possibility and other options exist [90, 91].

One possibility is to treat $\Lambda$ as a dynamical quantity by attributing its energy density to a scalar field potential $V(\phi)$, known as quintessence [92, 93]. Another option is to modify GR itself, altering the behavior of gravity to explain the Universe acceleration [94]. Interestingly, many dark energy models in the literature can effectively be described by a perfect fluid with a time-dependent equation of state $w_{\rm DE}(a)$, as generally defined by Eq. (2.24) [3]. These models satisfy the continuity equation, whose solution is given by Eq. (2.28), and can be characterized by the energy-momentum tensor of a perfect fluid (see Eq. (2.22)).

For the cosmological constant case, $P_\Lambda = -\rho_\Lambda \propto \Lambda$, resulting in $w_\Lambda = -1$. In dynamical dark energy scenarios like quintessence, $w_{\rm DE}$ can exceed $-1$ but remains significantly below zero. By measuring the dark energy density at different cosmic times (redshifts), we can constrain $w_{\rm DE}$ and distinguish between various dark energy scenarios.

## 2.5 Thermodynamics in an expanding Universe

### 2.5.1 Basic definitions

In section 2.3, we discussed the energy density and pressure of cosmological species modeled as perfect fluids without providing a formal definition of these quantities.

For a weakly interacting gas of particles $i$ with mass $m_i$ and internal degrees of freedom $g_i$, the number density $n_i$, energy density $\rho_i$, and pressure $P_i$ can be expressed in terms of the phase-space distribution function $f_i(\vec{p})$ [1]

$$
\begin{aligned}
n_i &= \frac{g_i}{(2\pi)^3} \int d^3p\, f(\vec{p})\,, \\
\rho_i &= \frac{g_i}{(2\pi)^3} \int d^3p\, E_i(\vec{p})\, f(\vec{p})\,, \\
P_i &= \frac{g_i}{(2\pi)^3} \int d^3p\, \frac{|\vec{p}|^2}{3E_i}\, f(\vec{p})\,,
\end{aligned}
\tag{2.79}
$$

where $E_i = \sqrt{|\vec{p}|^2 + m_i^2}$. In the case of *kinetic equilibrium*, the phase-space distribu-

| Limit | Particle type | $n_i$ | $\rho_i$ | $P_i$ |
|---|---|---|---|---|
| $m_i, \mu_i \ll T$ | Bosons | $\frac{\zeta(3)}{\pi^2} g_i T^3$ | $\frac{\pi^2}{30} g_i T^4$ | $\frac{\rho_i}{3}$ |
| | Fermions | $\frac{3}{4}\frac{\zeta(3)}{\pi^2} g_i T^3$ | $\frac{7}{8}\frac{\pi^2}{30} g_i T^4$ | $\frac{\rho_i}{3}$ |
| $m_i \gg T$ | Bosons | $g_i \left(\frac{m_i T}{2\pi}\right)^{3/2} e^{-\frac{m_i}{T}}$ | $m_i$ | $n_i T \ll \rho_i$ |
| | Fermions | $g_i \left(\frac{m_i T}{2\pi}\right)^{3/2} e^{-\frac{m_i}{T}}$ | $m_i$ | $n_i T \ll \rho_i$ |

Table 2.1: Solution for particle number density $n_i$, energy density $\rho_i$, and pressure $P_i$ for species $i$ in the relativistic ($m_i, \mu_i \ll T$) and non-relativistic ($m_i \gg T$) limits. In the non-relativistic regime, bosons and fermions behave similarly, following the Maxwell-Boltzmann distribution for $n_i$. $\zeta$ is the Riemann Zeta function and $\zeta(3) \approx 1.2$.

tion $f_i$ follows either the Fermi-Dirac or Bose-Einstein distributions

$$f_i(\vec{p}) = \frac{1}{\exp\left[(E_i - \mu_i)/T\right] \pm 1}\,, \tag{2.80}$$

with $+1$ for bosons and $-1$ for fermions. The chemical potential $\mu_i$ represents the energy required to change the particle number by one unit. If the species is in *chemical equilibrium*, the chemical potential $\mu_i$ is related to those of other participating species in the interaction. For example, in the case of the reaction $i + j \leftrightarrow k + l$, the chemical equilibrium condition is given by $\mu_i + \mu_j = \mu_k + \mu_l$.

The equilibrium distributions in Eq. (2.80) allow us to calculate the number density, energy density, and pressure of species $i$. Two important limits can be explicitly solved: the relativistic limit ($m_i \ll T$) and the non-relativistic limit ($m_i \gg T$) [2, 4, 95]. The results are summarized in Table 2.1. Notably, relativistic particles significantly contribute to the total number density, while non-relativistic particles become cosmologically irrelevant as the Universe cools down. This confirms the dominance of radiation in the early Universe, as discussed in section 2.3.

In the presence of multiple species with temperatures $T_i$ in the thermal bath, it is convenient to express the total energy density and pressure in terms of the photon

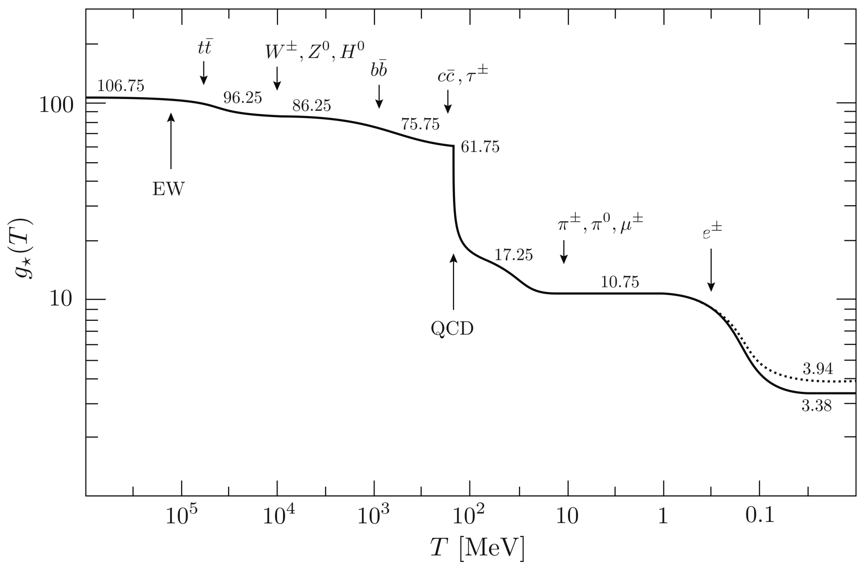


Figure 2.5: Evolution of the relativistic degrees of freedom $g_\star(T)$, defined in Eq. (2.82), assuming the SM particle content. At energies above the Higgs mass, we have $g_b \equiv \sum_{i=\text{bosons}} g_i = 28$, accounting for photons (2), $W^\pm$ and $Z$ bosons $(3\cdot 3)$, gluons $(8\cdot 2)$, and the Higgs boson (1). Similarly, $g_f \equiv \sum_{i=\text{fermions}} g_i = 90$ due to quarks $(6 \cdot 12)$, charged leptons $(3 \cdot 4)$, and neutrinos $(3 \cdot 2)$. The total is given by $g_\star = g_b + \frac{7}{8} g_f = 106.75$. The dotted line represents the number of effective degrees of freedom in entropy, $g_{\star s}(T)$ (see Eq (2.87)). Figure taken from [8].

temperature. Neglecting contributions from non-relativistic species, we have

$$\rho_r = \frac{\pi^2}{30} g_\star(T)\, T^4\,, \qquad P_r = \rho_r/3\,, \tag{2.81}$$

where $g_\star$ is the total number of effectively massless degrees of freedom

$$g_\star(T) = \sum_{i=\text{bosons}} g_i \left(\frac{T_i}{T}\right)^4 + \frac{7}{8} \sum_{i=\text{fermions}} g_i \left(\frac{T_i}{T}\right)^4. \tag{2.82}$$

The temperature evolution of $g_\star(T)$ is shown in Fig. 2.5 and depends on the number of relativistic species in thermal equilibrium at temperature $T$. The Hubble parameter during the early radiation-dominated epoch, when the total energy density of the Universe was essentially $\rho_r$, can be derived as [1]

$$H(T) = 1.66 \sqrt{g_\star} \frac{T^2}{M_{Pl}}\,, \qquad t = \frac{1}{2H}\,. \tag{2.83}$$

Equation (2.81) can be conveniently written in terms of the photon contribution plus other relativistic species, such as neutrinos [96, 97]

$$\rho_r = \left[1 + \frac{7}{8}\left(\frac{4}{11}\right)^{4/3} N_{\text{eff}}\right] \rho_\gamma \,, \tag{2.84}$$

where $N_{\text{eff}}$ represents the effective number of relativistic species in the thermal bath. In the SM, with only 3 active neutrino species, $N_{\text{eff}} = 3.044$ [98–100], in agreement with the CMB measured value of $N_{\text{eff}}^{\text{CMB}} = 2.99 \pm 0.17$ [19].

In thermal equilibrium, the entropy per comoving volume $s$,

$$s \equiv \frac{S}{V} = \frac{\sum_{i=\text{species}}(\rho_i + P_i - \mu_i n_i)}{T} \,, \tag{2.85}$$

remains constant and is approximately given by

$$s = \frac{2\pi^2}{45} g_{\star s}(T)\, T^3 \,, \tag{2.86}$$

where $g_{\star s}(T)$ is defined as

$$g_{\star s}(T) = \sum_{i=\text{bosons}} g_i \left(\frac{T_i}{T}\right)^3 + \frac{7}{8} \sum_{i=\text{fermions}} g_i \left(\frac{T_i}{T}\right)^3 . \tag{2.87}$$

It is worth noting that if $T_i = T$ for all relativistic particles $i$, then $g_\star = g_{\star s}$, which is generally verified in the early Universe as shown in Fig. 2.5. Additionally, the quantity $s$ in Eq. (2.86) is related to the number density $n$ of relativistic particles (see Table 2.1) and one finds that $s = 1.80\, g_{\star s} n_\gamma$, so that today $s = 7.04\, n_\gamma$. [8]

### 2.5.2 The Boltzmann equation

During the early stages of the Universe, a significant portion of its constituents were in thermal equilibrium, allowing for an equilibrium description to be a valid approximation. However, there were notable departures from thermal equilibrium, including

[8]The baryon asymmetry of the Universe $\eta$ is defined as the ratio between the difference in the number density of baryons and anti-baryons and either the entropy density $s$ or $n_\gamma$. The relation between the two is $s = 7.04\, n_\gamma$. See section 3.1.3.

BBN and photon decoupling. These played a crucial role in the formation of important relics such as the light elements and the CMB.

A rough criterion to determine the coupling or decoupling of a particle species $i$ from the thermal bath relies on comparing its interaction rate per particle, $\Gamma_i$, with the expansion rate of the Universe, $H(t)$. If $\Gamma_i \gtrsim H$, the particle is frequently interacting with the plasma and is considered thermally coupled. Conversely, if $\Gamma_i \lesssim H$, the rapid expansion prevents the particle from encountering others, leading to its decoupling.

While this criterion serves as a useful guideline, a proper treatment of decoupling requires tracking the evolution of the particle's phase-space distribution function, $f_i(p^\mu, x^\mu)$, governed by the *Boltzmann equation*

$$\hat{L}[f_i] = C[f_i]\,, \tag{2.88}$$

where $C[f_i]$ is the collision operator and $\hat{L}$ is the Liouville operator. In the non-relativistic regime, the Liouville operator for the phase-space density $f_i(\vec{v}, \vec{r})$ of a particle species of mass $m_i$ subject to a force $\vec{F} = d\vec{p}/dt$ takes the form [1]

$$\hat{L}_{\rm NR} = \frac{d}{dt} + \frac{d\vec{x}}{dt}\cdot\vec{\nabla}_x + \frac{d\vec{v}}{dt}\cdot\vec{\nabla}_v = \frac{d}{dt} + \vec{v}\cdot\vec{\nabla}_x + \frac{\vec{F}}{m_i}\cdot\vec{\nabla}_v\,. \tag{2.89}$$

Its covariant relativistic generalization is

$$\hat{L}_{\rm GR} = p^\alpha\partial_\alpha - \Gamma^\alpha_{\mu\nu}p^\mu p^\nu\partial_\alpha\,, \tag{2.90}$$

where the gravitational effects enter through the Christoffel symbol, as we might expect from section 2.2.

In a spatially homogeneous and isotropic Universe, the Boltzmann equation (2.88) reduces to a familiar form when integrated over the particle momentum, resulting in

$$\dot{n}_i + 3Hn_i = \frac{g_i}{(2\pi)^3}\int\frac{d^3p}{E_i}\,C[f_i]\,, \tag{2.91}$$

with $n_i$ the particle number density defined in Eq. (2.79), and the over-dot means time-derivative.

The collision term for a simple process $i + j \leftrightarrow k + l$ involving species $i$, $j$, $k$, and $l$, is expressed by [6]

$$\begin{aligned}\frac{g_i}{(2\pi)^3}\int\frac{d^3p}{E_i}\,C[f_i] =& g_i g_j g_k g_l \int\frac{d^3p}{(2\pi)^3 2E_i}\int\frac{d^3p_j}{(2\pi)^3 2E_j}\int\frac{d^3p_k}{(2\pi)^3 2E_k}\int\frac{d^3p_l}{(2\pi)^3 2E_l}\\ &(2\pi)^4\delta^{(3)}(\vec{p}+\vec{p}_j-\vec{p}_k-\vec{p}_l)\delta(E_i+E_j-E_k-E_l)|\mathcal{M}|^2\\ &\left[f_k f_l(1\pm f_i)(1\pm f_j)-f_i f_j(1\pm f_k)(1\pm f_l)\right],\end{aligned} \tag{2.92}$$

where $|\mathcal{M}|^2$ is the square of the matrix element, averaged over initial and final spins, and the four-dimensional delta function enforces energy and momentum conservation. Moreover, the terms containing the $\pm$ sign are called blocking and stimulated emission factors and the $+$ sign applies to bosons, whereas the $-$ sign to fermions.

The terms in the collision term have distinct interpretations: the $3Hn_i$ term represents the dilution effect due to cosmic expansion, while the right-hand side captures interactions that alter the particle number density $n_i$. In the absence of interactions, the solution to the Boltzmann equation follows the expected behavior, with $n_i \propto a^{-3}$, where $a$ is the scale factor. The generalization to the collision term above in the case of more than two initial and final state particles can be found in Ref. [1].

To account for the expansion of the Universe, it is useful to consider the dimensionless comoving number density $Y_i \equiv n_i/s$, where $s$ is the entropy density defined by Eq. (2.86). This scaling allows us to remove the effect of cosmic expansion. By introducing the dimensionless rescaled time variable $x \equiv m_i/T$, the Boltzmann equation (2.91) during the radiation-dominated era can be simplified as follows

$$\frac{dY}{dx} = \frac{x}{H(m_i)s}\,\frac{g_i}{(2\pi)^3}\int\frac{d^3p}{E_i}\,C[f_i]\,, \tag{2.93}$$

where $H(m_i) = x^2 H(T)$, and $H(T)$ is given by Eq. (2.83).

With this formalism in place, we can now apply it to well-known examples, starting with the thermal decoupling of heavy particles, such as WIMPs, known as "thermal freeze-out" mechanism.

### 2.5.3 Thermal freeze-out

Let us consider a heavy, stable particle $\chi$ and its antiparticle $\bar{\chi}$, with mass $m_\chi$, both subjected to thermal equilibrium governed by the annihilation and pair-production processes

$$\chi\bar{\chi} \leftrightarrow f\bar{f}\,, \tag{2.94}$$

where $f$ and $\bar{f}$ represent lighter SM particles with zero chemical potentials. We assume a symmetric abundance between $\chi$ and $\bar{\chi}$, denoted as $n$, and $g_\chi$ represents the number of degrees of freedom for $\chi$ [9]. The Boltzmann equation (2.91) for the number density takes the form [1, 101, 102]

$$\dot{n} + 3Hn = -\langle\sigma_a v\rangle[n^2 - n_{\rm eq}^2]\,, \tag{2.95}$$

whereas for the dimensionless comoving density $Y = n/s$ is [1]

$$\frac{dY}{dx} = -\frac{xs\langle\sigma_a v\rangle}{H(m_\chi)}[Y^2 - Y_{\rm eq}^2]\,. \tag{2.96}$$

Here, $\langle\sigma_a v\rangle$ is the annihilation cross-section multiplied by the relative velocity averaged over the thermal distribution of $\chi$ particles. The expression for $\langle\sigma_a v\rangle$ involves the integral over the Mandelstam variable $s = (p_1^\mu + p_2^\mu)^2$, if the annihilation process in question is $1 + 2 \to 3 + 4$. Its general form is [101]

$$\langle\sigma_a v\rangle = \frac{1}{8m_\chi^2 T K_2^2(m_{\chi/T})}\int_{4m_\chi^2}^{\infty} ds\,\sqrt{s}(s - 4m_\chi^2)K_1(\sqrt{s}/T)\,\sigma_a(s)\,, \tag{2.97}$$

where $K_i$ are the modified Bessel functions of the second kind, and the cross section $\sigma_a$ depends on the particle physics model describing the annihilation. See Ref. [103] for some examples. For non-relativistic species, an approximate expression for $\langle\sigma_a v\rangle$

[9] The number of degrees of freedom is $g_\chi = 1$ for a real scalar, 2 for a complex scalar or a Weyl fermion (like a Majorana fermion), or 4 for a Dirac fermion.

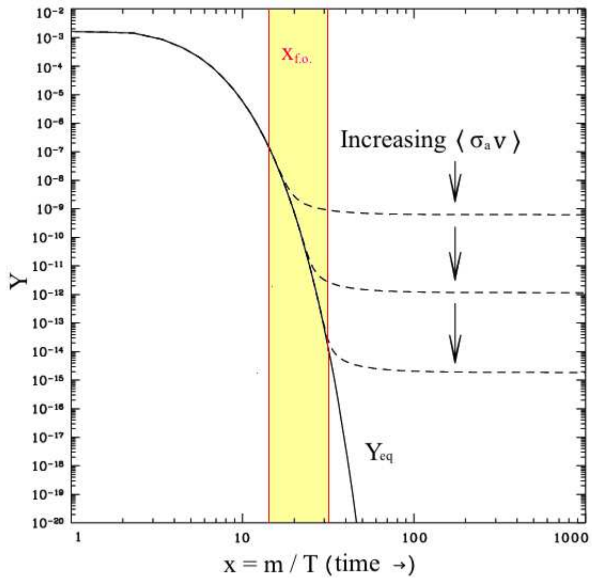


Figure 2.6: Evolution of the co-moving number density $Y$ of the DM particle $\chi$ with respect to the rescaled time variable $x = m_\chi/T$ during the epoch of DM thermal decoupling/freeze-out. Figure adapted from Ref. [104].

can be used instead

$$\langle\sigma_a v\rangle \approx \frac{\int\int d^3p_1 d^3p_2\, \sigma_a |\vec{v}_1 - \vec{v}_2|\, e^{-E_1/T} e^{-E_2/T}}{\int\int d^3p_1 d^3p_2\, e^{-E_1/T} e^{-E_2/T}}\,, \tag{2.98}$$

where we approximated the equilibrium number density $n_{\rm eq}$ as the Maxwell-Boltzmann distribution (see non-relativistic limit in Table 2.1). The quantity $Y_{\rm eq}$ is given by [103]

$$Y_{\rm eq}(x) = \frac{45}{4\pi^2}\frac{g_\chi}{g_{\star s}} x^2 K_2(x) \simeq \frac{45}{2\pi^4}\sqrt{\frac{\pi}{8}}\frac{g_\chi}{g_{\star s}} x^{3/2} e^{-x}\,, \tag{2.99}$$

where the last step is valid for $x \gg 1$.

Equation (2.96) is a Ricatti-type equation that does not have an exact closed-form analytical solution. A numerical solution, depicted in Fig. 2.6, is obtained with the initial condition $Y \simeq Y_{\rm eq}$ at $x \simeq 1$. Codes such as `micrOMEGAs` [105] and `DarkSUSY` [106] provide numerical solutions for the Boltzmann equation in various DM models, originally focusing on supersymmetric scenarios.

However, we can gain qualitative insights into the numerical solution by rewriting

Eq. (2.96) in the following suggestive form [1]

$$\frac{x}{Y_{\rm eq}}\frac{dY}{dx} = -\frac{\Gamma_a}{H}\left[\left(\frac{Y}{Y_{\rm eq}}\right)^2 - 1\right], \tag{2.100}$$

where $\Gamma_a \equiv n_{\rm eq}\langle\sigma_a v\rangle$, with $n_{\rm eq}$ being the equilibrium number density of the target DM particles, and we have used $H(T) = x^{-2}H(m_i)$.

In this form, we can see that the change in the comoving density $Y$ is controlled by the parameter $\Gamma_a/H$. As long as $\Gamma_a \gg H$, thermal equilibrium is maintained between $\chi$ and the photon bath, resulting in $Y(x) \simeq Y_{\rm eq}(x)$. However, since $\Gamma_a \propto n_{\rm eq}$ and decreases as the temperature $T$ decreases (see Table 2.1), annihilations become negligible when $\Gamma_a \simeq H$, typically occurring at $x = x_{\rm f.o.} \equiv m_\chi/T_{\rm f.o.}$, where $T_{\rm f.o.}$ is the "freeze-out" temperature. Therefore, we expect $Y(x \gtrsim x_{\rm f.o.}) = Y_{\rm eq}(x_{\rm f.o.})$. This behavior is precisely illustrated in Figure 2.6.

The freeze-out temperature can be naively estimated by the condition $\Gamma_a(x_{\rm f.o.}) \simeq H(x_{\rm f.o.})$. A more accurate approximation was derived in Refs. [1, 107, 108], resulting in

$$x_{\rm f.o.} \approx \ln y_{\rm f.o.} - \frac{1}{2}\ln\ln y_{\rm f.o.}\,, \qquad y_{\rm f.o.} = \frac{g_\chi}{2\pi^3}\sqrt{\frac{45}{8g_\star}}m_\chi M_{Pl}(n+1)\sigma_0\,, \tag{2.101}$$

where the annihilation cross-section is expanded in the low-temperature limit as

$$\langle\sigma_a v\rangle \approx \sigma_0\left(\frac{T}{m_\chi}\right)^n = \sigma_0 x^{-n}\,, \tag{2.102}$$

corresponding to a velocity expansion since $\langle v^2\rangle \sim T/m_\chi$. The case $n = 0$ corresponds to $s$-wave annihilation, $n = 2$ to $p$-wave annihilation, and so on [101] [10]. Solving Eq. (2.101) for $n = 0$, $m_\chi \sim 100$ GeV, and $\sigma_0 \sim \alpha_w^2/m_\chi^2$ with $\alpha_w \sim 10^{-2}$, we find that during the radiation-dominated era $x_{\rm f.o.} \sim 20$.

[10] The $s$-wave or $p$-wave annihilations of DM are related to the orbital and total angular momentum and spin properties of the initial and final states. In particular, Fermi statistics forces two identical DM fermions (assuming the DM antiparticle is its own particle) with orbital angular momentum $L$ and total spin $S$ to satisfy $(-1)^S = (-1)^L$. The total angular momentum of the $s$-wave state (characterized by $L = 0$ by definition) is $J \equiv L + S = 0$ and the $CP$ quantum number is given by $CP = (-1)^{L+1} = -1$, while the $p$-wave state has $CP = +1$ [109].

Using Eq. (2.102), the Boltzmann equation (2.96) can be written as [1]

$$\frac{dY}{dx} = -\frac{\lambda}{x^{n+2}}[Y^2 - Y_{\rm eq}^2]\,, \tag{2.103}$$

where $\lambda$ is defined as

$$\lambda \equiv \left[\frac{x\langle\sigma_a v\rangle s}{H(m_\chi)}\right]_{x=1} = \sqrt{\frac{\pi}{45}}\frac{g_{\star s}}{\sqrt{g_\star}}M_{Pl}m_\chi\sigma_0\,. \tag{2.104}$$

The present-day relic abundance of the species $\chi$ can be approximated by neglecting the $Y_{\rm eq}^2$ term on the right-hand side and integrating the differential equation from $x = x_{\rm f.o.}$ to $x = \infty$, giving [1, 108]

$$Y_0 \equiv Y(\infty) \approx \sqrt{\frac{45g_\star}{\pi g_{\star s}^2}}\frac{(n+1)\,x_{\rm f.o.}^{n+1}}{m_\chi M_{Pl}\,\sigma_0}\,. \tag{2.105}$$

It is important to note from Eq. (2.105) that $Y_0$ is inversely proportional to the annihilation cross-section and particle mass, indicating that a larger $\sigma_0$ corresponds to a lower expected relic density. For a non-relativistic particle $\chi$, the relic density becomes

$$\Omega_\chi \equiv \frac{\rho_\chi}{\rho_{\rm crit}} = \frac{n_\chi m_\chi}{\rho_{\rm crit}} = \frac{Y_0 s_0 m_\chi}{\rho_{\rm crit}} \approx \sqrt{\frac{45g_\star}{\pi g_{\star s}^2}}\frac{s_0}{\rho_{\rm crit}}\frac{(n+1)x_{\rm f.o.}^{n+1}}{M_{Pl}\sigma_0} \tag{2.106}$$

where $s_0$ is the entropy density (2.86) computed today. Remarkably, $\Omega_\chi$ is independent of the value of $m_\chi$ and should be compared to the observed DM density today.

In section 2.4, we found that the CMB, BBN, and BAO data imply $\Omega_c \simeq 0.27$ for the present-day CDM abundance. By using Eq. (2.106), we can solve for the cross-section and find

$$\sigma_0 \sim 10^{-9}\ {\rm GeV}^{-2} \sim 3\times 10^{-26}\ {\rm cm}^3\,{\rm s}^{-1}\,, \tag{2.107}$$

where we used $s_0 \simeq 2891/{\rm cm}^3$, $n = 0$, $g_\star \simeq 3.38$, and $g_{\star s} \simeq 3.94$ (see Fig. 2.5). This value of $\sigma_0$ corresponds to a typical weak-scale cross-section, which is of the order

$\sigma_0 \sim \alpha_w^2/m_\chi^2$ with $\alpha_w \sim 10^{-2}$ and $m_\chi \sim \mathcal{O}(100 \text{ GeV})$. Thus, having new physics near the weak scale appears to provide the correct DM relic density, a phenomenon referred to as the *WIMP miracle* [76].

Although the calculation above does not impose a constraint on the DM mass $m_\chi$, unitarity arguments based on the cross-section and the present-day DM abundance yield an upper limit on the cross-section, leading to the following model-independent bound [110]

$$\Omega_\chi h^2 \gtrsim 1.7 \times 10^{-6} \sqrt{x_{\text{f.o.}}}\, [m_\chi/(1\,\text{TeV})] \qquad \Longrightarrow \qquad m \lesssim 126\,\text{TeV}\,. \tag{2.108}$$

Furthermore, there exists a lower mass bound for WIMPs known as the Lee-Weinberg limit, which sets $m_\chi \gtrsim 2$ GeV to prevent overclosure of the Universe [111].

### 2.5.4 Asymmetric production

In the thermal freeze-out mechanism discussed earlier, we assumed the absence of a particle-antiparticle asymmetry in the early Universe. However, if this condition is not satisfied, the present-day relic abundance of DM could be generated through a mechanism similar to the one responsible for the baryon asymmetry observed in the Universe. This connection between the DM and baryon densities is known as Asymmetric DM (ADM) production [112], which was originally proposed to address the solar neutrino problem [113, 114].

In the following, we will present a general framework shared by many ADM models without focusing on a specific one, and refer the reader to Ref. [115] for a comprehensive review. A key observation is that the DM density is approximately five times higher than the baryonic density

$$\Omega_c \simeq 5\,\Omega_b\,, \tag{2.109}$$

as discussed in section 2.4, suggesting a possible common origin. Defining $\eta_{DM}$ as the asymmetry in the DM sector, if the present-day DM population is entirely asymmetric, this can explain Eq. (2.109) by tuning the DM mass $m_{DM}$ according to

$$m_{DM} = \left(\frac{\Omega_c}{\Omega_b}\right)\frac{\eta_B}{\eta_{DM}}\, m_p\,, \tag{2.110}$$

where $m_p \simeq 1$ GeV is the proton mass and we have taken $\Omega_{DM} \equiv \Omega_+ + \Omega_- \sim \Omega_+ = \Omega_c$ (assuming $\eta_{DM} > 0$), where $\Omega_+$ and $\Omega_-$ are the abundances of DM particles and antiparticles, respectively. If $\eta_{DM} \simeq \eta_B$, Eq. (2.110) leads to $m_{DM} \simeq 5$ GeV.

The final DM abundance is made asymmetric by suppressing the conventional symmetric component that arises from thermal freeze-out. This is typically achieved in the literature through the introduction in the dark sector of strong couplings analogous to QCD or the inclusion of new light states. These elements effectively lead to an annihilation cross section large enough to suppress the thermal symmetric component and avoid overclosure of the Universe [115].

Unlike the thermal freeze-out scenario, ADM models involve tracking the evolution of both the symmetric and asymmetric components of the relic number density. However, the computation closely resembles that of freeze-out as it relies on the Boltzmann transport equation, but with the presence of an asymmetry. [11] The latter addition implies that DM carries a chemical potential $\mu_{DM}$ [107]. It is important to note that this type of calculation assumes that DM is in thermal equilibrium with the photon bath, for which the sum of the chemical potentials of the incoming particles is equal to that of the outgoing particles [116]. While this assumption may not hold if there is a weakly coupled mediator between the visible and dark sectors [117], we simplify the analysis by assuming its validity in the following computation.

The DM relic density in ADM models is described in terms of the relic asymmetry, denoted as the present anti-DM to DM ratio $r_\infty = \Omega_-/\Omega_+$. This parameter plays a crucial role in determining the size of indirect signals from DM annihilation [115].

[11] In ADM models, a DM particle $\chi$ must be stable, heavy, not self-adjoint with an asymmetric abundance between particles and antiparticles, and subject to the annihilation process $\chi\bar{\chi} \to f\bar{f}$ with a large cross-section.

The absolute relic densities can be related to $r_\infty$ as follow [118]

$$\Omega_+ = \frac{1}{1-r_\infty}\frac{\eta_{DM} m_{DM} s_0}{\rho_{\rm crit}}\,, \qquad \Omega_- = \frac{r_\infty}{1-r_\infty}\frac{\eta_{DM} m_{DM} s_0}{\rho_{\rm crit}}\,. \tag{2.111}$$

The total relic density $\Omega_{DM} = \Omega_+ + \Omega_-$ is primarily determined by the DM mass $m_{DM}$ and its present asymmetry $\eta_{DM}$.

Using Eq. (2.111), we have

$$m_{DM} = \left(\frac{1-r_\infty}{1+r_\infty}\right)\left(\frac{\Omega_c}{\Omega_b}\right)\frac{\eta_B}{\eta_{DM}}\, m_p\,, \tag{2.112}$$

which reduces to Eq. (2.110) when $r_\infty = 0$, corresponding to pure asymmetric DM. The case with $r_\infty = 1$ corresponds to pure symmetric DM and leads to the thermal freeze-out scenario discussed in the previous section.

The number density of DM particles $n_+$ and antiparticles $n_-$ is described by a set of coupled Boltzmann equations, which can be written as [12]

$$\dot{n}_\pm + 3Hn_\pm = -\langle\sigma_a v\rangle[n_+ n_- - n_+^{\rm eq} n_-^{\rm eq}]\,, \tag{2.113}$$

where $n_\pm^{\rm eq} = n_{\rm eq}\, e^{\pm\mu_{DM}/T}$ with $n_{\rm eq}$ is the usual Maxwell-Boltzmann distribution. These equations can be simplified using the dimensionless quantities $x = m_{DM}/T$ and $Y_\pm = n_\pm/s$ from the previous section, resulting in

$$\frac{dY_\pm}{dx} = -\frac{xs\langle\sigma_a v\rangle}{H(m)}[Y_+Y_- - Y_{\rm eq}^2] = -\frac{\lambda}{x^{n+2}}\,[Y_+Y_- - Y_{\rm eq}^2]\,, \tag{2.114}$$

Here, $\lambda$ is given by Eq. (2.104), and the last step involves using $\langle\sigma_a v\rangle = \sigma_0\, x^{-n}$ as in Eq. (2.102). Notably, Eq. (2.114) resembles Eq. (2.103) derived in the thermal freeze-out mechanism, with the addition of a term that accounts for the interaction between particle and antiparticle densities.

Introducing the DM asymmetry as $\eta \equiv Y_+ - Y_-$ (the present value is $\eta_{DM}$ when

[12]The coupled Boltzmann equations in (2.113) are obtained under the following assumptions: (i) our particle species were in equilibrium with a thermal bath; (ii) there is no mass degeneracy between the two sectors; (iii) the dominant process that changes $n_\pm$ was annihilation; (iv) the annihilation process occurred far from a resonant threshold.

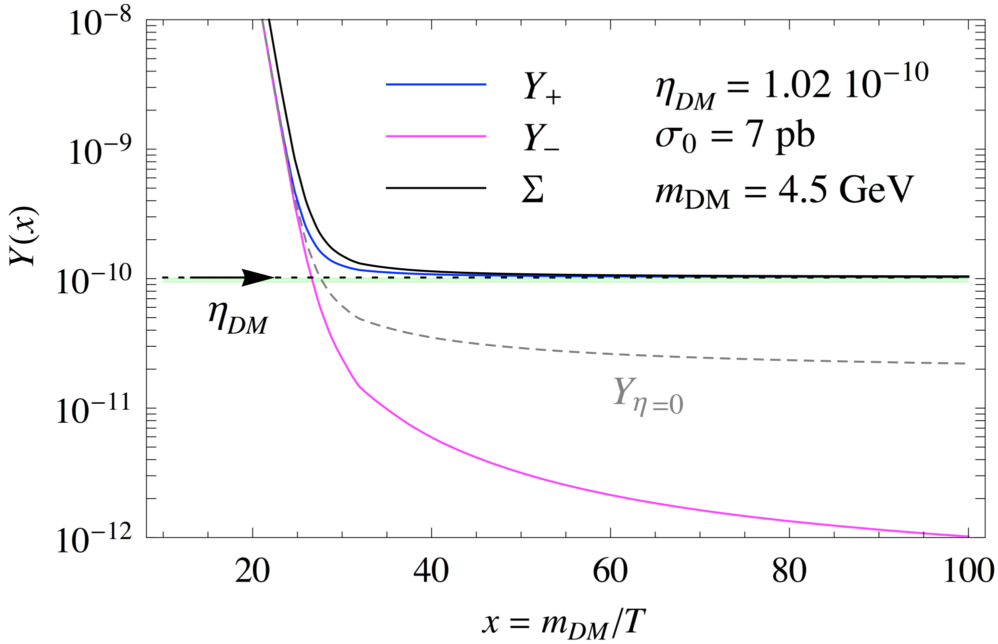


Figure 2.7: Evolution of $Y_\pm(x)$ (accounting for DM asymmetry $\eta_{DM} > 0$) and $Y_{\eta=0}$ (without asymmetry) after freeze-out. $\Sigma = Y_+ - Y_-$ represents the sum of relative co-moving number densities. Figure taken from Ref. [119].

$x \to \infty$), the above coupled Boltzmann equations can be solved numerically and an example of solution is shown in Figure 2.7. The asymmetry $\eta \neq 0$ enhances the depletion of the less abundant species ($n_-$) compared to the symmetric case. At late times, an approximate solution is obtained bu setting $Y_{\rm eq} \sim 0$. The expression for $Y_\pm(\infty)$ can be found to be

$$Y_\pm(\infty) \simeq \frac{\pm\eta_{DM}}{1 - [1 \mp \eta_{DM}/Y_\pm(x_{\rm f.o.})] \exp\left[\mp\eta_{DM}\lambda\, g_{\star s} g_\star^{-1/2}\, x_{\rm f.o.}^{-n-1}/(n+1)\right]}\,, \qquad (2.115)$$

where the freeze-out temperature $x_{\rm f.o.}$ is derived in Ref. [118].

The present ratio $r_\infty$ in ADM models can be estimated as

$$r_\infty \equiv \frac{Y_-(\infty)}{Y_+(\infty)} \simeq \frac{Y_-(x_{\rm f.o.})}{Y_+(x_{\rm f.o.})} \exp\left( - \frac{\eta_{DM}\lambda\, g_{\star s}(x_{\rm f.o.})}{\sqrt{g_\star(x_{\rm f.o.})}\, x_{\rm f.o.}^{n+1}(n+1)}\right). \qquad (2.116)$$

The first factor computed at $r_{\rm f.o.}$ is approximately equal to 1 and is derived numerically but an approximate analytical solution exists [117]. The magnitude of the ADM cross section $\sigma_0$ can be understood by comparing it to the symmetric cross section $\sigma_{0,\,\mathrm{sym}}$ corresponding to $r_\infty = 1$, obtaining

$$r_\infty \sim \exp\left( - \frac{\eta_{DM}\, g_{\star s}(x_{f.o.})}{\sqrt{g_\star(x_{f.o.})}\, Y^\infty_{\eta=0}\,(n+1)} \frac{\sigma_0}{\sigma_{0,\,\mathrm{sym}}} \right), \tag{2.117}$$

where $Y^\infty_{\eta=0} \equiv Y_0$ defined in Eq. (2.105), and we assumed for simplicity that both masses of the symmetric and asymmetric components are the same. By expressing $r_\infty$ in terms of $\sigma_0$ and $\sigma_{0,\,\mathrm{sym}}$, we find that $\sigma_0$ needs to be larger than $\sigma_{0,\,\mathrm{sym}}$ to efficiently annihilate the symmetric DM component (*i.e.* $r_\infty \lesssim 1$). A review on ADM scenarios can be found in Ref. [120].

### 2.5.5 Freeze-in

The two discussed mechanisms for producing the current DM abundance share a common feature: the production occurred through decoupling from a thermal bath at temperature $T$, with or without the presence of an initial DM asymmetry. However, it is possible for DM particles $\chi$ with mass $m_\chi$ to have such weak interactions that they never reached thermal equilibrium in the early Universe. This alternative mechanism, known as *freeze-in* [121], involves the production of DM through feeble interactions. The resulting particles are called Feebly-Interacting Massive Particles (FIMPs).

In the freeze-in scenario, due to the weak coupling between the primordial plasma and DM particles, the initial comoving abundance is approximately $Y \simeq 0$. The Boltzmann equation, Eq. (2.96), can be simplified to

$$\frac{dY}{dx} \simeq \frac{xs\langle\sigma_a v\rangle}{H(m_\chi)}\, Y^2_{\mathrm{eq}}\,, \tag{2.118}$$

which causes $Y(x)$ to slowly approach $Y_{\mathrm{eq}}$ from below. Unlike thermal freeze-out, the integration of Eq. (2.118) to estimate the relic abundance is dominated by the regime with small $x$ (high temperatures) [103]. Figure 2.9 illustrates an example of the time evolution of the comoving density resulting from integrating Eq. (2.118). The abundance of FIMP $\chi$ "freezes-in" at a certain point when the interaction rate

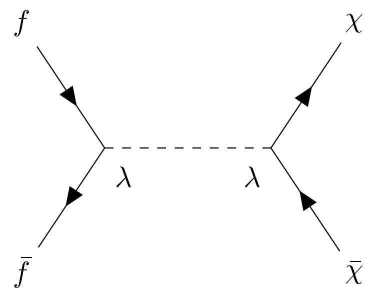


Figure 2.8: Annihilation process suppressed at high temperature, enabling freeze-in to occur.

becomes smaller than the expansion rate. The yield of freeze-in increases with the coupling strength between $\chi$ and the thermal bath.

Considering the $s$-channel process $f\bar{f} \to \chi\bar{\chi}$ mediated by a light boson, as shown in Fig. 2.8, with a coupling constant $\lambda$ between the mediator and particles $f$ or $\chi$, the annihilation cross section is $\langle\sigma_a v\rangle \sim \lambda^4 x^2/m_\chi^2$. The present-day relic abundance $Y_0$ is then approximately given by [103]

$$m_\chi Y_0 \sim 10^{-4}\lambda^4 M_{Pl} \simeq 4.3 \times 10^{-10} \text{ GeV} \tag{2.119}$$

to match the observed DM density. Inverting this formula yields $\lambda \sim 10^{-6}$, significantly smaller than the coupling constant required for thermal freeze-out, which is on the order of $\alpha_w \sim 10^{-2}$ (see Eq. (2.107)).

In order to compare thermal freeze-out and freeze-in processes, let us consider a common annihilation process with $\langle\sigma_a v\rangle \simeq \lambda^4/m_\chi^2$ as $T \to 0$, typically mediated by a massive gauge boson. Denoting $\langle\sigma_a v\rangle_0$ as the thermal freeze-out cross section, it can be shown that [103]

$$\frac{\langle\sigma_a v\rangle}{\langle\sigma_a v\rangle_0} \sim \left(\frac{0.1 \text{ eV}}{m_\chi}\right)^2. \tag{2.120}$$

Thus, for reasonably heavy DM particles, the freeze-in cross section is significantly lower than that for freeze-out by several orders of magnitude. An interesting application of the freeze-in mechanism is the production of ultra-heavy DM candidates (with masses up to $\sim 10^{16}$ GeV) that interact only via gravity with SM particles in the ther-

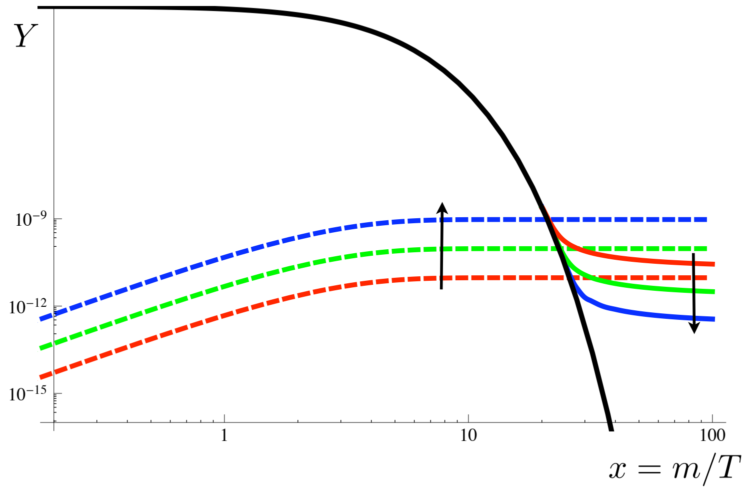


Figure 2.9: Evolution of DM relic abundance for freeze-out (solid curves) and freeze-in via Yukawa interaction (dashed curves) as a function of the dimensionless time $x \equiv m_\chi/T$. The black solid line represents the relic density in thermal equilibrium. The black arrows indicate the impact of increasing coupling strength for both processes. Freeze-in abundance dominates around $x \sim 2-5$, in contrast with freeze-out which occur at $x \sim 20$. Figure taken from [121].

mal primordial plasma, as these interactions are present regardless of model-building choices [122, 123].

## 2.6 Brief thermal history

The thermodynamics and particle physics in an expanding Universe, as described in sections 2.4 and 2.5, can be summarized by two guiding principles:

1. Particle interactions freeze out when their rate becomes smaller than the expansion rate;
2. Spontaneous symmetry breaking leads to phase transitions, such as the electroweak SSB discussed in section 2.4.1.2.

By considering these principles, we can reconstruct the thermal history of the Universe. Figure 2.10 provides a cartoon representation of this history, and Table 2.2 summarizes the main events. Notably, the events from approximately $10^{-10}$ seconds

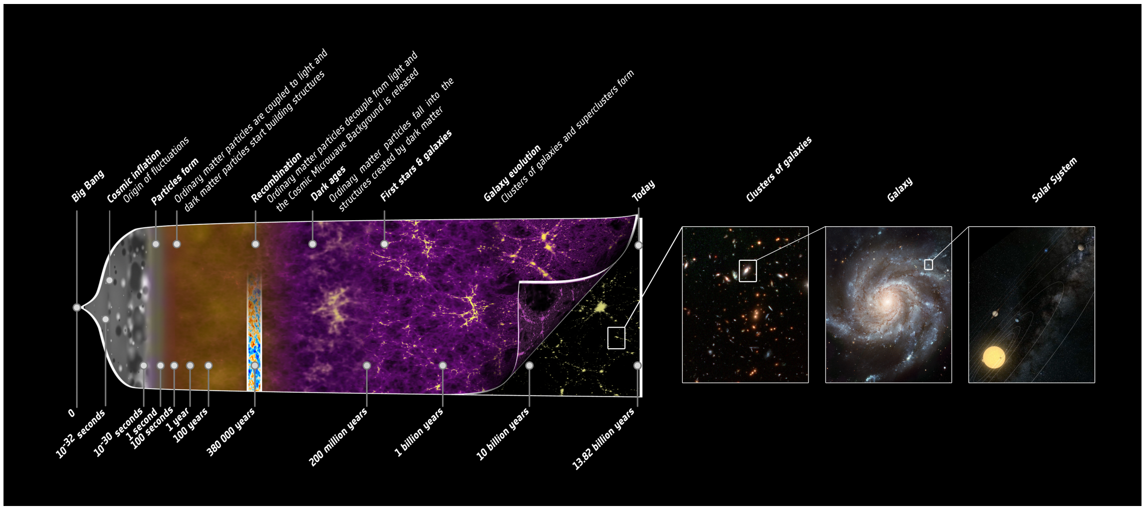


Figure 2.10: History of the Universe. Credits: NASA, Planck, Caltech (`https://www.nasa.gov/mission_pages/planck/multimedia/pia16876b.html`)

until the present are based on well-established laws of physics, including nuclear and atomic physics, in addition to gravity. We will now provide a brief overview of these events first.

In the early Universe, a plasma of relativistic particles, including quarks, leptons, gauge bosons, and the Higgs boson, prevailed. At temperatures above approximately 100 GeV, the electroweak symmetry was restored, resulting in massless weak gauge bosons associated with the $\mathrm{SU}(2)_L \otimes \mathrm{U}(1)_Y$ symmetry of the SM. The interactions were strong enough to maintain thermal equilibrium between quarks and leptons. As the temperature dropped below about 100 GeV, the electroweak symmetry was broken, and the $W^{\pm}$ and $Z$ bosons acquired mass through the Higgs mechanism. This led to a decrease in the cross-section of weak interactions and, as a result, neutrinos decoupled from the rest of the matter at approximately 1 MeV. Shortly after, at around 1 second, the temperature fell below the rest mass of electrons, causing efficient annihilation of electrons and positrons. Only a small matter-antimatter asymmetry, about one part in a billion, survived. The resulting photon-baryon fluid reached thermal equilibrium. Around $\sim 0.1$ MeV, strong interactions became significant, and protons and neutrons combined to form light elements (H, He, Li) during BBN at approximately $\sim 200$ seconds. At about 1 eV, or $10^{11}$ seconds, the matter and radiation densities became equal. Charged matter particles and photons were strongly coupled in the plasma, and density fluctuations propagated as cosmic sound waves. Around 0.1 eV, or $380,000$ years after the Big Bang, protons and electrons combined to form neutral hydrogen atoms. Photons decoupled, giving rise to the CMB radiation that we observe today.

CMB temperature anisotropies reveal primordial matter density fluctuations, which grew through gravitational instability to form the observed LSS in the late Universe. Clustering became more efficient as matter began to dominate the energy density of the Universe, with small scales becoming non-linear first. This led to hierarchical structure formation, where small-scale structures (*e.g.*, stars and galaxies) formed initially and subsequently merged into larger structures (clusters and superclusters of galaxies). Around redshift $z \sim 25$, high-energy photons from the first stars initiated the ionization of hydrogen in the intergalactic medium, a process known as "reionization", which completed at around $z \simeq 6$. Concurrently, the most massive stars depleted their nuclear fuel and underwent supernova explosions. At a redshift of approximately $z \sim 1$, a dark energy component with negative pressure began to dominate the evolution of the Universe.

As concerns events occurred within the first $\sim 10^{-11}$ seconds of the Universe history, the energy exceeds $\sim 1$ TeV, and direct experimental guidance is lacking. Our understanding of this period is based on extrapolating our present knowledge of the Universe and particle physics back to the Planck epoch, where quantum corrections to GR become significant at energies of $\sim 10^{18}$ GeV. The combination of electroweak and strong interactions likely occurred during the grand unification (GUT) phase transition, expected to have taken place at energies ranging from $10^{14}$ to $10^{16}$ GeV, based on the energy running of the SM couplings.

The fluctuations observed in the CMB temperature require the presence of primordial seed perturbations. The prevailing explanation is inflation, which postulates that these perturbations were generated during an early period around $10^{-34}$ seconds after the Big Bang. Inflation stretched small quantum fluctuations in the energy density to macroscopic scales, larger than the horizon at that time. Once a perturbation exited the horizon, it remained frozen with a constant amplitude until it re-entered the

| Event | Time | Energy | Redshift |
|---|---|---|---|
| Planck epoch? | $< 10^{-43}$ s | $\sim 10^{18}$ GeV | |
| Grand unification? | $\sim 10^{-36}$ s | $\sim 10^{15}$ GeV | |
| Inflation? | $\gtrsim 10^{-34}$ s | $\lesssim 10^{15}$ GeV | |
| Baryogenesis? | $< 10^{-10}$ s | $> 1$ TeV | |
| Electroweak unification | $\sim 10^{-10}$ s | $\sim 1$ TeV | |
| Quark-hadron transition | $\sim 10^{-4}$ s | $\sim 100$ MeV | |
| Nucleon freeze-out | $\sim 0.01$ s | $\sim 10$ MeV | |
| Neutrino decoupling | $\sim 1$ s | $\sim 1$ MeV | |
| BBN | $\sim 3$ min | $\sim 0.1$ MeV | |
| Matter-radiation equality | $\sim 10^4$ yrs | 1 eV | $\sim 10^4$ |
| Recombination | $\sim 10^5$ yrs | 0.1 eV | $\sim 1100$ |
| Dark ages | $10^5 - 10^8$ yrs | | $> 25$ |
| Reionization | $\sim 10^8$ yrs | | $25 - 6$ |
| Galaxy formation | $\sim 6 \times 10^8$ yrs | | $\sim 10$ |
| Dark energy | $\sim 10^9$ yrs | | $\sim 2$ |
| Solar system | $\sim 8 \times 10^9$ yrs | | $\sim 0.5$ |
| Today | $\sim 1.4 \times 10^{10}$ yrs | $\sim 1$ meV | 0 |

Table 2.2: Main events in the history of the Universe. Reproduced from Ref. [124].

horizon during the subsequent expansion of the Universe. The resulting fluctuations contributed to the acoustic peak structure observed in the CMB and the formation of galaxies and clusters of galaxies. Observations of the late-time CMB and LSS allow us to infer the primordial input spectrum by studying the evolution of perturbations after they re-entered the horizon. This provides insights into the physical conditions when the Universe was $\sim 10^{-34}$ seconds old.

Additionally, the presence of a baryon asymmetry in the Universe today suggests the occurrence of an event known as baryogenesis, which generated this asymmetry in the early Universe. Both inflation and baryogenesis will be the subjects of the next chapter.

# Bibliography


[1] E. W. Kolb and M. S. Turner, *The Early Universe*, vol. 69. 1990.

[2] S. Dodelson, *Modern Cosmology*. Academic Press, Amsterdam, 2003.

[3] S. Dodelson and F. Schmidt, *Modern Cosmology*. Academic Press, Amsterdam, 2020.

[4] V. Mukhanov, *Physical Foundations of Cosmology*. Cambridge University Press, Oxford, 2005.

[5] S. Weinberg, *Cosmology*. Oxford University Press, 2008.

[6] O. F. Piattella, *Lecture Notes in Cosmology*. UNITEXT for Physics. Springer, Cham, 2018. `arXiv:1803.00070 [astro-ph.CO]`.

[7] P. J. E. Peebles, *Principles of physical cosmology*. Princeton University Press, 1994.

[8] D. Baumann, *Cosmology*. Cambridge University Press, 7, 2022.

[9] Ø. Grøn, "The Discovery of the Expansion of the Universe," *Galaxies* **6** no. 4, (2018) 132.

[10] A. Friedman, "On the Curvature of space," *Z. Phys.* **10** (1922) 377–386.

[11] A. Friedmann, "On the Possibility of a world with constant negative curvature of space," *Z. Phys.* **21** (1924) 326–332.

[12] H. P. Robertson, "Kinematics and World-Structure," *Astrophys. J.* **82** (1935) 284–301.

[13] H. P. Robertson, "Kinematics and World-Structure. 3," *Astrophys. J.* **83** (1936) 257–271.

[14] A. G. Walker, "On Milne's theory of world-structure," *Proceedings of the London Mathematical Society* **2** no. 1, (1937) 90–127.

[15] G. Lemaitre, "The Expanding Universe," *Mon. Not. Roy. Astron. Soc.* **91** (1931) 490–501.

[16] G. Lemaitre, "The expanding universe," *Annales Soc. Sci. Bruxelles A* **53** (1933) 51–85.

[17] S. Weinberg, *Gravitation and Cosmology: Principles and Applications of the General Theory of Relativity*. John Wiley and Sons, New York, 1972.

[18] **Particle Data Group** Collaboration, R. L. Workman *et al.*, "Review of Particle Physics," *PTEP* **2022** (2022) 083C01.

[19] **Planck** Collaboration, N. Aghanim *et al.*, "Planck 2018 results. VI. Cosmological parameters," *Astron. Astrophys.* **641** (2020) A6, `arXiv:1807.06209 [astro-ph.CO]`. [Erratum: Astron.Astrophys. 652, C4 (2021)].

[20] W. L. Freedman, "Cosmology at a Crossroads," *Nature Astron.* **1** (2017) 0121, `arXiv:1706.02739 [astro-ph.CO]`.

[21] L. Verde, T. Treu, and A. G. Riess, "Tensions between the Early and the Late Universe," *Nature Astron.* **3** (7, 2019) 891, `arXiv:1907.10625 [astro-ph.CO]`.

[22] E. Di Valentino *et al.*, "Snowmass2021 - Letter of interest cosmology intertwined II: The hubble constant tension," *Astropart. Phys.* **131** (2021) 102605, `arXiv:2008.11284 [astro-ph.CO]`.

[23] E. Abdalla *et al.*, "Cosmology intertwined: A review of the particle physics, astrophysics, and cosmology associated with the cosmological tensions and anomalies," *JHEAp* **34** (2022) 49–211, `arXiv:2203.06142 [astro-ph.CO]`.

[24] M. D. Schwartz, *Quantum Field Theory and the Standard Model*. Cambridge University Press, 3, 2014.

[25] C. P. Burgess and G. D. Moore, *The standard model: A primer*. Cambridge University Press, 12, 2006.

[26] T.-P. .-.-.-. Cheng and L.-F. .-.-.-. Li, *Gauge Theory of Elementary Particle Physics*. Oxford University Press, Oxford, UK, 1984.

[27] P. Langacker, *The standard model and beyond*. 2010.

[28] C. Quigg, *Gauge Theories of the Strong, Weak, and Electromagnetic Interactions: Second Edition*. Princeton University Press, USA, 9, 2013.

[29] N. Cabibbo, "Unitary Symmetry and Leptonic Decays," *Phys. Rev. Lett.* **10** (1963) 531–533.

[30] M. Kobayashi and T. Maskawa, "CP Violation in the Renormalizable Theory of Weak Interaction," *Prog. Theor. Phys.* **49** (1973) 652–657.

[31] **ATLAS** Collaboration, G. Aad *et al.*, "Observation of a new particle in the search for the Standard Model Higgs boson with the ATLAS detector at the LHC," *Phys. Lett. B* **716** (2012) 1–29, `arXiv:1207.7214 [hep-ex]`.

[32] **CMS** Collaboration, S. Chatrchyan *et al.*, "Observation of a New Boson at a Mass of 125 GeV with the CMS Experiment at the LHC," *Phys. Lett. B* **716** (2012) 30–61, `arXiv:1207.7235 [hep-ex]`.

[33] P. Minkowski, "$\mu \to e\gamma$ at a Rate of One Out of $10^9$ Muon Decays?," *Phys. Lett. B* **67** (1977) 421–428.

[34] P. Ramond, "The Family Group in Grand Unified Theories," in *International Symposium on Fundamentals of Quantum Theory and Quantum Field Theory*. 2, 1979. `arXiv:hep-ph/9809459`.

[35] M. Gell-Mann, P. Ramond, and R. Slansky, "Complex Spinors and Unified Theories," *Conf. Proc. C* **790927** (1979) 315–321, `arXiv:1306.4669 [hep-th]`.

[36] T. Yanagida, "Horizontal gauge symmetry and masses of neutrinos," *Conf. Proc. C* **7902131** (1979) 95–99.

[37] R. N. Mohapatra and G. Senjanovic, "Neutrino Mass and Spontaneous Parity Nonconservation," *Phys. Rev. Lett.* **44** (1980) 912.

[38] S. Weinberg, "Baryon and Lepton Nonconserving Processes," *Phys. Rev. Lett.* **43** (1979) 1566–1570.

[39] J. Schechter and J. W. F. Valle, "Comment on the Lepton Mixing Matrix," *Phys. Rev. D* **21** (1980) 309.

[40] J. Schechter and J. W. F. Valle, "Neutrino Masses in SU(2) x U(1) Theories," *Phys. Rev. D* **22** (1980) 2227.

[41] J. Schechter and J. W. F. Valle, "Majorana Neutrinos and Magnetic Fields," *Phys. Rev. D* **24** (1981) 1883–1889. [Erratum: Phys.Rev.D 25, 283 (1982)].

[42] B. Pontecorvo, "Neutrino Experiments and the Problem of Conservation of Leptonic Charge," *Zh. Eksp. Teor. Fiz.* **53** (1967) 1717–1725.

[43] Z. Maki, M. Nakagawa, and S. Sakata, "Remarks on the unified model of elementary particles," *Prog. Theor. Phys.* **28** (1962) 870–880.

[44] V. N. Gribov and B. Pontecorvo, "Neutrino astronomy and lepton charge," *Phys. Lett. B* **28** (1969) 493.

[45] S. Antusch, C. Biggio, E. Fernandez-Martinez, M. B. Gavela, and J. Lopez-Pavon, "Unitarity of the Leptonic Mixing Matrix," *JHEP* **10** (2006) 084, `arXiv:hep-ph/0607020`.

[46] S. Antusch and O. Fischer, "Non-unitarity of the leptonic mixing matrix: Present bounds and future sensitivities," *JHEP* **10** (2014) 094, `arXiv:1407.6607 [hep-ph]`.

[47] G. 't Hooft, "Naturalness, chiral symmetry, and spontaneous chiral symmetry breaking," *NATO Sci. Ser. B* **59** (1980) 135–157.

[48] M. J. G. Veltman, "The Infrared - Ultraviolet Connection," *Acta Phys. Polon. B* **12** (1981) 437.

[49] S. P. Martin, "A Supersymmetry primer," *Adv. Ser. Direct. High Energy Phys.* **18** (1998) 1–98, `arXiv:hep-ph/9709356`.

[50] A. Hook, "TASI Lectures on the Strong CP Problem and Axions," *PoS* **TASI2018** (2019) 004, `arXiv:1812.02669 [hep-ph]`.

[51] L. F. Abbott and P. Sikivie, "A Cosmological Bound on the Invisible Axion," *Phys. Lett. B* **120** (1983) 133–136.

[52] M. Dine and W. Fischler, "The Not So Harmless Axion," *Phys. Lett. B* **120** (1983) 137–141.

[53] P. W. Graham, I. G. Irastorza, S. K. Lamoreaux, A. Lindner, and K. A. van Bibber, "Experimental Searches for the Axion and Axion-Like Particles," *Ann. Rev. Nucl. Part. Sci.* **65** (2015) 485–514, `arXiv:1602.00039 [hep-ex]`.

[54] L. Hui, J. P. Ostriker, S. Tremaine, and E. Witten, "Ultralight scalars as cosmological dark matter," *Phys. Rev. D* **95** no. 4, (2017) 043541, `arXiv:1610.08297 [astro-ph.CO]`.

[55] S. Dodelson and L. M. Widrow, "Sterile-neutrinos as dark matter," *Phys. Rev. Lett.* **72** (1994) 17–20, `arXiv:hep-ph/9303287`.

[56] M. Drewes *et al.*, "A White Paper on keV Sterile Neutrino Dark Matter," *JCAP* **01** (2017) 025, `arXiv:1602.04816 [hep-ph]`.

[57] E. Bulbul, M. Markevitch, A. Foster, R. K. Smith, M. Loewenstein, and S. W. Randall, "Detection of An Unidentified Emission Line in the Stacked X-ray spectrum of Galaxy Clusters," *Astrophys. J.* **789** (2014) 13, `arXiv:1402.2301 [astro-ph.CO]`.

[58] A. Boyarsky, O. Ruchayskiy, D. Iakubovskyi, and J. Franse, "Unidentified Line in X-Ray Spectra of the Andromeda Galaxy and Perseus Galaxy Cluster," *Phys. Rev. Lett.* **113** (2014) 251301, `arXiv:1402.4119 [astro-ph.CO]`.

[59] T. E. Jeltema and S. Profumo, "Discovery of a 3.5 keV line in the Galactic Centre and a critical look at the origin of the line across astronomical targets," *Mon. Not. Roy. Astron. Soc.* **450** no. 2, (2015) 2143–2152, `arXiv:1408.1699 [astro-ph.HE]`.

[60] M. E. Anderson, E. Churazov, and J. N. Bregman, "Non-Detection of X-Ray Emission From Sterile Neutrinos in Stacked Galaxy Spectra," *Mon. Not. Roy. Astron. Soc.* **452** no. 4, (2015) 3905–3923, `arXiv:1408.4115 [astro-ph.HE]`.

[61] D. Malyshev, A. Neronov, and D. Eckert, "Constraints on 3.55 keV line emission from stacked observations of dwarf spheroidal galaxies," *Phys. Rev. D* **90** (2014) 103506, `arXiv:1408.3531 [astro-ph.HE]`.

[62] T. E. Jeltema and S. Profumo, "Deep XMM Observations of Draco rule out at the 99% Confidence Level a Dark Matter Decay Origin for the 3.5 keV Line," *Mon. Not. Roy. Astron. Soc.* **458** no. 4, (2016) 3592–3596, `arXiv:1512.01239 [astro-ph.HE]`.

[63] M. Fabbrichesi, E. Gabrielli, and G. Lanfranchi, "The Dark Photon," `arXiv:2005.01515 [hep-ph]`.

[64] I. Y. Kobzarev, L. B. Okun, and I. Y. Pomeranchuk, "On the possibility of experimental observation of mirror particles," *Sov. J. Nucl. Phys.* **3** no. 6, (1966) 837–841.

[65] M. J. Strassler and K. M. Zurek, "Echoes of a hidden valley at hadron colliders," *Phys. Lett. B* **651** (2007) 374–379, `arXiv:hep-ph/0604261`.

[66] **ATLAS, CMS** Collaboration, N. Trevisani, "Collider Searches for Dark Matter (ATLAS + CMS)," *Universe* **4** no. 11, (2018) 131.

[67] A. Boveia and C. Doglioni, "Dark Matter Searches at Colliders," *Ann. Rev. Nucl. Part. Sci.* **68** (2018) 429–459, `arXiv:1810.12238 [hep-ex]`.

[68] A. Boveia *et al.*, "Recommendations on presenting LHC searches for missing transverse energy signals using simplified $s$-channel models of dark matter," *Phys. Dark Univ.* **27** (2020) 100365, `arXiv:1603.04156 [hep-ex]`.

[69] M. W. Goodman and E. Witten, "Detectability of Certain Dark Matter Candidates," *Phys. Rev. D* **31** (1985) 3059.

[70] A. K. Drukier, K. Freese, and D. N. Spergel, "Detecting Cold Dark Matter Candidates," *Phys. Rev. D* **33** (1986) 3495–3508.

[71] J. I. Read, "The Local Dark Matter Density," *J. Phys. G* **41** (2014) 063101, arXiv:1404.1938 [astro-ph.GA].

[72] T. Piffl *et al.*, "The RAVE survey: the Galactic escape speed and the mass of the Milky Way," *Astron. Astrophys.* **562** (2014) A91, arXiv:1309.4293 [astro-ph.GA].

[73] A. M. Green, "Astrophysical uncertainties on the local dark matter distribution and direct detection experiments," *J. Phys. G* **44** no. 8, (2017) 084001, arXiv:1703.10102 [astro-ph.CO].

[74] L. Necib, M. Lisanti, and V. Belokurov, "Inferred Evidence For Dark Matter Kinematic Substructure with SDSS-Gaia," arXiv:1807.02519 [astro-ph.GA].

[75] N. W. Evans, C. A. J. O'Hare, and C. McCabe, "Refinement of the standard halo model for dark matter searches in light of the Gaia Sausage," *Phys. Rev. D* **99** no. 2, (2019) 023012, arXiv:1810.11468 [astro-ph.GA].

[76] G. Jungman, M. Kamionkowski, and K. Griest, "Supersymmetric dark matter," *Phys. Rept.* **267** (1996) 195–373, arXiv:hep-ph/9506380.

[77] J. D. Lewin and P. F. Smith, "Review of mathematics, numerical factors, and corrections for dark matter experiments based on elastic nuclear recoil," *Astropart. Phys.* **6** (1996) 87–112.

[78] D. S. Akerib *et al.*, "Snowmass2021 Cosmic Frontier Dark Matter Direct Detection to the Neutrino Fog," in *Snowmass 2021*. 3, 2022. arXiv:2203.08084 [hep-ex].

[79] L. Vietze, P. Klos, J. Menéndez, W. C. Haxton, and A. Schwenk, "Nuclear structure aspects of spin-independent WIMP scattering off xenon," *Phys. Rev. D* **91** no. 4, (2015) 043520, arXiv:1412.6091 [nucl-th].

[80] P. Klos, J. Menéndez, D. Gazit, and A. Schwenk, "Large-scale nuclear structure calculations for spin-dependent WIMP scattering with chiral effective field theory currents," *Phys. Rev. D* **88** no. 8, (2013) 083516, `arXiv:1304.7684 [nucl-th]`. [Erratum: Phys.Rev.D 89, 029901 (2014)].

[81] R. Essig, J. Mardon, and T. Volansky, "Direct Detection of Sub-GeV Dark Matter," *Phys. Rev. D* **85** (2012) 076007, `arXiv:1108.5383 [hep-ph]`.

[82] R. Essig *et al.*, "Snowmass2021 Cosmic Frontier: The landscape of low-threshold dark matter direct detection in the next decade," in *Snowmass 2021*. 3, 2022. `arXiv:2203.08297 [hep-ph]`.

[83] T. R. Slatyer, "Les Houches Lectures on Indirect Detection of Dark Matter," *SciPost Phys. Lect. Notes* **53** (2022) 1, `arXiv:2109.02696 [hep-ph]`.

[84] L. Bergstrom, P. Ullio, and J. H. Buckley, "Observability of gamma-rays from dark matter neutralino annihilations in the Milky Way halo," *Astropart. Phys.* **9** (1998) 137–162, `arXiv:astro-ph/9712318`.

[85] J. F. Navarro, C. S. Frenk, and S. D. M. White, "The Structure of cold dark matter halos," *Astrophys. J.* **462** (1996) 563–575, `arXiv:astro-ph/9508025`.

[86] J. Einasto, "Kinematics and dynamics of stellar systems," *Trudy Astrofizicheskogo Instituta Alma-Ata* **5** (1965) 87–100.

[87] A. Burkert, "The Structure of dark matter halos in dwarf galaxies," *Astrophys. J. Lett.* **447** (1995) L25, `arXiv:astro-ph/9504041`.

[88] B. Moore, T. R. Quinn, F. Governato, J. Stadel, and G. Lake, "Cold collapse and the core catastrophe," *Mon. Not. Roy. Astron. Soc.* **310** (1999) 1147–1152, `arXiv:astro-ph/9903164`.

[89] M. Cirelli, G. Corcella, A. Hektor, G. Hutsi, M. Kadastik, P. Panci, M. Raidal, F. Sala, and A. Strumia, "PPPC 4 DM ID: A Poor Particle

Physicist Cookbook for Dark Matter Indirect Detection," *JCAP* **03** (2011) 051, arXiv:1012.4515 [hep-ph]. [Erratum: JCAP 10, E01 (2012)].

[90] M. Li, X.-D. Li, S. Wang, and Y. Wang, "Dark Energy," *Commun. Theor. Phys.* **56** (2011) 525–604, arXiv:1103.5870 [astro-ph.CO].

[91] C. P. Burgess, "The Cosmological Constant Problem: Why it's hard to get Dark Energy from Micro-physics," in *100e Ecole d'Ete de Physique: Post-Planck Cosmology*, pp. 149–197. 2015. arXiv:1309.4133 [hep-th].

[92] B. Ratra and P. J. E. Peebles, "Cosmological Consequences of a Rolling Homogeneous Scalar Field," *Phys. Rev. D* **37** (1988) 3406.

[93] C. Wetterich, "Cosmology and the Fate of Dilatation Symmetry," *Nucl. Phys. B* **302** (1988) 668–696, arXiv:1711.03844 [hep-th].

[94] A. Joyce, L. Lombriser, and F. Schmidt, "Dark Energy Versus Modified Gravity," *Ann. Rev. Nucl. Part. Sci.* **66** (2016) 95–122, arXiv:1601.06133 [astro-ph.CO].

[95] L. Bergstrom and A. Goobar, *Cosmology and particle astrophysics*. 1999.

[96] V. F. Shvartsman, "Density of relict particles with zero rest mass in the universe," *Pisma Zh. Eksp. Teor. Fiz.* **9** (1969) 315–317.

[97] G. Steigman, D. N. Schramm, and J. E. Gunn, "Cosmological Limits to the Number of Massive Leptons," *Phys. Lett. B* **66** (1977) 202–204.

[98] G. Mangano, G. Miele, S. Pastor, and M. Peloso, "A Precision calculation of the effective number of cosmological neutrinos," *Phys. Lett. B* **534** (2002) 8–16, arXiv:astro-ph/0111408.

[99] J. Froustey, C. Pitrou, and M. C. Volpe, "Neutrino decoupling including flavour oscillations and primordial nucleosynthesis," *JCAP* **12** (2020) 015, arXiv:2008.01074 [hep-ph].

[100] J. J. Bennett, G. Buldgen, P. F. De Salas, M. Drewes, S. Gariazzo, S. Pastor, and Y. Y. Y. Wong, "Towards a precision calculation of $N_{\rm eff}$ in the Standard Model II: Neutrino decoupling in the presence of flavour oscillations and finite-temperature QED," *JCAP* **04** (2021) 073, `arXiv:2012.02726 [hep-ph]`.

[101] P. Gondolo and G. Gelmini, "Cosmic abundances of stable particles: Improved analysis," *Nucl. Phys. B* **360** (1991) 145–179.

[102] M. Lisanti, "Lectures on Dark Matter Physics," in *Theoretical Advanced Study Institute in Elementary Particle Physics: New Frontiers in Fields and Strings*, pp. 399–446. 2017. `arXiv:1603.03797 [hep-ph]`.

[103] J. M. Cline, "TASI Lectures on Early Universe Cosmology: Inflation, Baryogenesis and Dark Matter," *PoS* **TASI2018** (2019) 001, `arXiv:1807.08749 [hep-ph]`.

[104] D. Hooper, "Particle Dark Matter," in *Theoretical Advanced Study Institute in Elementary Particle Physics: The Dawn of the LHC Era*, pp. 709–764. 2010. `arXiv:0901.4090 [hep-ph]`.

[105] G. Belanger, F. Boudjema, A. Pukhov, and A. Semenov, "MicrOMEGAs: A Program for calculating the relic density in the MSSM," *Comput. Phys. Commun.* **149** (2002) 103–120, `arXiv:hep-ph/0112278`.

[106] P. Gondolo, J. Edsjo, P. Ullio, L. Bergstrom, M. Schelke, and E. A. Baltz, "DarkSUSY: Computing supersymmetric dark matter properties numerically," *JCAP* **07** (2004) 008, `arXiv:astro-ph/0406204`.

[107] R. J. Scherrer and M. S. Turner, "On the Relic, Cosmic Abundance of Stable Weakly Interacting Massive Particles," *Phys. Rev. D* **33** (1986) 1585. [Erratum: Phys.Rev.D 34, 3263 (1986)].

[108] J. M. Cline, K. Kainulainen, P. Scott, and C. Weniger, "Update on scalar

singlet dark matter," *Phys. Rev. D* **88** (2013) 055025, `arXiv:1306.4710 [hep-ph]`. [Erratum: Phys.Rev.D 92, 039906 (2015)].

[109] C.-K. Chua and G.-G. Wong, "Study of Majorana Fermionic Dark Matter," *Phys. Rev. D* **94** no. 3, (2016) 035002, `arXiv:1512.01991 [hep-ph]`.

[110] K. Griest and M. Kamionkowski, "Unitarity Limits on the Mass and Radius of Dark Matter Particles," *Phys. Rev. Lett.* **64** (1990) 615.

[111] B. W. Lee and S. Weinberg, "Cosmological Lower Bound on Heavy Neutrino Masses," *Phys. Rev. Lett.* **39** (1977) 165–168.

[112] D. E. Kaplan, M. A. Luty, and K. M. Zurek, "Asymmetric Dark Matter," *Phys. Rev. D* **79** (2009) 115016, `arXiv:0901.4117 [hep-ph]`.

[113] S. Nussinov, "TECHNOCOSMOLOGY: COULD A TECHNIBARYON EXCESS PROVIDE A 'NATURAL' MISSING MASS CANDIDATE?," *Phys. Lett. B* **165** (1985) 55–58.

[114] G. B. Gelmini, L. J. Hall, and M. J. Lin, "What Is the Cosmion?," *Nucl. Phys. B* **281** (1987) 726.

[115] K. M. Zurek, "Asymmetric Dark Matter: Theories, Signatures, and Constraints," *Phys. Rept.* **537** (2014) 91–121, `arXiv:1308.0338 [hep-ph]`.

[116] J. A. Harvey and M. S. Turner, "Cosmological baryon and lepton number in the presence of electroweak fermion number violation," *Phys. Rev. D* **42** (1990) 3344–3349.

[117] T. Lin, H.-B. Yu, and K. M. Zurek, "On Symmetric and Asymmetric Light Dark Matter," *Phys. Rev. D* **85** (2012) 063503, `arXiv:1111.0293 [hep-ph]`.

[118] M. L. Graesser, I. M. Shoemaker, and L. Vecchi, "Asymmetric WIMP dark matter," *JHEP* **10** (2011) 110, `arXiv:1103.2771 [hep-ph]`.

[119] M. Cirelli, P. Panci, G. Servant, and G. Zaharijas, "Consequences of DM/antiDM Oscillations for Asymmetric WIMP Dark Matter," *JCAP* **03** (2012) 015, `arXiv:1110.3809 [hep-ph]`.

[120] K. Petraki and R. R. Volkas, "Review of asymmetric dark matter," *Int. J. Mod. Phys. A* **28** (2013) 1330028, `arXiv:1305.4939 [hep-ph]`.

[121] L. J. Hall, J. March-Russell, and S. M. West, "A Unified Theory of Matter Genesis: Asymmetric Freeze-In," `arXiv:1010.0245 [hep-ph]`.

[122] M. Garny, M. Sandora, and M. S. Sloth, "Planckian Interacting Massive Particles as Dark Matter," *Phys. Rev. Lett.* **116** no. 10, (2016) 101302, `arXiv:1511.03278 [hep-ph]`.

[123] M. Garny, A. Palessandro, M. Sandora, and M. S. Sloth, "Theory and Phenomenology of Planckian Interacting Massive Particles as Dark Matter," *JCAP* **02** (2018) 027, `arXiv:1709.09688 [hep-ph]`.

[124] D. Baumann, "Inflation," in *Theoretical Advanced Study Institute in Elementary Particle Physics: Physics of the Large and the Small*, pp. 523–686. 2011. `arXiv:0907.5424 [hep-th]`.

Chapter 3

# Problems in the Early and Late-time Universe

The $\Lambda$CDM model, as discussed in the previous chapter, has proven to be remarkably successful in explaining the history of the Universe from the time of BBN to the present. It is a reliable and extensively tested description of the Universe, with no definitive observational or experimental data contradicting its predictions.

However, similar to the SM of particle physics, the standard cosmological model has its limitations. These limitations do not involve internal inconsistencies within the theory but rather address questions that the model does not provide answers to, asking for extensions.

In the following section, we will provide a brief overview of the main limitations of the $\Lambda$CDM model and introduce two well-known solutions: inflation and baryogenesis. The remaining part of this thesis will attempt to address other limitations and aim to develop a comprehensive framework that can accommodate various shortcomings, including those of the SM such as neutrino masses, DM, and more.

## 3.1 Shortcomings of the $\Lambda$CDM model

### 3.1.1 Large-scale smoothness

CMB observations reveal that the Universe was highly uniform across the entire sky, with temperature fluctuations of the order of one part in $10^5$ [1–3]. One might assume that if the entire observable Universe had been in causal contact at the time of recombination ($t_{\rm rec} \sim 10^5$ years or $z_{\rm rec} \simeq 1100$), microphysical processes like Compton scattering between photons and baryons would have resulted in a common temperature among all species, smoothing out any primordial temperature fluctuations.

However, within the standard cosmological model, this scenario is not feasible due to the existence of the particle horizon. As defined in section 2.2, the particle horizon represents the maximum distance a photon could have traveled since time $t_i$ until a given time $t$. It can be expressed as

$$d_H(t) = a\,\chi_{\rm ph}(t) = a\int_{t_i}^{t}\frac{dt'}{a(t')} = \frac{a}{H_0}\int_{a(t_i)}^{a(t)}\frac{da'}{\sqrt{\Omega_r + \Omega_m a + \Omega_\Lambda a^4}}\,, \tag{3.1}$$

where $\chi_{\rm ph}$ is the comoving particle horizon defined in Eq. (2.11). Taking $t_i = a(t_i) = 0$, corresponding to the time of the Big Bang, the particle horizon $d_H(t)$ can be interpreted as the maximum size of a causally connected region at time $t$, within which one could expect homogeneity due to thermal equilibrium.

At the time of recombination, the radius of each causally connected region, represented by the particle horizon, was approximately

$$d_H(t_{\rm rec}) \simeq \frac{5\times10^{-5}}{H_0} \simeq 0.15\ h^{-1}\ {\rm Mpc}\,, \tag{3.2}$$

where we plugged in the values of $\Omega_r$, $\Omega_m$ and $\Omega_\Lambda$ given in section 2.4.

In contrast, the radius of the last scattering surface, which defines the observable

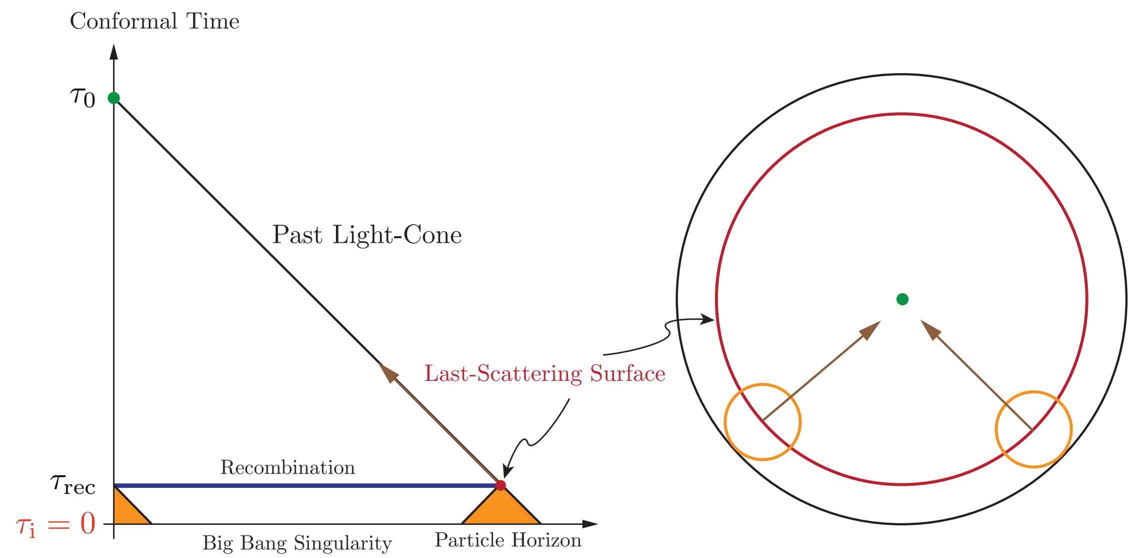

Figure 3.1: Conformal diagram illustrating the horizon problem in Big Bang cosmology. The orange circles represent causally disconnected regions of the CMB last-scattering surface (at recombination), while the green dot represents the observer. Figure from Ref. [4].

region of the CMB, was much larger

$$r_{ls}(t_{\rm rec}) = a\int_{t_{\rm rec}}^{t_0}\frac{dt'}{a(t')} = \frac{a}{H_0}\int_{a(t_{\rm rec})}^{1}\frac{da'}{\sqrt{\Omega_r+\Omega_m a+\Omega_\Lambda a^4}} \simeq \frac{3\times10^{-3}}{H_0} \simeq 9\ h^{-1}\ \mathrm{Mpc}\,, \tag{3.3}$$

where $t_0$ is the present time such that $a(t_0) = 1$, and we used the fact that CMB photons have been free-streaming from the surface of last scattering till today. This implies that CMB photons from regions with angular separations larger than $\Delta\theta \simeq 1.3°$ have not been in causal contact since their release, as illustrated in Figure 3.1. This discrepancy between the sizes of causally connected regions and of the observable CMB region is known as the *horizon problem*.

### 3.1.2 Spatial flatness

The spatial flatness of the Universe is a puzzle in the ΛCDM model. As presented in section 2.4, CMB data indicates a very small curvature parameter $\Omega_k \lesssim 0.001$ today [3], which is remarkable considering its time dependence. In fact, the Friedmann equation in (2.34) can be re-written as

$$\Omega_{\rm tot}(a) - 1 = \frac{k}{(aH)^2} \propto \begin{cases} t & \text{radiation domination}\,, \\ t^{2/3} & \text{matter domination}\,, \end{cases} \tag{3.4}$$

where $\Omega_{\rm tot}(a) = \sum_i \rho_i(a)/\rho_{\rm crit}(a)$ is the sum of all the species abundances present in the Universe, with $\rho_{\rm crit}(a) = 3H^2(a)/(8\pi G)$ [4]. In the last step of the previous equation, we used Eq. (2.31).

In either cases, the difference between $\Omega_{\rm tot}(a)$ and unity, as described by Eq. (3.4), increases with time, making a flat geometry unstable. Thus, a Universe so close to flatness today suggests an even closer proximity to flatness in the early Universe.

For instance, assuming the Einstein equations are valid since the Planck era ($t_{Pl} \sim 10^{-43}$ s after the Big Bang), when the temperature of the Universe was $T_{Pl} \sim 10^{19}$ GeV, it is possible to infer $|\Omega_{\rm tot} - 1|$ at $t_{Pl}$ knowing its value at present time ($t_0 \sim 10^{17}$ s, $T_0 \sim 10^{-13}$ GeV) as [4, 5]

$$\frac{|\Omega_{\rm tot} - 1|_{T\simeq T_{Pl}}}{|\Omega_{\rm tot} - 1|_{T\simeq T_0}} \approx \left(\frac{a_{Pl}}{a_0}\right)^2 \approx \left(\frac{T_0}{T_{Pl}}\right)^2 \approx \mathcal{O}(10^{-64})\,. \tag{3.5}$$

Similarly, at the time of BBN ($t_{\rm BBN} \sim 1$ s, $T_{\rm BBN} \sim 1$ MeV), we find

$$\frac{|\Omega_{\rm tot} - 1|_{T\simeq T_{\rm BBN}}}{|\Omega_{\rm tot} - 1|_{T\simeq T_0}} \approx \mathcal{O}(10^{-16})\,. \tag{3.6}$$

This unnatural fine-tuning of $|\Omega_{\rm tot}(a) - 1|$ close to zero at early times is known as the *flatness problem* in the ΛCDM model.

### 3.1.3 Baryon asymmetry

In section 1.2, we introduced the baryon-to-photon ratio $\eta$ as a measure of how many baryons over photons are present today. More precisely, the baryons here should be interpreted as the difference between baryons and antibaryons, because if they were present in the same amount in the early Universe we would expect they would have annihilated with each other and no baryonic matter should be visible. [1]

The asymmetry $\eta$ between baryons and antibaryons is called the baryon asymmetry of the Universe (BAU) and its value today can be summarized as [6]

$$\eta = \frac{n_B - n_{\bar{B}}}{n_\gamma} \simeq \begin{cases} [5.9 - 6.3] \times 10^{-10} & \text{BBN}\,, \\ [6.00 - 6.15] \times 10^{-10} & \text{CMB}\,, \end{cases} \tag{3.7}$$

or

$$\frac{n_B - n_{\bar{B}}}{s} = \frac{\eta}{7.04}\,, \tag{3.8}$$

where we used the entropy density as a reference, defined in section 2.5.1.

However, the standard cosmological model lacks a mechanism to generate the BAU. The process responsible for producing the asymmetry, known as baryogenesis, will be discussed in section 3.3.

### 3.1.4 Nature of dark matter and dark energy

As discussed extensively in the previous chapters, the origins and properties of two key components of the Universe's energy budget, DM and dark energy, remain a mystery. While the standard cosmological model provides predictions for their abundance and general characteristics, no specific model has been identified for DM and dark energy within the framework of the ΛCDM model.

### 3.1.5 Small-scale structure

In addition to the evidence for DM from Large-Scale Structure (LSS) discussed in section 1.5.4, N-body simulations have been conducted to study the behavior of collisionless and dissipationless CDM particles at smaller scales, corresponding to the size of galaxies. However, these simulations have revealed discrepancies when compared to observational data. Some notable inconsistencies include [7, 8]:

- The simulated DM halos prefer cuspy profiles, such as the NFW profile described

[1]Today we observe only matter, except for rare antiparticles produced by cosmic rays.

by Eq. (2.76). In contrast, observational data, particularly from dwarf galaxies, suggest that cored DM profiles provide a better fit to galaxy rotation curves [9]. This discrepancy is known as the *core-cusp problem*.

- Simulated halos predict a large number of substructures, resulting from earlier collapses on smaller scales. However, the observed number of satellite galaxies in the Milky Way is much smaller than expected, leading to the *missing satellite problem* [10, 11].

- Numerical simulations of CDM structure formation indicate an excessive amount of mass in the central regions (a few kpc) of halos and subhalos. This conflict is observed in satellites of our Galaxy and Andromeda galaxy [12] and is referred to as the *too-big-to-fail problem* [13].

Including baryonic physics in simulations offers a potential solution to some of the aforementioned challenges [14]. Analytical models combining supernova feedback and low star formation efficiency have shown promise in explaining why many DM subhalos around simulated Milky Way-like galaxies lack the visible component [7]. The Sloan Digital Sky Survey has identified some of these "invisible" satellite galaxies, known as ultra-faint dwarfs, with luminosities between $10^3$ and $10^5$ times that of the Sun [15]. Extrapolating these findings to the entire sky in the vicinity of the Milky Way suggests the existence of several hundred faint dwarf satellites, consistent with numerical simulations [16]. Thus, the missing satellite problem could potentially be resolved by the inclusion of baryonic physics [17].

Additionally, the effects of star formation and supernova feedback have been observed to flatten the central density of DM, transforming the cuspy profile predicted by CDM-only simulations into one with a nearly constant density core [18]. This alignment with observations is particularly evident in dwarf galaxies with stellar masses exceeding approximately $10^7\ M_\odot$, as determined from 21-cm measurements of nearby galaxies [19]. However, for galaxies with stellar masses below this threshold, analytical models indicate that the energy from supernovae alone is insufficient not only to create DM cores but also to resolve the too-big-to-fail problem [20, 21].

Alternatively, the discrepancies observed at small scales could indicate the presence of more intricate physics within the dark sector itself [22]. One possible explanation involves self-interacting DM (SIDM), where elastic scattering can modify halo mass profiles, leading to the formation of isothermal cores with nearly constant density [23]. In this scenario, particles in the outer regions exchange momentum with those in the central region, causing the central particles to gain energy and move outward [6, 24]. N-body simulations incorporating SIDM have supported this mechanism [25, 26]. The challenge of the missing satellite problem potentially finds a solution within the SIDM framework because SIDM tends to erase substructures by amplifying the impact of tidal disruption. This effect arises due to the fact that the SIDM density profiles are less concentrated than those in the standard ΛCDM scenario [23, 27].

The significant self-interaction of DM particles not only has the potential to resolve the core-cusp problem but also the too-big-to-fail and missing satellite problems, with cross sections $\sigma_s$ on the order of [27]

$$\frac{\sigma_s}{m_\chi} \sim (0.1 - 1)\, \frac{\mathrm{cm}^2}{g} \sim (0.2 - 2)\, \frac{\mathrm{barn}}{\mathrm{GeV}}\,. \tag{3.9}$$

These cross sections are approximately $10 - 100$ times smaller than those for nucleon-nucleon scattering and are consistent with constraints from the Bullet Cluster of $\sigma_s/m_\chi \lesssim 0.7\ \mathrm{cm}^2/\mathrm{g}$ [28].

In chapter 6, we will explore an alternative approach to addressing the core-cusp problem by exploiting DM oscillations and annihilations.

## 3.2 Inflation

The concept of inflation, proposed by Alan Guth in 1980 [29], offers a potential solution to the horizon and flatness problems in the early Universe. Here, we provide a brief overview of inflation based primarily on Ref. [6], while recommending Refs. [4, 5, 30–38] for a more comprehensive discussion.

Inflation involves a rapid expansion of the Universe before the era of radiation domination. This expansion allows for the separation of two points that were previously causally connected but are now at a much larger distance. This distance must exceed the size of the particle horizon at the end of inflation. Consequently, seemingly disconnected points in the present Universe were actually in thermal contact in the past, addressing the horizon problem. Similarly, the accelerated expansion during inflation stretches the fabric of space, resulting in an extremely small curvature for the Universe if the inflationary period is sufficiently long, thereby resolving the flatness problem.

More quantitatively and in its simplest incarnation, inflation is driven by a homogeneous scalar field $\phi$ called the inflaton, characterized by a flat potential $V(\phi)$. The flatness is measured by the potential slow-roll parameters $\epsilon$ and $\eta$ [2]

$$\epsilon = \frac{m_{Pl}^2}{2}\left(\frac{V'}{V}\right)^2, \qquad \eta = m_{Pl}^2\left(\frac{V''}{V}\right), \tag{3.10}$$

where $m_{Pl} = 2.44 \times 10^{18}$ GeV is the reduced Planck mass, and the prime indicates the derivative with respect to the field $\phi$.

The dynamics of the inflaton field, minimally-coupled to gravity, is governed by the action

$$\begin{aligned} S &= \int d^4x\,\sqrt{-g}\,\mathcal{L} = \int d^4x\,\sqrt{-g}\left[\frac{m_{Pl}^2}{2}R - \frac{1}{2}g^{\mu\nu}\partial_\mu\phi\partial_\nu\phi - V(\phi)\right] \\ &= S_{\rm EH} + S_\phi\,, \end{aligned} \tag{3.11}$$

where $\mathcal{L}$ is the total Lagrangian, $g$ is the determinant of the metric $g^{\mu\nu}$, $S_{\rm EH}$ is the so-called Einstein-Hilbert action and $S_\phi$ is the action of $\phi$. The energy-momentum tensor for $\phi$ can be derived by varying its action with respect to the metric.

By assuming a homogeneous field $\phi(t,\vec{x}) = \phi(t)$ and a FLRW metric (2.2), the

[2] The slow-roll parameters are more commonly defined via the Hubble parameter $H$ as: $\epsilon_1 = -\dot{H}/H^2 \simeq \epsilon$, $\epsilon_2 = \dot{\epsilon_1}/(H\epsilon_1) \simeq 4\epsilon - 2\eta$, $\epsilon_3 = \dot{\epsilon_2}/(H\epsilon_2)$, and so on. Here the over-dot means time-derivative. At leading order, the use of $\epsilon$ and $\eta$ in Eq. (3.10) instead of the generalized slow-roll parameters is essentially equivalent.

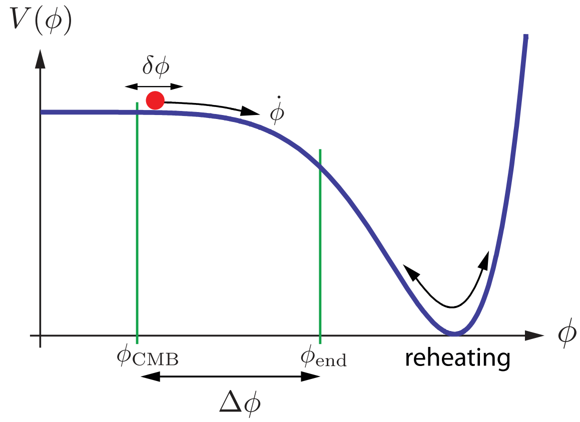


Figure 3.2: Evolution of the inflaton $\phi$ depicted as a ball rolling down a hill in the potential-energy plot $V(\phi)$ versus $\phi$. The acceleration phase, driven by the dominance of $V(\phi)$ over the kinetic term $\dot{\phi}/2$, ends at $\phi_{\rm end}$ when the two terms reach a comparable magnitude. Quantum perturbations $\delta\phi$ at $\phi_{\rm CMB}$ generate the observed CMB fluctuations. The energy stored in $\phi$ is later converted into radiation during reheating. Figure from Ref. [4].

scalar stress-energy tensor takes the form of a perfect fluid (2.23) described by

$$\begin{aligned} \rho_\phi &= \frac{1}{2}\dot{\phi}^2 + V(\phi)\,, \\ P_\phi &= \frac{1}{2}\dot{\phi}^2 - V(\phi)\,, \\ w_\phi &= \frac{P_\phi}{\rho_\phi} = \frac{\frac{1}{2}\dot{\phi}^2 - V(\phi)}{\frac{1}{2}\dot{\phi}^2 + V(\phi)}\,. \end{aligned} \tag{3.12}$$

When the potential $V$ dominates over the kinetic energy term $\dot{\phi}/2$, an accelerated expansion with $\omega_\phi \simeq -1$ similar to dark energy can be achieved. The Friedmann equation (2.29) can then be solved, resulting in

$$a(t) \sim \exp\left(\int H\,dt\right) \equiv e^N\,, \tag{3.13}$$

where $H \simeq \sqrt{V/(3m_{Pl}^2)} \equiv H_I \sim$ constant and $N$ is the so-called number of $e$-foldings. Here, we have assumed the inflaton $\phi$ dominates over the other components before the radiation era and the curvature term $\propto k$ is ignored because it will become negligible once inflation starts.

The dynamics of $\phi$ is governed by its equation of motion, obtained by varying the action in Eq. (3.11) with respect to $\phi$

$$\ddot{\phi} + 3H\dot{\phi} + V'(\phi) = 0 \,. \tag{3.14}$$

Figure 3.2 illustrates the evolution of $\phi$ for a generic potential $V(\phi)$. During the slow-roll phase, characterized by $\epsilon, \eta \ll 1$, the potential is sufficiently flat, and the acceleration term $\ddot{\phi}$ can be neglected in the equation of motion. This leads to

$$3H\dot{\phi} \approx -V'(\phi) \,, \tag{3.15}$$

which is the slow-roll equation of motion and it allows inflation to occur, with the kinetic term being subdominant compared to the potential.

As $\phi$ approaches the minimum of the potential, either $\epsilon$ or $\eta$ becomes larger than unity, and neglecting $\ddot{\phi}$ is no longer valid. Instead, the friction term $\propto H\dot{\phi}$ becomes negligible, and $\phi$ undergoes oscillations around the minimum of $V$ since

$$\ddot{\phi} \approx -V'(\phi) \,. \tag{3.16}$$

These oscillations lead to particle production and reheating of the Universe.

The reheating temperature $T_{\rm rh}$ can be estimated using the relation between time and temperature [6]

$$t \sim \frac{1}{\Gamma_\phi} \sim \frac{1}{H} \sim \frac{m_{Pl}}{\sqrt{\rho_\phi}} \sim \frac{m_{Pl}}{T_{\rm rh}^2} \,, \tag{3.17}$$

where $\Gamma_\phi$ is the decay rate of the inflaton. This estimation holds as long as $T_{\rm rh}$ remains below the energy scale of inflation, characterized by $V_i^{1/4}$, where $V_i$ represents the magnitude of the potential during the slow-roll phase [39, 40].

### 3.2.1 Solution to horizon and flatness problems

With the previous picture in mind, it is easy to understand now why inflation solves both the horizon and flatness problems.

Regarding the flatness problem, during inflation the Hubble rate $H_I$ is constant, and Eq. (3.4) simplifies to

$$|\Omega_{\rm tot}(a) - 1| = \frac{|k|}{(aH)^2} \sim a^{-2}\,. \tag{3.18}$$

To reproduce the observed value of $\Omega_{\rm tot}(a_0)$ close to unity today, the condition in Eq. (3.5) requires that $|\Omega_{\rm tot}(a) - 1|$ at the beginning of the radiation era (identified as the end of inflation at scale factor $a_{\rm end}$) should be on the order of

$$|\Omega_{\rm tot}(a_{\rm end}) - 1| \sim 10^{-60}\,. \tag{3.19}$$

By relating it to $|\Omega_{\rm tot}(a_i) - 1|$ at the beginning of inflation $a_i$ using Eq. (3.18), we find

$$\frac{|\Omega_{\rm tot}(a_{\rm end}) - 1|}{|\Omega_{\rm tot}(a_i) - 1|} = \left(\frac{a_i}{a_{\rm end}}\right)^2 = e^{-2N}\,, \tag{3.20}$$

where $N$ is the number of e-foldings defined in Eq. (3.13). Therefore, requiring $N \gtrsim 60$ is sufficient to naturally solve the flatness problem, even if $|\Omega_{\rm tot}(a_i) - 1|$ is of order unity.

The horizon problem is resolved within the inflationary scenario by considering the scale factor evolution given by Eq. (3.13), which can be re-written as

$$a(t) = a(0)\, e^{H_I t} \qquad \text{or} \qquad a(\tau) = -\frac{1}{H_I \tau}\,. \tag{3.21}$$

Unlike the standard Big Bang model where $a(0) = 0$ and $t = 0$ represents the singularity, inflation pushes the singularity to the infinite past ($t, \tau \to -\infty$). This implies that all points in the Universe were causally connected, as depicted in the top panel of Fig. 3.3. The choice of $t = -\infty$ as the time of the Big Bang is not necessary, and it is based on the assumption that Eq. (3.21) holds true for any time $t$, although we know it breaks down at the end of inflation.

The bottom panel of Fig. 3.3 provides an alternative understanding of how inflation solves the horizon problem. It compares the evolution of comoving scales with

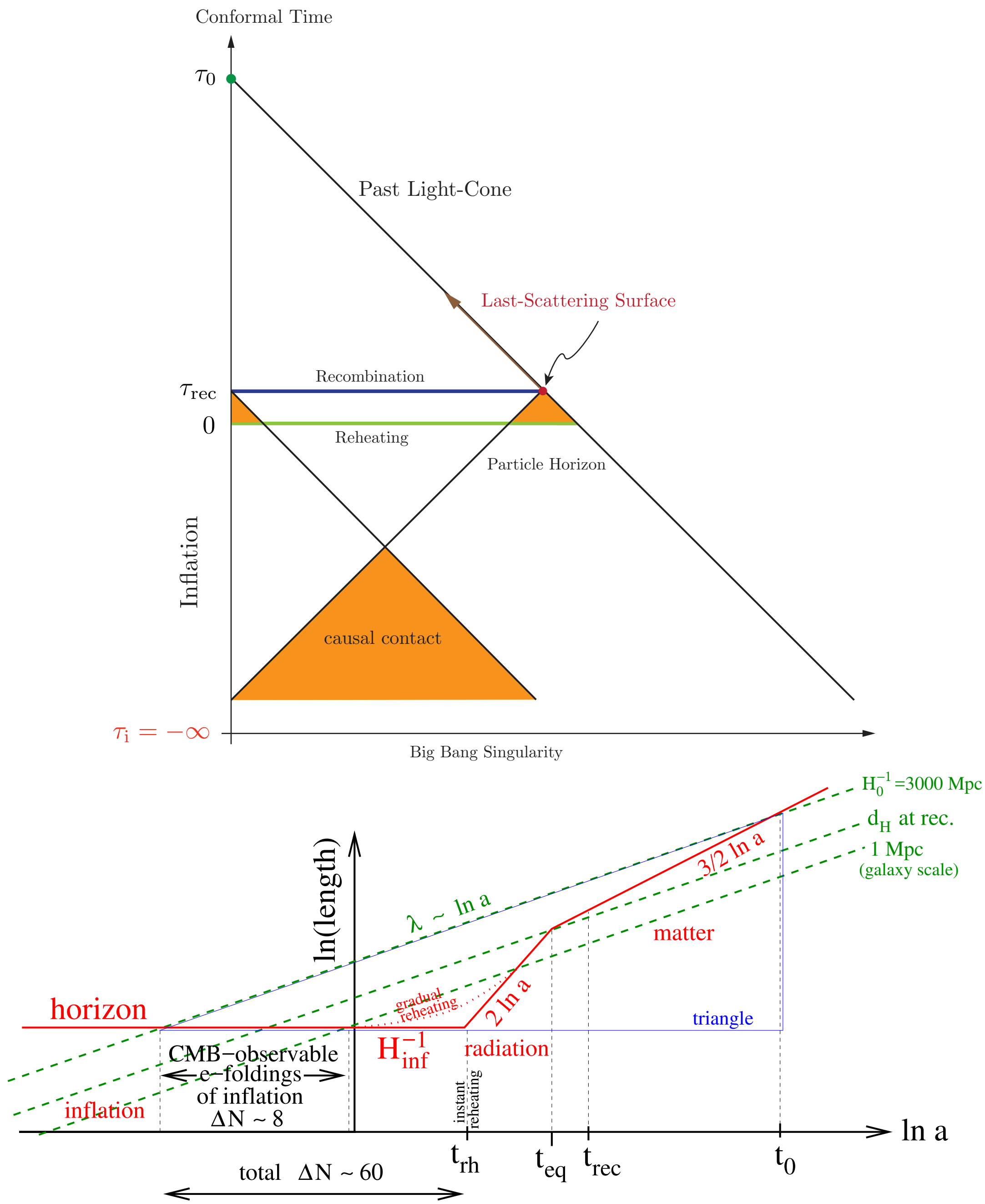


Figure 3.3: *Top*: Conformal-time diagram illustrating the inflationary scenario, where previously causally disconnected regions become in thermal contact in the past. Inflation extends the conformal time to negative values, leading to an "apparent" Big Bang at $\tau = 0$ corresponding to reheating, which is not a singularity. Figure taken from Ref. [4]. *Bottom*: Solution to the horizon problem shown through the evolution of comoving scales (green dashed curves) and the particle horizon (red solid curve) with the scale factor. From Ref. [6].

that of the particle horizon. In the standard Big Bang scenario, the current horizon scale (labeled by "$H_0^{-1} = 3000$ Mpc") shrinks as we go backward in time and always remains outside the particle horizon (red solid curve). However, if inflation lasted sufficiently long, the current horizon scale was inside the horizon in the distant past, allowing for causal processes to occur and make the Universe homogeneous.

Using the trigonometry of the aforementioned figure, we can estimate the minimum number of $e$-foldings $\Delta N$ required to solve the horizon problem. By focusing on the blue right triangle (labeled "triangle" in the figure) and assuming instantaneous reheating, we can approximate $\Delta N$ as [6]

$$\Delta N = \ln \frac{H_{\rm inf} T_0}{H_0 T_{\rm rh}} \,, \tag{3.22}$$

where $H_{\rm inf} \equiv H_I$, $T_0$ is the present-day temperature, and $T_{\rm rh}$ is the temperature at the time of reheating. Here, we have used the approximate relation between time $t$ (or scale factor $a$) and temperature, $T \sim a^{-1}$. A more precise derivation shows that the number of $e$-foldings $N_*$ until the end of inflation, when a comoving wave number scale $k_*$ crosses outside the horizon, is given by [41, 42]

$$N_* \approx 67 - \ln \frac{k_*}{a_0 H_0} + \frac{1}{4} \ln \frac{V_*^2}{m_{Pl}^4 \rho_{\rm end}} + \frac{1}{12} \ln \frac{T_{\rm rh}^4}{\rho_{\rm end}} \,, \tag{3.23}$$

where $\rho_{\rm end}$ is the value of $V(\phi)$ when inflation ends, and $V_*$ is the value of $V$ at horizon crossing. The latter is defined by

$$\frac{k_*}{a} = H \qquad \Longrightarrow \qquad H \simeq k_* e^{-Ht} = k_* e^{-N} \,, \tag{3.24}$$

where we have used Eq. (3.13) in the last step.

### 3.2.2 Connection with cosmological observables

Inflation not only solves the horizon and flatness problems but also provides a mechanism for generating the initial density perturbations required for the formation of cosmic structures [43–46]. These perturbations originate from quantum fluctuations of the inflaton field $\phi$ during inflation, as illustrated in Fig. 3.2. When two regions of the Universe have slightly different values of $\phi$, whose difference is $\delta\phi$, inflation ends at different times in each region, with a time difference of $\delta t \sim \delta\phi/\dot{\phi}$. This leads to local perturbations in the 3D curvature of a spatial slice at a fixed time. The magnitude of these perturbations, denoted by $\mathcal{R}_k$, can be estimated as [6]

$$\mathcal{R}_k \sim \frac{\delta a}{a} \sim H\delta t \sim \frac{H^2}{2\pi\dot{\phi}}\,, \tag{3.25}$$

where we have used that $a(t) \sim e^{Ht}$ during inflation. [3] In the last step, we used the fact that it is possible to show that the quantum fluctuation of a Fourier mode $k$ of the inflaton during inflation is [6, 48]

$$\delta\phi_k = \int d^3x\, e^{ik\cdot x}\, \delta\phi(x) \sim \frac{H}{2\pi} \tag{3.26}$$

for any $k$, implying that the fluctuations are nearly *scale invariant*. This scale invariance implies that $\mathcal{R}_k$ in Eq. (3.25) is also scale invariant, as $H$ and $\dot{\phi}$ change slowly during inflation. Using the slow-roll equation of motion (3.15), we can connect $\mathcal{R}_k$ to the inflaton potential $V(\phi)$ as [6]

$$\mathcal{R}_k \sim \frac{H^2}{2\pi\dot{\phi}} = \frac{H^3}{2\pi H\dot{\phi}} \sim \frac{V^{3/2}(\phi)}{2\pi\sqrt{3}\,V'(\phi)} \sim \sqrt{\frac{V(\phi)}{24\pi^2 m_{Pl}^4\epsilon}}\,, \tag{3.27}$$

where $\epsilon$ is the slow-roll parameter defined in Eq. (3.10). This expression is evaluated at the moment when the scale $k$ exits the horizon, namely at horizon crossing (3.24).

The correlation function of the 3D curvature is represented by the scalar power spectrum $P_s$, given by

$$\begin{aligned} P_s &= \int d^3x\, e^{ik\cdot x}\, \langle \mathcal{R}(0)\mathcal{R}(x)\rangle = |\mathcal{R}_k|^2 \sim \left(\frac{H^2}{2\pi\dot{\phi}}\right)^2 \sim \frac{V(\phi)}{24\pi^2 m_{Pl}^4\epsilon} \\ &\equiv A_s\left(\frac{k}{k_*}\right)^{n_s-1}\,, \end{aligned} \tag{3.28}$$

[3] For power-law inflation instead of exponential one, Eq. (3.25) would be modified (see Ref. [47]) since the metric fluctuations play a crucial role.

where $n_s$ represents the scalar spectral index and $A_s$ is the scalar amplitude. The value of $n_s$ characterizes the deviation from the scale-invariant Harrison-Zeldovich spectrum ($n_s = 1$), and it affects the amplitude of temperature fluctuations in the CMB angular power spectrum $C_\ell^{TT}$ defined in Eq. (1.14) [33, 49–51]. The Planck 2018 data provides the most recent measurements of $n_s$ and $A_s$ at 68% C.L., with values of [3]

$$n_s = 0.9649 \pm 0.0042\,, \qquad A_s = e^{3.044 \pm 0.014} \times 10^{-10}\,, \tag{3.29}$$

evaluated at the reference scale $k_* = 0.05$ Mpc$^{-1}$.

The prediction of the scalar spectral index within the framework of slow-roll inflation can be obtained from the scalar power spectrum (3.28). Specifically, we have

$$n_s - 1 = \frac{d \ln P_s}{d \ln k} \simeq \frac{d \ln P_s}{dN} \sim \left(3\frac{V'}{V} - 2\frac{V''}{V}\right)\frac{d\phi}{dN}\,, \tag{3.30}$$

where we have used Eq. (3.24) and $dN = H\,dt$ represents the change in the number of $e$-foldings. Using the slow-roll equation of motion (3.15) and $d\phi/dN = \dot{\phi}/H$, we arrive at the expression [6]

$$n_s - 1 = -6\epsilon + 2\eta + \mathcal{O}(\epsilon^2, \epsilon\eta, \eta^2)\,. \tag{3.31}$$

In addition to scalar perturbations, gravity waves, also known as tensor perturbations, acquire quantum fluctuations during inflation with an amplitude comparable to that of the inflaton field, given by [6, 33]

$$\delta(h_{\mu\nu})_k \sim \frac{H}{2\pi}\,. \tag{3.32}$$

The associated power spectrum, denoted as $P_t$, can be expressed as

$$P_t = \frac{2}{m_{Pl}^2}\left(\frac{H}{2\pi}\right)^2 \equiv A_t \left(\frac{k}{k_*}\right)^{n_t - 1}\,, \tag{3.33}$$

where $m_{Pl}$ is the reduced Planck mass. It is common to define the tensor-to-scalar

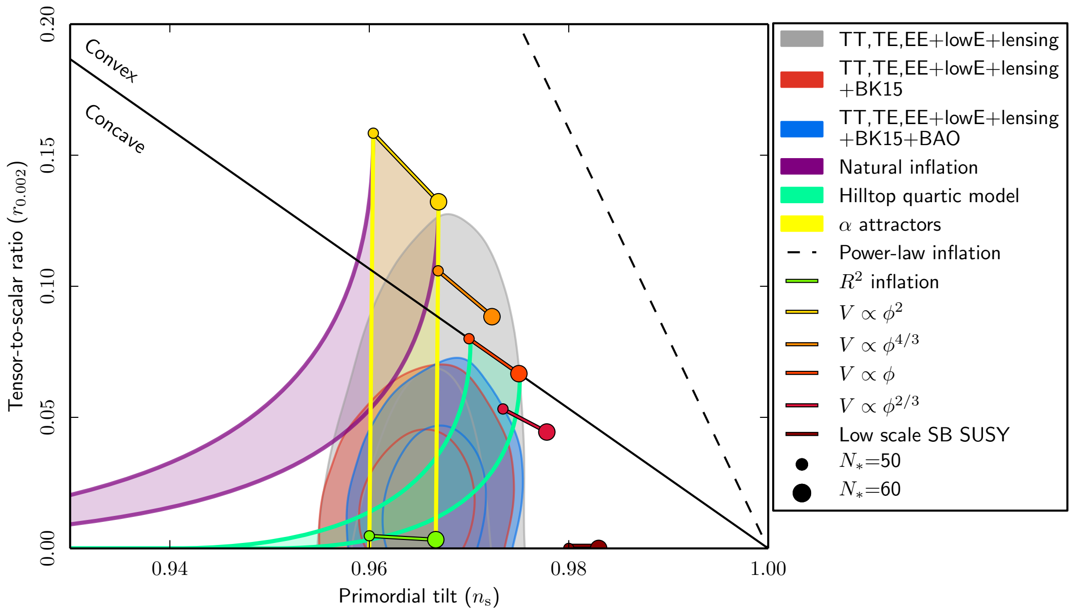


Figure 3.4: 68% and 95% C.L. constraints on $n_s$ and $r$ at $k = 0.002$ Mpc$^{-1}$ from Planck 2018 data alone and in combination with additional datasets. Theoretical predictions of popular inflationary models are included for comparison. From Ref. [52].

ratio, $r$, as

$$r = \frac{A_t}{A_s} = 16\epsilon\,, \tag{3.34}$$

which roughly quantifies the relative contributions of tensor and scalar perturbations to the angular power spectrum $C_\ell^{TT}$ at large scales. The absence of significant evidence for tensor perturbations imposes an upper limit [3]

$$r < 0.06\,, \tag{3.35}$$

evaluated at the reference scale $k_* = 0.002$ Mpc$^{-1}$.

#### 3.2.2.1 Current experimental bounds

CMB data tightly constrains the inflationary parameters $n_s$ and $r$, as shown in Fig. 3.4, along with a comparison to popular inflationary models.

One such model, known for its simplicity, is chaotic inflation [53]. It envisions the Universe starting in a disordered state, far from the potential's minimum, with energy density near the Planck scale. Inflation can initiate in any region, and once started, inhomogeneities are quickly smoothed out, leading to a much larger inflating region. The potential for chaotic inflation is given by

$$V(\phi) = \lambda\, m_{Pl}^4 \left(\frac{\phi}{m_{Pl}}\right)^p , \tag{3.36}$$

where $p > 0$. In this scenario, it is possible to show that [6]

$$n_s - 1 = -\frac{p+2}{(2N + p/2)} \simeq -\frac{(1+p/2)}{N} , \qquad r = \frac{4p}{N_*} , \tag{3.37}$$

where $N$ is the number of $e$-folding defined in Eq. (3.13) and $N_*$ is that at horizon crossing (3.24).

For an overview of the proposed inflationary models, refer to Refs. [6, 52, 54] and especially Ref. [55].

### 3.2.3 Beyond the simplest inflationary model

Inflation, as discussed so far, assumes a single scalar field with minimal coupling to gravity, driving the accelerated expansion and decaying into radiation, which starts the radiation-dominated era.

To provide a broader context for the rest of the thesis, particularly chapter 4, it is helpful to briefly mention additional technical aspects, including the generation of isocurvature perturbations and scenarios involving non-minimal coupling of the inflaton to gravity.

#### 3.2.3.1 Isocurvature perturbations

Single-field inflation predicts the generation of *adiabatic perturbations*, where different regions of the Universe have varying overdensities, but the fractional density perturbations are consistent across all species (baryons, CDM, photons, neutrinos). This is

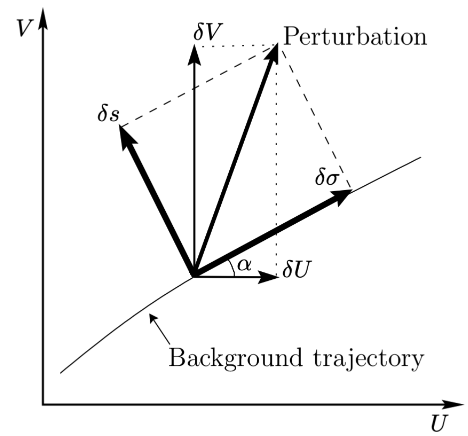


Figure 3.5: Decomposition of an arbitrary perturbation into adiabatic ($\delta\sigma$) and entropy ($\delta s$) components, with the angle of the tangent to the background trajectory denoted by $\alpha$. Figure adapted from Ref. [56].

expressed by the adiabatic condition

$$\frac{\delta\rho_b}{\rho_b} = \frac{\delta\rho_c}{\rho_c} = \frac{3}{4}\frac{\delta\rho_\gamma}{\rho_\gamma} = \frac{3}{4}\frac{\delta\rho_\nu}{\rho_\nu}\,, \tag{3.38}$$

with similar relations for velocities. This arises because inflation is driven by a single field, and each patch of the Universe during inflation is uniquely determined by the field's value, which governs a single temperature fluctuation controlling the densities. This is the reason of the factor 3/4 since $\rho_{\gamma,\nu} \sim T^4$ and $\rho_{b,c} \sim m\,T^3$. Precise observations of the CMB confirm the adiabatic nature of perturbations, limiting non-adiabatic contributions to be at most a percent-level fraction of the adiabatic ones [52].

In scenarios involving multi-field inflation, it is possible to have fluctuations among different particle species that violate Eq. (3.38). Additionally, particle number perturbations can occur between species, keeping the total $\delta\rho$ equal to zero. These fluctuations are known as *isocurvature perturbations* because they primarily affect the entropy of the system. Graphically, considering two canonically-normalized interacting fields $U$ and $V$, the adiabatic perturbation $\delta\sigma$ corresponds to the component of the two-field perturbation vector aligned with the background fields' evolution. On the other hand, fluctuations perpendicular to the background classical trajectory represent the isocurvature perturbations $\delta s$ [56, 57]. Refer to Fig. 3.5 for an illustration.

#### 3.2.3.2 Non-minimal coupling to gravity

The most favored inflationary models based on data have a non-minimal coupling of the inflaton to gravity. In the Jordan frame, in which the gravitational constant varies with time due to the evolution of the inflaton $\phi$, the Lagrangian is given by [6]

$$\mathcal{L}_J = \sqrt{-g_J}\left[\frac{1}{2}R_J(m_{Pl}^2 + \xi\phi^2) + \frac{1}{2}(\partial\phi)^2 - V(\phi)\right]. \tag{3.39}$$

To better understand the cosmology, we transition to the Einstein frame by performing a Weyl rescaling of the metric

$$g_E^{\mu\nu} = \frac{g_J^{\mu\nu}}{\Omega^2}, \qquad \Omega^2 = 1 + \xi\phi^2/m_{Pl}^2. \tag{3.40}$$

This transformation results in a complicated kinetic term for $\phi$, and the canonically normalized inflaton $\chi$ is related to $\phi$ by

$$\frac{d\chi}{d\phi} = \sqrt{\frac{\Omega^2 + 6\xi^2\phi^2/m_{Pl}^2}{\Omega^4}}. \tag{3.41}$$

In the Einstein frame, the Lagrangian takes the form

$$\mathcal{L}_E = \sqrt{-g_E}\left(\frac{1}{2}m_{Pl}^2 R_E + \frac{1}{2}(\partial\chi)^2 - \frac{V}{\Omega^4}\right), \tag{3.42}$$

which leads to a convex potential $V$ favored by Planck data.

## 3.3 Baryogenesis

In the context of inflation, the presence of the baryon asymmetry of the Universe (BAU) today (see section 3.1.3) suggests that the process responsible for its origin occurred after inflation. This is because any preexisting asymmetry would have been diluted by a factor of approximately $e^{-3N}$, where $N$ is the number of e-foldings.

There are three necessary conditions, known as the Sakharov conditions [58], for creating the BAU (see also Refs. [59–61]). These conditions are:

1. Baryon number ($B$) violation;

2. Out-of-equilibrium decay;

3. Symmetry violation of charge conjugation ($C$) and charge conjugation combined with parity ($CP$).

Let us briefly discuss the importance of satisfying these three requirements before introducing one of the most popular models for generating the BAU: leptogenesis.

### 3.3.1 $B$ violation

In section 2.4.1.1, we discovered that baryon and lepton numbers are accidental global symmetries in the SM. These symmetries are defined by the quantities

$$B = \int d^3x \, J_B^0(x) \,, \qquad L = \int d^3x \, J_L^0(x) \,, \tag{3.43}$$

where $J_B^0(x)$ and $J_L^0(x)$ are the zeroth components of the currents [62]

$$\begin{aligned} J_B^\mu &= \frac{1}{3} \sum_i^{N_f} \left( \bar{q}_{L_i} \gamma^\mu q_{L_i} - \bar{u}^c_{L_i} \gamma^\mu u^c_{L_i} - \bar{d}^c_{L_i} \gamma^\mu d^c_{L_i} \right) , \\ J_L^\mu &= \sum_i^{N_f} \left( \bar{\ell}_{L_i} \gamma^\mu \ell_{L_i} - \bar{e}^c_{L_i} \gamma^\mu e^c_{L_i} \right) . \end{aligned} \tag{3.44}$$

Here, $N_f = 3$ is the number of fermion generations, $q_L$ is the $\mathrm{SU}(2)_L$ quark doublet, while $u_L^c$ and $d_L^c$ refer to the right-handed quarks. Similarly, $\ell_L$ is the $\mathrm{SU}(2)_L$ lepton doublet and $e_L^c$ is the right-handed charged lepton.

While $B$ and $L$ in Eq. (3.43) are conserved at tree-level, they are not quantum-mechanically because of the Adler-Bell-Jackiw (ABJ) triangle anomaly (also known as chiaral anomaly) [63, 64]. In fact, the divergences of the currents in Eq. (3.44) do not vanish [65]

$$\partial_\mu J_B^\mu = \partial_\mu J_L^\mu = \frac{N_f}{64\pi^2} g^2 \epsilon^{\mu\nu\alpha\beta} W^a_{\mu\nu} W^a_{\alpha\beta} \,, \tag{3.45}$$

in the presence of a background $\mathrm{SU}(2)_L$ gauge field with field strength $W_{\mu\nu}$ and coupling constant $g$. The quantity $\epsilon^{\mu\nu\alpha\beta}$ is the Levi-Civita tensor. This equation reveals that the combination $(B-L)$ is a conserved charge, but $(B+L)$ is not. Although the violation of the $(B+L)$ symmetry is not observed in perturbative processes [66], it has significant implications in the early Universe, where non-perturbative processes could have occurred.

The violation of $(B+L)$ can be understood by examining the vacuum structure of the SU(2) gauge theory with spontaneously broken symmetries. Changes in $B$ and $L$ numbers are related to changes in the topological charge of the gauge field $W^a$ between two pure-gauge configurations (*i.e.* with $W^a_{\mu\nu}=0$ and zero energy) at initial time $t_i$ and final time $t_f$ [62, 66]. This relationship can be expressed as

$$\begin{aligned} B(t_f)-B(t_i) &= \int_{t_i}^{t_f} dt \int d^3x\, \partial_\mu J^\mu_B \\ &= N_f\left[\mathrm{N_{CS}}(t_f)-\mathrm{N_{CS}}(t_i)\right] \\ &= N_f\, \Delta\mathrm{N_{CS}} \equiv n\,, \end{aligned} \tag{3.46}$$

where $n$ is an integer known as the winding number and $\mathrm{N_{CS}}$ represents the topological charge or Chern-Simons number [67], defined by [66]

$$\mathrm{N_{CS}} = \int d^3x\, K^0\,, \qquad K^\mu = \frac{g^2}{32\pi^2}\epsilon^{\mu\nu\alpha\beta}\left(F^a_{\nu\alpha}A^a_\beta - \frac{g}{3}\epsilon_{abc}A^a_\nu A^b_\alpha A^c_\beta\right). \tag{3.47}$$

The presence of different pure-gauge configurations with different Chern-Simons number implies the existence of infinitely many degenerate ground states characterized by $\Delta\mathrm{N_{CS}} = \pm1, \pm2, \ldots$. To transition between these vacua, one must pass through configurations with non-vanishing field strength and energy, resulting in a potential barrier between each vacuum state. This barrier, depicted in the left panel of Fig. 3.6, has a height given by $E_{\rm sph} \simeq 8\pi\langle H(T)\rangle/g$, where $\langle H(T)\rangle$ is the Higgs field VEV at temperature $T$, and $\langle H(0)\rangle = \bar{v}$ with $\bar{v} = v/\sqrt{2} \approx 174$ GeV [66].

At zero temperature, vacuum-to-vacuum transitions occur only through tunneling, known as *instanton* configurations [65]. The tunneling rate per unit volume, estimated

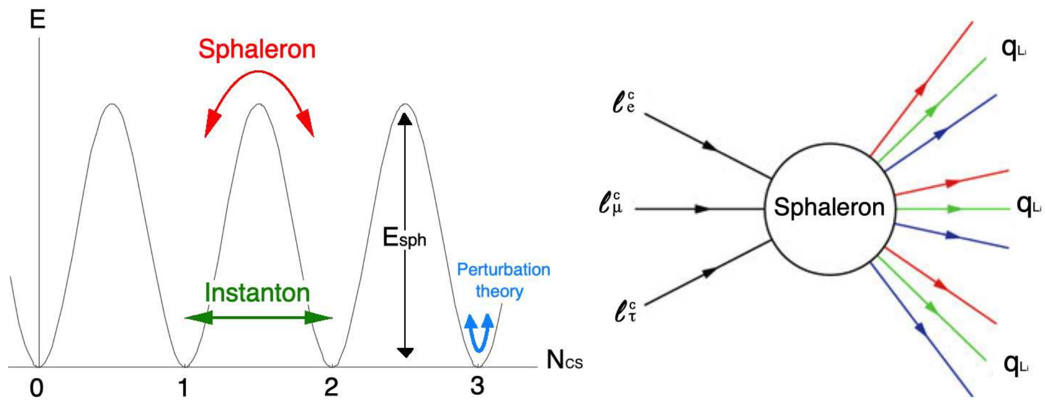


Figure 3.6: *Left*: Energy dependence of gauge field configurations with respect to the Chern-Simons number. Each minimum represents a valid perturbative vacuum state, while the instanton configuration determines the probability of tunneling between adjacent vacua. Sphalerons correspond to the potential's maxima (saddle points). Inspired by Ref. [68]. *Right*: Sphaleron transition conserving $(B-L)$. Figure adapted from Ref. [69].

as $\Gamma_{\text{inst}}/V \sim v^4\, e^{-2S} \sim v^4\, e^{-16\pi^2/g^2} \sim 10^{-160}\, v^4$ [6], is extremely small and unlikely to occur within the age of the Universe.

However, in the early Universe when all species were in thermal equilibrium, transitions between gauge vacua could occur through thermal fluctuations over the energy barrier instead of tunneling [70]. These transitions involve *sphalerons*, which are non-perturbative static field configurations that correspond to unstable solutions to the equation of motion [71] (see left panel of Fig. 3.6). Sphalerons allow for $(B+L)$-violating processes with a significant rate, as they are suppressed only by powers of the weak gauge coupling $g$ instead of exponential suppression.

During these transitions, the baryon and lepton numbers change by multiples of $N_f = 3$ units within the SM, as suggested by Eq. (3.46), resulting in the spontaneous production of 9 left-handed quarks (each quark has $B = 1/3$) and 3 left-handed leptons (each lepton has $L = 1$), one per generation [62, 66]. The associated Feynman diagram is displayed in the right panel of Fig. 3.6. The sphaleron rate per unit volume for $T \lesssim T_{\text{EW}} \simeq \mathcal{O}(100\text{ GeV})$ is given by [72]

$$\frac{\Gamma_{\text{sph}}}{V} \simeq \mathcal{O}(1)\left(\frac{E_{\text{sph}}}{T}\right)^3\left(\frac{M_W(T)}{T}\right)^4 T^4\, e^{-E_{\text{sph}}/T}\,, \tag{3.48}$$

where $M_W(T)$ is the temperature-dependent $W$ boson mass. On the other hand, for $T \gtrsim T_{\rm EW}$ it is approximately [73]

$$\frac{\Gamma_{\rm sph}}{V} \simeq 10^{-6}\, T^4 \,. \tag{3.49}$$

In a thermal volume $V \sim T^{-3}$, containing on average one particle of each type in the early-Universe plasma, the sphaleron rate scales as $\sim T$, which should be compared to the Hubble rate $H \sim T^2/m_{Pl}$. As a result, sphalerons come into equilibrium for $T \lesssim 10^{13}$ GeV and go out of equilibrium at the electroweak phase transition when the exponential suppression becomes effective [66]. Therefore, one of the criteria for baryogenesis, namely $B$ violation, is already present in the SM if the reheating temperature $T_{\rm rh} \gtrsim T_{\rm EW}$ following inflation.

In addition to the source of $B$ violation within the SM, beyond-SM theories can naturally include interactions that violate baryon number. Grand Unified Theory (GUT) models are a prominent example. In GUTs, where the strong and electroweak interactions are unified, quarks and leptons often belong to the same irreducible representation of the gauge group. This allows gauge bosons to mediate interactions that transform quarks into leptons or antiquarks, leading to $B$ violation [5].

### 3.3.2 Out-of-equilibrium decay

To generate and preserve the BAU, it is necessary to deviate from thermal equilibrium, because equilibrium processes have equal rates for their forward and backward reactions.

As discussed in section 2.5.2, a rule-of-thumb criterion to determine whether a particle physics process is in equilibrium in an expanding Universe is to compare the Hubble rate $H$ with the dominant particle interaction rate $\Gamma$. In the context of baryogenesis, $\Gamma$ corresponds to the decay rate, as decays typically regulate the relative number of particles and antiparticles.

By solving the Boltzmann equations for the number densities of particle and antiparticle species, considering an asymmetry parameter $\epsilon$ defined as [5]

$$\epsilon = \sum_f B_f \frac{\Gamma(X \to f) - \Gamma(\bar{X} \to \bar{f})}{\Gamma_X}\,, \tag{3.50}$$

where the sum runs over all final states $f$ with baryon number $B_f$ and $\Gamma_X$ is the total decay width of particle $X$, it can be shown that the net baryon abundance $Y_B$ is directly proportional to $\epsilon$. Most importantly, it is non-negligible whenever $\Gamma \ll H$, indicating that the system is out of equilibrium [6].

### 3.3.3 $C$ and $CP$ violation

The presence of $B$-violating interactions alone is not sufficient to generate a non-zero baryon asymmetry $\epsilon$, unless both $C$ and $CP$ are violated. In particular, $C$ violation ensures that the processes producing more baryons than anti-baryons are not counterbalanced by those producing more anti-baryons than baryons. Similarly, $CP$ violation is necessary to prevent the equal production of left-handed baryons and right-handed anti-baryons, as well as left-handed anti-baryons and right-handed baryons.

Although $C$ and $CP$ violations are observed in the SM, particularly in the CKM and possibly in the PMNS matrices [74] (see section 2.4.2.2), the amount of violation is insufficient to explain the observed baryon asymmetry [75]. This requires the presence of new physics processes beyond the SM.

Without delving into the specifics of any particular BSM model, there are three fundamental requirements to ensure $\epsilon \neq 0$ [5]:

1. $C$ and $CP$ violations should arise from the interference of loop diagrams with the tree-level diagram, necessitating the presence of complex coupling constants.

2. There must be at least two decaying particles that violate $B$, allowing for additional interactions. This prevents the removal of all phases of the complex couplings through field redefinitions.

3. The decaying particles must not be degenerate in mass to avoid complete cancellation of the baryon number produced by one particle with that produced by the other.

For a concrete example illustrating these requirements, we refer to Ref. [6].

### 3.3.4 Leptogenesis

Leptogenesis is a popular scenario for explaining the BAU because it can also address neutrino masses through the see-saw mechanism (see section 2.4.2.1).

The key elements involve introducing at least two families of heavy right-handed neutrinos $N_j$, which are singlets under the SM gauge group. These neutrinos couple to the lepton doublets and the Higgs field via Yukawa-like interactions described by

$$y_{\nu,\,ij}\bar{L}_i\tilde{H}N_{R,j} + \text{h.c.}\,. \tag{3.51}$$

Integrating out the heavy $N_j$ yields the Weinberg operator given by Eq. (2.57), with $z^{\nu}_{ij}/\Lambda_{\text{NP}} = (y_\nu M^{-1} y_\nu^T)_{ij}$, where $M$ represents the Majorana mass matrix of the heavy neutrinos. This leads to a mass term of the form $\frac{1}{2}M_j\bar{N}jN_j^c$, which violates lepton number by two units. After electroweak symmetry breaking, the SM neutrinos acquire small Majorana masses given by

$$m_{\nu,\,ij} = v^2(y_\nu M^{-1} y_\nu^T)_{ij}\,. \tag{3.52}$$

The out-of-equilibrium decays of $N_j \to L_i H^c$ can generate a lepton asymmetry, which can be partially converted into the baryon asymmetry through sphaleron interactions, with $Y_B \sim -Y_L/3$ [6]. Despite its simplicity as a theory of baryogenesis, leptogenesis suffers from a proliferation of free parameters, mainly associated with the phases in the Yukawa couplings $y_{\nu,\,ij}$, making it challenging to test experimentally.

# Bibliography


[1] D. J. Fixsen, E. S. Cheng, J. M. Gales, J. C. Mather, R. A. Shafer, and E. L. Wright, "The Cosmic Microwave Background spectrum from the full COBE FIRAS data set," *Astrophys. J.* **473** (1996) 576, `arXiv:astro-ph/9605054`.

[2] D. J. Fixsen, "The Temperature of the Cosmic Microwave Background," *Astrophys. J.* **707** (2009) 916–920, `arXiv:0911.1955 [astro-ph.CO]`.

[3] **Planck** Collaboration, N. Aghanim *et al.*, "Planck 2018 results. VI. Cosmological parameters," *Astron. Astrophys.* **641** (2020) A6, `arXiv:1807.06209 [astro-ph.CO]`. [Erratum: Astron.Astrophys. 652, C4 (2021)].

[4] D. Baumann, "Inflation," in *Theoretical Advanced Study Institute in Elementary Particle Physics: Physics of the Large and the Small*, pp. 523–686. 2011. `arXiv:0907.5424 [hep-th]`.

[5] E. W. Kolb and M. S. Turner, *The Early Universe*, vol. 69. 1990.

[6] J. M. Cline, "TASI Lectures on Early Universe Cosmology: Inflation, Baryogenesis and Dark Matter," *PoS* **TASI2018** (2019) 001, `arXiv:1807.08749 [hep-ph]`.

[7] D. H. Weinberg, J. S. Bullock, F. Governato, R. Kuzio de Naray, and A. H. G. Peter, "Cold dark matter: controversies on small scales," *Proc. Nat. Acad. Sci.* **112** (2015) 12249–12255, `arXiv:1306.0913 [astro-ph.CO]`.

[8] J. S. Bullock and M. Boylan-Kolchin, "Small-Scale Challenges to the ΛCDM Paradigm," *Ann. Rev. Astron. Astrophys.* **55** (2017) 343–387, `arXiv:1707.04256 [astro-ph.CO]`.

[9] W. J. G. de Blok, "The Core-Cusp Problem," *Adv. Astron.* **2010** (2010) 789293, `arXiv:0910.3538 [astro-ph.CO]`.

[10] B. Moore, S. Ghigna, F. Governato, G. Lake, T. R. Quinn, J. Stadel, and P. Tozzi, "Dark matter substructure within galactic halos," *Astrophys. J. Lett.* **524** (1999) L19–L22, arXiv:astro-ph/9907411.

[11] A. A. Klypin, A. V. Kravtsov, O. Valenzuela, and F. Prada, "Where are the missing Galactic satellites?," *Astrophys. J.* **522** (1999) 82–92, arXiv:astro-ph/9901240.

[12] E. J. Tollerud *et al.*, "The SPLASH Survey: Spectroscopy of 15 M31 Dwarf Spheroidal Satellite Galaxies," *Astrophys. J.* **752** (2012) 45, arXiv:1112.1067 [astro-ph.CO].

[13] M. Boylan-Kolchin, J. S. Bullock, and M. Kaplinghat, "Too big to fail? The puzzling darkness of massive Milky Way subhaloes," *Mon. Not. Roy. Astron. Soc.* **415** (2011) L40, arXiv:1103.0007 [astro-ph.CO].

[14] J. Zavala and C. S. Frenk, "Dark matter haloes and subhaloes," *Galaxies* **7** no. 4, (2019) 81, arXiv:1907.11775 [astro-ph.CO].

[15] **SDSS** Collaboration, V. Belokurov *et al.*, "Cats and Dogs, Hair and A Hero: A Quintet of New Milky Way Companions," *Astrophys. J.* **654** (2007) 897–906, arXiv:astro-ph/0608448.

[16] E. J. Tollerud, J. S. Bullock, L. E. Strigari, and B. Willman, "Hundreds of Milky Way Satellites? Luminosity Bias in the Satellite Luminosity Function," *Astrophys. J.* **688** (2008) 277–289, arXiv:0806.4381 [astro-ph].

[17] S. Y. Kim, A. H. G. Peter, and J. R. Hargis, "Missing Satellites Problem: Completeness Corrections to the Number of Satellite Galaxies in the Milky Way are Consistent with Cold Dark Matter Predictions," *Phys. Rev. Lett.* **121** no. 21, (2018) 211302, arXiv:1711.06267 [astro-ph.CO].

[18] F. Governato, A. Zolotov, A. Pontzen, C. Christensen, S. H. Oh, A. M. Brooks, T. Quinn, S. Shen, and J. Wadsley, "Cuspy No More: How Outflows Affect the

Central Dark Matter and Baryon Distribution in Lambda CDM Galaxies," *Mon. Not. Roy. Astron. Soc.* **422** (2012) 1231–1240, arXiv:1202.0554 [astro-ph.CO].

[19] F. Walter, E. Brinks, W. J. G. de Blok, F. Bigiel, R. C. Kennicutt, Jr., M. D. Thornley, and A. K. Leroy, "THINGS: The HI Nearby Galaxy Survey," *Astron. J.* **136** (1985) 2563–2647, arXiv:0810.2125 [astro-ph].

[20] J. Penarrubia, A. Pontzen, M. G. Walker, and S. E. Koposov, "The coupling between the core/cusp and missing satellite problems," *Astrophys. J. Lett.* **759** (2012) L42, arXiv:1207.2772 [astro-ph.GA].

[21] S. Garrison-Kimmel, M. Rocha, M. Boylan-Kolchin, J. Bullock, and J. Lally, "Can Feedback Solve the Too Big to Fail Problem?," *Mon. Not. Roy. Astron. Soc.* **433** (2013) 3539, arXiv:1301.3137 [astro-ph.CO].

[22] N. Arkani-Hamed, D. P. Finkbeiner, T. R. Slatyer, and N. Weiner, "A Theory of Dark Matter," *Phys. Rev. D* **79** (2009) 015014, arXiv:0810.0713 [hep-ph].

[23] D. N. Spergel and P. J. Steinhardt, "Observational evidence for selfinteracting cold dark matter," *Phys. Rev. Lett.* **84** (2000) 3760–3763, arXiv:astro-ph/9909386.

[24] E. Bertschinger, "Self - similar secondary infall and accretion in an Einstein-de Sitter universe," *Astrophys. J. Suppl.* **58** (1985) 39.

[25] M. Rocha, A. H. G. Peter, J. S. Bullock, M. Kaplinghat, S. Garrison-Kimmel, J. Onorbe, and L. A. Moustakas, "Cosmological Simulations with Self-Interacting Dark Matter I: Constant Density Cores and Substructure," *Mon. Not. Roy. Astron. Soc.* **430** (2013) 81–104, arXiv:1208.3025 [astro-ph.CO].

[26] M. Vogelsberger, J. Zavala, and A. Loeb, "Subhaloes in Self-Interacting Galactic Dark Matter Haloes," *Mon. Not. Roy. Astron. Soc.* **423** (2012) 3740, arXiv:1201.5892 [astro-ph.CO].

[27] S. Tulin and H.-B. Yu, "Dark Matter Self-interactions and Small Scale Structure," *Phys. Rept.* **730** (2018) 1–57, `arXiv:1705.02358 [hep-ph]`.

[28] S. W. Randall, M. Markevitch, D. Clowe, A. H. Gonzalez, and M. Bradac, "Constraints on the Self-Interaction Cross-Section of Dark Matter from Numerical Simulations of the Merging Galaxy Cluster 1E 0657-56," *Astrophys. J.* **679** (2008) 1173–1180, `arXiv:0704.0261 [astro-ph]`.

[29] A. H. Guth, "The Inflationary Universe: A Possible Solution to the Horizon and Flatness Problems," *Phys. Rev. D* **23** (1981) 347–356.

[30] D. Baumann, *Cosmology.* Cambridge University Press, 7, 2022.

[31] S. Dodelson, *Modern Cosmology.* Academic Press, Amsterdam, 2003.

[32] S. Dodelson and F. Schmidt, *Modern Cosmology.* Academic Press, Amsterdam, 2020.

[33] V. Mukhanov, *Physical Foundations of Cosmology.* Cambridge University Press, Oxford, 2005.

[34] S. Weinberg, *Cosmology.* Oxford University Press, 2008.

[35] O. F. Piattella, *Lecture Notes in Cosmology.* UNITEXT for Physics. Springer, Cham, 2018. `arXiv:1803.00070 [astro-ph.CO]`.

[36] P. J. E. Peebles, *Principles of physical cosmology.* Princeton University Press, 1994.

[37] R. H. Brandenberger, "Inflationary cosmology: Progress and problems," in *IPM School on Cosmology 1999: Large Scale Structure Formation.* 1, 1999. `arXiv:hep-ph/9910410`.

[38] W. H. Kinney, "TASI Lectures on Inflation," `arXiv:0902.1529 [astro-ph.CO]`.

[39] M. A. Amin, M. P. Hertzberg, D. I. Kaiser, and J. Karouby, "Nonperturbative Dynamics Of Reheating After Inflation: A Review," *Int. J. Mod. Phys. D* **24** (2014) 1530003, `arXiv:1410.3808 [hep-ph]`.

[40] R. Allahverdi, R. Brandenberger, F.-Y. Cyr-Racine, and A. Mazumdar, "Reheating in Inflationary Cosmology: Theory and Applications," *Ann. Rev. Nucl. Part. Sci.* **60** (2010) 27–51, `arXiv:1001.2600 [hep-th]`.

[41] A. R. Liddle and S. M. Leach, "How long before the end of inflation were observable perturbations produced?," *Phys. Rev. D* **68** (2003) 103503, `arXiv:astro-ph/0305263`.

[42] **Planck** Collaboration, P. A. R. Ade *et al.*, "Planck 2015 results. XX. Constraints on inflation," *Astron. Astrophys.* **594** (2016) A20, `arXiv:1502.02114 [astro-ph.CO]`.

[43] S. W. Hawking, "The Development of Irregularities in a Single Bubble Inflationary Universe," *Phys. Lett. B* **115** (1982) 295.

[44] A. A. Starobinsky, "Dynamics of Phase Transition in the New Inflationary Universe Scenario and Generation of Perturbations," *Phys. Lett. B* **117** (1982) 175–178.

[45] A. H. Guth and S. Y. Pi, "Fluctuations in the New Inflationary Universe," *Phys. Rev. Lett.* **49** (1982) 1110–1113.

[46] J. M. Bardeen, P. J. Steinhardt, and M. S. Turner, "Spontaneous Creation of Almost Scale - Free Density Perturbations in an Inflationary Universe," *Phys. Rev. D* **28** (1983) 679.

[47] V. F. Mukhanov and P. J. Steinhardt, "Density perturbations in multifield inflationary models," *Phys. Lett. B* **422** (1998) 52–60, `arXiv:astro-ph/9710038`.

[48] R. H. Brandenberger, "Lectures on the theory of cosmological perturbations," *Lect. Notes Phys.* **646** (2004) 127–167, `arXiv:hep-th/0306071`.

[49] V. F. Mukhanov, "CMB-slow, or how to estimate cosmological parameters by hand," *Int. J. Theor. Phys.* **43** (2004) 623–668, `arXiv:astro-ph/0303072`.

[50] S. Weinberg, "Fluctuations in the cosmic microwave background. 1. Form-factors and their calculation in synchronous gauge," *Phys. Rev. D* **64** (2001) 123511, `arXiv:astro-ph/0103279`.

[51] S. Weinberg, "Fluctuations in the cosmic microwave background. 2. C(l) at large and small l," *Phys. Rev. D* **64** (2001) 123512, `arXiv:astro-ph/0103281`.

[52] **Planck** Collaboration, Y. Akrami *et al.*, "Planck 2018 results. X. Constraints on inflation," *Astron. Astrophys.* **641** (2020) A10, `arXiv:1807.06211 [astro-ph.CO]`.

[53] A. D. Linde, "Chaotic Inflation," *Phys. Lett. B* **129** (1983) 177–181.

[54] **Particle Data Group** Collaboration, R. L. Workman *et al.*, "Review of Particle Physics," *PTEP* **2022** (2022) 083C01.

[55] J. Martin, C. Ringeval, R. Trotta, and V. Vennin, "The Best Inflationary Models After Planck," *JCAP* **03** (2014) 039, `arXiv:1312.3529 [astro-ph.CO]`.

[56] C. Gordon, D. Wands, B. A. Bassett, and R. Maartens, "Adiabatic and entropy perturbations from inflation," *Phys. Rev. D* **63** (2000) 023506, `arXiv:astro-ph/0009131`.

[57] C. T. Byrnes and D. Wands, "Curvature and isocurvature perturbations from two-field inflation in a slow-roll expansion," *Phys. Rev. D* **74** (2006) 043529, `arXiv:astro-ph/0605679`.

[58] A. D. Sakharov, "Violation of CP Invariance, C asymmetry, and baryon asymmetry of the universe," *Pisma Zh. Eksp. Teor. Fiz.* **5** (1967) 32–35.

[59] A. Y. Ignatiev, N. V. Krasnikov, V. A. Kuzmin, and A. N. Tavkhelidze, "Universal CP Noninvariant Superweak Interaction and Baryon Asymmetry of the Universe," *Phys. Lett. B* **76** (1978) 436–438.

[60] M. Yoshimura, "Unified Gauge Theories and the Baryon Number of the Universe," *Phys. Rev. Lett.* **41** (1978) 281–284. [Erratum: Phys.Rev.Lett. 42, 746 (1979)].

[61] D. Toussaint, S. B. Treiman, F. Wilczek, and A. Zee, "Matter - Antimatter Accounting, Thermodynamics, and Black Hole Radiation," *Phys. Rev. D* **19** (1979) 1036–1045.

[62] M.-C. Chen, "TASI 2006 Lectures on Leptogenesis," in *Theoretical Advanced Study Institute in Elementary Particle Physics: Exploring New Frontiers Using Colliders and Neutrinos*, pp. 123–176. 3, 2007. `arXiv:hep-ph/0703087`.

[63] S. L. Adler, "Axial vector vertex in spinor electrodynamics," *Phys. Rev.* **177** (1969) 2426–2438.

[64] J. S. Bell and R. Jackiw, "A PCAC puzzle: $\pi^0 \to \gamma\gamma$ in the $\sigma$ model," *Nuovo Cim. A* **60** (1969) 47–61.

[65] G. 't Hooft, "Symmetry Breaking Through Bell-Jackiw Anomalies," *Phys. Rev. Lett.* **37** (1976) 8–11.

[66] J. M. Cline, "Baryogenesis," in *Les Houches Summer School - Session 86: Particle Physics and Cosmology: The Fabric of Spacetime*. 9, 2006. `arXiv:hep-ph/0609145`.

[67] S.-S. Chern and J. Simons, "Characteristic forms and geometric invariants," *Annals Math.* **99** (1974) 48–69.

[68] S. Amoroso, D. Kar, and M. Schott, "How to discover QCD Instantons at the LHC," *Eur. Phys. J. C* **81** no. 7, (2021) 624, `arXiv:2012.09120 [hep-ph]`.

[69] N. D. Barrie, *An Asymmetric Universe from Inflation*, pp. 61–87. Springer International Publishing, Cham, 2018. https://doi.org/10.1007/978-3-319-94715-0_3.

[70] V. A. Kuzmin, V. A. Rubakov, and M. E. Shaposhnikov, "On the Anomalous Electroweak Baryon Number Nonconservation in the Early Universe," *Phys. Lett. B* **155** (1985) 36.

[71] F. R. Klinkhamer and N. S. Manton, "A Saddle Point Solution in the Weinberg-Salam Theory," *Phys. Rev. D* **30** (1984) 2212.

[72] P. B. Arnold and L. D. McLerran, "Sphalerons, Small Fluctuations and Baryon Number Violation in Electroweak Theory," *Phys. Rev. D* **36** (1987) 581.

[73] D. Bodeker, G. D. Moore, and K. Rummukainen, "Chern-Simons number diffusion and hard thermal loops on the lattice," *Phys. Rev. D* **61** (2000) 056003, arXiv:hep-ph/9907545.

[74] G. Elor *et al.*, "New Ideas in Baryogenesis: A Snowmass White Paper," in *Snowmass 2021*. 3, 2022. arXiv:2203.05010 [hep-ph].

[75] G. W. S. Hou, "Source of CP Violation for the Baryon Asymmetry of the Universe," *Int. J. Mod. Phys. D* **20** (2011) 1521–1532, arXiv:1101.2161 [hep-ph].

Chapter 4

# Affleck-Dine Inflation

**James M. Cline, Matteo Puel, and Takashi Toma**

*McGill University, Department of Physics, 3600 University Street, Montréal, QC H3A2T8 Canada*

Published in Physics Review D: Phys. Rev. D 101, 043014 (2020), [arXiv:1909.12300]

## 4.0 Prologue

In the previous chapter, we discussed inflation and baryogenesis as distinct events in the Universe's history. Notably, we emphasized that the BAU should have emerged after the inflationary phase to avoid being washed out. In this chapter, we will explore the intriguing possibility of a shared origin for these two events.

**Abstract**

The Affleck-Dine mechanism in its simplest form provides baryogenesis from the out-of-equilibrium evolution of a complex scalar field with a simple renormalizable potential. We show that such a model, supplemented by nonminimal coupling to gravity can also provide inflation, consistent with Planck constraints, simultaneously with the

generation of the baryon asymmetry. The predictions of the model include significant tensor-to-scalar ratio and possibly baryon isocurvature fluctuations. The reheating temperature is calculable, making the model fully predictive. We require color triplet scalars for reheating and transfering the primordial baryon asymmetry to quarks; these could be observable at colliders. They can also be probed at higher scales by searches for quark compositeness in dijet angular distributions, and flavor-changing neutral current effects.

## 4.1 Introduction

Theoretical mechanisms for baryogenesis abound and take many very different forms, but one common attribute is that they occur at some cosmological epoch following inflation. This seems like a necessity, since exponential expansion should dilute any preexisting baryon asymmetry. Warm inflation provides an exception; see Ref. [1]. In this work we show that it is possible to generate the baryon asymmetry of the Universe (BAU) during the course of ordinary cold inflation, if the inflaton carries baryon number.

One of the earliest proposed baryogenesis mechanisms was that of Affleck and Dine (AD) [2] in which a complex scalar field carrying baryon number can spontaneously create the BAU starting from field values displaced from the minimum of the potential. A baryon-violating coupling is required to satisfy Sakharov's requirements [3]. Although the AD mechanism is most commonly implemented in supersymmetric models whose potentials have nearly flat directions, it was originally demonstrated using a simple renormalizable potential of the form

$$V_J = m_\phi^2|\phi|^2 + \lambda|\phi|^4 + i\lambda'(\phi^4 - \phi^{*4}) \tag{4.1}$$

in the seminal reference [2]. (We use the subscript to denote the Jordan frame since a change of frames will be invoked below.) When $\lambda' = 0$, the potential has a U(1) global symmetry, that we will identify with baryon number. A generic initial condition such that $\langle\phi\rangle \neq 0$ spontaneously breaks CP and thermal equilibrium, as also required by Sakharov. The field winds around, at first generating baryon number, until Hubble damping of $\langle\phi(t)\rangle$ makes the $\lambda'$ interaction negligible, and baryon number becomes conserved.

The same kind of potential could be used for a two-field version of chaotic inflation [4]. Constraints from the Planck experiment now disfavor chaotic inflation with $\phi^2$ or $\phi^4$ potentials [5] since they predict too high tensor-to-scalar ratio $r$, given the measured value of the scalar perturbation spectral index $n_s = 0.965 \pm 0.004$. However this problem can be cured by adding a nonminimal coupling to gravity (we write $2\xi$ rather than $\xi$ to agree with the usual convention for inflation along a single component of the complex scalar),

$$\mathcal{L}_J = \frac{m_P^2}{2} R\left(1 + 2\xi|\phi|^2\right) \tag{4.2}$$

where $m_P = 2.44 \times 10^{18}\,\mathrm{GeV}$ is the reduced Planck mass, that we set to 1 unless explicitly shown. This introduces a noncanonical kinetic term for $\phi$ upon Weyl-transforming to the Einstein frame, and it flattens the potential at large field values to make the predictions of the model compatible with Planck observations, in the case of a real scalar field inflaton [6, 7]. Our goal is to determine whether this can still hold true for the two-field model, while at the same time generating the observed baryon asymmetry. A potential issue is that isocurvature perturbations can be produced in two-field models, and these are constrained by the Planck observations.

A similar idea was explored in Refs. [8, 9], using flat directions in supergravity models as the inflaton. Models with simpler potentials, more similar to the one we consider, were studied in Refs. [10, 11]. All of these previous studies are in the context of conventional chaotic inflation, and do not address the problem that the predictions of $r$ versus $n_s$ are excluded by Planck data. Isocurvature fluctuations are considered in Refs. [8, 10]. We disagree with the predictions of Ref. [8], which do not take into account the decay of the entropy perturbation between the horizon crossing and late times. The predictions of Ref. [10] for the power in entropy perturbations are consistent with ours, being below observable levels, but in the following we point out that the correlation between adiabatic and entropy modes can be large enough to be observed in current and upcoming CMB experiments.

## 4.2 Model

Equations (4.1) and (4.2) are sufficient to determine the inflationary trajectory until the epoch of reheating. It is convenient to make a Weyl rescaling of the metric, $g_{\mu\nu} \to \Omega^2 g_{\mu\nu}$, with $\Omega^2 = 1/(1 + 2\xi|\phi|^2)$. The Lagrangian in the Einstein frame, including gravity, is then

$$\mathcal{L}_E = \frac{1}{2}R + \Omega^4 \left( \frac{|\partial\phi|^2}{\Omega^2} + 3\xi^2(\partial|\phi|^2)^2 - V_J \right) . \tag{4.3}$$

Writing the complex scalar as $\phi = (X + iY)/\sqrt{2}$ and ignoring spatial gradients, the scalar kinetic term takes the form

$$\mathcal{L}_{\text{kin}} = \frac{1}{2}\Omega^2(\dot{X}^2 + \dot{Y}^2) + 3\Omega^4\xi^2(X\dot{X} + Y\dot{Y})^2 \tag{4.4}$$

with $\Omega^2 = 1/(1 + \xi(X^2 + Y^2))$. Thus $X$ and $Y$ are not canonically normalized fields. Instead of reexpressing them in terms of such fields, we will numerically solve the equations of motion for $X$ and $Y$ to determine the predictions for inflation and baryogenesis. Details of deriving the first-order equations convenient for numerical integration can be found for example in Ref. [12] [see Eqs. (2.100-2.101)]. We choose initial conditions close to the inflationary attractor solution, by setting the derivatives of the canonical momenta $\Pi_X = d\mathcal{L}/d\dot{X}$, $\Pi_Y = d\mathcal{L}/d\dot{Y}$ initially to zero.

More is needed in order to get reheating and transfer of the baryon asymmetry, initially stored in $\phi$, into quarks. A natural option for reheating is the Higgs portal coupling $\lambda_{\phi h}|\phi|^2|H|^2$. However since we also need a coupling to quarks, it is simpler to use the same interactions both for reheating and for transfer of the baryon asymmetry. This can be accomplished by introducing three QCD triplet scalars $\Phi_i$ carrying baryon number 2/3, with couplings

$$V_\Phi = \epsilon_{abd}\left(\lambda''\,\phi^*\,\Phi_1^a\Phi_2^b\Phi_3^d + y_1\Phi_1^a\,\bar{u}_R^b d_R^{c,d} + y_2\Phi_2^a\,\bar{u}_R^b d_R^{c,d} + y_3\Phi_3^a\,\bar{d}_R^b d_R^{c,d}\right) + \text{H.c.} \tag{4.5}$$

where $a, b, d$ are color indices, the quarks are right-handed [$\mathrm{SU}(2)_L$ singlets] and $d_R^c$ denotes the conjugate down-type quark. For simplicity we omit generation indices on the quarks and the Yukawa couplings $y_i$. These interactions allow for the decay $\phi \to uudddd$ via virtual $\Phi_i$ exchange, and imply that $\phi$ carries baryon number 2. The same conclusion holds if we choose $\Phi_1\bar{u}_R u_R^c$ and $\Phi_{2,3}\bar{d}_R d_R^c$ couplings instead of (4.5).

For small values of the $\lambda''$ coupling, we can view reheating as occurring through the perturbative decays $\phi \to \Phi_1\,\Phi_2\,\Phi_3$, which rapidly thermalize with the quarks and thereby the rest of the standard model degrees of freedom. Assuming that $\phi$ is much heavier than $\Phi_i$, the decay rate is

$$\Gamma_\phi = \frac{3\,\lambda''^2}{256\pi^3}\,m_\phi \tag{4.6}$$

## 4.3 Inflation + baryogenesis

An interesting aspect of our model is that the same parameters that influence inflationary observables can also affect the magnitude of the baryon asymmetry. Thus, although we describe the two processes separately, a fully viable model depends upon the interplay between the two.

### 4.3.1 Slow-roll parameters

Although we can solve for the inflaton trajectories without reference to the canonically normalized fields, that we will denote by $(U, V)$, it is necessary to know them for computing inflationary perturbations. It is straightforward to diagonalize the kinetic term (4.4) at a given point in field space to find

$$
\begin{aligned}
\begin{pmatrix} \dot{X} \\ \dot{Y} \end{pmatrix} &= \begin{pmatrix} c_\theta & -s_\theta \\ s_\theta & c_\theta \end{pmatrix} \begin{pmatrix} e_1 & 0 \\ 0 & e_2 \end{pmatrix} \begin{pmatrix} c_\psi & s_\psi \\ -s_\psi & c_\psi \end{pmatrix} \begin{pmatrix} \dot{U} \\ \dot{V} \end{pmatrix} \\
&\equiv Z_0 R_\psi \begin{pmatrix} \dot{U} \\ \dot{V} \end{pmatrix} \equiv Z \begin{pmatrix} \dot{U} \\ \dot{V} \end{pmatrix} \qquad (4.7)
\end{aligned}
$$

with $e_1 = \Omega^{-1}(1 + 6\Omega^2\xi^2(X^2 + Y^2))^{-1/2}$, $e_2 = \Omega^{-1}$, $\theta = \tan^{-1}(Y/X)$. Then $\mathcal{L}_{\rm kin} = \frac{1}{2}(\dot{U}^2 + \dot{V}^2)$. The matrix $Z$ allows us to transform slow-roll parameters computed in the original field basis (indices $i, j$) to those in the canonical basis (indices $m, n$):

$$
\begin{aligned}
\epsilon_m &= \frac{\left(Z_{im}\,\partial_i V_E\right)^2}{2V_E^2} \\
\eta_{mn} &= Z_{im} Z_{jn} \frac{\partial_i \partial_j V_E}{V_E} + Z_{im} \partial_i Z_{jn} \frac{\partial_j V_E}{V_E} \qquad (4.8)
\end{aligned}
$$

where $V_E = \Omega^4 V_J$ is the Einstein frame potential.

The extra rotation $R_\psi$ in Eq. (4.7) is not necessary for diagonalizing the kinetic term, but it is required in order to be able to interpret $Z$ as the Jacobian matrix $\partial(X, Y)/\partial(U, V)$. If we omit $R_\psi$ so that $Z = Z_0$, such an interpretation is not generally consistent since then the relations

$$
\begin{aligned}
U_{,YX} &= \partial_X (Z_0^{-1})_{12} = \partial_Y (Z_0^{-1})_{11} = U_{,XY} \\
V_{,YX} &= \partial_X (Z_0^{-1})_{22} = \partial_Y (Z_0^{-1})_{21} = V_{,XY} \qquad (4.9)
\end{aligned}
$$

may not be satisfied. We are free to set $\psi = 0$ at a given point in field space, such as the point of horizon crossing, but not its derivatives. Equations (4.9) with $Z_0 \to Z_0 R_\psi$ imply

$$
\begin{aligned}
(Z_0^{-1})_{22}\,\psi_{,X} - (Z_0^{-1})_{21}\,\psi_{,Y} &= (Z_0^{-1})_{12,X} - (Z_0^{-1})_{11,Y} \\
-(Z_0^{-1})_{12}\,\psi_{,X} + (Z_0^{-1})_{11}\,\psi_{,Y} &= (Z_0^{-1})_{22,X} - (Z_0^{-1})_{21,Y}\,.
\end{aligned}
$$

This has the solution

$$\begin{pmatrix} \psi_{,X} \\ \psi_{,Y} \end{pmatrix} = \det Z_0\,(Z_0^{-1})^T \begin{pmatrix} (Z_0^{-1})_{12,X} - (Z_0^{-1})_{11,Y} \\ (Z_0^{-1})_{22,X} - (Z_0^{-1})_{21,Y} \end{pmatrix}$$
$$= \Omega^2 \frac{e_1 e_2}{X^2+Y^2} \begin{pmatrix} -Y \\ X \end{pmatrix} . \tag{4.10}$$

The consistent identification of $Z$ with a Jacobian matrix ensures that $\eta_{mn}$ is symmetric in $mn$, even though the second term in (4.8) is not explicitly symmetric. Then we can write the second term in Eq. (4.8) as

$$\partial_i Z = (\partial_i Z_0)\, R_\psi + \psi_{,i} Z_0 \partial_\psi R_\psi \,. \tag{4.11}$$

To compute the adiabatic perturbation spectrum and the tensor-to-scalar ratio, we use the slow-roll formalism of Ref. [13], evaluating the slow-roll parameters (4.8) along the numerically determined inflationary solutions. This requires going from the $U, V$ basis of the canonical fields to the $\sigma, s$ basis of adiabatic/entropy directions, defined by

$$\begin{aligned} d\sigma &= c_\alpha dU + s_\alpha dV \\ ds &= -s_\alpha dU + c_\alpha dV \end{aligned} \tag{4.12}$$

with $\alpha = \tan^{-1}(\dot{V}/\dot{U})$. The rotated slow-roll parameters are given by [14]

$$\begin{aligned} \epsilon_\sigma &= (c_\alpha \partial_U V_E + s_\alpha \partial_V V_E)^2/(2V_E^2) \\ \epsilon_s &\cong 0 \\ \eta_{\sigma\sigma} &= c_\alpha^2 \eta_{UU} + 2c_\alpha s_\alpha \eta_{UV} + s_\alpha^2 \eta_{VV} \\ \eta_{ss} &= s_\alpha^2 \eta_{UU} - 2c_\alpha s_\alpha \eta_{UV} + c_\alpha^2 \eta_{VV} \\ \eta_{\sigma s} &= c_\alpha s_\alpha (\eta_{VV} - \eta_{UU}) + (c_\alpha^2 - s_\alpha^2)\eta_{UV} \end{aligned} \tag{4.13}$$

Then to leading order in the slow-roll expansion, the scalar spectral index and tensor-

| model | $m_\phi/m_P$ | $\lambda$ | $\lambda'$ | $\xi$ | $\lambda''$ | $X_0$ | $Y_0$ | $N_{\rm tot}$ | $N_*$ | $n_s$ | $r$ | $T_{RS}$ |
|---|---|---|---|---|---|---|---|---|---|---|---|---|
| 1 | $6.43\times10^{-7}$ | $8.73\times10^{-12}$ | $6.89\times10^{-13}$ | $5.96\times10^{-2}$ | $8.67\times10^{-5}$ | 18.4 | 6.63 | 65 | 53.1 | 0.962 | $1.4\times10^{-2}$ | $9\times10^{-2}$ |
| 2 | $4.67\times10^{-7}$ | $3.49\times10^{-11}$ | $6.68\times10^{-13}$ | 0.180 | $2.93\times10^{-5}$ | 23.7 | 0.91 | 146 | 52.0 | 0.961 | $7.2\times10^{-3}$ | $4\times10^{-5}$ |

Table 4.1: Parameters and initial values for two benchmark models, including the total number of $e$-foldings of inflation $N_{\rm tot}$, number of $e$-foldings before horizon crossing $N_*$, spectral index $n_s$ (evaluated at $k_* = 0.05\,{\rm Mpc}^{-1}$), tensor-to-scalar ratio $r$ and off-diagonal transfer matrix element $T_{RS}$, which is a measure of the correlation between adiabatic and isocurvature perturbations.

to-scalar ratio are [13]

$$\begin{aligned} n_s &= 1-(6-4c_\Delta^2)\epsilon_\sigma + 2s_\Delta^2\eta_{\sigma\sigma} + 4s_\Delta c_\Delta \eta_{\sigma s} + 2c_\Delta^2\eta_{ss} \\ r &= 16\epsilon_\sigma \end{aligned} \tag{4.14}$$

where $c_\Delta = -2\mathcal{C}\,\eta_{\sigma s}$, $s_\Delta = +\sqrt{1-c_\Delta^2}$, $\mathcal{C} = 2-\ln 2-\gamma \cong 0.73$ ($\gamma$ is the Euler constant), and the derivatives of $V_E$ with respect to $U$ and $V$ are computed similarly to Eq. (4.8). Including the effect of isocurvature modes ($T_{RS}$), which we will explain below, the scalar amplitude is

$$A_s = \frac{V_*}{24\pi^2\,\epsilon_\sigma}\left[1-2\epsilon_\sigma+2\mathcal{C}\left(3\,\epsilon_\sigma-\eta_{\sigma\sigma}-2\eta_{\sigma s}T_{RS}\right)\right] \tag{4.15}$$

with $V_* = V_E$ evaluated at horizon crossing and we have neglected terms of order $T_{RS}^2$.

We searched the parameter space via Markov Chain Monte Carlo (MCMC) to find models in agreement with Planck constraints on $A_s$, $n_s$, $r$ and the baryon asymmetry (discussed below). Two benchmark models are identified in Table 4.1. The correlation of $r$ with $n_s$ is shown over the interval $N_* = (50, 60)$ $e$-foldings, for several values of $\xi$ and fixed values of the potential parameters corresponding to the two benchmark models in Fig. 4.1.

On each curve a heavy dot is indicated to show the prediction of the model, for the chosen value of $\lambda''$, that determines the reheating temperature and thus the number of $e$-foldings $N_*$ between horizon crossing and the end of inflation. The value of $N_*$

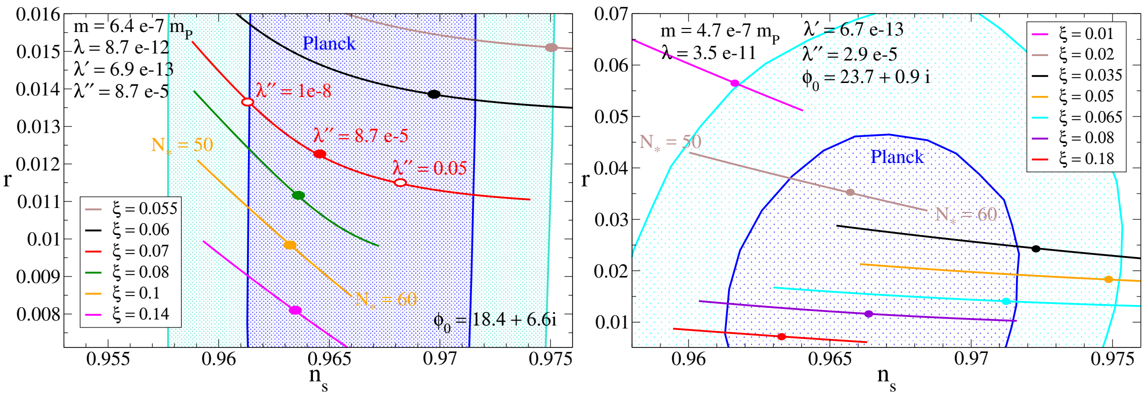


Figure 4.1: Scalar-to-tensor ratio versus spectral index for several values of the non-minimal coupling $\xi$, varied around the parameters of models 1 (left) and 2 (right) given in Table 4.1. The pivot scale is $k_* = 0.002\,\text{Mpc}^{-1}$ for comparison with the Planck $1\,\sigma$ and $2\,\sigma$ allowed regions. The number of $e$-foldings between horizon crossing and the end of inflation, $N_*$, is allowed to vary between 50 and 60, but the definite values shown by the solid dots are predicted by making a specific choice of $\lambda''$. The dependence on $\lambda''$ is shown on the $\xi = 0.07$ curve for model 1.

is determined by solving Eq. (47) of Ref. [5] (see also Ref. [15]),

$$N_* = 67 - \ln\left(\frac{k_*}{H_0}\right) + \frac{1}{4}\ln\left(\frac{V_*^2}{m_P^4\rho_{\text{end}}}\right) + \frac{1}{12}\ln\left(\frac{\rho_{\text{rh}}}{g_*\rho_{\text{end}}}\right) \tag{4.16}$$

where $H_0$ is the Hubble constant today, $\rho_{\text{end}}$ is the energy density at the end of inflation, $g_* = 106.75 + 18$ (counting the extra degrees of freedom from the colored scalars), and the reference scale $k_* = 0.002\,\text{Mpc}^{-1}$ for comparison with the Planck preferred regions in the $n_s$-$r$ plane. The energy density at the time of reheating is $\rho_{\text{rh}} = \frac{4}{3}\Gamma_\phi^2 m_P^2$, as explained below — see Eq. (4.24); this makes $N_*$ depend upon $\lambda''$ as $N_* \sim \frac{1}{3}\ln\lambda''$. Since $V_*$ appears in Eq. (4.16) but also depends upon $N_*$, we rescale the parameters of the potential while iteratively determining $N_*$, keeping $A_s = e^{3.044}\times 10^{-10}$ fixed to the observed central value [5]. To illustrate the dependence on $\lambda''$, we indicate two other horizon-crossing positions on the $\xi = 0.07$ curve of model 1, for larger and smaller values of $\lambda''$. The relation between $\lambda''$ and the reheat temperature will be discussed in Sec. 4.3.3.

The strong correlation between the tensor ratio $r$ and the nonminimal coupling $\xi$ is also clearly seen in the larger sample of models from two MCMC chains, Fig. 4.2

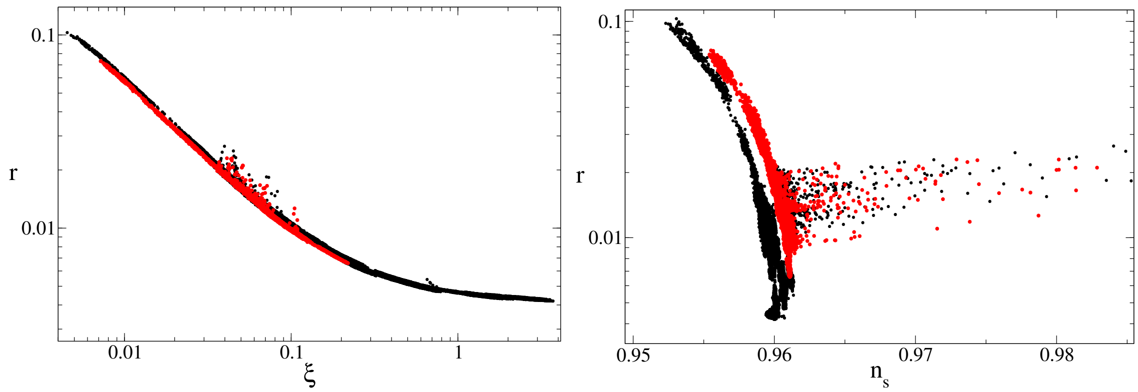


Figure 4.2: Scatter plots from the MCMC search of parameter space. Left: correlation of $r$ with $\chi$. Right: correlation of $r$ (evaluated at $k_* = 0.002\,\mathrm{Mpc}^{-1}$) with $n_s$ (at $k_* = 0.05\,\mathrm{Mpc}^{-1}$). Black versus red points correspond to two different chains as described in the text.

(left). The points shown have a total $\chi^2 < 10$, defining $\chi^2$ in the usual way in terms of the observables $r$, $n_s$ and $\eta_B$,

$$\chi^2 = \sum_i \frac{(x_i - \bar{x}_i)^2}{\delta x_i^2} \tag{4.17}$$

summed over observables $x_i$ with central value $\bar{x}_i$ and experimental error $\delta x_i$. The black points come from a chain where the experimental limit on $r$ was somewhat relaxed. The correlation between $r$ and $n_s$ within the chains is also notable, as shown in Fig. 4.2 (right). In both plots, one can notice a population of models scattered away from the main trends. These are special cases in which the total number of $e$-foldings of inflation are not much greater than the minimum required, $N_e \sim 60$. We will discuss these cases in more detail below.

### 4.3.2 Isocurvature fluctuations

During inflation, the components of the canonically normalized fields $U, V$ can fluctuate by order $H/(2\pi)$, where $H$ is the Hubble parameter. Fluctuations $d\sigma$ normal to the inflaton trajectory are entropy modes, and they could become observable isocurvature fluctuations if they decay into different species than the adiabatic fluctuations, that are parallel to the trajectory. The relation between adiabatic/entropy perturbations and the canonical field fluctuations is given in Eq. (4.12).

To find the observable entropy fluctuations, we need to compare $(d\sigma, ds)$ to the directions in field space that correspond to baryon number fluctuations $dB$, and the orthogonal direction, that will be related to $(dU, dV)$ through some different rotation angle $\beta$. Numerically we find that $\beta \cong 0$ during inflation, implying that the entropy perturbations are purely in the baryon number (compensated by radiation) to a good approximation, known as BDI (baryon density isocurvature). This can be seen starting from the definition of baryon density from the zeroth component of the baryon current carried by $\phi$,

$$n_B = j_B^0 = -2i(\phi\dot{\phi}^* - \phi^*\dot{\phi}) = 2(Y\dot{X} - X\dot{Y}) \tag{4.18}$$

leading to the fluctuation

$$\delta n_B = 2(\dot{X}\,\delta Y - \dot{Y}\,\delta X) + \ldots \tag{4.19}$$

where the omitted terms are subleading in the slow-roll approximation. The direction of the fluctuation (4.19) turns out numerically to be very nearly orthogonal to the inflaton trajectory in field space. Although both $\sigma$ and $s$ decay into quarks during reheating, only $s$ decays encode the baryon asymmetry, whereas $\sigma$ decays equally into quarks and antiquarks, that thermalize with the rest of the SM degrees of freedom.

We closely follow the formalism of Ref. [13] (see also Ref. [14]) to compute the power in isocurvature. The main task is to numerically solve the equations for the evolution of the perturbations $dU$, $dV$ between horizon crossing and the end of inflation,

$$
\begin{aligned}
dU'' &= -C_1 dU' - 3(\bar{\eta}_{UU} dU + \bar{\eta}_{UV} dV) + U' dC \\
&+ (U'^2)' dU + (U'V')' dV \\
dV'' &= -C_1 dV' - 3(\bar{\eta}_{VV} dV + \bar{\eta}_{UV} dU) + V' dC \\
&+ (V'^2)' dV + (U'V')' dU
\end{aligned}
\tag{4.20}
$$

and to relate them to the adiabatic/isocurvature perturbations $d\sigma$, $ds$ using Eq. 4.12). Here primes denote $d/dN_e$, $C_1 = 3 + H'/H$, and $dC = C_1(U'dU + V'dV)$. The barred parameters $\bar{\eta}_{ij}$ are defined as in Eq. (4.8), except that we divide by the total energy density $\rho = 3H^2$ instead of $V_E$, so that the equations remain valid even when the slow-roll approximation is not.

The transfer function for the curvature (adiabatic) and entropy perturbations is a matrix

$$
\begin{pmatrix} T_{RR} & T_{RS} \\ T_{SR} & T_{SS} \end{pmatrix}
\tag{4.21}
$$

that relates the amplitudes of $(d\sigma, ds)$ at horizon crossing to those at a later time, after inflation. We can get the matrix elements by solving the system (4.20) from the respective initial conditions $(d\sigma, ds) = (1, 0)$ and $(0, 1)$. The results are shown for the two benchmark models in Fig. 4.3. The adiabatic perturbation is conserved, resulting in $T_{RR} = 1$, and the $T_{SR}$ element is always very small, in accordance with the slow-roll prediction $T_{SR} = 0$ [13], meaning that there is negligible conversion of entropy to adiabatic modes.

Numerically it is difficult to evolve the transfer matrix deep into the post-inflationary phase, because of the fast oscillations of the fields. However since the solutions become quite smooth at this point, it seems reasonable to extrapolate them into the reheating era. Hence we have assumed that $T_{RR}$ and $T_{RS}$ continue to stay constant, and that $T_{SR}$ and $T_{SS}$ remain negligibly small, as Fig. 4.3 suggests. Once the inflaton decays, both adiabatic and entropy modes (which are approximately aligned with the modulus and phase of $\phi$) will decay into quarks and antiquarks. The only difference

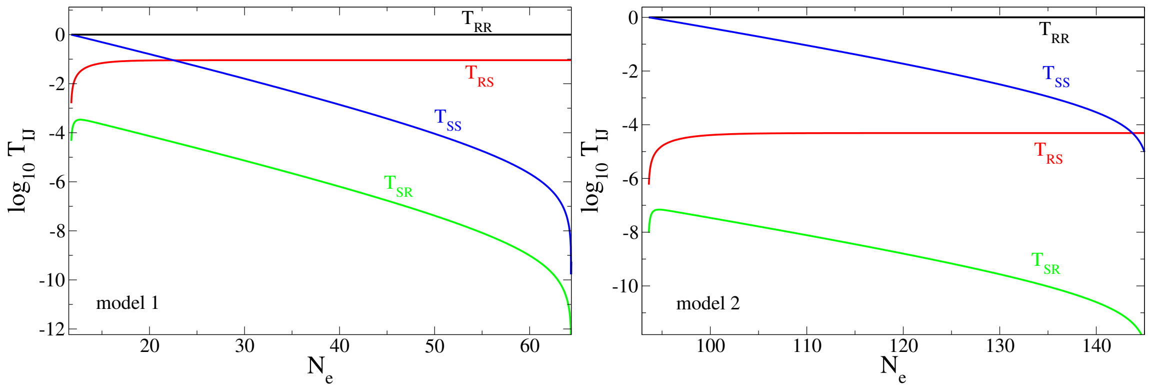

Figure 4.3: Evolution of transfer matrix elements for the adiabatic and isocurvature perturbations, versus number of $e$-foldings, for models 1 and 2 from Table 4.1.

between the two modes is that the isocurvature modes are also correlated with baryon number, which is conserved by this time, so that the baryon asymmetry encoded in $s$ is preserved during the decays.

For all cases in our MCMC, the entropy autocorrelation $T_{SS} \ll 0.1$ is too small to be observable, but in some cases like in model 1, the cross-correlation $T_{RS}$ is significant. It is related to the correlation angle, which to leading order in slow-roll parameters is given by [13]

$$\cos\Delta = \frac{T_{RS}}{\sqrt{1+T_{RS}^2}} \tag{4.22}$$

which is constrained by Planck as $|\cos\Delta| \lesssim$ 0.1-0.3, depending upon pivot scale $k_*$ and which datasets are combined. (Reference [5] notes that the constraints on BDI correlation are the same as for cold dark matter isocurvature.) Therefore model 1 is an example where the predicted BDI correlation is close to the experimental sensitivity.

The models with large BDI require somewhat special initial conditions, in which the total duration of inflation is not more than $\sim 80$ $e$-foldings. This is because significant curvature of the inflaton path in field space is needed during horizon crossing for generating isocurvature. Models with long periods of inflation tend to have such curvature earlier than horizon crossing, subsequently becoming nearly linear and thus resembling single-field inflation. This is illustrated for the two benchmark models in Fig. 4.4, that shows the field trajectories and horizon crossing points. It is further

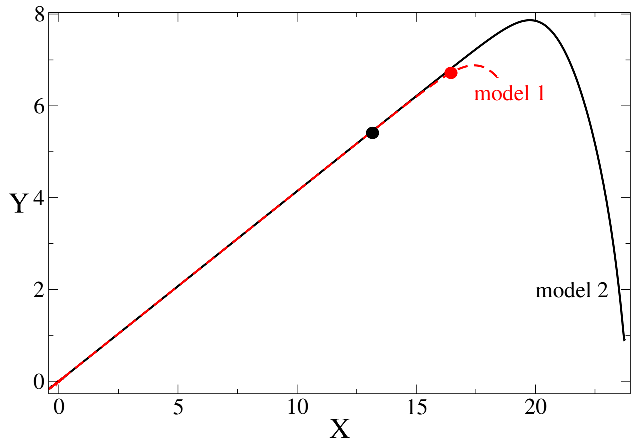


Figure 4.4: Inflaton trajectories in field space for the benchmark models. Horizon crossing is indicated by the heavy dot.

borne out by Fig. 4.5, showing the correlation between $|T_{RS}|$ and total number of $e$-foldings $N_{\rm tot}$ for models within an MCMC chain satisfying $\chi^2 < 10$. On the other hand, models like our benchmark model 2, having longer periods of inflation, lead to predictions that are relatively insensitive to the initial conditions, since the field trajectory settles into a unique trough in the potential.

### 4.3.3 Baryogenesis and reheating

To compute the baryon asymmetry, we use the baryon density stored in $\phi$, Eq. (4.18). It is convenient to compare this to the number density of $\phi$ particles, prior to reheating,

$$n_\phi = \frac{\rho_\phi}{m_\phi} \tag{4.23}$$

since the ratio $\eta = n_B/n_\phi$ reaches a constant value that we denote as $\eta_e$ at the end of inflation, during the period of $\phi$ oscillations around the minimum of the potential. The time evolution of $\eta$ is illustrated for model 1 in Fig. 4.6.

Reheating occurs at the time $t_{\rm rh} = 1/\Gamma_\phi$ where $\Gamma_\phi$ is the decay width of $\phi$. Defining

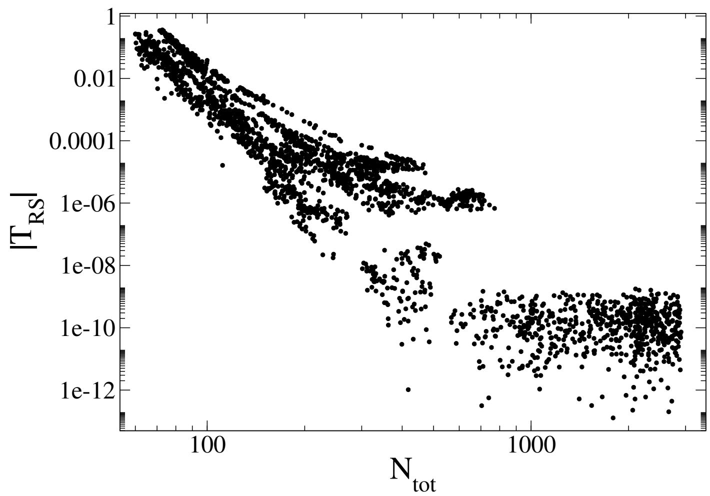


Figure 4.5: Scatter plot of isocurvature correlation $|T_{RS}|$ versus the total number of $e$-foldings of inflation $N_{\rm tot}$ from the MCMC.

$n_\phi = n_{\phi,e}$ at the end of inflation ($t = t_e$), $n_\phi$ at the time of reheating will be

$$
\begin{aligned}
n_{\phi,\rm rh} = n_{\phi,e}\left(\frac{a_e}{a_{\rm rh}}\right)^3 &= \frac{n_{\phi,e}}{\left(1+\frac{3}{2}\sqrt{\frac{m_\phi n_{\phi,e}}{3m_P^2}}(t_{\rm rh}-t_e)\right)^2} \\
&\cong \frac{4m_P^2\,\Gamma_\phi^2}{3m_\phi}
\end{aligned}
\tag{4.24}
$$

where we used the fact that the $\phi$ oscillations matter-dominate the Universe until reheating, and $t_{\rm rh} \gg t_e$. The value of $n_{\phi,\rm rh}$ is independent of $n_{\phi,e}$, so long as the latter is large enough to provide sufficient expansion of the Universe prior to reheating. This will be true if the energy density at the end of inflation is much greater than that at reheating.

The baryon-to-entropy ratio at reheating is given by

$$\eta_B = \eta_e \frac{n_{\phi,\rm rh}}{s} \tag{4.25}$$

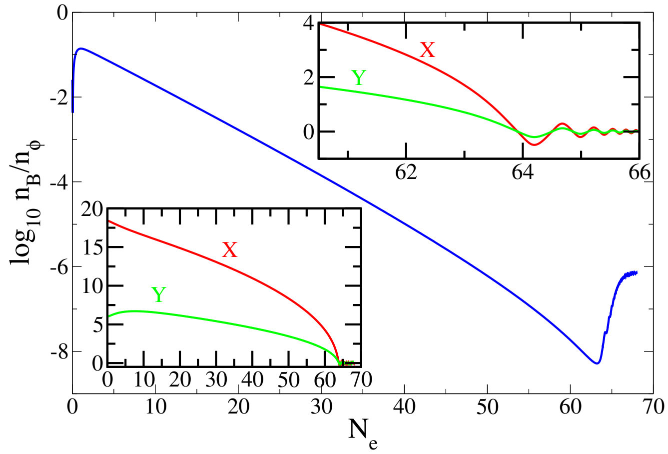


Figure 4.6: Baryon-to-inflaton ratio during inflation and shortly after its end, versus number of $e$-foldings $N_e$, for benchmark model 1. Insets show the evolution of the field components, $\phi = (X + iY)/\sqrt{2}$.

with $s = (2\pi^2/45) g_* T_{\rm rh}^3$ and reheat temperature [16]

$$\begin{aligned} T_{\rm rh} &= \left(\frac{90}{\pi^2 g_*}\right)^{1/4} (\Gamma_\phi\, m_P)^{1/2} \\ &= 1.7 \times 10^{14}\,\mathrm{GeV} \left(\frac{\lambda''}{10^{-2}}\right) \left(\frac{m_\phi/m_P}{5 \times 10^{-7}}\right)^{1/2} \end{aligned} \tag{4.26}$$

Including a factor of 36/111 [17] for the reduction of baryon number by redistribution into lepton number by sphalerons, it follows that

$$\eta_B \cong 6.1 \times 10^{-4}\, \eta_e\, \lambda'' \left(\frac{m_P}{m_\phi}\right)^{1/2} \tag{4.27}$$

which is conserved into the late Universe. The measured value is $\eta_B = 8.6 \times 10^{-11}$ [18].

The coupling $\lambda''$ should be small in order to justify the perturbative reheating assumption, but from the point of view of technical naturalness, it need not be very small. A three-loop diagram involving $\lambda''$ renormalizes the $\lambda|\phi|^4$ interaction, giving the estimate

$$\lambda'' \lesssim (16\pi^2)^{3/4} (\lambda/36)^{1/4} \cong 0.05 \tag{4.28}$$

to avoid destabilizing the inflationary potential by quantum corrections.

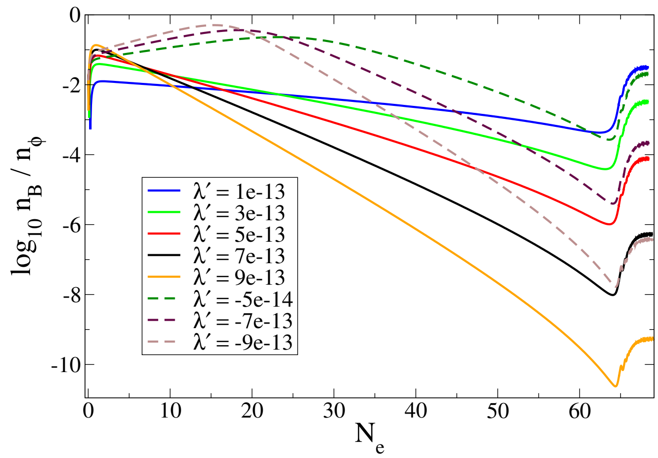


Figure 4.7: Baryon-to-inflaton ratio during inflation and shortly after its end, versus number of $e$-foldings $N_e$, for several values of $\lambda'$. Other potential parameters are fixed at those of model 1. The curves are in the same order as the key, from top to bottom at late times. Positive values of $\lambda'$ are shown with solid curves, negative with dashed.

The baryon asymmetry generated during inflation depends sensitively on the value of the $B$-violating coupling $\lambda'$. In Fig. 4.7 we again show how $\eta_B$ evolves with $N_e$ from the beginning of inflation until shortly after it ends, but for a range of different values of the baryon-violating coupling $\lambda'$. The effect of the $\phi$ oscillations can be seen briefly around $N_e = 65$, but these are quickly Hubble-damped and $\eta_B$ settles to a constant value that we have identified as $\eta_e$ in Eq. (4.25). The dependence of the final baryon asymmetry is not monotonic. At first this may be surprising, since one can derive the time-dependence of $n_B$ from the inflaton field equations,

$$\dot{n}_B = 2i(\phi^*\ddot{\phi} - \ddot{\phi}^*\phi) = -3Hn_B + 4\lambda'(\phi^4 + \phi^{*4}) \tag{4.29}$$

However one finds that $\lambda'$ has an important effect on the background inflaton trajectory, which explains the nonlinear dependence. This is illustrated in Fig. 4.8. Hence the processes of inflation and baryogenesis are nontrivially intertwined in our model: adjusting $\lambda'$ can affect not only $\eta_B$ but also the inflationary observables.

The effects of $B$ violation after inflation are negligible. At low energies, integrating out $\phi$ and $\Phi_i$ leads to a dimension-36 operator involving 24 quarks. It could induce conversion of four neutrons into their antiparticles in a neutron star, but the rate is

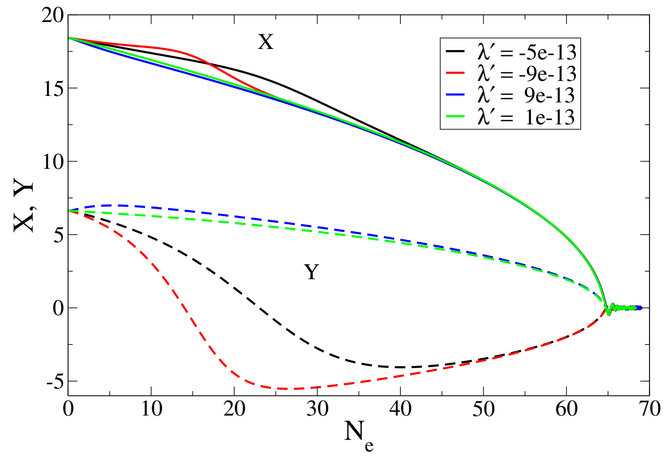


Figure 4.8: Inflaton trajectories $X(N_e)$ (solid) and $Y(N_e)$ (dashed) for four different values of the baryon-violating coupling $\lambda'$. Other parameters are fixed to those of model 1.

far too small to be significant. In the early Universe, we must check that the $\Delta B = 8$, $\Phi_i^{12}$ operator induced by $\phi$ exchange is out of equilibrium, to avoid washing out the $B$ asymmetry. The rate can be estimated as

$$\Gamma_{\Delta B=8} \sim \frac{\lambda'^2 \lambda''^8 T^{17}}{m_\phi^{16}} \lesssim \frac{T^2}{m_P} \tag{4.30}$$

By demanding that the decoupling temperature exceed the reheat temperature $T_{\rm rh}$ in Eq. (4.26), we find a constraint

$$\lambda'' \lesssim 20 \, \frac{m_\phi^{17/46}}{(\lambda')^{2/23}} \sim 1.5 \tag{4.31}$$

which is more lenient than the consistency requirement (4.28).

## 4.4 Particle physics implications

The colored scalars $\Phi_i$ can have observable effects at low energies. If sufficiently light, they can be pair-produced at LHC. The Yukawa interactions in Eq. (4.5) have the same form as $R$-parity violating coupling of squarks to quarks in supersymmetric models, leading to various mass exclusions in the range 80-525 GeV [19] or 100-600 GeV

| system | $K^0$-$\bar{K}^0$ | $K^0$-$\bar{K}^0$ | $B^0$-$\bar{B}^0$ | $B^0_s$-$\bar{B}^0_s$ |
|---|---|---|---|---|
| coefficient | $m_{\Phi_3}\,\mathrm{Re}[y_{3,dd}\,y^*_{3,ss}]^{-1/2}$ | $m_{\Phi_3}\,\mathrm{Im}[y_{3,dd}\,y^*_{3,ss}]^{-1/2}$ | $m_{\Phi_3}\,\lvert y_{3,dd}\,y^*_{3,bb}\rvert^{-1/2}$ | $m_{\Phi_3}\,\lvert y_{3,ss}\,y^*_{3,bb}\rvert^{-1/2}$ |
| limit | $1.1\times 10^3$ TeV | $2.1\times 10^4$ TeV | 990 TeV | 245 TeV |

Table 4.2: Lower limits from meson-antimeson mixing on parameters entering the Wilson coefficients of four-quark operators from integrating out the heavy color triplet $\Phi_3$.

[20], depending upon the flavor structure of the couplings.

However heavier colored scalars can be probed indirectly, using an effective field theory description where they are integrated out to give dimension-six, four-quark operators. For baryogenesis, the flavor structure of the new Yukawa couplings was not important, but at low energies it can have an observable effect on the angular distributions of jets at LHC, or flavor-changing neutral-currents like meson-antimeson oscillations. Using chiral Fierz identities [21], the effective Lagrangian is

$$\begin{aligned}\mathcal{L} = &-\sum_{A=1,2}\delta^{ae}_{bd}\,\frac{y_{A,ij}y^*_{A,kl}}{2m^2_{\Phi_A}}(\bar{u}^a_i\gamma^\mu P_R u_{k,b})(\bar{d}^e_j\gamma_\mu P_R d_{l,d})\\ &-\frac{y_{3,ii}y^*_{3,jj}}{m^2_{\Phi_3}}(\bar{d}^a_i\gamma^\mu P_R d_{j,a})(\bar{d}^b_i\gamma_\mu P_R d_{j,b})\end{aligned} \tag{4.32}$$

where $a, b, d, e$ are color indices, $i, j, k, l$ label flavor, and $P_R$ projects onto right-handed chirality. In the bottom line we have specialized to the case where $i \neq j$ and the operator contributes to meson-antimeson oscillations, since these combinations are much more severely constrained than the flavor-diagonal ones, or those connecting mesons of different masses.

From dijet angular distributions, the CMS Collaboration finds a limit of [22]

$$\left(\frac{m^2_\Phi}{yy^*}\right)^{1/2} \gtrsim 7\,\mathrm{TeV} \tag{4.33}$$

for flavor-diagonal operators, presumably of the first generation (since the limit on higher-generation quarks will be somewhat weakened by parton distribution functions). However $K^0$-$\bar{K}^0$, $B^0$-$\bar{B}^0$ and $B^0_s$-$\bar{B}^0_s$ mixing give more stringent constraints [23], shown in Table 4.2.

## 4.5 Conclusions

We have studied a new model of inflation with the novel feature that the inflaton carries baryon number, and it can produce the baryon asymmetry via the Affleck-Dine mechanism, mostly during inflation, with relatively small evolution over the few $e$-foldings after inflation ends. It is a simple but complete model, including a calculable perturbative reheating mechanism that allows one to make definite predictions for the inflationary observables, given a set of input parameters. One testable prediction is that the tensor-to-scalar ratio $r$ is likely to be observable, depending upon the value of the nonminimal coupling of the inflaton to gravity. For the values $\xi \sim 0.01 - 1$ considered in this work, we have found $r > 0.004$, which is within the sensitivity of upcoming CMB experiments. For example LiteBIRD will probe values down to $r \sim 10^{-3}$ [24].

Since ours is a two-field inflation model, another possible signal is correlated baryon isocurvature-adiabatic fluctuations that have been constrained by the Planck Collaboration. We have found that these can occur at an observable level if the total duration of inflation did not greatly exceed the canonical minimum number of $e$-foldings, $N_{\rm tot} \sim 60$. In this case the inflaton trajectory can turn significantly in field space around the time of horizon crossing. We are not aware of other models in the literature that predict baryon isocurvature perturbations.

The model relies upon new colored scalar particles in order to transfer the baryon asymmetry from the inflaton to the standard model quarks. These could have observable effects in laboratory experiments if sufficiently light, even at the scale of $10^4$ TeV for $K^0$-$\bar{K}^0$ oscillations. The colored scalars could also mediate purely hadronic rare flavor-changing decays, that we have not considered here. The new source of baryon violation needed for baryogenesis is however hidden at the high scale the inflaton mass $\sim 10^{-7}\, m_P$, out of reach of laboratory probes.

We have considered only the simplest scenario for reheating. It is possible that sufficiently large values of $\lambda''$ could lead to more efficient reheating through parametric resonance [16]. To our knowledge, this has not been previously studied for couplings of the form $\phi\Phi^3$ such as are present in our model. Moreover we have ignored the Higgs portal coupling $|\phi|^2|H|^2$ which could reduce the baryon asymmetry by producing extra radiation. We leave these issues for future study.

## Acknowledgment

We thank C. Byrnes and R. Namba for very helpful correpondence or discussions. Our work is supported by NSERC (Natural Sciences and Engineering Research Council, Canada). MP is supported by the Arthur B. McDonald Institute for Canadian astroparticle physics research.

## 4.6 Note added

After publication, we realized that our initial claim of potentially large isocurvature (DBI) perturbations for certain models was biased because we only considered one BDI variable. [1] In addition to the correlation angle $\cos\Delta$ in Eq. (4.22) [13]

$$\cos\Delta \equiv \frac{\mathcal{P}_{RS}}{\mathcal{P}_{RR}\mathcal{P}_{SS}} \simeq \frac{T_{RS}}{\sqrt{1+T_{RS}^2}} \sim T_{RS}\,, \tag{4.34}$$

the amount of BDI fluctuations is also characterized by the primordial isocurvature fraction [13]

$$\beta_{\rm iso}(k) \equiv \frac{\mathcal{P}_{SS}(k)}{\mathcal{P}_{RR}(k)+\mathcal{P}_{SS}(k)} \simeq \frac{T_{SS}^2}{1+T_{SS}^2+T_{RS}^2} \sim T_{SS}^2\,. \tag{4.35}$$

Here, $\mathcal{P}_{RR} \propto (1+T_{RS}^2)$ and $\mathcal{P}_{SS} \propto T_{SS}^2$ are the auto-correlation power spectra for the comoving curvature $R = H\,\delta\sigma/\dot{\sigma}$ and isocurvature perturbation $S = H\,\delta s/\dot{\sigma}$, respectively, and $\mathcal{P}_{RS} \propto T_{RS}T_{SS}$ is the cross-correlation spectrum of $R$ and $S$ [14]. Moreover, $\delta\sigma$ is the adiabatic and $\delta s$ is the isocurvature perturbation related to those for the canonically normalized fields by Eq. (4.12) (see also Fig. 3.5), and $T_{IJ}$ are the

[1] We thank Jean-Samuel Roux for bringing this to our attention.

transfer functions in Eq. (4.21). Both $\cos\Delta$ and $\beta_{\rm iso}(k)$ need to be evaluated at late times to compare them with the Planck constraints [5]

$$|\cos\Delta| \lesssim 0.1 - 0.3\,, \qquad \beta_{\rm iso}(k_* = 0.05\ \text{Mpc}^{-1}) \lesssim 0.01 - 0.3\,. \tag{4.36}$$

Since $\cos\Delta$ and $\beta_{\rm iso}(k)$ defined in Eqs. (4.34) and (4.35) are not independent, we expect a degeneracy between their experimental constraints. For instance, if isocurvature fluctuations are absent, $T_{RS}$ and $T_{SS}$ both go to zero (and hence $\mathcal{P}_{RS} \to 0$ and $\mathcal{P}_{SS} \to 0$), leading to $\cos\Delta$ becoming indeterminate and $\beta_{\rm iso} \to 0$. A similar situation arises if only $T_{SS} \to 0$, independently of the value of $T_{RS}$, as $\beta_{\rm iso} \to 0$ and $\cos\Delta$ remains indeterminate and can assume large values.

Our analysis indicates that the entropy auto-correlation $T_{SS} \ll 0.1$ is too small to be observed in all cases considered in our MCMC, implying $\beta_{\rm iso} \simeq 0$ and negligible DBI perturbations. This conclusion remains independent of the value of $\cos\Delta$, which can still assume large values. Supporting evidence for this is presented in Table 14 of Ref. [5], where the Planck Collaboration fixes $\cos\Delta = \pm 1$ in certain inflationary models. While these scenarios are not ruled out, they yield tighter bounds on $\beta_{\rm iso}$.

# Bibliography


[1] M. Bastero-Gil, A. Berera, R. O. Ramos, and J. a. G. Rosa, "Observational implications of mattergenesis during inflation," *JCAP* **10** (2014) 053, `arXiv:1404.4976 [astro-ph.CO]`.

[2] I. Affleck and M. Dine, "A New Mechanism for Baryogenesis," *Nucl. Phys. B* **249** (1985) 361–380.

[3] A. D. Sakharov, "Violation of CP Invariance, C asymmetry, and baryon asymmetry of the universe," *Pisma Zh. Eksp. Teor. Fiz.* **5** (1967) 32–35.

[4] A. D. Linde, "Chaotic Inflation," *Phys. Lett. B* **129** (1983) 177–181.

[5] **Planck** Collaboration, Y. Akrami *et al.*, "Planck 2018 results. X. Constraints

on inflation," *Astron. Astrophys.* **641** (2020) A10, arXiv:1807.06211 [astro-ph.CO].

[6] N. Okada, M. U. Rehman, and Q. Shafi, "Tensor to Scalar Ratio in Non-Minimal $\phi^4$ Inflation," *Phys. Rev. D* **82** (2010) 043502, arXiv:1005.5161 [hep-ph].

[7] A. Linde, M. Noorbala, and A. Westphal, "Observational consequences of chaotic inflation with nonminimal coupling to gravity," *JCAP* **03** (2011) 013, arXiv:1101.2652 [hep-th].

[8] Y.-Y. Charng, D.-S. Lee, C. N. Leung, and K.-W. Ng, "Affleck-Dine Baryogenesis, Split Supersymmetry, and Inflation," *Phys. Rev. D* **80** (2009) 063519, arXiv:0802.1328 [hep-ph].

[9] J. L. Evans, T. Gherghetta, and M. Peloso, "Affleck-Dine Sneutrino Inflation," *Phys. Rev. D* **92** no. 2, (2015) 021303, arXiv:1501.06560 [hep-ph].

[10] M. P. Hertzberg and J. Karouby, "Generating the Observed Baryon Asymmetry from the Inflaton Field," *Phys. Rev. D* **89** no. 6, (2014) 063523, arXiv:1309.0010 [hep-ph].

[11] N. Takeda, "Inflatonic baryogenesis with large tensor mode," *Phys. Lett. B* **746** (2015) 368–371, arXiv:1405.1959 [astro-ph.CO].

[12] J. M. Cline, "String Cosmology," in *Les Houches Summer School - Session 86: Particle Physics and Cosmology: The Fabric of Spacetime*. 12, 2006. arXiv:hep-th/0612129.

[13] C. T. Byrnes and D. Wands, "Curvature and isocurvature perturbations from two-field inflation in a slow-roll expansion," *Phys. Rev. D* **74** (2006) 043529, arXiv:astro-ph/0605679.

[14] C. Gordon, D. Wands, B. A. Bassett, and R. Maartens, "Adiabatic and entropy perturbations from inflation," *Phys. Rev. D* **63** (2000) 023506, arXiv:astro-ph/0009131.

[15] A. R. Liddle and S. M. Leach, “How long before the end of inflation were observable perturbations produced?,” *Phys. Rev. D* **68** (2003) 103503, `arXiv:astro-ph/0305263`.

[16] L. Kofman, A. D. Linde, and A. A. Starobinsky, “Towards the theory of reheating after inflation,” *Phys. Rev. D* **56** (1997) 3258–3295, `arXiv:hep-ph/9704452`.

[17] J. A. Harvey and M. S. Turner, “Cosmological baryon and lepton number in the presence of electroweak fermion number violation,” *Phys. Rev. D* **42** (1990) 3344–3349.

[18] **Planck** Collaboration, N. Aghanim *et al.*, “Planck 2018 results. VI. Cosmological parameters,” *Astron. Astrophys.* **641** (2020) A6, `arXiv:1807.06209 [astro-ph.CO]`. [Erratum: Astron.Astrophys. 652, C4 (2021)].

[19] **CMS** Collaboration, A. M. Sirunyan *et al.*, “Search for pair-produced resonances decaying to quark pairs in proton-proton collisions at $\sqrt{s} = 13$ TeV,” *Phys. Rev. D* **98** no. 11, (2018) 112014, `arXiv:1808.03124 [hep-ex]`.

[20] **ATLAS** Collaboration, M. Aaboud *et al.*, “A search for pair-produced resonances in four-jet final states at $\sqrt{s} = 13$ TeV with the ATLAS detector,” *Eur. Phys. J. C* **78** no. 3, (2018) 250, `arXiv:1710.07171 [hep-ex]`.

[21] C. C. Nishi, “Simple derivation of general Fierz-like identities,” *Am. J. Phys.* **73** (2005) 1160–1163, `arXiv:hep-ph/0412245`.

[22] **CMS** Collaboration, A. M. Sirunyan *et al.*, “Search for new physics in dijet angular distributions using proton–proton collisions at $\sqrt{s} = 13$ TeV and constraints on dark matter and other models,” *Eur. Phys. J. C* **78** no. 9, (2018) 789, `arXiv:1803.08030 [hep-ex]`. [Erratum: Eur.Phys.J.C 82, 379 (2022)].

[23] **UTfit** Collaboration, M. Bona, “Latest results for the Unitary Triangle fit from the UTfit Collaboration,” *PoS* **CKM2016** (2017) 096.

[24] M. Hazumi *et al.*, "LiteBIRD: A Satellite for the Studies of B-Mode Polarization and Inflation from Cosmic Background Radiation Detection," *J. Low Temp. Phys.* **194** no. 5-6, (2019) 443–452.

Chapter 5

# A little theory of everything, with heavy neutral leptons

**James M. Cline,[a] Matteo Puel,[a] and Takashi Toma[b]**

[a] *McGill University, Department of Physics, 3600 University St., Montréal, QC H3A2T8 Canada*

[b] *Institute of Liberal Arts and Science, Kanazawa University, Kakuma-machi, Kanazawa, Ishikawa 920-1192 Japan*

Published in the Journal of High Energy Physics: JHEP 2020, 39 (2020), [arXiv:2001.11505]

## 5.0 Prologue

The successful Affleck-Dine inflation mechanism in producing the observed baryon asymmetry of the Universe, as discussed in the previous chapter, motivates us to explore its potential to address other issues within the ΛCDM model (presented in chapter 3) and the SM of particle physics. This chapter demonstrates that by incorporating additional ingredients, a generalized Affleck-Dine inflationary model can naturally explain DM and neutrino masses, in addition to inflation and baryogenesis.

In the following paper, three concepts were referred to without elaboration, since they are well known in particle physics:

- The principle of minimal flavor violation (MFV) dictates that all flavor and $CP$-violating interactions should be tied to the known structure of the Yukawa couplings [1].
- A pseudo- or quasi-Dirac heavy neutral lepton $(N_L, N_R)^T$ is a pair of Majorana heavy neutrinos, $N_L = N_L^c$ and $N_R = N_R^c$, with a small mass splitting and a relative $CP$-sign between the two states. Hence, $N_L \neq N_R^c$ and $N_R \neq N_L^c$. In the limit of mass degeneracy, it would correspond to a Dirac neutrino.
- The principle of naturalness, as defined by 't Hooft (or technical naturalness), states that a quantity in nature should be small only if the underlying theory becomes more symmetric as that quantity tends to zero [2]. This implies that quantum corrections are less significant than tree-level contributions.

**Abstract**

Recently a new model of "Affleck-Dine inflation" was presented, that produces the baryon asymmetry from a complex inflaton carrying baryon number, while being consistent with constraints from the cosmic microwave background. We adapt this model such that the inflaton carries lepton number, and communicates the lepton asymmetry to the standard model baryons via quasi-Dirac heavy neutral leptons (HNLs) and sphalerons. One of these HNLs, with mass $\lesssim 4.5\,\mathrm{GeV}$, can be (partially) asymmetric dark matter (DM), whose asymmetry is determined by that of the baryons. Its stability is directly related to the vanishing of the lightest neutrino mass. Neutrino masses are generated by integrating out heavy sterile neutrinos whose mass is above the inflation scale. The model provides an economical origin for all of the major ingredients missing from the standard model: inflation, baryogenesis, neutrino masses, and dark matter. The HNLs can be probed in fixed-target experiments like SHiP, possibly manifesting $N$-$\bar{N}$ oscillations. A light singlet scalar, needed for depleting

the DM symmetric component, can be discovered in beam dump experiments and searches for rare decays, possibly explaining anomalous events recently observed by the KOTO collaboration. The DM HNL is strongly constrained by direct searches, and could have a cosmologically interesting self-interaction cross section.

## 5.1 Introduction

The standard model (SM) of particle physics is noted for being incomplete in numerous ways. It could be argued that the most urgently missing elements are an inflaton (or other source of primordial density perturbations), a mechanism for baryogenesis, dark matter (DM), and the origin of neutrino masses, since all of these relate to directly observed phenomena as opposed to problems of naturalness. It is tempting to seek relatively simple new physics models that can simultaneously address several of the missing pieces, or perhaps all.[1]

A notable example is the $\nu$MSM [4, 5], in which light sterile neutrinos can accomplish leptogenesis and provide a dark matter candidate while giving neutrino masses. Higgs inflation [6] can be invoked in this framework without needing any additional particles. A similar mechanism of getting an inflationary phase was also implemented in the scotogenic model [7, 8] to simultaneously explain inflation, dark matter, baryogenesis and neutrino masses, by introducing a scalar inert doublet coupled non-minimally to gravity and three right-handed neutrinos. Another example is the SMASH model [9] that assumes heavy right-handed neutrinos to explain neutrino mass and thermal leptogenesis, while introducing minimal extra matter content to produce axions as dark matter and a solution to the strong CP problem. The extra scalar field needed for breaking Peccei-Quinn symmetry can combine with the Higgs to give two-field inflation in the early Universe. The idea of explaining neutrino masses, baryon asymmetry, dark matter, inflation and solving the strong CP problem using three right-handed neutrinos and the extra fields of the KSVZ axion model

[1] Ref. [3] provides a recent attempt in this direction, in which an inflaton-like field is present, although the details of inflation are not yet worked out.

[10] was originally presented in Ref. [11]. There, the Higgs field was identified as the inflaton and the electroweak vacuum was shown to be stable for several choices of the model parameters. The problem of Higgs inflation, which is known to reduce the scale of perturbative unitarity breaking well below the Planck scale, was addressed by coupling the Higgs field nonminimally to gravity [12].

In the present work we suggest another way of completing the standard model, that does not rely upon leptogenesis as usually defined (through the CP-violating out-of-equilibrium decays of heavy neutrinos). The starting point is a model of inflation in which the Affleck-Dine mechanism [13] for creating a particle asymmetry occurs *during* inflation [14]. The asymmetry is originally stored in a complex inflaton field, that has the Lagrangian

$$\mathcal{L} = \frac{m_P^2}{2} R\left(1 + 2\xi|\phi|^2\right) + |\partial\phi|^2 - m_\phi^2|\phi|^2 - \lambda|\phi|^4 - i\lambda'(\phi^4 - \phi^{*4}) \tag{5.1}$$

(where $m_P$ is the reduced Planck scale) including a nonminimal coupling to gravity, needed to flatten the potential at large $|\phi|$, which makes the inflationary predictions compatible with Planck constraints [15]. In Ref. [14] we assumed that $\phi$ carried baryon number, which was transferred to the SM quarks through colored scalar mediators. Here we consider the case where $\phi$ carries lepton number, hence giving a new mechanism of leptogenesis. As usual, the resulting lepton asymmetry is transmitted to the baryons through the sphaleron interactions of the SM.

The challenge for such an approach is to find a way of transferring the lepton asymmetry from $\phi$ to the SM without it being washed out by the lepton-violating effects associated with neutrino mass generation. Indeed, if $\phi$ decays to heavy right-handed neutrinos that have large Majorana masses, the asymmetry gets washed out immediately and the situation reverts to standard leptogenesis being required. This suggests that $\phi$ should decay into quasi-Dirac neutrino mediators $N_i$, that mix with the SM neutrinos to transmit the asymmetry. Among the $N_i$ mediators, one can be stable and constitute a species of asymmetric dark matter, getting its relic density (partly) from the initial lepton asymmetry. The $N_i$ are an example of heavy neutral leptons (HNLs), a class of hypothetical particles that is being widely studied both theoretically and by upcoming experiments such as SHiP [16], MATHUSLA [17], FASER [18] and CODEX-b [19].

To deplete the symmetric component of the DM to a viable level, it is necessary to introduce a light mediator, which we take to be a scalar singlet $s$, so that $N_i\bar{N}_i \to ss$ annihilations are sufficiently strong. The DM can be fully or partially asymmetric depending on the coupling strength $g_s$. We will show that this interaction has interesting implications for direct detection, and for hints of anomalous rare $K_L \to \pi^0+$ invisible decays that have recently been reported by the KOTO experimental collaboration [20].

In our proposal, the HNLs do not explain the origin of light neutrino masses, but we hypothesize that their couplings to the SM $\nu$'s are related to those of the superheavy Majorana $\nu_R$'s that generate seesaw masses, by a principle similar to minimal flavor violation (MFV) [1]. The setup thereby also addresses the origin of neutrino mass and relates the HNL couplings to it in an essential way. Moreover a direct link is made between the stability of the dark matter candidate and the masslessness of the lightest SM neutrino.

In section 5.2 we specify the structure of couplings of the HNLs to the inflaton and SM particles, and its relation to neutrino mass generation. In section 5.3 we discuss constraints on the couplings such that the lepton asymmetry from inflation is transferred to the SM particles without being washed out. It is shown how the resulting baryon asymmetry determines the dark matter asymmetry and its mass. The relations between light $\nu$ properties and the HNL couplings are presented in section 5.4, and consequent predictions for the phenomenology of the HNLs. In section 5.5 we compile the experimental limits on the light singlet $s$, and identify a region of parameter space where the KOTO anomaly can be reconciled with DM direct detection limits. The latter are considered in detail in section 5.6, where we also treat the DM self-interactions and discuss possible DM indirect detection constraints. The technical naturalness of our setup is demonstrated in section 5.7, followed by conclusions in section 5.8. In appendix 5.A we derive the exact width for HNL decay into different-flavor charged leptons, which was given only in approximate form in previous papers.

## 5.2 Model

We assume the inflaton carries lepton number 2 (more correctly, $B - L = -2$ since $B - L$ symmetry is not broken by electroweak sphalerons), and couples to $N_N$ flavors of quasi-Dirac HNLs as

$$g_\phi \phi \bar{N}_{L,i} N_{L,i}^c + g_\phi \phi \bar{N}_{R,i} N_{R,i}^c + \text{H.c.} \tag{5.2}$$

$N_N$ is a free parameter; hereafter we take $N_N = 3$, which is the minimal number needed to get dark matter and the observed neutrino properties, through consistent assumptions about the flavor structure of the neutrino sector that will be explained presently. The HNLs couple to the SM lepton doublets as

$$\eta_{\nu,ij} \bar{N}_{R,i} H L_j \tag{5.3}$$

At energy scales relevant for inflation and below, it is consistent to assume that the only source of lepton number violation is through a small Majorana mass $\epsilon_\nu$ for the standard model neutrinos, which could be generated through the seesaw mechanism, by integrating out very heavy right-handed neutrinos, with mass $M_{\nu_R}$ above the scale of inflation. In the basis $\nu_L, N_R^c, N_L$, the neutrino mass matrix is

$$\begin{pmatrix} \epsilon_\nu & \eta_\nu^T \bar{v} & 0 \\ \eta_\nu \bar{v} & 0 & M_N \\ 0 & M_N & 0 \end{pmatrix} \tag{5.4}$$

where $\bar{v} \cong 174\,\text{GeV}$ is the complex Higgs VEV. We assume that $\epsilon_\nu$ has a flavor structure that is aligned with the couplings in (5.3) as

$$\epsilon_\nu = \bar{\mu}_\nu \, \eta_\nu^T \eta_\nu \tag{5.5}$$

where $\bar{\mu}_\nu$ is a scale that we will constrain below. This alignment ensures the stability of dark matter against oscillations with its antiparticle, if $\eta_\nu$ has one vanishing eigenvalue. In order to justify the ansatz, we will show that it is radiatively stable, due to an approximate SU(3) flavor symmetry for the $N_i$ leptons, that is broken in a minimal-flavor-violating (MFV) [1] manner, solely by the matrix $\eta_\nu$. For example, the flavor-diagonal couplings of the inflaton to $N_i$ could be perturbed by a term proportional to $\eta_\nu \eta_\nu^T$ without spoiling the viability of the framework.

By solving for the eigenvalues of (5.4), one finds that the light neutrino part $\epsilon_\nu$ induces a small Majorana mass matrix for the $N_i$'s of the form

$$\delta M = \frac{\bar{v}^2}{M_N^2}\, \eta_\nu \, \epsilon_\nu \, \eta_\nu^T \tag{5.6}$$

that leads to $N_i$-$\bar{N}_i$ oscillations. These are mildly constrained by the need for approximate lepton number conservation during the generation of the lepton asymmetry (apart from electroweak sphalerons), as we consider below.

## 5.3 Nonstandard leptogenesis and DM relic density

During inflation $\phi$ gets an asymmetry determined mostly by the couplings in Eq. (5.1) and to a smaller extent by the initial conditions of the inflaton, which provide the source of CP violation in the Affleck-Dine mechanism [13]. The details of asymmetry generation at the level of $\phi$ are exactly the same as discussed in Ref. [14]. The difference in the present work is that the $\phi$ asymmetry is transferred to the HNLs by the decays $\phi \to NN$ from the interaction (5.2). Whether reheating is perturbative or proceeds by parametric resonance is not crucial to the present discussion, where we assume that the created asymmetry results in the observed baryon asymmetry. This can always be achieved by appropriate choice of the $L$-violating parameter $\lambda'$, for example.[2]

[2]This observation is consistent with the results obtained by including the effects from nonlinear preheating dynamics on the generation of matter-antimatter asymmetry in Affleck-Dine inflationary scenarios [21].

### 5.3.1 Sharing and preserving the asymmetry

For simplicity, consider the case where $g_\phi$ is sufficiently small so that perturbative decays are the dominant mechanism for reheating, with reheat temperature of order

$$T_R \sim g_\phi (m_\phi m_P)^{1/2} \sim 10^{-3} g_\phi\, m_P \tag{5.7}$$

using the typical value $m_\phi \sim 10^{-6}\, m_P$ identified in Ref. [14]. Even for rather small values $g_\phi \lesssim 0.01$, this is well above the weak scale. Therefore it is easy for the HNLs to equilibrate with the SM through the interaction (5.3), which transmits the primordial $B-L$ asymmetry to the SM. The dominant process is $N_i$ (inverse) decays, whose rate is $\Gamma_d \cong 10^{-3}\eta_\nu^2 T$ [22] for $T \gtrsim 100\,\mathrm{GeV}$. Demanding that this comes into equilibrium before sphalerons freeze out, we find the lower bound $|\eta_\nu| \gtrsim 4\times 10^{-7}$ on the largest elements of $\eta_{\nu,ij}$.

We demand that no $L$-violating effects from the operator $\lambda'\phi^4$ in Eq. (5.1) ever come into equilibrium, since these would wash out the asymmetry. Above the scale $m_\phi$, this comes from $\phi\phi \to \phi^*\phi^*$ scatterings with rate $\sim \lambda'^2\, T$, that comes into equilibrium at $T \sim \lambda'^2 m_P \sim 10^{-24} m_P$, using the typical value $\lambda' \sim 10^{-12}$ found in Ref. [14]. This is far below $m_\phi$, hence it never comes into equilibrium. Instead the principal effect of $\lambda'$ is through the effective operator $(\lambda' g_\phi^4/m_\phi^8)(\bar{N}N^c)^4$ generated by integrating out the inflaton. This has a rate going as $\lambda'^2 g_\phi^8 m_\phi^{-16} T^{17}$, that goes out of equilibrium at $T \sim [m_\phi^{16}/(\lambda'^2 g_\phi^8 m_p)]^{1/15}$. Demanding that this remains below the reheat temperature gives an upper bound on $g_\phi$,

$$g_\phi \lesssim \left(\frac{m_\phi}{m_P}\right)^{17/23} \left(\frac{1}{\lambda'}\right)^{2/23} \cong 0.07 \tag{5.8}$$

which is not prohibitive.

The only other $L$-violating process operative at scales below that of inflation is $N$-$\bar{N}$ oscillations induced by the $\delta M$ matrix elements (5.6). These would wash out the $B$ and $L$ asymmetries if they were in equilibrium before sphaleron freezeout. The rate of $L$ violation is not simply the same as the oscillation rate $\sim 1/\delta M$, because flavornondiagonal interactions of $N$ with the plasma can measure the state of the oscillating $N$-$\bar{N}$ system before it has time to oscillate significantly, damping the conversions of $N \to \bar{N}$. The effective rate of $L$ violation can be parametrized as [23, 24]

$$\Gamma_{\Delta L} \sim \frac{M_N^2 \delta M^2}{M_N^2 \delta M^2 + T^2 \Gamma_m^2} \Gamma_m \tag{5.9}$$

where $\Gamma_m$ is the rate of processes that destroy the coherence of the $N$-$\bar{N}$ system. [3] For $T > T_{\rm EW} \sim 100\,{\rm GeV}$, (inverse) decays are dominant, but these quickly go out of equilibrium as $T$ falls below the mass of the Higgs boson. At temperatures somewhat below $T_{\rm EW}$, the elastic (but flavor-violating) $NL \to \bar{N}L$ scatterings mediated by Higgs exchange dominate, with $\Gamma_m = \Gamma_{\rm el} \sim \eta_\nu^4 T^5/m_h^4$. On the other hand, sphalerons are safely out of equilibrium since they are exponentially suppressed by the Boltzmann factor involving the sphaleron energy, which is above the TeV scale. Therefore it is sufficient to show that the rate (5.9) is out of equilibrium in this case, to establish that the washout process is innocuous. In other words, the following relation must be satisfied

$$\frac{\Gamma_{\Delta L}}{H} \sim \frac{M_N^2 \delta M^2 \ m_h^4 \ m_P}{\eta_\nu^4 \ T_{\rm EW}^9} < 1 \tag{5.10}$$

In section 5.4 we will show that the light neutrino mass matrix $m_\nu$ is approximately equal to $\epsilon_\nu$, which is generated by integrating out heavy neutrinos though the usual seesaw mechanism. This allows us to rewrite the HNL Majorana mass matrix $\delta M$ in Eq. (5.6) as $\delta M \sim \bar{v}^2 \eta_\nu^2 \, m_\nu / M_N^2 \sim U_{\ell i}^2 \, m_\nu$ where $U_{\ell i}$ is the mixing angle between HNLs and light neutrinos. Plugging the latter in Eq. (5.10), the $\eta_\nu$-dependence disappears and we can get a lower bound on the HNL Dirac mass, $M_N \gtrsim 4$ MeV. For higher values of $M_N$, the lepton-violating effects of $\delta M$ are therefore too small to affect the baryon asymmetry, but they can be observable in collider experiments that we will discuss in section 5.4.

DM-antiDM oscillations for asymmetric DM have been considered in Refs. [25, 26]. They can potentially regenerate the symmetric component of the DM and lead to its

[3] We will introduce an additional elastic scattering channel mediated by a singlet scalar $s$ below. These flavor-conserving interactions are not relevant for decohering the $N$-$\bar{N}$ oscillations [25].

dilution through annihilations. We avoid these constraints by the relation (5.6) that causes $\delta M$ to vanish when acting on the $N'$ DM state.

### 5.3.2 DM asymmetric abundance and maximum mass

The relic density for fully asymmetric DM is determined by its chemical potential, which in our framework is related to the baryon asymmetry in a deterministic way, since the DM initially has the same asymmetry as the remaining two HNLs. The relation between the DM and baryon asymmetries can be found by solving the system of equilibrium constraints, similarly to Ref. [27]. We generalize their network to include the extra HNL species, that satisfy the equilibrium condition

$$\mu_N = \mu_h + \mu_L \tag{5.11}$$

from the $\eta_\nu$ interactions. Eq. (5.11) only applies to the unstable HNL species since $N'$ is conserved, and its chemical potential is fixed by the initial lepton asymmetry

$$\mu_{N'} = \tfrac{1}{6} L_0 \tag{5.12}$$

The factor of 6 comes from having three HNL species, each with two chiralities. We recall that $L_0$ is determined by the inflationary dynamics, and is especially sensitive to the value of the coupling $\lambda'$. It is assumed that $\lambda'$ has been adjusted so that $L_0$ takes the value needed to yield the observed baryon asymmetry, which we relate to $L_0$ in the following.

Repeating the analysis of [27] we find the following equilibrium relations (setting the $W$ boson potential $\mu_W = 0$ since $T > T_{\rm EW}$):

$$\begin{aligned} L &= \tfrac{13}{3}\mu_\nu + \mu_h + 2\mu_{N'} \\ &= \tfrac{95}{21}\mu_\nu + 2\mu_{N'} \\ B &= -\tfrac{4}{3}\mu_\nu \\ \mu_{u_L} &= -\tfrac{1}{9}\mu_\nu, \quad \mu_h = \tfrac{4}{21}\mu_\nu \\ \mu_N &= \tfrac{11}{21}\mu_\nu \end{aligned} \tag{5.13}$$

where $L, B$ are the respective total chemical potentials for lepton and baryon number, $\mu_\nu$ is the sum of light neutrino chemical potentials, and $\mu_h$ is that of the Higgs. Since $B - L$ is conserved by sphalerons, we can relate these to the initial lepton asymmetry $L_0 = 6\mu_{N'} = (L - B)$: $\mu_\nu = \frac{84}{123}\mu_{N'}$, $B = -\frac{112}{123}\mu_{N'}$. This allows us to determine the maximum mass of $N'$ that gives the observed relic density:

$$m_{N'} = M_N \le \left|\frac{B}{\mu_{N'}}\right| \frac{\Omega_c}{\Omega_b}\, m_n = 4.5\,\text{GeV} \tag{5.14}$$

using the values $\Omega_c = 0.265$ and $\Omega_b = 0.0493$ from Ref. [28] and the nucleon mass $m_n$.

The inequality (5.14) is only saturated if the symmetric DM component is suppressed to a negligible level. Otherwise a smaller value of $m_{N'}$ is needed to compensate the presence of the symmetric component. We turn to the general case next.

### 5.3.3 Dark matter annihilation and relic density

In order to reduce the symmetric component of the DM to avoid overclosure of the Universe, an additional annihilation channel is needed. The $t$-channel Higgs-mediated annihilations $N'\bar{N}' \to L\bar{L}$ are not strong enough, leading to $\langle\sigma v\rangle \lesssim 10^{-32}$ cm$^3$/s, in light of the bound $|\eta_\nu| \lesssim 10^{-3}$ to be derived in section 5.4 below. We need an additional particle with sufficiently strong couplings to the DM.

The simplest possibility is to introduce a singlet scalar $s$, with interactions

$$g_s s \bar{N}_i N_i + \tfrac{1}{4}\lambda_s (s^2 - v_s^2)^2 + \lambda_{hs} h^2 s^2 \tag{5.15}$$

that at tree level are diagonal in the $N_i$ flavors, and lead to mixing of $s$ with the Higgs $h$. We will consider two cases: (i) $m_s < m_{N'}$ so that $N'\bar{N}' \to ss$ is allowed; (ii) $m_s \gtrsim 2\, m_{N'}$ so that there can be mild resonant enhancement of the $s$-channel cross section for $N'\bar{N}'$ annihilation to standard model particles, through the mixing of $s$ with the Higgs boson. For the nonresonant case, the $s$-channel amplitude for $N'\bar{N}' \to f\bar{f}$, where $f$ is the most strongly coupled kinematically accessible final state, is of the same order of magnitude as that for $N'$-nucleon scattering, which is strongly constrained by direct detection (section 5.6), making this contribution too small to be sufficient for annihilation. We will see that this limitation can be overcome by resonant enhancement without requiring too much fine tuning of masses.

#### 5.3.3.1 $N'\bar{N}' \to ss$ annihilation

We first consider the case when $m_s < m_{N'}$. The cross section for $N'\bar{N}' \to ss$ is $p$-wave suppressed. Parameterizing the Mandelstam variable as $s = 4m_{N'}^2(1+\epsilon)$ we find in the limit $m_s \ll m_{N'}$ and $\lambda_s \ll g_s$ that

$$\sigma \cong \frac{3\, g_s^4}{64\pi\, m_{N'}^2} \frac{\epsilon^{1/2}}{(1+\epsilon)^2} \tag{5.16}$$

(this is an analytic approximation to the exact result, which is more complicated). Carrying out the thermal average [29] with $x \equiv m_{N'}/T$ gives

$$\langle \sigma v \rangle \cong \frac{3\, g_s^4}{16\pi\, m_{N'}^2} F(x) \tag{5.17}$$

$$\begin{aligned} F(x) &= \frac{x}{K_2(x)^2} \int_0^\infty d\epsilon \left(\frac{\epsilon}{1+\epsilon}\right)^{3/2} K_1(2x\sqrt{1+\epsilon}) \\ &\cong 0.058 - 0.002\, x + 3.25 \times 10^{-5} x^2 - 1.87 \times 10^{-7} x^3 \end{aligned} \tag{5.18}$$

which is a good numerical approximation in the region $15 < x < 70$. For values $x \sim 20$ typical for freezeout, $F \cong 0.03$.

To find the relic abundance including both symmetric and asymmetric components, one can solve the Boltzmann equation for their ratio $r$ given in Ref. [30], which

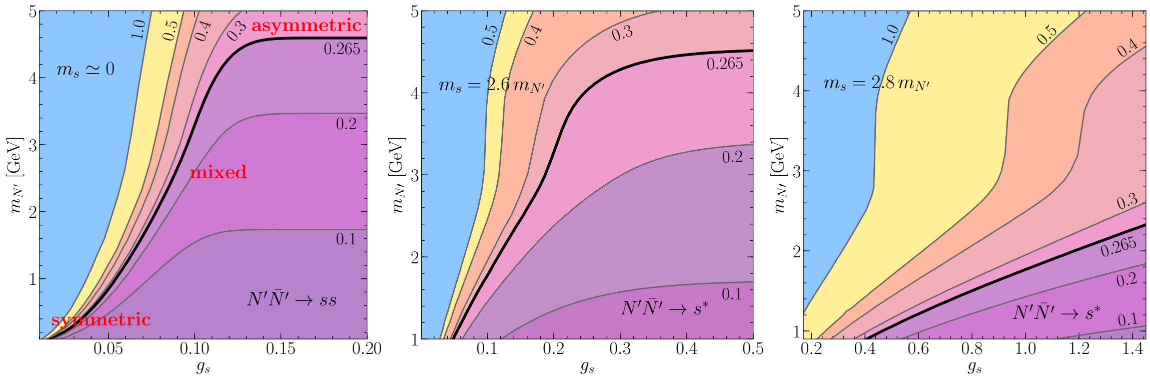


Figure 5.1: Contours of DM relic density $\Omega_{N'} \equiv \rho_{N'}/\rho_{\rm crit}$ in the plane of DM mass versus coupling to singlet, for three relations of singlet mass $m_s$ to the DM mass $m_{N'}$. Left: $m_s \ll m_{N'}$, with $N'\bar{N}' \to ss$ annihilation. Center: $m_s = 2.6\, m_{N'}$ with $N'\bar{N}' \to s^*$ (virtual $s$) annihilation. Right: like center, but with $m_s = 2.8\, m_{N'}$. The heavy contour labeled 0.265 corresponds to the observed relic density.

depends upon $\langle \sigma v \rangle$. Then as shown there, the fractional contribution of $N'$ to the energy density of the Universe is

$$\Omega_{N'} = \epsilon\, \eta_B\, m_{N'} \frac{s}{\rho_{\rm crit}} \left( \frac{1+r}{1-r} \right) \tag{5.19}$$

where $\eta_B = 8.8 \times 10^{-11}$ is the observed baryon-to-entropy ratio, $s$ is the entropy density, and $\epsilon = \eta_{N'}/\eta_B = 123/112$ in our model (see below Eq. (5.13)). Using Ref. [31], we checked whether the DM annihilation cross section might be Sommerfeld-enhanced since $m_s < m_{N'}$, but this was a negligible effect in the relevant parts of parameter space that we will specify below. In Figure 5.1 (left) we plot contours of $\Omega_{N'}$, the fractional contribution of the DM to the energy density of the Universe, in the plane of $m_{N'}$ versus $g_s$. For $g_s \gtrsim 0.14$ the maximum value in Eq. (5.14) is achieved, whereas for lower $g_s$, the symmetric component abundance is increased (while the asymmetric abundance remains fixed), corresponding to lower DM masses.

In the opposite regime $\lambda_s \gg g_s$, the annihilation $N'\bar{N}' \to ss$ could in principle be dominated by the $s$-channel diagram, giving the cross section

$$\langle \sigma v \rangle \cong \frac{1}{\pi} \left( \frac{3 \lambda_s v_s g_s}{8\, m_{N'}^2} \right)^2 \bar{F}(x), \tag{5.20}$$

in the case where $m_s \ll m_{N'}$, with

$$\bar{F}(x) = \frac{x}{K_2(x)^2} \int_0^\infty d\epsilon \, \frac{\epsilon^{3/2}}{(1+\epsilon)^{5/2}} \, K_1(2x\sqrt{1+\epsilon}) \tag{5.21}$$

For $x \sim 20$, $F \cong 0.01$ leading to the requirement that $g_s$ must be significantly larger than in the previous case to suppress the symmetric DM component. Such values are excluded by direct DM search constraints to be discussed in section 5.6 below. Hence there is no practical enlargement of the allowed parameter space from including the $s$-channel contribution.

#### 5.3.3.2 $N'\bar{N}' \to$ SM annihilation

In the other case where $m_s > m_{N'}$, the total annihilation cross section for $N'\bar{N}'$ into $\mu^+\mu^-$, $\pi^+\pi^-$, *etc.,* through the Higgs portal, does not depend upon the couplings of $s$ to the final state particles nor on the number of decay channels, in the limit of the narrow-width approximation for the intermediate virtual $s$. In this limit we can approximate the Breit-Wigner distribution for the $s$ propagator as a $\delta$ function, $(\pi/\Gamma_s)\delta(s - m_s^2)$ [$s$ is the Mandelstam variable], and the couplings in the singlet decay width $\Gamma_s$ cancel against those in the annihilation amplitude. One can think of this as the cross section for $N'\bar{N}' \to s$, which one integrates over the $\delta$ function when doing the thermal average. In this way we find

$$\langle \sigma v \rangle \cong \pi \frac{g_s^2}{2 m_{N'}^2} \, \frac{(y^2-1)^{3/2}\, x}{K_2(x)^2} \, K_1(2xy) \tag{5.22}$$

where $x = m_{N'}/T$ as usual, and $y \equiv m_s/(2\, m_{N'})$. It turns on steeply above the threshold $y = 1$ for resonant enhancement, and then quickly decays because of the Boltzmann suppression for $y \gg 1$. Nevertheless we find that it can be large enough for values of $y \lesssim 1.3 - 1.4$ that are not finely tuned to be close to 1, as we show in

Figure 5.1 (center and right plots).

We will see that for such parameter values, the $t$-channel exchange of $s$ for $N'$ scattering on nucleons can still be consistent with direct detection constraints. In this process, the suppression by the small coupling of $s$ to nucleons (through the singlet-Higgs mixing angle $\theta_s$) is not canceled by anything, in contrast to the $s$-channel resonance.

## 5.4 Neutrino properties and HNL constraints

Below the scales of electroweak symmetry breaking and the HNL mass $M_N$, the light neutrino mass matrix gets generated,

$$\begin{aligned} m_\nu &\cong \epsilon_\nu - \delta M' \\ \delta M' &\equiv \frac{\bar{v}^2}{M_N^2}\, \eta_\nu^T\, \epsilon_\nu\, \eta_\nu \end{aligned} \tag{5.23}$$

However $|\eta_\nu|\bar{v}/M_N \ll 1$ is the magnitude of the mixing between the light neutrinos and the HNLs, as we will discuss below, so that the correction $\delta M' \ll \epsilon_\nu$ can be ignored. We reiterate that $\epsilon_\nu$ is generated by the usual seesaw mechanism, integrating out sterile neutrinos whose mass is above all the other relevant scales in our model.

Recall that the stability of the dark matter $N'$ requires $\eta_\nu$ to be a matrix with one vanishing eigenvalue, which implies that the lightest neutrino is massless. This is an exact statement, not relying upon the neglect of $\delta M'$, since $\epsilon_\nu$ and $\delta M'$ are simultaneously diagonalizable by construction. This is a consequence of our MFV-like assumption that $\eta_\nu$ is the only source of flavor-breaking in the HNL/neutrino sector.

### 5.4.1 Explicit $\eta_\nu$ and HNL mixings

Using Eq. (5.5) we can solve for $\eta_\nu$ in terms of the neutrino masses and mixings,

$$\eta_\nu = O \left(\frac{D_\nu}{\bar{\mu}_\nu}\right)^{1/2} U_{\rm PMNS}^{-1} \tag{5.24}$$

where $D_\nu$ is the diagonal matrix of light $\nu$ mass eigenvalues, and $U_{\rm PMNS}$ is the $3\times 3$ PMNS matrix. The orthogonal matrix $O$ is undetermined since the $N_i$ are practically degenerate; for simplicity we set it to 1 in the following. Since we have assumed that one eigenvalue is vanishing, the other two are known,

$$\begin{aligned}
&D_{\nu 11}=0,\ D_{\nu 22}=\sqrt{\Delta m^2_{21}},\ D_{\nu 33}=\sqrt{\Delta m^2_{31}}, &&\text{NH}\\
&D_{\nu 33}=0,\ D_{\nu 22}=\sqrt{\Delta m^2_{32}},\ D_{\nu 11}=\sqrt{\Delta m^2_{32}-\Delta m^2_{21}}, &&\text{IH}
\end{aligned}\tag{5.25}$$

for the normal and inverted hierarchies, respectively.

The light neutrinos mix with $N_i$, with mixing matrix elements given by

$$U_{\ell i}\cong\frac{\eta^T_{\nu,\ell i}\bar{v}}{M_N}\tag{5.26}$$

where $\ell=e,\mu,\tau$ and $i=1,2,3$. Constraints on $U_{\ell i}$ arise from a variety of beam dump experiments and rare decay searches, summarized in Refs. [16, 32]. As we now discuss, the applicability of these limits depends upon whether the scalar singlet is heavier or lighter than the HNL's, since this determines the dominant decay modes of the latter.

#### 5.4.1.1 Unitarity constraints for $m_s < M_N$ case

If $m_s < M_N$, then many of the beam-dump and other limits on the mixing angles (5.26) versus $m_N$, shown in Figure 5.2, cannot be directly applied to our model because they assume that $N$ decays are mediated only by the weak interactions, through $N$-$\nu$ mixing, whereas we have a more efficient decay channel $N\to\nu s$, from the $g_s s\bar{N}_i N_i$ coupling and mixing. All of the bounds that rely upon detecting visible particles from the decay will now be sensitive to the singlet mass $m_s$ and mixing angle $\theta_s$ with the Higgs, and not just $M_N$. To modify these limits appropriately would require a dedicated reanalysis of each experiment, which is beyond the scope of our work.

However we can still make a definite statement about how weak the limit on $N$-$\nu$

mixing could possibly be, even in the case where the singlet escapes the detector unobserved, because electroweak precision data (EWPD) are only sensitive to the reduction in the SM couplings caused by the mixing, that we can readily calculate. This is most straightforward in the basis of the mass eigenstates, where $\eta_\nu$ is diagonal. Then the mass matrix (5.4) is block diagonal, and there is a mixing angle $\theta_i$ connecting each pair of light and heavy mass eigenstates. The relation between the flavor states (labeled by subscript $\alpha$) and the mass eigentstates (labeled by $i$) is

$$\nu_\alpha = (U_{\rm PMNS})_{\alpha i}\, \cos\theta_i\, \nu_i \equiv N_{\alpha i}\, \nu_i \tag{5.27}$$

In Refs. [33, 34], the matrix $N_{\alpha i}$ is introduced in this way to parametrize departures from unitarity in the lepton mixing matrix, and the magnitudes of $NN^\dagger$ are constrained by various precision electroweak data. The elements of such a matrix can be written in our model as

$$|NN^\dagger|_{\alpha\beta} \equiv \left| \sum_i N_{\alpha i} N^\dagger_{i\beta} \right| = \left| \delta_{\alpha\beta} - \sum_i (U_{\rm PMNS})_{\alpha i}\, \sin^2\theta_i\, (U_{\rm PMNS})^\dagger_{i\beta} \right| \tag{5.28}$$

Since most of the constraints on physical observables are often expressed in literature in terms of the Hermitian matrix $\varepsilon_{\alpha\beta}$, defined in $N = (1-\varepsilon)\, U_{\rm PMNS}$ [34], we have that the predicted $\varepsilon_{\alpha\beta}$ turns out to be [4]

$$\varepsilon_{\alpha\beta} = \tfrac{1}{2} \left| \sum_i (U_{\rm PMNS})_{\alpha i}\, \sin^2\theta_i\, (U_{\rm PMNS})^\dagger_{i\beta} \right| \tag{5.29}$$

The most stringent limits on $\varepsilon_{\alpha\beta}$ that can be applied to our model come from the measurement of the $W$ boson mass, which depends upon the combination [34]

$$\begin{aligned} M_W &\simeq M_W^{\rm SM} \left[ (NN^\dagger)_{ee} (NN^\dagger)_{\mu\mu} \right]^{1/4} \frac{s_W^{\rm SM}}{s_W} \\ &\cong M_W^{\rm SM}\, (1 + 0.20\, (\varepsilon_{ee} + \varepsilon_{\mu\mu})) \end{aligned} \tag{5.30}$$

where the SM radiative corrections, parametrized by the variable $\Delta r = 0.03672$ [35],

[4] The matrix $\varepsilon$ defined here is called $\eta$ in Ref. [34].

are included in the computation; they enter through the weak mixing angle [33],

$$s_W^2 = \frac{1}{2}\left[1 - \sqrt{1 - \frac{2\sqrt{2}\pi\alpha}{G_\mu M_Z^2}(1+\Delta r)\left[(NN^\dagger)_{ee}(NN^\dagger)_{\mu\mu}\right]^{1/2}}\,\right] \tag{5.31}$$

Using the experimental and SM values of $M_W$ in Eq. (5.30), we obtain a 95% C.L. upper bound on $(\varepsilon_{ee} + \varepsilon_{\mu\mu}) \leq 2.64 \times 10^{-3}$.

In our framework, the mixing angles $\theta_i$ in Eq. (5.29) can be computed explicitly, from the eigenvalues of $\eta_\nu$, up to multiplicative factors,

$$\theta_i \cong \frac{\eta_i\,\bar{v}}{M_N} \tag{5.32}$$

where $\eta_i$ is the eigenvalue of $\eta_\nu$ associated with the eigenvector that couples to $N_i$. For the normal hierarchy, we label $\eta_1 = 0$ for the massless state, while for inverted hierarchy $\eta_3 = 0$. Using (5.24), we can solve explicitly for $\eta_\nu$ in either mass scheme, up to the overall proportionality controlled by the parameter $\bar{\mu}_\nu$. Comparing the combination $(\varepsilon_{ee} + \varepsilon_{\mu\mu})$, computed from Eqs. (5.29) and (5.32), to the upper limit found above from $M_W$, yields lower bounds on the scale $\bar{\mu}_\nu$ in the two mass hierarchy choices, and upper bounds on the corresponding matrices $\eta_\nu$ and the mixing angles between HNLs and the light neutrinos. Defining $\bar{U}_\ell \equiv (\sum_i |U_{\ell i}|^2)^{1/2}$, we find for the normal mass hierarchy

$$\begin{aligned}
&\bar{\mu}_\nu > 5.9\ \text{keV} \times \left(\frac{4.5\ \text{GeV}}{M_N}\right)^2, && \text{NH}\\
&|\eta_\nu^T| < 10^{-3}\begin{vmatrix} 0 & 0.66 & -0.32 - 0.29\,i \\ 0 & 0.72 - 0.05\,i & 2.14 \\ 0 & -0.70 - 0.04\,i & 1.91 \end{vmatrix} \times \left(\frac{M_N}{4.5\ \text{GeV}}\right) \\
&\bar{U}_e < 0.031, \quad \bar{U}_\mu < 0.087, \quad \bar{U}_\tau < 0.078
\end{aligned} \tag{5.33}$$

The dependence on $M_N$ cancels out in the bounds on $U_{\ell i}$. The corresponding results for inverted hierarchy are

$$
\begin{aligned}
&\bar{\mu}_\nu > 13.6 \text{ keV} \times \left(\frac{4.5 \text{ GeV}}{M_N}\right)^2, \qquad\qquad\qquad \text{IH} \\
&|\eta_\nu^T| < 10^{-3} \begin{vmatrix} 1.57 & 1.06 & 0 \\ -0.75 - 0.17\, i & 1.02 - 0.12\, i & 0 \\ 0.75 - 0.15\, i & -1.23 - 0.10\, i & 0 \end{vmatrix} \times \left(\frac{M_N}{4.5 \text{ GeV}}\right) \\
&\bar{U}_e < 0.073, \quad \bar{U}_\mu < 0.050, \quad \bar{U}_\tau < 0.056
\end{aligned} \tag{5.34}
$$

In each case the column of zeros corresponds to the absence of coupling to the DM state $N'$; hence we identify $N' = N_1$ for the normal hierarchy and $N' = N_3$ for the inverted hierarchy.

We emphasize that the above bounds are robust, but might be strengthened, depending on the choices of $m_s$ and $\theta_s$, by reanalyzing limits from other experiments to take into account the observation of charged particles or neutral hadrons from $s$ decays following $N \to \nu s$. Hence the true limits are expected to lie somewhere between the (brown) EWPD line shown in Figure 5.2 for the normal (left) and inverted (right) hierarchy cases, and the more stringent limits that may arise from the other (typically beam dump) experiments.

The scale $\bar{\mu}_\nu$ determines how the couplings $y_\nu = k\eta_\nu$ of the light neutrinos to the superheavy Majorana neutrinos $\nu_R$ (as restricted by our MFV-like assumption) are enhanced relative to $\eta_\nu$ by a proportionality factor, $k = (M_{\nu_R}\bar{\mu}_\nu/\bar{v}^2)^{1/2}$. Perturbativity of $y_\nu$ limits $k \lesssim 0.5 \times 10^3$, hence the scale of the heavy neutrinos is bounded by $M_{\nu_R} \lesssim 10^{15}\,\text{GeV}$ for the value of $\bar{\mu}_\nu$ in Eq. (5.33). This is not restrictive, and can be made consistent with our assumption that the heavy neutrinos do not play a role during inflation or reheating, if the reheat temperature is sufficiently low.

#### 5.4.1.2 Laboratory constraints for $m_s > M_N$ case

If $m_s > M_N$, only three-body decays of HNL's are available, and they are dominated by weak interactions, induced by mixing of $N_i$ with the light $\nu$'s. There is also a 3-body decay $N \to \nu f \bar{f}$ by virtual $s$ exchange, but this is highly suppressed by the

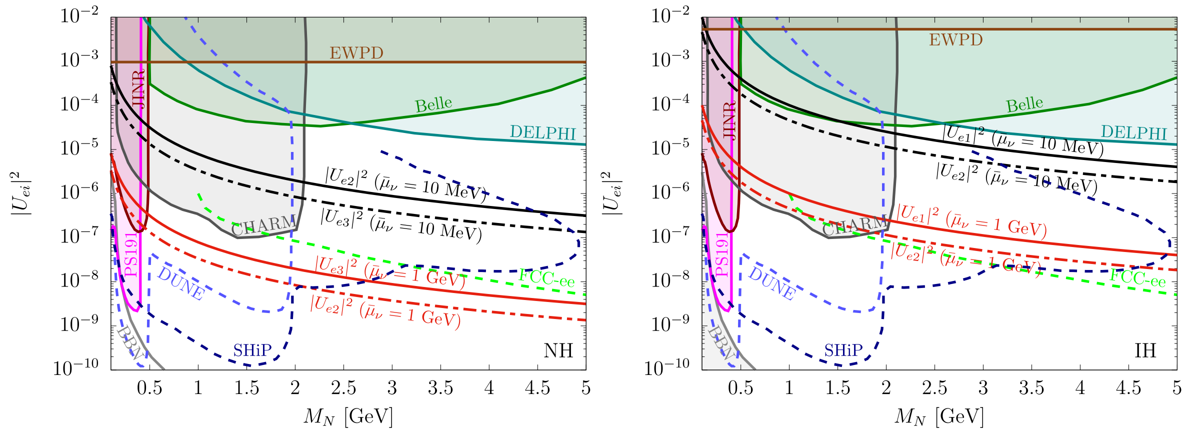

Figure 5.2: Summary of constraints on HNL mixing with electron neutrinos, over mass range of interest for our model (left: normal hierarchy, right: inverted hierarchy). Solid and dot-dashed black and red curves show the model's predictions for $U_{e2}$ ($U_{e1}$) (solid curves) and $U_{e3}$ ($U_{e2}$) (dot-dashed) in the normal (inverted) mass hierarchy, for two choices of the parameter $\bar{\mu}_\nu$ that determines the mixing through Eqs. (5.24, 5.26). $U_{e1} \equiv 0$ ($U_{e3} \equiv 0$) for the normal (inverted) hierarchy since $N_1 = N'$ ($N_3 = N'$) denotes the dark matter HNL. Laboratory constraints are taken from Ref. [16]. Although a more recent and comprehensive analysis of these bounds in the MeV–GeV mass range was made in Ref. [36], we noticed no appreciable difference for $M_N > 0.1$ GeV. We also do not display the preliminary limit from the NA62 experiment [37], which would be the strongest limit for $M_N$ between 0.15 and 0.45 GeV if confirmed. Sensitivity regions of future experiments FCC-ee [38], DUNE [39] and SHiP [40] are bounded by dashed curves.

small scalar mixing angle $\theta_s$ and the couplings $m_f/v$ to the Higgs. In this case, all of the constraints on $N$-$\nu$ mixing shown in Figure 5.2 unambiguously apply. For masses $M_N > 2$ GeV, the most stringent limit comes from searches for $Z \to N\nu$ decays by the DELPHI Collaboration [41]. Defining again $\bar{U}_\ell = (\sum_i |U_{\ell i}|^2)^{1/2}$, at our largest allowed mass $M_N = 4.5$ GeV, the bound is

$$\bar{U} \equiv \left(\sum_\ell \bar{U}_\ell^2\right)^{1/2} < 0.0039\,, \tag{5.35}$$

since DELPHI was sensitive to the total rate of $N_i$ production from $Z \to N_i\nu_\ell$ decays, times the total (semi)leptonic rate of $N_i$ decays.

Using Eqs. (5.24, 5.26), the bound (5.35) can be approximately saturated if $\bar{\mu}_\nu =$

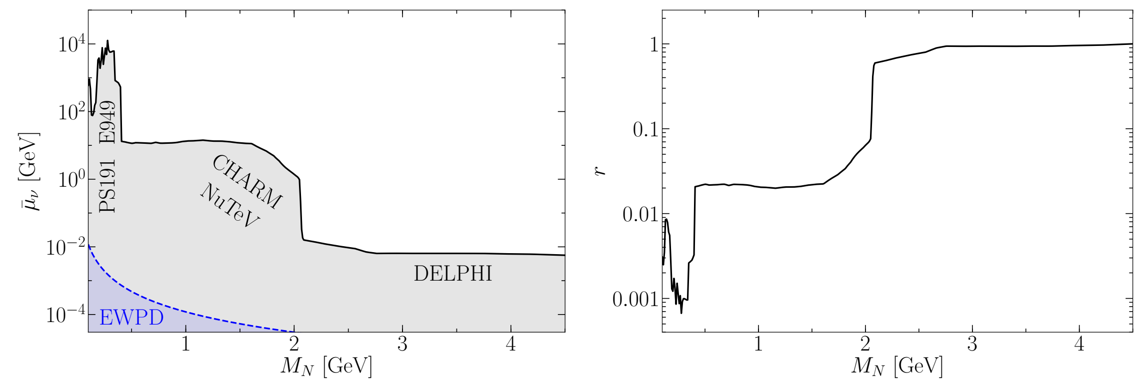


Figure 5.3: Left: minimum allowed mass scale $\bar{\mu}_\nu(M_N)$, predicted by our model for the normal mass hierarchy case, compatible with current constraints on the HNL mixings to light neutrinos [16]. The shaded gray region is excluded. Right: the ratio $r$ showing how the maximum allowed mixings (5.38) at $M_N = 4.5$ GeV are rescaled at lower $M_N$.

5.7 (9.8) MeV for the normal (inverted) hierarchy. Taking the PDG central values of the neutrino masses and mixings [35], we find

$$\eta_\nu^T \cong 10^{-5} \begin{pmatrix} 0 & 2.1 & -1.0 - 0.9\,i \\ 0 & 2.3 - 0.2\,i & 6.9 \\ 0 & -2.2 - 0.1\,i & 6.1 \end{pmatrix}$$
$$\bar{U}_e \cong 0.00099, \quad \bar{U}_\mu \cong 0.0028, \quad \bar{U}_\tau \cong 0.0025 \tag{5.36}$$

at $M_N = 4.5$ GeV for the normal hierarchy, and

$$\eta_\nu^T \cong 10^{-5} \begin{pmatrix} 5.8 & 3.9 & 0 \\ -2.8 - 0.6\,i & 3.8 - 0.4\,i & 0 \\ 2.8 - 0.6\,i & -4.6 - 0.4\,i & 0 \end{pmatrix}$$
$$\bar{U}_e \cong 0.0027, \quad \bar{U}_\mu \cong 0.0019, \quad \bar{U}_\tau \cong 0.0021 \tag{5.37}$$

for the inverted hierarchy. In each case the column of zeros corresponds to the absence of coupling to the DM state $N'$; hence we identify $N' = N_1$ for the normal hierarchy and $N' = N_3$ for the inverted hierarchy.

For the lighter mass range $M_N \sim (0.4 - 2)$ GeV, beam dump experiments such as CHARM [42] and NuTEV [43] give the strongest limits for electron and muon flavors, roughly $U_{ei}$, $U_{\mu i} \lesssim 6 \times 10^{-4}(M_N/\mathrm{GeV})^{-1.14}$. The largest allowed magnitudes of the HNL mixings $U_{\ell i}$ can be expressed as a function of $M_N$,

$$|U_{\ell i}| \cong r(M_N) \begin{pmatrix} 0 & 0.00083 & 0.00054 \\ 0 & 0.00090 & 0.0027 \\ 0 & 0.00087 & 0.0024 \end{pmatrix} \tag{5.38}$$

focusing on the normal hierarchy case. We determined the minimum allowed value of $\bar{\mu}_\nu$ for lower $M_N$, and the consequent scaling factor $r(M_N) = (5.7\,\mathrm{MeV}/\min(\bar{\mu}_\nu))^{1/2}$, from the limits summarized in figures 4.10–4.12 of Ref. [16]. These limits were rescaled and combined to account for the fact that our model has two HNLs, each of which mixes with all of the light flavors rather than just one $N_i$ that can mix with only one flavor at a time. The functions $\min(\bar{\mu}_\nu)$ and $r(M_N)$ are plotted in Figure 5.3. The various constraints on the HNL mixing with electron neutrinos in the mass range relevant for our model are shown for two choices of $\bar{\mu}_\nu$ in Figure 5.2, including future constraints from FCC-ee, DUNE and SHiP.

### 5.4.2 $N$-$\bar{N}$ oscillations

As mentioned in section 5.3.1, the $L$-violating mass term $\delta M$ causes $N$-$\bar{N}$ oscillations at a rate that is too small to destroy the lepton asymmetry in the early Universe, but fast enough to possibly be detected in laboratory searches. In the scenario where $m_s < M_N$, this effect cannot be observed because the decay products of $N_i \to \nu\mu^+\mu^-$ and $\bar{N}_i \to \bar{\nu}\mu^+\mu^-$ differ only by having a neutrino versus antineutrino in the final states. However if $m_s > M_N$, the situation is more interesting. For the values of $\bar{\mu}_\nu$

and $\eta_\nu$ in Eq. (5.36), the largest eigenvalue of $\delta M$ is given by [5]

$$\delta M = 3.1 \times 10^{-6}\,\mathrm{eV}\left(\frac{2\ \mathrm{GeV}}{M_N}\right)^2 , \tag{5.39}$$

It was recently shown by Ref. [44] that this is a promising value for inducing observable $N$-$\bar{N}$ oscillations at the SHiP experiment. These would be seen by production of $N\ell^+$ in a hadronic collision, followed by semileptonic decays $N \to \bar{N} \to \ell^+\pi$ (where $\pi$ represents a generic hadron). The smoking gun is the presence of like-sign leptons in the decay chain, that can only occur if $N$ oscillates to $\bar{N}$ within the detector.

### 5.4.3 Weak HNL decays

In the case where $m_s > M_N$ so that $N_i \to \nu s$ decays are blocked, the lifetime of the unstable $N_i$ leptons is determined by weak decays. These can be 2- or 3-body, $N_i \to \ell^- q\bar{q}$ (with $q\bar{q}$ hadronizing into a meson) and $N_i \to \nu\ell^+\ell^-$ by $W$ and $Z$ exchange, due to mixing of $N_i$ with the active neutrinos with mixing angles $U^T_{i\ell} \cong -U_{\ell i}$. Then the decay rate is of order

$$\Gamma_{N_i} \sim \sum_\ell \frac{|U_{\ell i}|^2 G_F^2 M_N^5}{192\,\pi^3} \tag{5.40}$$

This gives a lifetime of $\sim 10^{-3} - 10^{-4}\,\mathrm{s}$ for $M_N \sim 1\,\mathrm{GeV}$, making such $N_i$ decays harmless for big bang nucleosynthesis (BBN) or the CMB.

More quantitatively, we have evaluated the partial widths for $N_i \to \nu\gamma$, $N_i \to h^0\nu$, $N_i \to h^+\ell^-$, $N_i \to 3\nu$, $N_i \to \nu\ell^+\ell^-$, including the hadronic final states with $h^0 = \pi^0, \eta, \eta', \rho^0$, $h^+ = \pi^+, K^+, \rho^+, D^+$ as computed in Ref. [46] and [47]. [6] Focusing on the normal hierarchy case, we use the mixing matrix given by Eq. (5.26) with $\bar{\mu}_\nu$ shown in Figure 5.3, that leads to different lifetimes for the two unstable HNLs $N_2$ and $N_3$. The lifetimes are plotted in Figure 5.4, along with decay lengths in the case

[5] The eigenvalue of $\delta M$ computed in Eq. (5.39) is the maximum value allowed by current experimental constraints because $\delta M \propto \bar{\mu}_\nu^{-1}$ from Eqs. (5.6, 5.24) and the minimum of $\bar{\mu}_\nu$ is reached at $M_N = 4.5$ GeV as shown in Figure 5.3.

[6] The formula for the decay width of $N_i \to \nu\ell_1^+\ell_2^-$ found in the literature (see Refs. [46, 48]) assumes that $m_{\ell_1}$ is negligible compared to $m_{\ell_2}$. This is not as good an approximation for the case $\ell_1 = \mu$, $\ell_2 = \tau$ as for $\ell_1 = e$, $\ell_2 = \mu$. We provide the exact formula in Appendix 5.A.

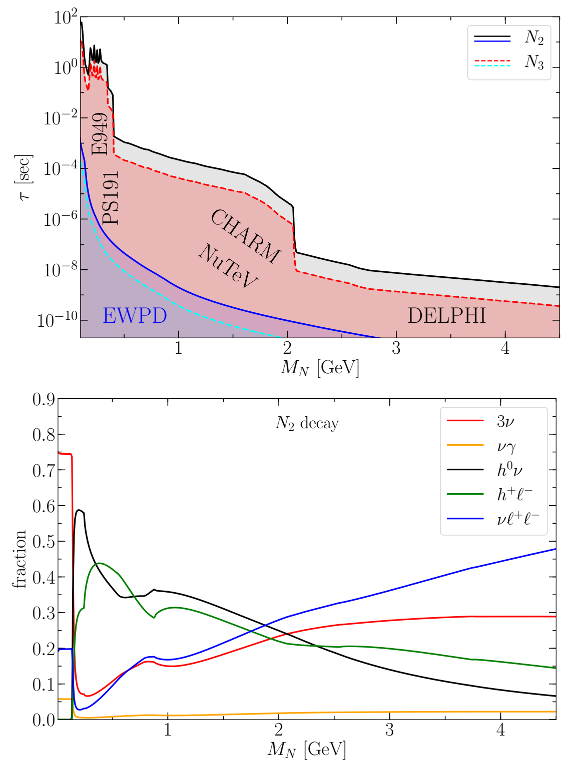


Figure 5.4: Top: Minimum lifetime (left) and decay length (right) of the HNLs $N_2$ and $N_3$, for the case of normal mass hierarchy. Upper curves are for mass $M_N < m_s$, lower curves for $M_N > m_s$, which determines whether weak decays or $N \to \nu\, s$ dominates. Decay length assumes energy $E = 25\,\mathrm{GeV}$, appropriate for SHiP experiment. The shaded regions are excluded. (The wiggles in the mass range $0.2 < M_N < 0.4$ GeV come from the E949 bound [45] present in figure 4.11 of Ref. [16], which also appear in Figure 5.3.) Bottom: branching ratios for $N_2$ (left) and $N_3$ (right) into various final states involving photon, hadrons, light neutrinos or charged leptons, for the case of weak decays, namely $M_N < m_s$.

of HNLs with energy $E = 25\,\mathrm{GeV}$ that would be relevant for the SHiP experiment. For $M_N \lesssim 0.3\,\mathrm{GeV}$, the lifetimes start to exceed 1 s, which for generic models of HNLs would come into conflict with nucleosynthesis. In our model, this need not be the case since the HNL abundance is suppressed by $N_i\bar{N}_i \to ss$ annihilations. Then it is the singlet that should decay before BBN, which generally occurs as long as $m_s > 2\,m_e$.

In Figure 5.4 the branching ratios for $N_2$ and $N_3$ to decay into the various final states (summing over flavors within each category) is also shown. Leptonic final states dominate for $M_N > 2$ GeV, while hadronic ones dominate for lower $M_N$.

### 5.4.4 Entropy and energy injection by late $N$ decays

If the Dirac HNLs $N_2$ and $N_3$ dominate the energy density of the Universe and are sufficiently long-lived, which may happen if the two-body decay $N_{2,3} \to \nu s$ is kinematically forbidden, a large amount of entropy may be injected by the decay of these particles after freezeout [49]. As a result, the produced dark matter relic abundance and baryon asymmetry can be diluted. Moreover one should take care that injected hadronic and electromagnetic energy does not disrupt the products of BBN.

In our model, since the freezeout of $N_2$ and $N_3$ occurs when they are nonrelativistic, the number density of these particles are highly suppressed. Therefore, the entropy and energy produced by the $N_{2,3}$ decays is negligible in terms of its cosmological impact. We illustrate this with an example; consider $M_N = 1\,\mathrm{GeV}$, and take the freezout temperature to be $T_f \sim M_N/20 \sim 0.05\,\mathrm{GeV}$, for which the number of degrees of freedom in the plasma is $g_* \cong 10$, and the decay rate is $\Gamma = 0.01\,\mathrm{s}^{-1}$. The thermal number density of the HNLs at $T = T_f$ is $n_N = 4\,(M_N T_f/(2\pi))^{3/2}\exp(-M_N/T_f)$, and its ratio to the entropy density at decoupling is denoted by $r_N = n_N/s$. Then Ref. [49] shows that the entropy injected by HNL decays in this case is

$$S \cong \left(1 + 3\left(\frac{2\pi^2\, g_*}{45}\right)^{1/3} \frac{(r_N\, m_N)^{4/3}}{(M_P\,\Gamma)^{2/3}}\right)^{3/4} \cong 1 + 4\times 10^{-9} \tag{5.41}$$

where $S = 1$ corresponds to the limit of no entropy production. This example shows that even when the lifetime is much longer than $1\,\mathrm{s}$, the abundance is too small to create any cosmological problem.

Previous studies show that even for decays as late as $100\,\mathrm{s}$, GeV-scale particles are only weakly constrained by BBN. Ref. [50] recently studied BBN constraints on models with late-decaying light particles, of mass up to $1\,\mathrm{GeV}$. It shows that there are no constraints on electromagnetic injection for lifetimes less than $10^4\,\mathrm{s}$, since nuclear photodissociation processes are suppressed at earlier times. Similarly, Ref. [51] finds no significant bounds from hadronic injections for GeV-scale particles decaying earlier

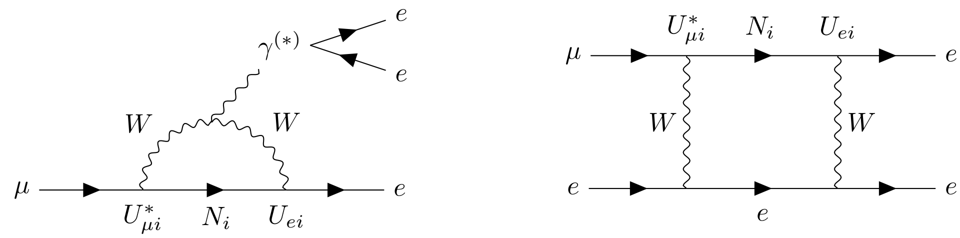


Figure 5.5: Diagrams leading to $\mu \to e\gamma$ and $\mu \to 3e$ from mixing of HNL's with the light neutrinos.

than 100 s.

### 5.4.5 Lepton flavor violation bounds

The mixing between light neutrinos and HNL's can lead to rare lepton-flavor violating processes, analogous to the well-studied case where TeV-scale $\nu_R$'s are responsible for the seesaw mass generation [52–57]. The decays $\mu \to e\gamma$ and $\mu \to 3e$ are induced by the digrams shown in Figure 5.5. The most constraining process currently is $\mu \to e\gamma$, which has a branching ratio of [58]

$$\mathrm{BR}(\mu \to e\gamma) = \frac{3\,\alpha_{\rm em}}{32\pi}\left|\sum_i U_{\mu i}U^*_{ei}\,\frac{M_N^2}{M_W^2}\right|^2 = \frac{3\,\alpha_{\rm em}}{32\pi}\,|NN^\dagger|^2_{\mu e}\,\frac{M_N^4}{M_W^4} \tag{5.42}$$

where $\alpha_{\rm em}$ is the electromagnetic fine structure constant and $|NN^\dagger|_{\mu e} \equiv |\sum_i N_{\mu i}N^\dagger_{ie}|$ with $N_{\alpha i}$ defined in Eq. (5.27). For the case of normal neutrino mass hierarchy, our least restrictive bound based on EWPD, Eq. (5.33), leads to $|\sum_i U_{\mu i}U^*_{ei}| < 1 \times 10^{-3}$, and the prediction that $\mathrm{BR}(\mu \to e\gamma) < 2.2 \times 10^{-15}$. This is still well below the current experimental bound of $4.2 \times 10^{-13}$ set by the MEG experiment [59].

From Ref. [60] we find the branching ratio for $\mu \to 3e$ in terms of $x \equiv M_N^2/M_W^2 \ll 1$,

$$\begin{aligned}\mathrm{BR}(\mu \to 3e) &\cong \frac{\alpha_{\rm em}^2}{16\pi^2\,\sin^4\theta_W}\left|\sum_i U_{\mu i}U^*_{ei}\right|^2 x^2\left(0.6\,\ln^2 x - 0.2\,\ln x + 2.2\right)\\ &< 1.6 \times 10^{-15}\end{aligned} \tag{5.43}$$

where the second line is the prediction using the value $|\sum_i U_{\mu i} U^*_{ei}| < 1 \times 10^{-3}$ mentioned before. The experimental limit $\mathrm{BR}(\mu \to 3e) < 1 \times 10^{-12}$, set by the SINDRUM experiment [61], is weaker than that of the radiative decay.

Although the lepton-flavor-violating processes currently do not constrain the model better than EWPD constraints, experimental improvements could change this in the coming years. For example the Mu3e experiment may eventually probe $\mu \to 3e$ down to the level of $10^{-16}$ branching ratio [62]. Moreover the process of $\mu N \to eN$ conversion in nuclei is expected to yield interesting limits in upcoming experiments, including Mu2e [63] at Fermilab and COMET [64] at KEK.

## 5.5 Constraints on the singlet

In recent years there have been intensive efforts to constrain the possible existence of light mediators connecting the SM to a hidden sector, the scalar singlet with Higgs portal being a prime example. The parameter space of $m_s$ and $\theta_s$ (the singlet-Higgs mixing angle) is constrained by a variety of beam-dump, collider and rare decay experiments, and by cosmology (big bang nucleosynthesis), astrophysics (supernova cooling) and dark matter direct searches. A large region of parameter space with $\theta_s \lesssim 10^{-3}$ and $m_s \lesssim 10\,\mathrm{GeV}$ remains open, and parts of this will be targeted by the upcoming SHiP experiment [16]. In Figure 5.6 we show some of the existing constraints, reproduced from Ref. [70].

The KOTO experiment has searched for the rare decay $K_L \to \pi^0 \nu\nu$ and set a new stringent upper limit of $3 \times 10^{-9}$ on its branching ratio [71, 72]. Recently four candidate events above expected backgrounds were reported [20], far in excess of the standard model prediction ($\mathrm{BR} = 3 \times 10^{-11}$ [35]). These could potentially be explained by the exotic decay mode $K_L \to \pi^0 s$, if $s$ is sufficiently long-lived to escape detection, or if it decays invisibly. Such an interpretation has been previously considered in Refs. [73–76]. In Figure 5.6, the $1\sigma$ and $2\sigma$ regions estimated in Ref. [74] for explaining the KOTO excess are shown in blue. Parts of these regions are excluded by other experiments, notably NA62 [77] and E949 [66], but a range around

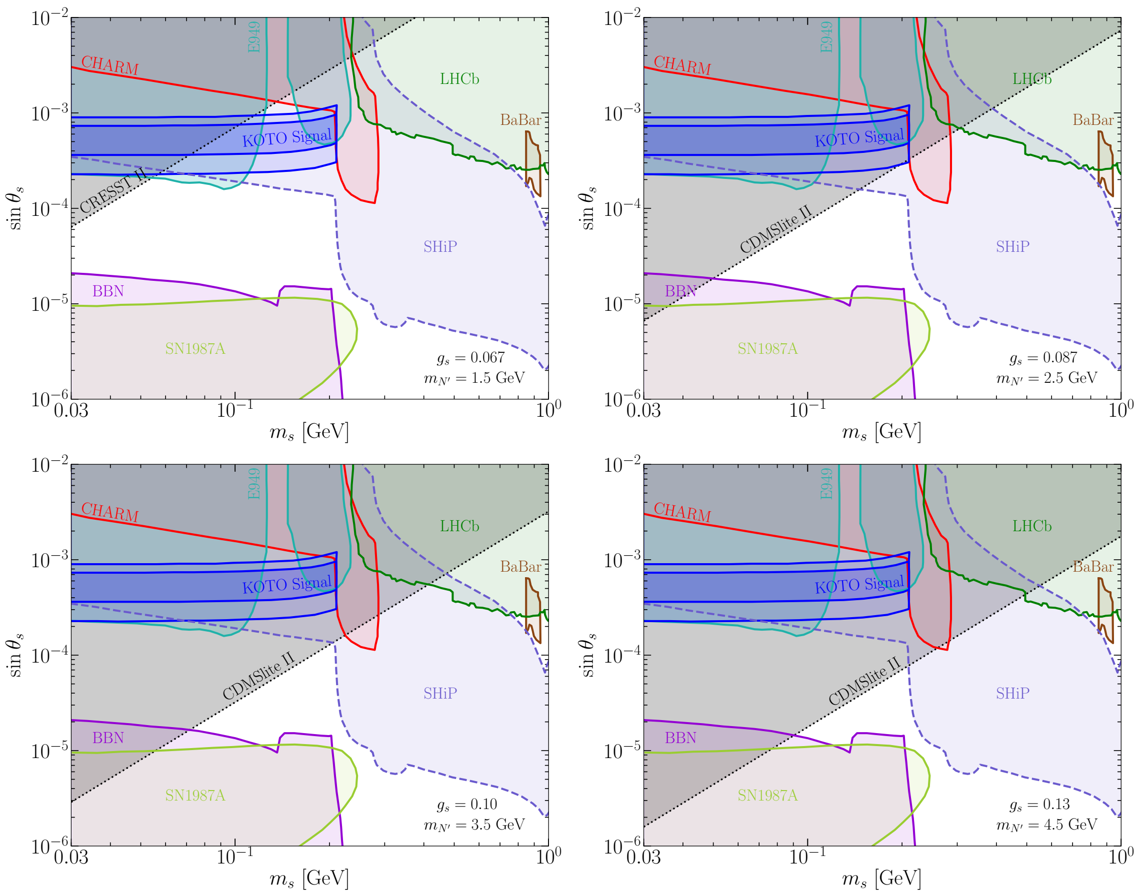


Figure 5.6: Constraints on a light singlet mediator, in the $m_s$-$\theta_s$ plane for the case $m_s < m_{N'}$. The four plots consider different values of the DM mass $m_{N'} = 1.5$, 2.5, 3.5, 4.5 GeV, for which the direct detection constraints (black dotted line) differ; all other constraints are the same. The dark blue regions are favored at $1\,\sigma$ and $2\,\sigma$ for the KOTO anomaly. The red, cyan, green and brown regions are excluded by CHARM [65], E949 [66], LHCb [67] and BaBar experiments [68], respectively. The violet and light-green regions are excluded by BBN [69] and supernova data [70]. Sensitivity projection for the SHiP experiment is indicated by the dashed blue-gray boundary. The experimental bounds, along with the projected sensitivity, are taken from Ref. [70].

$m_s \sim (120 - 160)\,\text{MeV}$ and $\theta_s \sim (2 - 9) \times 10^{-4}$ remains viable.

The four plots in Figure 5.6 pertain to different choices of the DM mass $m_{N'}$, for the purpose of showing constraints from direct detection, that we describe in the following section. It can be seen that the region favored by the KOTO excess events is excluded by DM direct searches except for light DM, with $m_{N'} \lesssim 2.5\,\text{GeV}$.

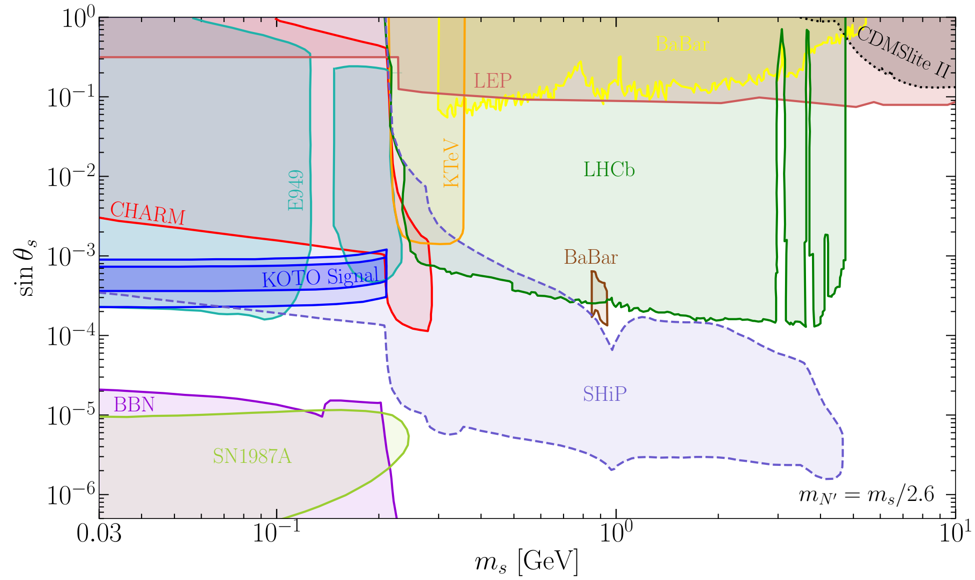


Figure 5.7: Constraints on a light singlet mediator, in the $m_s$-$\theta_s$ plane, for the case $m_s = 2.6\, m_{N'}$. The experimental bounds, along with the projected sensitivity, are the same as in Figure 5.6 and taken from Ref. [70]. The strongest direct detection constraint derived for our model comes from CDMSlite II experiment [78] and is shown with the black dotted line.

## 5.6 DM direct/indirect detection and self-interactions

In general, the interactions of DM with nucleons versus with other particles are independent processes, whose cross sections need not be related. In our model however, both are mediated by exchange of the singlet $s$, so it is natural to consider them together.

### 5.6.1 DM-nucleon scattering

The mixing of $s$ with the Higgs boson leads to spin-independent DM interactions with nucleons. In particular, the cross section for scattering on nucleons is

$$\sigma_{\rm SI}^p = \frac{g_s^2 m_{N'}^2 m_n^4 \sin^2 2\theta_s\, f_n^2}{4\pi \left(m_{N'} + m_n\right)^2 \bar{v}^2} \left(\frac{1}{m_h^2} - \frac{1}{m_s^2}\right)^2 , \tag{5.44}$$

where $m_n = 0.938$ GeV is the nucleon mass, $f_n = 0.30$ is the relative coupling of the Higgs to nucleons [79, 80], $m_h = 125$ GeV is the SM-like Higgs mass, $m_s$ is the singlet mass and $\theta_s$ is the $s$-$h$ mixing angle. (Recall that $\bar{v} \cong 174\,\text{GeV}$ is the complex Higgs field VEV.)

The strongest constraints from direct detection, in the mass range $m_{N'} < 4.5\,\text{GeV}$ predicted in our model, come from the experiments CRESST II [81], CDMSlite II [78] and LUX [82]. In the future these limits will be improved by SuperCDMS [83]. In all cases the sensitivity rapidly drops with lower DM mass because of the threshold for energy deposition. The DarkSide experiment [84] claims limits below those mentioned above, but their validity has been questioned in Ref. [85], and we omit them from our analysis.

Recently Ref. [86] cast doubts on the robustness of direct constraints on light dark matter in light of astrophysical uncertainties, especially that of the local escape velocity, that has been revisited using Gaia data [87]. It is claimed that the 2017 cross section bound from XENON1T [88] at DM mass 4 GeV is uncertain by six orders of magnitude. We checked their results using `DDCalc` [89], finding only two orders of magnitude uncertainty. More importantly, the astrophysical uncertainty on the more relevant newer constraints is only a few percent (due to the much lower thresholds of those experiments), hence irrelevant.

For a given value of DM mass $m_{N'}$, we can use the relic density constraint shown in Figure 5.1 to determine the coupling $g_s$. Then the predicted direct detection cross section (5.44) leads to a constraint in the $m_s$-$\theta_s$ plane, that we plot as a dashed curve in Figure 5.6 for the case $m_s < m_{N'}$. As mentioned above, for larger values of $m_{N'}$ the direct detection constraint is stronger, and the region favored by the KOTO anomaly is excluded.

For $m_s > m_{N'}$, and particularly in the region where $m_s \gtrsim 2\,m_{N'}$, the direct detection constraints are shown in Figure 5.7 for the case considered in the center panel of Figure 5.1, namely for $m_s = 2.6\,m_{N'}$. These bounds are much weaker than those in Figure 5.6 for any value of the DM mass $m_{N'}$ because of the relatively larger assumed value of $m_s$, as can be seen from Eq. (5.44).

### 5.6.2 DM indirect detection

Light dark matter models are typically constrained by indirect signals, like annihilation in the galaxy or the cosmic microwave background (CMB), enhanced by the relative large abundance of light DM. These signals are suppressed for asymmetric dark matter, by the absence of the symmetric component with which to annihilate, but DM accumulation in stars can provide significant constraints in the asymmetric case. Our model provides for a continuum of possibilities between the purely symmetric and asymmetric cases, depending on the strength of the coupling $g_s$ when $N'\bar{N}' \to ss$ is the dominant process, or a combination of $g_s$ and $m_s$ when $s$-channel annihilation dominates (recall Figure 5.1).

However in our scenario there are several reasons for annihilation signals to be suppressed at late times, even in the symmetric regime. For the case where $N'\bar{N}' \to ss$ dominates, the cross section is $p$-wave, which significantly relaxes indirect constraints because of the low DM velocity at times much later than freezeout [90]. An exception can occur if the DM particles annihilate to form a bound state [91], which is $s$-wave, and leads to much stronger CMB constraints than the $p$-wave process. However this only occurs for relatively heavy DM, with mass $\gtrsim 250\,\mathrm{GeV}$.

In addition, the $p$-wave process we consider from $N'\bar{N}' \to f\bar{f}$ targets parameter space with $m_s > 2\,m_{N'}$, such that $m_s$ is not too close to the threshold $2\,m_{N'}$. In this case the indirect signal is further suppressed, due to the low DM velocity in galaxies, $v \sim 10^{-3}\,c$, since the phase-space average of the annihilation cross section samples the resonant region much less than in the early Universe during freezeout. Indeed, following Refs. [90, 92], it is possible to estimate that for the values of $g_s$ and $m_{N'}$ contained in Figure 5.1 (center and right plots) the maximum ratio between the DM annihilation cross section today and that at the time of freezeout, given by Eq. (5.22), is of order of $\sim 10^{-14}$, which leads today to $\langle \sigma v \rangle \lesssim 10^{-37}$ cm$^3$/s. Such a value is well below the most stringent indirect detection constraint for $p$-wave annihilating DM of mass $m_{N'} \lesssim 4.5$ GeV [90].

Another possible signal that does not rely upon DM annihilation with itself, but rather on its interactions with standard model particles, is the effect of DM accumulation within stars. The most promising sites for capturing DM are neutron stars (NS's) because of their high density, which enhances the probability for DM particles to be captured and accumulate in the center of the NS during its lifetime.

For purely asymmetric DM, there is no DM annihilation in the NS core, and its accumulation may start to increase the star mass, destabilizing the delicate balance between the gravitational attraction and the Fermi pressure, and leading to the gravitational collapse of the NS into a black hole [93–96]. However, this effect is only relevant in the case of bosonic DM, where there is no compensating increase in the Fermi pressure, leading to severe constraints on the DM-nucleon and DM-lepton scattering cross-sections based on the estimated age of the oldest NSs observed so far [96, 97]. These bounds do not apply to the present model because of the fermionic nature of our DM candidate, and its GeV mass scale. For fermionic asymmetric DM, the destabilization can occur only for DM with mass larger than the PeV scale and having attractive self-interactions [98].

In the case where DM is partially or purely symmetric, which occurs for smaller values of $m_{N'}$ and $g_s$ in our model (recall Figure 5.1), the accumulated DM inside the NS core can annihilate and the annihilation products might thermalize, heating up the star and contributing to its luminosity [99, 100]. The latter is also increased by DM kinetic heating from multiple DM scatterings with the NS constituents, namely neutrons, electrons and muons, and this effect is independent of whether the DM is symmetric or asymmetric [99, 101]. However, the expected NS surface temperature generated only by DM annihilation and scattering is too low to be detected by current infrared telescopes. A future detection by, for instance, the James Webb Space Telescope, would set the strongest bound on the DM-nucleon and DM-lepton scattering cross-sections for DM masses below the GeV scale, which would constrain our model [101].

Other limits on DM-nucleon interaction can in principle be derived from DM capture by white dwarfs (WD's) [94]. Similarly to NS's, asymmetric DM accumulating in the WD core might destabilize the latter and spark fusion reactions that precede a

Type Ia supernova explosion [102]. However, in models where DM interactions with SM particles occur only via a light scalar mediator mixing with the Higgs boson, destabilization effects become important only for fermionic DM masses above $10^6$ GeV [103].

On the other hand, DM scattering and annihilation can heat up WD's and contribute to their luminosity. The difference between the WD and the NS case is that very old WD's with low surface temperature have been observed, in particular within the M4 globular cluster [104, 105]. Such observations have been used to claim very strong constraints on the DM-nucleon scattering cross section, $\sigma_{SI} \lesssim 10^{-42} - 10^{-43}$ cm$^2$ for DM masses in the range $10^{-2} - 10^7$ GeV [106, 107]. These limits were derived based on the assumption that the DM density within the M4 globular cluster is as high as $10^3$ GeV/cm$^3$, which can make the DM contribution to the WD luminosities as high as the observed values. However, as pointed out by Ref. [106], the value of the DM density in globular clusters is highly uncertain and under debate. Although values of $10^3$ GeV/cm$^3$ could be expected if globular clusters form within DM subhalos before falling into galactic halos [108], tidal stripping by subsequent mergers [109] provides a very efficient way of depleting DM in these systems, leaving them dominated today by just the stellar component [110]. The observation that the present-day dynamics of globular clusters can be explained without the need of DM suggests that these systems might form in molecular clouds in the gaseous disk of the galaxy instead of in DM overdensities [111–113]. It is therefore reasonable to assume that the DM density in the M4 globular cluster, which is about 2 kpc away from us in the direction towards the galactic center, could be as low as in the solar neighborhood, $\sim 0.3$ GeV/cm$^3$. This lower value would reduce the saturated DM heating luminosity by approximately three orders of magnitude, well below the observed one, and lead to no bound on the DM-nucleon scattering cross section at all. More promising WD candidates might be found in globular clusters in dwarf spheroidal galaxies of the Milky Way, where a significant amount of DM may have survived tidal stripping [114].

### 5.6.3 DM self-interactions

Dark matter can also interact with itself by exchange of the $s$, which is of interest for addressing small-scale structure problems of collisionless cold dark matter (see Ref. [115] for a review). Ref. [116] showed that the self-interaction cross section can be at an interesting level for solving these problems, while obtaining the right DM relic density, if both $m_{N'}$ and $m_s$ are light,

$$m_s \cong 1 \text{ MeV} \times \begin{cases} \left(\frac{m_{N'}}{0.55 \text{ GeV}}\right)^{3/4}, & \sigma/m_{N'} = 1 \text{ cm}^2/\text{g} \\ \left(\frac{m_{N'}}{0.25 \text{ GeV}}\right)^{3/4}, & \sigma/m_{N'} = 0.1 \text{ cm}^2/\text{g} \end{cases} \tag{5.45}$$

These relations, valid for approximately symmetric DM, correspond to self-interaction cross section per mass in the range $\sigma/m_{N'} = 0.1 - 1\,\text{cm}^2/\text{g}$, that are relevant for suppressing cusps in density profiles of dwarf spheroidal to Milky Way-sized galaxies.

Such light singlets in the MeV mass range are strongly constrained by direct detection. The prediction (5.44) is modified by the fact that the momentum transfer $q$ is no longer negligible compared to $m_s$, hence $m_s^2 \to m_s^2 + q^2$ in Eq. (5.44). We take $q = m_{N'}v_{N'}$ with DM velocity $v_{N'} \sim 300$ km/s to account for this. Figure 5.6 shows that for low $m_s$ there is an allowed window for $\sin\theta_s \sim 2 \times (10^{-5} - 10^{-4})$ between the BBN and E949 constraints, which persists to smaller values of $m_s \gtrsim 1$ MeV before being excluded by BBN as $m_s$ falls below the threshold for $s \to e^+e^-$ decay.

In Figure 5.8 we show the predicted spin-independent cross section versus $m_{N'}$ (black curves) for several choices of $\theta_s$ in the experimentally allowed range, fixing $g_s$ as in Figure 5.1 to give the right relic density, and $m_s$ (orange dash-dotted curve) as a function of $m_{N'}$ using (5.45). The plot on the left assumes the higher self-interaction cross section $\sigma/m = 1\,\text{cm}^2/\text{g}$. In this case, it is necessary to take the singlet mass $m_s \lesssim 0.7$ MeV and the DM mass $m_{N'} \lesssim 0.3$ GeV to respect the direct detection limit. This is ruled out by BBN since the decay $s \to e^+e^-$ are kinematically blocked, and will lead to overclosure by the singlets as $T$ falls below $m_s$. However, by adopting a lower self-interaction cross section $\sigma/m = 0.1$ cm$^2$/g (right plot of Figure 5.8), which may still be relevant for some of the small-scale structure issues, the allowed range

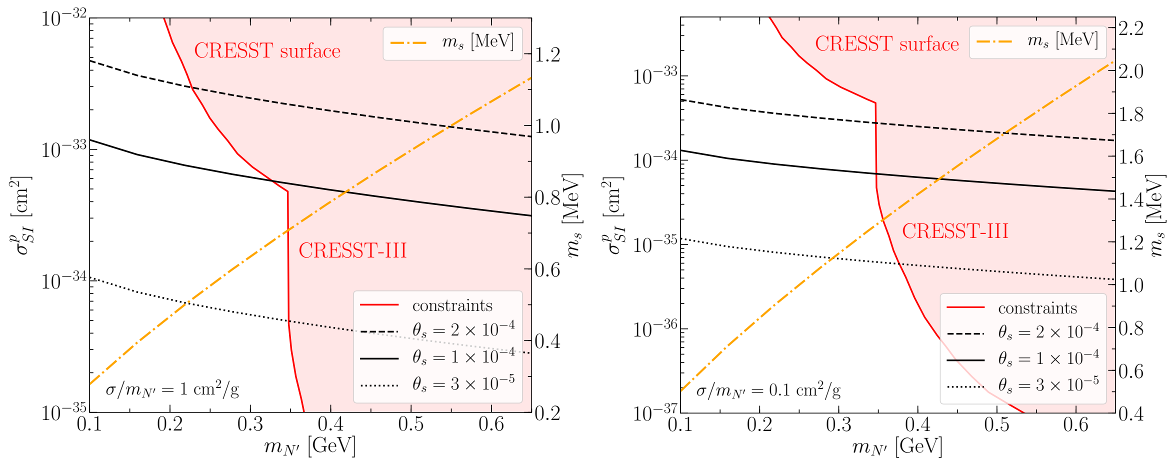


Figure 5.8: Predicted spin-independent cross section for DM scattering on nucleons versus DM mass $m_{N'}$, assuming approximately symmetric DM with a self-interaction cross section of $\sigma/m_{N'} = 1\,\mathrm{cm}^2/\mathrm{g}$ (left) or $0.1\,\mathrm{cm}^2/\mathrm{g}$ (right), for three choices of $\theta_s$ (dashed, solid black, dotted) and the envelope of experimental constraints (with the exception of DarkSide-50) copied from Ref. [117] (solid red). Dash-dotted curve shows the singlet mass $m_s$ versus $m_{N'}$.

of $m_{N'}$ and $m_s$ is increased to somewhat larger values with $m_s > 2\,m_e$, which can be compatible with BBN.

The previous determination holds in the region $m_{N'} \lesssim 3\,\mathrm{GeV}$ where the DM is to a good approximation symmetric, corresponding to the linearly increasing branch of the relic density contour in Figure 5.1 (left). For nearly asymmetric DM, the horizontal branch with $m_{N'} \cong 4.5$ GeV applies. Instead of Eq. (5.45), the desired self-interaction cross section requires a roughly linear relation $g_s \cong 0.75 + 4.43\,m_s/\mathrm{GeV}$ (valid for $m_s \sim 0.2-0.3$ GeV), that we determine by applying a Sommerfeld enhancement factor [118] to the tree-level, phase-space averaged transport scattering cross section given in Ref. [116], and requiring that the resulting cross section is $\sigma/m_{N'} = 1$ b/GeV $\cong 0.6$ cm$^2$/g for a mean DM velocity of 10 km/s, corresponding to dwarf spheroidal galaxies. To satisfy the CDMSLite II constraint $\sigma_{SI} < 1\times10^{-41}\,\mathrm{cm}^2$ at $m_{N'} = 4.5$ GeV [119], it is necessary to take small mixing $\theta_s \lesssim 6\times10^{-6}$, since $g_s \sim 2$ for $m_s \sim 0.2-0.3$ GeV, from imposing the desired value of $\sigma/m_{N'}$.

Hence we find two allowed regions for strong self-interactions, one marginal since

$m_s \gtrsim 1$ MeV close to BBN limits, with $\sigma/m_{N'} \sim 0.1$ cm$^2$/g at the low end of the range desired for small scale structure, and $m_{N'} \sim 0.35$ GeV. The other allows for a larger $\sigma/m_{N'} \gtrsim 0.6$ cm$^2$/g, with singlet parameters close to the SN1987A exclusion curve and $m_{N'} \cong 4.5$ GeV.

## 5.7 Naturalness

In our proposal, the flavor structure of neutrinos is controlled by the same matrix $\eta_{\nu,ij}$ that governs the HNL couplings, up to a proportionality constant, in the spirit of MFV. In order for DM to be stable, $\eta_{\nu,ij}$ must have rank two. The HNL mass matrix is proportional to the identity, up to corrections going as $\eta_\nu^2$. We do not provide any fundamental explanation of the origin of this structure; instead we content ourselves with the feature that it is technically natural in the sense of 't Hooft: all radiative corrections are consistent with our assumptions.

The stability of DM is most easily seen in the basis (5.36, 5.37), where $N'$ obviously decouples from the SM leptons. We assume this coincides with the mass eigenbasis, which is consistent since there are no interactions that can induce mass-mixing between $N'$ and the remaining $N_i$'s. Self-energy corrections involving $s$ exchange are flavor-diagonal. Those involving Higgs and leptons in the loop leave $m_{N'}$ unchanged, while renormalizing the $N_i$ mass matrix by

$$M_N\delta_{ij} \to M_N\delta_{ij} + O(1) \times \eta_{\nu,ik}\,\frac{m_{\ell_k}}{16\pi^2}\,\eta^\dagger_{\nu,kj} \tag{5.46}$$

where $m_{\ell_i}$ are the charged lepton masses. Given the smallness of $\eta_\nu \lesssim 10^{-4}$, these corrections are unimportant. Similarly the one-loop corrections to $\eta_\nu$ are negligible,

$$\eta_\nu \to \eta_\nu + \frac{O(1)}{16\pi^2}\,\eta_\nu\eta_\nu^\dagger\eta_\nu \tag{5.47}$$

and cannot induce couplings to $N'$. The only particles to which $N'$ couples are the singlet and the inflaton, Eqs. (5.2, 5.15), and these interactions are assumed to be flavor-conserving at tree level. Flavor-changing corrections to $g_s$ and $g_\phi$ of

$O(\eta_\nu^2/(16\pi^2)) \times g_{s,\phi}$ arise at the one-loop level and are negligible for our purposes.

There remains the infamous naturalness problem of the Higgs mass (weak scale hierarchy). This problem was addressed in the context of the seesaw mechanism in Ref. [120], where the weak scale was linked to that of the heavy Majorana neutrinos by radiative generation of the Higgs potential. A low scale for their masses is needed, $M_{\nu_R} \lesssim 10^7$ GeV [121], which would require a low reheat temperature in our scenario, and consequently small coupling $g_\phi \lesssim 10^{-8}$. Although peculiarly small, this value would still be compatible with the requirements of technical naturalness since it can only be multiplicatively renormalized.

The very light singlet could pose an analogous problem of fine-tuning. The first threshold encountered when running the renormalization scale up from low values is that of $N_i$, which contributes of order $\delta m_s \sim g_s M_N/(4\pi)$ to $m_s$. This can easily be compatible with the tree-level values of $m_s$ desired for large parts of the allowed parameter space (see Figures 5.1 and 5.6).

Next one encounters the Higgs threshold, which further shifts $m_s$ through the coupling $\lambda_{hs}$. The correction is of order $\delta m_s \sim \sqrt{\lambda_{hs}}\, m_h/4\pi$ which is related to the mixing angle by $\theta_s \sim \lambda_{hs} v v_s/m_h^2$, where $v$ and $v_s$ are the respective VEVs of the Higgs and the singlet. In turn, $v_s$ depends upon the $s$ self-coupling through $m_s^2 \sim \lambda_s v_s^2$. Using these and demanding that $\delta m_s \lesssim m_s$ gives the constraint $\sqrt{\lambda_s} \lesssim 16\pi^2 m_s^3 v/(\theta_s m_h^4)$. This can always be satisfied by choosing small enough $\lambda_s$, but the latter has a minimum natural value given by its one-loop correction $\delta\lambda_s \sim g_s^4/(16\pi^2)$.[7] Putting all of these together, we get a naturalness bound on the singlet mixing angle

$$\theta_s \lesssim \left(\frac{4\pi\, m_s}{m_h}\right)^3 \left(\frac{1}{\sqrt{\lambda_h}\, g_s^2}\right) \sim 0.008 \tag{5.48}$$

(taking $m_s \sim 0.3$ GeV and $g_s \sim 0.1$) which is compatible with the regions of interest for future discovery, including the anomalous KOTO events. Thus, somewhat surprisingly, the light scalar does not introduce a new hierarchy problem analogous to that of the Higgs mass, due to its relatively weak couplings.

[7] There is also a one-loop correction of order $\lambda_{hs}^2/16\pi^2$, but this leads to a weaker bound on $\theta_s$ than (5.48).

We do not address the smallness of $\theta_{QCD}$ in our "theory of everything," which was a motivation for Refs. [9, 11] to choose the QCD axion as their dark matter candidate. This neglect is consistent with our philosophy of focusing on technical naturalness rather than aesthetic values of couplings, since $\theta_{QCD}$ is known to be highly stable against radiative corrections [122].

## 5.8 Conclusions

It is interesting to construct scenarios that link the different particle physics ingredients known to be missing from the standard model, since it can lead to distinctive predictions. Here we have constructed a minimal scenario that explains inflation, baryogenesis, dark matter and neutrino masses, is highly predictive, and can be tested in numerous experimental searches for heavy neutral leptons, light dark matter, and light scalar mediators. At low energies, the only new particles are three quasi-Dirac HNLs, one of which is DM (and exactly Dirac), and a light singlet scalar.

One prediction of the model is that no new source of CP-violation is required for baryogenesis, which occurs through a novel form of leptogenesis here. In contrast to ordinary leptogenesis, the asymmetry is formed during inflation, and the right-handed neutrinos that generate light neutrino masses are too heavy to be produced during reheating. CP is spontaneously broken by the inflaton VEV during inflation, and the light HNLs transmit the lepton asymmetry from the inflaton to the SM. In Ref. [14] it was shown that observable isocurvature perturbations can arise, depending on the inflaton potential and initial conditions. In the present model, these would appear as correlated dark matter isocurvature and adiabatic perturbations.

Another prediction is that the two unstable HNLs $N_i$ should be degenerate to very high precision with the dark matter $N'$, split only by the correction (5.46) of order $10^{-2}$ eV. Similarly, the $N_i$ are Dirac particles to a very good approximation, with a lepton-violating Majorana mass of order $10^{-6}$ eV. This is too small to be detectable in neutrinoless double beta decay, but large enough to allow for a distinctive signature of lepton violation through $N$-$\bar{N}$ oscillations. The two $N_i$ HNLs can mix strongly enough with SM neutrinos to be discoverable at upcoming experiments like SHiP. The stability of $N'$ is directly linked to the masslessness of the lightest neutrino. This connection could be relaxed by slightly modifying the assumption that the HNL couplings are aligned with light neutrino masses through Eq. (5.5), without spoiling other features of our model. We further showed that lepton-flavor-violating decays like $\mu \to e\gamma$ and $\mu \to 3e$ may be generated by HNL exchange in loops, at a level that can be detected in future experiments.

In our framework, the dark matter $N'$ is partially asymmetric, and has a mass bounded by $m_{N'} \lesssim 4.5$ GeV. The bound is saturated when $N'$ is purely asymmetric, and its mass is determined by the observed value of the baryon asymmetry. Light DM can be accommodated by taking small values of the coupling $g_s$ between $N'$ and the singlet $s$, which controls $N'\bar{N}' \to ss$ annihilation; see Figure 5.1. In the mass range $(1-4.5)$ GeV, significant constraints are already placed by direct DM searches.

The light scalar singlet, whose mass must be less than $m_{N'}$ for efficient $N'\bar{N}' \to ss$ annihilation, can lead to striking signatures. For example the decay $K_L \to \pi s$ can explain anomalous excess events recently observed by the KOTO experiment, but only if $m_{N'} \lesssim 2.5$ GeV; otherwise direct detection constraints rule out this mode at the level suggested by the KOTO events, where $m_s \sim (100 - 200)$ MeV and $s$ mixes with the Higgs at the level $\theta_s \sim 5 \times 10^{-4}$. (The preferred parameter region for the KOTO anomaly is only a small part of the full allowed space of our model.) In a different part of parameter space with $m_s \sim (0.2 - 0.3)$ GeV, $m_{N'} \cong 4.5$ GeV and $\theta_s \lesssim 6 \times 10^{-6}$, the singlet mediates DM self-interactions with a cosmologically interesting cross section, $\sigma/m_{N'} \sim 0.6\ \mathrm{cm}^2/\mathrm{g}$.

## Acknowledgment

We thank J. Kopp for an insightful question that inspired this work, and G. Alonso-Álvarez, J. Bramante, T. Bringmann, L. Di Ciaccio, M. Fairbairn, E. Fernandez-Martinez, F. Kahlhoefer, C. Lacasta, E. Migliore, D. Morrissey, S. Petcov, M. Reina-Campos, P. Scott, J.-L. Tastet and J. Timmermans for helpful correspondence. Our research is supported by NSERC (Natural Sciences and Engineering Research Council, Canada). MP is supported by the Arthur B. McDonald Institute for Canadian astroparticle physics research.

## 5.9 Note added

The KOTO Collaboration reported that the four candidate events observed in the signal region for the rare decay $K_L \to \pi^0 \nu\bar{\nu}$, previously announced in Ref. [20], were found to be caused in reality by contamination from other SM decays. This finding makes the signal fully consistent with the background expectation, setting an upper limit of $4.9 \times 10^{-9}$ on the branching ratio of $K_L \to \pi^0 \nu\bar{\nu}$ [123, 124].

# Appendices

## 5.A Decay rate for $N_i \to \nu\ell^+\ell^-$

The matrix element for the process $N_i \to \nu_\beta \ell_\beta^+ \ell_\alpha^-$, where $\alpha, \beta = e,\ \mu,\ \tau$, is

$$\mathcal{M} = \frac{g_w^2}{8M_W^2} \left[\bar{u}(p_{\ell_\alpha^-})\, \gamma^\mu (1-\gamma^5)\, u(p_{N_i})\, U_{i\alpha}^*\right] \left[\bar{u}(p_{\nu_\beta})\, \gamma_\mu (1-\gamma^5)\, u(p_{\ell_\beta^+})\right] \tag{5.49}$$

whose square reduces to

$$\langle|\mathcal{M}|^2\rangle = \frac{G_F^2}{64}|U_{i\alpha}|^2 M_i E_\beta \left[\frac{M_i^2 + m_\beta^2 - m_\alpha^2}{2} - M_i E_\beta\right] \tag{5.50}$$

after averaging over the initial spin, summing over final spins and setting $m_{\nu_\beta} = 0$. Here, $G_F$ is the Fermi constant, $E_\beta$ is the energy of $\ell_\beta^+$ and we have defined for simplicity $M_i \equiv M_{N_i}$, $m_\alpha \equiv m_{\ell_\alpha^-}$ and $m_\beta \equiv m_{\ell_\beta^+}$. The decay rate $\Gamma$ can be obtained by plugging Eq. (5.50) in the standard decay formula (see Ref. [35]) and computing the three-body phase space integral. The common assumption made in the literature is to consider $m_\beta = 0$, which is well motivated for $\alpha = e,\ \mu$ and $\beta = \mu,\ e$. In these cases, the decay rate is [46, 48]

$$\Gamma = \frac{G_F^2 M_i^5}{192\pi^3}\,|U_{i\alpha}|^2\,\Big(1 - 8\,x_\alpha^2 + 8x_\alpha^6 - x_\alpha^8 - 12\,x_\alpha^4\,\log(x_\alpha^2)\Big) \tag{5.51}$$

where $x_\alpha = m_\alpha/M_i$. Such a simplified formula does not hold for $\alpha = \mu,\ \tau$ and $\beta = \tau,\ \mu$, where the muon mass is not negligible compared to the tau mass. The general expression reads

$$\begin{aligned}\Gamma = \frac{G_F^2 M_i^5}{192\pi^3}\,|U_{i\alpha}|^2 \Bigg\{ & 12\,|x_\beta^2 - x_\alpha^2|\,(x_\beta^2 + x_\alpha^2) \\ & \log\left[\frac{x_\beta^2 + x_\alpha^2 - (x_\beta^2 - x_\alpha^2)^2 - |x_\beta^2 - x_\alpha^2|\sqrt{(1-(x_\beta - x_\alpha)^2)(1-(x_\beta + x_\alpha)^2)}}{2\,x_\beta\,x_\alpha}\right] \\ & - 12\left[x_\beta^4 + x_\alpha^4 - 2x_\beta^4\,x_\alpha^4\right]\log\left[\frac{1 - x_\beta^2 - x_\alpha^2 - \sqrt{(1-(x_\beta - x_\alpha)^2)(1-(x_\beta + x_\alpha)^2)}}{2\,x_\beta\,x_\alpha}\right] \\ & + \sqrt{(1-(x_\beta - x_\alpha)^2)(1-(x_\beta + x_\alpha)^2)} \\ & \left[1 - 7\left(x_\beta^2 + x_\alpha^2\right)\left(1 + x_\beta^2\,x_\alpha^2\right) - 7\left(x_\beta^4 + x_\alpha^4\right) + 12\,x_\beta^2\,x_\alpha^2 + x_\beta^6 + x_\alpha^6\right]\Bigg\}\end{aligned} \tag{5.52}$$

where $x_\alpha \equiv m_\alpha/M_i$ and $x_\beta \equiv m_\beta/M_i$. It is easy to check that this formula reduces to Eq. (5.51) in the limit $m_\beta \to 0$.

# Bibliography


[1] G. D'Ambrosio, G. F. Giudice, G. Isidori, and A. Strumia, "Minimal flavor violation: An Effective field theory approach," *Nucl. Phys. B* **645** (2002) 155–187, `arXiv:hep-ph/0207036`.

[2] G. 't Hooft, "Naturalness, chiral symmetry, and spontaneous chiral symmetry breaking," *NATO Sci. Ser. B* **59** (1980) 135–157.

[3] G. Alonso-Álvarez, G. Elor, A. E. Nelson, and H. Xiao, "A Supersymmetric

Theory of Baryogenesis and Sterile Sneutrino Dark Matter from $B$ Mesons," *JHEP* **03** (2020) 046, arXiv:1907.10612 [hep-ph].

[4] T. Asaka and M. Shaposhnikov, "The $\nu$MSM, dark matter and baryon asymmetry of the universe," *Phys. Lett. B* **620** (2005) 17–26, arXiv:hep-ph/0505013.

[5] M. Shaposhnikov and I. Tkachev, "The nuMSM, inflation, and dark matter," *Phys. Lett. B* **639** (2006) 414–417, arXiv:hep-ph/0604236.

[6] F. L. Bezrukov and M. Shaposhnikov, "The Standard Model Higgs boson as the inflaton," *Phys. Lett. B* **659** (2008) 703–706, arXiv:0710.3755 [hep-th].

[7] S. Choubey and A. Kumar, "Inflation and Dark Matter in the Inert Doublet Model," *JHEP* **11** (2017) 080, arXiv:1707.06587 [hep-ph].

[8] D. Borah, P. S. B. Dev, and A. Kumar, "TeV scale leptogenesis, inflaton dark matter and neutrino mass in a scotogenic model," *Phys. Rev. D* **99** no. 5, (2019) 055012, arXiv:1810.03645 [hep-ph].

[9] G. Ballesteros, J. Redondo, A. Ringwald, and C. Tamarit, "Unifying inflation with the axion, dark matter, baryogenesis and the seesaw mechanism," *Phys. Rev. Lett.* **118** no. 7, (2017) 071802, arXiv:1608.05414 [hep-ph].

[10] M. A. Shifman, A. I. Vainshtein, and V. I. Zakharov, "Can Confinement Ensure Natural CP Invariance of Strong Interactions?," *Nucl. Phys. B* **166** (1980) 493–506.

[11] A. Salvio, "A Simple Motivated Completion of the Standard Model below the Planck Scale: Axions and Right-Handed Neutrinos," *Phys. Lett. B* **743** (2015) 428–434, arXiv:1501.03781 [hep-ph].

[12] A. Salvio, "Critical Higgs inflation in a Viable Motivated Model," *Phys. Rev. D* **99** no. 1, (2019) 015037, arXiv:1810.00792 [hep-ph].

[13] I. Affleck and M. Dine, "A New Mechanism for Baryogenesis," *Nucl. Phys. B* **249** (1985) 361–380.

[14] J. M. Cline, M. Puel, and T. Toma, "Affleck-Dine inflation," *Phys. Rev. D* **101** no. 4, (2020) 043014, `arXiv:1909.12300 [hep-ph]`.

[15] **Planck** Collaboration, Y. Akrami *et al.*, "Planck 2018 results. X. Constraints on inflation," *Astron. Astrophys.* **641** (2020) A10, `arXiv:1807.06211 [astro-ph.CO]`.

[16] S. Alekhin *et al.*, "A facility to Search for Hidden Particles at the CERN SPS: the SHiP physics case," *Rept. Prog. Phys.* **79** no. 12, (2016) 124201, `arXiv:1504.04855 [hep-ph]`.

[17] D. Curtin *et al.*, "Long-Lived Particles at the Energy Frontier: The MATHUSLA Physics Case," *Rept. Prog. Phys.* **82** no. 11, (2019) 116201, `arXiv:1806.07396 [hep-ph]`.

[18] J. L. Feng, I. Galon, F. Kling, and S. Trojanowski, "ForwArd Search ExpeRiment at the LHC," *Phys. Rev. D* **97** no. 3, (2018) 035001, `arXiv:1708.09389 [hep-ph]`.

[19] V. V. Gligorov, S. Knapen, M. Papucci, and D. J. Robinson, "Searching for Long-lived Particles: A Compact Detector for Exotics at LHCb," *Phys. Rev. D* **97** no. 1, (2018) 015023, `arXiv:1708.09395 [hep-ph]`.

[20] S. Shinohara, "Search for the rare decay $K_L \to \pi^0 \nu \bar{\nu}$ at J-PARC KOTO experiment." `https://indico.cern.ch/event/769729/contri-butions/3510939/`, September, 2019. KAON2019, Perugia, Italy.

[21] K. D. Lozanov and M. A. Amin, "End of inflation, oscillons, and matter-antimatter asymmetry," *Phys. Rev. D* **90** no. 8, (2014) 083528, `arXiv:1408.1811 [hep-ph]`.

[22] B. A. Campbell, S. Davidson, J. R. Ellis, and K. A. Olive, "On the baryon, lepton flavor and right-handed electron asymmetries of the universe," *Phys. Lett. B* **297** (1992) 118–124, `arXiv:hep-ph/9302221`.

[23] J. M. Cline, "Constraints on almost Dirac neutrinos from neutrino - anti-neutrino oscillations," *Phys. Rev. Lett.* **68** (1992) 3137–3140.

[24] T. Bringmann, J. M. Cline, and J. M. Cornell, "Baryogenesis from neutron-dark matter oscillations," *Phys. Rev. D* **99** no. 3, (2019) 035024, `arXiv:1810.08215 [hep-ph]`.

[25] S. Tulin, H.-B. Yu, and K. M. Zurek, "Oscillating Asymmetric Dark Matter," *JCAP* **05** (2012) 013, `arXiv:1202.0283 [hep-ph]`.

[26] M. Cirelli, P. Panci, G. Servant, and G. Zaharijas, "Consequences of DM/antiDM Oscillations for Asymmetric WIMP Dark Matter," *JCAP* **03** (2012) 015, `arXiv:1110.3809 [hep-ph]`.

[27] J. A. Harvey and M. S. Turner, "Cosmological baryon and lepton number in the presence of electroweak fermion number violation," *Phys. Rev. D* **42** (1990) 3344–3349.

[28] **Planck** Collaboration, N. Aghanim *et al.*, "Planck 2018 results. VI. Cosmological parameters," *Astron. Astrophys.* **641** (2020) A6, `arXiv:1807.06209 [astro-ph.CO]`. [Erratum: Astron.Astrophys. 652, C4 (2021)].

[29] P. Gondolo and G. Gelmini, "Cosmic abundances of stable particles: Improved analysis," *Nucl. Phys. B* **360** (1991) 145–179.

[30] M. L. Graesser, I. M. Shoemaker, and L. Vecchi, "Asymmetric WIMP dark matter," *JHEP* **10** (2011) 110, `arXiv:1103.2771 [hep-ph]`.

[31] R. Iengo, "Sommerfeld enhancement: General results from field theory diagrams," *JHEP* **05** (2009) 024, `arXiv:0902.0688 [hep-ph]`.

[32] M. Drewes and B. Garbrecht, "Combining experimental and cosmological constraints on heavy neutrinos," *Nucl. Phys. B* **921** (2017) 250–315, arXiv:1502.00477 [hep-ph].

[33] S. Antusch and O. Fischer, "Non-unitarity of the leptonic mixing matrix: Present bounds and future sensitivities," *JHEP* **10** (2014) 094, arXiv:1407.6607 [hep-ph].

[34] E. Fernandez-Martinez, J. Hernandez-Garcia, and J. Lopez-Pavon, "Global constraints on heavy neutrino mixing," *JHEP* **08** (2016) 033, arXiv:1605.08774 [hep-ph].

[35] **Particle Data Group** Collaboration, M. Tanabashi *et al.*, "Review of Particle Physics," *Phys. Rev. D* **98** no. 3, (2018) 030001.

[36] D. A. Bryman and R. Shrock, "Constraints on Sterile Neutrinos in the MeV to GeV Mass Range," *Phys. Rev. D* **100** (2019) 073011, arXiv:1909.11198 [hep-ph].

[37] **NA62** Collaboration, "HNL production and exotic searches at NA62." https://indico.cern.ch/event/769729/contributions/3511127/attachments/1907464/3150874/goudzovski_130919.pdf, 2019. KAON2019, Perugia, Italy.

[38] **FCC-ee study Team** Collaboration, A. Blondel, E. Graverini, N. Serra, and M. Shaposhnikov, "Search for Heavy Right Handed Neutrinos at the FCC-ee," *Nucl. Part. Phys. Proc.* **273-275** (2016) 1883–1890, arXiv:1411.5230 [hep-ex].

[39] I. Krasnov, "DUNE prospects in the search for sterile neutrinos," *Phys. Rev. D* **100** no. 7, (2019) 075023, arXiv:1902.06099 [hep-ph].

[40] **SHiP** Collaboration, C. Ahdida *et al.*, "Sensitivity of the SHiP experiment to Heavy Neutral Leptons," *JHEP* **04** (2019) 077, arXiv:1811.00930 [hep-ph].

[41] **DELPHI** Collaboration, P. Abreu *et al.*, "Search for neutral heavy leptons produced in Z decays," *Z. Phys. C* **74** (1997) 57–71. [Erratum: Z.Phys.C 75, 580 (1997)].

[42] **CHARM** Collaboration, F. Bergsma *et al.*, "A Search for Decays of Heavy Neutrinos in the Mass Range 0.5-GeV to 2.8-GeV," *Phys. Lett. B* **166** (1986) 473–478.

[43] **NuTeV, E815** Collaboration, A. Vaitaitis *et al.*, "Search for neutral heavy leptons in a high-energy neutrino beam," *Phys. Rev. Lett.* **83** (1999) 4943–4946, `arXiv:hep-ex/9908011`.

[44] J.-L. Tastet and I. Timiryasov, "Dirac vs. Majorana HNLs (and their oscillations) at SHiP," *JHEP* **04** (2020) 005, `arXiv:1912.05520 [hep-ph]`.

[45] **E949** Collaboration, A. V. Artamonov *et al.*, "Search for heavy neutrinos in $K^+ \to \mu^+ \nu_H$ decays," *Phys. Rev. D* **91** no. 5, (2015) 052001, `arXiv:1411.3963 [hep-ex]`. [Erratum: Phys.Rev.D 91, 059903 (2015)].

[46] L. M. Johnson, D. W. McKay, and T. Bolton, "Extending sensitivity for low mass neutral heavy lepton searches," *Phys. Rev. D* **56** (1997) 2970–2981, `arXiv:hep-ph/9703333`.

[47] P. B. Pal and L. Wolfenstein, "Radiative Decays of Massive Neutrinos," *Phys. Rev. D* **25** (1982) 766.

[48] D. Gorbunov and M. Shaposhnikov, "How to find neutral leptons of the $\nu$MSM?," *JHEP* **10** (2007) 015, `arXiv:0705.1729 [hep-ph]`. [Erratum: JHEP 11, 101 (2013)].

[49] F. Bezrukov, H. Hettmansperger, and M. Lindner, "keV sterile neutrino Dark Matter in gauge extensions of the Standard Model," *Phys. Rev. D* **81** (2010) 085032, `arXiv:0912.4415 [hep-ph]`.

[50] J. Coffey, L. Forestell, D. E. Morrissey, and G. White, "Cosmological Bounds on sub-GeV Dark Vector Bosons from Electromagnetic Energy Injection," *JHEP* **07** (2020) 179, `arXiv:2003.02273 [hep-ph]`.

[51] M. Pospelov and J. Pradler, "Metastable GeV-scale particles as a solution to the cosmological lithium problem," *Phys. Rev. D* **82** (2010) 103514, `arXiv:1006.4172 [hep-ph]`.

[52] S. T. Petcov, "The Processes $\mu \to e + \gamma, \mu \to e + \bar{e}, \nu' \to \nu + \gamma$ in the Weinberg-Salam Model with Neutrino Mixing," *Sov. J. Nucl. Phys.* **25** (1977) 340. [Erratum: Sov.J.Nucl.Phys. 25, 698 (1977), Erratum: Yad.Fiz. 25, 1336 (1977)].

[53] S. M. Bilenky, S. T. Petcov, and B. Pontecorvo, "Lepton Mixing, mu –> e + gamma Decay and Neutrino Oscillations," *Phys. Lett. B* **67** (1977) 309.

[54] T. P. Cheng and L.-F. Li in *Proceedings of the Coral Gables Conference*, S. Perlmutter, ed. Plenum, New York, 1977.

[55] W. J. Marciano and A. I. Sanda, "Exotic Decays of the Muon and Heavy Leptons in Gauge Theories," *Phys. Lett. B* **67** (1977) 303–305.

[56] B. W. Lee, S. Pakvasa, R. E. Shrock, and H. Sugawara, "Muon and Electron Number Nonconservation in a V-A Gauge Model," *Phys. Rev. Lett.* **38** (1977) 937. [Erratum: Phys.Rev.Lett. 38, 1230 (1977)].

[57] B. W. Lee and R. E. Shrock, "Natural Suppression of Symmetry Violation in Gauge Theories: Muon - Lepton and Electron Lepton Number Nonconservation," *Phys. Rev. D* **16** (1977) 1444.

[58] L. Calibbi and G. Signorelli, "Charged Lepton Flavour Violation: An Experimental and Theoretical Introduction," *Riv. Nuovo Cim.* **41** no. 2, (2018) 71–174, `arXiv:1709.00294 [hep-ph]`.

[59] **MEG** Collaboration, A. M. Baldini *et al.*, "Search for the lepton flavour violating decay $\mu^+ \to \mathrm{e}^+\gamma$ with the full dataset of the MEG experiment," *Eur. Phys. J. C* **76** no. 8, (2016) 434, `arXiv:1605.05081 [hep-ex]`.

[60] D. N. Dinh, A. Ibarra, E. Molinaro, and S. T. Petcov, "The $\mu - e$ Conversion in Nuclei, $\mu \to e\gamma, \mu \to 3e$ Decays and TeV Scale See-Saw Scenarios of Neutrino Mass Generation," *JHEP* **08** (2012) 125, `arXiv:1205.4671 [hep-ph]`. [Erratum: JHEP 09, 023 (2013)].

[61] **SINDRUM** Collaboration, U. Bellgardt *et al.*, "Search for the Decay mu+ —> e+ e+ e-," *Nucl. Phys. B* **299** (1988) 1–6.

[62] **Mu3e** Collaboration, A.-K. Perrevoort, "Searching for Lepton Flavour Violation with the Mu3e Experiment," *PoS* **NuFact2017** (2017) 105, `arXiv:1802.09851 [physics.ins-det]`.

[63] **Mu2e** Collaboration, A. Baldini *et al.*, "Charged Lepton Flavour Violation using Intense Muon Beams at Future Facilities,".

[64] **COMET** Collaboration, D. Shoukavy, "COMET status and plans," *EPJ Web Conf.* **212** (2019) 01006.

[65] **CHARM** Collaboration, F. Bergsma *et al.*, "Search for Axion Like Particle Production in 400-GeV Proton - Copper Interactions," *Phys. Lett. B* **157** (1985) 458–462.

[66] **BNL-E949** Collaboration, A. V. Artamonov *et al.*, "Study of the decay $K^+ \to \pi^+\nu\bar{\nu}$ in the momentum region $140 < P_\pi < 199$ MeV/c," *Phys. Rev. D* **79** (2009) 092004, `arXiv:0903.0030 [hep-ex]`.

[67] **LHCb** Collaboration, R. Aaij *et al.*, "Differential branching fraction and angular analysis of the $B^+ \to K^+\mu^+\mu^-$ decay," *JHEP* **02** (2013) 105, `arXiv:1209.4284 [hep-ex]`.

[68] **BaBar** Collaboration, J. P. Lees *et al.*, "Search for Long-Lived Particles in $e^+e^-$ Collisions," *Phys. Rev. Lett.* **114** no. 17, (2015) 171801, arXiv:1502.02580 [hep-ex].

[69] A. Fradette and M. Pospelov, "BBN for the LHC: constraints on lifetimes of the Higgs portal scalars," *Phys. Rev. D* **96** no. 7, (2017) 075033, arXiv:1706.01920 [hep-ph].

[70] M. W. Winkler, "Decay and detection of a light scalar boson mixing with the Higgs boson," *Phys. Rev. D* **99** no. 1, (2019) 015018, arXiv:1809.01876 [hep-ph].

[71] **KOTO** Collaboration, M. A. Hutcheson, "Status on the Search for $K_L^0 \to \pi^0 \nu\bar{\nu}$ with the KOTO Experiment," in *Meeting of the Division of Particles and Fields of the American Physical Society*. 10, 2019. arXiv:1910.07585 [hep-ex].

[72] **KOTO** Collaboration, B. Beckford, "New results on the search for rare kaon events with the KOTO detector," 10, 2019. arXiv:1910.07148 [hep-ex].

[73] T. Kitahara, T. Okui, G. Perez, Y. Soreq, and K. Tobioka, "New physics implications of recent search for $K_L \to \pi^0 \nu\bar{\nu}$ at KOTO," *Phys. Rev. Lett.* **124** no. 7, (2020) 071801, arXiv:1909.11111 [hep-ph].

[74] D. Egana-Ugrinovic, S. Homiller, and P. Meade, "Light Scalars and the Koto Anomaly," *Phys. Rev. Lett.* **124** no. 19, (2020) 191801, arXiv:1911.10203 [hep-ph].

[75] P. S. B. Dev, R. N. Mohapatra, and Y. Zhang, "Constraints on long-lived light scalars with flavor-changing couplings and the KOTO anomaly," *Phys. Rev. D* **101** no. 7, (2020) 075014, arXiv:1911.12334 [hep-ph].

[76] J. Liu, N. McGinnis, C. E. M. Wagner, and X.-P. Wang, "A light scalar explanation of $(g-2)_\mu$ and the KOTO anomaly," *JHEP* **04** (2020) 197, arXiv:2001.06522 [hep-ph].

[77] G. Ruggero, "Latest measurement of $K^+ \to \pi^+ \nu \bar{\nu}$ with the NA62 experiment at CERN." https://indico.cern.ch/event/769729/contri-butions/3510938/, September, 2019. KAON2019, Perugia, Italy.

[78] **SuperCDMS** Collaboration, R. Agnese *et al.*, "New Results from the Search for Low-Mass Weakly Interacting Massive Particles with the CDMS Low Ionization Threshold Experiment," *Phys. Rev. Lett.* **116** no. 7, (2016) 071301, arXiv:1509.02448 [astro-ph.CO].

[79] J. M. Cline, K. Kainulainen, P. Scott, and C. Weniger, "Update on scalar singlet dark matter," *Phys. Rev. D* **88** (2013) 055025, arXiv:1306.4710 [hep-ph]. [Erratum: Phys.Rev.D 92, 039906 (2015)].

[80] J. Ellis, N. Nagata, and K. A. Olive, "Uncertainties in WIMP Dark Matter Scattering Revisited," *Eur. Phys. J. C* **78** no. 7, (2018) 569, arXiv:1805.09795 [hep-ph].

[81] **CRESST** Collaboration, G. Angloher *et al.*, "Results on light dark matter particles with a low-threshold CRESST-II detector," *Eur. Phys. J. C* **76** no. 1, (2016) 25, arXiv:1509.01515 [astro-ph.CO].

[82] **LUX** Collaboration, D. S. Akerib *et al.*, "Improved Limits on Scattering of Weakly Interacting Massive Particles from Reanalysis of 2013 LUX Data," *Phys. Rev. Lett.* **116** no. 16, (2016) 161301, arXiv:1512.03506 [astro-ph.CO].

[83] **SuperCDMS** Collaboration, R. Agnese *et al.*, "Projected Sensitivity of the SuperCDMS SNOLAB experiment," *Phys. Rev. D* **95** no. 8, (2017) 082002, arXiv:1610.00006 [physics.ins-det].

[84] **DarkSide** Collaboration, P. Agnes *et al.*, "Low-Mass Dark Matter Search with the DarkSide-50 Experiment," *Phys. Rev. Lett.* **121** no. 8, (2018) 081307, arXiv:1802.06994 [astro-ph.HE].

[85] E. Bernreuther, F. Kahlhoefer, M. Krämer, and P. Tunney, "Strongly interacting dark sectors in the early Universe and at the LHC through a simplified portal," *JHEP* **01** (2020) 162, `arXiv:1907.04346 [hep-ph]`.

[86] Y. Wu, K. Freese, C. Kelso, P. Stengel, and M. Valluri, "Uncertainties in Direct Dark Matter Detection in Light of Gaia's Escape Velocity Measurements," *JCAP* **10** (2019) 034, `arXiv:1904.04781 [hep-ph]`.

[87] A. J. Deason, A. Fattahi, V. Belokurov, N. W. Evans, R. J. J. Grand, F. Marinacci, and R. Pakmor, "The local high-velocity tail and the Galactic escape speed," *Mon. Not. Roy. Astron. Soc.* **485** no. 3, (2019) 3514–3526, `arXiv:1901.02016 [astro-ph]`.

[88] **XENON** Collaboration, E. Aprile *et al.*, "First Dark Matter Search Results from the XENON1T Experiment," *Phys. Rev. Lett.* **119** no. 18, (2017) 181301, `arXiv:1705.06655 [astro-ph.CO]`.

[89] **GAMBIT Dark Matter Workgroup** Collaboration, T. Bringmann *et al.*, "DarkBit: A GAMBIT module for computing dark matter observables and likelihoods," *Eur. Phys. J. C* **77** no. 12, (2017) 831, `arXiv:1705.07920 [hep-ph]`.

[90] R. Diamanti, L. Lopez-Honorez, O. Mena, S. Palomares-Ruiz, and A. C. Vincent, "Constraining Dark Matter Late-Time Energy Injection: Decays and P-Wave Annihilations," *JCAP* **02** (2014) 017, `arXiv:1308.2578 [astro-ph.CO]`.

[91] H. An, M. B. Wise, and Y. Zhang, "Strong CMB Constraint On P-Wave Annihilating Dark Matter," *Phys. Lett. B* **773** (2017) 121–124, `arXiv:1606.02305 [hep-ph]`.

[92] J. M. Cline and T. Toma, "Pseudo-Goldstone dark matter confronts cosmic ray and collider anomalies," *Phys. Rev. D* **100** no. 3, (2019) 035023, `arXiv:1906.02175 [hep-ph]`.

[93] I. Goldman and S. Nussinov, "Weakly Interacting Massive Particles and Neutron Stars," *Phys. Rev. D* **40** (1989) 3221–3230.

[94] G. Bertone and M. Fairbairn, "Compact Stars as Dark Matter Probes," *Phys. Rev. D* **77** (2008) 043515, `arXiv:0709.1485 [astro-ph]`.

[95] A. de Lavallaz and M. Fairbairn, "Neutron Stars as Dark Matter Probes," *Phys. Rev. D* **81** (2010) 123521, `arXiv:1004.0629 [astro-ph.GA]`.

[96] S. D. McDermott, H.-B. Yu, and K. M. Zurek, "Constraints on Scalar Asymmetric Dark Matter from Black Hole Formation in Neutron Stars," *Phys. Rev. D* **85** (2012) 023519, `arXiv:1103.5472 [hep-ph]`.

[97] C. Kouvaris and P. Tinyakov, "Can Neutron stars constrain Dark Matter?," *Phys. Rev. D* **82** (2010) 063531, `arXiv:1004.0586 [astro-ph.GA]`.

[98] M. I. Gresham and K. M. Zurek, "Asymmetric Dark Stars and Neutron Star Stability," *Phys. Rev. D* **99** no. 8, (2019) 083008, `arXiv:1809.08254 [astro-ph.CO]`.

[99] M. Baryakhtar, J. Bramante, S. W. Li, T. Linden, and N. Raj, "Dark Kinetic Heating of Neutron Stars and An Infrared Window On WIMPs, SIMPs, and Pure Higgsinos," *Phys. Rev. Lett.* **119** no. 13, (2017) 131801, `arXiv:1704.01577 [hep-ph]`.

[100] C. Kouvaris, "WIMP Annihilation and Cooling of Neutron Stars," *Phys. Rev. D* **77** (2008) 023006, `arXiv:0708.2362 [astro-ph]`.

[101] N. F. Bell, G. Busoni, and S. Robles, "Capture of Leptophilic Dark Matter in Neutron Stars," *JCAP* **06** (2019) 054, `arXiv:1904.09803 [hep-ph]`.

[102] J. Bramante, "Dark matter ignition of type Ia supernovae," *Phys. Rev. Lett.* **115** no. 14, (2015) 141301, `arXiv:1505.07464 [hep-ph]`.

[103] J. F. Acevedo and J. Bramante, "Supernovae Sparked By Dark Matter in White Dwarfs," *Phys. Rev. D* **100** no. 4, (2019) 043020, arXiv:1904.11993 [hep-ph].

[104] H. B. Richer *et al.*, "Hubble space telescope observations of white dwarfs in the globular cluster m4," *Astrophys. J. Lett.* **451** (1995) L17, arXiv:astro-ph/9507109.

[105] L. R. Bedin, M. Salaris, G. Piotto, J. Anderson, I. R. King, and S. Cassisi, "The End of the White Dwarf Cooling Sequence in M4: an efficient approach," *Astrophys. J.* **697** (2009) 965–979, arXiv:0903.2839 [astro-ph.GA].

[106] M. McCullough and M. Fairbairn, "Capture of Inelastic Dark Matter in White Dwarves," *Phys. Rev. D* **81** (2010) 083520, arXiv:1001.2737 [hep-ph].

[107] B. Dasgupta, A. Gupta, and A. Ray, "Dark matter capture in celestial objects: Improved treatment of multiple scattering and updated constraints from white dwarfs," *JCAP* **08** (2019) 018, arXiv:1906.04204 [hep-ph].

[108] P. J. E. Peebles, "Dark matter and the origin of galaxies and globular star clusters," *Astrophys. J* **277** (1984) 470.

[109] B. F. *et al.*. Griffen, "Globular Cluster Formation Within The Aquarius Simulation," *Mon. Not. Roy. Astron. Soc.* **405** (2010) 375, arXiv:0910.0310 [astro-ph.GA].

[110] M. A. Beasley, "Globular Cluster Systems and Galaxy Formation," in *Reviews in Frontiers of Modern Astrophysics*, pp. 245–277. Springer International Publishing, 2020.

[111] A. V. Kravtsov and O. Y. Gnedin, "Formation of globular clusters in hierarchical cosmology," *Astrophys. J.* **623** (2005) 650–665, arXiv:astro-ph/0305199.

[112] D. Hooper, D. Spolyar, A. Vallinotto, and N. Y. Gnedin, "Inelastic Dark Matter As An Efficient Fuel For Compact Stars," *Phys. Rev. D* **81** (2010) 103531, `arXiv:1002.0005 [hep-ph]`.

[113] I. Claydon, M. Gieles, A. L. Varri, D. C. Heggie, and A. Zocchi, "Spherical models of star clusters with potential escapers," *Mon. Not. Roy. Astron. Soc.* **487** (2019) 147, `arXiv:1903.05954 [astro-ph.GA]`.

[114] R. Krall and M. Reece, "Last Electroweak WIMP Standing: Pseudo-Dirac Higgsino Status and Compact Stars as Future Probes," *Chin. Phys. C* **42** no. 4, (2018) 043105, `arXiv:1705.04843 [hep-ph]`.

[115] S. Tulin and H.-B. Yu, "Dark Matter Self-interactions and Small Scale Structure," *Phys. Rept.* **730** (2018) 1–57, `arXiv:1705.02358 [hep-ph]`.

[116] S. Tulin, H.-B. Yu, and K. M. Zurek, "Resonant Dark Forces and Small Scale Structure," *Phys. Rev. Lett.* **110** no. 11, (2013) 111301, `arXiv:1210.0900 [hep-ph]`.

[117] **LUX** Collaboration, D. S. Akerib *et al.*, "Results of a Search for Sub-GeV Dark Matter Using 2013 LUX Data," *Phys. Rev. Lett.* **122** no. 13, (2019) 131301, `arXiv:1811.11241 [astro-ph.CO]`.

[118] S. Cassel, "Sommerfeld factor for arbitrary partial wave processes," *J. Phys. G* **37** (2010) 105009, `arXiv:0903.5307 [hep-ph]`.

[119] **CDEX** Collaboration, H. Jiang *et al.*, "Limits on Light Weakly Interacting Massive Particles from the First 102.8 kg $\times$ day Data of the CDEX-10 Experiment," *Phys. Rev. Lett.* **120** no. 24, (2018) 241301, `arXiv:1802.09016 [hep-ex]`.

[120] I. Brivio and M. Trott, "Radiatively Generating the Higgs Potential and Electroweak Scale via the Seesaw Mechanism," *Phys. Rev. Lett.* **119** no. 14, (2017) 141801, `arXiv:1703.10924 [hep-ph]`.

[121] I. Brivio and M. Trott, "Examining the neutrino option," *JHEP* **02** (2019) 107, `arXiv:1809.03450 [hep-ph]`.

[122] J. R. Ellis and M. K. Gaillard, "Strong and Weak CP Violation," *Nucl. Phys. B* **150** (1979) 141–162.

[123] **KOTO** Collaboration, J. K. Ahn *et al.*, "Study of the $K_L \to \pi^0 \nu \bar{\nu}$ Decay at the J-PARC KOTO Experiment," *Phys. Rev. Lett.* **126** no. 12, (2021) 121801, `arXiv:2012.07571 [hep-ex]`.

[124] **KOTO** Collaboration, K. Shiomi, "Search for the $K_L \to \pi^0 \nu \bar{\nu}$ decay at the J-PARC KOTO experiment," *J. Phys. Conf. Ser.* **2446** no. 1, (2023) 012003.

Chapter 6

# Late-Time Dark Matter Oscillations and the Core-Cusp Problem

**James M. Cline,[a] Guillermo Gambini,[a,b] Samuel D. McDermott,[c] and Matteo Puel [a]**

[a] *McGill University, Department of Physics, 3600 University Street, Montréal, QC H3A2T8 Canada*

[b] *Instituto de Física Gleb Wataghin, UNICAMP, Rua Sérgio Buarque de Holanda 777, 13083-859, Campinas-SP, Brasil*

[c] *Theory Division, Fermi National Accelerator Laboratory, Kirk Road, Batavia, IL 60510, U.S.A*

Published in the Journal of High Energy Physics: JHEP 2021, 223 (2021), [arXiv:2010.12583]

## 6.0 Prologue

In the previous chapter, we proposed a "little theory of everything" to address inflation, baryogenesis, neutrino masses, and (asymmetric) DM within a unified framework, filling the gaps in the ΛCDM model and in the SM of particle physics.

In this scenario, a small Majorana mass was induced for the heavy neutral leptons (HNLs), which played a crucial role in transferring the primordial asymmetry from the inflaton field to the SM particles, causing particle-antiparticle oscillations. Such oscillations could be used also as a way of testing the model in laboratory searches. However, the HNL acting as DM candidate avoided particle-antiparticle oscillations due to the masslessness of one active SM neutrino.

Considering a small Majorana mass term $\delta m \neq 0$ also for DM particles, their particle-antiparticle oscillations can potentially regenerate the symmetric component of DM, leading to its dilution through annihilation. Depending on the value of $\delta m$, DM annihilation may be reactivated at late times, offering a potential solution to the core-cusp problem at galactic scales, a long-standing issue in the ΛCDM model (see section 3.1.5). This chapter will explore this intriguing scenario.

**Abstract**

The core-cusp problem persists as an unresolved tension between the predictions of ΛCDM cosmology and observations of dark matter (DM) profiles in dwarf spheroidal and other galaxies. We present a novel scenario for converting cusps into cores through reactivation of DM annihilation in galaxies at late times. This can happen in asymmetric DM models when there is a very small DM-number violating mass term that causes oscillations between DM and its antiparticle. Using analytic methods as well as gravitational N-body simulations, we show that this mechanism can robustly eliminate cusps from galactic DM profiles for light fermionic DM of mass $m_\chi \sim (0.1 - 1)$ GeV and a lighter mediator into which the DM can annihilate. We identify regions of parameter space where annihilation of DM particles is more efficient than elastic scattering at reducing the inner density of the DM profile. Dark matter annihilation is therefore a qualitatively distinct alternative to the mechanism of elastic self-interacting dark matter for addressing the cusp-core problem.

## 6.1 Introduction

In many respects the standard ΛCDM paradigm of cosmology gives an extremely good description of the observed Universe. But it has long been recognized that simulations of structure formation that neglect the presence of baryons predict singular (cuspy) density profiles of the dark matter (DM) toward the centers of galaxies, whereas observations suggest flatter (cored) distributions [1]. More recent simulations include the effects of baryonic feedback, which can expel material from denser regions and help to ameliorate this discrepancy, but there is not yet any consensus that this provides a complete solution. Moreover in systems like dwarf spheroidals, where baryons are relatively scarce, one does not expect baryons to have a significant impact on the small scale structure. These issues have been reviewed in Ref. [2].

Another proposed solution is self-interacting dark matter (SIDM) [3, 4], with a scattering cross section at the level of

$$\frac{\sigma}{m_\chi} \sim (0.1 - 1)\,\frac{\mathrm{cm}^2}{\mathrm{g}} \tag{6.1}$$

that is close to upper bounds from colliding galaxy clusters, such as the Bullet Cluster [5], even though it may be not so robust [6]. N-body simulations incorporating such interactions have shown that cross sections consistent with eq. (6.1) can produce cored DM profiles in a wide range of systems [7, 8]. However, more recent studies indicate that a constant cross section is not the ideal solution, since then $\langle\sigma v\rangle$ increases with the size of the system, contrary to the observation that cores are less pronounced on the scales of galactic clusters. A weak velocity dependence of the form $\sigma \sim 1/v$ is found to give a better fit to the full range of structures [9].

The most common assumption is that the DM self-interaction is in the form of elastic scattering, but a more exotic possibility was proposed in Ref. [10], in which fusion of DM particles into bound objects is the interaction leading to cored profiles. Like other exothermic processes, this has the advantage of predicting a cross section with $\sigma v$ remaining constant at low velocities, as desired for fitting the DM profiles of both large and small galactic structures. Other interesting possibilities to achieve the correct velocity-dependence of SIDM have been studied, for instance in the context of resonant SIDM [11–13], puffy DM [14], self-heating DM [15–18], maximally SIDM [19] and DM bound states produced in the early Universe by three-body recombination [20, 21].

Here we explore a different alternative, motivated by the fact that DM annihilation is also an exothermic process with $\sigma v$ becoming constant as $v \to 0$. The challenge for such a scenario is to explain how annihilations could go out of equilibrium in the early Universe, but then come back at late times [22]. In fact, a mechanism to do this is well known in the context of asymmetric dark matter, where there is an asymmetry between the DM $\chi$ and its antiparticle $\bar{\chi}$. By allowing for a small mass term that violates the conservation of DM number, oscillations between $\chi$ and $\bar{\chi}$ can reactivate the annihilations at late times [23–26].

The reactivation of DM annihilation at late times is usually seen as a danger to be avoided, since it is known that the DM density should not change appreciably between the era of the CMB (redshift $z \sim 1100$) and structure formation [27, 28], but in the present work we demonstrate that this mechanism can efficiently produce cored profiles in galaxies without changing the total DM density significantly. The reason is that the efficiency of oscillations leading to regeneration of the anti-DM component can depend strongly on density, so that annihilations are effective in the centers of galaxies but not in the outer regions.

For a more quantitative investigation, one should integrate quantum Boltzmann equations for the density matrix, that account for the coherence of states undergoing oscillations, analogous to those used for the study of neutrino oscillations in a medium. This formalism was initially worked out for DM in Ref. [25], and some important corrections were realized in Ref. [26], which we follow closely in the present work.

We consider two models of quasi-Dirac fermionic DM $\chi$ of mass $m_\chi$. In the first, the dark matter couples to a lighter vector boson $V^\mu$ (Model 1), with effective Lagrangian

$$\mathcal{L}_1 \supset -\frac{1}{2} m_V^2 V_\mu^2 - g' \bar{\chi} \not{V} \chi \,. \tag{6.2}$$

In Model 1, the dark matter freeze-out and the late-time depletion are both allowed by the annihilation process $\chi\bar{\chi} \to VV$. In the second model, dark matter couples to a complex scalar $\Phi = \phi + ia$ (Model 2),

$$\mathcal{L}_2 \supset -\frac{1}{2}m_\phi^2\phi^2 - \frac{1}{2}m_a^2 a^2 - g'\bar{\chi}(\phi + ia\gamma_5)\chi\,. \tag{6.3}$$

Model 2 allows freeze-out and late-time depletion from $\chi\bar{\chi} \to \phi a$ (which unlike $\chi\bar{\chi} \to \phi\phi$ or $\chi\bar{\chi} \to aa$ is $s$-wave, hence not suppressed at low velocities). The coupling between $\chi$ and either kind of boson is denoted as $g'$, and its associated fine-structure constant is $\alpha' = g'^2/4\pi$. The DM-violating mass term is

$$\mathcal{L}_m = \frac{1}{2}\delta m\left(\bar{\chi}\chi^c + \text{H.c.}\right)\,. \tag{6.4}$$

The parameter $\delta m$ violates not only dark matter number, but also the gauge symmetry of Model 1, which is additionally broken by the Stueckelberg mass term for the vector. It would be possible to replace both of these explicit breakings by a Higgs mechanism, but for simplicity we adopt the simpler effective theory.

We begin by making preliminary estimates to identify viable regions of the parameter space, in section 6.2. The essential details of the density matrix Boltzmann equation formalism are reviewed in section 6.3. In section 6.4 we will show that, for appropriate choices of the model parameters, integration of the Boltzmann equations in the early Universe leads to the conventional freeze-out of DM annihilations, leaving only the asymmetric component of the DM. This justifies the initial conditions for the second step, described in section 6.5, where we re-solve the analogous Boltzmann equations in the background of an already-formed galaxy and show how an initial cusp gets erased by reactivated annihilation following $\chi$-$\bar{\chi}$ oscillations. This is a somewhat crude approach since it considers formation of the galaxy to happen suddenly and neglects the role of gravity in shaping the DM halo. In section 6.6, we improve on this by carrying out a gravitational N-body simulation of galaxy evolution, in a code adapted to properly account for the new physics effects. Conclusions are given in section 6.7, and details of the quantum Boltzmann and N-body simulation methods are presented in the appendices.

## 6.2 Analytic estimates

Before embarking on a detailed analysis, we analytically estimate the regions of parameter space that are of interest for our mechanism. First, the annihilation cross sections at threshold for the two models are

$$\langle\sigma v\rangle_a = \frac{\pi\,\alpha'^2}{m_\chi^2} \times \begin{cases} (1-r_m^2)^{3/2}/(1-r_m^2/2)^2, & \text{Model 1} \\ (1-r_m^2/4), & \text{Model 2} \end{cases} \tag{6.5}$$

where $r_m$ is the ratio of the mediator to the DM mass, $r_m = m_V/m_\chi$ for $\chi\bar{\chi} \to VV$ (Model 1) or $r_m = m_\phi/m_\chi$ for $\chi\bar{\chi} \to \phi a$ (Model 2). In the latter, we have assumed for simplicity that $m_a \ll m_\phi$, and neglected the $p$-wave suppressed channels $\chi\bar{\chi} \to \phi\phi$, $aa$.

To compare eq. (6.5) to the desired cross section (6.1), consider a reference velocity $v_0 = 100\,\mathrm{km/s}$ characteristic of DM in a Milky-Way-like galaxy, and the upper value in the range (6.1), giving $\sigma v/m_\chi \sim 100\,\mathrm{cm^2\,km/s/g} \sim 0.2 \times (100\,\mathrm{MeV}/m_\chi)\,\mathrm{GeV^{-2}}$. Equating this to $\langle\sigma v\rangle_a$ suggests the constraint

$$\alpha' \cong 0.7\left(\frac{m_\chi}{\mathrm{GeV}}\right)^{3/2} \tag{6.6}$$

For example with $m_\chi = 100\,\mathrm{MeV}$, $\alpha' \cong 0.02$; we will adopt these as approximate benchmark values. However nothing prevents us from taking somewhat heavier DM, up to $m_\chi \sim 1\,\mathrm{GeV}$; above this, the theory starts to be strongly coupled.

It is impossible to avoid $\chi\chi$ elastic scattering mediated by the annihilation products, and we choose to constrain these cross sections so that they are below the level that would change the DM density profile independently of the annihilation effect, which is the focus of this work. The elastic scattering cross sections at low velocities are

$$\sigma_s \cong 4\pi\alpha'^2\, m_\chi^2 \begin{cases} m_V^{-4}, & \text{Model 1} \\ m_\phi^{-4} + (5/4)v^4 m_a^{-4}, & \text{Model 2} \end{cases} \tag{6.7}$$

where $v = v_{\rm rel}/2$ is the center-of-mass velocity. Here, all the relevant channels contributing to the $\chi\chi$ and $\chi\bar{\chi}$ scatterings are included and the cross sections for these two processes turn out to be the same in the low-velocity limit. To avoid that the scattering self-interactions play a leading role in the galactic dynamics, we require that $\sigma_s v_{\rm rel} \ll \langle\sigma_a v\rangle$. This implies $(m_{V,\phi}/m_\chi)^4 \gg 4v_{\rm rel}$, which is most stringent for large systems, galaxy clusters, that have the highest DM velocities. For example, the cluster A2537 has velocity dispersion $\sigma_v \sim 1000\,{\rm km/s}$ [29], with $v_{\rm rel} = (4/\sqrt{\pi})\sigma_v$ (assuming the velocity is Maxwell-Boltzmann distributed), and demanding that $\sigma_s v_{\rm rel} < 0.3\,\langle\sigma_a v\rangle$ gives the constraints

$$\begin{aligned} &0.6 < r_m < 0.94, \;\text{Model 1} \\ &0.6 < r_m < 1.99, \;\text{Model 2} \end{aligned} \tag{6.8}$$

where the upper limits come about because of phase space suppression of the annihilation.[1]

The pseudoscalar mass $m_a$ should not be arbitrarily small, since its virtual contributions can become Sommerfeld enhanced if $m_a \ll \alpha' m_\chi,\ v m_\chi$ [30–32]. In the present work we avoid these complications by considering $m_a \sim m_\chi/10$, which is small enough to ignore it in phase space integrals and its $d$-wave suppressed contribution to scattering in eq. (6.7), but large enough to avoid nonperturbative effects, as well as cosmological problems in the era of Big Bang Nucleosynthesis.

The $\chi$-number violating mass $\delta m$ must be small enough so that $\chi$-$\bar{\chi}$ oscillations have not yet started at the time of DM freeze-out, $T_{\chi,{\rm fo}} \sim m_\chi/20$, where we allow for a lower temperature

$$T_\chi \equiv \xi T < T \tag{6.9}$$

in the dark sector, as discussed in more detail in Sec. 6.4.3. For annihilations to

[1] We assumed $m_a \ll m_\phi$ in the last limit, for the process $\chi\chi \to \phi a$.

recouple during structure formation, the oscillations should start before the epoch of structure formation, $t_s \sim 0.1\,\mathrm{Gyr}$. On the other hand, we will show in Sect. 6.4 that too-early onset of recoupled annihilations tend to change the DM relic density more than is allowed by CMB constraints [27, 28]. This leads to a window of allowed values, whose upper limit depends upon details of the scenarios we will discuss,

$$\begin{aligned} \frac{1}{t_s} \lesssim \delta m \lesssim & \begin{cases} \dfrac{16.3\,\delta_\eta^{1/2}\,m_\chi^{1/2}}{g_*^{1/4}\overline{\langle\sigma v\rangle}_s\langle\sigma v\rangle_a^{1/2}\eta_{\rm DM}^{3/2}M_p^{5/2}}, & \text{Model 1} \\ \dfrac{342\,\delta_\eta^{1/2}}{g_*^{1/2}\langle\sigma v\rangle_a^2\,\eta_{\rm DM}^2\,M_p^3}, & \text{Model 2} \end{cases} \\ \implies 10^{-31}\,\mathrm{eV} \lesssim \delta m \lesssim & \begin{cases} 5\times 10^{-28}\,\mathrm{eV}, & \text{Model 1} \\ 3\times 10^{-30}\,\mathrm{eV}, & \text{Model 2} \end{cases} , \end{aligned} \tag{6.10}$$

where $\eta_{\rm DM}$ is the DM asymmetry and $\delta_\eta$ is the fractional change in $\eta_{\rm DM}$ allowed by the CMB constraints. The numerical values are indicative, based on the limited parameter choices we have investigated here. It is possible that the upper limits could be relaxed in a wider search of parameter space. The analytic expressions in eq. (6.10) are derived in Appendix 6.D.

## 6.3 Oscillation formalism

In the presence of DM oscillations, the distinction between particle and antiparticle becomes time-dependent. If we define a basis

$$|\chi\rangle = \begin{pmatrix} 1 \\ 0 \end{pmatrix}, \quad |\bar\chi\rangle = \begin{pmatrix} 0 \\ 1 \end{pmatrix}, \tag{6.11}$$

then it is straightforward to show that the time dependence of a state that is initially pure $|\chi\rangle$ is

$$|\chi(t)\rangle = e^{-im_\chi t}\begin{pmatrix} c_\varphi \\ -is_\varphi \end{pmatrix} \tag{6.12}$$

with $c_\varphi = \cos\varphi$, $s_\varphi = \sin\varphi$, $\varphi = \delta m\, t$. To this state we can associate the density matrix for a single-particle state,

$$n_1 = |\chi(t)\rangle \langle\chi(t)| = \begin{pmatrix} c_\varphi^2 & i c_\varphi s_\varphi \\ -i c_\varphi s_\varphi & s_\varphi^2 \end{pmatrix} . \tag{6.13}$$

Naively it might seem like appreciable amounts of $\bar\chi$ appear as soon as $\varphi \sim 1$ and $\chi\bar\chi$ annihilations could recommence, but this need not be true if all the particles in the plasma are oscillating with the same phase. Ref. [26] showed that recoupling of annihilation depends on the nature of the interactions. Interactions of fermionic DM with vectors $V$ are called "flavor sensitive," while interactions of $\chi$ with scalars or pseudoscalars are "flavor blind," leading to very different behaviors of the annihilation probabilities. In the collision of two particles with respective phases $\varphi$ and $\varphi'$, the annihilation rates are modulated by the factors

$$\chi\bar\chi \to VV: \quad \sin^2(\varphi - \varphi')\ \text{(flavor sensitive)}\,, \tag{6.14}$$

$$\chi\bar\chi \to \phi a: \quad \sin^2(\varphi + \varphi')\ \text{(flavor blind)}\,. \tag{6.15}$$

In the first case, a bath starting as pure $|\chi\rangle$ and maintaining phase coherence never undergoes annihilations since $\varphi - \varphi'$ remains zero, despite the oscillations. In the second, the modulation factor averages to $1/2$ for fast oscillations, and is therefore effective even when the particles stay in phase with each other.

For a thermal bath, the matrix $n_1$ in eq. (6.13) is replaced by an integral over the corresponding matrix distribution function $\mathcal{F}(k)$ for the states of momentum $k$,

$$n = (2s+1)\int \frac{d^3k}{(2\pi)^3}\,\mathcal{F}(k)\,, \tag{6.16}$$

where $s = 1/2$ for fermions as we consider. Then $n_{11}$ ($n_{22}$) represents the number density of particles (antiparticles) defined with respect to the basis $\{|\chi\rangle, |\bar\chi\rangle\}$ as in (6.11); the off-diagonal elements keep track of the coherence between these two states.

The Boltzmann equation for $n$ reduces to the usual form when we consider only the diagonal elements, but it has additional terms due to the off-diagonal elements, which depend on whether the interactions are flavor-sensitive or flavor-blind.

### 6.3.1 Model 1: vector mediator

We first consider the flavor-sensitive case, applicable to Model 1, for which the Boltzmann equation is

$$\begin{aligned}\dot{n} + 3Hn = &-i[\mathcal{H}_0, n] - \frac{3}{2}\langle\sigma v\rangle_s\,(\mathrm{Tr}\,n)\begin{pmatrix}0 & n_{12}\\ n_{21} & 0\end{pmatrix}\\ &-\langle\sigma v\rangle_a\left(\det n - n_{\mathrm{eq}}^2\right)\mathbb{1}\,,\end{aligned}\tag{6.17}$$

where $H$ is the Hubble parameter, the thermally averaged free Hamiltonian is

$$\begin{aligned}\mathcal{H}_0 &= \langle E\rangle\,\mathbb{1} + \left\langle\frac{m_\chi\,\delta m}{E}\right\rangle\begin{pmatrix}0 & 1\\ 1 & 0\end{pmatrix}\\ &\cong m_\chi\,\mathbb{1} + \delta m\begin{pmatrix}0 & 1\\ 1 & 0\end{pmatrix}\,,\end{aligned}\tag{6.18}$$

$\langle\sigma v\rangle_s$ is the $\chi\chi$ or $\chi\bar{\chi}$ scattering cross section (that coincides at low energies), $\langle\sigma v\rangle_a$ is the $\chi\bar{\chi}\to VV$ annihilation cross section, and $n_{\mathrm{eq}}$ is the equilibrium number density. The scattering term in eq. (6.17) is derived in appendix 6.A, while the other terms can be found in Ref. [26].[2] Eq. (6.17) is the appropriate form for cosmology; in section 6.5 we will discuss how it can be applied in a galactic environment.

The scattering term in (6.17) has the effect of damping the off-diagonal elements of $n$, which destroys the coherence of the quantum superpositions and effectively measures the state of an oscillating system. The loss of coherence results in $\det n \neq 0$, which activates the annihilations. Since $\langle\sigma v\rangle_s$ is proportional to the DM velocity, this makes the effect stronger in systems with large velocity dispersions. We will see in section 6.5 that this is contrary to observations, disfavoring Model 1 taken by itself.

The origin of the factor (6.14) can be heuristically understood from (6.17) by

[2]Ref. [26] derived the scattering term for $\chi f\to\chi f$ with $f$ being a different particle in the plasma.

interpreting the annihilation term $\det n\,\mathbb{1}$ as the matrix [26]

$$\begin{aligned}\det n\,\mathbb{1} &\to \frac{1}{2}(n_1\sigma_2 n_2^T\sigma_2 + n_2\sigma_2 n_1^T\sigma_2)\\ &= \frac{1}{2}\sin^2(\varphi_1-\varphi_2)\,\mathbb{1}\,,\end{aligned} \tag{6.19}$$

where $n_1$, $n_2$ represent the density matrices (6.13) of two particles, having respective phases $\varphi_1$, $\varphi_2$, and $\sigma_2$ is the Pauli matrix.[3]

Similarly, the effect of the scattering term can be understood by replacing $n \to n_1$ everywhere except in the trace, where $\mathrm{Tr}\,n \to \mathrm{Tr}\,n_2$, which does not depend on $\varphi_2$, and just represents the total density $n$ of DM scattering on particle 1. Then the off-diagonal parts of the Boltzmann equation determine the damping of $\varphi_1$ as

$$\frac{d}{dt}(c_{\varphi_1}s_{\varphi_1}) \sim -\frac{3}{2}n\langle\sigma v\rangle_s c_{\varphi_1}s_{\varphi_1}\,, \tag{6.20}$$

which has the solution $c_\varphi s_\varphi \sim \exp(-\frac{3}{2}\Gamma_s t)(c_\varphi s_\varphi)_0$, where $\Gamma_s = n\langle\sigma v\rangle_s$ is the elastic scattering rate.

### 6.3.2 Model 2: scalar mediators

For scalar interactions, the Boltzmann equation simplifies, because elastic scattering no longer has any effect on the density matrix. The form of the annihilation term is also changed, in a way that makes it lead to decoherence by itself

$$\begin{aligned}\dot{n} + 3Hn &= -i[\mathcal{H}_0, n] \\ &\quad - \langle\sigma v\rangle_a\left[\begin{pmatrix}\det' n & (\mathrm{Tr}\,n)n_{12}\\ (\mathrm{Tr}\,n)n_{21} & \det' n\end{pmatrix} - n_{\mathrm{eq}}^2\,\mathbb{1}\right].\end{aligned} \tag{6.21}$$

Here we define $\det' n \equiv n_{11}n_{22} + n_{21}n_{21}$. In contrast to eq. (6.17) for the vector model, there is no dependence on the DM velocity in (6.21), leading one to expect a more

[3] In the notation of Ref. [26], $\sigma_1 n^T\sigma_1 = \bar{n}$ and $\sigma_3 = O_-$. Appendix 6.B implies that the actual matrix structure is more complicated than (6.19), but this form is adequate for our application of it in section 6.5, which can only account for coherence effects in an approximate way. In particular, the off-diagonal elements are not exactly zero, but they average to zero over the ensemble.

similar level of cusp erasure in both large and small galactic systems, independently of the differences in their velocity dispersions.

The analogous reasoning that led to eq. (6.19) can be applied in the simpler case where $\varphi_1 = \varphi_2 = \varphi$ since the annihilation term no longer vanishes in that limit, giving

$$\begin{aligned} \det{}' n &\to \frac{1}{2}\{n, \sigma_1 n^T \sigma_1\} \\ &= \frac{1}{2}\sin^2 2\varphi\, \mathbb{1} + \frac{1}{2}\sin 2\varphi\, \sigma_2\,. \end{aligned} \tag{6.22}$$

The diagonal term goes to (6.15) when the two phases are different from each other. The off-diagonal term leads to phase damping similarly to (6.20), but now with $c_\varphi s_\varphi \sim \exp(-\Gamma_a t)(c_\varphi s_\varphi)_0$, where $\Gamma_a$ is the conventional annihilation rate, without the $\sin^2 2\varphi$ modulation factor.

## 6.4 Early cosmology

For small values of $\delta m \lesssim 10^{-30}\,\mathrm{eV}$, oscillations are unimportant until the epoch when structure formation begins. For larger values of $\delta m$ they can cause annihilations to temporarily recouple, further reducing the density of the asymmetric component, before structure formation begins and annihilations are reactivated once again. In this section we illustrate these possibilities by solving the Boltzmann equation at early times. This is meant to provide the initial conditions before the effects of oscillations on structure formation begin, that we will investigate in the following sections.

### 6.4.1 Model 1

Like for conventional freeze-out, it is convenient to use $x \equiv m_\chi/T$ as the independent variable, and the abundance $Y \equiv n/s$ as the dependent variable, where $s = 2\pi^2 g_{*s} m_\chi^3/(45x^3)$ is the entropy density and $Y$ is now a matrix. The Boltzmann equation becomes

$$Y' = -\frac{i}{xH}[\mathcal{H}_0, Y] - \xi^3 \frac{3\langle\sigma v\rangle_s s}{2xH}\begin{pmatrix} 0 & Y_{12} \\ Y_{21} & 0 \end{pmatrix} \mathrm{Tr}\, Y$$
$$- \xi^3 \frac{\langle\sigma v\rangle_a s}{xH}\left(\det Y - Y_{\rm eq}^2\right) \mathbb{1}\,. \tag{6.23}$$

Here $H \cong 1.66\sqrt{g_*} m_\chi^2/(M_p x^2)$ is the Hubble parameter, and we have allowed for the DM temperature to differ from that of the standard model by putting the appropriate factors of $\xi = T_\chi/T$. The averaged scattering cross section is

$$\langle\sigma v\rangle_s = \sigma_0 \sqrt{\frac{\xi}{x}}, \qquad \sigma_0 \cong 8\pi\alpha'^2 \frac{m_\chi^2}{m_V^4}\,, \tag{6.24}$$

and the equilibrium abundance is

$$Y_{\rm eq} \cong \frac{45\, x^3}{2\pi^4\, g_{*s}} \frac{K_2(\xi x)}{\xi x} \tag{6.25}$$

in the Maxwell-Boltzmann approximation. It is the abundance of just the DM particle $\chi$, not including the antiparticle.

There is an additional possible source of decoherence that is not captured by eq. (6.23). The full Hamiltonian (6.18), before taking the non-relativistic limit, depends on the momentum $k$ of the state, which is neglected in (6.23). This causes states of different momenta to oscillate at slightly different frequencies $\delta\omega \sim \delta m\,(k^2/2m_\chi^2)$, giving rise to thermal decoherence even in the absence of scattering. To fully investigate this effect would require solving for the full distribution function $\mathcal{F}(k)$, which is numerically prohibitive. Instead we model it in an approximate way, by splitting the integral over $k$ in (6.16) into two bins of small and large momenta, $Y = Y_s + Y_l$. The averaged Hamiltonians $\mathcal{H}_{s,l}$ for the respective bins are shown in eq. (6.57). The resulting coupled Boltzmann equations are given in eqs. (6.53). They have a more complicated matrix structure than (6.23), but the sum of the two agrees with (6.23). We found this additional source of decoherence to have a negligible effect, compared to that due to the scatterings.

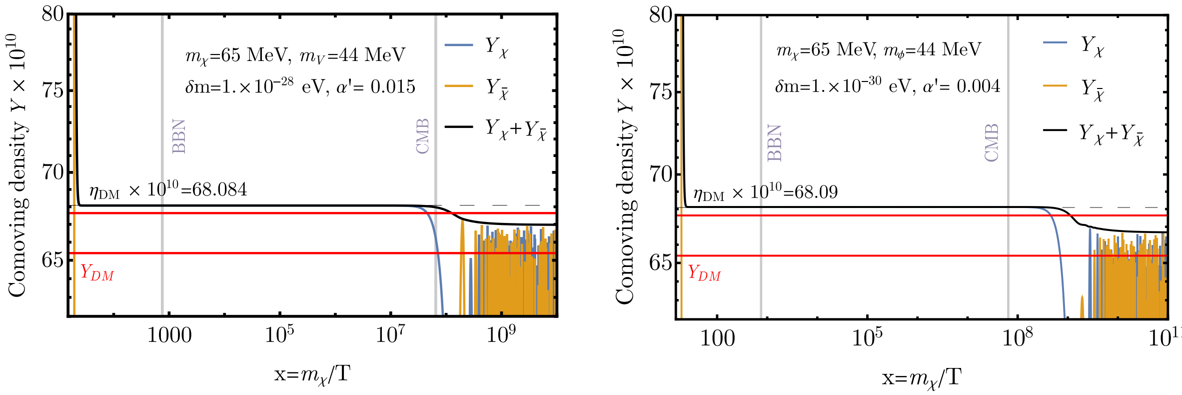


Figure 6.4.1: Cosmological evolution of $\chi$, $\bar{\chi}$ and total abundances for Model 1 (left) and Model 2 (right). The model parameter values are indicated in the plots. We indicate the approximate time of BBN and CMB with faint gray vertical lines. The ratio of dark to visible sector temperatures is taken to be $\xi = 1$.

The left panel of Fig. 6.4.1 shows the effect of thermal decoherence in the evolution of the oscillating dark matter in the vector model at early, intermediate, and late times. We see that after oscillations commence at late times (values of $x \sim 10^7 - 10^8$ in the two models), annihilations recouple briefly before freezing out again. The dark matter density, $Y = Y_{\bar{\chi}} + Y_\chi$, is reduced by $\lesssim \mathcal{O}(5\%)$, which is roughly compatible with observations of density perturbations in the CMB [27]. These constraints were refined in Ref. [28], which limits the change in the DM abundance $Y$ as a function of the redshift of the transition as well as its duration, with respect to CMB data. We have checked in detail that the examples shown in Fig. 6.4.1 are compatible with the limits found there.

On the other hand, we observe that increasing $\delta m$ has the effect of shifting the recoupling of annihilation to earlier times, and also inducing much larger changes in $\Delta Y$, that would be in conflict with the CMB. By varying $\delta m$ and comparing to the excluded regions from Ref. [28], we arrive at the approximate upper bounds shown in eq. (6.10). It is possible that models saturating these limits could ameliorate current tensions in the different measurements of $H_0$ [33] and $\sigma_8$ [34]. We leave further exploration of these implications for future work.

### 6.4.2 Model 2

The cosmological version of the Boltzmann equation (6.21) is

$$
\begin{aligned}
Y' = &- \frac{i}{xH}\,[\mathcal{H}_0, Y] \\
&- \xi^3 \frac{\langle \sigma v \rangle_a\, s}{xH} \left[ \begin{pmatrix} \det' Y & Y_{12}\,\mathrm{Tr}\,Y \\ Y_{21}\,\mathrm{Tr}\,Y & \det' Y \end{pmatrix} - Y_{\mathrm{eq}}^2\, \mathbb{1} \right] ,
\end{aligned}
\tag{6.26}
$$

where scatterings no longer play any role. Its solution is shown in the right panel of Fig. 6.4.1. The implications of the brief recoupling in dark matter annihilation are similar as in Model 1.

### 6.4.3 Constraints on $N_{\mathrm{eff}}$

As usual for dark matter models coupled to light mediators, indirect detection constraints from X-ray and gamma-ray telescopes require the hidden sector to be largely secluded from the Standard Model. Moreover, the force mediators like the vector $V$ of Model 1 or the scalars $\phi$ and $a$ of Model 2, which are the products of $\chi\bar{\chi}$ annihilation, must decay into radiation of some sort to avoid dominating the energy density of the Universe at low temperatures, for example at the time of BBN. The simplest solution to these possible issues is to introduce a dark radiation species, such as massless sterile neutrinos $\nu'$, that couple to the mediators and allow for the decays $V, \phi, a \to \nu'\bar{\nu}'$. As long as these new species have a mass smaller than $\sim$ eV, they will not come to matter-dominate the Universe before the formation of the CMB.

Even this single light degree of freedom might be detected by precise probes of the energy content of the early Universe at BBN [35, 36] and CMB [37], which constrain the number of new relativistic degrees of freedom. For single-parameter extensions of $\Lambda$CDM, the constraints are of order $\Delta N_{\mathrm{eff}} \lesssim 0.2$, but known parameter degeneracy with the helium abundance $Y_p$ and possible hints of beyond-$\Lambda$CDM physics such as neutrino masses or the $H_0$ tension can partially relax these constraints to the level of $\Delta N_{\mathrm{eff}} \lesssim 0.5$ [35–37].[4] In any case, these would robustly exclude the 1.75 (3.5) degrees

[4] see Eqs. 68-69 and 81 of Ref. [37] or Fig. 11 and Table 5 of Ref. [36].

of freedom contributed by a fully thermalized Majorana (Dirac) fermion. This does not occur in our setup because the two sectors are assumed to remain secluded.

If we allow for an initial discrepancy between the Standard Model and dark sector temperatures, $T_{d,0} = \xi_0 T_{\gamma,0}$, the predicted contribution to the effective number of relativistic species at any temperature within our framework is given by

$$\begin{aligned}\Delta N_{\text{eff}}(T_\gamma) &= \frac{4}{7}\,\xi_0^4\,g_*^d\left[\left(\frac{11}{4}\right)^{\Theta(m_e-T_\gamma)}\frac{g_{*S0}^d}{g_{*S}^d}\,\frac{g_{*S}}{g_{*S0}}\right]^{4/3} \\ &= 0.43\,\xi_0^4\left(\frac{g_*^d}{7/2}\right)^{-1/3}\left(\frac{g_{*S0}^d}{11}\,\frac{106.75}{g_{*S0}}\right)^{4/3} \end{aligned} \tag{6.27}$$

where $g_*^d$, $g_{*S}^d$ and $g_{*S}$, are the number of degrees of freedom in energy and entropy in the dark sector and in entropy in the visible sector, respectively, and all of them are evaluated at $T_\gamma$. In going from the first to the second line, the Standard Model degrees of freedom in entropy before and after $e^+e^-$ freezeout cancel the change in neutrino temperature, as expected. We normalize to the values appropriate for a dark sector containing one light and one heavy Dirac fermion, a vector, and a complex scalar (required to give the vector a mass), reflecting the field content of Model 1. In the case of a dark sector with two heavy and one light Majorana fermion plus a complex scalar, as in the minimal case to generate the phenomenology of Model 2, one obtains the smaller result $\Delta N_{\text{eff}} \simeq 0.31\,\xi_0^4$.

In either case, the CMB and BBN limits in single-parameter extensions of $\Lambda$CDM are in tension with the models if $\xi_0 = 1$, but the most stringent BBN and CMB limits are satisfied for $\xi_0 \simeq 0.9$, which requires only a moderate difference in inflationary reheating efficiencies for the two sectors [38, 39]. Even if $\xi_0 = 1$, either model is compatible with CMB and BBN limits once uncertainties in $Y_p$ or other quantities are more conservatively taken into account [35–37]. In the near future, high-resolution studies of the CMB damping tail will improve these bounds by an order of magnitude [40].

## 6.5 Structure formation

We start with an approximate treatment of the effect of $\chi$-$\bar{\chi}$ oscillations on galactic dynamics, by imagining that an NFW-shaped halo with

$$\rho_{\chi,0} = \frac{\rho_s}{(r/r_s)(1+r/r_s)^2} \tag{6.28}$$

has already formed at some time $t_0$, with the initial condition on the matrix density that

$$n_{ij}(r;t_0) = \frac{\rho_{\chi,0}(r)}{m_\chi}\,\delta_{i1}\delta_{j1} \tag{6.29}$$

at each position $r$ in the collapsed system: this corresponds to a pure $\chi$ state, in which oscillations have not yet had any effect.

To apply the Boltzmann equation (6.17) in a galactic environment that has separated from the Hubble expansion, we drop the $3Hn$ term, and set $n_{\rm eq} = 0$, since the annihilation products escape without further interactions. For example with fiducial parameters $\alpha' = 0.02$, $m_\chi = 100\,\mathrm{MeV}$, and central densities $\rho_\chi \sim 1\,\mathrm{GeV/cm^3}$, the mean free path for $\phi\chi \to \phi\chi$ or $V\chi \to V\chi$ scattering is of order $(\alpha'^2\rho_\chi/m_\chi^3)^{-1} \sim 10^{21}$ kpc. In principle, the Boltzmann equation in an inhomogeneous environment could contain extra terms, coming from the Liouville operator

$$\hat{L}[\mathcal{F}] \equiv \left(\frac{\partial}{\partial t} + \frac{\vec{k}}{m_\chi}\cdot\vec{\nabla} + \vec{F}(r)\cdot\vec{\nabla}_k\right)\mathcal{F}(t,\vec{x},\vec{k}) \tag{6.30}$$

acting on the density matrix $\mathcal{F}$, where $\vec{F}(r)$ is the gravitational force at a given radius in the halo. However in the approximation used in this section, we are assuming as an initial condition an already-formed NFW halo in which the velocity distribution is isotropic. Therefore in the integral of eq. (6.30) over $d^3k$ to convert $\mathcal{F} \to n$, all terms average to zero except for $\dot{n}$. Hence the diffusion of dark matter particles that is modeled in $N$-body simulations is not captured in the Boltzmann equation (6.17), although the quantum coherence effects are. We supplement this analysis by a complementary $N$-body approach in section 6.6, which will corroborate the qualitative features found here.[5]

We evolve the initial density (6.29) at each radial position $r$, up to a final time $t_f$ of order 10 Gyr. This leads to a modified density profile $\rho_\chi = (n_{11}+n_{22})\, m_\chi$, that is to be compared to present-day observations. In addition to knowing the initial density profile, it is also necessary (for Model 1 only) to specify the DM velocity profile, since the relative velocity enters into the scattering rate through $\langle \sigma v \rangle_s$ (whereas the annihilation rate is insensitive to $v_{\rm rel}$). We have adopted the analytic solution for the radial velocity dispersion $\sigma_r(r)$ from Ref. [41] (see eq. (14) of that reference), derived by solving the Jeans equation for an NFW profile. This determines $\sigma_r(r)$ for given NFW parameters $r_s$, $\rho_s$. The latter can be related to the virial radius $r_{200}$, concentration $c_{200}$, mass $M_{200}$ and velocity $V_{200}$ through

$$\begin{aligned}
\frac{\rho_s}{\rho_c} &= \frac{200}{3}\, c_{200}^3\, g(c_{200})\,, \\
r_{200} &= c_{200}\, r_s\,, \\
M_{200} &= \frac{4\pi}{3}\, 200\, r_{200}^3\, \rho_c\,, \\
V_{200}^2 &= \frac{G M_{200}}{r_{200}}\,,
\end{aligned} \tag{6.31}$$

where $\rho_c$ is the present critical density, and $g(c) = [\ln(1+c) - c/(1+c)]^{-1}$.

### 6.5.1 Model 1

We applied this procedure first within Model 1 for a particular dwarf spheroidal galaxy, DDO 154 [43], that has been discussed from the point of view of self-interacting dark matter in Ref. [42]. There the NFW parameters were determined using data from Ref. [44] and the mass-concentration relation from Ref. [45]. The resulting NFW profile is shown in Fig. 6.5.1 (top left). This profile disagrees with the observed

[5] To model effects of anisotropic velocity distribution, one could for example assume that $\mathcal{F}$ factorizes into spatial and $\vec{k}$-dependent functions, $\mathcal{F} = n(r) f(k_r, k_t)$, where $k_r$ and $k_t$ are the radial and tangential momentum components, and take an additional moment $\int d^3k\, k_r$ of the Boltzmann equation to obtain coupled equations for $n$ and $f$. We have checked that $f$ is in fact isotropic in the $N$-body simulations described below; hence we do not pursue such a more detailed investigation in the present work.

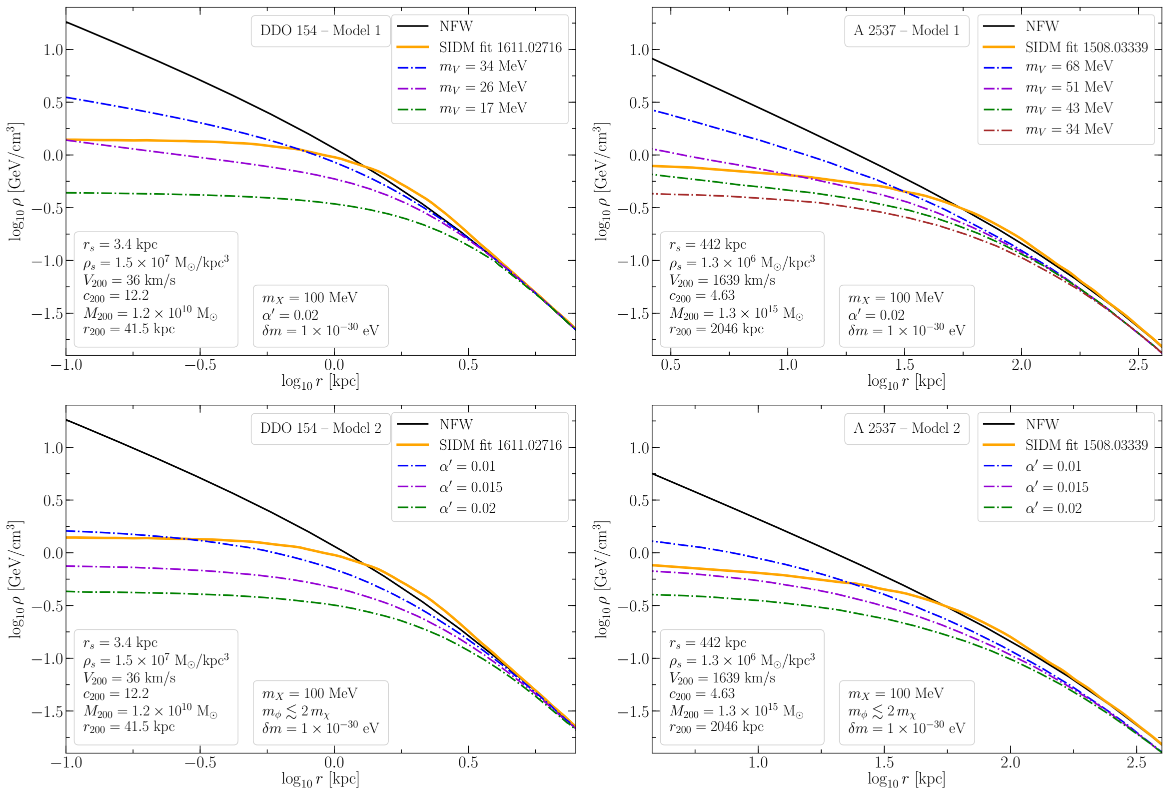


Figure 6.5.1: Left: density profiles for dwarf galaxy DDO 154. NFW and modified profiles from SIDM are from Ref. [42] (solid curves), while dot-dashed curves are the predictions of Model 1 (Model 2) for different indicated values of the vector mediator mass $m_V$ (dark fine-structure constant $\alpha'$). Right: corresponding results for galaxy cluster A2537, where SIDM result is from Ref. [9]. Top row is for Model 1 (vector), bottom for Model 2 (scalar).

rotation curve in the inner part of the galaxy, whereas the solid "SIDM" curve, which arises from elastic DM self-interactions adjusted to the appropriate cross section, gives a good fit.

The dot-dashed curves show the results for our model, with $m_\chi = 100\,\mathrm{MeV}$, $\alpha' = 0.02$, and several values of $m_V$. The profile is significantly cored, depending on the value of $m_V$, and has a different shape from that predicted by SIDM. The closest match between the SIDM profile and ours is produced for $m_V = 34\,\mathrm{MeV}$, which however is inconsistent with the constraint (6.8). It means that we should not neglect the effects of elastic scattering by itself, which go into the usual SIDM treatment. This problem can be overcome by simultaneously increasing $m_V$ and $\alpha'$; for example $m_V = 60\,\mathrm{MeV}$ and $\alpha' = 0.1$ gives a reasonable fit. However neither of

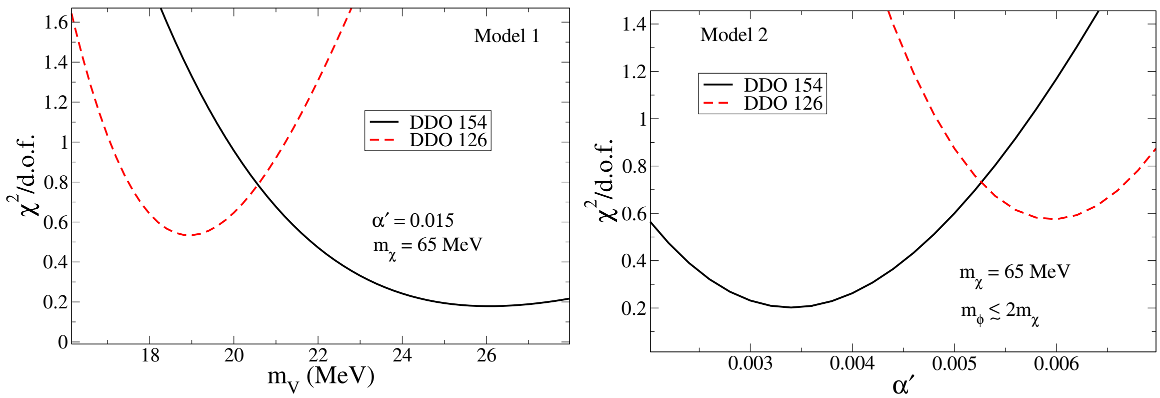


Figure 6.5.2: Left: $\chi^2$ per degree of freedom versus the vector mediator mass $m_V$ in Model 1, for fits to the circular velocities of dwarf spheroidals DDO 154 and 126, with DM mass $m_\chi = 65\,\text{MeV}$. Right: similar to left, for Model 2 with varying $\alpha'$. In either model, acceptable joint fits can be found by taking intermediate values of $m_V$ or $\alpha'$, respectively.

these models are consistent with data from galaxy clusters, as we discuss next.

Ref. [9] presents evidence for the DM profiles of galaxy clusters also being cored, to a somewhat lesser extent than dwarf spheroidal galaxies. These larger systems have much higher velocity dispersions, which leads to a stronger reduction of the central density by our mechanism, using Model 1. This is shown for the cluster A2537 in Fig. 6.5.1 (top right), where for the same values $m_\chi = 100\,\text{MeV}$ and $\alpha' = 0.02$ as before, the best match to the SIDM curve is for $m_V \cong 51\,\text{MeV}$; the lower value of $m_V = 34\,\text{MeV}$, favored by dwarf spheroidals, leads to unacceptably large suppression of the central density to be compatible with measured stellar velocity profiles. More detailed quantitative comparisons between the theory and data will be presented in section 6.6, in terms of the predicted versus observed velocity profiles.

One may also wonder to what extent a given model can match the observed properties of different spheroidal dwarf galaxies, whose density profiles can be diverse. Although an exhaustive comparison is beyond the scope of the present work, we have studied a contrasting example, DDO 126, whose DM density profile (like that of DDO 154) was estimated by Ref. [44]. The best fits to the circular velocity measurements for the two galaxies occur at different values of the model parameters, as shown in the left panel of Fig. 6.5.2, where we fixed $m_\chi = 65\,\text{MeV}$, $\alpha' = 0.015$ and allowed $m_V$

to vary. (Notice we have chosen a lower value of $m_\chi$ in this example; it is motivated by the discussion in section 6.5.3.) However, an acceptable fit to both systems can be found at an intermediate value $m_V \cong 20.6\,\mathrm{MeV}$, resulting in $\chi^2/\mathrm{d.o.f.} \cong 0.8$ for either system. We have allowed for systematic uncertainty in the magnitude of the DM density profiles, reflecting an estimated $\sim 25\%$ uncertainty in the baryonic content of the galaxies [9]. Since the baryons comprise $\sim 10\%$ of these systems, this translates to a 2.5% uncertainty in the overall DM densities, that we have marginalized over to slightly improve the fits.

### 6.5.2 Model 2

In Model 2, the situation is the opposite, though with a smaller discrepancy. In this case nothing depends on the scalar mass $m_\phi$, as long as it satisfies the consistency condition (6.8). For a fixed value of $m_\chi$ (here still at $100\,\mathrm{MeV}$), only $\alpha'$ matters. The SIDM profile can be approximately matched by taking $\alpha' \cong 0.01$ in the DDO 154 dwarf galaxy, while for the same parameter choices, the predicted inner profile of cluster A2537 lies somewhat above the SIDM fit, a factor of 1.7 higher as illustrated in the density profiles shown in Fig. 6.5.1.

We have found that this qualitative difference between scalar and vector mediators is generic: the velocity dependence of the decoherence mechanism in Model 1 makes it more effective for cusp suppression in high-velocity systems (clusters), whereas the lack of such dependence in Model 2 leads it to be more efficient in higher density systems (dwarfs).

The mild tension in simultaneously explaining the density profiles of different spheroidal dwarf galaxies, described for Model 1, is also present in model 2, as illustrated in the right panel of Fig. 6.5.2 for the case of $m_\chi = 65\,\mathrm{MeV}$: the best fits occur at different values of $\alpha'$ for the DDO 154 and DDO 126 galaxies. Like for Model 1, it is not a serious difficulty since an intermediate choice $\alpha' \cong 0.0053$ results in an acceptable $\chi^2/\mathrm{d.o.f.} = 0.72$ for both systems. We leave a more exhaustive study, both of the allowed parameter space and including more galaxies, for future work.

### 6.5.3 Hybrid models

The previous results suggest that the challenges for Models 1 or 2 to simultaneously fit the rotation curves of both dwarf galaxies and clusters could be overcome in a model with both mediators present. Here we present an example that supports this hypothesis, leaving for future work a more rigorous or detailed analysis.

Since it is technically difficult to implement both kinds of mediators simultaneously, we will be content here to give an example in which a vector mediator gives a good fit to a cluster, while leaving a dwarf galaxy relatively unaffected, and at the same time a scalar mediator that achieves the opposite. Since each model has a relatively small effect on one of the systems, it seems likely that by combining them, one can add the coring effects to both systems in a roughly linear fashion.

For example we find that for lighter DM with $m_\chi = 65\,\mathrm{MeV}$, and Model 1 parameters $\alpha' = 0.015$, $m_V = 44\,\mathrm{MeV}$, we fit the observed stellar line-of-sight velocity dispersion profile (described in more detail in the next section) for A2537 extremely well, while leaving the predicted circular velocity $V_{\mathrm{circ}}(r)$ in DDO 154 too high from not sufficiently reducing the central density in the dwarf system. On the other hand, choosing a lower coupling $\alpha' = 0.004$ in Model 2 gives an excellent fit to the DDO 154 rotation curve, while having a small impact on the inner profile of A2537. These outcomes are shown in Fig. 6.5.3, indicating that by combining the two mediators, it is possible to get as good a fit as an elastic SIDM model with a velocity-dependent cross section that is tuned to fit both systems. In elastic SIDM, a cross section of $\sigma/m \cong 3\,\mathrm{cm}^2/\mathrm{g}$ [42] is needed to agree with dwarf spheroidals, whereas a smaller value $\sim 0.1\,\mathrm{cm}^2/\mathrm{g}$ is used to explain clusters [9].

## 6.6 N-body simulations

To more quantitatively predict the evolution of galactic structures in our scenario, we have performed N-body simulations that take into account the peculiar interactions described by the Boltzmann approach of the previous sections. The two approaches should be viewed as complementary since each has its own limitations. The challenge

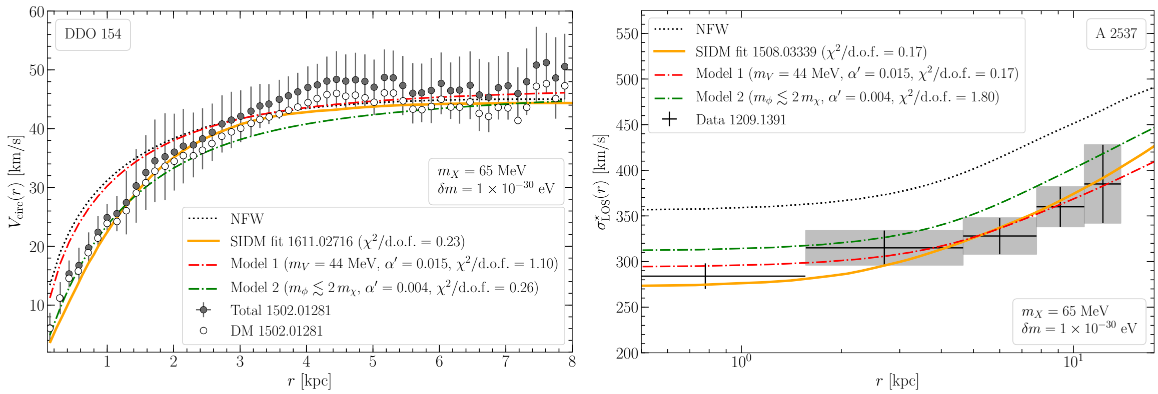


Figure 6.5.3: Illustration of how combining vector and scalar mediators could give a good simultaneous fit for both dwarf spheroidals (left) and clusters (right). Left: predicted circular velocities due to the DM component alone from the same two models and from SIDM (Ref. [42]), and data from Ref. [44]. In each case, one mediator dominates the coring effect of the central profile in one system, while having little effect in the other system. Right: stellar velocity dispersion along the line-of-sight for cluster A2537, with predictions based on the DM density profile from two of our models, from SIDM (Ref. [9]) and data from Ref. [29].

for N-body simulations, even if modified to account for self-interactions, is that they treat test particles classically, with scatterings occurring probabilistically rather than quantum mechanically. For conventional self-interactions this is not a serious limitation, but in the present context, the overall coherence of the DM ensemble is of primary importance.

To address this, we have modified the public version of the `GADGET-2` code [46, 47], which is widely used to generate N-body cosmological simulations. [6] The novel feature, apart from including DM scattering and annihilation (see appendix 6.C for implementation details and code tests), is to keep track of the phase $\varphi$ of each test particle, that describes the oscillations as in eq. (6.12). We assume that all particles in the halo are initially in phase with each other. Depending on whether the model is flavor-sensitive (Model 1) or flavor-blind (Model 2), this phase plays different roles, and evolves differently. In the absence of interactions, the phase of each particle would evolve trivially as $\varphi = \delta m\, t$. To mock up the behavior predicted by the quantum Boltzmann equations while still treating the particles classically, we implement

[6] `https://wwwmpa.mpa-garching.mpg.de/gadget/`

scattering as follows.

**Model 1.** Elastic scatterings damp the quantum coherence, as described by the off-diagonal elements of the collision term in (6.17). Integrating the off-diagonal elements over a collision time $\Delta t = 1/\Gamma_s = (n\langle\sigma v\rangle_s)^{-1}$ leads to a phase change $\Delta \ln(c_\varphi s_\varphi) = -3/2$, as shown in eq. (6.20). For strongly damped systems such that $\Gamma_s > \delta m$, this can be modeled by replacing the phase of each particle undergoing elastic scattering by

$$\varphi \to (\varphi \bmod 2\pi)\, e^{-3/2}\,, \tag{6.32}$$

leading to decoherence of the ensemble, that allows annihilations to occur. The annihilation probability of two particles with respective phases $\varphi_1$ and $\varphi_2$ is reduced relative to its usual value by the factor $\sin^2(\varphi_1 - \varphi_2)$, as derived in eq. (6.19).

**Model 2.** In this case, the scattering self-interactions have no effect on the phases, and they play exactly the same role as in conventional SIDM. Instead, decoherence is caused by the annihilation interactions themselves. The phase reduction described above now becomes a factor of $e^{-1}$ each time an annihilation *would have* occurred, for a fully decoherent mixture of $\chi$ and $\bar{\chi}$. The annihilation probability is modulated by the different factor $\sin^2(\varphi_1 + \varphi_2)$ as was explained below eq. (6.22).

As initial conditions for DM halos corresponding to the dwarf galaxy DDO 154 and the galaxy cluster A2537, we took Hernquist profiles [48], which are described by the total mass $M$ and the scale radius $a$. Unlike NFW, these profiles have finite mass without any need of truncation and they are perfectly stable in time when evolved with collisionless DM [49, 50], as we show in appendix 6.C.

To match the initial N-body profiles to the ones assumed in section 6.5, we used the procedure described in Ref. [49]. It consists of choosing the value of the Hernquist mass $M$ as the virial mass $M_{200}$ of the NFW profile and requiring the two density profiles to coincide in the inner region where $r \ll r_{200}$. The latter condition gives a relation between the Hernquist scale radius $a$ and the NFW one $r_s$, namely

$$a = r_s\sqrt{2\left[\ln\left(1 + c_{200}\right) - c_{200}/(1 + c_{200})\right]}\,, \tag{6.33}$$

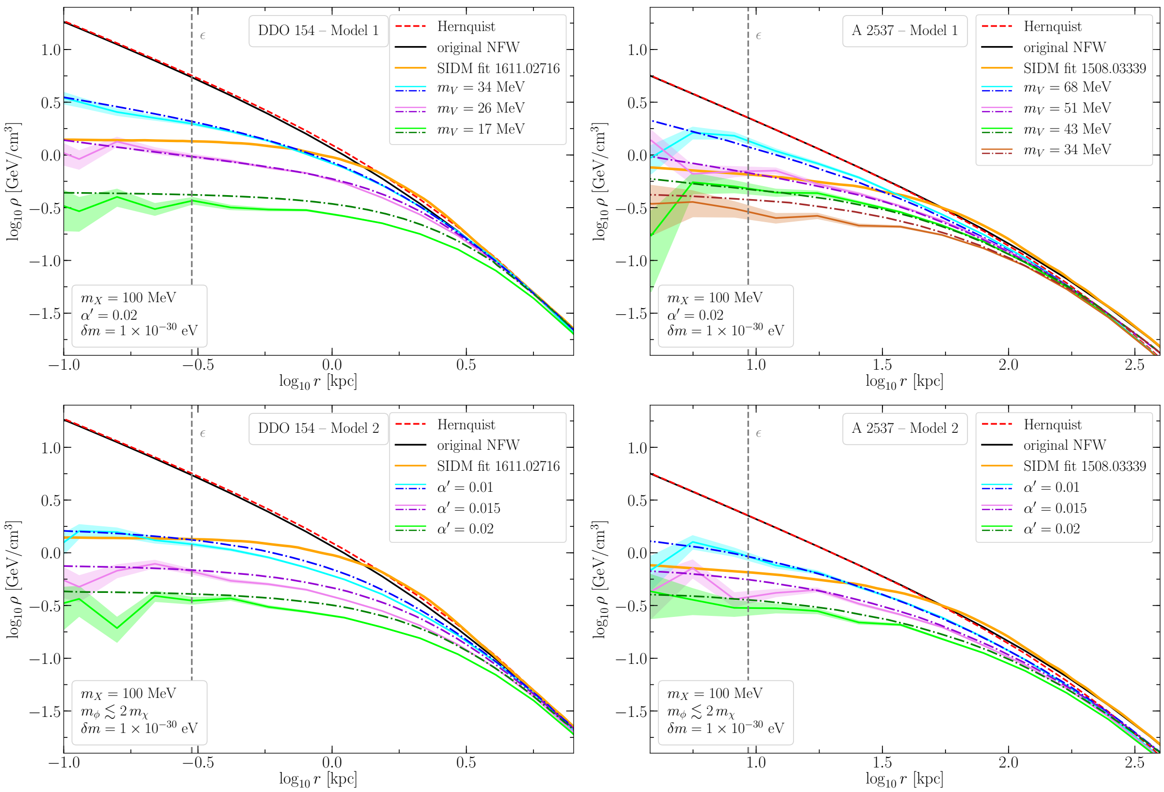


Figure 6.6.1: Like Fig. 6.5.1, but including comparison with the N-body simulation results. The latter are shown as solid lines surrounded by the $1\sigma$ uncertainty band, obtained by assuming that the number of particles in each bin is Poisson-distributed. The black solid curve corresponds to the original NFW profile, whereas the matched Hernquist profile is shown with the red dashed line. The other dot-dashed curves are the results of Fig. 6.5.1. The orange solid line is the SIDM prediction from Ref. [42] for DDO 154 and from Ref. [9] for A2537. The dashed vertical line shows the position of the gravitational softening length $\epsilon$ used in the simulations.

where $c_{200} = r_{200}/r_s$ is the concentration index. The values of $c_{200}$ we use for our examples are displayed in Fig. 6.5.1. The comparison between the original NFW and the matched Hernquist profile for our simulated halos is shown in Fig. 6.6.1. The agreement between these two profiles is excellent in the inner halo regions of interest for our study, suggesting that the simulation outcomes should model to a very good approximation the same dynamics as in our complementary treatment of section 6.5, on the subgalactic or subcluster scales where they are most relevant.

Fig. 6.6.1 shows the results of the N-body simulations for both Model 1 and Model 2 and their comparison with those obtained previously in Fig. 6.5.1. The overall agreement observed for both DM models suggests that the N-body simulations model reasonably well the physics encapsulated in the quantum Boltzmann equation, where the coherence of DM particles plays a decisive role. Differences between the simulation and the approximate approaches are perhaps more evident in the dwarf galaxy because gravitational effects and DM dynamics have a relatively larger effect in small systems than in large ones.

To compare our model predictions with existing data, we converted our results for the DM density into observed quantities, namely the circular velocity for dwarf systems and the projected stellar velocity along the line-of-sight for galaxy clusters. The former is defined as $V_{\rm circ}(r) = [G\,M(r)/r]^{1/2}$, where $M(r)$ is the enclosed mass at radius $r$. The left panels of Fig. 6.6.2 show our DM predictions for the rotation curve of DDO 154 dwarf galaxy within the two classes of models considered in this paper compared to current data. The grey points show the total circular velocity of the dwarf as observed by the LITTLE THINGS survey [44], whereas the white points represent just the DM contribution to $V_{\rm circ}(r)$, obtained by subtracting the gas and star components after carefully modelling their distribution within the galaxy [44]. The vector model with $m_V = 34$ MeV provides the best fit to data among the models displayed in the top panel of Fig. 6.6.2, with a $\chi^2$/d.o.f. $< 1$, comparable to the SIDM curve found in Ref. [42]. For the scalar case, a choice of $\alpha'$ somewhat smaller than 0.01 would provide good agreement between our model and observations as shown in the bottom left panel of the same figure.

For relaxed clusters dominated by a central early-type galaxy, such as in A2537, it is possible to measure the stellar line-of-sight velocity dispersion profiles $\sigma^\star_{\rm LOS}(r)$ with spatially-resolved spectroscopy [29, 51]. In order to convert our model predictions into $\sigma^\star_{\rm LOS}(r)$, we used the procedure outlined in appendix A of Ref. [52] combined with the information for A2537 cluster contained in Ref. [29]. In particular, as done in the latter reference, we modeled the stellar luminosity density $\nu_\star(r)$ with a dual pseudo isothermal elliptical profile (dPIE) [53] and converted it into a baryonic density via the relation

$$\rho_b(r) = \Upsilon_{\star V}\,\nu_\star(r)\,. \tag{6.34}$$

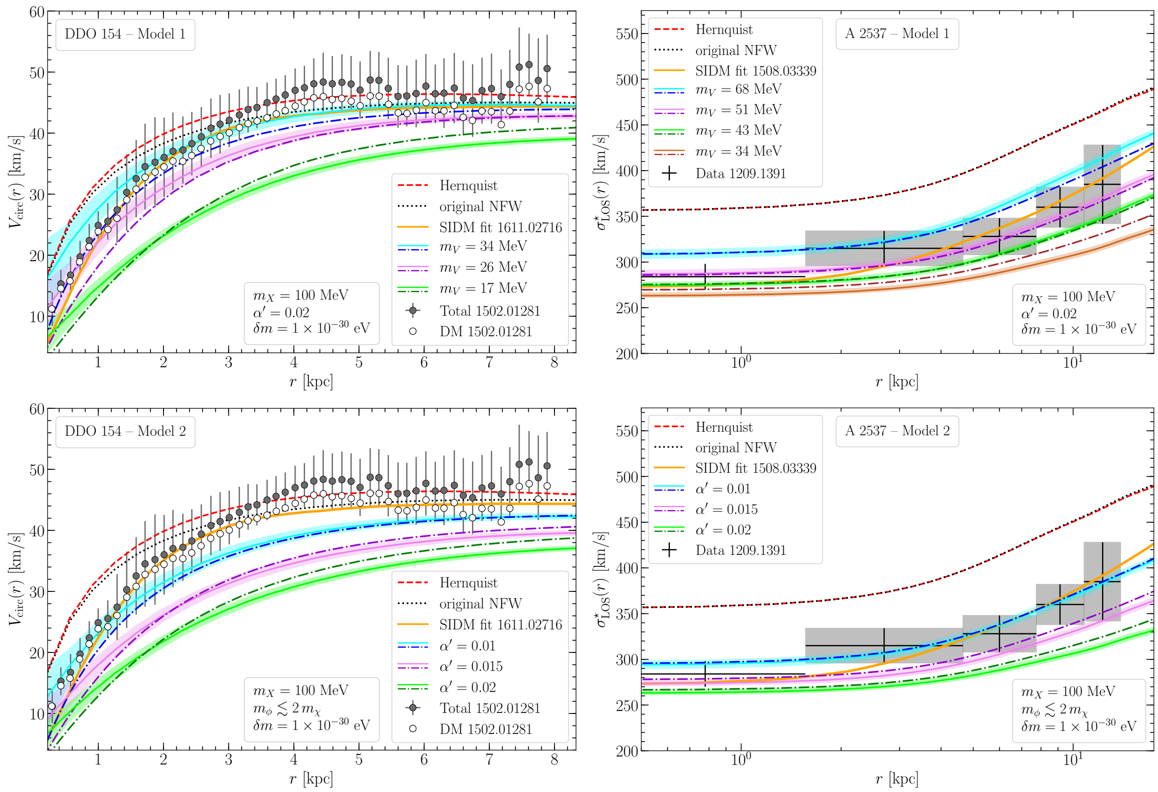


Figure 6.6.2: Comparison between our model predictions and observational data. Left: circular velocity as a function of distance from the galactic center of the dwarf DDO 154. The data points and the corresponding error bars are taken from Ref. [44]. In particular, the grey dots show the total effect of DM, gas and stars on the rotation curve, whereas the white dots show just the DM contribution obtained after a careful modelling of stars and gas components (see Ref. [44] for details). Right: projected stellar velocity dispersion along the line-of-sight as a function of radial distance for the cluster A2537. The data points and the error bars are taken from Ref. [29]. In all panels, N-body simulation results are shown as solid lines surrounded by the $1\sigma$ uncertainty band, obtained by assuming that the number of particles in each bin is Poisson-distributed. The black dotted curve corresponds to the original NFW profile, whereas the matched Hernquist profile is shown with the red dashed line. The other dot-dashed curves are the results of Fig. 6.5.1. The orange solid line is the SIDM prediction from Ref. [42] for DDO 154 and from Ref. [9] for A2537.

Here $\Upsilon_{\star V} \equiv M_\star / L_V$ is the stellar mass-to-light ratio in the V-luminosity band, which is usually assumed to be spatially-independent across the cluster [29, 52]. The value of $\Upsilon_{\star V}$ could be inferred from the stellar population synthesis (SPS) up to an unknown initial mass function (IMF) and therefore one usually parametrizes this ignorance with the free parameter $\log(\Upsilon_{\star V}/\Upsilon_{\star V}^{\rm SPS})$, where $\Upsilon_{\star V}^{\rm SPS}$ is the SPS predicted mass-to-light ratio for a given IMF. We considered a Chabrier IMF [54] as done in Ref. [29] and fixed the value of $\log(\Upsilon_{\star V}/\Upsilon_{\star V}^{\rm SPS})$ for the A2537 cluster by matching the baryonic density computed by eq. (6.34) with that obtained in Ref. [9]. The results of this procedure are shown in the right panels of Fig. 6.6.2 for both the vector and scalar models. Good agreement between them and the existing data is obtained for a wide set of parameters in both classes of models because of the large error bars in the observational data.

The N-body approach allows us to distinguish between the complementary effects of ordinary self-interactions by scattering, versus the novel one from annihilations, which we have investigated in both Models 1 and 2. To estimate the annihilation contribution to the total profile, we turned off the elastic scattering processes. Similarly, the scattering contribution can be estimated by turning off the annihilations. The top panels of Fig. 6.6.3 show that the major effect in shaping the halo density profile is given by DM annihilation for the choices of parameters both in Model 1 and Model 2 considered in this paper. This verifies that the annihilation mechanism, investigated here for the first time in quantitative detail, has the capacity to alleviate the small-scale structure problems of CDM in the way originally suggested by [22].

The comparison between annihilation and scattering is more evident by looking at their effect on the velocity dispersion of DM particles within the halo. As well-known in standard SIDM, particle scatterings lead to a net energy transfer between the outer and inner parts of the halo, causing an increase in the velocity dispersion in the central region with respect to the collisionless cold DM case [3, 8]. However, such an effect is absent in the DM annihilation scenario if the annihilation products are not reabsorbed within the halo, as occurs for the choice of parameters for both Model 1 and Model 2 considered in this paper (see discussion at the beginning of section 6.5). On the contrary, the halo is expected to become overall colder than that in the collisionless cold DM scenario because high-velocity particles have higher chance to find a partner to annihilate with than low-velocity particles. This is nicely displayed in the bottom panels of Fig. 6.6.3, where the velocity dispersion of DDO 154 shows a net decrease at intermediate distances from the galactic center because

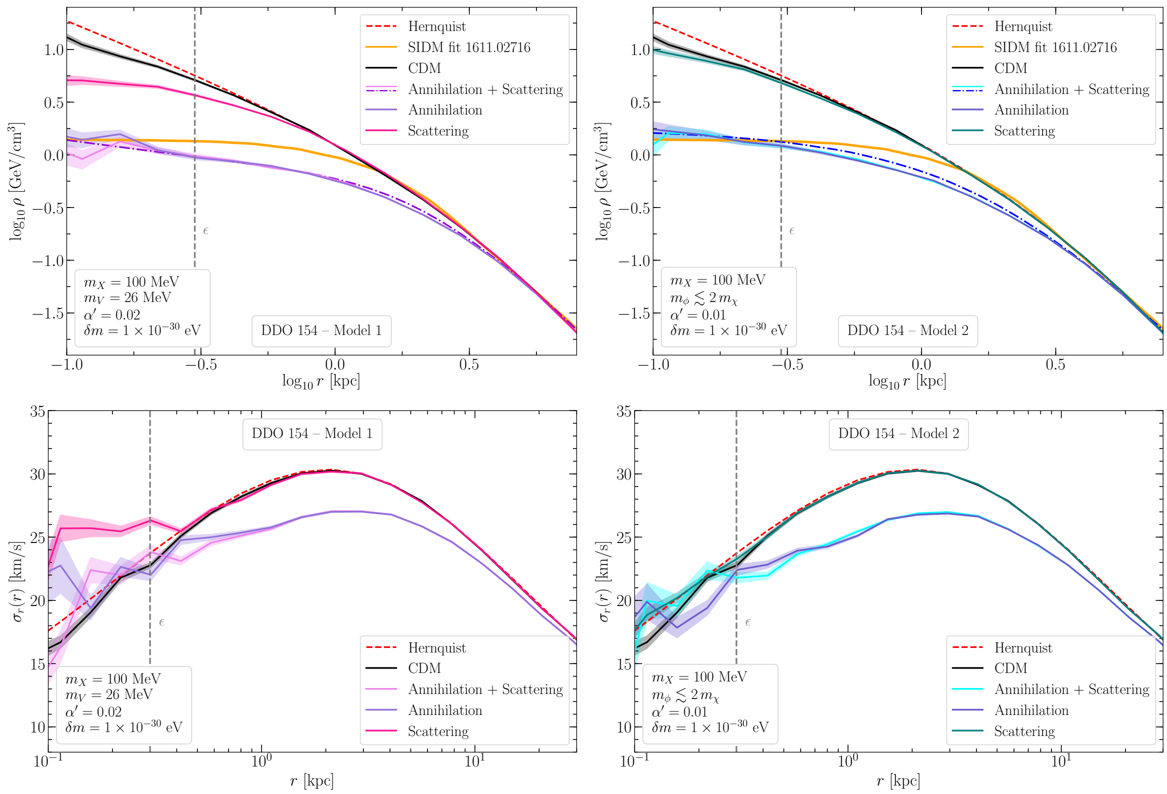


Figure 6.6.3: Top: Radial density profile of the dwarf galaxy DDO 154 for Model 1 with $m_V = 26$ MeV (left) and for Model 2 with $\alpha' = 0.01$ (right) from N-body simulations. The other model parameters are the same as in Fig. 6.6.1. The contributions of DM scattering and DM annihilation to the total profile are shown separately. The black solid curve corresponds to the result with just collisionless cold DM and the Hernquist profile for the initial halo is shown with the red dashed line. The gray dashed vertical line shows the position of the gravitational softening length $\epsilon$ used in the simulations. Bottom: Corresponding radial velocity dispersion of DDO 154 for the same Model 1 and Model 2 considered in the top row.

particles there have normally a larger radial velocity.

Using dark matter annihilation to solve the core-cusp problem naturally gives a roughly constant value of the rate of core formation [10], as is suggested by fits to astrophysical objects spanning five decades in mass [9]. Relying on dark matter dynamics to resolve these issues is potentially under some tension from the measurement of cusps in the centers of classical dwarf spheroidal galaxies [55, 56] and from recently discovered ultrafaint galaxies [57], although out-of-equilibrium dynamics like tidal effects of the host galaxy may play a role in contributing to the diversity of these systems [58–62]. Doing self-consistent fits to the observational data across many different systems will be critical for determining if the mechanism we investigate in this paper is as quantitatively successful as the elastic SIDM mechanism has been. Exploring this model in cosmological N-body simulations to compare against the subhalo abundance, for instance, will also be an important route for future work.

## 6.7 Conclusions

The long-standing discrepancies between gravitational N-body simulations of structure formation in the $\Lambda$CDM paradigm and observations of cored density profiles continue to motivate exploration of alternative dark matter models and mechanisms. In this work we have revived one of the earliest such proposals [22] by showing that dark matter annihilations in galactic structures can be responsible for erasure of the cusps, using distinctive properties of asymmetric dark matter (ADM). The key idea is that very strong annihilations would freeze out early in cosmic history, solving the problem of removing the "symmetric" ADM relic density, and are reactivated at late times relevant for structure formation by oscillations of DM into its antiparticle. The preferred annihilation rate per unit mass $\sigma v/m_\chi \sim 100\,\mathrm{cm}^2/\mathrm{g}$ km/s can be fit in our model by dark matter and mediator masses of order $30\,\mathrm{MeV} \simeq m_{V,\phi,a} \lesssim m_\chi \simeq 100\,\mathrm{MeV}$, a perturbative self-coupling as given in Eq. (6.6), and a Majorana mass term $\delta m$ within the range $(10^{-31} - 10^{-28})\,\mathrm{eV}$.

To obtain a large-enough annihilation cross section while respecting perturbativity of couplings constrains the DM and the mediator of the strong hidden force to be light, typically below 100 MeV. We have illustrated the mechanism in two representative models, with vector or scalar mediators respectively, and using two complementary approaches to model the structure formation dynamics. A fully consistent simulation is challenging because it must incorporate the quantum coherence of the oscillating dark matter while tracking the spatially-dependent annihilation rates within a DM halo. Our N-body simulations, which treat the coherence in an approximate way, give relatively close results to a quantum Boltzmann equation approach, which models the structure formation less rigorously. We have tested the scenario on two representative dwarf spheroidal galaxies, as well as a galactic cluster. Both methods lead to significant coring of the density profile, qualitatively similar to the effects of elastic SIDM scattering that have been widely used to address the cusp-core problem.

Like the elastic SIDM paradigm, the new mechanism we propose here does not, in its simplest forms, address the diversity of halo profiles on all scales. In elastic SIDM this is accomplished by assuming velocity-dependent scattering, with a cross section that goes down at larger DM speeds. Within our mechanism, scalar mediators generically have a relatively stronger coring effect on small halos than larger (less dense) ones, while vector mediators have the opposite behavior. We presented evidence that the combination of both mediators could provide a good universal fit, leaving a detailed investigation for future study.

## Acknowledgment

We thank A. Benson, S. Tulin and A. Robertson for very helpful correspondence. JC and SDM thank the CERN Department of Theoretical Physics for its hospitality and stimulating environment during the inception of this work. We acknowledge Calcul Quebéc (`https://www.calculquebec.ca`) and Compute Canada (`https://www.computecanada.ca`) for supercomputing resources. JC and GG are supported by NSERC (Natural Sciences and Engineering Research Council, Canada). GG acknowledges support from CNPq grant No.141699/2016-7, FAEPEX grant No. 2039/20, and FAPESP grant No. 2014/19164-6, as well as the support from Global Affairs Canada and McGill Space Institute. MP is supported by the Arthur B. McDonald Institute for Canadian astroparticle physics research. Fermilab is operated by Fermi Research Alliance, LLC under Contract No. DE-AC02-07CH11359 with the United States Department of Energy.

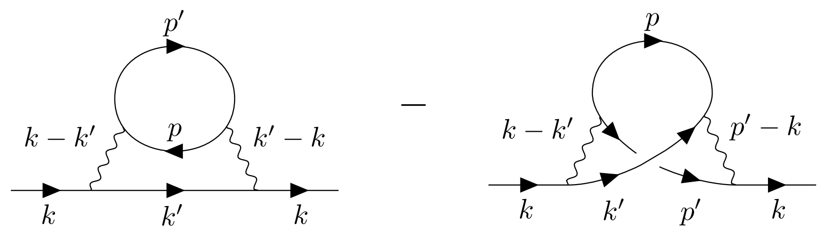


Figure 6.A.1: Self-energy diagrams for the vector model

# Appendices

## 6.A Scattering term in Model 1

In this appendix we derive the collision term for elastic scattering of $\chi\chi$ or $\chi\bar{\chi}$ through exchange of the vector boson, needed for the quantum Boltzmann equations. The diagrams in Fig. 6.A.1 are the analog of Fig. 4b in Ref. [26]. We can read off the imaginary part of the self-energies $\Sigma^{>,<}$, in analogy to their eq. (A26) of Ref. [26],

$$
\begin{aligned}
\Sigma^{>,<}(k) = i\frac{g'^4}{4}\int dk' dp' dp\,(2\pi)^4\delta^{(4)}(k+p-k'-p')& \\
\cdot\ \Bigg[\frac{1}{((k-k')^2-m_V^2)^2}\,O_-\gamma^\mu S_{k'}^{>,<}O_-\gamma^\nu\,\mathrm{Tr}\left(S_p^{<,>}O_-\gamma_\mu S_{p'}^{>,<}O_-\gamma_\nu\right)& \\
-\ \frac{1}{((k-k')^2-m_V^2)((p-p')^2-m_V^2)}\,O_-\gamma^\mu S_{p'}^{>,<}O_-\gamma^\nu S_p^{<,>}O_-\gamma_\mu S_{k'}^{>,<}O_-\gamma_\nu\Bigg]&,
\end{aligned}
\tag{6.35}
$$

where $dp = d^4p/(2\pi)^4$ and the Green's functions are given by

$$
\begin{aligned}
S_k^< &= -2\pi\delta(k^2-m^2)(\not{k}+m_\chi)\left[\theta_{k^0}\mathcal{F}_k-\theta_{-k^0}(1-\bar{\mathcal{F}}_k)\right]\,, \\
S_k^> &= +2\pi\delta(k^2-m^2)(\not{k}+m_\chi)\left[\theta_{k^0}(1-\mathcal{F}_k)-\theta_{-k^0}\bar{\mathcal{F}}_k\right]\,.
\end{aligned}
\tag{6.36}
$$

Here $\bar{\mathcal{F}}$ is the matrix with the diagonal entries interchanged, as in (11) of [26], and $O_- = \mathrm{diag}(1,-1)$. The trace is over both Dirac and flavor indices. We also define

$$
\tilde{\mathcal{F}} = O_-\mathcal{F}O_-\,,\quad \tilde{\bar{\mathcal{F}}} = O_-\bar{\mathcal{F}}O_-\,. \tag{6.37}
$$

This has the effect of reversing the signs of the off-diagonal elements.

Considering the relevant physical processes, it is not necessary to take account of all eight of the terms that arise from each diagram, from the products of the $S^{>,<}$ functions. First, since annihilation diagrams are suppressed while $k^0 > 0$, we can ignore $k'^0 < 0$, which would give the $s$-channel diagram. Second, by energy conservation, we must have either $p^0 > 0$ and $p'^0 > 0$, representing $\chi\chi$ scattering, or $p^0 < 0$ and $p'^0 < 0$, representing $\chi\bar{\chi}$ scattering. Let us first write the terms that arise from the middle line of (6.35), apart from the factors of $2\pi\delta(\dots)$

$$\begin{aligned}
&\frac{1}{((k-k')^2-m_V^2)^2}\gamma^\mu(\not{k}'+m_\chi)\gamma^\nu\,\mathrm{Tr}\left((\not{p}+m_\chi)\gamma_\mu(\not{p}'+m_\chi)\gamma_\nu\right)\;\times\\
&\quad\Sigma_k^>:\quad(1-\tilde{\mathcal{F}}_{k'})\left[\theta_{p^0}\theta_{p'^0}\,\mathrm{Tr}\left((-\mathcal{F}_p)(1-\tilde{\mathcal{F}}_{p'})\right)+\theta_{-p^0}\theta_{-p'^0}\,\mathrm{Tr}\left((1-\bar{\mathcal{F}}_p)(-\bar{\tilde{\mathcal{F}}}_{p'})\right)\right]\,,\\
&\quad\Sigma_k^<:\qquad\;-\tilde{\mathcal{F}}_{k'}\left[\theta_{p^0}\theta_{p'^0}\,\mathrm{Tr}\left((1-\mathcal{F}_p)(-\tilde{\mathcal{F}}_{p'})\right)+\theta_{-p^0}\theta_{-p'^0}\,\mathrm{Tr}\left((-\bar{\mathcal{F}}_p)(1-\bar{\tilde{\mathcal{F}}}_{p'})\right)\right]\,.
\end{aligned}\tag{6.38}$$

Similarly the last line of (6.35) contributes

$$\begin{aligned}
&-\frac{1}{((k-k')^2-m_V^2)((p-p')^2-m_V^2)}\gamma^\mu(\not{p}'+m_\chi)\gamma^\nu(\not{p}+m_\chi)\gamma_\mu(\not{k}'+m_\chi)\gamma_\nu\;\times\\
&\quad\Sigma_k^>:\quad(1-\tilde{\mathcal{F}}_{p'})\left[\theta_{p^0}\theta_{p'^0}\left((-\mathcal{F}_p)(1-\tilde{\mathcal{F}}_{k'})\right)+\theta_{-p^0}\theta_{-p'^0}\left((1-\bar{\mathcal{F}}_p)(-\bar{\tilde{\mathcal{F}}}_{k'})\right)\right]\,,\\
&\quad\Sigma_k^<:\qquad\;-\tilde{\mathcal{F}}_{p'}\left[\theta_{p^0}\theta_{p'^0}\left((1-\mathcal{F}_p)(-\tilde{\mathcal{F}}_{k'})\right)+\theta_{-p^0}\theta_{-p'^0}\left((-\bar{\mathcal{F}}_p)(1-\bar{\tilde{\mathcal{F}}}_{k'})\right)\right]\,.
\end{aligned}\tag{6.39}$$

The collision term comes from $\Sigma^{>,<}$ by

$$\mathcal{C}_s = i\int\frac{d^4k}{(2\pi)^4}\,\mathrm{tr}\left[\left(\frac{\not{k}+m_\chi}{4m_\chi}\right)\left(\{\Sigma_k^<,S_k^>\}-\{\Sigma_k^>,S_k^<\}\right)\right]\tag{6.40}$$

where unlike Tr above, tr denotes only the trace over Dirac matrices. Since we are interested in low densities, we can neglect terms of order $\mathcal{F}^3$, which means that we need only keep terms of order

$$\Sigma_k^< : O(\mathcal{F}^2)\,, \quad S_k^> : O(1)\,, \quad \Sigma_k^> : O(\mathcal{F})\,, \quad S_k^< : O(\mathcal{F})\,. \tag{6.41}$$

After carrying out the Dirac traces and combining like terms, we find that the respective contributions from the two diagrams are

$$\begin{aligned}
\mathcal{C}_1 &= -4g'^4 \int d\Pi_k d\Pi_{k'} d\Pi_p d\Pi_{p'}\, \frac{(2\pi)^4\delta^{(4)}(k+p-k'-p')}{((k-k')^2-m_V^2)^2} \\
&\quad \times \left[(k\cdot p)(k'\cdot p') + (k\cdot p')(k'\cdot p) - m_\chi^2(k\cdot k' + p\cdot p') + 2m_\chi^4\right] \\
&\quad \times \theta_{k^0}\theta_{k'^0}\Big\{\theta_{p^0}\theta_{p'^0}\Big[\tilde{\mathcal{F}}_{k'}\,\mathrm{Tr}\,\tilde{\mathcal{F}}_{p'} - \mathcal{F}_k\,\mathrm{Tr}\,\mathcal{F}_p\Big] + \theta_{-p^0}\theta_{-p'^0}\Big[\tilde{\mathcal{F}}_{k'}\,\mathrm{Tr}\,\bar{\mathcal{F}}_p - \mathcal{F}_k\,\mathrm{Tr}\,\bar{\tilde{\mathcal{F}}}_{p'}\Big]\Big\}\,, \\
\mathcal{C}_2 &= -4g'^4 \int d\Pi_k d\Pi_{k'} d\Pi_p d\Pi_{p'}\, \frac{(2\pi)^4\delta^{(4)}(k+p-k'-p')}{((k-k')^2-m_V^2)((p-p')^2-m_V^2)} \\
&\quad \times \left[(k\cdot p)(k'\cdot p') - \frac{1}{2}m_\chi^2(k\cdot k' + p\cdot p' + k\cdot p + k\cdot p' + k'\cdot p + k'\cdot p') + m_\chi^4\right] \\
&\quad \times \theta_{k^0}\theta_{k'^0}\Big\{\theta_{p^0}\theta_{p'^0}\Big[\tilde{\mathcal{F}}_{p'}\tilde{\mathcal{F}}_{k'} - \frac{1}{2}\{\mathcal{F}_p,\mathcal{F}_k\}\Big] + \theta_{-p^0}\theta_{-p'^0}\Big[\tilde{\mathcal{F}}_{p'}\bar{\mathcal{F}}_p - \frac{1}{2}\{\bar{\tilde{\mathcal{F}}}_{k'},\mathcal{F}_k\}\Big]\Big\}\,,
\end{aligned} \tag{6.42}$$

where $d\Pi_p = d^4p\,\delta(p^2-m_\chi^2)/(2\pi)^3$.

In the non-relativistic limit, it further simplifies since the squared matrix element in brackets is equal to $2\,m_\chi^4$ for $\mathcal{C}_1$, while for $\mathcal{C}_2$ it depends on which of the theta functions are taken: $[\ldots] = -m_\chi^4$ for positive energies and $+m_\chi^4$ for negative energies. The resulting collision term is

$$\begin{aligned}
\mathcal{C}_s = -\frac{g'^4}{4(2\pi)^8 m_V^4} \int d^3k \cdots d^3p'\,\delta^{(4)}(\cdots)\,\Big[4\left(\tilde{\mathcal{F}}_{k'}\,\mathrm{Tr}\,\mathcal{F}_{p'} - \mathcal{F}_k\,\mathrm{Tr}\,\mathcal{F}_p\right) \\
- \tilde{\mathcal{F}}_{p'}\tilde{\mathcal{F}}_{k'} + \frac{1}{2}\{\mathcal{F}_p,\mathcal{F}_k\} + \tilde{\mathcal{F}}_p\bar{\mathcal{F}}_{p'} - \frac{1}{2}\{\bar{\tilde{\mathcal{F}}}_{k'},\mathcal{F}_k\}\Big]\,.
\end{aligned} \tag{6.43}$$

Here, we used the identities $\mathrm{Tr}\,\tilde{\mathcal{F}}_p = \mathrm{Tr}\,\bar{\mathcal{F}}_p = \mathrm{Tr}\,\bar{\tilde{\mathcal{F}}}_p = \mathrm{Tr}\,\mathcal{F}_p$, as well as the fact that any terms with negative energies can be transformed to the corresponding phase space integrals with positive energy by changing $p \leftrightarrow p'$.

The next step is to make the ansatz

$$\mathcal{F}_k = e^{-\beta\omega_k}\frac{n}{n_{\rm eq}}\,, \tag{6.44}$$

where $\omega_k \cong m_\chi + k^2/2m_\chi \equiv m_\chi + E_k$,

$$n = \begin{pmatrix} n_{11} & n_{12} \\ n_{21} & n_{22} \end{pmatrix}\,, \tag{6.45}$$

and $n_{\rm eq}$ is the equilibrium number density. Then the momentum integrals can be carried out to get collision terms as a function of the density matrix $n$

$$\begin{aligned}\mathcal{C}_s = &-\frac{g'^4\, e^{-2\beta m_\chi}}{4(2\pi)^8 m_V^4\, n_{\rm eq}^2}\int d^3k\cdots d^3p'\,\delta^{(4)}(\cdots)\Big[e^{-\beta(E_k+E_p)}\left[4(\tilde{n}-n)\,{\rm Tr}\,n - \tilde{n}^2 + n^2\right) \\ &+ e^{-\beta(E_p+E_{p'})}\tilde{n}\bar{n} - e^{-\beta(E_k+E_{k'})}\frac{1}{2}\{\tilde{\bar{n}}, n\}\Big]\,. \end{aligned}\tag{6.46}$$

The integrals are all equal to $(m_\chi T)^{9/2}/T$ times a dimensionless number, and there are only two different possibilities, depending upon whether the two energies in the Boltzmann factors are both initial/final state, or one initial and one final. We get

$$\mathcal{C}_s = -\frac{g'^4\, m_\chi^{3/2}T^{1/2}}{16\pi\, m_V^4}\left[I_s\,\left(4(\tilde{n}-n)\,{\rm Tr}\,n - \tilde{n}^2 + n^2\right) + I_d\left(\tilde{n}\bar{n} - \frac{1}{2}\{\tilde{\bar{n}}, n\}\right)\right]\,, \tag{6.47}$$

where the two dimensionless integrals are

$$\begin{aligned} I_s &= \frac{1}{8\pi^4}\int d^3p\, d^3k\, d^3p'\, d^3k'\,\delta^{(4)}(p+k-p'-k')\, e^{-(p^2+k^2)/2} \\ &= \frac{1}{8\pi^4}\int d^3p\, d^3k\, d^3p'\,\delta(\vec{p}\cdot\vec{k})\, e^{-(\vec{p}+\vec{p}')^2/2-(\vec{k}+\vec{p}')^2/2} \cong 2.26\,, \\ I_d &= \frac{1}{8\pi^4}\int d^3p\, d^3k\, d^3p'\, d^3k'\,\delta^{(4)}(p+k-p'-k')\, e^{-(p^2+p'^2)/2} \\ &= \frac{1}{8\pi^4}\int d^3p\, d^3k\, d^3p'\,\delta(\vec{p}\cdot\vec{k})\, e^{-(\vec{p}+\vec{p}')^2/2-p'^2/2} = \infty\,, \end{aligned}\tag{6.48}$$

and the zeroth component of the delta function is in terms of the non-relativistic dimensionless energies. The second forms of the integrals, in which the delta function of energies simplifies, are obtained by shifting $\vec{p}\to\vec{p}+\vec{p}'$ and $\vec{k}\to\vec{k}+\vec{p}'$. We evaluated

$I_s$ numerically. The divergent integral is inconsequential because it multiplies $\tilde{n}\bar{n} - \frac{1}{2}\{\bar{\tilde{n}}, n\} \equiv 0$, which vanishes identically. In retrospect we understand that this term is unphysical, since it corresponds to the interference of the $t$- and $u$-channel scattering diagrams, which vanishes for scattering of $\chi$ with $\bar{\chi}$. The relevant matrix evaluates to

$$4(\tilde{n} - n)\,\mathrm{Tr}\, n - \tilde{n}^2 + n^2 = -6(n_{11} + n_{22}) \begin{pmatrix} 0 & n_{12} \\ n_{21} & 0 \end{pmatrix}, \tag{6.49}$$

so the collision term from scattering is

$$\mathcal{C}_s = \frac{3 I_s g'^4\, m_\chi^{3/2} T^{1/2}}{8\pi m_V^4} (n_{11} + n_{22}) \begin{pmatrix} 0 & n_{12} \\ n_{21} & 0 \end{pmatrix} \equiv \frac{3}{2}\langle\sigma v\rangle_s (n_{11} + n_{22}) \begin{pmatrix} 0 & n_{12} \\ n_{21} & 0 \end{pmatrix}, \tag{6.50}$$

which would appear in eq. (20) of Ref. [26]. The normalization of $\langle\sigma v\rangle_s$ is chosen to agree with the usual definition, in which the low-energy cross section is $\sigma \approx g^4 m_\chi^2/(4\pi m_v^4)$, and the thermal averaging is done as in Ref. [63].

## 6.B Thermal decoherence in the Boltzmann equation

For the vector model, we have simulated the effect of thermal decoherence due to the oscillation rate depending on the momentum in the quantum Boltzmann equation for the density matrix

$$\frac{d\mathcal{F}_k}{dt} - Hk\frac{d\mathcal{F}_k}{dk} = -i[\mathcal{H}_k, \mathcal{F}] + \mathcal{C}[\mathcal{F}], \qquad \mathcal{H}_k = \omega_k \mathbb{1} + \frac{m_\chi \delta m}{\omega_k} \begin{pmatrix} 0 & 1 \\ 1 & 0 \end{pmatrix}, \tag{6.51}$$

where $H$ is the Hubble rate and $\omega_k = \sqrt{k^2 + m_\chi^2}$. The $k$-dependence in the second term of the Hamiltonian implies that high-$k$ parts of the distribution oscillate with slightly lower frequency than low-$k$ parts, which is an additional source of decoherence that is neglected by integrating over momenta to reduce eq. (6.51) to an equation for the number density matrix $n$. Our goal is to verify that this neglect is justified. For the scalar model, this issue is less important since decoherence is not a requirement for annihilations to occur.

To model the effect one would like to divide the particle distribution into several momentum bins. We will be content to take just two, labeled by $s, l$ for small and large momenta, relative to the midpoint of the distribution. Accordingly, we split the density matrix into

$$n_t = n_s + n_l \tag{6.52}$$

and one finds separate Boltzmann equations for each component, that are coupled to each other through the collision terms. The Boltzmann equations take the form

$$\begin{aligned} \dot{n}_s + 3Hn_s &= -i[H_s, n_s] - \frac{\langle\sigma v\rangle_s}{8}\left(S_s + S\right) - \frac{\langle\sigma v\rangle_a}{2}\left(A_s - n_{\rm eq}^2\right) \,, \\ \dot{n}_l + 3Hn_l &= -i[H_l, n_l] - \frac{\langle\sigma v\rangle_s}{8}\left(S_l + S\right) - \frac{\langle\sigma v\rangle_a}{2}\left(A_l - n_{\rm eq}^2\right) \,, \end{aligned} \tag{6.53}$$

where $\langle\sigma v\rangle_{s,a}$ are the scattering and annihilation cross sections, the matrices $S_i$, $S$, $A_i$ are defined as

$$S_i = \begin{pmatrix} n_{i,11}(6n_{11} + 8n_{22}) - n_{i,12}n_{21} - n_{i,21}n_{12} & 7n_{i,12}n_t - n_{i,t}n_{12} \\ 7n_{i,21}n_t - n_{i,t}n_{21} & n_{i,22}(8n_{11} + 6n_{22}) - n_{i,12}n_{21} - n_{i,21}n_{12} \end{pmatrix}, \tag{6.54}$$

$$S = \begin{pmatrix} -3n_{11}^2 - 4n_{11}n_{22} + n_{12}n_{21} & 3n_{12}n_t \\ 3n_{21}n_t & -3n_{22}^2 - 4n_{11}n_{22} + n_{12}n_{21} \end{pmatrix}, \tag{6.55}$$

$$A_i = \begin{pmatrix} 2\, n_{i,11}n_{22} - (n_{i,12}n_{21} + n_{i,21}n_{12}) & (n_{i,12}n_t - n_{i,t}n_{12}) \\ (n_{i,21}n_t - n_{i,t}n_{21}) & 2\, n_{i,22}n_{11} - (n_{i,12}n_{21} + n_{i,21}n_{12}) \end{pmatrix}, \tag{6.56}$$

and we defined $n_{ij} = n_{s,ij} + n_{l,ij}$, $n_t = n_{11} + n_{22}$, and $n_{i,t} = n_{i,11} + n_{i,22}$. These expressions can be read from the form of the collision and annihilation terms in terms of the $\mathcal{F}$ matrices, before doing the final integral over the momentum $k$ of the particle whose distribution is being tracked in the Boltzmann equation. If one adds the two equations together, they revert to the standard equation in terms of $n_t$ alone. The decoherence effect comes from the fact that the free Hamiltonians $\mathcal{H}_{s,l}$ are slightly different for the two components, which for non-relativistic particles is

$$\mathcal{H}_{s,l} \cong m_\chi \begin{pmatrix} 1 & 0 \\ 0 & 1 \end{pmatrix} + \delta m \begin{pmatrix} 0 & 1 \\ 1 & 0 \end{pmatrix} + \frac{\langle k^2 \rangle_{s,l}}{2m_\chi} \left[ 1 - \frac{\delta m}{m_\chi} \begin{pmatrix} 0 & 1 \\ 1 & 0 \end{pmatrix} \right] . \tag{6.57}$$

The important feature is the difference between $\langle k^2 \rangle_l$ and $\langle k^2 \rangle_s$, so for simplicity one could take, for example, $\langle k^2 \rangle_s = \frac{1}{2} \langle k^2 \rangle$ and $\langle k^2 \rangle_l = \frac{3}{2} \langle k^2 \rangle$, which is a temperature-dependent split. For temperatures such that scattering is still in equilibrium, we can estimate $\langle k^2 \rangle \sim 3m_\chi^2 / x$, where $x = m_\chi / T$. After scatterings freeze out, the wavenumber redshifts as $1/a$, so $\langle k^2 \rangle \sim 3m_\chi^2 \, x_f / x^2$.

This effect can be important only in the early Universe when the momenta are sufficiently large that $k^2 / m_\chi^2$ is not negligible. We have applied this formalism to check the early-Universe solutions of section 6.4. We found no appreciable effect from this extra source of decoherence.

## 6.C N-body simulation details

In this appendix, we describe the scattering and annihilation algorithms used in the simulations presented in this paper. Validation tests of the code are also presented and discussed.

### 6.C.1 Scattering

Elastic scattering between DM particles has been implemented stochastically on top of `GADGET-2` in the same way as done by Ref. [50], which was derived directly from the classical Boltzmann equation [7]. We summarize below the main relevant information and refer the reader to Ref. [50] for a more detailed description.

The scattering rate for a DM particle of mass $m_\chi$ at position $\vec{r}_i$ and velocity $\vec{v}_i$, moving in an equal-mass particle background characterized by a normalized velocity distribution $f_v(\vec{r}, \vec{v})$ and a local density $\rho(\vec{r})$, is

$$\Gamma_{i,\,\mathrm{scatt}} = \int f_v(\vec{r}_i, \vec{v}) \, \rho(\vec{r}_i) \, \frac{\sigma}{m_\chi} \, |\vec{v}_i - \vec{v}| \, d\vec{v} \, . \tag{6.58}$$

Here $\sigma/m_\chi$ is the DM scattering cross section per unit particle mass, which can be velocity-dependent. In simulations, individual physical particles cannot be resolved and all the properties of the latter should be translated to those of the simulation particles. For instance $\sigma/m_\chi$ should be replaced by $\sigma_p/m_p$, where $\sigma_p$ and $m_p$ are the scattering cross section and the mass of the simulation particles, respectively. In a similar manner, the quantities $f_v(\vec{r},\vec{v})$ and $\rho(\vec{r})$ should be estimated from the volume within a sphere of radius $h_S$, called *scatter search radius*, centered at the DM particle position $\vec{r}_i$. Assuming all the simulation particles within the scattering volume contribute equally, independently of their location (top-hat kernel), eq. (6.58) can be written as a sum over the $N_p$ neighboring particles [50]

$$\Gamma_{i,\,\mathrm{scatt}} = \sum_{j=1}^{N_p} \frac{\sigma_p\,|\vec{v}_i - \vec{v}_j|}{\frac{4}{3}\pi h_S^3}\,. \tag{6.59}$$

Hence the probability for particles $i$ and $j$, separated by a distance smaller than $h_S$, to scatter within the next time step of size $\Delta t$, is given by

$$\begin{aligned} P_{ij,\,\mathrm{scatt}} &= \left(\frac{\sigma}{m_\chi}\right)\rho_{ij}\,|\vec{v}_i - \vec{v}_j|\,\Delta t\,, \\ \rho_{ij} &= \begin{cases} \frac{3\,m_p}{4\,\pi h_S^3} & 0 \le \tilde{r} \le h_S \\ 0 & \tilde{r} > h_S \end{cases} \end{aligned} \tag{6.60}$$

where $\tilde{r} \equiv |\vec{r}_i - \vec{r}_j|$ and $\rho_{ij}$ is the target density, which is constant in this case because it is estimated using a top-hat kernel function. This is the simplest choice, but not the most common one used to implement DM self-interaction in N-body simulations. For instance, refs. [7, 8, 64] used a cubic spline kernel $W(r, h_S)$ like the one already used in `GADGET` to compute the gravitational force in the context of smoothed-particle hydrodynamics (SPH) [65]. Such a kernel allows nearby particles separated by a distance less than $h_S$ to have higher scatter probability than those further apart because $W$ is a smoothing function peaked at $\tilde{r} = 0$. For appropriate choices of $h_S$, both the top-hat and cubic spline kernels provide results in agreement with analytical expectations [7, 8, 50, 64] and with each other, within numerical uncertainties [50].

Therefore, we preferred using the simple and intuitive top-hat kernel with $\rho_{ij}$ given by eq. (6.60) and with a fixed value of $h_S$ of the same order of the gravitational softening length $\epsilon$. In particular, we consider $h_S = \epsilon$ as chosen by Ref. [50] because it gives the expected scattering rate, as discussed in section 6.C.3.

To see which particles do actually scatter at each time step, the probability in eq. (6.60) is computed for each pair of nearby particles and compared with a random number drawn from a uniform distribution. For isotropic scattering and equal-mass particles, the post-scatter velocities are computed as $\vec{v}'_{i,j} = \vec{v}_{\rm CM} \pm (v_{\rm rel}/2)\,\hat{e}$, where $\vec{v}_i$ and $\vec{v}_j$ are the initial velocities, $\vec{v}_{\rm CM}$ is the center-of-mass velocity between particle $i$ and $j$, $v_{\rm rel}$ is the magnitude of their relative velocity and $\hat{e}$ is a randomly oriented unit vector.

This scattering algorithm is very similar to that used in several SIDM cosmological simulations [6, 8, 66–71], which mainly differ in the number of neighbors within the scattering volume. The majority of these simulations have treated the DM scattering as isotropic, which usually results from a short-range interaction mediated by a massive particle. In particular the mediator mass $m_{V,\phi}$ should be much heavier than the DM particle momenta, which translates into $m_{V,\phi} \gg 10^{-3}\, m_\chi$ for DM particles moving in Milky-Way-like galaxies today. If this is not the case, the cross section will depend on the momentum exchange, which increases with the collision velocity or the scattering angle, leading typically to velocity-dependent anisotropic scatterings. The latter are common in long-range interactions via light or massless mediators, which occur in several motivated DM scenarios such as mirror [72–74], atomic [75–78] and hidden sector DM models [79–83]. The simplest way to take them into account is to assume the scattering is still isotropic but the cross section $\sigma$ in eq. (6.60) is replaced by the *momentum transfer cross section* $\sigma_T$, defined as [84–86]

$$\sigma_T = \int_0^\pi \frac{d\sigma}{d\Omega}\,(1-\cos\theta)\,d\Omega\,, \tag{6.61}$$

where $\theta$ and $d\Omega$ are the scattering and solid angles, respectively. Here, the differential cross section $d\sigma/d\Omega$ can be derived within the Born approximation [87] from particle scattering mediated by a Yukawa interaction [4, 88]

$$\frac{d\sigma}{d\Omega} = \frac{\sigma_s}{4\pi}\left(1 + \frac{v_{\rm rel}^2}{\omega^2}\sin^2\frac{\theta}{2}\right)^{-2}, \tag{6.62}$$

where $\sigma_s$ is given by eq. (6.7) and $\omega = r_m\, c$ with $r_m = m_V/m_\chi$ or $r_m = m_\phi/m_\chi$ depending on the model under consideration. In the limit $v_{\rm rel} \ll \omega$, $d\sigma/d\Omega$ becomes velocity-independent, $\sigma = \int (d\sigma/d\Omega)\, d\Omega \approx \sigma_s$ and the scattering is isotropic. In the opposite regime, eq. (6.62) scales as $\propto v_{\rm rel}^{-4}$ like in Rutherford scattering which is mediated by the Coulomb potential. The approximation of using $\sigma_T$ instead of $\sigma$ as the scattering cross section captures most of the effects of more complicated scattering dynamics where the DM velocity distribution is close to isotropic, which is the case of dwarf galaxies [86] [7]. This is because $\sigma_T$ estimates the average forward momentum lost during the collision, and several simulations used it to model DM long-range interactions [8, 91–94]. Ref. [89] proposed an alternative definition of $\sigma_T$, namely

$$\sigma_{\tilde{T}} = 2\int \frac{d\sigma}{d\Omega}\,(1 - |\cos\theta|)\, d\Omega\,, \tag{6.63}$$

to account for particle indistinguishability, which implies that $d\sigma/d\Omega$ is invariant under $\cos\theta \to -\cos\theta$. The overall factor of 2 is used to give $\sigma_{\tilde{T}} \approx \sigma$ in the isotropic regime, as done in Ref. [95]. This new definition of the scattering cross section has been shown to provide better results than $\sigma_T$ in simulations of isolated DM halos [90]. An even better description of anisotropic scattering within the isotropic approximation seems to be given by the replacement of $\sigma$ with the *viscosity (or conductivity) cross section* [86]

$$\sigma_V = \frac{3}{2}\int \frac{d\sigma}{d\Omega}\,(1 - \cos^2\theta)\, d\Omega \tag{6.64}$$

because $\sigma_V$ takes into account of both forward and backward scatterings at the same time in addition to particle indistinguishability. Again, in order to match $\sigma_V \approx \sigma$

[7] Although in most astrophysical systems DM is expected to have an approximately isotropic velocity distribution, this is not the case of colliding galaxy clusters where there is a preferred direction along which DM particles collide [89, 90].

in the isotropic regime, the original expression is multiplied by an overall factor of 3/2. In the present case, the DM particles are treated as being distinguishable since they have an associated oscillation phase $\varphi$, which might evolve differently during the simulation from particle to particle as discussed in section 6.6.

As noticed by Ref. [4], $\sigma_V$ differs just by a $\mathcal{O}(1)$ factor from $\sigma_T$ and $\sigma_{\tilde{T}}$ for distinguishable particles and apart from the rescaling factor, any of them can be taken as good measures of DM self-interactions, since systematic uncertainties in astrophysical observations are still too big to allow for discrimination between the different prescriptions. They become identical in the isotropic regime where $v_{\rm rel} \ll \omega$, which is well satisfied for the choice of model parameters and DM halos considered in this paper (see section 6.5). We have chosen $\sigma_T$ because of its wide use in SIDM simulations, and we checked *a posteriori* that the use of the other prescriptions lead to the same simulation results for the DM models considered in this paper.

With eq. (6.62), which is valid within the Born approximation for $r_m \gg \alpha'$ (recall $\alpha'$ is the dark fine-structure constant), the momentum transfer cross section in eq. (6.61) and its modified version in eq. (6.63) turn out to be [96, 97]

$$\begin{aligned} \sigma_T &= \sigma_s \, \frac{2\,\omega^4}{v_{\rm rel}^4} \left[ \ln\left(1 + \frac{v_{\rm rel}^2}{\omega^2}\right) - \frac{v_{\rm rel}^2}{\omega^2 + v_{\rm rel}^2} \right], \\ \sigma_{\tilde{T}} &= \sigma_s \, \frac{4\,\omega^4}{v_{\rm rel}^4} \left[ 2\,\ln\left(1 + \frac{v_{\rm rel}^2}{2\,\omega^2}\right) - \ln\left(1 + \frac{v_{\rm rel}^2}{\omega^2}\right) \right], \end{aligned} \tag{6.65}$$

and, analogously, the viscosity cross section in eq. (6.64) becomes

$$\sigma_V = \sigma_s \, \frac{6\,\omega^4}{v_{\rm rel}^4} \left[ \left(1 + \frac{2\,\omega^2}{v_{\rm rel}^2}\right) \ln\left(1 + \frac{v_{\rm rel}^2}{\omega^2}\right) - 2 \right]. \tag{6.66}$$

The tests for the code implementations of DM scattering are presented in section 6.C.3.

### 6.C.2 Annihilation

We have implemented DM annihilation in a stochastic way similar to what was done for scattering. To the best of our knowledge, the first self-consistent implementation of DM annihilation in N-body simulations was performed in Ref. [98], followed by

Ref. [99], where the energy released from annihilations to the surrounding gas particles was properly accounted for throughout the simulation. We followed a simplified version of this annihilation algorithm, without including the energy transfer between different particle species, because our simulation considers only DM particles $\chi$ and the annihilation products escape the galaxies without affecting their environment and therefore the observable quantities.

In detail, the annihilation rate for a DM particle of mass $m_\chi$ at position $\vec{r}_i$, moving in an equal-mass particle background of density $\rho(\vec{r})$, is

$$\Gamma_{i,\,\mathrm{ann}} = \rho(\vec{r}_i)\,\frac{\langle\sigma_{\mathrm{ann}} v\rangle}{m_\chi}\,, \tag{6.67}$$

where $\langle\sigma_{\mathrm{ann}} v\rangle$ is the velocity-averaged annihilation cross section. Depending on the particle nature of DM, the estimation of $\rho(\vec{r})$ can include all the DM particles in the system (for Majorana fermions or real scalars) or just antiparticles (for Dirac fermions or complex scalars). Following the same steps as in section 6.C.1 and introducing the *annihilation search radius* $h_A$, we can generalize eq. (6.67) and write the probability for DM particles $i$ and $j$, separated by a distance smaller than $h_A$, to annihilate within the next time step of size $\Delta t$ as

$$\begin{aligned} P_{ij,\,\mathrm{ann}} &= \left(\frac{\langle\sigma_{\mathrm{ann}} v\rangle_{ij}}{m_\chi}\right)\rho_{ij}\,\Delta t\,, \\ \rho_{ij} &= \begin{cases} \frac{3\,m_p}{4\,\pi h_A^3} & 0 \le \tilde{r} \le h_A \\ 0 & \tilde{r} > h_A \end{cases} \end{aligned} \tag{6.68}$$

where $\tilde{r} \equiv |\vec{r}_i - \vec{r}_j|$ and $\rho_{ij}$ is the target density, which is estimated using a top-hat kernel function. The velocity-averaged annihilation cross section $\langle\sigma_{\mathrm{ann}} v\rangle_{ij}$ depends generally on the relative velocity $v_{\mathrm{rel}} = |\vec{v}_i - \vec{v}_j|$ between particles $i$ and $j$. In the non-relativistic limit, valid in the context of galaxies, it is usually expanded in powers of $v_{\mathrm{rel}}$ as

$$\langle\sigma_{\mathrm{ann}} v\rangle_{ij} \simeq \sigma_{\mathrm{ann},\,s} + \sigma_{\mathrm{ann},\,p}\, v_{\mathrm{rel}}^2 + \mathcal{O}(v_{\mathrm{rel}}^4)\,, \tag{6.69}$$

where $\sigma_{\mathrm{ann},\,s}$ and $\sigma_{\mathrm{ann},\,p}$ are constants corresponding to the $s$-wave and the $p$-wave annihilation terms, respectively. For the models considered in this paper, only $\sigma_{\text{ann},s}$ contributes to $\langle\sigma_{\text{ann}}v\rangle_{ij}$, which is given by what we refer to as $\langle\sigma v\rangle_a$ in eq. (6.5). This makes the annihilation probability in eq. (6.68) velocity-independent. As in the scattering case, the annihilation search radius $h_A$ entering the density $\rho_{ij}$ is in principle a free parameter that should be chosen to reproduce analytical results. As we will discuss in section 6.C.3, $h_A = \epsilon$ turns out to be the best choice (recall $\epsilon$ is the gravitational softening length). To see which particles annihilate at each time step, the probability in eq. (6.68) is computed for each pair of nearby simulation particles and compared to a random number. If the latter is below than the former, annihilation happens and the two particles in the event are removed from the system.

### 6.C.3 Validation tests

The simplest test for both our scattering and annihilation algorithms is a uniform cube of $N_c$ particles moving through a background of stationary particles with constant number density $n_b$. All the particles making up the simulated system have the same mass $m_p$. To allow simple predictions, we impose that the cube particles move with constant speed $v_0$ along the same axis, they can scatter with constant cross section $\sigma_p$ at most once, and gravity is turned off [50].

The scattering or annihilation rate for each simulation particle in the cube is $\Gamma = n_b\, m_p(\sigma v_0/m_\chi)$, where $m_\chi$ and $\sigma$ are respectively the mass and the cross section of the physical particles, whose properties have been translated into those of the simulation particles via $\sigma_p = m_p\,(\sigma/m_\chi)$. Naively, we can estimate the expected number of interactions after a time $t$ as

$$N_{\text{exp}} = N_c\,\Gamma\,t = N_c\,n_b\,m_p(\sigma v_0/m_\chi)\,t\,. \tag{6.70}$$

This expression has however several limitations because not only it does not take into account that not all the particles in the cube have interacted between zero and time $t$ but also that those that have scattered or annihilated could do it just once. These effects are properly captured by considering how the number of cube particles changes

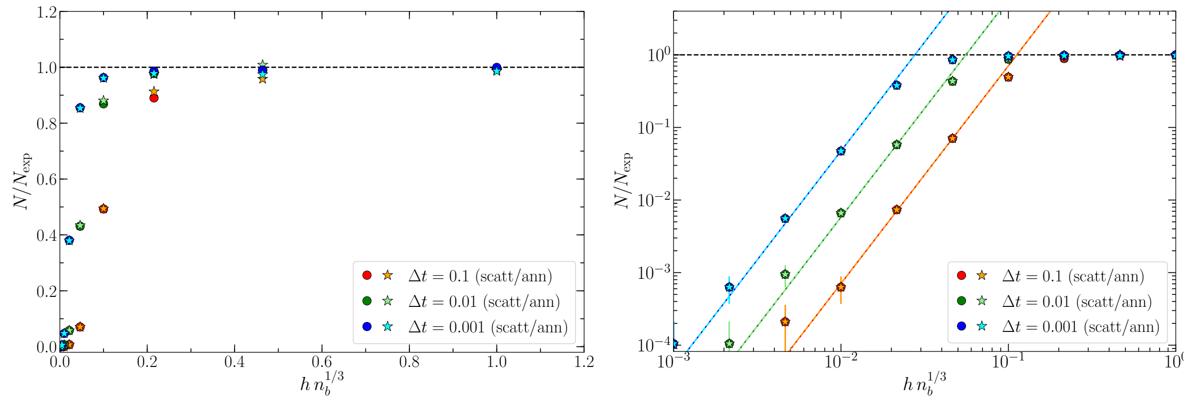


Figure 6.C.1: Ratio of the number of cube particles scattering (annihilating) in our test simulations to the expected number of the same events given by eq. (6.72), as a function of the scatter (annihilation) search radius $h$. Points correspond to the results of simulations where only scattering was turned on, whereas stars are used for simulations in which only annihilation took place. Different color points represent different choices of the simulation time step $\Delta t$, which is measured in units of $\ell/v_0$ with $\ell$ being the side of the cube. The left and right plots show the same data with different axis scales, linear on the left and logarithmic on the right. The solid (dashed) lines in the right panel show $N \propto h^3$, which is the result expected from "probability saturation," as originally noticed by Ref. [50]. The error bars show the $1\sigma$ uncertainty assuming $N$ is Poisson distributed.

with time, which can be described by

$$\frac{dN_c}{dt} = -\Gamma\, t\,. \tag{6.71}$$

With this in mind, the expected number of scattering or annihilating particles in the simulation after a time $t$ can be better expressed by

$$N_{\rm exp} = N_c(0)\,\{1 - \exp\left[-n_b\, m_p\, (\sigma v_0/m_\chi)\, t\right]\}\,, \tag{6.72}$$

where $N_c(0)$ is the initial number of particles in the cube.

The comparison between $N_{\rm exp}$ and the number $N$ of cube particles that have scattered (annihilated) in our test simulations is plotted in Fig. 6.C.1 as a function of the scatter (annihilation) search radius $h$. Here, each point corresponds to a simulation where only scattering was turned on, while stars are used for simulations in which only annihilation was active. As already noticed in refs. [7, 50], $N$ falls below than expected only for $h$ smaller than 20% of the mean background interparticle separation, but this minimum value depends heavily on the chosen time step $\Delta t$ [50], as confirmed by Fig. 6.C.1. The $h$-dependence of the number $N$ of scattering or annihilating particles in simulations arises in the "probability-saturated" regime, where the probability for a particle to scatter or annihilate within a time step, given by eqs. (6.60) or (6.68), becomes greater than unity. The latter probability enters the definition of $N$, which depends on it ($\propto h^{-3}$) and on the number of neighbouring particles that a particle finds at each time step ($\propto h^3$). This makes $N$ generally insensitive to $h$, except in the probability-saturated regime, where $N \propto h^3$ as shown by the solid and dashed lines in the right panel of Fig. 6.C.1. In order to avoid probability saturation, a shorter time step should be used when using smaller $h$, since the probability for a pair of particles to scatter or annihilate is proportional to $\Delta t/h^3$.

Although Ref. [50] suggested that probabilities exceeding unity within each time step should not appear in SIDM simulations powered by `GADGET` for reasonable values of $\sigma/m_\chi$, we decided to implement a time-step criterion. In particular, similar to what was done in Ref. [69], an individual particle time step $\Delta t$ is modified by rearranging eq. (6.60) as

$$\Delta\tilde{t} = \frac{4\,\pi h_S^3}{3\,m_p}\,\frac{m_\chi}{\sigma\,v_{\rm rel}}\,P_{\rm max} \tag{6.73}$$

if the probability of interaction for any pair involving such a particle was greater than $P_{\rm max} = 0.1$ during the last tree-walk. This restriction is important only for scattering particles, because annihilating particles are removed from the system as soon as the interaction takes place and therefore their time step becomes meaningless. Although limiting the individual time step makes the Monte Carlo method more computationally costly, it allows for suppression of the probability of having multiple scatterings in the same $\Delta t$, which is an important issue in SIDM simulations.

For simulations with only scattering, the directions and velocities of the scattered particles can also be compared to the expected normalized distributions. The latter can be obtained by transforming the differential cross section from the centre-of-mass frame of the collision to the simulation frame. For isotropic scatterings, these

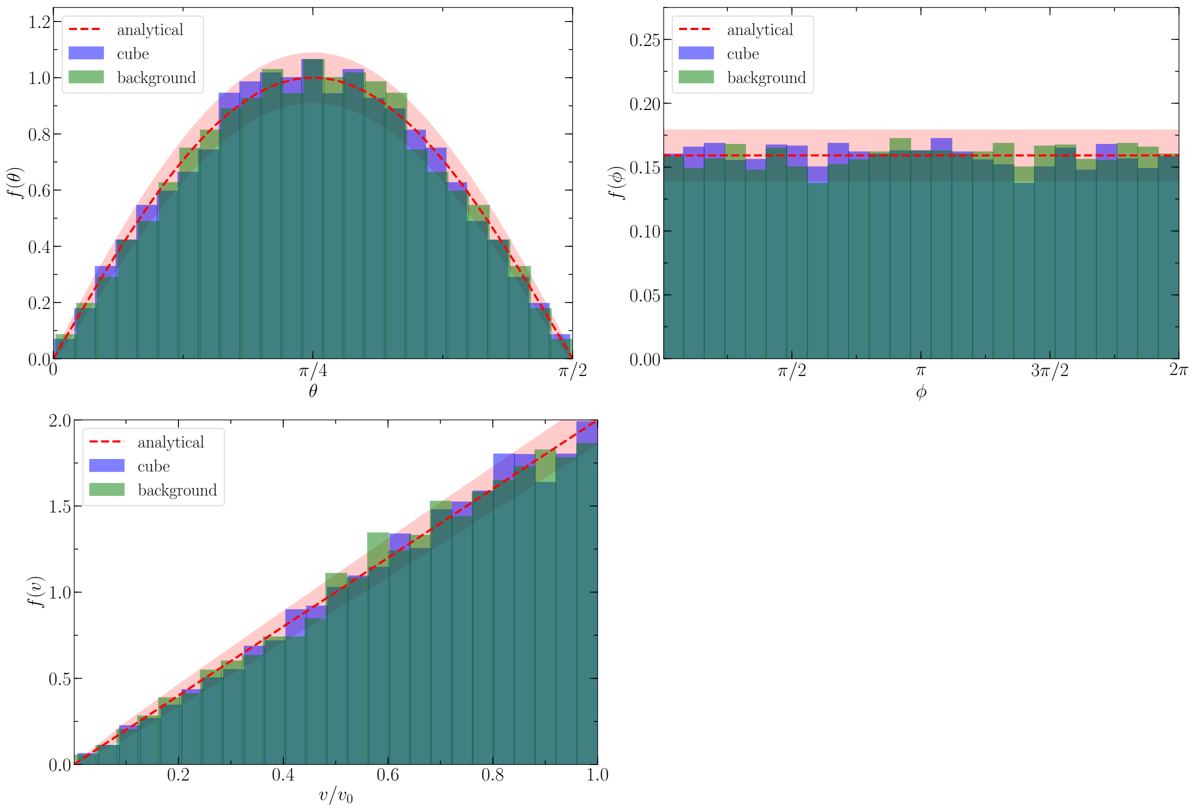


Figure 6.C.2: Distributions of polar and azimuthal angles (top) and velocity magnitude (bottom) of scattered particles in one of our test simulations. The expected results are the red dashed lines, and their $1\sigma$ uncertainty regions are shaded red, computed assuming that the number of particles in each bin is Poisson distributed.

distributions turn out to be the same for both background and cube particles and take a simple form, with $f(\theta) = \sin 2\theta$, $f(\phi) = (2\pi)^{-1}$ and $f(v) = 2v$, where the latter is valid for $v \leq v_0$, and becomes zero otherwise. Fig. 6.C.2 shows the comparison between the expected distributions and those reconstructed from one of our test simulations, which agree to within $1\sigma$ uncertainty.

Another important test of our code is to check whether particle scattering and annihilation are well modeled in isolated DM halos. We focus on halos with Hernquist profile [48], whose density distribution can be written as

$$\rho(r = x\,a) = \frac{\rho_H}{x\,(1+x)^3}\,, \tag{6.74}$$

where $\rho_H \equiv M/(2\pi a^3)$, $M$ is the total halo mass and $a$ the scale radius. We have chosen this type of halo because it has a finite mass without need of truncation and the phase-space distribution function $f(E)$, with $E$ being the particle energy, has an analytic form [48]. The latter property allows to easily generate equilibrium initial conditions for N-body simulations and compute scattering or annihilation quantities analytically. The initial conditions for particle positions and velocities making up our test halos have been generated randomly from the Hernquist distribution function $f(E)$ using the von Neumann rejection method [100], as originally done in Ref. [101]. To prevent centroid motion of the generated DM halo during the simulation, we set its initial centre-of-mass position and velocity to zero by an overall boost.

Since we consider a large range of halo masses in this paper, ranging from $10^{10}$ to $10^{15}$ $M_\odot$, we tested our code with simulated Hernquist halos having different values of $M$ and $a$, finding good agreement between the analytical expectations and the simulation outcomes for all of them. As a prototype example, we focus here just on an isolated Hernquist halo with total mass $M = 10^{14}$ $M_\odot$ and scale radius $a = 225$ kpc. The simulations for such a halo were run with $N = 128^3$ particles, each having mass $m_p \simeq 4.8 \times 10^8$ $M_\odot$, and the Plummer-equivalent gravitational softening length was set to $\epsilon = 4.4$ kpc. We evolved the generated halos with collisionless DM first to study their stability and to check whether cores can form as numerical artifacts. The results for our prototype halo as a function of the simulation time are shown in the top left plot of Fig. 6.C.3. For a suitable choice of time-integration and tree-force accuracy parameters, $\eta = 0.005$ and $\alpha = 0.0012$ respectively, the density and velocity distributions remained unchanged except for the formation of a small constant core with size similar to the gravitational softening length $\epsilon$, as observed by Ref. [50].

When DM scattering is turned on, these cores quickly become larger because particles scatter mostly in high density regions until the cores settle to a size that is independent of the value of $\sigma/m_\chi$ [66]. The right panel of Fig. 6.C.3 shows the results for the density profile of our prototype halo at different simulation times for a constant scattering cross section per unit DM mass of 1.0 $\mathrm{cm}^2/\mathrm{g}$. The resulting

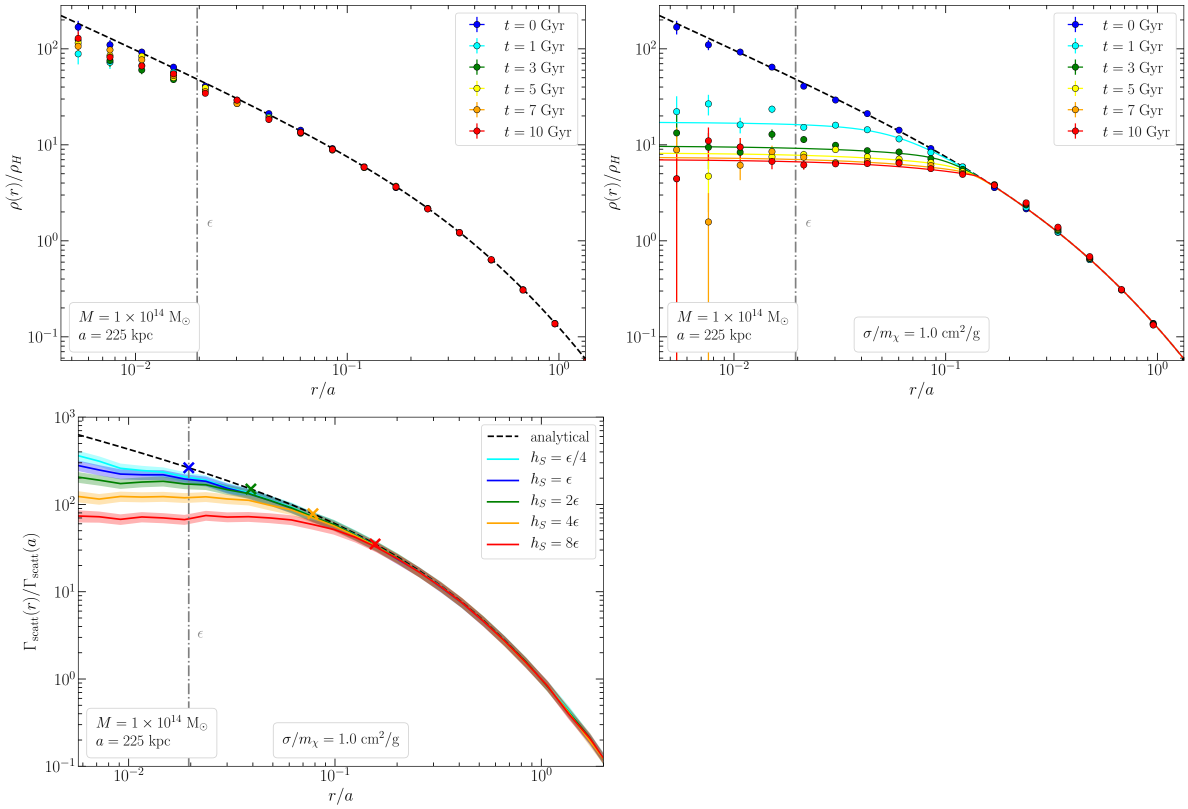


Figure 6.C.3: Top: Radial density profile of a DM halo with Hernquist mass $M = 10^{14}$ M$_\odot$ and radius $a = 225$ kpc as a function of the distance $r$, in units of $\rho_H = M/(2\pi a^3)$ and $a$ respectively. The black dashed line displays the original density profile in eq. (6.74). The left panel shows the halo stability across a time window of 10 Gyr. The right panel shows how the density profile evolves with time assuming particle scattering with constant $\sigma/m_\chi = 1.0$ cm$^2$/g. Here we chose the scatter search radius as $h_S = \epsilon$. The solid lines correspond to the best-fit cored-Hernquist profiles, given by eq. (6.75), where $r_c$ and $\beta$ are left as free parameters. The $1\sigma$ error bar for each data point is computed assuming that the number of particles in each bin is Poisson distributed. Bottom: Extracted scattering rate per particle for the same Hernquist profile DM halo after 3 Gyr, for different choices of the scatter search radius $h_S$, and its comparison with the theoretical expectation. Although the simulations were run with $\sigma/m_\chi = 1.0$ cm$^2$/g, the result is independent of the scattering cross section since a ratio is considered. The colored crosses along the analytical curve correspond to the radius equal to $h_S$. The $1\sigma$ uncertainty for each colored line is computed assuming that the number of particles in each bin is Poisson distributed and displayed with a same-color shaded region. In all three panels, the gray dot-dashed vertical line shows the position of the gravitational softening length $\epsilon$ used in all simulations for the considered halo. We used a time-integration parameter of $\eta = 0.005$ and tree-force accuracy of $\alpha = 0.0012$ in each simulation run.

profiles are well fitted by a cored-Hernquist profile of the form [90]

$$\rho(x) = \frac{\rho_H}{(1+x)^3} \frac{1}{[x^\beta + (r_c/a)^\beta]^{1/\beta}} \,, \tag{6.75}$$

where $x \equiv r/a$, $r_c$ is the core-radius and $\beta$ is an index controlling the sharpness of the transition from $\rho \propto x^{-1}$ to a constant density. Leaving $r_c$ and $\beta$ as free parameters in the fit, we found that their best-fit values across a time evolution of 10 Gyr are $r_c/a \in (0.06, 0.14)$ and $\beta \in (3.5, 62.0)$, in agreement with refs. [66, 90].

The results shown in the right panel of Fig. 6.C.3 have been obtained by choosing the scatter search radius equal to the gravitational softening length in the computation of the scattering probability, given by eq. (6.60). This was done in light of the result shown in the bottom panel of Fig. 6.C.3, where the scattering rate extracted from simulations is compared to the analytical prediction. In particular, the latter can be computed by integrating eq. (6.58) over the velocity distribution function, obtaining the average rate for particles at position $\vec{r}$ [50]

$$\Gamma_{\rm scatt}(\vec{r}) = \frac{\langle \sigma\, v_{\rm pair}\rangle(\vec{r})\, \rho(\vec{r})}{m_\chi} \,, \tag{6.76}$$

where $\rho(\vec{r})$ is given by eq. (6.74) and $\langle \sigma\, v_{\rm pair}\rangle = \sigma\, \langle v_{\rm pair}\rangle$ if the scattering cross section is velocity-independent. The mean pairwise particle velocity $\langle v_{\rm pair}\rangle$ can be computed from the one-dimensional velocity dispersion $\sigma_{1D}$ for Hernquist halos [48]

$$\begin{aligned} \sigma_{1D}^2 = \frac{G\,M}{12\,a} \Bigg\{ & 12\,x\,(1+x)^3\, \ln\left(\frac{1+x}{x}\right) \\ & - \frac{x}{1+x}\left[25 + 52\,x + 42\,x^2 + 12\,x^3\right] \Bigg\} \end{aligned} \tag{6.77}$$

as $\langle v_{\rm pair}\rangle = (4/\sqrt{\pi})\,\sigma_{1D}$, where we have assumed the velocities are isotropic and follow a Maxwell-Boltzmann distribution. From simulations, the scattering rate per particle as a function of the radius $r$ can be estimated as the ratio between the number of particles that have scattered within the radial bin including $r$, and the time averaged number of particles within the same bin [50]. To avoid any modification of the density profile and velocity distribution due to DM self-interactions that would lead the scattering rate not to follow the analytic prediction, we turned off the change in the momenta of the scattered particles in the simulations used in the bottom panel of Fig. 6.C.3.

Such a plot clearly shows that our code accurately reproduces the scattering rate within the halo except for distances less than $h_S$, where the extracted rate falls below the analytic result. This can be explained by the fact that the scatter search radius acts as a scale below which the particle density entering the scattering probability becomes smooth, preventing a faithful reconstruction of the real density. Although it suggests choosing a small value of $h_S$ in order to correctly capture the scattering dynamics in small high-density regions, there is a natural lower bound for $h_S$ set by the gravitational softening length $\epsilon$. As we have found in simulation runs for collisionless DM, the density gets affected by a small core of size of the order of the softening length, which arises from smoothing the gravitational potential at $r < \epsilon$ and thus the particle distribution at these scales. This explains why $\Gamma_{\rm scatt}$ ceases to change for scales smaller than $\epsilon$ in simulations where $h_S < \epsilon$, as displayed in the bottom panel of Fig. 6.C.3. Therefore, reducing $h_S$ to values below $\epsilon$ cannot improve the agreement between the extracted rate and the analytic result, but rather it tends to create probability saturation problems that can be solved by choosing smaller time steps or a time-step delimiter, as already discussed above. Considering all these factors and the results in the bottom panel of Fig. 6.C.3, we find that setting $h_S = \epsilon$ provides the best reconstruction of scattering dynamics at low scales, and it limits the occurrence of events where the scattering probability becomes greater than unity.

With the same Hernquist halos it is possible to also test the goodness of our annihilation algorithm. For instance, the annihilation rate extracted from simulations can be compared to the analytic result, which is given by eq. (6.76) with the replacement of $\langle \sigma \, v_{\rm pair} \rangle$ with $\langle \sigma_{\rm ann} \, v \rangle$. The extracted annihilation rate as a function of the radius $r$ has been obtained in the same way as done for scattering events, namely as the ratio between the number of annihilated particles located in the radial bin including $r$ and the time averaged number of particles within the same bin. To allow for a direct

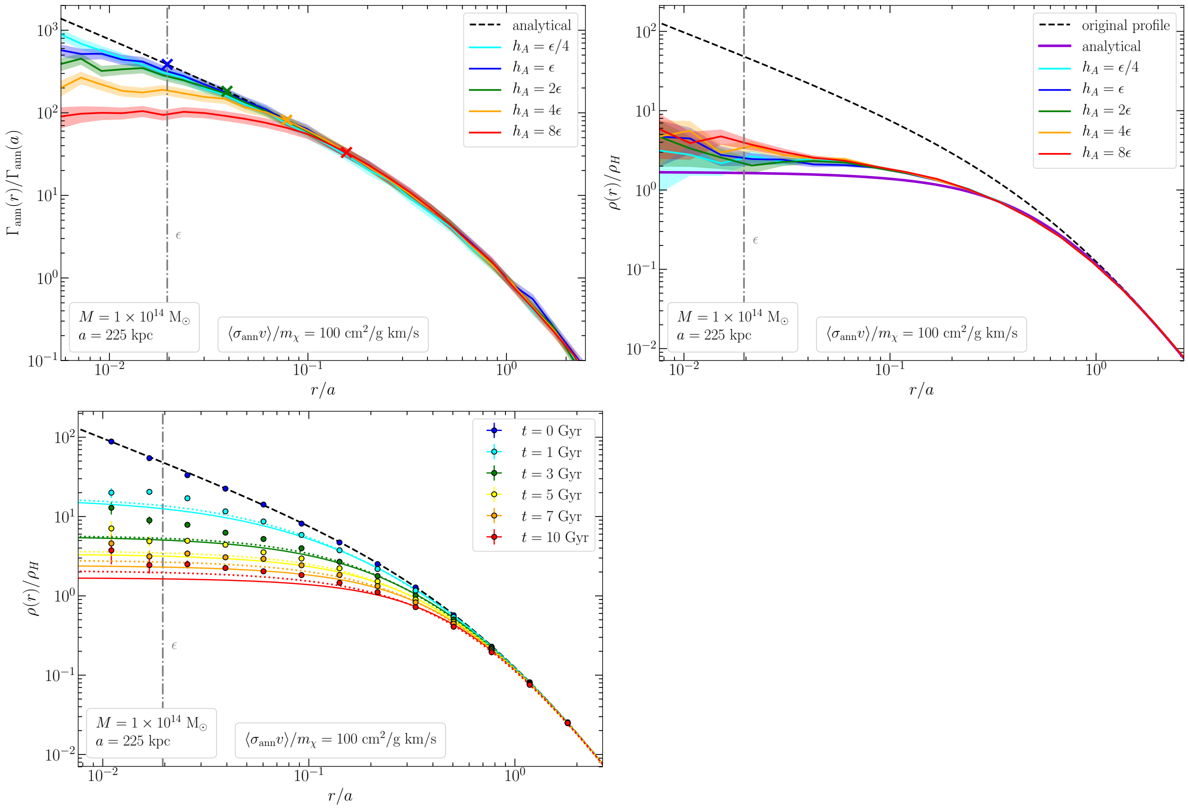


Figure 6.C.4: Top left: Similar to the bottom panel of Fig. 6.C.3, but for the extracted annihilation rate per particle and different choices of the annihilation search radius $h_A$. The simulations for the prototype Hernquist halo were run with $\langle\sigma_{\rm ann} v\rangle/m_\chi = 100$ cm$^2$/g km/s. Top right: Radial density profile of the prototype Hernquist halo undergoing DM annihilation for 10 Gyr, for different choices of $h_A$. The black dashed line displays the original density profile in eq. (6.74). The violet solid line corresponds to the theoretical prediction given by eq. (6.80) at $(t - t_{\rm ini}) = 10$ Gyr. Bottom: Similar to the right panel of Fig. 6.C.3, but for particle annihilation with the same constant velocity-averaged cross section considered above. Here we chose the annihilation search radius as $h_A = \epsilon$. Each colored solid curve shows the analytical expectation given by eq. (6.80) at the time of the corresponding same-color data points. The dotted lines represent the best-fit cored-Hernquist profiles, given by eq. (6.75), where $r_c$ and $\beta$ are left as free parameters.

comparison to the analytical result we did not remove the annihilated particles from the system, but the annihilation algorithm was used to count and localize the particles that actually annihilate. The results from this comparison are shown in the top left panel of Fig. 6.C.4, where we have chosen a constant ($s$-wave) velocity-averaged annihilation cross section per unit DM mass of 100 cm$^2$/g km/s. Similarly to what was observed in the scattering case, choosing an annihilation search radius $h_A$ equal to the gravitational softening length $\epsilon$ provides the best reconstruction of the annihilation rate. This is because the particle distribution at scales below $h_A$ and $\epsilon$ are smoothed, leading to a decreased annihilation rate compared to the true unsmoothed one.

The effect that DM annihilation has on the time evolution of the halo density profile was first studied by Ref. [22], which proposed the following analytic formula for $\rho(r,t)$

$$\frac{d}{dt}\left(\frac{\rho(r,t)}{\rho_A}\right) = -\frac{1}{t_0}\left(\frac{\rho(r,t)}{\rho_A}\right)^2, \tag{6.78}$$

where $\rho_A \equiv m_\chi/(\langle\sigma_{\rm ann}\, v\rangle\, t_0)$ and $t_0$ is the age of the Universe today. This equation comes directly from the definition of the DM annihilation rate and can be easily adapted to our simulation setup, where the annihilation probability is given by eq. (6.68), by replacing $\rho_A$ with $\rho_A/2$. The factor $1/2$ arises because the halo density is reduced by two units of the simulation particle mass in each annihilation event. The general solution of eq. (6.78) is given by

$$\begin{aligned} \rho(r,t) &= \left[\frac{1}{\rho_{\rm core}(t)} + \frac{1}{\rho(r,t_{\rm ini})}\right]^{-1}, \\ \rho_{\rm core}(t) &\equiv \frac{m_\chi}{2\,\langle\sigma_{\rm ann}\, v\rangle\,(t-t_{\rm ini})}, \end{aligned} \tag{6.79}$$

where the latter definition is valid for our simulations and $t_{\rm ini}$ is the initial time, which can be taken as the time when the simulation starts and the density profile is $\rho(r,t_{\rm ini})$. One observes that the core density $\rho_{\rm core}(t)$ is generally greater than $\rho_A$ and the equality is reached when $(t-t_{\rm ini}) = t_0$.

Focusing on just DM halos with initial Hernquist profile and taking $t_{\rm ini} = 0$, we find that the density profile of halos undergoing DM annihilation should be described after a time $t$ by

$$\rho(x,t) = \frac{\rho_H}{x\,(1+x)^3 + \rho_H/\rho_{\rm core}(t)} \tag{6.80}$$

with $x \equiv r/a$, which has been obtained by substituting eq. (6.74) into eq. (6.79). The halo density is therefore characterized by a core of constant density $\rho_{\rm core}(t)$ at small scales. The bottom panel of Fig. 6.C.4 shows the evolution of the density profile of the prototype Hernquist halo in the simulation at different times $t$ and its comparison with the theoretical prediction.

Although the data points and the solid lines given by eq. (6.80) match very well at large radii, there is some disagreement at small distances. These differences are not eliminated by changing the annihilation search radius, as shown by the right panel of Fig. 6.C.4, where the analytical prediction is compared to the simulation outcome at $t = 10$ Gyr for different values of $h_A$. A graphical comparison between the analytical curve and the colored lines suggests that eq. (6.80) does not provide a good fit to the simulation data at low scales, independently of the choice of $h_A$, although it accurately captures the physics at large radii. We confirmed this observation by fitting the simulation data with eq. (6.80), in which $\rho_{\rm core}(t)$ was left as a free parameter, leading to agreement within $1\sigma$ between the best fit value and that computed by eq. (6.79) at different times $t$, independently of the value of $h_A$.

In analogy to the case of scattering, as shown in the top right panel of Fig. 6.C.3, we investigated the cored-Hernquist profile function given by eq. (6.75) for fitting the annihilation data displayed in the bottom panel of Fig. 6.C.4, leaving $r_c$ and $\beta$ as free parameters. The results of this fit are shown with colored dotted lines in the same panel, with best-fit values $r_c/a \in (0.06, 0.48)$ and $\beta \in (1.2, 2.0)$. They do not give significant improvement with respect to eq. (6.80).

## 6.D Upper bounds for the DM-number violating mass

In this appendix, we will investigate the upper bound on the Majorana mass $\delta m$. This parameter determines the timescale on which annihilations recouple after the initial asymmetric dark matter freezeout epoch. For convenience, we define $\alpha = Y_{11} - Y_{22}, \beta = Y_{12} - Y_{21}, \theta = Y_{12} + Y_{21}$, $\gamma = Y_{11} + Y_{22}$, $s = \bar{s} m_\chi^3/x^3$, $H = \kappa m_\chi^2/x^2$, where $\bar{s} = \frac{2\pi^2}{45} g_{*s}$, $\kappa = \frac{1.66}{M_p}\sqrt{g_*}$.

### 6.D.1 Flavor-blind interactions

From the Boltzmann equations after freeze-out we get

$$x^2\beta' - \left(\frac{\bar{s}\,\langle\sigma v\rangle_a\,m_\chi}{\kappa}\eta_{DM}\right)\beta - \left(\frac{2i\delta m}{\kappa\,m_\chi^2}\eta_{DM}\right)x^3 = 0, \tag{6.81}$$

with $\beta(\bar{x}) = 0$ as initial condition. Here we used $\alpha \approx Y_{11} \approx \eta_{DM}$ (this does not imply $\alpha' = 0$), as we are working before the moment of residual annihilations. The solution to this equation can be approximated to $\beta(x) \approx iBx(A+x)/2$, where

$$A \equiv \frac{\bar{s}\,\langle\sigma v\rangle_a\,m_\chi}{\kappa}\eta_{DM}, \qquad B \equiv \frac{2\,\delta m}{\kappa\,m_\chi^2}\eta_{DM}. \tag{6.82}$$

Plugging this result into the Boltzmann equations for $Y_{11}$ and $Y_{22}$, we get

$$\begin{aligned} 16\,\eta_{DM}\,Y_{11}' &= B^2(A+x)\left(A(A+x)-4\right), \\ 16\,\eta_{DM}\,Y_{22}' &= B^2(A+x)\left(A(A+x)+4\right), \end{aligned} \tag{6.83}$$

with initial conditions $Y_{11}(\bar{x}) = \eta_{DM}$ and $Y_{22}(\bar{x}) = 0$.

Taking the solutions for $Y_{11}$ and $Y_{22}$ and solving for $x$ when $Y_{11}(\bar{\bar{x}}) = Y_{22}(\bar{\bar{x}})$ gives

$$\bar{\bar{x}} = 1.53\frac{m_\chi}{\sqrt{\delta m\,M_p}}g_*^{1/4}. \tag{6.84}$$

Now that we have found $\gamma = Y_{11} + Y_{22}$ near the epoch of residual annihilations, let us calculate how much it can deviate from $\eta_{DM}$. Defining the fractional change in the dark matter comoving density from $\gamma = \eta_{DM}\,(1-\delta_\eta)$, we get

$$\delta m \lesssim \frac{342}{\sqrt{g_*}}\frac{\delta_\eta^{1/2}}{\langle\sigma v\rangle_a^2\,\eta_{DM}^2 M_p^3}, \tag{6.85}$$

for $x > \bar{\bar{x}}$. As a numerical example, for our set of parameters and taking $\delta_\eta \simeq 3\%$ (as limited by the change in the dark matter density after the formation of the CMB [27]), we get $\delta m \lesssim 3 \times 10^{-30}$ eV. This bound will be relaxed if the second epoch of annihilation freezes out before the formation of the CMB [28].

### 6.D.2 Flavor-sensitive interactions

In this case, the equation for $\beta$ reads

$$x^{5/2}\beta' + \left(\frac{3I_s g'^4 m_\chi^3 \bar{s}\,\eta_{DM}}{8\pi\kappa m_V^4}\right)\beta - \left(\frac{2i\delta m\,\eta_{DM}}{\kappa m_\chi^2}\right)x^{7/2} = 0 \tag{6.86}$$

where we considered $\alpha \approx \eta_{DM}$ and

$$\langle\sigma v\rangle_s = \frac{I_s g'^4 m_\chi^2}{4\pi m_V^4}\frac{1}{\sqrt{x}} = \overline{\langle\sigma v\rangle}_s \frac{1}{\sqrt{x}}. \tag{6.87}$$

This time, $A$ is redefined to

$$A \equiv \frac{3I_s g'^4 m_\chi^3 \bar{s}\,\eta_{DM}}{8\pi\kappa m_V^4}. \tag{6.88}$$

Working with our set of parameters, it is possible to approximate the solution of eq. (6.86) to

$$\beta(x) \approx i\left(\frac{2}{3}\right)^{7/3} A^{4/3} B\,\Gamma\left(-\frac{4}{3}, \frac{2A}{3x^{3/2}}\right), \tag{6.89}$$

where the incomplete gamma function is defined by $\Gamma(a,z) = \int_z^\infty t^{a-1}e^{-t}dt$. Now we can use this result and solve for $\alpha$. Taking the limit $\Gamma(s,r)/r^s = -1/s$ when $r \to 0$ for $Re(s) < 0$, we get

$$\alpha(x) = \eta_{DM}\left(1 - \frac{\delta m^2}{2\kappa^2 m_\chi^4}x^4\right). \tag{6.90}$$

Solving $\alpha = 0$ for $x$ gives us the previous result of eq. (6.84).

Now, let us rearrange the Boltzmann equations as an equation for the total DM comoving density $\gamma$

$$xH\gamma' = -\frac{1}{2}\langle\sigma v\rangle_a\, s\left(\gamma^2 - \Upsilon^2\right) \tag{6.91}$$

and an equation for its "late-time equilibrium" function $\Upsilon = \frac{\sqrt{f(x)}}{2\delta m}$,

$$f' = -3\overline{\langle\sigma v\rangle}_s \frac{s}{\sqrt{x}}\eta_{DM} x H(\alpha')^2, \tag{6.92}$$

where

$$f = (xH\alpha')^2 + 4\delta m^2\alpha^2. \tag{6.93}$$

We will not attempt to solve the full set of equations from before freeze-out to today. Instead, let's try to evolve our functions from their states in the flat land to new states in the region of residual annihilations.

As we are working with smaller and smaller values of $\delta m$, let us explore what happens when $\delta m \to 0$. In this limit, there should be no residual annihilations, i.e. the total DM density must follow a constant equilibrium function, $\lim_{\delta m \to 0} \Upsilon = \eta_{DM}$. Consequently,

$$\lim_{\delta m \to 0} f(x) = 4\delta m^2 \eta_{DM}^2. \tag{6.94}$$

From this result, and equations (6.92) and (6.93) we get, $\alpha' \to 0$ and $\alpha \to \eta_{DM}$, in this limit. Also, $\beta \to 0$. Thus, $\Upsilon^2 \to \alpha^2$. Now, eq. (6.90) was obtained using $\alpha \approx \eta_{DM}$. Performing the inverse substitution we get

$$\alpha(z) = \frac{\eta_{DM}}{\left(1 + \frac{z^2}{2}\right)}, \tag{6.95}$$

where we defined $z \equiv \frac{\delta m}{\kappa m_\chi^2} x^2$. From now on, we will use $z$ instead of $x$. For example, from eq. (6.90), the moment when $Y_{11} = Y_{22}$, i.e. $\alpha = 0$ , is given by $z = \sqrt{2}$. Now, the equation we need to solve is,

$$z^{3/2}\delta_\eta'(z) = W\,\eta_{DM}\left[1 - 2\delta_\eta(z) - \frac{1}{\left(1 + \frac{z^2}{2}\right)^2}\right], \tag{6.96}$$

where we have parametrized the total DM density as $\gamma = \eta_{DM}(1 - \delta_\eta)$, where $\delta_\eta \ll 1$ and we have used $(1 - \delta_\eta)^2 \approx 1 - 2\delta_\eta$. Also, we defined

$$W \equiv \frac{\langle \sigma v \rangle_a\, \bar{s}}{4\kappa^{3/2}} \sqrt{\delta m} = \overline{W}\sqrt{\delta m}. \tag{6.97}$$

To a good approximation, we obtain

$$\delta_\eta(z) \approx \frac{\overline{W}\,\eta_{DM}}{2}\sqrt{\delta m}\frac{z^{3/2}}{2 + z^2}. \tag{6.98}$$

In this way,

$$\delta m \approx \frac{1521}{\sqrt{g_*}} \frac{\delta_\eta^2}{\langle\sigma v\rangle_a^2 \eta_{DM}^2 M_p^3} \frac{(2+z^2)^2}{z^3}. \tag{6.99}$$

Before getting an upper bound for $\delta m$, let us go back to eq. (6.92) and eq. (6.93). These can be merged into

$$x^{5/2}\alpha'' + \left(2A - x^{3/2}\right)\alpha' + \left(\frac{B}{\eta_{DM}}\right)^2 x^{9/2}\alpha = 0. \tag{6.100}$$

We notice there is a dramatic change in this equation when the damping term changes sign. For this reason, we will take

$$\bar{\bar{x}} = \left[\frac{3}{1.66\sqrt{g_*}}\overline{\langle\sigma v\rangle}_s \bar{s}\, m_\chi M_p\, \eta_{DM}\right]^{2/3} \tag{6.101}$$

as a better approximation for the starting point for residual annihilations. Numerically, this gives us $\bar{\bar{z}} \ll 1$, so we can make the following approximation

$$\frac{(2+\bar{\bar{z}}^2)^2}{\bar{\bar{z}}^3} \to \frac{4}{\bar{\bar{z}}^3}. \tag{6.102}$$

Since this is our starting point, for any $z > \bar{\bar{z}}$ we have from eq. (6.99)

$$\delta m < 16.3 \frac{m_\chi^{1/2}}{g_*^{1/4}} \frac{\delta_\eta^{1/2}}{\overline{\langle\sigma v\rangle}_s \langle\sigma v\rangle_a^{1/2} \eta_{DM}^{3/2} M_p^{5/2}}. \tag{6.103}$$

As we can see, for a fixed $\delta m$, the change in the DM comoving density $\delta_\eta$ goes to zero when we turn off scatterings. For our parameters, we obtain $\delta m < 5 \times 10^{-28}$ eV.

# Bibliography


[1] P. Salucci, "The distribution of dark matter in galaxies," *Astron. Astrophys. Rev.* **27** no. 1, (2019) 2, `arXiv:1811.08843 [astro-ph.GA]`.

[2] D. H. Weinberg, J. S. Bullock, F. Governato, R. Kuzio de Naray, and A. H. G.

Peter, "Cold dark matter: controversies on small scales," *Proc. Nat. Acad. Sci.* **112** (2015) 12249–12255, `arXiv:1306.0913 [astro-ph.CO]`.

[3] D. N. Spergel and P. J. Steinhardt, "Observational evidence for selfinteracting cold dark matter," *Phys. Rev. Lett.* **84** (2000) 3760–3763, `arXiv:astro-ph/9909386`.

[4] S. Tulin and H.-B. Yu, "Dark Matter Self-interactions and Small Scale Structure," *Phys. Rept.* **730** (2018) 1–57, `arXiv:1705.02358 [hep-ph]`.

[5] M. Markevitch, A. Gonzalez, D. Clowe, A. Vikhlinin, L. David, W. Forman, C. Jones, S. Murray, and W. Tucker, "Direct constraints on the dark matter self-interaction cross-section from the merging galaxy cluster 1E0657-56," *Astrophys. J.* **606** (2004) 819–824, `arXiv:astro-ph/0309303`.

[6] S. Y. Kim, A. H. Peter, and D. Wittman, "In the Wake of Dark Giants: New Signatures of Dark Matter Self Interactions in Equal Mass Mergers of Galaxy Clusters," *Mon. Not. Roy. Astron. Soc.* **469** no. 2, (2017) 1414–1444, `arXiv:1608.08630 [astro-ph.CO]`.

[7] M. Rocha, A. H. Peter, J. S. Bullock, M. Kaplinghat, S. Garrison-Kimmel, J. Onorbe, and L. A. Moustakas, "Cosmological Simulations with Self-Interacting Dark Matter I: Constant Density Cores and Substructure," *Mon. Not. Roy. Astron. Soc.* **430** (2013) 81–104, `arXiv:1208.3025 [astro-ph.CO]`.

[8] M. Vogelsberger, J. Zavala, and A. Loeb, "Subhaloes in Self-Interacting Galactic Dark Matter Haloes," *Mon. Not. Roy. Astron. Soc.* **423** (2012) 3740, `arXiv:1201.5892 [astro-ph.CO]`.

[9] M. Kaplinghat, S. Tulin, and H.-B. Yu, "Dark Matter Halos as Particle Colliders: Unified Solution to Small-Scale Structure Puzzles from Dwarfs to Clusters," *Phys. Rev. Lett.* **116** no. 4, (2016) 041302, `arXiv:1508.03339 [astro-ph.CO]`.

[10] S. D. McDermott, "Is Self-Interacting Dark Matter Undergoing Dark Fusion?," *Phys. Rev. Lett.* **120** no. 22, (2018) 221806, `arXiv:1711.00857 [hep-ph]`.

[11] X. Chu, C. Garcia-Cely, and H. Murayama, "Velocity Dependence from Resonant Self-Interacting Dark Matter," *Phys. Rev. Lett.* **122** no. 7, (2019) 071103, `arXiv:1810.04709 [hep-ph]`.

[12] X. Chu, C. Garcia-Cely, and H. Murayama, "A Practical and Consistent Parametrization of Dark Matter Self-Interactions," *JCAP* **06** (2020) 043, `arXiv:1908.06067 [hep-ph]`.

[13] Y.-D. Tsai, R. McGehee, and H. Murayama, "Resonant Self-Interacting Dark Matter from Dark QCD," `arXiv:2008.08608 [hep-ph]`.

[14] X. Chu, C. Garcia-Cely, and H. Murayama, "Finite-size dark matter and its effect on small-scale structure," *Phys. Rev. Lett.* **124** no. 4, (2020) 041101, `arXiv:1901.00075 [hep-ph]`.

[15] X. Chu and C. Garcia-Cely, "Core formation from self-heating dark matter," *JCAP* **07** (2018) 013, `arXiv:1803.09762 [hep-ph]`.

[16] A. Kamada and H. J. Kim, "Escalating core formation with dark matter self-heating," *Phys. Rev. D* **102** no. 4, (2020) 043009, `arXiv:1911.09717 [hep-ph]`.

[17] A. Kamada, H. J. Kim, H. Kim, and T. Sekiguchi, "Self-Heating Dark Matter via Semiannihilation," *Phys. Rev. Lett.* **120** no. 13, (2018) 131802, `arXiv:1707.09238 [hep-ph]`.

[18] A. Kamada, H. J. Kim, and H. Kim, "Self-heating of Strongly Interacting Massive Particles," *Phys. Rev. D* **98** no. 2, (2018) 023509, `arXiv:1805.05648 [hep-ph]`.

[19] A. Kamada, H. J. Kim, and T. Kuwahara, "Maximally self-interacting dark matter: models and predictions," `arXiv:2007.15522 [hep-ph]`.

[20] E. Braaten, D. Kang, and R. Laha, "Production of dark-matter bound states in the early universe by three-body recombination," *JHEP* **11** (2018) 084, arXiv:1806.00609 [hep-ph].

[21] E. Braaten, D. Kang, and R. Laha, "Dark Matter Bound States from Three-Body Recombination," *Springer Proc. Phys.* **238** (2020) 1001–1006, arXiv:1905.04558 [hep-ph].

[22] M. Kaplinghat, L. Knox, and M. S. Turner, "Annihilating the cold dark matter cusp crisis," *Phys. Rev. Lett.* **85** (2000) 3335, arXiv:astro-ph/0005210.

[23] T. Cohen and K. M. Zurek, "Leptophilic Dark Matter from the Lepton Asymmetry," *Phys. Rev. Lett.* **104** (2010) 101301, arXiv:0909.2035 [hep-ph].

[24] M. R. Buckley and S. Profumo, "Regenerating a symmetry in asymmetric dark matter," *Phys. Rev. Lett.* **108** (Jan, 2012) 011301. https://link.aps.org/doi/10.1103/PhysRevLett.108.011301.

[25] M. Cirelli, P. Panci, G. Servant, and G. Zaharijas, "Consequences of DM/antiDM Oscillations for Asymmetric WIMP Dark Matter," *JCAP* **03** (2012) 015, arXiv:1110.3809 [hep-ph].

[26] S. Tulin, H.-B. Yu, and K. M. Zurek, "Oscillating Asymmetric Dark Matter," *JCAP* **05** (2012) 013, arXiv:1202.0283 [hep-ph].

[27] V. Poulin, P. D. Serpico, and J. Lesgourgues, "A fresh look at linear cosmological constraints on a decaying dark matter component," *JCAP* **08** (2016) 036, arXiv:1606.02073 [astro-ph.CO].

[28] T. Bringmann, F. Kahlhoefer, K. Schmidt-Hoberg, and P. Walia, "Converting nonrelativistic dark matter to radiation," *Phys. Rev. D* **98** no. 2, (2018) 023543, arXiv:1803.03644 [astro-ph.CO].

[29] A. B. Newman, T. Treu, R. S. Ellis, D. J. Sand, C. Nipoti, J. Richard, and E. Jullo, "The Density Profiles of Massive, Relaxed Galaxy Clusters: I. The Total Density Over 3 Decades in Radius," *Astrophys. J.* **765** (2013) 24, arXiv:1209.1391 [astro-ph.CO].

[30] B. Bellazzini, M. Cliche, and P. Tanedo, "Effective theory of self-interacting dark matter," *Phys. Rev. D* **88** no. 8, (2013) 083506, arXiv:1307.1129 [hep-ph].

[31] F. Kahlhoefer, K. Schmidt-Hoberg, and S. Wild, "Dark matter self-interactions from a general spin-0 mediator," *JCAP* **08** (2017) 003, arXiv:1704.02149 [hep-ph].

[32] P. Agrawal, A. Parikh, and M. Reece, "Systematizing the Effective Theory of Self-Interacting Dark Matter," *JHEP* **10** (2020) 191, arXiv:2003.00021 [hep-ph].

[33] N. Blinov, C. Keith, and D. Hooper, "Warm Decaying Dark Matter and the Hubble Tension," *JCAP* **06** (2020) 005, arXiv:2004.06114 [astro-ph.CO].

[34] G. F. Abellan, R. Murgia, V. Poulin, and J. Lavalle, "Hints for decaying dark matter from $S_8$ measurements," arXiv:2008.09615 [astro-ph.CO].

[35] R. H. Cyburt, B. D. Fields, K. A. Olive, and T.-H. Yeh, "Big Bang Nucleosynthesis: 2015," *Rev. Mod. Phys.* **88** (2016) 015004, arXiv:1505.01076 [astro-ph.CO].

[36] B. D. Fields, K. A. Olive, T.-H. Yeh, and C. Young, "Big-Bang Nucleosynthesis After Planck," *JCAP* **03** (2020) 010, arXiv:1912.01132 [astro-ph.CO].

[37] **Planck** Collaboration, N. Aghanim *et al.*, "Planck 2018 results. VI. Cosmological parameters," arXiv:1807.06209 [astro-ph.CO].

[38] P. Adshead, Y. Cui, and J. Shelton, "Chilly Dark Sectors and Asymmetric Reheating," *JHEP* **06** (2016) 016, `arXiv:1604.02458 [hep-ph]`.

[39] P. Adshead, P. Ralegankar, and J. Shelton, "Reheating in two-sector cosmology," *JHEP* **08** (2019) 151, `arXiv:1906.02755 [hep-ph]`.

[40] D. Green *et al.*, "Messengers from the Early Universe: Cosmic Neutrinos and Other Light Relics," *Bull. Am. Astron. Soc.* **51** no. 7, (2019) 159, `arXiv:1903.04763 [astro-ph.CO]`.

[41] E. L. Lokas and G. A. Mamon, "Properties of spherical galaxies and clusters with an NFW density profile," *Mon. Not. Roy. Astron. Soc.* **321** (2001) 155, `arXiv:astro-ph/0002395`.

[42] A. Kamada, M. Kaplinghat, A. B. Pace, and H.-B. Yu, "How the Self-Interacting Dark Matter Model Explains the Diverse Galactic Rotation Curves," *Phys. Rev. Lett.* **119** no. 11, (2017) 111102, `arXiv:1611.02716 [astro-ph.GA]`.

[43] C. Carignan and K. C. Freeman, "DDO 154: A "Dark" Galaxy?," *Astrophys. J. L.* **332** (1988) L33.

[44] S.-H. Oh *et al.*, "High-resolution mass models of dwarf galaxies from LITTLE THINGS," *Astron. J.* **149** (2015) 180, `arXiv:1502.01281 [astro-ph.GA]`.

[45] A. A. Dutton and A. V. Macció, "Cold dark matter haloes in the Planck era: evolution of structural parameters for Einasto and NFW profiles," *Mon. Not. Roy. Astron. Soc.* **441** no. 4, (2014) 3359–3374, `arXiv:1402.7073 [astro-ph.CO]`.

[46] V. Springel, "The Cosmological simulation code GADGET-2," *Mon. Not. Roy. Astron. Soc.* **364** (2005) 1105–1134, `arXiv:astro-ph/0505010`.

[47] V. Springel, N. Yoshida, and S. D. White, "GADGET: A Code for collisionless and gasdynamical cosmological simulations," *New Astron.* **6** (2001) 79, `arXiv:astro-ph/0003162`.

[48] L. Hernquist, "An Analytical Model for Spherical Galaxies and Bulges," *Astrophys. J.* **356** (1990) 359.

[49] V. Springel, T. Di Matteo, and L. Hernquist, "Modeling feedback from stars and black holes in galaxy mergers," *Mon. Not. Roy. Astron. Soc.* **361** (2005) 776–794, `arXiv:astro-ph/0411108`.

[50] A. Robertson, R. Massey, and V. Eke, "What does the Bullet Cluster tell us about self-interacting dark matter?," *Mon. Not. Roy. Astron. Soc.* **465** no. 1, (2017) 569–587, `arXiv:1605.04307 [astro-ph.CO]`.

[51] A. B. Newman, T. Treu, R. S. Ellis, and D. J. Sand, "The density profiles of massive, relaxed galaxy clusters. ii. separating luminous and dark matter in cluster cores," *Astrophys. J.* **765** (2013) 25, `arXiv:1209.1392 [astro-ph.CO]`.

[52] L. Sagunski, S. Gad-Nasr, B. Colquhoun, A. Robertson, and S. Tulin, "Velocity-dependent Self-interacting Dark Matter from Groups and Clusters of Galaxies," `arXiv:2006.12515 [astro-ph.CO]`.

[53] A. Eliasdottir, M. Limousin, J. Richard, J. Hjorth, J.-P. Kneib, P. Natarajan, K. Pedersen, E. Jullo, and D. Paraficz, "Where is the matter in the Merging Cluster Abell 2218?," `arXiv:0710.5636 [astro-ph]`.

[54] G. Chabrier, "Galactic stellar and substellar initial mass function," *Publ. Astron. Soc. Pac.* **115** (2003) 763–796, `arXiv:astro-ph/0304382`.

[55] J. Read, M. Walker, and P. Steger, "The case for a cold dark matter cusp in Draco," *Mon. Not. Roy. Astron. Soc.* **481** no. 1, (2018) 860–877, `arXiv:1805.06934 [astro-ph.GA]`.

[56] K. Hayashi, M. Chiba, and T. Ishiyama, "Diversity of dark matter density profiles in the Galactic dwarf spheroidal satellites," `arXiv:2007.13780 [astro-ph.GA]`.

[57] K. Hayashi, M. Ibe, S. Kobayashi, Y. Nakayama, and S. Shirai, "Probing Dark Matter Self-interaction with Ultra-faint Dwarf Galaxies," arXiv:2008.02529 [astro-ph.CO].

[58] J. Kummer, M. Brüggen, K. Dolag, F. Kahlhoefer, and K. Schmidt-Hoberg, "Simulations of core formation for frequent dark matter self-interactions," *Mon. Not. Roy. Astron. Soc.* **487** no. 1, (2019) 354–363, arXiv:1902.02330 [astro-ph.CO].

[59] V. H. Robles, T. Kelley, J. S. Bullock, and M. Kaplinghat, "The Milky Way's halo and subhaloes in self-interacting dark matter," *Mon. Not. Roy. Astron. Soc.* **490** no. 2, (2019) 2117–2123, arXiv:1903.01469 [astro-ph.GA].

[60] O. Sameie, H.-B. Yu, L. V. Sales, M. Vogelsberger, and J. Zavala, "Self-Interacting Dark Matter Subhalos in the Milky Way's Tides," *Phys. Rev. Lett.* **124** no. 14, (2020) 141102, arXiv:1904.07872 [astro-ph.GA].

[61] F. Kahlhoefer, M. Kaplinghat, T. R. Slatyer, and C.-L. Wu, "Diversity in density profiles of self-interacting dark matter satellite halos," *JCAP* **12** (2019) 010, arXiv:1904.10539 [astro-ph.GA].

[62] C. A. Correa, "Constraining Velocity-dependent Self-Interacting Dark Matter with the Milky Way's dwarf spheroidal galaxies," *arXiv e-prints* (July, 2020) arXiv:2007.02958, arXiv:2007.02958 [astro-ph.GA].

[63] P. Gondolo and G. Gelmini, "Cosmic abundances of stable particles: Improved analysis," *Nucl. Phys. B* **360** (1991) 145–179.

[64] M. Vogelsberger, J. Zavala, K. Schutz, and T. R. Slatyer, "Evaporating the Milky Way halo and its satellites with inelastic self-interacting dark matter," arXiv:1805.03203 [astro-ph.GA].

[65] J. J. Monaghan and J. C. Lattanzio, "A refined particle method for astrophysical problems," *Astron. and Astrophys.* **149** no. 1, (Aug., 1985) 135–143.

[66] C. Kochanek and M. J. White, "A Quantitative study of interacting dark matter in halos," *Astrophys. J.* **543** (2000) 514, arXiv:astro-ph/0003483.

[67] N. Yoshida, V. Springel, S. D. White, and G. Tormen, "Weakly self-interacting dark matter and the structure of dark halos," *Astrophys. J.* **544** (2000) L87–L90, arXiv:astro-ph/0006134.

[68] R. Dave, D. N. Spergel, P. J. Steinhardt, and B. D. Wandelt, "Halo properties in cosmological simulations of selfinteracting cold dark matter," *Astrophys. J.* **547** (2001) 574–589, arXiv:astro-ph/0006218.

[69] J. Koda and P. R. Shapiro, "Gravothermal collapse of isolated self-interacting dark matter haloes: N-body simulation versus the fluid model," *Mon. Not. Roy. Astron. Soc.* **415** (2011) 1125, arXiv:1101.3097 [astro-ph.CO].

[70] A. B. Fry, F. Governato, A. Pontzen, T. Quinn, M. Tremmel, L. Anderson, H. Menon, A. Brooks, and J. Wadsley, "All about baryons: revisiting SIDM predictions at small halo masses," *Mon. Not. Roy. Astron. Soc.* **452** no. 2, (2015) 1468–1479, arXiv:1501.00497 [astro-ph.CO].

[71] O. D. Elbert, J. S. Bullock, M. Kaplinghat, S. Garrison-Kimmel, A. S. Graus, and M. Rocha, "A Testable Conspiracy: Simulating Baryonic Effects on Self-Interacting Dark Matter Halos," *Astrophys. J.* **853** no. 2, (2018) 109, arXiv:1609.08626 [astro-ph.GA].

[72] S. Blinnikov and M. Khlopov, "Possible astronomical effects of mirror particles," *Sov. Astron.* **27** (1983) 371–375.

[73] Z. Berezhiani, A. Dolgov, and R. Mohapatra, "Asymmetric inflationary reheating and the nature of mirror universe," *Phys. Lett. B* **375** (1996) 26–36, arXiv:hep-ph/9511221.

[74] R. Foot, "Mirror matter-type dark matter," *Int. J. Mod. Phys. D* **13** (2004) 2161–2192, arXiv:astro-ph/0407623.

[75] J. M. Cline, Z. Liu, and W. Xue, "Millicharged Atomic Dark Matter," *Phys. Rev. D* **85** (2012) 101302, arXiv:1201.4858 [hep-ph].

[76] J. M. Cline, Z. Liu, G. Moore, and W. Xue, "Scattering properties of dark atoms and molecules," *Phys. Rev. D* **89** no. 4, (2014) 043514, arXiv:1311.6468 [hep-ph].

[77] J. M. Cline, Z. Liu, G. Moore, and W. Xue, "Composite strongly interacting dark matter," *Phys. Rev. D* **90** no. 1, (2014) 015023, arXiv:1312.3325 [hep-ph].

[78] F.-Y. Cyr-Racine and K. Sigurdson, "Cosmology of atomic dark matter," *Phys. Rev. D* **87** no. 10, (2013) 103515, arXiv:1209.5752 [astro-ph.CO].

[79] J. L. Feng, M. Kaplinghat, H. Tu, and H.-B. Yu, "Hidden Charged Dark Matter," *JCAP* **07** (2009) 004, arXiv:0905.3039 [hep-ph].

[80] R. Foot and S. Vagnozzi, "Dissipative hidden sector dark matter," *Phys. Rev. D* **91** (2015) 023512, arXiv:1409.7174 [hep-ph].

[81] R. Foot and S. Vagnozzi, "Solving the small-scale structure puzzles with dissipative dark matter," *JCAP* **07** (2016) 013, arXiv:1602.02467 [astro-ph.CO].

[82] K. K. Boddy, J. L. Feng, M. Kaplinghat, and T. M. P. Tait, "Self-Interacting Dark Matter from a Non-Abelian Hidden Sector," *Phys. Rev. D* **89** no. 11, (2014) 115017, arXiv:1402.3629 [hep-ph].

[83] K. K. Boddy, M. Kaplinghat, A. Kwa, and A. H. G. Peter, "Hidden Sector Hydrogen as Dark Matter: Small-scale Structure Formation Predictions and the Importance of Hyperfine Interactions," *Phys. Rev. D* **94** no. 12, (2016) 123017, arXiv:1609.03592 [hep-ph].

[84] J. L. Feng, M. Kaplinghat, and H.-B. Yu, "Halo Shape and Relic Density Exclusions of Sommerfeld-Enhanced Dark Matter Explanations of Cosmic Ray Excesses," *Phys. Rev. Lett.* **104** (2010) 151301, arXiv:0911.0422 [hep-ph].

[85] M. R. Buckley and P. J. Fox, "Dark Matter Self-Interactions and Light Force Carriers," *Phys. Rev. D* **81** (2010) 083522, `arXiv:0911.3898 [hep-ph]`.

[86] S. Tulin, H.-B. Yu, and K. M. Zurek, "Beyond Collisionless Dark Matter: Particle Physics Dynamics for Dark Matter Halo Structure," *Phys. Rev. D* **87** no. 11, (2013) 115007, `arXiv:1302.3898 [hep-ph]`.

[87] M. Born, "Quantenmechanik der Stoßvorgänge," *Z. Phys.* **38** no. 11-12, (1926) 803–827.

[88] M. Ibe and H.-b. Yu, "Distinguishing Dark Matter Annihilation Enhancement Scenarios via Halo Shapes," *Phys. Lett. B* **692** (2010) 70–73, `arXiv:0912.5425 [hep-ph]`.

[89] F. Kahlhoefer, K. Schmidt-Hoberg, M. T. Frandsen, and S. Sarkar, "Colliding clusters and dark matter self-interactions," *Mon. Not. Roy. Astron. Soc.* **437** no. 3, (2014) 2865–2881, `arXiv:1308.3419 [astro-ph.CO]`.

[90] A. Robertson, R. Massey, and V. Eke, "Cosmic particle colliders: simulations of self-interacting dark matter with anisotropic scattering," *Mon. Not. Roy. Astron. Soc.* **467** no. 4, (2017) 4719–4730, `arXiv:1612.03906 [astro-ph.CO]`.

[91] J. Zavala, M. Vogelsberger, and M. G. Walker, "Constraining Self-Interacting Dark Matter with the Milky Way's dwarf spheroidals," *Mon. Not. Roy. Astron. Soc.* **431** (2013) L20–L24, `arXiv:1211.6426 [astro-ph.CO]`.

[92] M. Vogelsberger and J. Zavala, "Direct detection of self-interacting dark matter," *Mon. Not. Roy. Astron. Soc.* **430** no. 3, (2013) 1722–1735, `1211.1377`.

[93] M. Vogelsberger, J. Zavala, C. Simpson, and A. Jenkins, "Dwarf galaxies in CDM and SIDM with baryons: observational probes of the nature of dark matter," *Mon. Not. Roy. Astron. Soc.* **444** no. 4, (2014) 3684–3698, `arXiv:1405.5216 [astro-ph.CO]`.

[94] M. Vogelsberger, J. Zavala, F.-Y. Cyr-Racine, C. Pfrommer, T. Bringmann, and K. Sigurdson, "ETHOS – an effective theory of structure formation: dark matter physics as a possible explanation of the small-scale CDM problems," *Mon. Not. Roy. Astron. Soc.* **460** no. 2, (2016) 1399–1416, arXiv:1512.05349 [astro-ph.CO].

[95] A. Robertson, R. Massey, V. Eke, J. Schaye, and T. Theuns, "The surprising accuracy of isothermal Jeans modelling of self-interacting dark matter density profiles," arXiv:2009.07844 [astro-ph.CO].

[96] J. L. Feng, M. Kaplinghat, and H.-B. Yu, "Sommerfeld Enhancements for Thermal Relic Dark Matter," *Phys. Rev. D* **82** (2010) 083525, arXiv:1005.4678 [hep-ph].

[97] S. A. e. a. Khrapak, "Scattering in the Attractive Yukawa Potential: Application to the Ion-Drag Force in Complex Plasmas," *IEEE Transactions on Plasma Science* **32** no. 2, (2004) 555–560.

[98] N. Iwanus, P. J. Elahi, and G. F. Lewis, "Dark matter annihilation feedback in cosmological simulations – I: Code convergence and idealized haloes," *Mon. Not. Roy. Astron. Soc.* **472** no. 1, (2017) 1214–1225, arXiv:1707.06770 [astro-ph.CO].

[99] F. List, N. Iwanus, P. J. Elahi, and G. F. Lewis, "A Novel Scheme for Dark Matter Annihilation Feedback in Cosmological Simulations," *Mon. Not. Roy. Astron. Soc.* **489** no. 3, (2019) 4217–4232, arXiv:1908.05812 [astro-ph.CO].

[100] J. von Neumann, "Various techniques used in connection with random digits," in *Monte Carlo Method*, A. S. Householder, G. E. Forsythe, and H. H. Germond, eds., vol. 12 of *National Bureau of Standards Applied Mathematics Series*, ch. 13, pp. 36–38. US Government Printing Office, Washington, DC, 1951.

[101] S. J. Aarseth, M. Henon, and R. Wielen, "A Comparison of Numerical Methods for the Study of Star Cluster Dynamics," *Astron. & Astrophys.* **37** no. 1, (1974) 183–187.

# Chapter 7

# Blazar constraints on neutrino-dark matter scattering

**James M. Cline, Shan Gao, Fangyi Guo, Zhongan Lin, Shiyan Liu, Matteo Puel, Phillip Todd, and Tianzhuo Xiao**

*McGill University, Department of Physics, 3600 University Street, Montréal, QC H3A2T8 Canada*

Published in Physics Review Letters: PRL 130 (2023) 9, 091402, [arXiv:2209.02713].

## 7.0 Prologue

In the "little theory of everything" presented in chapter 5, neutrinos and DM particles played pivotal roles. This naturally raises the question of whether any potential interaction between these two species could be constrained through astrophysical or cosmological observations.

In this chapter and in the next, we will explore potential and promising sources of neutrinos, such as active galactic nuclei (AGNs). AGNs are compact regions at the center of galaxies with luminosities far exceeding that produced by the stellar population alone. The non-stellar radiation from an AGN originates from the accretion of matter by a supermassive black hole at the galaxy's center [1], resulting in a highly energetic jet of plasma perpendicular to the accretion disk. The inclination of the AGN system relative to the observer determines the different AGN types [2–4]. When the relativistic jet points directly toward the observer, they are known as *blazars*. On the other hand, if the observer sees the jet from the side, they are referred to as *radio galaxies* [5].

The properties of an AGN are described by its spectral energy distribution (SED), the energy-dependent spectrum of electromagnetic emission. In blazars, the UV and X-ray parts of the SED are attributed to synchrotron emission from electrons moving in the highly magnetized jet. For the $\gamma$-ray part of the SED, three scenarios have been proposed based on which process dominates [5]:

- *Leptonic models* suggest that $\gamma$ rays are mainly produced by inverse-Compton scattering, where high-energy electrons interact with low-energy photons in the jet and transfer part of their energy to them.

- *Hadronic models* propose that proton synchrotron radiation is the primary source of $\gamma$ rays.

- *Lepto-hadronic models* predict that the $\gamma$-ray part of the spectrum is generated by secondary leptons produced in proton-photon interactions within the jet.

Neutrinos can only be produced in proton-photon interactions, such as the photo-meson processes

$$\begin{aligned} & p+\gamma \to p+\pi^0 && \pi^0 \to 2\gamma\,, \\ & \left.\begin{aligned} & p+\gamma \to n+\pi^+ \\ & p+\gamma \to p+\pi^+ +\pi^- \end{aligned}\right\} && \begin{aligned} & \pi^+ \to \mu^+ + \nu_\mu \to e^+ + \nu_e + \bar{\nu}_\mu + \nu_\mu\,, \\ & \pi^- \to \mu^- + \bar{\nu}_\mu \to e^- + \bar{\nu}_e + \nu_\mu + \bar{\nu}_\mu\,, \end{aligned} \end{aligned} \tag{7.1}$$

which rule out leptonic models as neutrino sources. Pure hadronic models are also disfavored because they require extremely high proton density and luminosities exceeding the Eddington limit [1], which are in conflict with the electromagnetic SED

[1]The Eddington limit is the maximum luminosity achievable by an AGN when the outward radiation force of the gas orbiting the central engine is balanced with the inward gravitational force.

data. Moreover, these models require very strong magnetic fields and the predicted neutrino flux at high energies contradicts the IceCube observed flux for the blazar TXS 0506+056 [6]. [2] Thus, lepto-hadronic models are the favored scenario for producing $\gamma$ rays and neutrinos that are compatible with observations if no DM-neutrino interaction is involved. In the case where such interaction exists, we will show in the rest of the chapter that hadronic models would lead to stronger constraints on the scattering cross section than lepto-hadronic ones, making the latter the most conservative choice.

It is worth noting that the above conclusion is based on one-zone emission models, where all radiative and neutrino processes originate from a single spherical emitting region in the jet [9]. However, if multiple emitting regions are considered, pure hadronic models remain still viable [10].

Regarding the nature of DM considered in this chapter, we focus on the keV-GeV mass range. This choice is motivated by the fact that within this parameter space, direct detection constraints on DM become less stringent. However, the results we derive are applicable to a broader range of DM masses, specifically $m_\chi \gtrsim 10^{-6}$ eV. In this regime, the DM spike formed around a black hole could potentially be detected by upcoming space-based gravitational wave observatories [11, 12].

A final remark concerns the size of the DM spike, which should be thought to be independent of the specific nature of the DM particle, as its determination should rely on observational considerations. Specifically, the mass of the central black hole (BH) is determined based on the enclosed mass within a certain spherical region centered at the galactic center. Consequently, it is reasonable to assume that the inferred BH mass is a combination of both the DM spike and the true mass of the BH itself, given that these two components cannot be distinguished from an observational standpoint. Therefore, when estimating the size of the DM spike, it should be considered at least as large as the radius of the spherical shell used to estimate the BH mass [13].

[2] The association between the single neutrino event observed by IceCube and the blazar TXS 0506+056 was confirmed by follow-up measurements from several electromagnetic satellites, which observed the blazar undergoing a flaring-stage [7]. Prior to the 2017 observation, IceCube found a $\sim 3.5\sigma$ evidence for other neutrinos coming from the same blazar in its 9.5 years of data [8].

**Abstract**

Neutrino emission in coincidence with gamma rays has been observed from the blazar TXS 0506+056 by the IceCube telescope. Neutrinos from the blazar had to pass through a dense spike of dark matter (DM) surrounding the central black hole. The observation of such a neutrino implies new upper bounds on the neutrino-DM scattering cross section as a function of the DM mass. The constraint is stronger than existing ones for a range of DM masses, if the cross section rises linearly with energy. For constant cross sections, competitive bounds are also possible, depending on details of the DM spike.

## 7.1 Introduction

The possible interactions of dark matter (DM) with ordinary matter have been constrained in many ways. The most challenging category is DM-neutrino interactions, due to the difficulty of observing neutrinos. A promising strategy is to consider astrophysical sources of high-energy neutrinos that could accelerate light DM particles to energies that would make them detectable in ground-based DM and neutrino search experiments [14–16]. This only works if, in addition to DM-$\nu$ interactions, there can also be scattering of DM from nuclei or electrons in the detector.

A more model independent strategy is to use the fact that a 290 TeV neutrino, known as event IC-170922A, has been observed by the IceCube experiment and was identified as coming from the blazar TXS 0506+056 [7]. Reference [17] set limits on the DM-$\nu$ scattering cross section using the fact that the neutrino had to pass through cosmological and galactic DM between the blazar and the Earth. In this paper, we derive stronger limits, using the fact that the neutrino also had to traverse the dense DM spike surrounding the supermassive black hole powering TXS 0506+056.

IceCube additionally reported a statistical excess of lower energy neutrinos prior the 2017 flare of TXS 0506+056 [8], but the claimed excess is too large to be explained by state-of-the-art one-zone blazar models, likely requiring more complicated modelling [18–23]. Hence we do not include it in the present analysis. There have also been several candidate associations between neutrinos detected by IceCube and known $\gamma$-ray blazars subsequent to IC-170922A (e.g. [24–31]). Since none of them have been confirmed by the IceCube Collaboration, we do not include them in this study.

## 7.2 Expected neutrino events

We start by describing the theoretical models of neutrino emission from blazars and the expected flux from TXS 0506+056. The observed spectra of electromagnetic emission from blazars is well described by lepto-hadronic models [6, 9, 22, 23, 32], in which protons and electrons are shock-accelerated to create a relativistic jet in a magnetized region that produces synchrotron radiation. The jet extends to distances $\sim 10^{11}\,\mathrm{km}$ [6, 23], around 1000 times smaller than the extent of the DM spike to be described in Section 7.3. Proton-photon interactions in the jet produce pions, whose decays are the source of high-energy neutrinos.

Purely hadronic models are also able to fit the combined electromagnetic spectra at optical, x-ray and gamma-ray frequencies, but they lead to either a detectable neutrino flux at much higher energies or a negligible low flux at energies compatible with IC-170922A [6, 9]; hence we focus on lepto-hadronic models in the following. The impact of different choices is discussed at the end of section 7.4. Under the steady state approximation, the hadronic model of Ref. [6] predicts a neutrino flux between $E_\nu \sim 100\,\mathrm{TeV}$ and $10\,\mathrm{EeV}$, that peaks at a value $E_\nu \sim 10\,\mathrm{PeV}$, which is orders of magnitude higher than IC-170922A. We find that the probability of observing a neutrino with energy $\lesssim 300\,\mathrm{TeV}$ is $\sim 3\,\%$ in this model. Hence we consider it to be disfavored for explaining IC-170922A.

On the other hand, the neutrino flux predicted by the lepto-hadronic model of Ref. [23], based on a fully time-dependent approach, peaks near $E_\nu = 100\,\mathrm{TeV}$ and is compatible with the observation. Within the quasi-two neutrino oscillation approximation [23], the flux is well fit by the formula

$$\log_{10}\Phi_\nu(E_\nu) = -F_0 - \frac{F_1\,x}{1+F_2|x|^{F_3}} \tag{7.2}$$

with $F_0 = 13.22, F_1 = 1.498, F_2 = -0.00167, F_3 = 4.119$, and $x = \log_{10}(E_\nu/\mathrm{TeV}) \in [-1.2,\,4.2]$. The expected number of muon neutrino events observed at IceCube is given by

$$N_{\rm pred} = t_{\rm obs}\int dE_\nu\,\Phi_\nu(E_\nu)\,A_{\rm eff}(E_\nu)\,, \tag{7.3}$$

where $t_{\rm obs}$ is the time interval of observation, $\Phi_\nu$ is the predicted neutrino flux from the blazar, and $A_{\rm eff}$ is an effective area for detection, which depends on the geometry of the source direction and $E_\nu$, and encodes the probability for a neutrino to convert to a muon through weak interactions. Data for $A_{\rm eff}$ from TXS 0506+056 is provided by IceCube [33].[3] For the campaign IC86c during JD (Julian day) 57 161−58 057 that observed IC-170922A, $t_{\rm obs} = 898\,\mathrm{d}$, and the reconstructed energy was $E_\nu = 290\,\mathrm{TeV}$. This yields $N_{\rm pred} \approx 2.0$ from the flux (7.2), compatible with the observed event. We adopt this as the input model for constraining the DM-$\nu$ cross section in the following.

## 7.3 Dark matter spike

The overdensity of DM surrounding the central black hole plays a crucial role for constraining $\nu$-DM scattering from the blazar. The possibility of adiabatic accretion of DM around the black hole (BH) was first considered by Gondolo and Silk in Ref. [34]. They derived an inner radius for the spike of $r_i = 4R_S$, where $R_S = 2GM_{BH}$ is the BH Schwarzschild radius, and an outer profile $\rho'(r) \cong N\,(1 - 4R_S/r)^3\,r^{-\alpha}$ with $\alpha = (9-2\gamma)/(4-\gamma) \in [2.25,\,2.5]$, depending on the inner cusp of the initial DM halo density, $\rho \sim r^{-\gamma}$, with $0 \le \gamma \le 2$. The normalization $N$ of $\rho'$ can be determined using the finding that the mass of the spike is of the same order as $M_{BH}$ [35], $4\pi\int_{r_i}^{r_o} dr\,r^2\rho' \cong M_{BH}$, within a radius of typical size $r_o \cong 10^5\,R_S$ [13]. The BH

[3] The effective area can be fit in the region $x \in [-1,\,6]$ by $\log_{10} A_{\rm eff}/\mathrm{cm}^2 \cong 3.57 + 2.007\,x - 0.5263\,x^2 + 0.0922\,x^3 - 0.0072\,x^4$.

mass of the blazar TXS 0506+056 is estimated to be $3.09 \times 10^8\ M_\odot$ [36]. In Ref. [37], it was argued that gravitational scattering of DM with stars in the central region would lead to dynamical relaxation to a less cuspy profile with $\alpha = 3/2$; hence we also consider this possibility below.

The spike density is reduced relative to these initial profiles if there is subsequent DM annihilation, leading to a maximum density of $\rho_c = m_\chi/(\langle\sigma_a v\rangle\, t_{BH})$, where $m_\chi$ is the DM mass, $\langle\sigma_a v\rangle$ is an effective annihilation cross section, and $t_{BH}$ is the age of the BH. The spike density then becomes $\rho_\chi = \rho_c\rho'/(\rho_c + \rho')$. The quantity $\langle\sigma_a v\rangle$ is "effective" in the sense that it could be negligible even if the actual annihilation cross section is large. This would be the case for asymmetric dark matter, in which the symmetric component has completely annihilated away in the early Universe. Then annihilations would have no effect at later times, when the DM spike is formed. To illustrate the range of possible outcomes from varying $\langle\sigma_a v\rangle$, we follow Ref. [16] by considering three benchmark models BM1–BM3, in which $\langle\sigma_a v\rangle = (0,\, 0.01,\, 3) \times 10^{-26}\,\mathrm{cm}^3/\mathrm{s}$, respectively, and $t_{BH} = 10^9\,\mathrm{yr}$. These models assumed $\alpha = 7/3$ in $\rho' \sim r^{-\alpha}$. We also consider models BM1′–BM3′ using the less cuspy value $\alpha = 3/2$.

The probability for neutrinos to scatter from DM in the spike depends on the DM column density,

$$\Sigma_\chi = \int_{R_{\rm em}}^{\infty} dr\, \rho_\chi \cong A_\Sigma \left(\frac{m_\chi}{1\,\mathrm{MeV}}\right)^{1-B_\Sigma}\ \mathrm{MeV}\,, \tag{7.4}$$

where $R_{\rm em} \approx R'\,\delta \sim 2 \times 10^{17}$ cm is the distance from the central BH to the position in the jet where neutrinos and photons are likely to be produced [36]. $R' \sim 10^{16}$ cm is the comoving size of the spherical emission region and $\delta \sim 20$ is the Doppler factor for the lepto-hadronic model of Ref. [23]. One finds that $\Sigma_\chi/m_\chi$ can be accurately fit by a power law, $\Sigma_\chi/m_\chi = A_\Sigma\,(\mathrm{MeV}/m_\chi)^{B_\Sigma}$, with $B_\Sigma = 1$ for the case of $\langle\sigma_a v\rangle = 0$, and a fractional power when annihilation occurs. The parameters $A_\Sigma$, $B_\Sigma$ for the benchmark models are given in Table 7.3.1. Although the DM spike does not extend to arbitrary distances, the integral in (7.4) converges around $10\,R_S$ in the case of no DM annihilation, and at larger radii $\sim (10^6 - 10^8)\,R_S$ for the cases with annihilation.

| $\langle\sigma_a v\rangle$ | Model | $\alpha$ | $\log_{10} A_\Sigma$ | $B_\Sigma$ | Model | $\alpha$ | $\log_{10} A_\Sigma$ | $B_\Sigma$ |
|---|---|---|---|---|---|---|---|---|
| 0 | BM1 | 7/3 | 31.4 | 1 | BM1′ | 3/2 | 31.9 | 1 |
| 0.01 | BM2 | 7/3 | 30.0 | 0.48 | BM2′ | 3/2 | 30.8 | 0.73 |
| 3 | BM3 | 7/3 | 28.7 | 0.43 | BM3′ | 3/2 | 29.5 | 0.66 |

Table 7.3.1: Normalization $A_\Sigma$ and exponent $B_\Sigma$ of power law fit to DM spike column density per mass $\Sigma/m_\chi$; see Eq. (7.4). Models are distinguished by different values of the effective DM annihilation cross section (in units of $10^{-26}\,\mathrm{cm}^3/\mathrm{s}$) and the spike profile exponent $\alpha$. $A_\Sigma$ is in units of $\mathrm{cm}^{-2}$.

## 7.4 Neutrino attenuation by DM

One can make an initial estimate for the maximum DM-$\nu$ scattering cross section $\sigma_{\nu\chi}$ as being inverse to the column density $\Sigma_\chi/m_\chi$ of the DM spike surrounding the central BH of TXS 0506+056. To be more quantitative, we recompute the expected number of IceCube events from the 2017 flare that led to the observed event, taking into account the attenuation from scattering on DM. The analogous computation for scattering of neutrinos by galactic DM has been considered in Ref. [38]. The evolution of the flux due to scattering is described by the cascade equation,

$$\frac{d\Phi}{d\tau}(E_\nu) = -\sigma_{\nu\chi}\Phi + \int_{E_\nu}^{\infty} dE_\nu' \, \frac{d\sigma_{\nu\chi}}{dE_\nu}(E_\nu' \to E_\nu)\, \Phi(E_\nu')\,, \tag{7.5}$$

where $\tau = \Sigma(r)/m_\chi = \int^r dr\, \rho_\chi/m_\chi$ is the accumulated column density. The second term represents the effect of neutrino energies being redistributed, rather than simply being lost from the beam.

To proceed, we must make an assumption about the energy dependence of the cross section. In section 7.6 we will discuss particle physics models that predict $\sigma_{\nu\chi}(E_\nu)$. A particularly simple and well-motivated choice is linear energy dependence,

$$\sigma_{\nu\chi} = \sigma_0\, E_\nu/E_0\,, \tag{7.6}$$

taking the reference energy $E_0 = 290\,\mathrm{TeV}$ to be that of the observed event. Approximating the scattering as being isotropic in the center-of-mass frame, one can show that $d\sigma_{\nu\chi}/dE_\nu = \sigma_{\nu\chi}/E_\nu' = \sigma_0/E_0$. The cascade equation can be discretized, choosing equal logarithmic intervals $\Delta x$ in $x = \log_{10}(E_\nu/\mathrm{TeV})$. Defining a dimensionless column density $y = (m_\chi/\Sigma_\chi)\,\tau$, it takes the form

$$\frac{d\Phi_i}{dy} = A\left(-\hat{E}_i\Phi_i + \Delta x \ln 10 \sum_{j=i}^{N} \hat{E}_j\Phi_j\right) \tag{7.7}$$

where $A = (\Sigma_\chi/m_\chi)(\sigma_0/\hat{E}_0)$, $\hat{E}_i = 10^{x_i}$ is the energy in TeV units, $\hat{E}_0 = 290$ and $y \in [0, 1]$.

To solve Eq. (7.7), one can either evolve the initial condition from $y = 0$ to $y = 1$ by incrementing in $y$, or use the algorithm presented in Ref. [39]. We have checked that both methods give the same results, resulting in the 90% Confidence Level (C.L.) limit

$$A \equiv \frac{\Sigma_\chi \sigma_0}{m_\chi\, \hat{E}_0} < 0.0047 \tag{7.8}$$

by demanding the number of events giving a neutrino of energy $E_\nu \geq 290\,\mathrm{TeV}$ be greater than 0.1. The corresponding constraints in the plane of $\sigma_0$ versus $m_\chi$ are plotted in Fig. 7.4.1 for the six DM spike models. The constraint (7.8) can be expressed as $\sigma_0 < 1.4\, m_\chi/\Sigma_\chi$, in agreement with the initial estimate. The effects of other kinds of energy dependence of $\sigma_{\nu\chi}$ are considered in Section 7.6. [4]

We find that the constraint (7.8) is strengthened by a factor of $\sim 4 - 10$ for hadronic production models, like those of Refs. [6, 23], relative to lepto-hadronic ones. In fact, a nonvanishing $\sigma_{\nu\chi}$ at such levels could reduce the too-high energies predicted by hadronic models, to better explain the IC-170922A event, but interpreted as an upper limit it is more stringent than Eq. (7.8), hence our adoption of lepto-hadronic models is a conservative choice.

[4] If the cross section is exactly constant, the second term of the cascade equation (7.5) is zero and the neutrino flux is exponentially suppressed according to $\Phi \sim \exp\left(-\sigma_{\nu\chi}\,\Sigma_\chi/m_\chi\right)$. The corresponding 90% C.L. bound on $\sigma_0$ becomes $\sigma_0 \lesssim 1.7\, m_\chi/\Sigma_\chi$, which is very similar to the result obtained for the case of linear energy-dependent $\sigma_{\nu\chi}$.

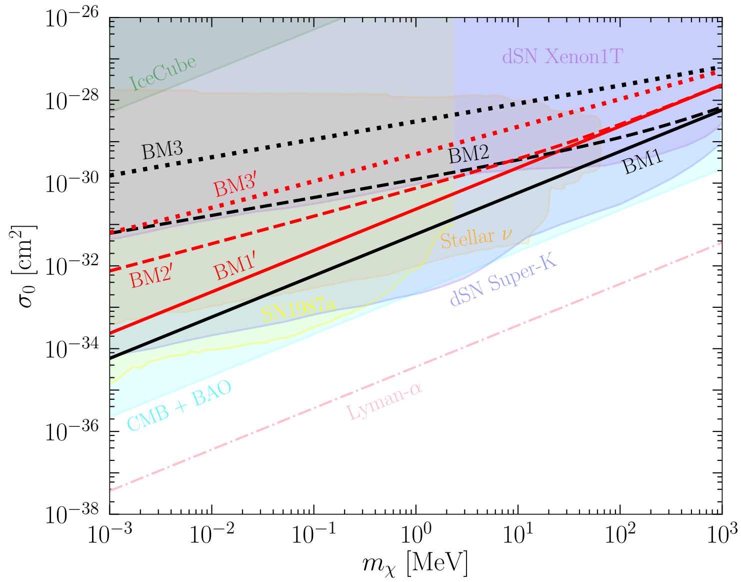


Figure 7.4.1: 90% C.L. upper limits on the $\nu$-DM scattering cross section at reference energy $E_0 = 290\,\mathrm{TeV}$, for the six benchmark DM spike models. Previous constraints are shown for comparison, assuming energy-independent cross section: (cyan) CMB and baryon acoustic oscillations [40]; (pink) Lyman-$\alpha$ preferred model [41]; (dark violet, blue) diffuse supernova neutrinos [15]; (orange) stellar neutrinos [42]; (yellow) supernova SN1987A [43]; (green) IceCube bound from TXS 0506+056 [17].

## 7.5 Comparison to previous limits

A model-independent signal of neutrino-DM interactions is the suppression in the primordial density fluctuations at temperatures $\sim$ 1 eV, which would produce detectable effects in the cosmic microwave background (CMB) and matter power spectrum [40, 41, 44–47]. For a constant scattering cross section, Ref. [47] derived a limit of $\sigma_{\nu\chi} \lesssim 10^{-36}\,(m_\chi/\mathrm{MeV})$ cm$^2$ for massless neutrinos, which becomes weaker by about 5 orders of magnitude if a neutrino mass of $\sim$ 0.06 eV is properly included [40]. A more recent analysis using Lyman-$\alpha$ forest data found a mild preference for DM interacting with massive neutrinos, which requires confirmation [41].

Besides its effect on cosmology, DM-$\nu$ scattering can also be probed in direct detection experiments and neutrino observatories, if further assumptions about the DM interaction with either leptons or nucleons are made. A prominent example involves boosting DM within our galaxy by astrophysical neutrinos such as those coming from stars [42, 48], diffuse supernovae [15, 49–51] or from supernova SN1987A [43], leading

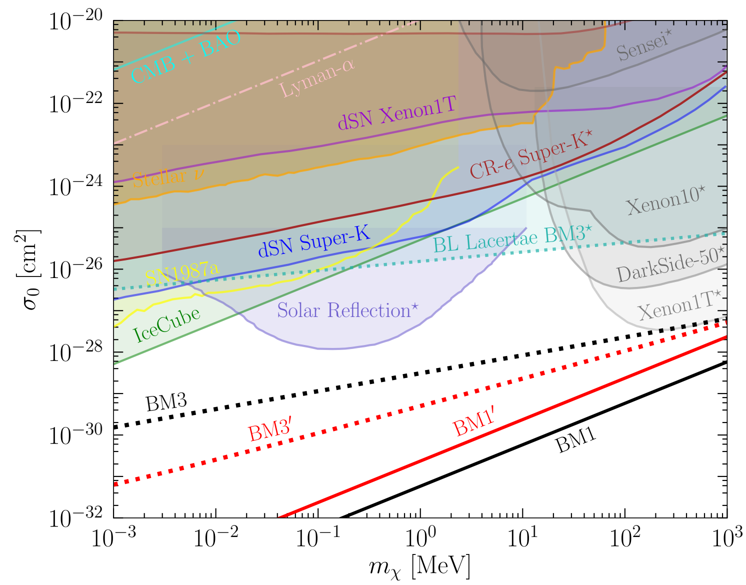


Figure 7.5.1: Previous constraints on $\nu$-DM and $e$-DM scattering, rescaled to $E_0 =$ 290 TeV assuming $\sigma_{\nu\chi} \propto E_\nu$, compared to the least (BM3, BM3′) and most restrictive (BM1, BM1′) new limits of Fig. 7.4.1. The $\nu$-DM scattering bounds are the same as in Fig. 7.4.1, while for $e$-DM scattering they are labelled with $\star$ and are as follows: (slate blue) solar reflection [59], (brown) Super-K for DM boosted by cosmic-ray electrons, (turquoise) blazar BL Lacertae for BM3 model [16], (gray) direct detection for light DM interacting with electrons [60–63].

to larger energy deposition than could occur for light DM particles. Alternative ways to probe DM scattering with neutrinos is via attenuation of neutrino fluxes from supernovae [44, 52] and the galactic center [53], delayed neutrino propagation [54–56], and through effects in the extragalactic distribution and spectra of PeV neutrinos [57, 58].

Figure 7.5.1 shows a compilation of the most stringent bounds on $\sigma_{\nu\chi}$ after rescaling them to the common energy scale $E_0 = 290$ TeV, assuming Eq. (7.6). Here we include also constraints on DM-electron scattering, since it is natural for neutrinos and electrons to interact with DM with the same strength, as discussed in the next section. DM-$e$ scattering can be probed in a variety of ways. It would alter the CMB anisotropies, the shape of the matter power spectrum and the abundance of Milky Way satellites [64–66], cause CMB spectral distortions [67, 68], and heat or cool the gas in dwarf galaxies [69]. Similarly to the neutrino case, DM particles can be boosted by cosmic rays [70–90], particles in the solar interior [59] or in the relativistic jets of blazars [14, 16] and be directly detected. Standard direct detection constraints on light DM particles can apply [60–63, 91–100]. DM-electron scattering can alter the cosmic ray spectrum [101] and potentially heat neutron stars [102–104] and white dwarfs [105].

The new blazar limits on $\sigma_{\nu\chi}$ shown in Fig. 7.5.1, assuming $\sigma_{\nu\chi} \propto E_\nu$, are several orders of magnitude stronger than existing ones for sub-GeV DM, when the latter are rescaled to the blazar neutrino energy. In the case of light mediators that could lead to a constant-in-energy cross section, we lose this advantage, as shown in Fig. 7.4.1.

## 7.6 Particle physics models

The simplest models for DM-$\nu$ scattering involve the exchange of a vector boson $Z'$ between DM and neutrinos. We assume coupling $g_\nu$ to all flavors of neutrinos, and coupling $g_\chi$ to DM, taken to be a complex scalar; by dimensional analysis, the results are expected to be insensitive to the spin of the DM. [Exact expressions for $\sigma(E)$ in various models can be found in the appendix of Ref. [38].] At energies $E_\nu \gg m_\chi$, the cross section goes as

$$\sigma_{\nu\chi} \cong \frac{g_\nu^2 g_\chi^2}{4\pi\, m_{Z'}^2}\left[1 - \frac{m_{Z'}^2}{s}\ln\left(1 + \frac{s}{m_{Z'}^2}\right)\right], \tag{7.9}$$

where $s \cong 2m_\chi E_\nu$. For $m_{Z'}^2 > m_\chi E_\nu \gtrsim 1\,\mathrm{GeV}^2$ (considering $m_\chi$ as low as 1 keV), $\sigma_{\nu\chi}$ rises linearly with $E_\nu$ by expanding the logarithm to second order in $s/m_{Z'}^2$, while for $E_\nu \gg m_{Z'}^2/m_\chi$, $\sigma_{\nu\chi}$ saturates to a constant value. The corresponding differential cross section that appears in the second term of the cascade equation (7.5) is

$$\frac{d\sigma_{\nu\chi}}{dE_\nu}(E'_\nu \to E_\nu) = \frac{(g_\nu^2 g_\chi^2/4\pi)(m_\chi\, E_\nu/E'_\nu)}{(m_{Z'}^2 + 2m_\chi(E'_\nu - E_\nu))^2}\,. \tag{7.10}$$

This model is similar to that in Eq. (7.6) in having $\sigma_{\nu\chi} \propto E_\nu$ at low energy, but it is physically distinct because the differential scattering implied by (7.10) is not isotropic. One can show that its behavior in the cascade equation is determined by

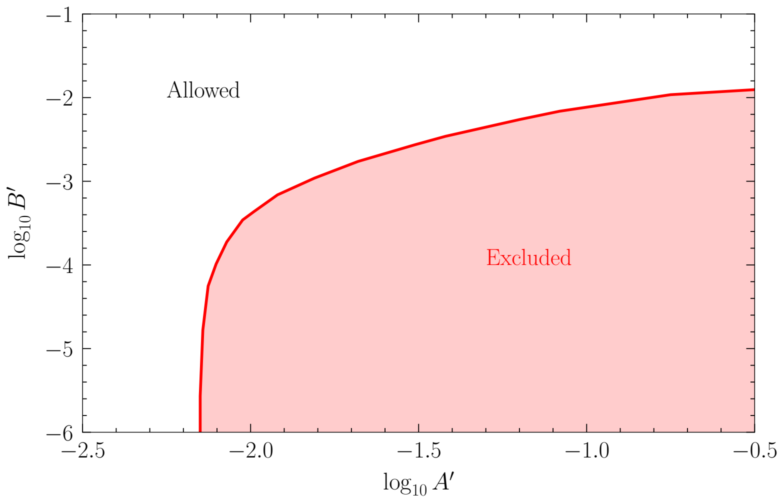


Figure 7.6.1: Constraint on the dimensionless parameters defined in Eq. (7.11) in the model with a $Z'$ mediator.

just two (dimensionless) parameters, that we take to be

$$A' = \frac{g_\nu^2 g_\chi^2 \, \Sigma_\chi \cdot (1\,\text{TeV})}{4\pi \, m_{Z'}^4}, \quad B' \equiv \frac{m_\chi \cdot (1\,\text{TeV})}{m_{Z'}^2}. \tag{7.11}$$

With this choice, $A'$ plays the same role of $A$ in Eq. (7.7) in the low-energy regime where $\sigma_{\nu\chi} \sim g_\nu^2 g_\chi^2 m_\chi E_\nu/(4\pi m_{Z'}^4)$. By solving the cascade equation on a grid of values in the $A'$-$B'$ plane, again demanding at least 0.1 predicted IceCube events above 290 TeV, we obtain the constraint shown in Fig. 7.6.1. We translate the $A'$ versus $B'$ bound into the microscopic model parameters, $g_\nu g_\chi$ versus $m_{Z'}$ in Fig. 7.6.2, for some choices of the DM spike models and DM masses. For comparison, the most stringent related constraint from $Z \to 4\nu$ is also shown [106, 107], for the case that $g_\chi = g_\nu$.

In a realistic model, $Z'$ should couple not only to neutrinos, but to charged leptons in the $\mathrm{SU}(2)_L$ doublets, and to baryons so that the theory is anomaly-free. This leads to numerous further constraints in the parameter space of $g_\nu$ versus $m_{Z'}$, which are beyond the scope of the present work. This aspect will be considered in a follow-up paper [108].

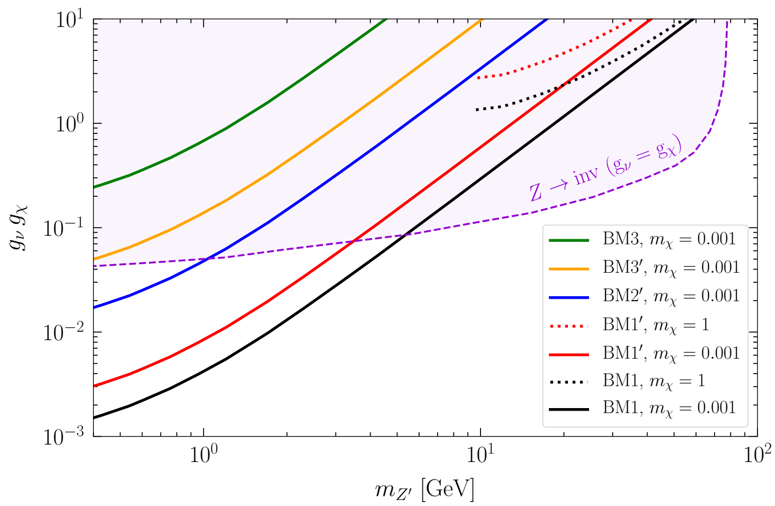


Figure 7.6.2: Upper limit on the product of the couplings $g_\nu g_\chi$ versus $m_{Z'}$ in the vector boson mediator model, for several choices of DM spike model and mass $m_\chi$, indicated in MeV units. Laboratory bound from $Z \to 4\nu$ [106, 107] is shown for the case $g_\chi = g_\nu$.

## 7.7 Summary and conclusions

It is not disputed that dark matter accumulates in the vicinity of supermassive black holes that power active galactic nuclei, but there are significant uncertainties from astrophysics, including the initial neutrino flux, the location along the jet where neutrinos are likely to be produced, the density profile of the DM spike, and the effective DM annihilation cross section. Despite these uncertainties, we find strong and conservative constraints on the elastic scattering cross section $\sigma_{\nu\chi}$ for DM-neutrino scattering, so long as the IceCube event IC-170922A indeed came from the blazar TXS 0506+056 during its 2017 flare, as is widely believed.

Since the single event has a unique neutrino energy $E_0$, our constraint applies to $\sigma_{\nu\chi}$ at that energy. A natural hypothesis is that such interactions arise from exchange of a massive mediator, which leads to the prediction of linear energy dependence $\sigma_{\nu\chi} = \sigma_0\, E_\nu / E_0$ at sufficiently low energies. Under that assumption, we compared our limit to previous ones in the literature, which are set at much lower energies.

Even in the least optimistic case (models BM3–BM3′), our limits improve on the existing ones by several orders of magnitude, if rescaled to $E_0$, for sub-GeV DM masses (see Fig. 7.5.1). The stronger of our constraints (BM1–BM1′) are likely to be applicable in the case of asymmetric DM, where the effective annihilation cross section is essentially zero, due to the negligible proportion of a symmetric component that is necessary to have annihilation. Our constraints are weakened if the mediator mass is sufficiently small, which causes the cross section to stop rising with energy at a scale of order $m_{Z'}^2/m_\chi$, becoming constant at higher energies, and thereby reducing the leverage of our bound coming from the 290 TeV scale (see Fig. 7.4.1).

A further natural assumption, motivated by $\mathrm{SU}(2)_L$ gauge symmetry in the standard model, is that charged leptons should have an equal cross section with DM relative to neutrinos, allowing us to compare to existing electron-DM scattering constraints. Here too our constraints improve on previous limits, for linearly rising cross sections.

We look forward to future observations by neutrino telescopes that may confirm the multimessenger signals from blazars, and perhaps lead to refined constraints on lepton-DM scattering.


## Acknowledgment

We thank Sargis Gasparyan, Rebecca Leane, Kohta Murase, Foteini Oikonomou, Paolo Padovani, Ken Ragan, Aaron Vincent and Jin-Wei Wang for helpful correspondence. This work was supported by the Natural Sciences and Engineering Research Council (NSERC) of Canada.


## Bibliography


[1] **Event Horizon Telescope** Collaboration, K. Akiyama *et al.*, "First M87 Event Horizon Telescope Results. I. The Shadow of the Supermassive Black Hole," *Astrophys. J. Lett.* **875** (2019) L1, `arXiv:1906.11238 [astro-ph.GA]`.

[2] R. Antonucci, "Unified models for active galactic nuclei and quasars," *Ann. Rev. Astron. Astrophys.* **31** (1993) 473–521.

[3] C. M. Urry and P. Padovani, "Unified schemes for radio-loud active galactic nuclei," *Publ. Astron. Soc. Pac.* **107** (1995) 803, `arXiv:astro-ph/9506063`.

[4] L. J. Kewley, B. Groves, G. Kauffmann, and T. Heckman, "The Host Galaxies and Classification of Active Galactic Nuclei," *Mon. Not. Roy. Astron. Soc.* **372** (2006) 961–976, `arXiv:astro-ph/0605681`.

[5] M. Cerruti, "Leptonic and Hadronic Radiative Processes in Supermassive-Black-Hole Jets," *Galaxies* **8** no. 4, (2020) 72, `arXiv:2012.13302 [astro-ph.HE]`.

[6] M. Cerruti, A. Zech, C. Boisson, G. Emery, S. Inoue, and J. P. Lenain, "Leptohadronic single-zone models for the electromagnetic and neutrino emission of TXS 0506+056," *Mon. Not. Roy. Astron. Soc.* **483** no. 1, (2019) L12–L16, `arXiv:1807.04335 [astro-ph.HE]`. [Erratum: Mon.Not.Roy.Astron.Soc. 502, L21–L22 (2021)].

[7] **IceCube, Fermi-LAT, MAGIC, AGILE, ASAS-SN, HAWC, H.E.S.S., INTEGRAL, Kanata, Kiso, Kapteyn, Liverpool Telescope, Subaru, Swift NuSTAR, VERITAS, VLA/17B-403** Collaboration, M. G. Aartsen *et al.*, "Multimessenger observations of a flaring blazar coincident with high-energy neutrino IceCube-170922A," *Science* **361** no. 6398, (2018) eaat1378, `arXiv:1807.08816 [astro-ph.HE]`.

[8] **IceCube** Collaboration, M. G. Aartsen *et al.*, "Neutrino emission from the direction of the blazar TXS 0506+056 prior to the IceCube-170922A alert," *Science* **361** no. 6398, (2018) 147–151, `arXiv:1807.08794 [astro-ph.HE]`.

[9] S. Gao, A. Fedynitch, W. Winter, and M. Pohl, "Modelling the coincident observation of a high-energy neutrino and a bright blazar flare," *Nature Astron.* **3** no. 1, (2019) 88–92, `arXiv:1807.04275 [astro-ph.HE]`.

[10] R. Xue, R.-Y. Liu, M. Petropoulou, F. Oikonomou, Z.-R. Wang, K. Wang, and X.-Y. Wang, "A two-zone model for blazar emission: implications for TXS

0506+056 and the neutrino event IceCube-170922A," arXiv:1908.10190 [astro-ph.HE].

[11] O. A. Hannuksela, K. C. Y. Ng, and T. G. F. Li, "Extreme dark matter tests with extreme mass ratio inspirals," *Phys. Rev. D* **102** no. 10, (2020) 103022, arXiv:1906.11845 [astro-ph.CO].

[12] M. Baryakhtar *et al.*, "Dark Matter In Extreme Astrophysical Environments," in *Snowmass 2021*. 3, 2022. arXiv:2203.07984 [hep-ph].

[13] M. Gorchtein, S. Profumo, and L. Ubaldi, "Probing Dark Matter with AGN Jets," *Phys. Rev. D* **82** (2010) 083514, arXiv:1008.2230 [astro-ph.HE]. [Erratum: Phys.Rev.D 84, 069903 (2011)].

[14] J.-W. Wang, A. Granelli, and P. Ullio, "Direct Detection Constraints on Blazar-Boosted Dark Matter," *Phys. Rev. Lett.* **128** (2022) 221104, arXiv:2111.13644 [astro-ph.HE].

[15] D. Ghosh, A. Guha, and D. Sachdeva, "Exclusion limits on dark matter-neutrino scattering cross section," *Phys. Rev. D* **105** no. 10, (2022) 103029, arXiv:2110.00025 [hep-ph].

[16] A. Granelli, P. Ullio, and J.-W. Wang, "Blazar-boosted dark matter at Super-Kamiokande," *JCAP* **07** no. 07, (2022) 013, arXiv:2202.07598 [astro-ph.HE].

[17] K.-Y. Choi, J. Kim, and C. Rott, "Constraining dark matter-neutrino interactions with IceCube-170922A," *Phys. Rev. D* **99** no. 8, (2019) 083018, arXiv:1903.03302 [astro-ph.CO].

[18] A. Keivani *et al.*, "A Multimessenger Picture of the Flaring Blazar TXS 0506+056: implications for High-Energy Neutrino Emission and Cosmic Ray Acceleration," *Astrophys. J.* **864** no. 1, (2018) 84, arXiv:1807.04537 [astro-ph.HE].

[19] K. Murase, F. Oikonomou, and M. Petropoulou, "Blazar Flares as an Origin of High-Energy Cosmic Neutrinos?," *Astrophys. J.* **865** no. 2, (2018) 124, arXiv:1807.04748 [astro-ph.HE].

[20] A. Reimer, M. Boettcher, and S. Buson, "Cascading Constraints from Neutrino-emitting Blazars: The Case of TXS 0506+056," *Astrophys. J.* **881** no. 1, (2019) 46, arXiv:1812.05654 [astro-ph.HE]. [Erratum: Astrophys.J. 899, 168 (2020)].

[21] X. Rodrigues, S. Gao, A. Fedynitch, A. Palladino, and W. Winter, "Leptohadronic Blazar Models Applied to the 2014–2015 Flare of TXS 0506+056," *Astrophys. J. Lett.* **874** no. 2, (2019) L29, arXiv:1812.05939 [astro-ph.HE].

[22] M. Petropoulou *et al.*, "Multi-Epoch Modeling of TXS 0506+056 and Implications for Long-Term High-Energy Neutrino Emission," *Astrophys. J.* **891** (2020) 115, arXiv:1911.04010 [astro-ph.HE].

[23] S. Gasparyan, D. Bégué, and N. Sahakyan, "Time-dependent lepto-hadronic modelling of the emission from blazar jets with SOPRANO: the case of TXS 0506 + 056, 3HSP J095507.9 + 355101, and 3C 279," *Mon. Not. Roy. Astron. Soc.* **509** no. 2, (2021) 2102–2121, arXiv:2110.01549 [astro-ph.HE].

[24] X. Rodrigues, S. Garrappa, S. Gao, V. S. Paliya, A. Franckowiak, and W. Winter, "Multiwavelength and Neutrino Emission from Blazar PKS 1502 + 106," *Astrophys. J.* **912** no. 1, (2021) 54, arXiv:2009.04026 [astro-ph.HE].

[25] P. Giommi, P. Padovani, F. Oikonomou, T. Glauch, S. Paiano, and E. Resconi, "3HSP J095507.9+355101: a flaring extreme blazar coincident in space and time with IceCube-200107A," *Astron. Astrophys.* **640** (2020) L4, arXiv:2003.06405 [astro-ph.HE].

[26] **Fermi-LAT, ASAS-SN, IceCube** Collaboration, S. Garrappa *et al.*, "Investigation of two Fermi-LAT gamma-ray blazars coincident with

high-energy neutrinos detected by IceCube," *Astrophys. J.* **880** no. 2, (2019) 880:103, `arXiv:1901.10806 [astro-ph.HE]`.

[27] M. Kadler *et al.*, "Coincidence of a high-fluence blazar outburst with a PeV-energy neutrino event," *Nature Phys.* **12** no. 8, (2016) 807–814, `arXiv:1602.02012 [astro-ph.HE]`.

[28] N. Sahakyan, P. Giommi, P. Padovani, M. Petropoulou, D. Bégué, B. Boccardi, and S. Gasparyan, "A multi-messenger study of the blazar PKS 0735+178: a new major neutrino source candidate," `arXiv:2204.05060 [astro-ph.HE]`.

[29] **IceCube** Collaboration, R. Abbasi *et al.*, "Search for Multi-flare Neutrino Emissions in 10 yr of IceCube Data from a Catalog of Sources," *Astrophys. J. Lett.* **920** no. 2, (2021) L45, `arXiv:2109.05818 [astro-ph.HE]`.

[30] P. Giommi, T. Glauch, P. Padovani, E. Resconi, A. Turcati, and Y. L. Chang, "Dissecting the regions around IceCube high-energy neutrinos: growing evidence for the blazar connection," *Mon. Not. Roy. Astron. Soc.* **497** no. 1, (2020) 865–878, `arXiv:2001.09355 [astro-ph.HE]`.

[31] A. Franckowiak *et al.*, "Patterns in the Multiwavelength Behavior of Candidate Neutrino Blazars," *Astrophys. J.* **893** no. 2, (2020) 162, `arXiv:2001.10232 [astro-ph.HE]`.

[32] A. Mucke and R. J. Protheroe, "A Proton synchrotron blazar model for flaring in Markarian 501," *Astropart. Phys.* **15** (2001) 121–136, `arXiv:astro-ph/0004052`.

[33] **IceCube** Collaboration. `https://icecube.wisc.edu/data-releases/2018/07/`.

[34] P. Gondolo and J. Silk, "Dark matter annihilation at the galactic center," *Phys. Rev. Lett.* **83** (1999) 1719–1722, `arXiv:astro-ph/9906391`.

[35] P. Ullio, H. Zhao, and M. Kamionkowski, "A Dark matter spike at the galactic center?," *Phys. Rev. D* **64** (2001) 043504, arXiv:astro-ph/0101481.

[36] P. Padovani, F. Oikonomou, M. Petropoulou, P. Giommi, and E. Resconi, "TXS 0506+056, the first cosmic neutrino source, is not a BL Lac," *Mon. Not. Roy. Astron. Soc.* **484** no. 1, (2019) L104–L108, arXiv:1901.06998 [astro-ph.HE].

[37] O. Y. Gnedin and J. R. Primack, "Dark Matter Profile in the Galactic Center," *Phys. Rev. Lett.* **93** (2004) 061302, arXiv:astro-ph/0308385.

[38] C. A. Argüelles, A. Kheirandish, and A. C. Vincent, "Imaging Galactic Dark Matter with High-Energy Cosmic Neutrinos," *Phys. Rev. Lett.* **119** no. 20, (2017) 201801, arXiv:1703.00451 [hep-ph].

[39] A. C. Vincent, C. A. Argüelles, and A. Kheirandish, "High-energy neutrino attenuation in the Earth and its associated uncertainties," *JCAP* **11** (2017) 012, arXiv:1706.09895 [hep-ph].

[40] M. R. Mosbech, C. Boehm, S. Hannestad, O. Mena, J. Stadler, and Y. Y. Y. Wong, "The full Boltzmann hierarchy for dark matter-massive neutrino interactions," *JCAP* **03** (2021) 066, arXiv:2011.04206 [astro-ph.CO].

[41] D. C. Hooper and M. Lucca, "Hints of dark matter-neutrino interactions in Lyman-$\alpha$ data," *Phys. Rev. D* **105** no. 10, (2022) 103504, arXiv:2110.04024 [astro-ph.CO].

[42] Y. Jho, J.-C. Park, S. C. Park, and P.-Y. Tseng, "Cosmic-Neutrino-Boosted Dark Matter ($\nu$BDM)," arXiv:2101.11262 [hep-ph].

[43] Y.-H. Lin, W.-H. Wu, M.-R. Wu, and H. T.-K. Wong, "Searching for Afterglow: Light Dark Matter boosted by Supernova Neutrinos," arXiv:2206.06864 [hep-ph].

[44] G. Mangano, A. Melchiorri, P. Serra, A. Cooray, and M. Kamionkowski, "Cosmological bounds on dark matter-neutrino interactions," *Phys. Rev. D* **74** (2006) 043517, arXiv:astro-ph/0606190.

[45] C. Boehm, M. J. Dolan, and C. McCabe, "A Lower Bound on the Mass of Cold Thermal Dark Matter from Planck," *JCAP* **08** (2013) 041, arXiv:1303.6270 [hep-ph].

[46] B. Bertoni, S. Ipek, D. McKeen, and A. E. Nelson, "Constraints and consequences of reducing small scale structure via large dark matter-neutrino interactions," *JHEP* **04** (2015) 170, arXiv:1412.3113 [hep-ph].

[47] R. J. Wilkinson, C. Boehm, and J. Lesgourgues, "Constraining Dark Matter-Neutrino Interactions using the CMB and Large-Scale Structure," *JCAP* **05** (2014) 011, arXiv:1401.7597 [astro-ph.CO].

[48] Y. Zhang, "Speeding up dark matter with solar neutrinos," *PTEP* **2022** no. 1, (2022) 013B05, arXiv:2001.00948 [hep-ph].

[49] Y. Farzan and S. Palomares-Ruiz, "Dips in the Diffuse Supernova Neutrino Background," *JCAP* **06** (2014) 014, arXiv:1401.7019 [hep-ph].

[50] A. Das and M. Sen, "Boosted dark matter from diffuse supernova neutrinos," *Phys. Rev. D* **104** no. 7, (2021) 075029, arXiv:2104.00027 [hep-ph].

[51] D. Bardhan, S. Bhowmick, D. Ghosh, A. Guha, and D. Sachdeva, "Boosting through the Darkness," arXiv:2208.09405 [hep-ph].

[52] P. Fayet, D. Hooper, and G. Sigl, "Constraints on light dark matter from core-collapse supernovae," *Phys. Rev. Lett.* **96** (2006) 211302, arXiv:hep-ph/0602169.

[53] **IceCube** Collaboration, A. McMullen, A. Vincent, C. Arguelles, and A. Schneider, "Dark matter neutrino scattering in the galactic centre with

IceCube," *JINST* **16** no. 08, (2021) C08001, arXiv:2107.11491 [astro-ph.HE].

[54] S. Koren, "Neutrino – Dark Matter Scattering and Coincident Detections of UHE Neutrinos with EM Sources," *JCAP* **09** (2019) 013, arXiv:1903.05096 [hep-ph].

[55] K. Murase and I. M. Shoemaker, "Neutrino Echoes from Multimessenger Transient Sources," *Phys. Rev. Lett.* **123** no. 24, (2019) 241102, arXiv:1903.08607 [hep-ph].

[56] J. A. Carpio, A. Kheirandish, and K. Murase, "Time-delayed neutrino emission from supernovae as a probe of dark matter-neutrino interactions," arXiv:2204.09650 [hep-ph].

[57] J. H. Davis and J. Silk, "Spectral and Spatial Distortions of PeV Neutrinos from Scattering with Dark Matter," arXiv:1505.01843 [hep-ph].

[58] W. Yin, "Highly-boosted dark matter and cutoff for cosmic-ray neutrinos through neutrino portal," *EPJ Web Conf.* **208** (2019) 04003, arXiv:1809.08610 [hep-ph].

[59] H. An, M. Pospelov, J. Pradler, and A. Ritz, "Directly Detecting MeV-scale Dark Matter via Solar Reflection," *Phys. Rev. Lett.* **120** no. 14, (2018) 141801, arXiv:1708.03642 [hep-ph]. [Erratum: Phys.Rev.Lett. 121, 259903 (2018)].

[60] **SENSEI** Collaboration, L. Barak *et al.*, "SENSEI: Direct-Detection Results on sub-GeV Dark Matter from a New Skipper-CCD," *Phys. Rev. Lett.* **125** no. 17, (2020) 171802, arXiv:2004.11378 [astro-ph.CO].

[61] R. Essig, T. Volansky, and T.-T. Yu, "New Constraints and Prospects for sub-GeV Dark Matter Scattering off Electrons in Xenon," *Phys. Rev. D* **96** no. 4, (2017) 043017, arXiv:1703.00910 [hep-ph].

[62] **DarkSide-50** Collaboration, P. Agnes *et al.*, "Search for dark matter particle interactions with electron final states with DarkSide-50," `arXiv:2207.11968 [hep-ex]`.

[63] **XENON** Collaboration, E. Aprile *et al.*, "Light Dark Matter Search with Ionization Signals in XENON1T," *Phys. Rev. Lett.* **123** no. 25, (2019) 251801, `arXiv:1907.11485 [hep-ex]`.

[64] C. Dvorkin, K. Blum, and M. Kamionkowski, "Constraining Dark Matter-Baryon Scattering with Linear Cosmology," *Phys. Rev. D* **89** no. 2, (2014) 023519, `arXiv:1311.2937 [astro-ph.CO]`.

[65] M. A. Buen-Abad, R. Essig, D. McKeen, and Y.-M. Zhong, "Cosmological constraints on dark matter interactions with ordinary matter," *Phys. Rept.* **961** (2022) 1–35, `arXiv:2107.12377 [astro-ph.CO]`.

[66] D. V. Nguyen, D. Sarnaaik, K. K. Boddy, E. O. Nadler, and V. Gluscevic, "Observational constraints on dark matter scattering with electrons," *Phys. Rev. D* **104** no. 10, (2021) 103521, `arXiv:2107.12380 [astro-ph.CO]`.

[67] Y. Ali-Haïmoud, J. Chluba, and M. Kamionkowski, "Constraints on Dark Matter Interactions with Standard Model Particles from Cosmic Microwave Background Spectral Distortions," *Phys. Rev. Lett.* **115** no. 7, (2015) 071304, `arXiv:1506.04745 [astro-ph.CO]`.

[68] Y. Ali-Haïmoud, "Testing dark matter interactions with CMB spectral distortions," *Phys. Rev. D* **103** no. 4, (2021) 043541, `arXiv:2101.04070 [astro-ph.CO]`.

[69] D. Wadekar and G. R. Farrar, "Gas-rich dwarf galaxies as a new probe of dark matter interactions with ordinary matter," *Phys. Rev. D* **103** no. 12, (2021) 123028, `arXiv:1903.12190 [hep-ph]`.

[70] C. V. Cappiello and J. F. Beacom, "Strong New Limits on Light Dark Matter

from Neutrino Experiments," *Phys. Rev. D* **100** no. 10, (2019) 103011, arXiv:1906.11283 [hep-ph]. [Erratum: Phys.Rev.D 104, 069901 (2021)].

[71] Y. Ema, F. Sala, and R. Sato, "Light Dark Matter at Neutrino Experiments," *Phys. Rev. Lett.* **122** no. 18, (2019) 181802, arXiv:1811.00520 [hep-ph].

[72] Q.-H. Cao, R. Ding, and Q.-F. Xiang, "Searching for sub-MeV boosted dark matter from xenon electron direct detection," *Chin. Phys. C* **45** no. 4, (2021) 045002, arXiv:2006.12767 [hep-ph].

[73] C. Xia, Y.-H. Xu, and Y.-F. Zhou, "Constraining light dark matter upscattered by ultrahigh-energy cosmic rays," *Nucl. Phys. B* **969** (2021) 115470, arXiv:2009.00353 [hep-ph].

[74] J. B. Dent, B. Dutta, J. L. Newstead, I. M. Shoemaker, and N. T. Arellano, "Present and future status of light dark matter models from cosmic-ray electron upscattering," *Phys. Rev. D* **103** (2021) 095015, arXiv:2010.09749 [hep-ph].

[75] T. Bringmann and M. Pospelov, "Novel direct detection constraints on light dark matter," *Phys. Rev. Lett.* **122** no. 17, (2019) 171801, arXiv:1810.10543 [hep-ph].

[76] J. B. Dent, B. Dutta, J. L. Newstead, and I. M. Shoemaker, "Bounds on Cosmic Ray-Boosted Dark Matter in Simplified Models and its Corresponding Neutrino-Floor," *Phys. Rev. D* **101** no. 11, (2020) 116007, arXiv:1907.03782 [hep-ph].

[77] W. Wang, L. Wu, J. M. Yang, H. Zhou, and B. Zhu, "Cosmic ray boosted sub-GeV gravitationally interacting dark matter in direct detection," *JHEP* **12** (2020) 072, arXiv:1912.09904 [hep-ph]. [Erratum: JHEP 02, 052 (2021)].

[78] G. Guo, Y.-L. S. Tsai, and M.-R. Wu, "Probing cosmic-ray accelerated light dark matter with IceCube," *JCAP* **10** (2020) 049, arXiv:2004.03161 [astro-ph.HE].

[79] S.-F. Ge, J. Liu, Q. Yuan, and N. Zhou, "Diurnal Effect of Sub-GeV Dark Matter Boosted by Cosmic Rays," *Phys. Rev. Lett.* **126** no. 9, (2021) 091804, arXiv:2005.09480 [hep-ph].

[80] Y. Jho, J.-C. Park, S. C. Park, and P.-Y. Tseng, "Leptonic New Force and Cosmic-ray Boosted Dark Matter for the XENON1T Excess," *Phys. Lett. B* **811** (2020) 135863, arXiv:2006.13910 [hep-ph].

[81] W. Cho, K.-Y. Choi, and S. M. Yoo, "Searching for boosted dark matter mediated by a new gauge boson," *Phys. Rev. D* **102** no. 9, (2020) 095010, arXiv:2007.04555 [hep-ph].

[82] Z.-H. Lei, J. Tang, and B.-L. Zhang, "Constraints on cosmic-ray boosted dark matter in CDEX-10 *," *Chin. Phys. C* **46** no. 8, (2022) 085103, arXiv:2008.07116 [hep-ph].

[83] G. Guo, Y.-L. S. Tsai, M.-R. Wu, and Q. Yuan, "Elastic and Inelastic Scattering of Cosmic-Rays on Sub-GeV Dark Matter," *Phys. Rev. D* **102** no. 10, (2020) 103004, arXiv:2008.12137 [astro-ph.HE].

[84] Y. Ema, F. Sala, and R. Sato, "Neutrino experiments probe hadrophilic light dark matter," *SciPost Phys.* **10** no. 3, (2021) 072, arXiv:2011.01939 [hep-ph].

[85] V. V. Flambaum, L. Su, L. Wu, and B. Zhu, "Constraining sub-GeV dark matter from Migdal and Boosted effects," arXiv:2012.09751 [hep-ph].

[86] N. F. Bell, J. B. Dent, B. Dutta, S. Ghosh, J. Kumar, J. L. Newstead, and I. M. Shoemaker, "Cosmic-ray upscattered inelastic dark matter," *Phys. Rev. D* **104** (2021) 076020, arXiv:2108.00583 [hep-ph].

[87] J.-C. Feng, X.-W. Kang, C.-T. Lu, Y.-L. S. Tsai, and F.-S. Zhang, "Revising inelastic dark matter direct detection by including the cosmic ray acceleration," *JHEP* **04** (2022) 080, arXiv:2110.08863 [hep-ph].

[88] W. Wang, L. Wu, W.-N. Yang, and B. Zhu, “The Spin-dependent Scattering of Boosted Dark Matter,” arXiv:2111.04000 [hep-ph].

[89] C. Xia, Y.-H. Xu, and Y.-F. Zhou, “Production and attenuation of cosmic-ray boosted dark matter,” *JCAP* **02** no. 02, (2022) 028, arXiv:2111.05559 [hep-ph].

[90] J. Bramante, B. J. Kavanagh, and N. Raj, “Scattering Searches for Dark Matter in Subhalos: Neutron Stars, Cosmic Rays, and Old Rocks,” *Phys. Rev. Lett.* **128** no. 23, (2022) 231801, arXiv:2109.04582 [hep-ph].

[91] R. Essig, A. Manalaysay, J. Mardon, P. Sorensen, and T. Volansky, “First Direct Detection Limits on sub-GeV Dark Matter from XENON10,” *Phys. Rev. Lett.* **109** (2012) 021301, arXiv:1206.2644 [astro-ph.CO].

[92] **SuperCDMS** Collaboration, R. Agnese *et al.*, “First Dark Matter Constraints from a SuperCDMS Single-Charge Sensitive Detector,” *Phys. Rev. Lett.* **121** no. 5, (2018) 051301, arXiv:1804.10697 [hep-ex]. [Erratum: Phys.Rev.Lett. 122, 069901 (2019)].

[93] **SuperCDMS** Collaboration, D. W. Amaral *et al.*, “Constraints on low-mass, relic dark matter candidates from a surface-operated SuperCDMS single-charge sensitive detector,” *Phys. Rev. D* **102** no. 9, (2020) 091101, arXiv:2005.14067 [hep-ex].

[94] **DarkSide** Collaboration, P. Agnes *et al.*, “Constraints on Sub-GeV Dark-Matter–Electron Scattering from the DarkSide-50 Experiment,” *Phys. Rev. Lett.* **121** no. 11, (2018) 111303, arXiv:1802.06998 [astro-ph.CO].

[95] **SENSEI** Collaboration, M. Crisler, R. Essig, J. Estrada, G. Fernandez, J. Tiffenberg, M. Sofo haro, T. Volansky, and T.-T. Yu, “SENSEI: First Direct-Detection Constraints on sub-GeV Dark Matter from a Surface Run,” *Phys. Rev. Lett.* **121** no. 6, (2018) 061803, arXiv:1804.00088 [hep-ex].

[96] **SENSEI** Collaboration, O. Abramoff *et al.*, "SENSEI: Direct-Detection Constraints on Sub-GeV Dark Matter from a Shallow Underground Run Using a Prototype Skipper-CCD," *Phys. Rev. Lett.* **122** no. 16, (2019) 161801, `arXiv:1901.10478 [hep-ex]`.

[97] **XENON** Collaboration, E. Aprile *et al.*, "Emission of single and few electrons in XENON1T and limits on light dark matter," *Phys. Rev. D* **106** no. 2, (2022) 022001, `arXiv:2112.12116 [hep-ex]`.

[98] **DAMIC** Collaboration, A. Aguilar-Arevalo *et al.*, "Constraints on Light Dark Matter Particles Interacting with Electrons from DAMIC at SNOLAB," *Phys. Rev. Lett.* **123** no. 18, (2019) 181802, `arXiv:1907.12628 [astro-ph.CO]`.

[99] **EDELWEISS** Collaboration, Q. Arnaud *et al.*, "First germanium-based constraints on sub-MeV Dark Matter with the EDELWEISS experiment," *Phys. Rev. Lett.* **125** no. 14, (2020) 141301, `arXiv:2003.01046 [astro-ph.GA]`.

[100] **PandaX-II** Collaboration, C. Cheng *et al.*, "Search for Light Dark Matter-Electron Scatterings in the PandaX-II Experiment," *Phys. Rev. Lett.* **126** no. 21, (2021) 211803, `arXiv:2101.07479 [hep-ex]`.

[101] C. V. Cappiello, K. C. Y. Ng, and J. F. Beacom, "Reverse Direct Detection: Cosmic Ray Scattering With Light Dark Matter," *Phys. Rev. D* **99** no. 6, (2019) 063004, `arXiv:1810.07705 [hep-ph]`.

[102] N. F. Bell, G. Busoni, and S. Robles, "Capture of Leptophilic Dark Matter in Neutron Stars," *JCAP* **06** (2019) 054, `arXiv:1904.09803 [hep-ph]`.

[103] N. F. Bell, G. Busoni, S. Robles, and M. Virgato, "Improved Treatment of Dark Matter Capture in Neutron Stars," *JCAP* **09** (2020) 028, `arXiv:2004.14888 [hep-ph]`.

[104] N. F. Bell, G. Busoni, S. Robles, and M. Virgato, "Improved Treatment of

Dark Matter Capture in Neutron Stars II: Leptonic Targets," *JCAP* **03** (2021) 086, `arXiv:2010.13257 [hep-ph]`.

[105] N. F. Bell, G. Busoni, M. E. Ramirez-Quezada, S. Robles, and M. Virgato, "Improved treatment of dark matter capture in white dwarfs," *JCAP* **10** (2021) 083, `arXiv:2104.14367 [hep-ph]`.

[106] M. S. Bilenky, S. M. Bilenky, and A. Santamaria, "Invisible width of the Z boson and 'secret' neutrino-neutrino interactions," *Phys. Lett. B* **301** (1993) 287–291.

[107] J. M. Berryman *et al.*, "Neutrino Self-Interactions: A White Paper," in *2022 Snowmass Summer Study*. 3, 2022. `arXiv:2203.01955 [hep-ph]`.

[108] J. M. Cline and M. Puel, "NGC 1068 constraints on neutrino-dark matter scattering," *JCAP* **06** (2023) 004, `arXiv:2301.08756 [hep-ph]`.

Chapter 8

# NGC 1068 constraints on neutrino-dark matter scattering

**James M. Cline, and Matteo Puel**

*McGill University, Department of Physics, 3600 University Street, Montréal, QC H3A2T8 Canada*

Published in Journal of Cosmology and Astroparticle Physics: JCAP 06 (2023) 004, [arXiv:2301.08756].

## 8.0 Prologue

In the previous chapter, we used blazars to set strong limits on the DM-neutrino scattering cross section. However, other AGN types can also be employed for this purpose if neutrinos from these sources are detected by ground-based neutrino observatories.

Recently, IceCube detected several neutrinos originating from the nearby radio galaxy, NGC 1068. Unlike blazars, radio galaxies are obscured by a thick torus of gas and dust, preventing the escape of $\gamma$-rays [1]. Neutrino emission in radio galaxies occurs in regions closer to the supermassive black hole, such as in the corona, which is an ultra-bright, billion-degree ring of high-energy particles surrounding the black

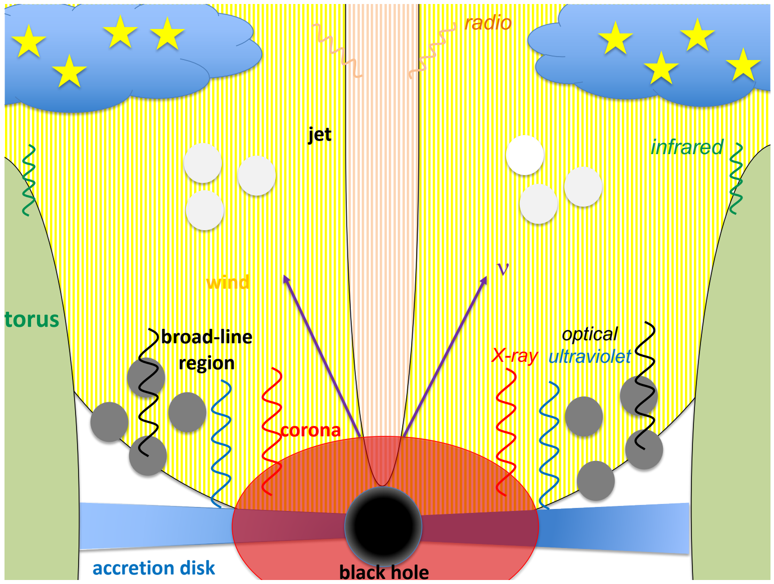

Figure 8.0.1: Schematic picture of a radio galaxy producing neutrinos. Gas accreting onto a supermassive black hole forms an accretion disk and hot corona emitting optical, UV, and X-rays. This electromagnetic radiation is obscured by the surrounding gas and dust. Infrared radiation comes from a dusty torus. Winds and jets may also be launched. Figure taken from Ref. [1].

hole's event horizon [2]. An illustration of the structure of a radio galaxy is provided in Fig. 8.0.1.

The smaller neutrino-emitting region in radio galaxies, compared to blazars, suggests that constraints on DM-neutrino cross section inferred from the interactions between neutrinos and the DM spike could potentially become stronger than those derived in the previous chapter. We will explore this possibility in the following.

### Abstract

The IceCube collaboration has observed the first steady-state point source of high-energy neutrinos, coming from the active galaxy NGC 1068. If neutrinos interacted strongly enough with dark matter, the emitted neutrinos would have been impeded by the dense spike of dark matter surrounding the supermassive black hole at the galactic center, which powers the emission. We derive a stringent upper limit on the scattering cross section between neutrinos and dark matter based on the observed events and

theoretical models of the dark matter spike. The bound can be stronger than that obtained by the single IceCube neutrino event from the blazar TXS 0506+056 for some spike models.

## 8.1 Introduction

Neutrinos and dark matter (DM) are the most weakly coupled particles in the Universe; it is intriguing to imagine that they might interact very weakly with each other. Much effort has been made to search for signals of $\nu$-DM interactions, through their effects on cosmology [3–8], astrophysics [3, 9–15], and direct detection of boosted DM [16–22] and fermionic absorption DM [23–30]. Neutrino emission from active galactic nuclei (AGN) can provide a sensitive probe of $\nu$-DM scattering, in particular from the blazar TXS 0506+056, from which a 290 TeV neutrino was observed by IceCube [31]. It was pointed out in Ref. [32] that the ensuing constraints could be significantly improved by taking into account the dense "spike" of DM that is believed to accrue around the supermassive black hole (SMBH) that powers the AGN engine.

Recently the IceCube collaboration reported observing $79^{+22}_{-20}$ neutrinos from the nearby active galaxy NGC 1068, mostly with energies of $\sim (1-15)\,\mathrm{TeV}$, the first continuously emitting point source of neutrinos to be discovered [33]. Unlike a blazar, in which the jet points toward Earth, NGC 1068 is a radio galaxy, with the jet pointing $\sim 90°$ away [34, 35], thereby exposing Earth to the equatorial emissions perpendicular to the jet. The neutrino emission in this case can be dominated by regions closer to the SMBH, where the DM spike plays a more important role. We thus anticipate that it can further strengthen the constraints on $\nu$-DM scattering, beyond what is possible with a blazar. In the following, we will show this is indeed the case.

## 8.2 Neutrino flux

We use similar methodology to that in Ref. [32]. To set a constraint on the $\nu$-DM scattering cross section using AGNs as neutrino sources one must specify the initial

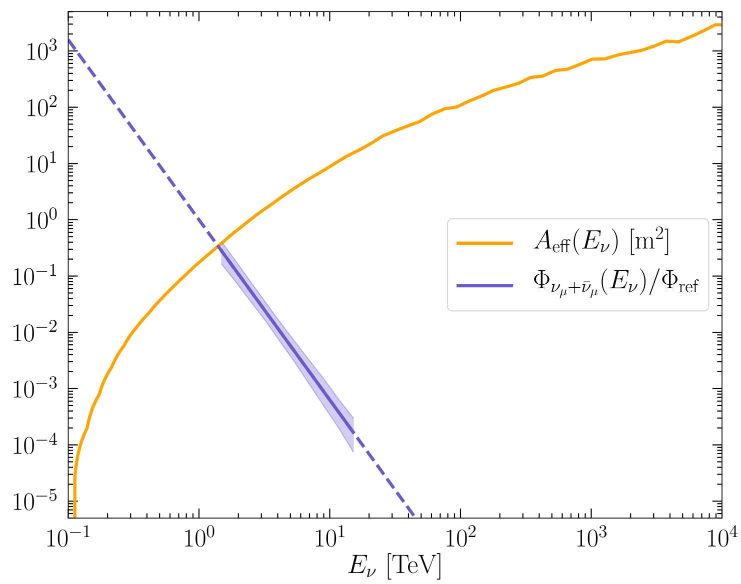


Figure 8.1.1: Normalized neutrino flux $\Phi_{\nu_\mu+\bar{\nu}_\mu}(E_\nu)/\Phi_{\rm ref}$ and IceCube effective area $A_{\rm eff}(E_\nu)$ from the direction of NGC 1068. The flux, described by Eq. (8.1), is shown in slate blue along with its 95% confidence region [33]. The orange curve is the effective area, which is taken from Ref. [36].

neutrino spectrum and the density of the DM spike. The IceCube collaboration has found that the neutrino flux at Earth is well-described in the energy range $E_\nu \in [1.5, 15]$ TeV by an unbroken power-law of the form [33]

$$\Phi_{\nu_\mu+\bar{\nu}_\mu}(E_\nu) = \Phi_{\rm ref}\left(\frac{E_\nu}{E_{\rm ref}}\right)^{-\gamma} \tag{8.1}$$

based on the observation of $\approx 80$ events. Here, $E_{\rm ref} = 1$ TeV, $\Phi_{\rm ref} \approx 5\times10^{-11}$ TeV$^{-1}$cm$^{-2}$s$^{-1}$ and $\gamma \approx 3.2$. This flux, shown in Fig. 8.1.1, accounts for the muon neutrino and anti-neutrino contributions only since these are what the IceCube detector can measure; it is expected that all flavors contribute equally to the spectrum, due to neutrino oscillations over cosmic distances, for sources dominated by pion decay [37, 38]. Therefore we can view Eq. (8.1) as the flux where neutrino oscillations are included and the all-flavor flux would be a factor of 3 higher.

In the following, we will carry out two complementary statistical analyses for setting limits on the $\nu$-DM scattering cross section, based on different reasonable null hypotheses. In the first approach, we will assume that the initial neutrino flux coincides with the one observed by IceCube, and derive 90% C.L. limits on $\sigma_{\nu\chi}$ by requiring this assumed initial flux not be attenuated too much. In the alternative approach, carried out in Section 8.5, we will instead assume the initial flux is that predicted by theoretical models from the literature. It will be shown that the two methodologies give results that are in agreement up to factors of a few.

As a consistency check, we first recomputed the number of expected muon neutrino events observed by IceCube in the case of no $\nu$-DM scattering,

$$N_{\rm pred} = t_{\rm obs} \int dE_\nu \, \Phi_\nu(E_\nu) \, A_{\rm eff}(E_\nu) \,, \tag{8.2}$$

where $\Phi_\nu \equiv \Phi_{\nu_\mu+\bar{\nu}_\mu}$ is the flux in Eq. (8.1), $t_{\rm obs} \approx 3186$ days [33] is the observing time, and $A_{\rm eff}$ is the detector's effective area, shown in Fig. 8.1.1. The relevant events were observed between 2011 and 2020, and data for $A_{\rm eff}$ from the direction of NGC 1068 is provided by IceCube [36]. Integrating Eq. (8.2) over the range $E_\nu \in [10^{-1}, 10^4]$ TeV [33] gives $N_{\rm pred} \approx 80$ events as expected. Since IceCube considered the flux in Eq. (8.1) to be reliably determined only within the smaller energy range $E_\nu \in [1.5, 15]$ TeV, we find that the corresponding number of predicted muon neutrinos is reduced to $N_{\rm pred} \approx 31 \pm 7$.

## 8.3 Dark matter spike profile

The second ingredient needed to set a constraint on $\nu$-DM scattering is the density profile of the DM spike. The accretion of DM onto the SMBH has been widely studied in the literature, *e.g.,* Refs. [39–47]. If the accretion is adiabatic and relativistic effects are neglected, it can be shown that an initially cuspy DM profile of the form

$$\rho(r) \simeq \rho_s \left(\frac{r}{r_s}\right)^{-\gamma} \tag{8.3}$$

in the region close to the SMBH, with $r_s$ the scale radius and $\rho_s$ the scale density, evolves into a spike whose density is [39]

$$\rho'(r) \simeq \rho_R \left(1 - \frac{4R_S}{r}\right)^3 \left(\frac{R_{sp}}{r}\right)^\alpha . \tag{8.4}$$

Here $R_S = 2GM_{\rm BH}$ is the Schwarzschild radius, $R_{sp}$ is the characteristic size of the spike and $\rho_R \approx \rho'(R_{sp})$. The slope $\alpha$ of the spike profile in Eq. (8.4) was found in Ref. [39] to be related to the slope of the initial profile $\gamma$ in Eq. (8.3) by $\alpha = (9 - 2\gamma)/(4 - \gamma)$. For $0 \leq \gamma \leq 2$, $\alpha$ can vary between 2.25 to 2.5 and for a Navarro-Frenk-White (NFW) profile $\gamma = 1$ and $\alpha = 7/3$.

### 8.3.1 Spike relaxation

However, the likely presence of a dense stellar component in the inner region of the galaxy can induce gravitational scattering off of DM, causing a softening of the spike profile to a slope of $\alpha = 3/2$, independently of the value of $\gamma$ [42–45]. We consider both the cases of $\alpha = 7/3$ and $\alpha = 3/2$, with $\gamma = 1$. More precisely, the modification of the slope of the spike due to stellar scattering with DM is relevant only within the influence radius of the SMBH, $r_h$ [43], which is generally smaller than the size of the spike $R_{sp}$.[1] Therefore, for the case of $\alpha = 3/2$, the spike profile in Eq. (8.4) should be modified by

$$\rho'_{3/2}(r) \simeq \begin{cases} \rho_N \left(1 - \dfrac{4R_S}{r}\right)^3 \left(\dfrac{r_h}{r}\right)^{3/2} & r_i \leq r \leq r_h \\ \rho'_N \left(\dfrac{R_{sp}}{r}\right)^{7/3} & r \geq r_h \end{cases} \tag{8.5}$$

[1]The influence radius is defined as $r_h = GM_{BH}/\sigma_\star^2$, where $\sigma_\star$ is the stellar velocity dispersion. This is the radius within which the gravitational effects of the SMBH directly affect the motion of the surrounding stars.

where $r_i = 4R_S$ is the inner radius of the spike, and the outer profile at $r \geq r_h$ converges to that predicted by Ref. [39] for $r \geq r_h \gg R_S$, which we rewrite as

$$\rho'_{7/3}(r) \simeq \rho_N \left(1 - \frac{4R_S}{r}\right)^3 \left(\frac{R_{sp}}{r}\right)^{7/3}, \qquad r \geq r_i\,. \tag{8.6}$$

### 8.3.2 Effect of DM annihilation

If DM particles are allowed to annihilate, the spike profile in the innermost region tends to a maximum density $\rho_c = m_\chi/(\langle\sigma_a v\rangle\, t_{\rm BH})$, where $m_\chi$ is the DM mass, $\langle\sigma_a v\rangle$ is an effective annihilation cross section,[2] and $t_{\rm BH}$ is the age of the SMBH. We take the latter to be $t_{\rm BH} \simeq 10^9$ yrs for NGC 1068, which is well motivated by studies on the mass assembly history of SMBH at high redshift [48]. This value is also similar to that adopted for the blazar TXS 0506+056 [32, 49–51], which allows a fair comparison between the new limits derived in this paper and the previous ones. Considering that the spike profile should merge onto the pre-existing galaxy profile for $r \geq R_{sp}$, which we take as a NFW halo of the form

$$\rho_{\rm NFW}(r) = \rho_s \left(\frac{r}{r_s}\right)^{-1} \left(1 + \frac{r}{r_s}\right)^{-2}, \tag{8.7}$$

then the total DM density can be written as [39, 40, 51–53]

$$\rho_\chi(r) = \begin{cases} 0 & r \leq r_i \\ \dfrac{\rho'_\alpha(r)\,\rho_c}{\rho'_\alpha(r) + \rho_c} & r_i \leq r \leq R_{sp} \\ \dfrac{\rho_{\rm NFW}(r)\,\rho_c}{\rho_{\rm NFW}(r) + \rho_c} & r \geq R_{sp} \end{cases} \tag{8.8}$$

where $\rho'_\alpha(r)$ is given by Eq. (8.5) for $\alpha = 3/2$ and by Eq. (8.6) for $\alpha = 7/3$. In Eq. (8.8) we accounted for the possibility that DM annihilation is strong enough to deplete the outer NFW halo as well, in addition to the internal spike.[3]

[2] If the dark matter is asymmetric, then the effective $\langle\sigma_a v\rangle = 0$, even if the actual $\langle\sigma_a v\rangle$ is large, since in that case annihilations cannot occur within the DM spike.

[3] We found that the DM profile considered in Ref. [51] suffers from the lack of the additional DM annihilation in the outer halo for some values of $m_\chi$ and $\langle\sigma_a v\rangle$. This problem does not occur for the

### 8.3.3 Fixing spike parameters

We have to determine $\rho_N$, $\rho'_N$, $r_h$ and $R_{sp}$ for the spike density $\rho'_\alpha(r)$, and $\rho_s$ and $r_s$ for the NFW halo. Concerning the latter two parameters, they are determined by the virial mass of NGC 1068, which can be inferred independently of the DM spike, since the latter cannot appreciably impact the overall halo shape. More precisely, N-body simulations in a ΛCDM Universe predict that the DM halo is related to the SMBH mass via [54]

$$M_{\rm BH} \sim 7 \times 10^7\, M_\odot \left(\frac{M_{\rm DM}}{10^{12}\ M_\odot}\right)^{4/3}, \tag{8.9}$$

which is consistent with relations found in Refs. [55, 56].

Estimates of the NGC 1068 SMBH mass vary. From the water maser emission line, Ref. [57] estimated a central mass of $M_{\rm BH} \sim 1\times10^7\ M_\odot$ within a radius of about 0.65 pc $\simeq 6.5\times10^5\ R_S$, which we can take as a proxy for the influence radius $r_h$ of the SMBH. Similar values of $M_{\rm BH}$ were found by Refs. [58–62], but estimates as large as $M_{\rm BH} \sim (7-10)\times10^7\ M_\odot$ have been inferred from the polarized broad Balmer and the neutral FeK$\alpha$ emission lines [63]. In the following, we consider $M_{\rm BH} = 1\times10^7\ M_\odot$ for which $r_h$ is provided, but we checked that the impact of considering different SMBH masses within the range $\sim 10^7 - 10^8\ M_\odot$ would impact our results by at most one order of magnitude in the case without DM-annihilation, making them stronger for smaller values of $M_{\rm BH}$.

From Eq. (8.9) we find that the DM halo mass for NGC 1068 is of order $M_{\rm DM} \simeq 2.3 \times 10^{11}\ M_\odot$, which is consistent within a factor of $\lesssim 4$ with the predictions from Refs. [55, 56, 64, 65] and input parameters from Refs. [66, 67]. Taking $M_{\rm DM}$ to be the virial mass for a NFW halo, we can then use Ref. [68] to infer $r_s \simeq 13$ kpc and $\rho_s \simeq 0.35$ GeV/cm$^3$. The halo parameters we estimated are reasonable in the sense that they are similar to those of the Milky Way galaxy [39, 40, 69], which is known to host a SMBH with similar mass to that in NGC 1068 [70].

The normalization $\rho_N$ of the profiles in Eqs. (8.5) and (8.6) depends only upon the combination $\mathcal{N} \equiv \rho_N\, r_h^{3/2}$ or $\mathcal{N} \equiv \rho_N\, R_{sp}^{7/3}$, respectively, which can be determined

NGC 1068 case because the outer halo turns out to give a negligible contribution.

| $\langle\sigma_a v\rangle$ | Model | $\alpha$ | Model | $\alpha$ |
|---|---|---|---|---|
| 0 | BM1 | 7/3 | BM1′ | 3/2 |
| 0.01 | BM2 | 7/3 | BM2′ | 3/2 |
| 3 | BM3 | 7/3 | BM3′ | 3/2 |

Table 8.3.1: Models considered in this paper, distinguished by different values of the effective DM annihilation cross section (in units of $10^{-26}\,\mathrm{cm}^3/\mathrm{s}$) and the spike-profile exponent $\alpha$. They are the same as considered in Ref. [32]. The case $\langle\sigma_a v\rangle \cong 0$ could correspond to asymmetric or freeze-in dark matter.

by the mass of the SMBH [40, 41, 52, 53, 71]

$$M_{\mathrm{BH}} \approx 4\pi \int_{r_i}^{r_h} dr\, r^2\, \rho_\chi(r)\,, \tag{8.10}$$

where $r_h$ is the radius of influence of the black hole and $\rho_\chi(r)$ is given by Eq. (8.8). The integral in Eq. (8.10) is dominated by the contribution from $r \gg r_i$, in which regime $\rho_\chi(r) \simeq \rho'_\alpha(r)$ since $\rho_c \gg \rho'_\alpha(r)$. Therefore, we find that $\mathcal{N}$ obtained from Eq. (8.10) is approximately given by

$$\mathcal{N} \simeq \frac{M_{\mathrm{BH}}}{4\pi\left[f_\alpha(r_h) - f_\alpha(r_i)\right]}\,, \tag{8.11}$$

where

$$f_\alpha(r) \equiv r^{-\alpha}\left(\frac{r^3}{3-\alpha} + \frac{12R_S\, r^2}{\alpha-2} - \frac{48R_S^2\, r}{\alpha-1} + \frac{64R_S^3}{\alpha}\right). \tag{8.12}$$

For the $\alpha = 3/2$ case, the normalization density $\rho'_N$ in Eq. (8.5) is determined by requiring the profile $\rho'_{3/2}(r)$ to match at $r = r_h$, giving $\rho'_N \simeq \rho_N\,(r_h/R_{sp})^{7/3}$ $\simeq \mathcal{N}\, r_h^{5/6}/R_{sp}^{7/3}$. On the other hand, the value of $R_{sp}$ can be obtained from the matching condition between the spike and the outer halo, namely $\rho'_N$, $\rho_N \simeq \rho_s(R_{sp}/r_s)^{-\gamma}$ for $\alpha = 3/2$, 7/3, respectively, since $R_S \ll r_h < R_{sp} \ll r_s$. This translates into

$$R_{sp} \simeq \begin{cases} \left(\dfrac{\mathcal{N}}{\rho_s r_s}\right)^{3/4} r_h^{5/8}\,, & \alpha = 3/2 \\ \left(\dfrac{\mathcal{N}}{\rho_s r_s}\right)^{3/4}, & \alpha = 7/3 \end{cases}\,, \tag{8.13}$$

where $\mathcal{N}$ is given by Eq. (8.11). We find that $R_{sp} \sim 0.7$ kpc $\gg r_h$ for the parameter

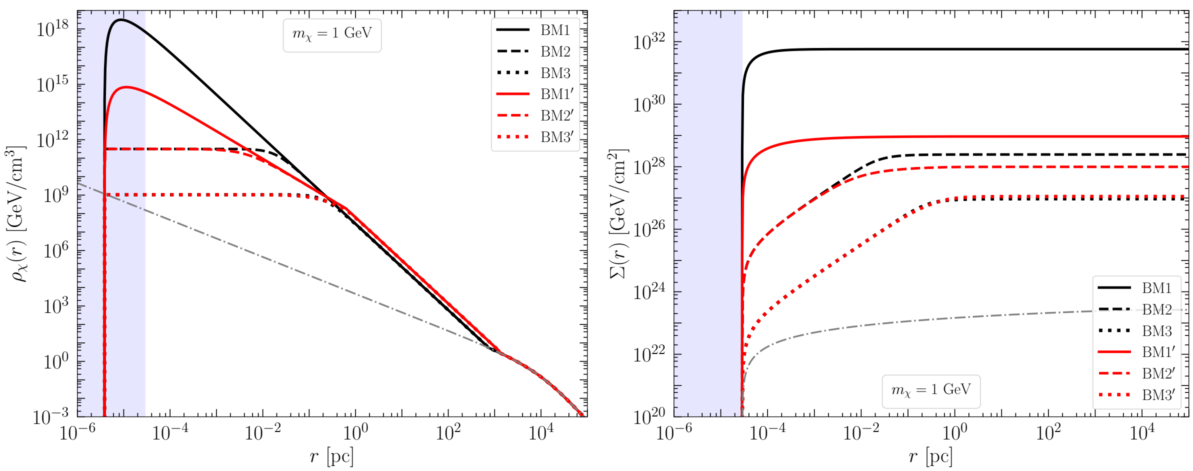


Figure 8.3.1: DM density profile $\rho_\chi(r)$ for the galaxy NGC 1068 (*left*), given by Eq. (8.8), and its corresponding accumulated DM column density $\Sigma(r)$ (*right*), given by Eq. (8.14), as a function of the distance from the galactic centre, for the different benchmark models considered in Table 8.3.1. The DM mass is fixed to $m_\chi = 1$ GeV. The gray dot-dashed curve represents the contribution of the NFW host-halo alone, described by the density in Eq. (8.7). Its contribution to $\Sigma(r)$ is negligible compared to that of the spike. The blue shaded region delimits the region within the galaxy where neutrinos are not likely to be emitted. Its right edge corresponds to the value of $R_{\rm em}$ used in Eq. (8.14).

values used in this paper. The DM profile of NGC 1068, described by Eq. (8.8), is shown in the left panel of Fig. 8.3.1 for different choices of the effective DM annihilation cross section $\langle\sigma_a v\rangle$ and the spike-profile exponent $\alpha$, according to the benchmark models considered in Ref. [32] and summarized in Table 8.3.1.

### 8.3.4 DM column density

An important quantity for $\nu$-DM scattering is the DM column density, which is the projection of the 3D density of DM along the line-of-sight, integrating over the distance that neutrinos travel during their journey to Earth. The accumulated column density is defined by

$$\Sigma(r) = \int_{R_{\rm em}}^{r} dr'\, \rho_{\rm DM}(r') \approx \int_{R_{\rm em}}^{r} dr'\, \rho_\chi(r')\,, \tag{8.14}$$

where $R_{\rm em}$ is the distance from the SMBH to the position in the radio galaxy where neutrinos are first likely to be produced. Neutrinos with energy below 100 TeV are believed to be generated through hadronic interactions occurring in the AGN corona [72–84], whose radius has been estimated to be a few tens of the Schwarzschild radius $R_S$ [1, 80–82, 85, 86]. We take $R_{\rm em} \simeq 30\, R_S$ as in Ref. [82], whose neutrino spectrum matches well the IceCube observation from NGC 1068, and supported by a model-independent study in Ref. [1]. In the second step of Eq. (8.14), we neglected the cosmological and Milky-Way DM contributions to $\Sigma(r)$ (see for instance Ref. [87]) because they are orders of magnitude smaller than that given by the DM spike profile [32, 51].

The right panel of Fig. 8.3.1 shows the accumulated DM column density as a function of the distance from the central SMBH, for the different benchmark models of Table 8.3.1. Given that $\Sigma(r)$ stays constant for $r \gtrsim \mathcal{O}(100\ \text{pc})$, similarly to that found in Ref. [49, 50] for the blazar TXS 0506+056, we can take the DM column density at the Earth location, roughly distant $D_L \simeq 14.4$ Mpc from NGC 1068 [88, 89], to be approximately $\Sigma(D_L) \cong \Sigma(r \simeq 100\ \text{pc}) \equiv \Sigma_\chi$.

In contrast to Ref. [51], we find that the inclusion of the halo of the host galaxy (which becomes important for $r \gtrsim R_{sp}$) gives a negligible contribution to $\Sigma_\chi$, as also suggested by Ref. [50]. This can be explained by the fact that the normalization of the outer halo $\rho_s$ cannot be inferred through the SMBH mass, given by Eq. (8.10), since the latter can constrain at most the DM spike normalization density $\rho_N$. Instead, $\rho_s$ should be chosen so that the total DM mass of the host halo matches reasonable values as found by observations and cosmological simulations, since the spike makes a negligible contribution to the total halo mass.

We note that a more accurate description of the adiabatic accretion of DM onto SMBH would require the inclusion of relativistic effects. Ref. [46] found that not only the inner radius of the DM spike reduces to $r_i = 2R_S$ from its nonrelativistic value of $4R_S$, but also the spike reaches significantly higher densities. For a rotating SMBH, the density enhancement is even more important [47]. However, such relativistic effects become irrelevant for distances $r \gtrsim 20\, R_S$ [46], which is where neutrinos are likely to be produced in NGC 1068.

## 8.4 Constraints on neutrino-dark matter scattering

If neutrinos scatter with DM along their journey to the detector, the attenuation of the neutrino flux can be described by a form of the Boltzmann equation known as the cascade equation [32, 90, 91]

$$\frac{d\Phi}{d\tau}(E_\nu) = -\sigma_{\nu\chi}\Phi + \int_{E_\nu}^{\infty} dE'_\nu \, \frac{d\sigma_{\nu\chi}}{dE_\nu}(E'_\nu \to E_\nu) \, \Phi(E'_\nu) \, , \tag{8.15}$$

where $\tau = \Sigma(r)/m_\chi$ is the accumulated column density, defined in Eq. (8.14), over the DM mass and $E_\nu$ and $E'_\nu$ are the energies of the outgoing and incoming neutrino, respectively. The first term of the cascade equation describes the flux depletion of neutrinos with energy $E_\nu$ due to their interaction with the surrounding DM, whereas the second term corresponds to the effect of energy redistribution of the neutrinos from high to low energy.

The cascade equation is designed to predict the change in the energy spectrum due to downscattering, for high-energy beams that are scattered predominantly in the forward direction. If $d\sigma_{\nu\chi}/dE_\nu$ is nonzero, then it can be seen that $\int_0^\infty dE_\nu d\Phi/d\tau = 0$, indicating that the total number of particles in the beam is conserved, and only their spectrum changes. On the other hand, if one sets $d\sigma_{\nu\chi}/dE_\nu = 0$, the equation describes the inelastic process of neutrino absorption in which there is no final-state energy $E_\nu$. For elastic scattering with constant cross section, the neutrino does not lose energy in the process (only its direction changes), translating into $d\sigma_{\nu\chi}/dE_\nu \propto \delta(E'_\nu - E_\nu)$ and resulting in a conserved flux according to eq. (8.15).

As will be shown in Section 8.6, another situation where the cross section is approximately constant is the high-energy regime of a model with a mediator of mass $m_{Z'} \ll \sqrt{E_\nu m_\chi}$. Even though $d\sigma/dE_\nu$ is not strictly zero in that case, we showed in Ref. [32] that to a good approximation, it can be neglected for such high energies, and we will use this approximation where appropriate below. Including or neglecting the second term in the cascade equation therefore corresponds to different microscopic origins of the scattering, and the results should be interpreted accordingly when comparing to specific particle physics models.

We consider two different cases that describe important regimes for the cross section in particular particle physics models [32]:

(a) $\sigma_{\nu\chi} \simeq \sigma_0 = \text{const}$;

(b) $\sigma_{\nu\chi} \simeq \sigma_0 \, (E_\nu / E_0)$, with $E_0 = \text{const}$.

For the former case, Eq. (8.15) leads to an exponential attenuation of the neutrino flux according to $\Phi(E_\nu) \sim \Phi_\nu(E_\nu) \exp\left(-\sigma_0 \, \Sigma_\chi / m_\chi\right)$, where $\Phi_\nu(E_\nu)$ is the initial flux at the source location, given by Eq. (8.1), and $\Phi(E_\nu)$ is the final flux at the detector location.

To set limits on the scattering cross section, we require the number of neutrinos reaching the detector at Earth to be no less than what IceCube observed. In particular, the 90% Confidence Level (C.L.) upper limit on $\sigma_0$ follows from demanding that the number of events in the energy range $E_\nu \in [1.5, 15]$ TeV exceed $\simeq 22.2$; this is the 90% C.L. lower limit on the number $31 \pm 7$ of observed IceCube events, assuming a Gaussian distribution. For energy-independent scattering and initial flux given by Eq. (8.1), this corresponds to a flux attenuation of $\sim 30\%$, resulting in the bound [4]

$$\sigma_0 < 0.34 \, \frac{m_\chi}{\Sigma_\chi} \, . \tag{8.16}$$

The left panel of Fig. 8.4.1 shows the resulting constraints for the different benchmark models of Table 8.3.1.

The new bounds for the four annihilating DM models (BM2, BM2′, BM3 and BM3′) are a factor 2-3 stronger than those inferred from the blazar TXS 0506+056 by Ref. [32], as can be seen by comparing the black dotted curve with the dotted green one in Fig. 8.4.1. On the other hand, the constraint from TXS 0506+056 on

[4]For the IceCube observation of a single neutrino from the blazar TXS 0506+056, the 90% C.L. lower limit on the Poisson-distributed number of observed events is $\simeq 0.1$ [92], as used in Ref. [32]. This corresponds to a 90% absorption of the initial flux if the scattering cross section is energy-independent, as previously considered in the literature [32, 51, 87].

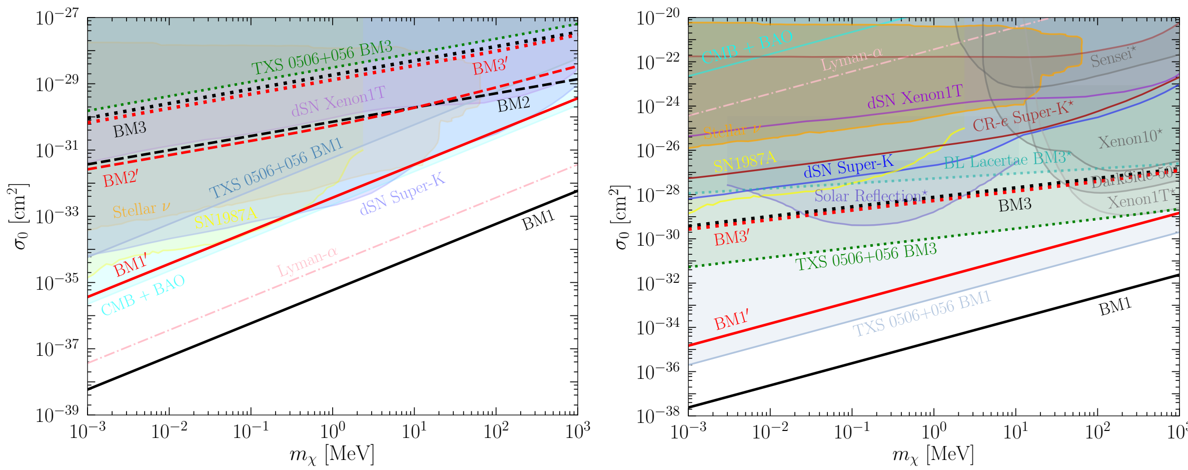


Figure 8.4.1: *Left:* 90% C.L. upper limits on the $\nu$-DM scattering cross section, assumed to be energy-independent, for the six benchmark DM spike models of Table 8.3.1, compared to previous constraints. The latter are: (cyan) CMB and baryon acoustic oscillations [7]; (pink) Lyman-$\alpha$ preferred model [8]; (dark violet, blue) diffuse supernova neutrinos [20]; (orange) stellar neutrinos [17]; (yellow) supernova SN1987A [22]; (green, light steel blue) least and most restrictive bounds, namely for BM3 and BM1 respectively, from TXS 0506+056 [32]. *Right:* Same, but assuming linear energy-dependent $\nu$-DM and $e$-DM scattering cross-sections. All the constraints are rescaled to the energy $E_0 = 10$ TeV according to the relation $\sigma_{\nu\chi} = \sigma_0(E_\nu/E_0)$. Only the least (BM3, BM3′) and most restrictive (BM1, BM1′) new limits are shown. The $\nu$-DM scattering bounds are the same as those in the left panel, while for $e$-DM scattering they are labelled with $\star$ and are: (slate blue) solar reflection [93], (brown) Super-K for DM boosted by cosmic-ray electrons, (turquoise) blazar BL Lacertae for BM3 model [50], (gray) direct detection for light DM interacting with electrons [94–97].

$\sigma_0\Sigma_\chi/m_\chi$ was $\sim 50$ times stronger than the analogous one derived here, Eq. (8.16). The apparent discrepancy arises because $\Sigma_\chi$ for NGC 1068 is much greater than that for TXS 0506+056. Indeed, the total DM density profile $\rho_\chi(r)$ for TXS 0506+056 peaks at larger distances from the galactic centre than that for NGC 1068, with a smaller spike amplitude, given that the mass of the SMBH within the former galaxy is larger than the one in NGC 1068, and so are the corresponding Schwarzschild radii. In other words, the smaller the black hole mass, the larger is the effect of the DM spike, which would peak at a distance closer to the galactic centre compared to a heavier black hole. This effect is even more pronounced in the nonannihilating DM models BM1 and BM1′, which give stronger limits than those obtained in Ref. [32]

for TXS 0506+056, thanks also to the smaller value of $R_{\rm em}$ for the radio galaxy than that for the blazar. In particular the limit for the model BM1 surpasses any existing bounds on $\sigma_{\nu\chi}$ in the literature by several orders of magnitude.

For the linear energy-dependent $\sigma_{\nu\chi} = \sigma_0(E_\nu/E_0)$ case, the cascade equation (8.15) can be solved by discretizing it in equal logarithmic energy intervals and using the methods outlined in Refs. [32, 91]. The 90% C.L. limit on $\sigma_0$ is derived in the same way as described for the energy-independent case. Taking $E_0 = 10$ TeV, which lies within the range of validity of the IceCube flux in Eq. (8.1), we find that

$$\sigma_0 < 1.25\,\frac{m_\chi}{\Sigma_\chi}\,, \tag{8.17}$$

which is roughly a factor of four times weaker than the energy-independent scattering case considered above, given by Eq. (8.16). The corresponding limits on $\sigma_0$ for the different benchmark models are shown on the right panel of Fig. 8.4.1, where the strongest constraints on the $\nu$-DM scattering existing in the literature are included, after being rescaled to the common energy scale $E_0$ using the relation $\sigma_{\nu\chi} = \sigma_0\,(E_\nu/E_0)$.

Bounds on electron-DM scattering are also included in the right panel of Fig. 8.4.1 (labelled with $\star$), since it is natural for DM to interact with neutrinos and charged leptons with equal strength, due to the $\mathrm{SU}(2)_L$ gauge symmetry of the standard model. We refer the reader to Ref. [32] for the description of the existing limits. We do not include the recent bounds on $\sigma_{e\chi}$ inferred by Ref. [98] because they are model-dependent. Our new limits on $\sigma_0$, shown in the right panel for the case of $\sigma_{\nu\chi} \propto E_\nu$, are generally weaker than the constraints implied by the 290 TeV neutrino event from TXS 0506+056, except for the most optimistic BM1 spike model [5].

[5] It was recently argued that the 290 TeV IceCube neutrino from the blazar TXS 0506+056 might have originated from a region closer to the central black hole, such as the corona, rather than coming from the jet [99]. This is based on the observation by the MASTER Collaboration of a rapid change in the optical luminosity of the blazar between one minute and two hours after the IceCube detection [100], which raises the question whether such fast variability could occur at very large distances from the central engine, pertaining to the jet. If this was indeed true, the bounds on $\sigma_0$ derived in Ref. [32] at energy $E_0 = 290$ TeV would become stronger by about a factor of 50 (5) for the BM1 (BM1$'$) model, assuming the initial neutrino flux used there can still be valid. We thank Francis Halzen for brining this to our attention.

| Color in Fig. 8.4.2 | Ref. of $\Phi_\nu$ (color curve) | $\sigma_{\nu\chi} \sim$ const $[m_\chi/\Sigma_\chi]$ | $\sigma_{\nu\chi} \sim E_\nu$ $[m_\chi/\Sigma_\chi]$ |
|---|---|---|---|
| slate blue (IceCube) | Fig. 4 of [33] (slate blue) | $\sigma_0 < 0.34$ | $\sigma_0 < 1.25$ |
| brown | Fig. 2 of [80] (blue, upper) | $\sigma_0 < 0.27$ | $\sigma_0 < 1.33$ |
| lime | Fig. 1 of [83] (red) | $\sigma_0 < 0.36$ | $\sigma_0 < 1.13$ |
| hot pink | Fig. 4 of [83] (deep pink, upper) | $\sigma_0 < 1.52$ | $\sigma_0 < 5.32$ |
| medium orchid | Fig. 12 of [83] (green, thin) | $\sigma_0 < 0.11$ | $\sigma_0 < 0.34$ |
| deep sky blue | Fig. 5 of [101] (black-green) | $\sigma_0 < 0.44$ | $\sigma_0 < 1.67$ |
| crimson | Fig. 3 left of [1] (black) | $\sigma_0 < 0.29$ | $\sigma_0 < 1.09$ |
| gold | Fig. 3 right of [1] (black) | $\sigma_0 < 0.17$ | $\sigma_0 < 0.64$ |
| green | Fig. 6 of [102] (green, dashed) | $\sigma_0 < 0.30$ | $\sigma_0 < 1.06$ |
| orange | Fig. 6 of [102] (orange, solid) | $\sigma_0 < 0.03$ | $\sigma_0 < 0.10$ |

Table 8.4.1: 90% C.L. upper bounds on $\sigma_0$ (in units of $m_\chi/\Sigma_\chi$) for different initial neutrino fluxes $\Phi_\nu$, both for energy-independent and energy-dependent scattering cross sections. The first column contains the color of the curve used in Fig. 8.4.2, the second column displays the reference and figure where each input flux is taken and what color is used to show the curve there. The third and fourth columns contain our derived bounds on $\sigma_0$. The first row corresponds to the bounds in Eqs. (8.16) and (8.17) using the IceCube observed flux in Eq. (8.1) as the input spectrum.

## 8.5 Astrophysical uncertainties

The results derived in the previous sections and summarized in Fig. 8.4.1 are subject to astrophysical uncertainties, which we elaborate on in this section. So far, we considered variations in the shape of the DM spike profile, by allowing for a range of possible values of the profile exponent $\alpha$ and DM annihilation cross section $\langle\sigma_a v\rangle$. Another parameter is the size of the emission region, characterized by the radial distance $R_{\rm em}$ from the central black hole beyond which neutrinos are likely to be produced. A third is the initial neutrino flux $\Phi_\nu$. In the foregoing analysis, we kept the latter two quantities fixed, namely to $R_{\rm em} \simeq 30\, R_S$ and $\Phi_\nu = \Phi_{\nu_\mu+\bar{\nu}_\mu}$, as given by Eq. (8.1).

A largely model-independent study on the connection between neutrinos and gamma rays in NGC 1068, based on the recent IceCube $\approx 80$ events, found that neutrinos in the TeV range are most likely to be emitted from regions within $\sim 30-100\, R_S$ from the galactic center [1]. Dimensional analysis arguments on neutrino production in AGN obscured cores reach similar conclusions [99]. Allowing for $R_{\rm em} \simeq 100\, R_S$, the value of $\Sigma(r)$ implied by Eq. (8.14) would decrease by a factor of $\sim 4$ (2) for the non-annihilation DM model BM1 (BM1′), weakening the corresponding constraints

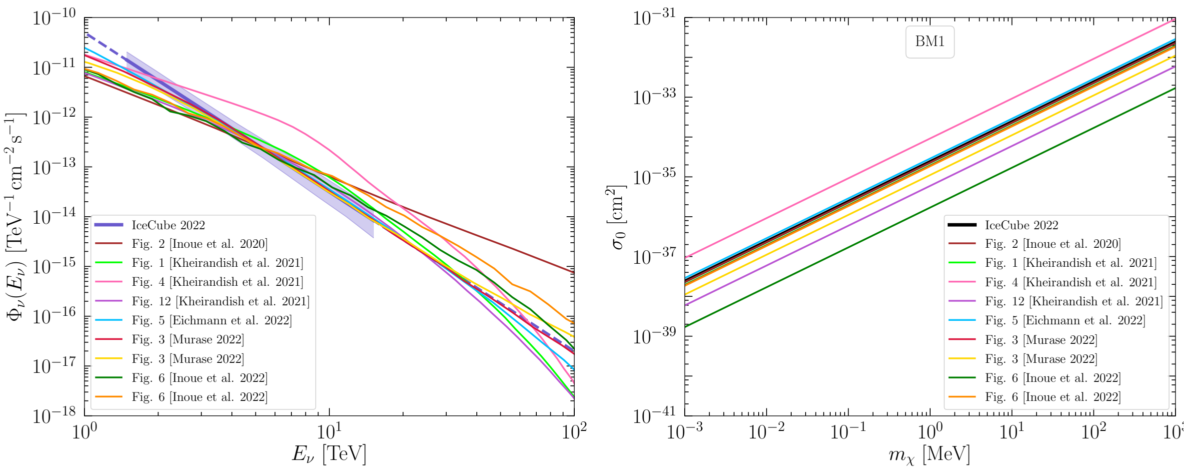


Figure 8.4.2: *Left:* The initial neutrino fluxes $\Phi_\nu$ used in this paper and summarized in Table 8.4.1. The corresponding models used to explain the observational data are, in order of appearance: (slate blue) corona $pp$ scenario with gyrofactor $\eta_g = 30$, which is the mean free path of a particle in units of the gyroradius [80], (lime) stochastic scenario with high cosmic ray (CR) pressure and with x-ray luminosity $L_X = 10^{43}$ erg/s [83], (hot pink) same with $L_X = 10^{43.8}$ erg/s [83], (medium orchid) magnetic reconnection fast acceleration scenario with injected CR power-law exponent $s = 1$, acceleration efficiency $\eta_{\rm acc} = 300$ and maximum proton energy $E_p^{\rm rec} = 0.1$ PeV [83], (deep sky blue) corona plus starburst model [101], (crimson) minimal $pp$ scenario [1], (gold) minimal $p\gamma$ scenario [1], (green) wind plus torus model with magnetic field strength $B = 1130$ G and gyrofactor $\eta_g = 4$ [102], (orange) same with $B = 510$ G and $\eta_g = 1$. The slate blue curve is the IceCube observed flux in Eq. (8.1) as shown in Fig. 8.1.1. *Right:* 90% C.L. limits on the cross section $\sigma_0$ at energy $E_\nu = 10$ TeV in the linear energy-dependent scattering scenario, for the spike model BM1 and for different choices of the initial flux $\Phi_\nu$. The black curve is the result shown in the right panel of Fig. 8.4.1 using the IceCube observed flux in Eq. (8.1) as the input spectrum. The rest of the color coding is the same in both panels.

on $\sigma_0$ by the same factor.

Concerning the initial neutrino flux, we recomputed the limits by considering dozens of predicted neutrino spectra for NGC 1068 found in the literature. These vary in terms of source modeling, production mechanisms for both photons and neutrinos, and model parameters [1, 80, 82, 83, 101–106]. Among them, only the nine examples shown in the left panel of Fig. 8.4.2 give at least as many expected muon neutrinos as observed by IceCube within the energy range $E_\nu \in [1.5, 15]$ TeV, according to Eq. (8.2) in the absence of $\nu$-DM scattering. Carrying out the same analysis as in the previous section, we derived the 90% C.L. upper limits on $\sigma_0$ for all of these initial neutrino spectra, for both the energy-independent and linear energy-dependent scattering cases.

The results are summarized in Table 8.4.1 and shown in the right panel of Fig. 8.4.2 for the example of the BM1 spike model. Although there is a factor of $\sim 10-15$ ($50-60$) scatter in the upper limits of $\sigma_0$ for the energy-dependent (energy-independent) scattering cross section limit inferred from the nine fluxes, only one of them provides a weaker limit (by a factor of $4-5$) than we obtained using Eq. (8.1) as the input flux. The associated spectrum, taken from Fig. 4 of Ref. [83] (hot pink curve in Fig. 8.4.2), was derived within the stochastic acceleration scenario with high cosmic ray pressure for the largest x-ray luminosity $L_X \simeq 10^{43.8}$ erg/s allowed by observations [107]; hence it could be considered to be an outlier. We refer the reader to Ref. [83] for model details.

Since all but one of the available initial neutrino spectra give stronger constraints on $\sigma_0$ than we obtained using the IceCube observed flux in Eq. (8.1), the latter can be viewed as not only the most model-independent option, but it also gives a conservative choice for setting limits on $\nu$-DM interactions [6].

## 8.6 $Z'$ interpretation

To relate the derived constraints to an underlying particle physics model, we consider a new gauge boson $Z'$ that couples equally to all three flavors of leptons with strength $g_\nu$. It is not sufficient for our purpose to couple to a single flavor, because the new interaction induces a neutrino self-energy in the dark matter spike [112], analogous to the Wolfenstein potential for electron neutrinos in the matter. We find that for the cross sections of interest, it suppresses oscillations, such that the other two flavors would escape from the DM spike unimpeded. A simple anomaly-free choice is to

[6] Most, if not all, of the initial neutrino fluxes we tested were tuned to reproduce both the NGC 1068 electromagnetic data [106–110] and the IceCube neutrino data [33, 111]. It is possible that by relaxing the requirement that the neutrino spectrum emitted by the source should be consistent with IceCube observations, the flux normalization may be higher than that assumed so far in the literature, giving more room for nonstandard neutrino interactions, such as $\nu$-DM scattering, to match IceCube data and potentially weakening the constraints derived in this paper. We leave this question for future investigation.

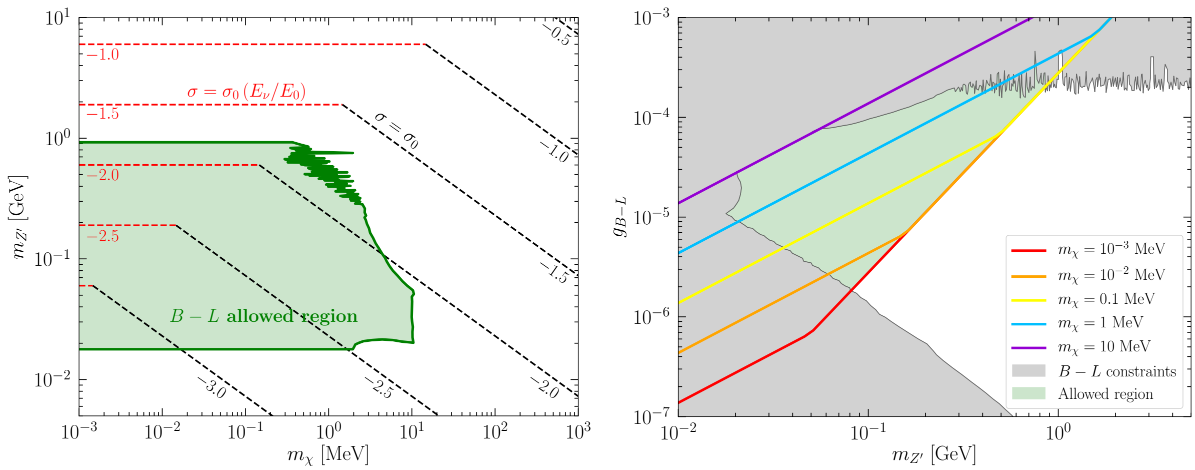


Figure 8.6.1: *Left:* Dashed lines are contours of $\log_{10}(\sqrt{g_\nu g_\chi}) \equiv \log_{10} g_{\text{eff}}$ corresponding to the limit on the cross section from dark matter spike model BM1. Horizontal red (diagonal black) lines indicate where the cross section is approximately linear in (constant with) $E_\nu$. Green region is that allowed for $U(1)'$ corresponding to $B - L$ gauge symmetry. *Right:* Constraints in the plane of $g_{B-L} = g_\nu$ versus $m'_Z$. Gray regions are excluded by laboratory and astrophysical probes taken from Ref. [113]. Colored lines are contours of constant dark matter mass such that the NGC 1068 constraint is saturated, for the BM1 DM spike model, with $g_\chi = 1$. The green shaded region corresponds to the same as in the left panel.

couple $Z'$ to baryon minus lepton number, $B - L$.

For definiteness, we take the dark matter $\chi$ to be a complex scalar, with $B - L$ charge $g_\chi$, while the leptons have charge $g_\nu$. The cross section for neutrinos of energy $E_\nu$ to scatter on DM at rest has the limiting behaviors [32]

$$\sigma = \frac{g_\chi^2 g_\nu^2}{4\pi m_{Z'}^2} \begin{cases} 1, & E_\nu \gg m_{Z'}^2/m_\chi \\ m_\chi E_\nu / m_{Z'}^2, & E_\nu \ll m_{Z'}^2/m_\chi \end{cases} . \tag{8.18}$$

This demonstrates the relevance of the choices of $\sigma$ being constant or linearly rising with $E_\nu$.

The left panel of Fig. 8.6.1 illustrates the typical values of $m_{Z'}$ and the effective coupling $g_{\text{eff}} = \sqrt{g_\chi g_\nu}$ that would saturate the constraint in Fig. 8.4.1 arising from the BM1 spike model. The dashed lines indicate contours of $\log_{10} g_{\text{eff}}$ for given choices of $m_{Z'}$ and $m_\chi$. The entire region shown is consistent with perturbative unitarity, for $m_{Z'} \lesssim 130\,\text{GeV}$. However, $g_\nu$ is constrained by numerous experimental tests of the

$B-L$ model, summarized for example in Ref. [113]. The allowed parameter space is indicated in Fig. 8.6.1 by the shaded green region, assuming that $g_\chi \lesssim 1$. To match to the weaker limits corresponding to a different spike model $X$, the values of the couplings would have to be rescaled as $g_{\rm eff} \to g_{\rm eff} \times (\sigma_X/\sigma_{BM1})^{1/4}$. For example with the BM1′ model, $g_{\rm eff}$ increases by a factor of $\sim 3$, hence $\log_{10} g_{\rm eff} \to (\log_{10} g_{\rm eff} + 0.5)$.

A complementary view of our new constraint, versus existing limits on $g_\nu$ versus $m_{Z'}$, is shown in the right panel of Fig. 8.6.1. The gray region is excluded by laboratory and astrophysical considerations. The colored curves are contours of constant $m_\chi$ that saturate the BM1 constraint derived above, for the case of $g_\chi = 1$. For smaller values of $g_\chi$, the curves would move upward by the factor $1/g_\chi$. The break in the curves for $m_\chi \lesssim 0.1\,\text{MeV}$ occurs at the transition between constant cross section and $\sigma$ linearly rising with energy. The shaded green region therefore corresponds to parameter space where our new constraint can be saturated while remaining consistent with other probes of the $B-L$ model.

## 8.7 Dark matter relic density

It is striking that the $\nu$-DM interaction may play a crucial role in determining the relic density of the dark matter, through the annihilation process $\nu\nu \to \chi\bar{\chi}$. For $m_\chi \gtrsim 1\,\text{MeV}$, this could occur through thermal freezeout, or by having an initial asymmetry between $\chi$ and its antiparticle, giving asymmetric DM (ADM). The thermally averaged annihilation cross section (times relative velocity) should satisfy $\langle\sigma_a v\rangle \sim 3 \times 10^{-26}\,\text{cm}^3/\text{s}$ [114] for symmetric DM, and it should be greater for ADM, in order to suppress the symmetric component.

For lighter DM with $m_\chi \lesssim 1\,\text{MeV}$, thermal production is not viable since it results in warm dark matter, which is observationally disfavored. Instead, the annihilation process can slowly build up the DM density over time, while remaining out of thermal equilibrium. This is the freeze-in mechanism [115], which requires much smaller values of $\langle\sigma_a v\rangle$.

Although the annihilation cross section is not identical to the elastic scattering cross section, they are closely related in typical particle physics models. In the model with a massive $Z'$ gauge boson, at low energies the effective interaction Lagrangian is

$$\mathcal{L} = \frac{1}{\Lambda^2}(\chi^* \overleftrightarrow{\partial}_\mu \chi)(\bar{\nu}\gamma^\mu \nu) \tag{8.19}$$

in the case of complex scalar DM, where $\Lambda = m_{Z'}/\sqrt{g_\nu g_\chi}$, the ratio of the $Z'$ mass to its couplings. Then the elastic cross section scales as $\sigma \sim m_\chi E_\nu/\Lambda^4$, while the annihilation cross section behaves as

$$\langle \sigma_a v \rangle \sim \begin{cases} m_\chi^2/\Lambda^4, & T \ll m_\chi \\ T^2/\Lambda^4\,, & m_{Z'} > T \gg m_\chi \\ (g_\nu g_\chi)^2/T^2, & T \gg m_{Z'} \end{cases} \tag{8.20}$$

The low-$T$ limit is appropriate for the case of freeze-out, while the high-$T$ limit dominates in the case of freeze-in. The third line of Eq. (8.20) indicates the behavior ensuing when the effective description in Eq. (8.19) breaks down due to the $Z'$ propagator.

The freeze-in production is determined by the Boltzmann equation (see for example Ref. [116])

$$\frac{dY_\chi}{dx} = \frac{x\, s\, \langle \sigma_a v \rangle}{H(m_\chi)} Y_{eq}^2\,, \tag{8.21}$$

where $Y_\chi$ is the DM abundance, $x = m_\chi/T$, $s$ is the entropy density, $H(m_\chi)$ is the Hubble parameter at $T = m_\chi$, and $Y_{eq}$ is the $\chi$ equilibrium density. DM production is dominated by the high-$T$ contributions near $T \sim m_{Z'}$. Integrating Eq. (8.21) and imposing the observed relic density $Y_\chi m_\chi \cong 4 \times 10^{-10}$ GeV [117], we find that

$$\left(\frac{\Lambda}{m_\chi}\right)^4 \sim 5 \times 10^6 \left(\frac{\ln(m_{Z'}/m_\chi)}{g_*^{3/2}}\right)^{1/4}\,, \tag{8.22}$$

which can be used to estimate the magnitude of $\sigma_0$ for the case of $\nu$-DM scattering with linear energy dependence.

This procedure results in the heavy orange line (labeled "freeze-in") on Fig. 8.7.1. Values above the line would lead to overabundant dark matter, in the absence of

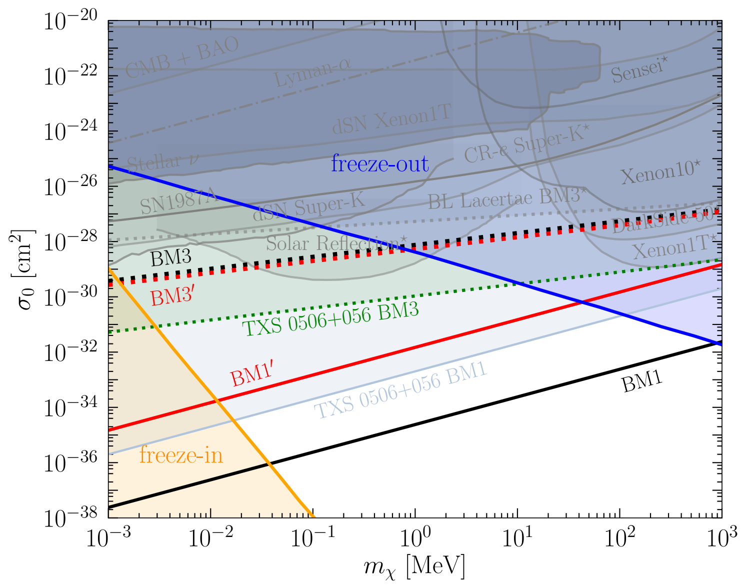


Figure 8.7.1: 90% C.L. upper limits on the $\nu$-DM and $e$-DM scattering cross sections at the reference energy $E_0 = 10$ TeV, assuming they scale as $\sigma_{\ell\chi} \propto E_\nu$ with $\ell = \nu, e$ as shown in the right panel of Fig. 8.4.1. The regions of parameter space where freeze-out (blue curve) and freeze-in (orange curve) mechanisms can lead to the correct DM relic density are also shown. In particular, models for which $(m_\chi, \sigma_0)$ is above the blue or below the orange curves can accommodate only a sub-dominant faction of DM in the case of fully symmetric DM or leads to a suppression of the symmetric component in the case of ADM.

an additional annhilation channel. Similarly, one can estimate that $m_\chi/\Lambda^2 \sim 5 \times 10^{-5}\,\mathrm{GeV}^{-1}$ for the desired relic abundance through thermal freeze-out. This determines $\sigma_0$ versus $m_\chi$ as shown by the heavy blue line (labeled "freeze-out") in Fig. 8.7.1. Values of $\sigma_0$ above the line correspond to a subdominant DM component, in the case of fully symmetric DM, or suppression of the symmetric component in the case of ADM. Dark matter in the region of parameter space between the two lines would require some additional interactions for achieving the observed relic density.

Comparing to the results of the previous section, we see that the freeze-out scenario is not viable for pure $B - L$ gauge models that saturate the BM1 constraint, but freeze-in is consistent.

## 8.8 Conclusions

IceCube has now observed neutrinos from two active galactic nuclei, and other researchers have suggested that additional AGNs have produced excess IceCube events with lower statistical significance [118–125]. It seems likely that in the coming years, more such sources will be discovered, which may further strengthen constraints on dark matter-neutrino interactions.

In the present work, we derived new limits on $\nu$-DM scattering, which depend strongly on the details of the DM spike density surrounding the AGN's central supermassive black hole, in particular, the power $\alpha$ in the assumed density profile $\rho \sim r^{-\alpha}$. Previous work on the blazar TXS 0506+056 considered only the case $\alpha = 7/3$ [51, 87], which neglects relaxation of the initial DM spike by gravitational scattering with stars, whereas $\alpha \to 3/2$ when this effect is maximal. Here we have considered both possibilities, as did by Ref. [98] in the context of dark matter boosted by electrons in the blazar jet. Probably $\alpha = 3/2$ is more realistic due to the complex stellar environment in AGNs [126], but we do not feel qualified to make a definitive statement, and we defer to workers who specialize on this issue to confirm such a statement, which would significantly reduce the astrophysical uncertainty of the constraints.

Other astrophysical uncertainties that can significantly affect the predictions for AGNs concern the position $R_{\mathrm{em}}$ within the relativistic jet where neutrinos are likely to be produced, and the choice of the initial neutrino flux $\Phi_\nu$. In these respects, radio galaxies like NGC 1068 allow for more robust predictions than blazars. Observations of different radio galaxies (see e.g. [85, 86]) suggest that the black hole corona, where neutrinos with energy of $\sim \mathcal{O}(10\ \mathrm{TeV})$ can be generated, has to extend at most several tens of the Schwarzschild radii $R_S$ from the galactic center [1, 99], which is one to two orders of magnitude smaller than the radius of the neutrino-emitting region in blazar jets [127]. Furthermore, the initial neutrino flux we used to set constraints on the $\nu$-DM scattering comes directly from the IceCube observation of NGC 1068 and does not rely on the result of numerical simulations, which might be affected by simplifying assumptions in modelling the astrophysical source. Choosing a different initial neutrino spectrum, as derived from theoretical modeling or simulations of NGC 1068, generally strengthens our results or, in the worst case scenario, weakens the limits by a factor of a few.

The remaining important uncertainty is on whether dark matter can annihilate within the DM spike, and this cannot be easily resolved. However we can say that a consistent picture emerges if the DM obtains its relic density through freeze-in, mediated by the same interactions that we are constraining. In this case the DM annihilation cross section can be much smaller than the values where annihilation would significantly deplete the spike, and our strongest limits would then apply.

## Acknowledgment

We thank Andrew Benson, Daryl Haggard and Shengqi Yang for helpful information about NGC 1068 structure, Paolo Gondolo about the profile of the dark matter spike, Kohta Murase for clarification on the neutrino emitting region and astrophysical uncertainties, Francis Halzen for an alternative interpretation of the IceCube neutrino event from TXS 0506+056, and Matthew Lundy and Samantha Wong for stimulating discussion. We also thank Ken Ragan, Aaron Vincent and Andreas Warburton for clarifications and suggestions that improved the original manuscript. This research was supported by the Natural Sciences and Engineering Research Council (NSERC) of Canada.

## Bibliography

[1] K. Murase, "Hidden Hearts of Neutrino Active Galaxies," *Astrophys. J. Lett.* **941** no. 1, (2022) L17, `arXiv:2211.04460 [astro-ph.HE]`.

[2] S. M. Tang and S. N. Zhang, "A possible mechanism for hot corona formation around black holes," in *Astrophysics and Space Science Library*, K. S. Cheng, K. C. Leung, and T. P. Li, eds., vol. 298. 1, 2003.

[3] G. Mangano, A. Melchiorri, P. Serra, A. Cooray, and M. Kamionkowski, "Cosmological bounds on dark matter-neutrino interactions," *Phys. Rev. D* **74** (2006) 043517, arXiv:astro-ph/0606190.

[4] C. Boehm, M. J. Dolan, and C. McCabe, "A Lower Bound on the Mass of Cold Thermal Dark Matter from Planck," *JCAP* **08** (2013) 041, arXiv:1303.6270 [hep-ph].

[5] B. Bertoni, S. Ipek, D. McKeen, and A. E. Nelson, "Constraints and consequences of reducing small scale structure via large dark matter-neutrino interactions," *JHEP* **04** (2015) 170, arXiv:1412.3113 [hep-ph].

[6] R. J. Wilkinson, C. Boehm, and J. Lesgourgues, "Constraining Dark Matter-Neutrino Interactions using the CMB and Large-Scale Structure," *JCAP* **05** (2014) 011, arXiv:1401.7597 [astro-ph.CO].

[7] M. R. Mosbech, C. Boehm, S. Hannestad, O. Mena, J. Stadler, and Y. Y. Y. Wong, "The full Boltzmann hierarchy for dark matter-massive neutrino interactions," *JCAP* **03** (2021) 066, arXiv:2011.04206 [astro-ph.CO].

[8] D. C. Hooper and M. Lucca, "Hints of dark matter-neutrino interactions in Lyman-$\alpha$ data," *Phys. Rev. D* **105** no. 10, (2022) 103504, arXiv:2110.04024 [astro-ph.CO].

[9] P. Fayet, D. Hooper, and G. Sigl, "Constraints on light dark matter from core-collapse supernovae," *Phys. Rev. Lett.* **96** (2006) 211302, arXiv:hep-ph/0602169.

[10] **IceCube** Collaboration, A. McMullen, A. Vincent, C. Arguelles, and A. Schneider, "Dark matter neutrino scattering in the galactic centre with IceCube," *JINST* **16** no. 08, (2021) C08001, arXiv:2107.11491 [astro-ph.HE].

[11] S. Koren, "Neutrino – Dark Matter Scattering and Coincident Detections of

UHE Neutrinos with EM Sources," *JCAP* **09** (2019) 013, arXiv:1903.05096 [hep-ph].

[12] K. Murase and I. M. Shoemaker, "Neutrino Echoes from Multimessenger Transient Sources," *Phys. Rev. Lett.* **123** no. 24, (2019) 241102, arXiv:1903.08607 [hep-ph].

[13] J. A. Carpio, A. Kheirandish, and K. Murase, "Time-delayed neutrino emission from supernovae as a probe of dark matter-neutrino interactions," arXiv:2204.09650 [hep-ph].

[14] J. H. Davis and J. Silk, "Spectral and Spatial Distortions of PeV Neutrinos from Scattering with Dark Matter," arXiv:1505.01843 [hep-ph].

[15] W. Yin, "Highly-boosted dark matter and cutoff for cosmic-ray neutrinos through neutrino portal," *EPJ Web Conf.* **208** (2019) 04003, arXiv:1809.08610 [hep-ph].

[16] Y. Zhang, "Speeding up dark matter with solar neutrinos," *PTEP* **2022** no. 1, (2022) 013B05, arXiv:2001.00948 [hep-ph].

[17] Y. Jho, J.-C. Park, S. C. Park, and P.-Y. Tseng, "Cosmic-Neutrino-Boosted Dark Matter ($\nu$BDM)," arXiv:2101.11262 [hep-ph].

[18] Y. Farzan and S. Palomares-Ruiz, "Dips in the Diffuse Supernova Neutrino Background," *JCAP* **06** (2014) 014, arXiv:1401.7019 [hep-ph].

[19] A. Das and M. Sen, "Boosted dark matter from diffuse supernova neutrinos," *Phys. Rev. D* **104** no. 7, (2021) 075029, arXiv:2104.00027 [hep-ph].

[20] D. Ghosh, A. Guha, and D. Sachdeva, "Exclusion limits on dark matter-neutrino scattering cross section," *Phys. Rev. D* **105** no. 10, (2022) 103029, arXiv:2110.00025 [hep-ph].

[21] D. Bardhan, S. Bhowmick, D. Ghosh, A. Guha, and D. Sachdeva, "Boosting through the Darkness," arXiv:2208.09405 [hep-ph].

[22] Y.-H. Lin, W.-H. Wu, M.-R. Wu, and H. T.-K. Wong, "Searching for Afterglow: Light Dark Matter boosted by Supernova Neutrinos," `arXiv:2206.06864 [hep-ph]`.

[23] J. A. Dror, G. Elor, R. McGehee, and T.-T. Yu, "Absorption of sub-MeV fermionic dark matter by electron targets," *Phys. Rev. D* **103** no. 3, (2021) 035001, `arXiv:2011.01940 [hep-ph]`. [Erratum: Phys.Rev.D 105, 119903 (2022)].

[24] J. A. Dror, G. Elor, and R. Mcgehee, "Directly Detecting Signals from Absorption of Fermionic Dark Matter," *Phys. Rev. Lett.* **124** no. 18, (2020) 18, `arXiv:1905.12635 [hep-ph]`.

[25] J. A. Dror, G. Elor, and R. Mcgehee, "Absorption of Fermionic Dark Matter by Nuclear Targets," *JHEP* **02** (2020) 134, `arXiv:1908.10861 [hep-ph]`.

[26] **PandaX** Collaboration, L. Gu *et al.*, "First Search for the Absorption of Fermionic Dark Matter with the PandaX-4T Experiment," *Phys. Rev. Lett.* **129** no. 16, (2022) 161803, `arXiv:2205.15771 [hep-ex]`.

[27] **PandaX** Collaboration, D. Zhang *et al.*, "Search for Light Fermionic Dark Matter Absorption on Electrons in PandaX-4T," *Phys. Rev. Lett.* **129** no. 16, (2022) 161804, `arXiv:2206.02339 [hep-ex]`.

[28] **MAJORANA** Collaboration, I. J. Arnquist *et al.*, "Exotic dark matter search with the Majorana Demonstrator," `arXiv:2206.10638 [hep-ex]`.

[29] **EXO-200** Collaboration, S. A. Kharusi *et al.*, "Search for MeV Electron Recoils from Dark Matter in EXO-200," `arXiv:2207.00897 [hep-ex]`.

[30] **CDEX** Collaboration, W. H. Dai *et al.*, "Exotic Dark Matter Search with the CDEX-10 Experiment at China's Jinping Underground Laboratory," *Phys. Rev. Lett.* **129** no. 22, (2022) 221802, `arXiv:2209.00861 [hep-ex]`.

[31] **IceCube, Fermi-LAT, MAGIC, AGILE, ASAS-SN, HAWC, H.E.S.S., INTEGRAL, Kanata, Kiso, Kapteyn, Liverpool Telescope, Subaru, Swift NuSTAR, VERITAS, VLA/17B-403** Collaboration, M. G. Aartsen *et al.*, "Multimessenger observations of a flaring blazar coincident with high-energy neutrino IceCube-170922A," *Science* **361** no. 6398, (2018) eaat1378, `arXiv:1807.08816 [astro-ph.HE]`.

[32] J. M. Cline, S. Gao, F. Guo, Z. Lin, S. Liu, M. Puel, P. Todd, and T. Xiao, "Blazar Constraints on Neutrino-Dark Matter Scattering," *Phys. Rev. Lett.* **130** no. 9, (2023) 091402, `arXiv:2209.02713 [hep-ph]`.

[33] **IceCube** Collaboration, R. Abbasi *et al.*, "Evidence for neutrino emission from the nearby active galaxy NGC 1068," *Science* **378** no. 6619, (2022) 538–543, `arXiv:2211.09972 [astro-ph.HE]`.

[34] D. M. Crenshaw and S. B. Kraemer, "Resolved spectroscopy of the narrow-line region in ngc 1068: kinematics of the ionized gas," *Astrophys. J. Lett.* **532** (2000) L101, `arXiv:astro-ph/0002438`.

[35] W. Jaffe *et al.*, "The central dusty torus in the active nucleus of NGC 1068," *Nature* **429** (2004) 47–49.

[36] **IceCube** Collaboration. `https://icecube.wisc.edu/data-releases/2022/11/`.

[37] M. Bustamante, J. F. Beacom, and W. Winter, "Theoretically palatable flavor combinations of astrophysical neutrinos," *Phys. Rev. Lett.* **115** no. 16, (2015) 161302, `arXiv:1506.02645 [astro-ph.HE]`.

[38] C. A. Argüelles, T. Katori, and J. Salvado, "New Physics in Astrophysical Neutrino Flavor," *Phys. Rev. Lett.* **115** (2015) 161303, `arXiv:1506.02043 [hep-ph]`.

[39] P. Gondolo and J. Silk, "Dark matter annihilation at the galactic center," *Phys. Rev. Lett.* **83** (1999) 1719–1722, `arXiv:astro-ph/9906391`.

[40] P. Ullio, H. Zhao, and M. Kamionkowski, "A Dark matter spike at the galactic center?," *Phys. Rev. D* **64** (2001) 043504, `arXiv:astro-ph/0101481`.

[41] M. Gorchtein, S. Profumo, and L. Ubaldi, "Probing Dark Matter with AGN Jets," *Phys. Rev. D* **82** (2010) 083514, `arXiv:1008.2230 [astro-ph.HE]`. [Erratum: Phys.Rev.D 84, 069903 (2011)].

[42] D. Merritt, "Evolution of the dark matter distribution at the galactic center," *Phys. Rev. Lett.* **92** (2004) 201304, `arXiv:astro-ph/0311594`.

[43] O. Y. Gnedin and J. R. Primack, "Dark Matter Profile in the Galactic Center," *Phys. Rev. Lett.* **93** (2004) 061302, `arXiv:astro-ph/0308385`.

[44] D. Merritt, S. Harfst, and G. Bertone, "Collisionally Regenerated Dark Matter Structures in Galactic Nuclei," *Phys. Rev. D* **75** (2007) 043517, `arXiv:astro-ph/0610425`.

[45] S. L. Shapiro and D. C. Heggie, "Effect of stars on the dark matter spike around a black hole: A tale of two treatments," *Phys. Rev. D* **106** no. 4, (2022) 043018, `arXiv:2209.08105 [astro-ph.GA]`.

[46] L. Sadeghian, F. Ferrer, and C. M. Will, "Dark matter distributions around massive black holes: A general relativistic analysis," *Phys. Rev. D* **88** no. 6, (2013) 063522, `arXiv:1305.2619 [astro-ph.GA]`.

[47] F. Ferrer, A. M. da Rosa, and C. M. Will, "Dark matter spikes in the vicinity of Kerr black holes," *Phys. Rev. D* **96** no. 8, (2017) 083014, `arXiv:1707.06302 [astro-ph.CO]`.

[48] O. Piana, P. Dayal, M. Volonteri, and T. R. Choudhury, "The mass assembly of high-redshift black holes," *Monthly Notices of the Royal Astronomical Society* **500** no. 2, (Oct, 2020) 2146–2158. `https://doi.org/10.1093%2Fmnras%2Fstaa3363`.

[49] J.-W. Wang, A. Granelli, and P. Ullio, "Direct Detection Constraints on Blazar-Boosted Dark Matter," *Phys. Rev. Lett.* **128** (2022) 221104, arXiv:2111.13644 [astro-ph.HE].

[50] A. Granelli, P. Ullio, and J.-W. Wang, "Blazar-boosted dark matter at Super-Kamiokande," *JCAP* **07** no. 07, (2022) 013, arXiv:2202.07598 [astro-ph.HE].

[51] F. Ferrer, G. Herrera, and A. Ibarra, "New constraints on the dark matter-neutrino and dark matter-photon scattering cross sections from TXS 0506+056," arXiv:2209.06339 [hep-ph].

[52] T. Lacroix, C. Bœhm, and J. Silk, "Ruling out thermal dark matter with a black hole induced spiky profile in the M87 galaxy," *Phys. Rev. D* **92** no. 4, (2015) 043510, arXiv:1505.00785 [astro-ph.GA].

[53] T. Lacroix, M. Karami, A. E. Broderick, J. Silk, and C. Boehm, "Unique probe of dark matter in the core of M87 with the Event Horizon Telescope," *Phys. Rev. D* **96** no. 6, (2017) 063008, arXiv:1611.01961 [astro-ph.GA].

[54] T. Di Matteo, R. A. C. Croft, V. Springel, and L. Hernquist, "Black hole growth and activity in a lambda CDM universe," *Astrophys. J.* **593** (2003) 56–68, arXiv:astro-ph/0301586.

[55] L. Ferrarese, "Beyond the bulge: a fundamental relation between supermassive black holes and dark matter halos," *Astrophys. J.* **578** (2002) 90–97, arXiv:astro-ph/0203469.

[56] M. Baes, P. Buyle, G. K. T. Hau, and H. Dejonghe, "Observational evidence for a connection between supermassive black holes and dark matter haloes," *Mon. Not. Roy. Astron. Soc.* **341** (2003) L44, arXiv:astro-ph/0303628.

[57] L. J. Greenhill, C. R. Gwinn, R. Antonucci, and R. Barvainis, "Vlbi imaging of water maser emission from the nuclear torus of ngc 1068," *Astrophys. J. Lett.* **472** (1996) L21, arXiv:astro-ph/9609082.

[58] F. L. J. Greenhill and C. R. Gwinn, "VLBI Imaging of Water Maser Emission from a Nuclear Disk in NGC 1068," *Astrophysics and Space Science* **248** no. 1-2, (1997) 261–267.

[59] J.-M. Hure, "Origin of non-keplerian motions of masers in ngc 1068," *Astron. Astrophys.* **395** (2002) L21–L24, `arXiv:astro-ph/0210180`.

[60] G. Lodato and G. Bertin, "Non-Keplerian rotation in the nucleus of NGC 1068: Evidence for a massive accretion disk?," *Astron. Astrophys.* **398** (2003) 517–524, `arXiv:astro-ph/0211113`.

[61] J.-H. Woo and C. M. Urry, "AGN black hole masses and bolometric luminosities," *Astrophys. J.* **579** (2002) 530–544, `arXiv:astro-ph/0207249`.

[62] F. Panessa, L. Bassani, M. Cappi, M. Dadina, X. Barcons, F. J. Carrera, L. C. Ho, and K. Iwasawa, "On the X-ray, optical emission line and black hole mass properties of local Seyfert galaxies," *Astron. Astrophys.* **455** (2006) 173, `arXiv:astro-ph/0605236`.

[63] T. Minezaki and K. Matsushita, "A New Black Hole Mass Estimate for Obscured Active Galactic Nuclei," *Astrophys. J.* **802** (2015) 98, `arXiv:1501.07522`.

[64] J. S. Bullock, T. S. Kolatt, Y. Sigad, R. S. Somerville, A. V. Kravtsov, A. A. Klypin, J. R. Primack, and A. Dekel, "Profiles of dark haloes. Evolution, scatter, and environment," *Mon. Not. Roy. Astron. Soc.* **321** (2001) 559–575, `arXiv:astro-ph/9908159`.

[65] B. M. Sabra, C. Saliba, M. Abi Akl, and G. Chahine, "The black hole-dark matter halo connection," *Astrophys. J.* **803** no. 1, (2015) 5, `arXiv:1502.00775 [astro-ph.GA]`.

[66] E. Brinks, E. D. Skillman, R. J. Terlevich, and E. Terlevich, "HI Observations of NGC 1068," *Astrophys. Space Sci* **248** no. 1-2, (Feb., 1997) 23–31.

[67] G. Paturel, C. Petit, P. Prugniel, G. Theureau, J. Rousseau, M. Brouty, P. Dubois, and L. Cambresy, "HYPERLEDA. I. Identification and designation of galaxies," *Astron. Astrophys.* **412** (2003) 45–55. `http://leda.univ-lyon1.fr`.

[68] G. Gentile, C. Tonini, and P. Salucci, "Lambda CDM Halo Density Profiles: Where do actual halos converge to NFW ones?," *Astron. Astrophys.* **467** (2007) 925–931, `arXiv:astro-ph/0701550`.

[69] M. Cautun, A. Benitez-Llambay, A. J. Deason, C. S. Frenk, A. Fattahi, F. A. Gómez, R. J. J. Grand, K. A. Oman, J. F. Navarro, and C. M. Simpson, "The Milky Way total mass profile as inferred from Gaia DR2," *Mon. Not. Roy. Astron. Soc.* **494** no. 3, (2020) 4291–4313, `arXiv:1911.04557 [astro-ph.GA]`.

[70] E. H. T. Collaboration, "First Sagittarius A$^\star$ Event Horizon Telescope Results. I. The Shadow of the Supermassive Black Hole in the Center of the Milky Way," *Astrophys. J. Letters* **930** no. 2, (2022) L12. `https://dx.doi.org/10.3847/2041-8213/ac6674`.

[71] M. Cermeño, C. Degrande, and L. Mantani, "Signatures of leptophilic t-channel dark matter from active galactic nuclei," *Phys. Rev. D* **105** no. 8, (2022) 083019, `arXiv:2201.07247 [hep-ph]`.

[72] J. I. Katz, "Nonrelativistic Compton scattering and models of quasars.," *Astrophys. J.* **206** (Jun, 1976) 910–916.

[73] G. S. Bisnovatyi-Kogan and S. I. Blinnikov, "Disk accretion onto a black hole at subcritical luminosity.," *Astron. and Astrophys.* **59** (Jul, 1977) 111–125.

[74] D. Eichler, "High-energy neutrino astronomy: a probe of galactic nuclei?," *Astrophys. J.* **232** (Aug, 1979) 106–112.

[75] L. A. Pozdnyakov, I. M. Sobol, and R. A. Syunyaev, "Comptonization and the

shaping of X-ray source spectra - Monte Carlo calculations," *Soviet Ast.* **2** (Jan, 1983) 189–331.

[76] A. A. Galeev, R. Rosner, and G. S. Vaiana, "Structured coronae of accretion disks.," *Astrophys. J.* **229** (Apr, 1979) 318–326.

[77] M. C. Begelman, B. Rudak, and M. Sikora, "Consequences of Relativistic Proton Injection in Active Galactic Nuclei," *Astrophys. J.* **362** (Oct, 1990) 38.

[78] F. W. Stecker, C. Done, M. H. Salamon, and P. Sommers, "High-energy neutrinos from active galactic nuclei," *Phys. Rev. Lett.* **66** no. 21, (May, 1991) 2697–2700.

[79] O. Kalashev, D. Semikoz, and I. Tkachev, "Neutrinos in IceCube from active galactic nuclei," *J. Exp. Theor. Phys.* **120** no. 3, (2015) 541–548, `arXiv:1410.8124 [astro-ph.HE]`.

[80] Y. Inoue, D. Khangulyan, and A. Doi, "On the Origin of High-energy Neutrinos from NGC 1068: The Role of Nonthermal Coronal Activity," *Astrophys. J. Lett.* **891** no. 2, (2020) L33, `arXiv:1909.02239 [astro-ph.HE]`.

[81] Y. Inoue, D. Khangulyan, S. Inoue, and A. Doi, "On high-energy particles in accretion disk coronae of supermassive black holes: implications for MeV gamma rays and high-energy neutrinos from AGN cores," `arXiv:1904.00554 [astro-ph.HE]`.

[82] K. Murase, S. S. Kimura, and P. Meszaros, "Hidden Cores of Active Galactic Nuclei as the Origin of Medium-Energy Neutrinos: Critical Tests with the MeV Gamma-Ray Connection," *Phys. Rev. Lett.* **125** no. 1, (2020) 011101, `arXiv:1904.04226 [astro-ph.HE]`.

[83] A. Kheirandish, K. Murase, and S. S. Kimura, "High-energy Neutrinos from Magnetized Coronae of Active Galactic Nuclei and Prospects for Identification

of Seyfert Galaxies and Quasars in Neutrino Telescopes," *Astrophys. J.* **922** no. 1, (2021) 45, arXiv:2102.04475 [astro-ph.HE].

[84] K. Murase, D. Guetta, and M. Ahlers, "Hidden Cosmic-Ray Accelerators as an Origin of TeV-PeV Cosmic Neutrinos," *Phys. Rev. Lett.* **116** no. 7, (2016) 071101, arXiv:1509.00805 [astro-ph.HE].

[85] Y. Inoue and A. Doi, "Detection of Coronal Magnetic Activity in Nearby Active Supermassive Black Holes," *Astrophys. J.* **869** no. 2, (2018) 114, arXiv:1810.10732 [astro-ph.HE].

[86] J. F. Gallimore, S. A. Baum, and C. P. O'Dea, "The parsec-scale radio structure of ngc 1068 and the nature of the nuclear radio source," *Astrophys. J.* **613** (2004) 794–810, arXiv:astro-ph/0406062.

[87] K.-Y. Choi, J. Kim, and C. Rott, "Constraining dark matter-neutrino interactions with IceCube-170922A," *Phys. Rev. D* **99** no. 8, (2019) 083018, arXiv:1903.03302 [astro-ph.CO].

[88] R. B. Tully, *Nearby galaxies catalog.* Cambridge University Press, 1988.

[89] J. Bland-Hawthorn, J. F. Gallimore, L. J. Tacconi, E. Brinks, S. A. Baum, R. R. J. Antonucci, and G. N. Cecil, "The Ringberg Standards for NGC 1068," *Astrophys. Space Sci* **248** no. 1-2, (Feb, 1997) 9–19.

[90] C. A. Argüelles, A. Kheirandish, and A. C. Vincent, "Imaging Galactic Dark Matter with High-Energy Cosmic Neutrinos," *Phys. Rev. Lett.* **119** no. 20, (2017) 201801, arXiv:1703.00451 [hep-ph].

[91] A. C. Vincent, C. A. Argüelles, and A. Kheirandish, "High-energy neutrino attenuation in the Earth and its associated uncertainties," *JCAP* **11** (2017) 012, arXiv:1706.09895 [hep-ph].

[92] G. J. Feldman and R. D. Cousins, "A Unified approach to the classical statistical analysis of small signals," *Phys. Rev. D* **57** (1998) 3873–3889, arXiv:physics/9711021.

[93] H. An, M. Pospelov, J. Pradler, and A. Ritz, "Directly Detecting MeV-scale Dark Matter via Solar Reflection," *Phys. Rev. Lett.* **120** no. 14, (2018) 141801, `arXiv:1708.03642 [hep-ph]`. [Erratum: Phys.Rev.Lett. 121, 259903 (2018)].

[94] **SENSEI** Collaboration, L. Barak *et al.*, "SENSEI: Direct-Detection Results on sub-GeV Dark Matter from a New Skipper-CCD," *Phys. Rev. Lett.* **125** no. 17, (2020) 171802, `arXiv:2004.11378 [astro-ph.CO]`.

[95] R. Essig, T. Volansky, and T.-T. Yu, "New Constraints and Prospects for sub-GeV Dark Matter Scattering off Electrons in Xenon," *Phys. Rev. D* **96** no. 4, (2017) 043017, `arXiv:1703.00910 [hep-ph]`.

[96] **DarkSide-50** Collaboration, P. Agnes *et al.*, "Search for dark matter particle interactions with electron final states with DarkSide-50," `arXiv:2207.11968 [hep-ex]`.

[97] **XENON** Collaboration, E. Aprile *et al.*, "Light Dark Matter Search with Ionization Signals in XENON1T," *Phys. Rev. Lett.* **123** no. 25, (2019) 251801, `arXiv:1907.11485 [hep-ex]`.

[98] S. Bhowmick, D. Ghosh, and D. Sachdeva, "Blazar boosted Dark Matter – direct detection constraints on $\sigma_{e\chi}$ : Role of energy dependent cross sections," `arXiv:2301.00209 [hep-ph]`.

[99] F. Halzen, "IceCube: the First Decade of Neutrino Astronomy," *in preparation* (2023) .

[100] V. M. Lipunov *et al.*, "Optical Observations Reveal Strong Evidence for High Energy Neutrino Progenitor," *Astrophys. J.* **896** no. 2, (6, 2020) L19, `arXiv:2006.04918 [astro-ph.HE]`.

[101] B. Eichmann, F. Oikonomou, S. Salvatore, R.-J. Dettmar, and J. Becker Tjus, "Solving the Multimessenger Puzzle of the AGN-starburst Composite Galaxy NGC 1068," *Astrophys. J.* **939** no. 1, (2022) 43, `arXiv:2207.00102 [astro-ph.HE]`.

[102] S. Inoue, M. Cerruti, K. Murase, and R.-Y. Liu, "High-energy neutrinos and gamma rays from winds and tori in active galactic nuclei," `arXiv:2207.02097 [astro-ph.HE]`.

[103] L. A. Anchordoqui, J. F. Krizmanic, and F. W. Stecker, "High-Energy Neutrinos from NGC 1068," *PoS* **ICRC2021** (2021) 993, `arXiv:2102.12409 [astro-ph.HE]`.

[104] T. M. Yoast-Hull, J. S. G. III, E. G. Zweibel, and J. E. Everett, "Active Galactic Nuclei, Neutrinos, and Interacting Cosmic Rays in NGC 253 and NGC 1068," *Astrophys. J.* **780** (2014) 137, `arXiv:1311.5586 [astro-ph.HE]`.

[105] A. Lamastra, F. Fiore, D. Guetta, L. A. Antonelli, S. Colafrancesco, N. Menci, S. Puccetti, A. Stamerra, and L. Zappacosta, "Galactic outflow driven by the active nucleus and the origin of the gamma-ray emission in NGC 1068," *Astron. Astrophys.* **596** (2016) A68, `arXiv:1609.09664 [astro-ph.HE]`.

[106] **MAGIC** Collaboration, V. A. Acciari *et al.*, "Constraints on gamma-ray and neutrino emission from NGC 1068 with the MAGIC telescopes," *Astrophys. J.* **883** (2019) 135, `arXiv:1906.10954 [astro-ph.HE]`.

[107] A. Marinucci *et al.*, "NuSTAR catches the unveiling nucleus of NGC 1068," *Mon. Not. Roy. Astron. Soc.* **456** no. 1, (2016) L94–L98, `arXiv:1511.03503 [astro-ph.HE]`.

[108] M. A. Prieto, J. Reunanen, K. R. W. Tristram, N. Neumayer, J. A. Fernandez-Ontiveros, M. Orienti, and K. Meisenheimer, "The spectral energy distribution of the central parsecs of the nearest AGN," *Mon. Not. Roy. Astron. Soc.* **402** (2010) 724–744, `arXiv:0910.3771 [astro-ph.CO]`.

[109] **Fermi-LAT** Collaboration, M. Ajello *et al.*, "3FHL: The Third Catalog of Hard Fermi-LAT Sources," *Astrophys. J. Suppl.* **232** no. 2, (2017) 18, `arXiv:1702.00664 [astro-ph.HE]`.

[110] **Fermi-LAT** Collaboration, S. Abdollahi *et al.*, "*Fermi* Large Area Telescope Fourth Source Catalog," *Astrophys. J. Suppl.* **247** no. 1, (2020) 33, `arXiv:1902.10045 [astro-ph.HE]`.

[111] **IceCube** Collaboration, M. G. Aartsen *et al.*, "Time-Integrated Neutrino Source Searches with 10 Years of IceCube Data," *Phys. Rev. Lett.* **124** no. 5, (2020) 051103, `arXiv:1910.08488 [astro-ph.HE]`.

[112] K.-Y. Choi, E. J. Chun, and J. Kim, "Neutrino Oscillations in Dark Matter," *Phys. Dark Univ.* **30** (2020) 100606, `arXiv:1909.10478 [hep-ph]`.

[113] M. Bauer, P. Foldenauer, and J. Jaeckel, "Hunting All the Hidden Photons," *JHEP* **07** (2018) 094, `arXiv:1803.05466 [hep-ph]`.

[114] G. Steigman, B. Dasgupta, and J. F. Beacom, "Precise Relic WIMP Abundance and its Impact on Searches for Dark Matter Annihilation," *Phys. Rev. D* **86** (2012) 023506, `arXiv:1204.3622 [hep-ph]`.

[115] L. J. Hall, K. Jedamzik, J. March-Russell, and S. M. West, "Freeze-In Production of FIMP Dark Matter," *JHEP* **03** (2010) 080, `arXiv:0911.1120 [hep-ph]`.

[116] J. M. Cline, "TASI Lectures on Early Universe Cosmology: Inflation, Baryogenesis and Dark Matter," *PoS* **TASI2018** (2019) 001, `arXiv:1807.08749 [hep-ph]`.

[117] **Planck** Collaboration, N. Aghanim *et al.*, "Planck 2018 results. VI. Cosmological parameters," *Astron. Astrophys.* **641** (2020) A6, `arXiv:1807.06209 [astro-ph.CO]`. [Erratum: Astron.Astrophys. 652, C4 (2021)].

[118] X. Rodrigues, S. Garrappa, S. Gao, V. S. Paliya, A. Franckowiak, and W. Winter, "Multiwavelength and Neutrino Emission from Blazar PKS 1502 + 106," *Astrophys. J.* **912** no. 1, (2021) 54, `arXiv:2009.04026 [astro-ph.HE]`.

[119] P. Giommi, P. Padovani, F. Oikonomou, T. Glauch, S. Paiano, and E. Resconi, "3HSP J095507.9+355101: a flaring extreme blazar coincident in space and time with IceCube-200107A," *Astron. Astrophys.* **640** (2020) L4, `arXiv:2003.06405 [astro-ph.HE]`.

[120] **Fermi-LAT, ASAS-SN, IceCube** Collaboration, S. Garrappa *et al.*, "Investigation of two Fermi-LAT gamma-ray blazars coincident with high-energy neutrinos detected by IceCube," *Astrophys. J.* **880** no. 2, (2019) 880:103, `arXiv:1901.10806 [astro-ph.HE]`.

[121] M. Kadler *et al.*, "Coincidence of a high-fluence blazar outburst with a PeV-energy neutrino event," *Nature Phys.* **12** no. 8, (2016) 807–814, `arXiv:1602.02012 [astro-ph.HE]`.

[122] N. Sahakyan, P. Giommi, P. Padovani, M. Petropoulou, D. Bégué, B. Boccardi, and S. Gasparyan, "A multi-messenger study of the blazar PKS 0735+178: a new major neutrino source candidate," `arXiv:2204.05060 [astro-ph.HE]`.

[123] **IceCube** Collaboration, R. Abbasi *et al.*, "Search for Multi-flare Neutrino Emissions in 10 yr of IceCube Data from a Catalog of Sources," *Astrophys. J. Lett.* **920** no. 2, (2021) L45, `arXiv:2109.05818 [astro-ph.HE]`.

[124] P. Giommi, T. Glauch, P. Padovani, E. Resconi, A. Turcati, and Y. L. Chang, "Dissecting the regions around IceCube high-energy neutrinos: growing evidence for the blazar connection," *Mon. Not. Roy. Astron. Soc.* **497** no. 1, (2020) 865–878, `arXiv:2001.09355 [astro-ph.HE]`.

[125] A. Franckowiak *et al.*, "Patterns in the Multiwavelength Behavior of Candidate Neutrino Blazars," *Astrophys. J.* **893** no. 2, (2020) 162, `arXiv:2001.10232 [astro-ph.HE]`.

[126] A. B. Romeo and K. Fathi, "What powers the starburst activity of NGC 1068? Star-driven gravitational instabilities caught in the act," *Mon. Not.*

*Roy. Astron. Soc.* **460** no. 3, (2016) 2360–2367, arXiv:1602.03049 [astro-ph.GA].

[127] P. Padovani, F. Oikonomou, M. Petropoulou, P. Giommi, and E. Resconi, "TXS 0506+056, the first cosmic neutrino source, is not a BL Lac," *Mon. Not. Roy. Astron. Soc.* **484** no. 1, (2019) L104–L108, arXiv:1901.06998 [astro-ph.HE].

Chapter 9

# Conclusions

In this thesis, we explored some experimentally-viable extensions of the $\Lambda$CDM model, addressing various challenges in the standard cosmological picture, including inflation, baryogenesis, dark matter (DM), neutrino masses, and the core-cusp problem.

Chapter 4 introduced a scenario where the inflaton field carries baryon number and features a potential similar to the Affleck-Dine one. This setup allows the generation of a baryon asymmetry during inflation, which can persist until the present day. Notably, this model makes clear predictions for inflationary observables with just a few new input parameters. Among these predictions, a significant tensor-to-scalar ratio $r$ stands out as a testable quantity that upcoming CMB-polarization experiments, like LiteBIRD [1], could potentially measure. Contrary to initial claims, isocurvature perturbations are too small to be observable when both isocurvature observables are taken into consideration (see section 4.6).

The transfer of the baryon asymmetry from the inflaton to the SM particles is achieved by three new scalar color-charged particles, which could be observable at colliders if they are sufficiently light. If pseudo-Dirac heavy neutral leptons (HNLs) are used for this transfer instead (with the inflaton carrying lepton number now), the model naturally explains the DM nature, its abundance, and neutrino masses. This is the "little theory of everything" presented in chapter 5, which is a very minimal model in the sense that it requires only three new HNLs and a new scalar particle at low energies. Moreover, it is highly predictive providing testable signatures in laboratory experiments. Two HNLs are predicted to be unstable and highly degenerate, with a mass close to a stable third HNL acting as the DM candidate. DM in this scenario is partially asymmetric with a Dirac mass below 4.5 GeV. Additionally, a light scalar singlet, coupling with the Higgs boson and responsible for depleting the symmetric DM component, can mediate intriguing DM self-interactions, which potentially address small-scale structure problems in the ΛCDM model (see section 3.1.5). While we showed that the scalar singlet might also have explained the KOTO anomaly in certain parameter regions, it was later found that the anomaly was merely due to previously-unknown systematics (section 5.9).

Among the small-scale structure problems, the most well-known one is the core-cusp problem. While the standard new-physics explanation involves self-interacting DM (SIDM) with elastic scattering to erase cusps, we proposed an alternative solution in chapter 6: strong DM annihilation can also lead to the formation of cored profiles. However, DM annihilation, especially with large cross sections, typically poses a problem as it depletes the DM abundance, which is tightly constrained by observations between the cosmic microwave background (CMB) era and the epoch of structure formation. We found a way to overcome this issue by considering asymmetric DM with a small Majorana mass. In this scenario, strong annihilations freeze out early in the cosmic history, effectively resolving the problem of removing the symmetric ADM relic density. Furthermore, these annihilations can be reactivated at later times during structure formation. It is important to note that this mechanism, like elastic SIDM, can not address the diversity of DM halo profiles on all scales in its simplest form. To achieve this, a combination of a scalar and vector light mediators is likely required, contrary to what occurs in elastic SIDM where a rather fine-tuned velocity-dependent scattering cross section is invoked.

Regarding the models presented in chapters 4, 5 and 6, certain simplifications were made to facilitate the analysis. For instance, in the Affleck-Dine inflationary model, we considered the simplest scenario of perturbative reheating and neglected any direct coupling between the inflaton and the Higgs field. Relaxing the former assumption could lead to a larger coupling between the inflaton and the color-charged scalars, potentially affecting reheating efficiency through parametric resonance. Additionally, allowing direct inflaton decay into Standard Model (SM) particles through the Higgs portal might impact the baryon asymmetry if $CP$-violating decays occur in the Higgs sector [2, 3].

Furthermore, in the "little theory of everything" we assumed one of the SM neutrinos to be exactly massless to ensure the stability of the DM candidate. However, this perfect DM stability is not strictly required to remain consistent with cosmological observables (see *e.g.* Refs. [4, 5]). The effects discussed in chapter 6 at galactic scales may be applicable to a generalized version of the "little theory of everything", where a small Majorana mass for DM particles is allowed. Though the mass ranges for DM and the mediator responsible for annihilation differ slightly between the two scenarios, as presented in chapters 5 and 6, further analysis is needed to draw definitive conclusions, which we plan for future studies.

The conclusions derived in chapter 6 for the oscillating asymmetric dark matter (ADM) model are also limited, and a more comprehensive analysis with both scalar and vector mediators should be undertaken. Additionally, we focused on model parameter regions where DM scattering was negligible compared to annihilation. Allowing both DM channels to be important might significantly alter our conclusions, potentially requiring just one particle to mediate both processes and relaxing the fine-tuned value of the Majorana mass of the DM particles. This is an intriguing avenue which we think is worth exploring in the future because it contains all the characteristics that a generic DM model could have: annihilation and scattering.

Shifting focus to chapters 7 and 8, we demonstrated that active galactic nuclei (AGNs) serve as powerful probes of DM interactions with SM particles, particularly with neutrinos (for the case with other SM particles, see Refs. [6–9]). DM accretes onto black holes similarly to visible matter, forming over time a DM overdensity in the central region known as a spike. Therefore particles produced in the AGN jet or in the corona have to travel through this DM spike before being able to reach Earth and likely be detected. The latter could be hampered if there exists a non-negligible interaction between DM and the particles produced by the AGN. The detection of neutrinos from the blazar TXS 0506+056 and the radio galaxy NGC 1068 by IceCube enabled us to set strong limits on DM-neutrino scattering in a model-independent manner, relying solely on an energy-dependence assumption for the cross section.

AGNs, as the most powerful sources of high-energy neutrinos [10], offer an excellent opportunity to explore DM interactions in an energy regime almost unexplored, because of the lack of high-energy physics processes where both neutrinos and DM are involved. Neutrino observations from a larger AGN population in the future could tightly constrain DM scatterings with SM particles at energies ranging from TeV to PeV, potentially excluding significant portions of the dark-sector parameter space.

However, the results from chapters 7 and 8 are subject to uncertainties arising from our limited understanding of the extreme AGN environment. For instance, the density profile of the DM spike, $\rho \propto r^{-\alpha}$, depends on whether baryons play a role in DM accretion onto the central black hole, leading to different exponents $\alpha \simeq 1.5-2.3$. Additionally, DM annihilation can alter the spike shape, significantly affecting the derived DM-neutrino bounds.

On the astrophysical side, the aforementioned bounds depend on the location of the neutrino emitting region within AGNs, which remains largely unknown. This uncertainty in the location is especially relevant for blazars, where neutrinos are believed to be produced within the relativistic jet, extending to distances $\sim 10^{11}$ km from the central engine. In contrast, neutrino emission from radio galaxies arises in the corona, which is a region roughly two orders of magnitude smaller than the size of the jet. Moreover, the initial neutrino spectrum emitted from the source, before being affected by DM scattering, is not directly observable and relies on simulations with many free parameters. These parameters are inferred by fitting the model to the electromagnetic spectrum (SED) observed from AGNs. The lack of experimental data in certain energy ranges, like X-rays and MeV $\gamma$-rays, makes it challenging to determine the correct normalization of the neutrino spectrum [11]. The situation is even more complicated when DM interactions are included. The introduction of new DM parameters can become degenerate with those controlling neutrino emission [11], requiring a direct integration of DM interactions in AGN modeling for reliable constraints on neutrino secret interactions, such as those involving DM [12]. This challenging task will be the focus of future studies.

Overall, this thesis presents a collection of innovative ideas aimed at overcoming the limitations encountered by the standard cosmological model and the SM of particle physics when confronted with experimental observations. The research presented here opens up exciting avenues for further exploration, and there is no boundary to our capacity for imagination when it comes to uncovering the mysteries of the Universe. The quest to deepen our understanding of fundamental physics and cosmology continues, and I am grateful to have been part of this journey.

# Bibliography


[1] **LiteBIRD** Collaboration, E. Allys *et al.*, "Probing Cosmic Inflation with the LiteBIRD Cosmic Microwave Background Polarization Survey," *PTEP* **2023** no. 4, (2023) 042F01, `arXiv:2202.02773 [astro-ph.IM]`.

[2] A. Mendez and A. Pomarol, "Signals of CP violation in the Higgs sector," *Phys. Lett. B* **272** (1991) 313–318.

[3] Y. Chen, A. Falkowski, I. Low, and R. Vega-Morales, "New Observables for CP Violation in Higgs Decays," *Phys. Rev. D* **90** no. 11, (2014) 113006, `arXiv:1405.6723 [hep-ph]`.

[4] S. De Lope Amigo, W. M.-Y. Cheung, Z. Huang, and S.-P. Ng, "Cosmological Constraints on Decaying Dark Matter," *JCAP* **06** (2009) 005, `arXiv:0812.4016 [hep-ph]`.

[5] S. J. Clark, K. Vattis, and S. M. Koushiappas, "Cosmological constraints on late-universe decaying dark matter as a solution to the $H_0$ tension," *Phys. Rev. D* **103** no. 4, (2021) 043014, `arXiv:2006.03678 [astro-ph.CO]`.

[6] J.-W. Wang, A. Granelli, and P. Ullio, "Direct Detection Constraints on

Blazar-Boosted Dark Matter," *Phys. Rev. Lett.* **128** no. 22, (2022) 221104, `arXiv:2111.13644 [astro-ph.HE]`.

[7] A. Granelli, P. Ullio, and J.-W. Wang, "Blazar-boosted dark matter at Super-Kamiokande," *JCAP* **07** no. 07, (2022) 013, `arXiv:2202.07598 [astro-ph.HE]`.

[8] F. Ferrer, G. Herrera, and A. Ibarra, "New constraints on the dark matter-neutrino and dark matter-photon scattering cross sections from TXS 0506+056," *JCAP* **05** (2023) 057, `arXiv:2209.06339 [hep-ph]`.

[9] G. Herrera and K. Murase, "Probing Light Dark Matter through Cosmic-Ray Cooling in Active Galactic Nuclei," `arXiv:2307.09460 [hep-ph]`.

[10] K. Murase, *Active Galactic Nuclei as High-Energy Neutrino Sources*, pp. 15–31. 2017. `arXiv:1511.01590 [astro-ph.HE]`.

[11] K. Murase, 2023. private communication.

[12] K. Ioka and K. Murase, "IceCube PeV–EeV neutrinos and secret interactions of neutrinos," *PTEP* **2014** no. 6, (2014) 061E01, `arXiv:1404.2279 [astro-ph.HE]`.